

目 录

一、教研业绩

1. 教学研究项目

- 1.1 华南农业大学广州合成材料研究院有限公司大学生社会实践教学基地（省级大学生实践教学基地）1
- 1.2 智慧植保导向下的精准农业人才培养体系构建（广东省质量工程项目）..16
- 1.3 化学类一流本科专业科技创新-毕业论文-实习-就业“四位一体化”教学改革与实践（广东省教育教学研究和改革项目）22

2. 编写教材

- 2.1 物理化学（ISBN：978-7-5655-2890-3）46

二、科研项目

1. 主持

- 1.1 向香蕉球茎积累的纳米咯菌腈递送载体构建及靶向传导机制（国家自然科学基金项目，32572864）有关佐证材料.....57
- 1.2 γ -氨基丁酸介导纳米咯菌腈对香蕉枯萎病的靶向治疗（广东省基础与应用基础研究基金，2023A1515010609）有关佐证材料.....59
- 1.3 广东省农业纳米共性关键技术研发创新团队专题专家（广东省农业农村厅，2019KJ140）有关佐证材料.....65
- 1.4 高效纳米农药的控释材料研发(广东省科学技术厅，2023B0202080001-1-5)有关佐证材料.....75
- 1.5 纳米导向农药的减施增效技术集成与应用（国家科学技术部，2018YFD020030401）有关佐证材料.....79
- 1.6 L-半胱氨酸介导鱼藤酮的输机理及可视化研究（广东省教育厅，4900-215100）有关佐证材料.....84
- 1.7 香蕉绿色生产关键技术集成应用与示范（横向项目，xh20250518）有关佐证材料.....87
- 1.8 高效纳米农药对作物隐蔽性病虫害的靶向防控（绿色农药全国重点实验室，GPLSCAU202407）有关佐证材料.....91

2. 主要参加

2.1 东莞市植物重大及入侵害虫绿色监测防控技术推广示范应用（广东省农业 厅，441900230000000001952）有关佐证材料.....	103
---	-----

三、论文、著作等

1. 检索证明.....	110
2. 以第一作者发表本专业论文情况	
2.1 Uptake and imaging of glycine functionalized gold nanoclusters in <i>Spodoptera frugiperda</i> (Sf9) cells (Journal of Cluster Science, 2021)	116
2.2 Enhanced intracellular uptake in vitro by glucose-functionalized nanopesticides (New Journal of Chemistry, 2017)	125
2.3 Preparation, characterization and intracellular imaging of 2,4-dichlorop- henoxya-cetic acid conjugated gold nanorods (Journal of Nanoscience and Nanotechnology, 2016)	132
2.4 Biosynthesis of silver and gold nanoparticles using Huangdan (<i>Camellia sinensis</i>) leaf extract (Synthesis and Reactivity in Inorganic Metal-organic and Nano-metal Chemistry, 2015)	139
2.5 Biosynthesis of gold nanoparticles using novel Bamboo (<i>Bambusa chungii</i>) leaf extracts (Journal of Nanoscience and Nanotechnology, 2015)	146
3. 以通讯作者发表本专业论文情况	
3.1 Gaba-decorated nanocarrier for smart delivery of fludioxonil for targeted control of banana wilt disease (Journal of Agricultural and Food Chemistry, 2024)	150
3.2 Optimized nanopesticide delivery of thiamethoxam to cowpeas (<i>Vigna unguiculata</i>) controls thrips (<i>Megalurothrips usitatus</i>) and reduces toxicity to non-target worker bees (<i>Apis mellifera</i>) (Science of the Total Environment, 2024).....	163
3.3 A Pyr-loaded polymer microparticle for effectively controlling <i>Solenopsis invicta</i> (Hymenoptera: Formicidae) in the nest (Colloids and Surfaces B: Biointerfaces, 2024)	177
3.4 ConA-loaded PEGylated graphene oxide for targeted nanopesticide carriers	

against <i>magnaporthe oryzae</i> (ACS Applied Nano Materials, 2023)	187
3.5 Enzyme-responsive lignin nanocarriers for triggered delivery of abamectin to control plant root-knot nematodes (<i>Meloidogyne incognita</i>) (Journal of Agricultural and Food Chemistry, 2023)	198
3.6 Targeted delivery of emamectin benzoate by functionalized polysuccinimide nanoparticles for the flowering cabbage and controlling <i>Plutella xylostella</i> (Pest Management Science, 2022)	208
3.7 Graphene oxide as a pesticide carrier for enhancing fungicide activity against <i>Magnaporthe oryzae</i> (New Journal of Chemistry, 2021)	220
3.8 Phloem delivery of fludioxonil by plant amino acid transporter-mediated polysuccinimide nanocarriers for controlling fusarium wilt in banana (Journal of Agricultural and Food Chemistry, 2021)	230
3.9 Long-lasting repellent activities of eco-friendly polyurethane system for controlled citral against melon fly (Crop Protection, 2021)	241
3.10 Development of multifunctional avermectin poly(succinimide) nanoparticles to improve bioactivity and transportation in rice (Journal of Agricultural and Food Chemistry, 2018)	251
3.11 A novel water-based chitosan-La pesticide nanocarrier enhancing defense responses in rice (<i>Oryza sativa L</i>) growth (Carbohydrate Polymers, 2018)	261
3.12 Chitosan-based nanoparticles of avermectin to control pine wood nematodes (International Journal of Biological Macromolecules, 2018)	269
3.13 高效输导咯菌腈纳米杀菌剂的制备及其性能研究 (仲恺农业工程学院学报, 2024)	275

四、科研成果

1. 知识产权

1.1 专利授权证书：一种酶响应纳米农药及制备方法与应用（专利号：202211160312X）.....	281
1.2 专利授权证书：一种植物韧皮部输导的纳米农药的制备方法及应用202010455763.0）	283

五、其他业绩

1. 指导学生学科竞赛

1.1 指导学生参加学科竞赛（广东省第十二届大学生材料创新大赛总决赛 三等奖，2023）.....285

1.2 指导学生参加学科竞赛（广东省第十二届大学生材料创新大赛分赛区 三等奖，2023）.....286

1.3 指导学生参加学科竞赛（广东省第十届大学生材料创新大赛总决赛 三等奖，2020）.....287

1.4 指导学生参加学科竞赛（广东省第十届大学生材料创新大赛分赛区三等奖，2020）.....288

2. 年度考核结果

2.1 2018 和 2022 年度考核结果（优秀）.....289

广东省本科高校大学生实践教学基地

建设任务书



学校名称：

基地名称：华南农业大学广州合成材料研究院
有限公司大学生实践教学基地

基地负责人：

张声森

主要面向专业：

材料化学、材料科学与工程、
应用化学

依托单位：

广州合成材料研究院有限公司

所属行业：

研究和技术服务业

填表日期：

2025 年 10 月 14 日

广东省教育厅 制

填写说明

一、本项目申报须附学校与基地依托单位正式签订的《合作培养协议书》，作为申报支撑材料；

二、申报表中各项内容用“小四”号仿宋体填写。

三、有可能涉密和不宜大范围公开的内容不可作为申报内容填写。

四、如表格篇幅不够，可以自行调整，但页码须保持清晰。

五、请在本任务书第3页（空白）处补充任务书目录。

六、著作、教材、论文须已刊登在正式期刊上或为正式出版物，截止时间为申报当年9月30日。

建设任务书目录¹

一、基本情况	3
二、运行情况	6
2-1. 基地发展历程及现有合作基础	6
2-2. 基地立项成为省级基地的必要性	7
三、建设目标、内容和计划	7
3-1. 基地主要建设目标	7
3-2. 建设内容与计划	8
四、基地建设支持保障措施	9
4-1. 基地管理运行体系	9
4-2. 基地师资队伍	10
4-3. 基地建设投入	10
五、预期建设成果和推广共享计划	11
5-1. 预期建设成果	11
5-2. 成果推广共享计划	11
六、建设经费预算	13
七、学校意见	14

¹ 目录请根据任务书填写情况进行编辑，注明纲目及对应页码。

一、基本情况

社会实践基地名称		华南农业大学广州合成材料研究院有限公司大学生实践教学基地						
基地依托单位		广州合成材料研究院有限公司						
基地依托单位地址		广州市天河区车陂西路 396 号			基地建立时间		2015 年	
基地所面向的主要专业		材料化学、材料科学与工程、应用化学			年接待实践学生人数		60	
是否签订正式合作协议		是		协议签订时间	2024 年		协议年限	4 年
基地依托单位基本情况		法人代表	戚建强			联系人		李欣
		联系人电话	1353521323			联系人所在部门及职务		材料检测事业部总经理助理
		单位性质	国有企业			主管部门		中国中化控股有限责任公司
基地负责人	姓名	张声森	性别	男	出生年月	1978.9	民族	汉
	单位、职务	材料与能源学院、工会主席	专业技术职务	教授	学历/学位	研究生/博士	毕业院校	华南理工大学
	电子邮箱	zhangss@scau.edu.cn				联系电话	13622886156	
	教学工作经历	<p>(1) 2014 年起在华南农业大学工作，先后在理学院应用化学系和材料与能源学院材料化学系担任专业教师，主讲《无机及分析化学》和《分析化学》等本科生课程。</p> <p>(2) 2015 年起负责材料与能源学院材料化学专业的教学实习基地建设和教学工作，建成 3 个校级教学实践基地（含华南农业大学广州合成材料研究院有限公司校级实习基地（附件 2））和 10 个院级教学实习基地。</p>						

教学工作经历	<p>(3) 2019 年至 2024 年担任材料与能源学院材料化学系系主任，主持系的全面行政管理工作，具体包括人才培养、科学研究、师资建设、社会服务和国际化建设等工作。</p> <p>(4) 每年指导硕士研究生完成毕业论文 2-4 名，指导本科生完成毕业论文 4-5 名。</p> <p>(5) 以第一作者身份在中文核心期刊上发表教学改革类论文 2 篇，在普通刊物上发表论文 3 篇。(附件 3)</p> <p>(6) 指导本科生以第一作者身份发表 4 篇 SCI 收录的科研论文。(附件 4)</p> <p>(7) 2020 年，获华南农业大学“丁颖杯”与“挑战杯”广东赛区优秀指导教师奖。(附件 5)</p> <p>(8) 2020 年，指导本科生方玉璇等申请的项目“丝网型 TiO_2 纳米管阵列的制备及其光催化降解甲醛气体的研究”获国家级立项，并入选第十三届全国大学生创新创业年会。(附件 6)</p> <p>(9) 2020 年，获得华南农业大学材料与能源学院教学效果优秀一等奖。(附件 7)</p> <p>(10) 2020 年，指导本科生方玉璇等获得广东省大学生材料创新大赛无机非金属材料分赛区二等奖(附件 8)</p> <p>(11) 2021 年，主持广东省教育研究与改革项目，题为“化学类一流本科专业科技创新-毕业论文-实习-就业‘四位一体化’教学改革与实践”，并已按时完成结题。(附件 9)</p> <p>(12) 2021 年，指导的本科生方玉璇的毕业论文获评全国能源动力类专业百篇优秀毕业论文。(附件 10)</p> <p>(13) 2022 年，指导的硕士研究生许传毅同学荣获国家级奖学金。(附件 11)</p> <p>(14) 2023 年，指导本科生何咏然等人申请的“可见光驱动 $\text{Co}_3\text{O}_4/\text{BiOBr}-\text{Pt}$ 异质结催化剂净化有机磷农药废水”项目获大学生创新创业训练计划省级立项。(附件 12)</p> <p>(15) 2023 年，指导本科生骆依文等人申请的“改性碳基催化剂活化过硫酸盐降解有机污染物的研究”项目获大学生创新创业训练计划省级立项。(附件 13)</p> <p>(16) 2023 年，指导的硕士研究生许传毅获得华南农业大学优秀毕业生荣誉称号。(附件 14)</p> <p>(17) 2024 年，指导本科生李佳鑫等人申请的“NiO_x/C 光热助催化剂的构建及其光催化活化过硫酸盐净化垃圾渗滤液研究”项目获大学生创新创业训练计划国家级立项。(附件 15)</p>
--------	---

教学工作经历	(18) 2024 年，指导的硕士研究生唐城阳同学荣获国家级奖学金。(附件 16)
在基地建设中的主要职责	<p>基地负责人张声森曾主持建设 3 个校级实践教学基地——华南农业大学广州合成材料研究院有限公司、广州飞胜智能科技股份有限公司、广州美维电子有限公司，以及十余个材料与能源学院院级实习基地。所建基地多次考核优秀，获评示范基地，为新基地的建设与运行积累了丰富经验。</p> <p>1. 构建校企实践导师团队。联合材料化学、材料科学与工程、应用化学等相关专业理论教师、实践课教师，以及企业导师共同组建一支专业互补、老中青结合的实践教学团队。制定师资队伍培养制度，指导青年教师深入企业实践锻炼，打造职业道德规范、技能娴熟、善于沟通、责任心强的新农科高质量实践导师队伍。</p> <p>2. 制订校外实践计划。结合课程大纲和企业生产实际，与导师团队制定详实的实践计划（含实践目的、内容、时间安排等），完善协同考评制度（含出勤率、过程考核、结果考核等），形成实践教学与课堂教学互融互促的局面，实现“理论教学、实践教学、人才培养”融合渗透，提升人才培养质量。</p> <p>3. 指导实习实践活动。根据既定实践教学任务，及时联系校企导师，指导学生实践，关注学生实习实训期间的思想动态、心理状况、实习进度和生活环境，解答学生实践中的疑问，确保实习实践活动顺利完成。</p> <p>4. 评估和总结实践成果。实践结束后，认真组织实习汇报、批改实习报告，收集学生实习反馈意见，评估学生实践中的表现和收获。同时加强与基地沟通，收集双方导师对实践教学工作的建议，整理撰写总结报告，为后续实践教学提供参考借鉴。</p> <div data-bbox="699 1429 1145 1865"></div> <p>图 1 基地负责人在基地建设中的主要职责</p>

二、运行情况

2-1. 基地发展历程及现有合作基础（介绍自基地合作协议签署以来基地的建设发展情况、实践教学基础条件、现行合作机制及主要合作成果，800 字以内）

（一）基地建设发展情况

华南农业大学材料与能源学院与广州合成材料研究院有限公司（以下简称“广州合材”）自 2015 年建立院级实习基地以来，校企合作不断深化。2019 年，实习基地升级为校级实习基地，标志着双方合作进入新阶段。2024 年，双方续签校级实习基地协议，合作期限延长至 2028 年，进一步巩固了长期稳定的合作关系。

在近十年的合作期间，实习基地始终为学院学生提供了高质量的实践平台。2015 年至 2019 年，广州合材每年平均接纳约 60 名毕业生进行实习（附件 17）；受疫情影响，2020-2023 年暂停集中实习；2024 年，实习项目得以恢复，共接纳 62 名毕业实习生，继续保持了稳定的培养规模。此外，该基地于 2020 年被评为“优秀校级实习基地”（附件 18），并在 2024 年通过评估，再次获评“合格校级实习基地”（附件 19），充分体现了其实习基地建设的规范性与可持续性。

（二）实践教学基础条件

广州合材隶属于中国中化控股有限责任公司，是一家专注于化工新材料研究开发、检测评估及整体解决方案的国有企业。为高新技术企业、广东省标准领军企业和国家级中小企业公共服务示范平台（附件 20）。公司技术实力雄厚，汇聚大量高素质专业人才，其中中高级职称人员占比达 50%。在材料老化研究领域，公司积累了超过 50 年的专业数据，形成了深厚的技术沉淀。近三年，公司在石油化工领域的卓越贡献，并获得多项奖项（附件 21），包括科技进步奖（2022）、全国优秀标准项目（2023）、期刊百强（2023）、省级优秀科技期刊（2024）和中石油优秀标准奖（2024）。公司建有先进的研发平台和完善的生产设施，拥有 60 余间功能实验室，总面积 12000 平方米，配备 300 多台高精度实验检测仪器，价值 5000 多万元。广州合材为学生提供丰富的实践机会，涵盖高分子材料的合成、性能测试、产品开发及产业化应用等多个环节，并安排经验丰富的技术骨干担任实习指导教师，提供专业化实训指导。

（三）现行合作机制

双导师制：2021 年，广州合材副院长杨育农受聘为我院校外指导教师，2024 年增聘谢宇芳副总经理为校外指导教师，进一步强化了校企联合培养机制。（附件 22）

学术交流与思想教育：2021 年，杨育农副院长来校为材料化学专业新生作专题报告《正确的世界观与高分子材料》，深化了学生对行业的认知。（附件 23）

动态评估与优化：学院与企业定期对实习效果进行评估，根据反馈调整培养方案，确保实习质量。

（四）主要合作成果和产生的成效

- 1) **人才培养成效显著：**2015-2024 年累计培养实习生 400 余人，2024 年接纳 62 人，部分毕业生成为企业技术骨干。

- 2) **校企资源共享**：学院借助企业资源优化实践课程设计，企业通过学生实习发掘优秀人才，实现双赢。
- 3) **社会影响力提升**：基地的持续建设为同类院校的校企合作提供了示范，增强了学校在材料领域的产学研结合能力。
- 4) **基地荣誉**：2020 年、2024 年分获“优秀”和“合格”校级实习基地称号（附件 18-19）。未来，双方将继续深化合作，拓展科研项目联合攻关、共建实验室等新模式，进一步提升实习基地的育人水平和社会服务能力。

2-2. 基地立项成为省级基地的必要性（500 字以内）

（一）提升人才培养质量，服务区域产业发展

广东省是我国新材料产业的重要基地，对高分子材料、能源材料、材料老化研究等领域的高素质应用型人才需求旺盛。华南农业大学材料与能源学院与广州合材的实习基地已具备扎实的合作基础，若升级为省级基地，可进一步优化实践教学体系，培养更符合行业需求的高水平人才，助力粤港澳大湾区新材料产业高质量发展。

（二）深化产学研协同，促进科技成果转化

广州合材在合成材料研发领域具有显著技术优势，而学院在新能源材料、高分子改性等方面具备科研实力。省级基地的设立将推动校企联合攻关，加速实验室成果向产业化应用转化，提升广东新材料产业的创新竞争力。

（三）优化资源共享，发挥示范引领作用

目前该基地已形成稳定的校企协同育人机制，并获评校级优秀实习基地。升级为省级基地后，可争取更多政策与资金支持，完善实训平台建设，同时为省内高校提供可复制的校企合作模式，推动全省应用型人才培养水平的整体提升。

（四）增强学生就业竞争力，拓宽职业发展渠道

省级基地的认定将进一步提升实习的规范性和含金量，使学生获得更系统的工程实践训练，提高就业竞争力。此外，基地可依托省级平台与更多企业建立合作网络，为学生提供更广阔的就业和发展机会。

综上，将该实习基地立项为省级基地，既是深化产教融合、服务区域经济的必然要求，也是提升人才培养质量、增强学科影响力的重要举措，具有显著的现实意义和发展价值。

三、建设目标、内容和计划

3-1. 基地主要建设目标（包括人才培养目标和社会服务目标两个方面，300 字以内）

（一）人才培养目标

- 1) 构建“产学研用”一体化实践教学体系，培养具有扎实理论基础、突出工程实践能力和创新精神的新材料领域高素质应用型人才。
- 2) 通过“双导师制”联合培养模式，强化学生的专业技能和职业素养，培养质量进一

步提升。推动学生就业对口率提升至 85%以上，力争孵化省级以上创新创业项目 2-3 项/年。

3) 通过“双导师制”联合培养模式，强化学生的专业技能和职业素养，培养质量进一步提升。推动学生就业对口率提升至 85%以上，力争孵化省级以上创新创业项目 2-3 项/年。

4) 建立阶梯式实践能力培养方案，使学生在材料研发、性能测试、生产工艺等环节获得系统训练。

将德育（职业伦理教育）、智育（专业技术实践）、美育（材料设计美学）、体育（实验室安全训练）、劳育（生产一线操作）贯穿实践全过程，培养德才兼备的高素质应用型人才。

（二）社会服务目标

1) 打造区域性新材料人才培养高地，为粤港澳大湾区新材料产业输送专业技术人才。

2) 推动校企协同创新，每年开展 2-3 项联合技术攻关，促进科研成果转化。

3) 发挥示范辐射作用，为省内 1-2 所高校提供可复制的校企协同育人模式，服务地方经济社会发展。



图 2 基地主要建设目标

3-2. 建设内容与计划（包括实践教学课程体系建设以及实现建设目标所采取的建设举措、建设步骤安排等，重点说明如何依托基地更好实施实践教学及实现德育、美育、劳动教育与专业教育相统一，800 字以内）

依托广州合成材料研究院有限公司雄厚的科研实力和完善的产业平台，结合华南农业大学材料与能源学院材料化学、材料科学与工程、应用化学等专业的教学需求，基地将围绕“以实践促专业，以劳动铸品格”的理念，打造产学研用融合的实践教学体系。

（一）实践教学课程体系建设

将与学院联合构建“实验基础—工程实训—企业课题—科研创新”四层次实践课程体系。设置与企业技术紧密对接的模块内容，如高分子合成与改性、结构材料性能分析、新材料制备工艺等，与《高分子化学》《材料分析测试》《精细化工合成》等核心课程联动，构建课内外、校内外一体化的教学链条。探索“订单式实习”和“项目式训练”结合模式，提升学生实践解决问题能力。

（二）建设举措与步骤安排

- 1) 第一阶段（2025.10-2026.09）：完成基地管理制度建设与实践教学大纲修订；遴选首批企业导师并开展师资培训；组织小批量学生进行试点实习，验证课程匹配度和实施效果。
- 2) 第二阶段（2026.10-2027.09）：正式批量化组织学生进入基地实习实训，稳定每年60-100人次规模；设立“本科毕业实习工作站”与“创新创业训练平台”，推动课题、竞赛、论文一体联动。
- 3) 第三阶段（2027.10-2028.09）：拓展多元协同机制，推动与企业共建联合实验室、研究平台；建设线上实习资源库，实现“校外基地+云课堂”双平台支撑；持续迭代教学内容、成果评估机制与师生双向交流通道。

（三）教育融合内容落实

- 1) **德育**：依托杨育农副院长、谢宇芳副总经理等企业导师资源，以专题讲座、职业访谈形式，引导学生树立正确价值观、职业观。
- 2) **美育**：结合材料设计与产品美学，引导学生参与“材料与生活美学”创新训练项目，提升综合素养。
- 3) **劳动教育**：通过参与企业实际生产、样品测试与工艺操作，强化学生工程实践能力与敬业精神，实现“知行合一、德技双修”。

通过本大学生社会实践基地的建设，将实现理论教学与产业需求深度融合，为学生成长成才与地方产业高质量发展提供坚实支撑。



图3 基地主要建设内容与计划

四、基地建设支持保障措施

4-1. 基地管理运行体系（重点说明学校与合作单位如何协作，以高效完成实践教学任务，确保基地平稳运行，500字以内）

为确保实践教学基地高效、规范、可持续运行，华南农业大学材料与能源学院与广州合成材料研究院有限公司建立了“校企协同、分工明确、动态调整”的运行管理机制。

- 1) **建立联席协调机制。**由学院分管教学副院长牵头，联合基地负责人组成“实践教学基地管理小组”，定期召开联席会议，协调实习安排、课程衔接、实训内容优化等事务，保障教学与产业实际有效对接。
- 2) **实行双重管理模式。**学院指派实践教学负责人统筹学生选派、安全教育、学业评估等工作；企业指定专人担任基地联系人，负责学生实训安排、现场指导与日常管理，确保实习期间教学活动有序开展。
- 3) **完善规章制度建设。**双方共同制定《基地学生实习管理办法》《安全操作规范》《企业导师职责制度》等，明确各方职责、流程及安全规范，做到有章可循、管理闭环。
- 4) **推进信息化管理。**依托校内实践教学管理系统，实时记录学生实习动态与导师反馈，确保实践过程可监控、可评估、可追溯，提升管理效率与透明度。
- 5) **建立多元评价机制。**实习结束后，学生、企业导师与校内指导教师三方共同参与评价，涵盖技能掌握、职业素养、安全规范等维度，推动实践质量持续改进。

通过上述协同管理体系建设，基地实现了资源互补、职责清晰、运行高效的目标，为实践教学任务的高质量完成提供坚实保障。

4-2. 基地师资队伍（重点说明基地共建各方参与师资队伍建设情况及师资队伍如何实现对基地实践教学的支撑和保障，500 字以内）

本大学生社会实践教学基地由校企双方共同组建高水平、结构合理的师资队伍，形成“专业教师+行业专家”协同育人的指导体系，为实践教学提供坚实支撑。

校内师资队伍主要由华南农业大学材料与能源学院承担，由张声森教授担任基地负责人，长期从事材料化学实践教学与基地建设工作。团队成员包括贾金亮副教授、雷炳富教授、杨卓鸿教授、杨宇副教授、蔡欣副教授、高琼芝副教授、杨思源副教授等，涵盖材料化学、应用化学、材料物理与性能测试等多个方向，具备丰富的教学与科研经验，能够全面支撑相关专业的实习指导、课程设计及课题培训工作。

校外师资队伍由广州合成材料研究院有限公司提供，现有指导教师 11 人，包括教授级高级工程师 3 人、高级工程师 8 人，具有硕博学历的占 64%，专业覆盖高分子化学与物理、材料学、化学工程与技术、有机化工等核心方向（附件 24）。主要成员包括李欣、彭军、覃红阳、冯志新、吴舜娟、王瑞萍等，长期从事高分子材料老化、性能评价与工程应用研究，具备扎实的工程背景和项目实战经验。

此外，企业副总经理谢宇芳和副院长杨育农已先后受聘为校外指导教师，积极参与学生思想引导与职业生涯教育。

校企联合实施“双导师制”，通过导师协同制定实习方案、全过程跟进指导、共同参与教学评估，确保学生在知识应用、技能提升、职业素养等方面获得全方位培养。

4-3. 基地建设投入（重点说明基地共建各方对基地的人力、物力、财力等投入情况，500 字以内）

为保障实践教学基地的持续运行与高质量发展，华南农业大学材料与能源学院与广州

合成材料研究院有限公司在基地建设中实行共建共管、资源共享，并协同投入人力、物力与财力。

- 1) **在人力投入方面**，学院配备专职教师团队由张声森教授牵头，组织开展实践教学设计、实习组织与学生指导等工作。企业方面，广州合材遴选 12 名资深工程技术人员担任指导教师，建立了以教授级高工、高级工程师为主的指导团队，并指定专人负责与学院的对接与学生管理，形成完整的教学组织体系。
- 2) **在物力投入方面**，广州合材向学生开放多个核心实验平台与中试设备，包括材料合成、老化试验、性能测试等实验场所，为专业实训和科研训练提供完备条件；学院也同步提供相关课程教学仪器、教学资料与在线教学平台资源，实现教学资源协同使用与内容共享。
- 3) **在财力投入方面**，学院每年按比例安排专项实践教学经费用于师资交通、保险保障、教材印刷、管理运行等基本支出；企业承担学生实习期间安全保障、现场培训和耗材费用，并资助院方老师指导费、交通费、保险费及优秀奖励 1 万元/年。此外，企业对学生提供资助，本科生 1000 元/月，研究生 1500 元/月，确保实习活动顺利进行。

未来，双方还将联合申报省级实践教学项目和产教融合资金，加大投入力度，推动建设升级为区域示范性实践基地，持续提升服务专业教育和区域产业的能力。

五、预期建设成果和推广共享计划

5-1. 预期建设成果(包括但不限于人才培养、软硬件建设及服务社会等方面，要求成果具体、明确、可测，300 字以内)

本基地建设完成后，预计在以下方面取得显著成果：

- 1) 通过大学生社会实践教学基地的建设，强化本科生专业知识与工程技能训练，实习结束后学生能通过实践考核与综合评价，合格率达 95%以上。
- 2) 总结基地建设教学改革经验，计划发表教改论文 1 篇，共享经验。
- 3) 组织学生满意度调查，基地综合满意度平均分达 8 分以上（满分 10 分）。
- 4) 指导学生参与企业科研课题，联合撰写科研论文 1 篇以上，联合申请专利 1 项以上，提升学生创新实践能力。
- 5) 实习学生能掌握主要生产工艺流程及质量控制关键点，部分学生进入基地企业就业或被纳入“优秀实习生人才库”。
- 6) 提供行业培训与技术服务，服务粤港澳大湾区新材料产业发展，逐步建设为区域性协同育人和技术支持中心。

5-2. 成果推广共享计划（包括采取何种手段、途径，面向哪些对象或学校进行共享推广以及预计起到何种作用，300 字以内）

本基地将通过多渠道、多形式推动建设成果的共享与推广，提升示范效应。

- 1) 依托华南农业大学本科教育教学改革平台和学院官网，定期发布基地建设动态、教

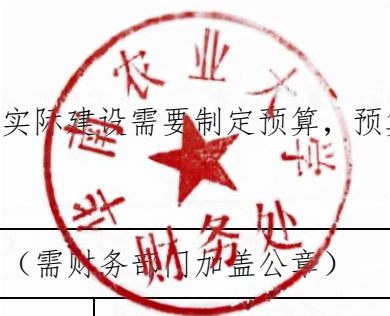
学成果与学生实习案例，供校内外借鉴。

- 2) 以基地为依托，接收周边高校材料、化学类专业学生联合实习与短期访学，扩大资源共享范围。
- 3) 通过发表教学改革论文、案例教材建设等形式，总结可复制、可推广的实践教学经验，面向全省推广应用。
- 4) 研究成果通过研究论文发表和专利申请等途径向社会进行推广。

通过以上措施，基地将辐射带动粤港澳大湾区高校协同育人水平提升，助力区域材料产业和高素质技术人才培养体系建设。

六、建设经费预算

(根据项目获得省级立项后实际建设需要制定预算，预算要经学校财务部门审核批准)



预算经费总额	10（万元）（需财务部门加盖公章）	
科目名称	预算额	项目支出用途
出版/文献/信息传播/知识产权事务费	2.00	出版/文献/信息传播/知识产权事务费等
咨询费	1.00	指在基地建设过程中支付咨询专家的费用
设备费及材料费	4.00	项目实施过程中加工设备更新以及茶叶材料费等
差旅费	3.00	往返基地交通费，开展实践教学研讨、调研发生的会议费差旅费等

七、学校意见

学校保证给予该项目建设(研究)所需的各项条件,包括足额的经费支持,并严格遵守省教育厅项目管理规定,督促和保障项目顺利实施。

主管校长签字: 薛红已 学校(公章):
2025年11月24日



广东省质量工程项目 验收登记表

项目类别：	教改项目
项目名称：	智慧植保导向下的精准农业人才培养体系构建
所在学校：	华南农业大学
项目负责人：	徐汉虹
项目参与人： (限前 5 人， 不含 项目负责人)	刘家莉、兰玉彬、曹广祥、李兆栋、 贾金亮
立项时间：	2020 年 12 月 9 日
填表时间：	2024 年 2 月 23 日

广东省教育厅 制
二〇二三年

六、项目校内管理部门初步审核意见

(须从管理部门层面对项目建设成效进行客观评价，明确该项目是否已经具备资格可以参加校内结题，并附学校管理部门初步审核意见)


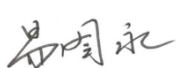
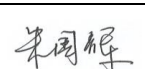
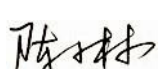
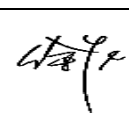
该项目已按照项目申报书完成预期研究改革内容，项目总体执行情况良好，研究成果丰硕，研究成果对于新农科建设下植物保护人才培养体系的创新，尤其是培养适应市场需求和智慧农业发展的新型植物保护人才具有重大实践意义，尤其是在课程改革上具有创新性和较好的示范效应，有进一步推广的意义和价值。同意该项目按期结题。

部门负责人签章:

2024年2月28日



七、项目结题专家及意见

结题评审 专家信息 (专家至少5人以上,其中校外专家不少于2/3)	序号	姓名	职称/职务	所在单位	联系方式	专家签名(电子签名)
	1	吴学宏	教授	中国农业大学	13601272810	
	2	易图永	教授/副院长	湖南农业大学	13574127831	
	3	朱国辉	教授/副院长	华南农业大学	13660276645	
	4	陈小林	教授	华中农业大学	13667127102	
	5	徐彪	教授/副院长	仲恺农业工程学院	13610109631	
专家组意见(300字以内)	<p>(需将项目建设任务执行情况、成果完成情况、成果实践应用情况、项目创新点、项目经费支持情况、建设存在的主要问题、改进建议等具体说明,并给出总体评价,请附项目结题时专家评审原始材料)</p> <p>该项目结合国家实施重大战略以及社会生产需求,提出以智慧植保为导向建立农业人才培养体系,意义重大。该项目围绕人才培养大纲修订、校企联合、产学研一体化、优化教学平台、跨学科教学团队组建等方面进行建设,超额完成了任务书中的预期建设成果,尤其是《智慧植保》及《植保大数据》两门交叉课程的开设以及国家级课程、国家级教材的建设将有力地促进新农科人才培养体系的构建,从而在全国涉农高校的人才培养理念以及培养模式创新等方面起到示范作用,积极地推动提升学生综合素质的教学改革。项目成员获得国家级或省部级教学竞赛奖彰显出其较高的教学水平。</p> <p>综上,该项目结题报告优秀,建议总结和凝练教学成果,申报省部级以上教学奖励。</p>					

2021年省教学质量与教学改革工程拟立项项目名单

1、2021年度省实验教学示范中心拟立项项目名单

序号	项目类别	学校	项目名称	负责人
1	实验教学示范中心	中山大学	航空航天工程实验教学示范中心	蒋建平
2	实验教学示范中心	中山大学	中山大学化工基础实验教学中心	欧阳钢锋
3	实验教学示范中心	中山大学	集成电路工程与技术实验教学示范中心	余峻聪
4	实验教学示范中心	暨南大学	口腔医学实验教学示范中心	黄跃
5	实验教学示范中心	暨南大学	网络空间安全实验教学示范中心	翁健
6	实验教学示范中心	华南农业大学	华南农业大学植物保护学院实验教学示范中心	李云锋
7	实验教学示范中心	南方医科大学	临床技能模拟实训实验教学示范中心	蔡文智
8	实验教学示范中心	华南师范大学	材料化学专业实验教学示范中心	石光
9	实验教学示范中心	华南师范大学	广东省软件工程实验教学示范中心	曾碧卿
10	实验教学示范中心	广东工业大学	数字经济实验教学示范中心	谢卫红
11	实验教学示范中心	汕头大学	光电信息科学与工程实验教学示范中心	李鹏程
12	实验教学示范中心	汕头大学	口腔医学实验教学示范中心	辛蔚妮
13	实验教学示范中心	广东财经大学	新商科实验教学示范中心（佛山校区）	丁友刚
14	实验教学示范中心	广东医科大学	广东医科大学医学影像学实验教学示范中心	徐晓红

9、2021年度省高等教育教学改革拟立项项目名单

序号	项目类别	学校	项目名称	负责人
1	高等教育教学改革	中山大学	粤港澳大湾区国际化人才培养视域下的全球史课程双语教学改革	曹鸿
2	高等教育教学改革	中山大学	儿科学基于BOPPPS模型的SPOC教学与高素质创新型人才培养评价体系的构建与实践	陈纯
3	高等教育教学改革	中山大学	构建标准化妇检三维动画和智能化妇检 反馈模型在妇科检查教学中的应用	陈圣福
4	高等教育教学改革	中山大学	基于“五个融合”的《海洋生态学》一流本科课程改革与实践	何蕾
5	高等教育教学改革	中山大学	Simodont虚拟仿真系统在口腔修复学临床实习教学中的应用	黄雪清
6	高等教育教学改革	中山大学	新时代大学生劳动教育的价值向度与实践路径	胡莹
7	高等教育教学改革	中山大学	中国共产党广东历史融入高校思政课教学研究	姜帆
8	高等教育教学改革	中山大学	创新实践能力的团队化、探索式、自主性培养创新模式	刘昆
9	高等教育教学改革	中山大学	“中山大学”号科考船实践教学体系的构建和实施	黎伟标
10	高等教育教学改革	中山大学	基于转化医学理念与临床深度融合的病理生理学教学模式改革	陆立鹤
11	高等教育教学改革	中山大学	大类培养背景下新工科类基础课程-大学化学课程改革与实践	乔正平
12	高等教育教学改革	中山大学	配位超分子笼物理化学研究方法---化学强基班实验教材建设	苏成勇
13	高等教育教学改革	中山大学	以加强数学应用能力与提升数学素养为抓手的高校公共数学课教学改革与实践	万安华
14	高等教育教学改革	中山大学	人工智能背景下肺结节影像诊断教学模式改革研究	王国杰

79	高等教育教学改革	华南农业大学	新文科背景下以乡村振兴为导向的涉农卓越法律人才培养的创新研究与实践	陈维君
80	高等教育教学改革	华南农业大学	农业院校生物化学课程思政教学设计与实践	朱国辉
81	高等教育教学改革	华南农业大学	合理增负背景下大学生实践操作技能提升的实效性研究——以《小动物内科学实验》课程为例	郭剑英
82	高等教育教学改革	华南农业大学	适应新工科/新农科/新文科渗透交叉需要的测绘工程专业人才培养模式改革研究与实践	王长委
83	高等教育教学改革	华南农业大学	“双万计划”背景下农林院校金课建设常态化路径研究-以华南农业大学为例	邓晓华
84	高等教育教学改革	华南农业大学	新文科背景下艺术类专业跨学科融合的实践教学体系创新研究	邹岚
85	高等教育教学改革	华南农业大学	产教融合背景下包装工程专业校企双元育人机制研究	范小平
86	高等教育教学改革	华南农业大学	基于课程思政背景下的《学校社会工作》课程多维联动研究	韩丽
87	高等教育教学改革	华南农业大学	农业院校生物学拔尖人才培养模式改革与实践	邓诣群
88	高等教育教学改革	华南农业大学	三全育人理念下农业院校课程思政建设模式探索—以华南农业大学为例	李艳丽
89	高等教育教学改革	华南农业大学	基于TRIZ理论的《大学生创新创业基础》改革实践	王春铭
90	高等教育教学改革	华南农业大学	基于ESG整合思政与专业教育的《财务报告分析》混合式教学改革与实践	陈艳艳
91	高等教育教学改革	华南农业大学	“思维导图+TBL”教学模式的探索与实践 --以农林类非生物学专业《生物化学》课程为例	蒋珺
92	高等教育教学改革	华南农业大学	“双一流”视角下艺术类专业教学改革项目质量评价模式研究	王芳
93	高等教育教学改革	华南农业大学	基于新农科视野下人文素质课程混合式实训教学模式的创新与实践	吴琪
94	高等教育教学改革	华南农业大学	化学类一流本科专业科技创新-毕业论文-实习-就业“四位一体化”教学改革与实践	张声森

广东省高等教育教学研究和改革项目

申 请 书

项目名称 化学类一流本科专业科技创新-毕业论文-
实习-就业“四位一体化”教学改革与实践

项目负责人 张声森

职 称 副研究员

所在学校 华南农业大学

申报日期 2021 年 8 月 10 日

广东省教育厅 制

2021 年 10 月

申请者的承诺与成果使用授权

本人自愿申报广东省本科院校教育教学改革项目，认可所填写的《广东省本科院校教育教学改革项目》（以下简称为《申请书》）为有约束力的协议，并承诺对所填写的《申请书》所涉及各项内容的真实性负责，保证没有知识产权争议。课题申请如获准立项，在研究工作中，接受广东省教育厅或其授权（委托）单位、以及本人所在单位的管理，并对以下约定信守承诺：

1. 遵守相关法律法规。遵守我国著作权法和专利法等相关法律法规；遵守我国政府签署加入的相关国际知识产权规定。

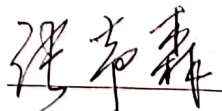
2. 遵循学术研究的基本规范，恪守学术道德，维护学术尊严。研究过程真实，不得以任何方式抄袭、剽窃或侵吞他人学术成果，杜绝伪注、伪造、篡改文献和数据等学术不端行为；成果真实，不重复发表研究成果；维护社会公共利益，维护广东省高等教育教学改革项目的声誉和公信力，不以项目名义牟取不当利益。

3. 遵守广东省本科院校教育教学改革项目有关管理规定以及广东省财务规章制度。

4. 凡因项目内容、成果或研究过程引起的法律、学术、产权或经费使用问题引起的纠纷，责任由相应的项目研究人员承担。


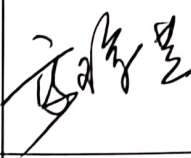
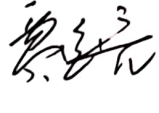
5. 项目立项未获得资助项目或获得批准的资助经费低于申请的资助经费时，同意承担项目并按申报预期完成研究任务。

6. 同意广东省教育厅或其授权（委托）单位有权基于公益需要公布、使用、宣传《项目申请·评审书》内容及相关成果。

项目负责人（签章）：

2021年11月12日

		2014-2016 年下半年	基础实验化学 A1	13-16 级食品 工程、环境 科学等	年均 128	材料与能源 学院		
		2017-2020 年上半年	基础实验化学 B2	18-20 级包装 工程、林业 工程等	年均 96	材料与能源 学院		
	曾主持项目情 况(限填近 3 年 主持项目情况)	项目 级别	项目名称				获批时间	
		国家 级项目	双极一体化自偏压光催化体系的构建及其净化有机废水耦合制氢性能和机理研究(国家自然科学基金面上项目,主持)				2021 年	
		省级 项目	双极同基自偏压光催化体系的构建及其净化有机废水耦合制氢研究(广东省自然科学基金,主持)				2019 年	
项 目 组	总人数	职称			学位			
		高 级	中 级	初 级	博 士 后	博 士	硕 士	参加单位数
		6	0	0	0	6	0	1
	主要成员 (不含主持 人)	姓 名	性 别	出 生 年 月	职 称	工 作 单 位	分 工	签 名
		刘英菊	女	1978.07	教授	材料与能源学院	讨论制定项目相关方案	刘英菊
		杨卓鸿	男	1975.02	教授	材料与能源学院	实践基地建设	杨卓鸿

		倪春林	男	1965.01	教授	材料与能源学院	实践基地建设	
		高琼芝	女	1974.02	副教授	材料与能源学院	项目方案实施	
		贾金亮	男	1979.08	副教授	材料与能源学院	成果的推广应用	

二、立项依据¹

2-1 项目实施的意义和现状分析（要求必须立足合本专业、本学院、本校或全省教学改革实际，从问题出发有针对性地提出）

2.1 项目研究的意义

（1）“四位一体化”教学改革有利于一流化学类专业的建设。

实习（包括专业实习和毕业实习）和毕业论文（设计）是高校人才培养方案中最重要的两个实践教学环节，是培养学生实践能力、创新能力、综合素质的重要手段，也是本科生四年大学学习成果的一次全面检验、总结和提高。《国务院关于加快发展现代职业教育的决定》和《现代职业教育体系建设规划（2014—2020年）》指出，地方本科院校应该向应用技术类型高校转型发展。地方本科院校转型的发展，就是要发挥其学科优势，建立应用型人才培养新模式，培养面向生产一线的应用型人才。在人才培养方面，不再单纯强调专业教学的理论性、系统性，而是强调人才培养的针对性及实用性，更加突出社会需求、就业导向，实施面向职业实践的创新性人才培养方案。在当前理工类本科专业，特别是化学类等相关专业的培养过程中，科技创新日益受到广泛重视，已经成为国内众多高等院校高年级本科生的基本必修课程之一。地方高校在向应用技术类型高校转型的形势下，如何服务地方和培养创新应用型人才，找到学校在区域经济社会发展中的作用，尤其是加强包括实习、毕业论文（设计）在内的实践教学环节与地方社会经济的联系，培养复合型、应用型人才，是当前地方高校重要的研究课题。我校一流化学类建设专业，包括应用化学（国家一流本科专业建设点）和材料化学（广东省一流本科专业建设点）两个专业（佐证材料1），是高校实践教学比较强的专业，所以实践教学环节对培养服务地方建设的创新应用型人才

¹ 表格不够，可自行拓展加页；但不得附其他无关材料。下同。

和毕业生就业有着非常重要的作用，同时，我校化学类的本科生还有一门《创新性实验》课程，此课程着重科技创新性人才的培养，是在开始毕业论文之前，和毕业论文、实习具有很强的连贯性。探索科技创新、毕业论文（设计）、实习和就业“四位一体化”模式意义重大。

（2）“四位一体化”教学改革有利于新时代创新性人才的培养。

普通高等学校理科本科生实习和毕业论文（设计）的安排和实施已成为高校教学和社会关注的热点问题，因为毕业实习和毕业论文的质量影响着本科生的培养质量及就业后社会对学生的满意度。然而，学生人数增加、实习时间较短、企业不愿意接收、实习基地不足且难以保证或实践基地变动过于频繁、学生及教师对实习不够重视等一系列问题都会导致实习质量下降，使人才培养目标不能很好地实现，从而又影响到毕业生的就业质量。从用人单位的调查反馈来看，当今大学毕业生动手能力不强、实践能力不足、科技创新意识不强，工作适应能力较低，部分毕业生要经过半年甚至更长时间的培训和实践锻炼才能胜任本职工作，这些因素对毕业生的就业产生了负面的影响。所以，如何深化科技创新、毕业论文、实习与就业一体化教育模式的改革，提高一流专业建设点的学生培养质量，进一步帮助培养出“双一流”建设背景下适应学科专业发展与新时代发展需求的创新性人才，是当前以及未来很长一段时期内化学类相关专业人才培养与本科教学研究中的重点改革目标之一，同时也是亟待攻克的一大难点。

2.2 项目的现状分析

（1）科技创新中的“创新性实验”课程的现状与不足。

在我们十多年来的不断探索与课程实践中，尽管创新性实验在化学类专业人才的素质培养、本科毕业设计、创新氛围建设乃至反哺教师科研工作等方面发挥了积极有益的作用，但在新形势下的专业教学实践改革与实施过程中依然存在以下几个主要问题：1）学生在创新性实验关键环节中的参与度与能动性较低，师生思维互动亟待加强。尽管专业教师一直鼓励学生积极参与实验课题的内容与方案设计，但多年来的教学实践表明，大多数学生受限于传统理论教学和其它实验教学的教学模式，在创新性实验的立题选题、实验方案设计制订以及新实验的现象观察。2）学生的主观积极性不够高，在自主性、研究探索兴趣以及团队协作等方面整体表现不理想。针对创新性实验的课程性质与实践目标，实施过程中一般主要通过两种方式确立创新性实验的研究：第一种方式是让学生自行设计创新性实验的内容与方法，指导老师负责给出一些参考的创新性实验课题资料等，在学生自行确立实验

课题后进行适当引导，促成创新性实验研究。第二种方式是学生自愿选择参与教师的研究项目，并在一学期内相对独立地完成指导老师指导的一项小课题研究内容。两种创新性实验的研究方式相较而言，显然前者较后者对学生综合素质的锻炼和主动创新能力的培养作用更为显著。然而遗憾的是，近年来学生小组基本选择第二种参与型方式，缺乏对创新性研究的基本热情和积极性，在完成创新性实验的过程中在个人自主性和团队合作配合等方面表现均不够理想，且对探索性研究的认识 and 关注度匮乏，不利于推动创新性实验的教学改革与发展。3) 缺乏对创新性实验过程与实施质量进行实时记录、反馈评效的有效方法和长效机制。在以往的创新性实验的实施过程中，每一个实验/课题小团队由学生（小组）及其指导教师组成，由于各个课题在实验内容方面一般不会重叠交叉，因此在实施阶段多个实验小团队之间缺乏深入有效的沟通和交流，特别是有关创新性实验过程中的一些有趣发现和重要实验数据的跟踪与记录基本处于空白，对于实验过程中出现的有关课程设计合理性等相关问题缺乏良好的分析汇总。

(2) 本科生实习的现状与不足。

1) 专业实习情况：通过专业实习使学生初步了解相关实习厂（或车间）的实际生产过程，包括生产原材料、生产工艺及流程、生产工艺条件、生产设备及控制、产品等；加深对专业理论和生产工艺原理及过程的理解，增加对本专业的感性认识，并学习简单的生产技能；通过同工人、工程技术人员、生产及管理人员的接触和了解、增加对社会的认识、提高其社会适应能力。我校化学类专业的实习手段通常主要是组织学生参观化学材料的合成、加工和应用企业，实习安排第七学期，时间为1周（[佐证材料2](#)），经费安排只解决学生来回交通费用，对维持实习基地具有重大的挑战。该课程设置加深了学生对专业课的学习并产生了兴趣，因此引起了学生和学校各方的高度重视。但近年来，学校和学院对学生考研越来越重视，专业实习经常安排在考研后的一周，经常为年底，时间较为紧张。另外，随着我国制造业的进步，企业产品质量的进一步严格监控，对原来可以接收整班学生参观认知实习的大型企业越来越少，认识实习的单位范围在不断收缩，要顺利圆满进行就越发困难。

2) 毕业实习情况：我校化学类毕业实习为实践必修课，是本专业教学过程中一个重要的实践环节，是学生学习本专业的专业课程之后，并具有一定的专业理论知识的基础上，将理论知识与生产实际相结合的过程。毕业实习是培养学生创新意识和实践能力、实现专业培养目标的重要实践教学环节。使学生掌握与材料化学专业有关的生产实际和组织管理

知识技能，培养学生适应社会的重要教学环节。通过毕业实习，可以使学生加深对本专业理论知识的理解，了解实际过程中对于专业知识和个人素质的要求，做好理论与实践的结合作，缩短学生毕业后进入实际工作岗位的适应期，实现培养高素质应用型人才的目的。我校化学类学生的毕业实习一般设在第八学期连续实习 5 周，是将所学知识应用于实践并接受实践的检验、将所学知识融于企业运行，和企业需求接轨的一个重要教学环节，并为大学生的毕业设计提供理论和实践的强有力的支持。但在近几年的实施过程中毕业实习中存在一些问题，主要有以下几方面：**(a) 实习经费问题。**与课堂教学不同的是，毕业实习需要较多的经费投入。一般情况下，接受实习生的企业或单位需要收取一定的费用作为对学生的管理费用。目前的现实情况是毕业实习投入的经费已无法满足学生毕业实习过程的费用。根据学校的制度经过计算我院每个班的用于学生实验的经费为 2000 元，平均每个学生不到 70 元（佐证材料 3），远远不能满足学生毕业实习的基本需要，在一定程度上也影响了毕业实习的效果，也未达到毕业实习的最终目的。因此，如何提高学生毕业实习经费是化学类专业需要考虑的问题。**(b) 实习基地建设问题。**学院缺乏长期合作的实习基地建设和投入。学院初期实习基地合作单位不稳定，部分企业对开展本科生毕业实习的积极性不高，随意性较大。部分实习合作单位对实习学生人数和实习时间要求较高，导致学院与其无法长期进行合作。对于已签订协议的实习基地，实习建设投入不足，缺乏系统的实习流程内容。我校化学类专业实习合作企业大部分为民营企业，规模较小，缺乏足够的住宿条件，大部分企业不能满足十人以上学生规模实习，只能按不同企业分组实习。因此，由于毕业实习企业不同，导致我院化学类专业学生毕业实习质量参差不齐。**(c) 实习内容问题。**以我校化学类专业毕业实习为例，实习单位主要以化学材料制造和分析检测公司为主。从现场实习情况来看，大部分企业不要求学生到车间进行生产实习。即使被安排到车间，学生只从事打扫卫生，较轻的部件装卸搬动等体力活。一方面，由于车间属于危险区域，需对学生安全负责，部分企业担心在生产实习过程中出现安全事故而承担相应责任，所以只安排学生办公室实习。另一方面，实习时间短，企业教会学生后，实习就面临结束的情况。因此，企业不愿意浪费较多的人力时间培训学生，从而导致学生在企业实习时基本面临无事可做的窘境。而对于材料的研发和大型仪器检测等工作，大部分实习学生并未参与，从而出现实习内容与专业不符而达不到实习目的的问题。**(d) 实习考核方式问题。**实习考核方式较简单，以我院化学类专业为例，毕业实习考核是以学生个人自评、企业考核和任课教师考核三方面组成。由于成绩给定方式相对固定简单，部分学生实习的积极性

不高，对实习过程不够重视。为满足实习报告格式和内容要求，部分学生强行凑字数，导致实习报告质量良莠不齐，不能很好展现学生实习效果，从而未能有效达到毕业实习设定的目的及要求。

(3) 本科毕业论文设计的现状与不足。我校化学类的本科生毕业论文安排在第七和第八学期，其完成主要有如下六个环节：导师拟定题目-师生互选-开题-实验-撰写论文-答辩。近年来，由于扩招和就业形势严峻等多方面的原因，本科毕业论文的总体质量出现下降趋势，特别是在创新性培养方面有明显的不足，主要有以下几个原因。**(a) 导师科研项目不足。**由于我校化学类专业的导师要承担我校的全部化学基础课，约有一半老师忙于上课，科研项目较少，创新性科研较弱，且每位导师平均下来要带的学生数是 4-5 位，同时导师还需要花大量的时间培养研究生，因此对大学生的创新性能力的培养上心有余而力不足的现实。由于学生多而专业教师少，教师的指导工作量过大，又有繁重的教学工作，无暇给予学生及时的指导和检查；有些毕业设计课题缺少实践平台，只能作理论分析。在选题时，为回避实践环节，很多选择了与实际相脱离的综述类题目或虚拟设计题目；还有的学生选题和指导教师的研究方向不一致，教师难以对学生进行具体的指导，学生又忙于找工作等，造成很多学生论文不规范，质量很低，甚至抄袭论文，没有起到培养综合能力和科研水平的作用。**(b) 学生的主观能动性不强。**在导师安排的本科毕业论文的题目中，有很多结果是未知的，需要学生在整个毕业论文的过程中要发挥主观能动性。特别是开题前的文献调研、实验中的问题解决和实验数据的分析需要学生很强的主动性才能增强其逻辑思维、创新思维和分析能力。然而，在实际毕业论文的全过程中，学生同时面临着毕业实习、找工作问题，以及准备考研的同学学习重心放在复习备考上，毕业论文经常安排在考试结束后，导致毕业论文的时间相当紧张，创新性研究很难系统的开展。另外有些同学认为毕业后不从事科研工作，因此对毕业论文积极性不高，对待毕业论文完全按照老师的安排，创新能力更难培养。**(c) 本科生毕业论文安排经费不足。**根据我们目前的本科生毕业论文管理制度，每位学生安排的实验经费是 500 元（佐证材料 4），根据化学类本科生毕业论文的要求，需要有完整的研究过程。在实验过程中需要大量的实验数据的测试和表征，所安排的毕业论文经费是远远不够。而创新性能力的培养需要通过大量的实验数据进行分析，根据实验结果进一步改进实验，都是未知的实验，需要花费大量的试剂和表征测试费，导致指导教师在知道本科生完成毕业论文的过程中年减少了对本科生创新能力的培养。

(4) 学生就业的现状与不足。学生就业是高校当前的热点、难点工作，化学类专业

毕业生找工作难也是很普遍的现象。有些学生毕业文凭到手，就是失业的开始，所以学生一进入大学就开始忧心自己将来的就业问题。进入大四年级，就业、考研开始实际操作，已无法安心学习，特别是第八学期的实习、毕业论文等重要的实践教学环节不能安心去做，使毕业生的质量降低，更增加了学生就业的难度。另一方面，企业所需要的各类专业人才紧缺，招不到适合自己企业需要的员工，有的应聘大学生专业水平过低，有的所学专业知识和企业需求不一致，难以达成协议。因此，就业难是高校和学生的共同呼声，也是高校发展必须要解决的一道难题。

在当前我校一流专业建设点的本科化学类专业（应用化学和材料化学）的教学规划中，科技创新、毕业设计、实习与就业工作四者分别设置，由于科技创新的培养贯穿大二到大四，同时学生在进入大四后，实践教学无法安排，缺少完成各项任务的平台，学生“一心四用”，很难高质量的完成。实际上，四者之间是一个有机的整体，可以作为同一项工程进行改革与实践。采用科技创新、毕业设计、实习与就业工作“四位一体化”创新模式，可以在很大程度上解决这一矛盾。

主要参考文献：

- [1] 赵晓波，化学一流本科专业建设的研究与实践，教育教学论坛，40 (2020) 39-241.
- [2] 蔡欣，禹筱元，罗颖，高琼芝，张声森，杨思源，材料类专业创新性实验的教学改革探索与实践，广东化工，45 (2018) 235-236+251.
- [3] 倪春林，张展基，陈建平，郑文旭，农业院校化学类专业大学生创新能力培养的探索与实践，实验室科学，15 (2012) 160-163.
- [4] 张起祥，李祖欣，毕业设计、毕业实习与就业一体化改革模式探析，黑龙江高教研究，209 (2011) 163-165.
- [5] 陈建兵，叶三梅，产教融合背景下应用型本科高校毕业实习与毕业论文一体化的改革研究——以池州学院高分子材料与工程专业为例，高分子通报，5 (2020) 63-68.
- [6] 温永红，王世颖，高洪涛，詹天荣，新时代背景下省属高校本科生毕业实习-毕业论文-就业一体化教学模式探索与实践，大学化学，35 (2020) 7-12.
- [7] 蔡岗，吴凌燕，何凯萍，高校实践教学改革中的校企合作创新平台建设，福建电脑，

11 (2016) 52-52.

[8] 李立清, 吴盼旺, 李渊, 陈火平, 刘晋彪, 季淑蕊, 新型工科专业校企合作实践教学模式研究, 教育现代化, 7 (2020) 102-103+112.

[9] 杨振华, 周攀, 周兆锋, 张彪, "双一流"背景下新能源材料与器件本科专业拔尖人才培养体系的设计与构建, 科教文汇, 4 (2021) 5-6.

[10] 廖庆喜, 张拥军, 廖宜涛, 黄小毛, 基于学科交叉融合的农业工程类一流专业建设探索与实践, 高等工程教育研究, 178 (2019) 17-21.

2-2 项目实施基础 (包括与本项目有关的工作积累和已取得的工作成绩; 学校对项目的支持情况, 含有关政策、经费及其使用管理机制、保障条件等, 可附文件材料)

1.与本项目有关的工作积累和已取得的工作成绩

(1) 申请团队具备扎实的教学与科研基础, 具有良好的工作积累

本项目申请团队现有教授 3 名, 副教授及副研究员 3 名, 项目组的 6 名教师均指导过专业实习、毕业实习、毕业论文和就业相关工作, 具有丰富的一线教学和人才培养经验。申请团队 6 名成员中包括博士生导师 2 名、硕士生导师 4 名; 近 5 年主持承担的国家及省部级各类教学和科研项目共 20 项 (经费达 800 多万元); 主持应用化学国家一流专业建设项目 1 项 (负责人: 刘英菊)。已发表教改论文 20 余篇 (申请团队已取得的代表性教改论文和教学成果请参见 2.1 和 2.2 附录)。

其中, 项目负责人张声森, 毕业于华南理工大学获工业催化专业博士学位。自 2014 年加入华南农业大学至今每年承担化学类的理论与实验教学任务, 完成教学学时超过 300 学时, 自材料与能源学院成立以来, 每年和本项目参与成员贾金亮一起指导材料化学专业学生的专业见习和毕业实习的相关工作。申请人在教学工作中坚持认真负责, 始终兢兢业业, 不断学习注重积累提升教学技能和教学水平。在科研工作上踏实进取, 作为硕士生导师注重创新人才的培养与发展; 目前主持国家自然科学基金面上项目 1 项, 广东省自然科学基金 2 项以及广东省科技厅公益研究与能力建设专项资金 1 项, 已发表多篇教改论文和 80 余篇 SCI 学术论文。在培养本科生方面: 1) 共指导了 28 位本科生的创新&毕业论文设计; 2) 指导大学生创新创业训练项目有国家级 1 项, 省级 1 项, 校级 1 项。2020 年国家级项目代表广东省参加全国第十三届大学生创新创业年会 (全省 15 项, 全校 3 项), 助力我校获得年度优秀组织奖 (此工作进入了 2020 年度校长工作报告)。3) 指导 5 届材料化学专业的专业见习和毕业实习。4) 担任 14 和 18 级两届学生班主任。七年的大学教学科研实践表

明，良好的科研工作积累与持续创新的学术兴趣不仅可以为本科教学提供丰富的学科发展相关的前沿素材与研究成果，也在很大程度上不断回馈促进本科生培养工作的发展。

项目参与成员杨卓鸿、刘英菊和倪春林教授在化学类本科专业的人才培养与教学质量管控等方面具有深刻的认识，积累了多年的专业教学与科研工作经验。项目组成员刘英菊教授和高琼芝副教授均曾获学校十佳教师奖，刘英菊教授还获得华南农业大学教学名师奖。因此，项目组成员具备培养“四位一体化”创新性、综合性人才的扎实工作基础。

2.1 附录：近 5 年申请团队已取得的代表性教改论文成果一览表：

序号	作者及其排名	论文题目	期刊	级别	年份及卷期号
1	张声森/第 1, 高琼芝/第 4, 倪春林/第 7	以油茶壳为原料制备吸附剂及其净化抗生素废水性能 ——“新农科”理念下培养“新农人”的综合研究性实验设计	化学通报	核心期刊	2020, 83(9): 844-849
2	高琼芝/第 1; 刘英菊/第 2; 张声森/第 3	“翻转课堂”教学法在无机及分析化学课程教学中的实践与效果分析	大学化学	普通期刊	2021, 36, 2010065 (1-10)
3	倪春林/第 1	基于复合抗菌材料制备与性能综合实验教学	实验技术与管理	核心期刊	2020,37(08): 80-83+87
4	倪春林/第 1	绿色荧光晶态材料的制备与性能实验设计	实验室研究与探索	核心期刊	2020, 39(12): 38-41
5	杨卓鸿/第 2	农业院校理工科研究生拔尖创新人才培养模式探索	实验技术与管理	核心期刊	2020,37(08): 37-41
6	倪春林/第 1	锌卟啉功能化薄膜材料的制备与性能综合实验设计	实验室研究与探索	核心期刊	2019, 38(6): 38-41
7	杨卓鸿/第 2	化工原理课程知识共性关联探究及教学实践	实验室研究与探索	核心期刊	2019,38(12): 190-195
8	倪春林/第 1	农业院校研究生“现代化学化工实验技术”课程的设计与教学实践	化学教育	普通期刊	2018, 6: 61-65
9	倪春林/第 2, 刘英菊/第 4, 杨卓鸿/第 5	桐油的光化学反应创新实验设计及其教学实践	实验室研究与探索	核心期刊	2018,37(9): 231-235 +290
10	倪春林/第 1	农业院校研究生创新实验项目的设计与实践	实验室研究与	核心期刊	2017, 36(1): 169-172

			探索		
2.2 附录：近 5 年申请团队已取得的教学成果一览表：					
序号	获奖者及排名	获奖内容	获奖级别	获奖年度	
1	张声森	指导本科生创新创业项目代表广东省参加全国第十三届大学生创新创业年会	省级	2020 年	
2	张声森	“丁颖杯”暨“挑战杯”广东课外学术科技竞赛优秀指导教师	校级	2021 年	
3	张声森	华南农业大学材料与能源学院 2018-2020 年度优秀班主任	院级	2020 年	
4	张声森	华南农业大学材料与能源学院青年教师教学竞赛二等奖	院级	2020 年	
5	倪春林/第一	“应用化学专业实验教学团队”，获“广东省教学团队”称号，2019 年。	省级	2019 年	
6	倪春林/第一	“具有农科特色的化学和材料类人才培养模式创新实验区”获“广东省人才培养模式创新实验区”牌匾	省级	2018 年	
7	杨卓鸿	“四链协同驱动农业院校化工材料类研究生拔尖人才培养模式建设与实践” 教学成果二等奖	校级	2021 年	
8	刘英菊	华南农业大学教学名师奖	校级	2019 年	
9	刘英菊	华南农业大学教学优秀奖	校级	2017 年	
10	倪春林/第一	“开放式农科化学实验教学平台的建设与学生创新能力的培养” 教学成果一等奖	校级	2017 年	
11	高琼芝	华南农业大学教学十佳教师	校级	2017 年	

2. 单位对项目的支持情况

华南农业大学材料与能源学院一流化学类专业包含材料化学和应用化学两个专业，是高校实践教学比较强的专业，所以实践教学环节对培养服务地方建设的材料应用型人才和毕业生就业有着非常重有的作用。我校和学院对化学类的学生的实践培养和就业情况相当重视。在有限的资源条件下，千方百计的探索化学类学生的专业实习、毕业实习、毕业论文(设计)和就业工作的最优化。本项目充分考虑大四学生的校内课程和实习经费两方面的问题。特别是在教学经费方面，通过四位一体化的模式把教学经费化零为整、统一安排，保证了经费的支持，在同样的教学经费的支持下，能系统化提升学生的素养，培养出高质量的化学类学生。若本项目获得立项，将有1万元经费支持，如再获得省级立项将总计有2万元经费支持，由于本项目的实施需要企业参与合作实施，寻找合适的企业并进行有效的沟通是本项目的重点，因此本项目的经费主要用于与企业的对接中产生的差旅费和交通费、以及相关材料的打印费，可以满足本项目的实施。

另外，我校高度重视和支持教师从事教学研究和改革探索，学院对教师发表核心期刊教改论文给予报销版面费的支持，因此在本项目预算中无需预算版面费。

在学校和学院实习实验教学经费等支持下，近年来我院教学和科研环境大大改善，三个专业现有的实习基地超过20个。本项目在实施过程中，已经具备了项目建设所需的各项软件、硬件条件，目前暂时不存在缺少的条件。

3. 项目负责人和项目组成员所承担的教学改革和科研项目情况

近年来项目申请人主持教学类项目1项，主持各类科研项目6项，其中包括国家自然科学基金面上项目1项、省级项目3项。项目申请人及参与人已取得的代表性教学改革和科研项目及代表性高水平科研论文请分别参见2.3和2.4附录。

2.3 附录 近年来项目组成员主持承担的主要教学改革和科研项目一览表

序号	主持人	项目类别及项目名称	经费	年度	级别	项目类型
1	张声森	国家自然科学基金(22078118)，双极一体化自偏压光催化体系的构建及其净化有机废水耦合制氢性能和机理研究	63 万	2020	国家级	科研项目
2	张声森	广东省自然科学基金(2019A1515011138)，双极同基自偏压光催化体系的构建及其净化有机废水耦合制氢研究	10 万	2019	省级	科研项目
3	张声森	广东省自然科学基金(2019A1515011138)，阴	10 万	2017	省级	科研

		阳两极一体化自偏压光电池的设计及其光催化分解水制氢性能研究				项目
4	张声森	广州市科技计划项目(201803030003), 具有等离子共振效应的纳米 Cu 修饰氢化一维 TiO ₂ 纳米材料的制备及其太阳能光催化分解水制氢性能研究	30 万	2016	省级	科研项目
5	张声森	材料类专业创新教育的实验教学模式改革研究与实践	0.2 万	2016	院级	教研项目
6	刘英菊	国家自然科学基金项目(21874048), 基于功能化二硫化钼构筑比率型免疫传感器对赭曲霉毒素广谱性识别的研究	62 万	2019	国家级	科研项目
7	杨卓鸿	国家自然科学基金项目(51673075), 植物油紫外光化学反应调控机制及其应用研究	72.6 万	2017	国家级	科研项目
8	倪春林	广东省高等教育教学改革项目(粤教高函[2020]20 号), “三全育人”背景下《无机功能材料》课程思政的建设与实践	2 万	2019	省级	教改项目
9	倪春林	广东省质量工程项目(2019-5-16), 制药工程专业实践课程教学团队	3 万	2019	省级	质量工程
10	倪春林	广东省学位与研究生教育改革研究项目(2018JGXM17, 《现代化学化工实验技术》课程体系的优化建设与教学模式改革	2 万	2017	省级	教改项目
11	倪春林	广东省实验教学示范中心(粤教高函[2017]214 号), 生物化工与制药实验教学示范中心,	150 万	2017	省级	教改项目
12	刘英菊	广东省自然科学基金(2021A1515010208), 基于纳米金属仿生酶构筑光电双通道免疫传感器对保健品中罗格列酮的检测	10 万	2021	省级	科研项目
13	杨卓鸿	省级促进经济高质量发展专项(海洋工程装备专题): 石墨烯改性环氧树脂基海洋防腐涂料研究及产业化应用, 2021/04-2023/03, 500 万	500 万	2021	省级	科研项目
14	杨卓鸿	广东省科技计划项目(2020A0505100051), 基于生物质纳米孔碳/金属复合催化材料的高性能锂硫电池研究	50 万	2021	省级	科研项目
15	高琼芝	华南农业大学教学质量工程项目(zlgc19034), 无机及分析化学	3 万	2019	校级	质量工程

2.4 附录 近年来项目组成员发表的15篇代表性高水平SCI学术论文

序号	论文题目	作者及排序	刊物名称	发表时间
1	Boosting photocatalytic hydrogen evolution using a noble-metal-free cocatalyst: CuNi@C	张声森/通讯作	Applied Catalysis B-Environmental	2021 年

	with oxygen-containing functional groups	者		
2	A CuNi alloy-carbon layer core-shell catalyst for highly efficient conversion of aqueous formaldehyde to hydrogen at room temperature	张声森/ 通讯作者	ACS Applied Materials & Interfaces	2021年
3	Surface oxidized nano-cobalt wrapped by nitrogen-doped carbon nanotubes for efficient purification of organic wastewater	张声森/ 通讯作者	Separation and Purification Technology	2021年
4	FeCo alloy@N-doped graphitized carbon as an efficient cocatalyst for enhanced photocatalytic H ₂ evolution by inducing accelerated charge transfer.	张声森/ 通讯作者	Journal of Energy Chemistry	2021年
5	FeNi intermetallic compound nanoparticles wrapped with N-doped graphitized carbon: a novel cocatalyst for boosting photocatalytic hydrogen evolution	张声森/ 通讯作者	Journal of Materials Chemistry A	2020年
6	Designing robust anatase-branch @hydrogenated-rutile-nanorod TiO ₂ as accurate and sensitive photoelectrochemical sensors	张声森/ 通讯作者	Sensors and Actuators B-Chemical	2020年
7	ZnO/CdS/PbS nanotube arrays with multi-heterojunctions for efficient visible-light-driven photoelectrochemical hydrogen evolution	张声森/ 通讯作者	Chemical Engineering Journal	2019年
8	Bifunctional CdS@Co ₉ S ₈ /Ni ₃ S ₂ catalyst for efficient electrocatalytic and photo-assisted electrocatalytic overall water splitting	高琼芝/ 通讯作者, 张声森/通讯作者	Journal of Materials Chemistry A	2020年
9	Construction of CdS/B-TiO ₂ nanorods photoelectrochemical immunosensor for the detection of microcystin-LR using SiO ₂ @G-quadruplex as multi-amplifier	刘英菊/ 通讯作者, 张声森/通讯作者	Sensors and Actuators B: Chemical	2018年
10	Capsulation of AuNCs with AIE effect into metal-organic framework for the marriage of fluorescence and colorimetric biosensor to detect organophosphorus pesticides	刘英菊/ 通讯作者	Analytical Chemistry	2021年
11	In-situ phosphatizing of cobalt-molybdenum	刘英菊/	Chemical	2021年

	nanosheet arrays on self-supporting rGO/CNTs film as efficient electrocatalysts for hydrogen evolution reaction	通讯作者	Engineering Journal	
12	Phloem delivery of fludioxonil by plant amino acid transporter-mediated polysuccinimide nanocarriers for controlling Fusarium Wilt in banana	贾金亮/ 通讯作者	Journal of Agricultural Food Chemistry	2021年
13	Compressible nanowood/polymer composite adsorbents for wastewater purification applications	杨卓鸿/ 通讯作者	Composites Science and Technology	2020年
14	A novel multi-functional bio-based reactive diluent derived from cardanol for high bio-content UV-curable coatings application	杨卓鸿/ 通讯作者	Progress in Organic Coatings	2020年
15	Visible-light-driven photocatalytic system based on a nickel complex over CdS materials for hydrogen production from water	倪春林/ 通讯作者	Applied Catalysis B-Environmental	2017年

三、项目实施方案及实施计划

3-1 具体改革内容、改革目标和拟解决的关键问题

1.1 具体改革内容

(1) 创建科技创新、毕业设计、实习与就业工作四位一体化教学模式。在学生学习主题上前三者要趋于一致，相互连贯。通过专业实习了解毕业实习的内容，通过毕业实习提高毕业设计的质量，通过毕业实习学生提前进入企业生产实践，全面了解企业生产的需求，从而增加了就业机会。

(2) 建立四位一体化实习基地。根据珠三角化学类企业较多，学生就业门路宽的特点，积极主动联系相关企业，共建实习基地，扩大学生实习的范围，延长实产学合作，加强和学院教师有科研合作的企业建设四位一体化实习基地，探索实践教学新模式，创建国家一流专业。

(3) 针对学生的具体情况，设计多种“四位一体化”教学形式。当前，大学生的出路主要是两条，分别是考研和就业。针对这两部分同学，分别设置校企联合培养，但主次不同的两种四位一体化教学形式。对于考研的同学，鼓励采取 i) 以校为主的校企相结合四位一体化教学形式；对于就业的同学，鼓励采取 ii) 企业（也即实习基地）为主

的校企相结合的四位一体化教学形式。

(4) 提前启动毕业设计、实习与学生就业工作。结合各专业的培养目标，适度加大了毕业设计、毕业实习的时间，如将毕业实习提前到第七学期初，既大四开学后启动毕业实习工作，提前让学生介入企业的实习，经过将近一年的培训和业务的熟悉，毕业之后学生就可以直接在该实习企业或校内科研团队工作。这对于培养学生理论和实践相结合以及创新能力具有重要作用。同时进行毕业论文设计，学生可以根据在企业的实习情况和现有的项目，自己选择合适的题目进行毕业设计，并由企业有经验的工程师和教师共同指导毕业设计，使得毕业设计更贴近实际。

(5) 修订专业的培养方案。通过科技创新、毕业设计、实习与就业工作“四位一体化”模式的初步研究与实践，在培养方案中，突出实践教学对学生能力、专业素质的培养，加强毕业设计、专业实习等实践环节的改革，使学生下到工厂、企业实习实践的时间延长。各主要专业课程安排在前三年，减少第四学年的计划课程，以便于学生进行专业实习、毕业实习与毕业设计学习的连贯性。

1.2 改革目标

将我校化学类本科一流专业的科技创新、毕业设计、实习与就业工作安排有机融合在一起，通过多种“四位一体化”的教学形式，结合生产实际的毕业设计的综合培养和训练，提高毕业实习和毕业设计的质量，全方位提升学生的科研创新能力和专业素质，进而可以实现高质量的就业和升学深造，推进化学类本科一流专业的建设。

1.3 拟解决的关键问题

通过化学类一流本科专业实习-毕业实习-毕业论文-就业“四位一体化”教学的改革与实践项目，拟解决的关键问题有三个：

(1) 拟解决毕业实习虚假与低效的问题。所谓毕业实习虚假就是学生不去实习，找某个单位开一个虚假证明，学生敷衍塞责，应付以对，虚假实习；所谓毕业实习低效就是学生实习走过场，身到心不到，与课堂理论教学相比，学生实习没有获得感。四位一体化改革要求知行统一，真题真做，实习和论文相结合。如果毕业生不去实习，不去认真实习，就不可能发现问题，写出满意的论文，获得满意的成绩。

(2) 拟解决学生就业率不高问题。通过专业实习-毕业实习-毕业论文-就业四个环节时间合并，同时开展，延长至整个大四学年，学生结合就业意向寻找实习单位，通过实习解决毕业设计中的实践问题，提高毕业设计质量，并且丰富毕业实习的内容，实现

由学生到技术人员的角色转换，提前融入生产实践，可直接在实习单位实现就业，或为就业创造机会。

(3) 拟解决教学经费不足问题。我校化学类的专业实习、毕业实习以及毕业论文设计的经费各自分散且不足，通过四位一体化可以用把三个环节安排的教学经费进行统一整合，合理安排，有效解决生均培养经费不足的问题。

2. 实施方案、实施方法、具体实施计划（含年度进展情况）及可行性分析

2.1 实施方案

(1) “四位一体化”导师制的建立。由于科技创新可以从大二就开始培养，从大二开始就建立校内导师制，大三开始可以进一步增加企业导师制，使学生可以在创新性实验、毕业论文、实习和就业都有导师进行指导。具体实施如下 (i) 征集学生意见。在创新性实验开展初期，向学生介绍该门科技创新课程的教学目标与实施策略，征集学生对该课程的合理建议，进一步调整创新性实验初步实施方案。建立科技创新性实验课程互动的微信群，为交流共享提供及时有效的平台。(ii) 确立分组，选择创新性实验/课题题目。学生结合自己的实际情况和兴趣自由选择创新性实验指导教师，和指导教师共同探讨确定课题题目，以 2~3 人为一个创新实验小组。(iii) 学生开展前期文献调研和资料收集。(iv) 在导师的指导下，学生设计、制定、分拆基本的创新性实验方案，在实验开展过程中根据分步实验效果调整优化实验方案。(v) 在导师的指导下，学生开展科技创新实验。采集实验数据，进行材料表征测试等，完成基本的实验研究内容，并及时处理分析所得实验数据。

(2) 建设四位一体化实践教学基地。和现有的教学实习基地基础上进行积极沟通，升级为四位一体化实习基地，同时开通新的四位一体化实习基地。也即同一学生的专业实习、毕业实习和毕业论文在学校导师的指导下在相同的实践基地中进行，达到三方面的内容具有连贯性和系统性，达到学生和企业的深度了解，提高就业率和就业质量。目前和化学类一流专业保持积极联系并有培养学生的实习基地有共同组建实习实践教学基地 18 家，其中包括省级基地 1 家、校级基地 5 家、院级基地 12 家，涵盖了国家高新技术企业、普通民企和事业单位。实践教学基地依托单位主要包括上达电子（深圳）股份有限公司、校级实习基地广东蓝洋科技有限公司、广东科迪新材料科技有限公司、广东川奥高新科技有限公司、广州合成材料研究院有限公司、广州飞胜高分子材料有限公

司、广州市福田化学工业涂料有限公司、佛山市方普防护有限公司、佛山霖环保科技有限公司、合众（佛山）化工有限公司、东莞长联新材料科技股份有限公司、东莞市信远无纺布有限公司、东莞市优越检测技术服务股份有限公司州汇标检测技术中心、广州市出入境检验检疫局新沙办事处、广东省环境监测中心、广州致辉精化股份有限公司等企业事业单位。

（3）提前启动毕业论文设计、实习与学生就业工作。将专业实习提前到第6学期，毕业设计提前到第7学期初，中期启动毕业实习工作。（i）专业实习、毕业论文（设计）、毕业实习延续到学生毕业前夕，增加了毕业论文的时间。如在第七学期初就让学生开始毕业论文选题，在校期间完成毕业论文的基本框架，掌握做毕业论文的基本方法和基本内容，以便在下到企业实习中，结合实际生产情况做好相关的调研、设计工作。（ii）提前让学生介入相同的企业的进行专业实习和毕业实习，并配备相应教师进行现场协管和锻炼。如在第七学期的一定时间内让学生进入企业实习，经过一段时间的培训和业务熟悉，在最后一个学期的真正实习阶段，学生已经可以完全介入企业的运作了，这对于学生理论和实践相结合、培养实践能、创新能力具有重要作用。

（4）实习和毕业设计统一安排。在培养方案中，将各主要专业课程向前三学年转移，减少第四学年的计划课程。第七学期开始毕业设计，包括落实任务、查阅资料，掌握毕业设计的基本程序、要求，完成文献综述、外文翻译，完成毕业论文的总体框架设计。学生在校完成毕业论文总体框架后，下到企业、实习基地边实习边做毕业设计，多数学生可请公司的技术人员做兼职指导教师，学生课题也有一部分来自企业的指导教师，实现校企共同指导毕业设计。毕业设计的内容可联系企业的实际项目做研究内容、方法的调整，甚至重新开展课题研究。做到理论联系实际，提高学生的科研能力，提高毕业设计的质量。

（5）实习与就业一体化设计。改进学生就业指导工作，设立“大学生就业指导”课程，将学生就业工作纳入人才培养计划。引导学生认清形势，转变观念，准确定位。采取请企业经理作报告，介绍行业现状、企业需求情况，请优秀毕业生回校现身说法等多种形式，教育学生如何通过毕业实习全面提升自己的就业竞争力，引导学生争取在实习单位就业，充分利用实习时间，寻求就业。引导学生树立“先就业后择业”的就业观念，以发展的眼光对待就业问题，鼓励毕业生发挥自己的聪明才智，积极参与实习和投身就业工作。

2.2 实施方法

把大学生从三年级开始实践教学作为高校的专项工作，统一规划。建立以实习为平台、以就业为导向、毕业设计为关键考核点的教学管理机制。

(1) 从大二开始就实行学生导师制，学生的科技创新、实习、就业 和毕业设计由同一教师 (或导师组) 统一指导，全程 负责。由于指导毕业设计时和学生的长期接触和业务指导，教师了解学生，学生信任指导教师，可以有针对性地指导学生实习、就业，效果极为显著。

(2) 在学生到企业实习期间，配备相应的企业导师进行现场协管和锻炼，这也是提高教师工程设计能力的企业运作方法。既加强了对学生实习期间相关教学指导，同时也提高了教师的现场解决问题能力，使他们懂得一套工程设计的企业运作模式。

(3) 领导定期巡视，现场指导实习与就业工作。把学生的毕业设计、实习、就业作为大四年级学生的中心工作纳入学校工作日程，建立学生实习就业档案，学院领导定期巡视，检查和指导实习就业相关工作。

2.3 具体实施计划

本项目由材料与能源学院材料化学系和应用化学系教师共同承担，项目计划实施周期为 2 年，分四个阶段进行。

第一阶段 (2021.09-2021.11): 在我校化学类 2020 级学生中征集学生的建议，建立科技创新导师制。在 2018 级化学类学生在教学实践基地实习期间，和学生及和实习基地的相关到导师和相应的负责人总结实习时获得的经验和存在的问题，探讨四位一体化基地的建设，初步形成一套较为完整的四位一体化的具体实施方案。

第二阶段 (2021.12-2022.08): 安排 2019 级化学类专业学生到多个相应的实践基地进行专业实习，动员对实践基地的行业有兴趣的学生把专业实习和毕业实习以及毕业论文都安排和实践基地相应的课题，同时联系校内专业相近的老师进行联合指导，完成专业实习，参与四位一体化教学；四位一体化实践教学基地的建设。

第三阶段 (2022.09-2023.11): 安排 2019 级材料类专业学生到相应的实践基地进行实习，对参加四位一体化的学生安排在相应的企业进行毕业实习；四位一体化实践教学基地的建设；动员 2020 级学生参与四位一体化教学；发表教改论文 1 篇。

第四阶段 (2023.12-2023.08): 指导参与四位一体化教学的学生继续在企业进行毕业论文的相关实验和撰写，促进学生在相应的实践基地就业。撰写研究论文及项目结题报

告；发表相关教改论文 1 篇。

2.3 可行性分析

本项目是经过大量调研我校国家一流本科建设专业应用化学和省级一流本科建设专业材料化学科技创新、毕业设计、实习与就业工作背景，并结合申请人工作积累的基础上提出的，在理论和实践上是切实可行。

(1) 理论上可行：科技创新、毕业设计、实习与就业工作“四位一体化”创新模式，实现学生、学校和企业三方三赢。(i) 学生提前介入企业运行，实现由学生到企业技术人员角色转换，可直接就业或为就业创造条件，毕业实习为毕业设计提供实践平台，提供支撑，提高毕业设计水平；(ii) 学生带着毕业设计课题参与企业运行，请企业技术人员做兼职指导教师，毕业设计水平提高了，也丰富了实习内容，大大强化了学生专业能力、科研能力。专业水平的提升，增加了就业资本，提高了就业质量。实习时间延长，实习单位欢迎程度明显提升。(iii) 实习时间延长，实习单位欢迎程度明显提升。学生有充足的时间参与到学校及企业实习的各个环节，提升了学生对理论和专业技能的认知，有利于学生理论技能和专业技能水平的提高，也直接促进了学生在实习单位就业，高质量就业。(iv) 一体化实习基地的建设促使学校专业程度不断提升，为学校实现人才培养目标提供了强有力的保障。因此，从学生、学校和企业三方面的角度出发，“四位一体化”教学改革与实践理论上是可行的。

(2) 实施过程可行：“四位一体化”教学改革与实践在实施过程中充分考虑大四学生的校内课程和实习经费两方面的问题是否可行。(i) 当前我校一流化学类专业本科的校外实践基地都在珠三角区域内（佐证材料 5），来回路程不会超过 1.5 小时车程。大四学生的课可以适当减少并集中安排在一星期的 2-3 天，这样学生长期在企业实习过程，可以通过灵活安排学校课程和实习工作都不耽误，在实施过程中不会对学生的校内课程有影响。(ii) 教学经费方面，传统的专业实习、毕业实习和毕业论文的经费是各自安排，导致三方面的教学都面临着实习经费不足的问题，通过四位一体化的模式把教学经费化零为整、统一安排，保证了经费的支持。从企业的角度出发，由于实习时间延长，学生在中后期也能为企业创造一定的效益，企业对学生的教学投入更多，进一步保证经费的充足。

(3) 项目的研究团队合理：本项目研究团队共有 6 人，其中教授 3 人，副研究员 1 人，副教授 2 人。项目申请人张声森副研究和刘英菊教授分别为材料化学系和应用化学系主任（佐证材料 6），对两个系的情况掌握清楚，能及时了解学生的动态和教师的情

况，能使本项目顺利开展；同时刘英菊教授是国家一流专业应用化学建设试点的负责人（佐证材料7），清楚一流专业需要培养什么样的创新型、复合型化学类一流人才，能在本项目建设方向上提出正确意见；杨卓鸿教授为我院分管科研的副院长（佐证材料8），对本项目的科技创新的开展能提供有力的指导和支持；倪春林教授已经主持了十多个与本科教学相关省级项目（佐证材料9），对项目如何开展和方向具有丰富的经验；高琼芝副教授为我校的十佳教师（佐证材料10），多年负责材料化学专业的本科毕业论文的统筹安排，能为本科毕业论文的开展提供有效的方案；贾金亮副教授和项目申请人连续6年一起负责材料化学专业的专业实习和毕业实习，熟悉学生实习的安排，且和现有实习基地联系紧密（佐证材料11）。总之，本项目团队组织合理，是本项目顺利开展的有力保障。

总之，本项目建立在我校化学类专业当前学生、学校和实践基地三方面的现状和理论分析的基础上，既考虑了毕业班学生的校内课程，又考虑了实践基地的实际需求和经费的支持，在理论上和实施过程中切实可行，团队组织合理，能很好的完成预期目标。

3-3 项目预期成果及其实践运用预期（包括成果形式、预期推广、应用范围、受益面等）

（1）成果形式：

- 1) 提供“四位一体化”教学改革实施方案1份；
- 2) 建设“四位一体化”实践基地2个；
- 3) 发表相关教学研究论文2篇。

（2）预期推广：

先在华南农业大学化学类本科一流专业建设点（应用化学和材料化学两个专业）进行试点，再在其它专业比如和化学类密切相关的环境类和材料类专业进行推广。

（3）项目受益面及预期效果：

1) 项目受益面：华南农业大学材料化学与应用化学专业的学生，以及开设相关专业课程的广东省高校或其它农林院校。

2) 预期可达到的效果：（i）科技创新、毕业设计、实习与就业工作“四位一体化”创新模式教学计划；（ii）获得一套新的富有成效的“四位一体化”完整实施方案；（iii）强化学生专业能力、科研能力，增加学生就业资本，提高就业质量。（iv）建设一批优质的教学实践基地。

3-4 本项目的特色与创新点（佐证材料12）

(1) 人才培养不是仅仅局限于学校的角度进行探讨，而是从企业(市场)需求着手，精心设计，校内教学与校外教学相结合，将科技创新、毕业设计、实习与就业四者有机融合，在做好每一环节工作的同时，强化了四者之间的关系。

(2) 加强了校企合作，通过学生毕业设计校企联合指导，解决了专业教师工作任务繁重而无暇指导学生毕业设计的局面；解决了毕业设计课题因缺少实践平台，理论脱离实际的现象；指导教师深入企业，也提高了教师自身实际工作经验，避免了对学生毕业设计指导中“空对空”的情况。

(3) 以实习促就业，通过实习被用人单位留用。工业企业招聘新员工一般要有试用期、培训期，学生提前到企业实习，并延长实习时间，企业可以在这一段时间以较小的资源完成对实习生的考查、培训。符合企业的运行机制，也增加了学生就业的机会。

四、建设经费预算（根据项目获得省级立项后实际建设需要制定预算，预算要经学校财务部门审核批准）

预算经费总额	(万元) (需财务部门加盖公章)	
科目名称	预算额	项目支出用途
材料费（含打印费、耗材费）	0.1	本项目调研及相关文件资料的制作费和打印费
基地建设费	1.3	用于基地学生实验的器材和试剂
软件服务费（含课堂录像及网站制作）	0.2	项目实施过程中录制微视频
交通费	0.3	学生在市内开展调研学习的交通费用
差旅费	0.9	前往企业进行洽谈沟通的差旅费
其他费用	0.1	计算机设备维修维护费等费用
出版/文献/信息传播/知识产权事务费	0.1	查询相关资料信息费

五. 项目佐证材料清单

(可以证明项目立项必要性、可行性、创新性的相关佐证材料,请分条列明,限20条以内,内容另附)

本项目立项必要性佐证材料:

- 佐证材料 1: 国家和省级一流本科专业建设点证明材料;
- 佐证材料 2: 专业实习、毕业实习时间安排;
- 佐证材料 3: 华南农业大学实习经费管理办法;
- 佐证材料 4: 华南农业大学材料与能源学院毕业论文经费管理办法。

本项目立项可行性佐证材料:

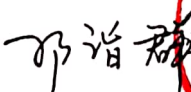
- 佐证材料 5: 材料化学和应用化学在珠三角的校级实习基地建设协议;
- 佐证材料 6: 张声森和刘英菊分别为材料化学系和应用化学系主任任命文件;
- 佐证材料 7: 刘英菊教授为国家一流专业应用化学建设试点的负责人证明;
- 佐证材料 8: 杨卓鸿教授为我院分管科研的副院长证明;
- 佐证材料 9: 倪春林教授近三年主持的四个与本科教学相关省级项目;
- 佐证材料 10: 高琼芝副教授为我校的十佳教师证书;
- 佐证材料 11: 张声森和贾金亮担任毕业实习、专业实习课程证明。

本项目立项的创新性佐证材料:

- 佐证材料 12: 本项目创新性证明。

六、项目负责人所在院系及学校意见

同意

主管校长签字:  学校(公章):

2021年11月17日



教育部高等农林院校理科基础课程
教学指导委员会推荐示范教材



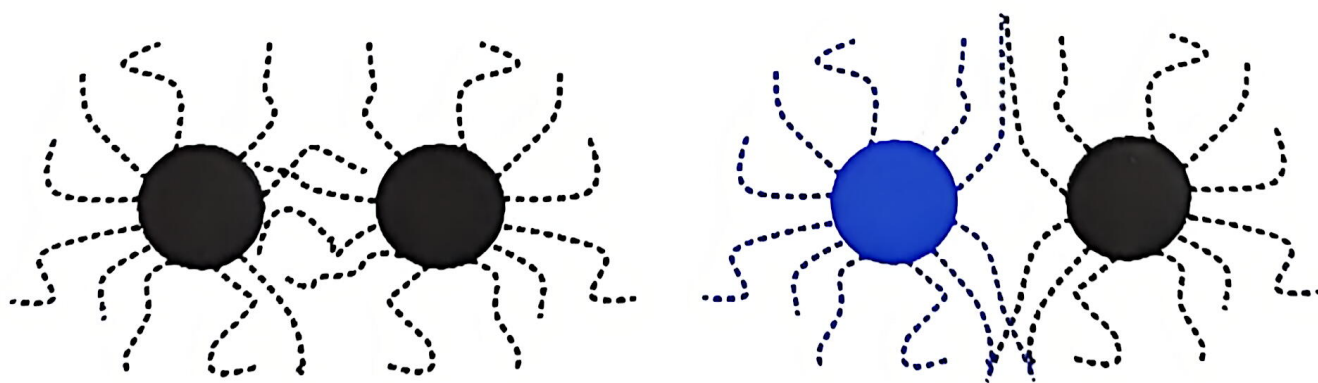
普通高等教育“十四五”规划教材

Physical Chemistry

物理化学

第3版

徐悦华 王 静 贾金亮◎主编



中国农业大学出版社
China Agricultural University Press

内 容 简 介

本书是教育部高等农林院校理科基础课程教学指导委员会推荐示范教材,由华南农业大学、南京农业大学等6所高等院校的物理化学教师共同修订编写。本书包括热力学第一定律、热力学第二定律、混合物和溶液、相平衡、化学平衡、电解质溶液、电化学、化学动力学基础、表面物理化学和胶体化学等共10章内容。本书主要突出物理化学的基础性和交叉性两大特点,重点阐述基本概念和基本理论,力求叙述简明扼要,突出内容的科学性和先进性,培养学生的创新思维和创新能力;章末列有阅读材料和拓展材料,适当介绍学科的新进展,力求达到知识、能力和素质的统一。每章配有思考题、习题以及一两个习题解答视频,书末附有参考答案。本书可作为高等农林院校相关专业物理化学课程的教材,也可作为其他院校相关专业的教材或科研技术人员的参考书。

图书在版编目(CIP)数据

物理化学/徐悦华,王静,贾金亮主编. —3版. —北京:中国农业大学出版社,2022.12
ISBN 978-7-5655-2890-3

I. ①物… II. ①徐…②王…③贾… III. ①物理化学-高等学校-教材 IV. ①O64

中国版本图书馆 CIP 数据核字(2022)第 222720 号

书 名 物理化学 第3版

作 者 徐悦华 王 静 贾金亮 主编

策划编辑 梁爱荣

责任编辑 梁爱荣

封面设计 李尘工作室

出版发行 中国农业大学出版社

社 址 北京市海淀区圆明园西路2号

邮政编码 100193

电 话 发行部 010-62733489,1190

读者服务部 010-62732336

编辑部 010-62732617,2618

出 版 部 010-62733440

网 址 <http://www.caupress.cn>

E-mail cbsszs@cau.edu.cn

经 销 新华书店

印 刷 涿州市星河印刷有限公司

版 次 2023年3月第3版 2023年3月第1次印刷

规 格 185 mm×260 mm 16开本 24.75印张 600千字

定 价 79.00元

图书如有质量问题本社发行部负责调换

C 目录

CONTENTS

绪论	1
第 1 章 热力学第一定律	3
1.1 热力学基本概念	3
1.1.1 系统和环境	3
1.1.2 状态和状态函数	4
1.1.3 过程和途径	5
1.1.4 热和功	5
1.1.5 热力学能	5
1.2 热力学第一定律	6
1.2.1 热力学第一定律的表述	6
1.2.2 热力学第一定律的数学表达式	6
1.3 功与过程	7
1.3.1 功与途径	7
1.3.2 可逆过程	8
1.4 热与过程	9
1.4.1 等容热	9
1.4.2 等压热与焓	10
1.4.3 热容	10
1.5 理想气体的热力学	12
1.5.1 Joule 实验	12
1.5.2 理想气体的热容	13
1.5.3 理想气体的 ΔU 和 ΔH 的计算	14
1.5.4 理想气体的绝热可逆过程	14
1.6 热化学	15
1.6.1 反应进度	16
1.6.2 化学反应的热效应	17
1.6.3 热化学方程式	18
1.6.4 Hess 定律	19
1.6.5 几种热效应	20
1.6.6 Kirchhoff 定律	23

本章小结	
阅读材料	
拓展材料	
思考题	
习题	
第 2 章 热力学第二定律	
2.1 热力学第二定律的经典表述	
2.1.1 自发过程的共同特征	
2.1.2 热力学第二定律的经典表述	
2.2 热力学第二定律的熵表述	
2.2.1 Carnot 循环与 Carnot 定理	
2.2.2 熵的概念	
2.2.3 热力学第二定律的数学表达式	
2.2.4 熵增加原理和熵判据	
2.3 熵变的计算	3
2.3.1 理想气体单纯 p, V, T 变化过程的熵变	3
2.3.2 相变过程的熵变	4
2.3.3 热力学第三定律和化学变化过程的熵变	4
2.3.4 熵的统计意义	45
2.4 Helmholtz 自由能与 Gibbs 自由能	46
2.4.1 Helmholtz 自由能及判据	46
2.4.2 Gibbs 自由能及判据	47
2.4.3 热力学判据小结	48
2.5 热力学函数间的关系	48
2.5.1 热力学函数之间的关系	48
2.5.2 热力学基本方程	49
2.5.3 特征偏微商和 Maxwell 关系式	49
2.6 ΔG 的计算	51
2.6.1 单纯 p, V, T 变化过程中的 ΔG	51
2.6.2 相变过程中的 ΔG	53
2.6.3 化学变化过程中的 ΔG	55
2.7 Gibbs 自由能变随温度及压力的变化	57
2.7.1 Gibbs 自由能变与温度的关系	57
2.7.2 Gibbs 自由能变与压力的关系	58
* 2.8 不可逆过程热力学简介	59
2.8.1 熵产生和熵流	60
2.8.2 熵与生命	60
本章小结	61

3

4.1.2 相律	95
4.2 单组分系统相图及其应用	97
4.2.1 Clapeyron 方程	97
4.2.2 水的相图	99
4.2.3 超临界流体及其应用	100
4.3 二组分双液系统相图及其应用	102
4.3.1 理想的完全互溶双液系统的相图	102
4.3.2 非理想的完全互溶双液系统的相图	105
*4.3.3 部分互溶双液系统的相图	107
*4.3.4 完全不互溶双液系统的相图	108
4.4 二组分固液系统相图及其应用	109
本章小结	110
阅读材料	111
拓展材料	112
思考题	112
习题	114
第 5 章 化学平衡	116
5.1 化学反应的方向和限度	117
5.2 化学反应等温式与平衡常数	118
5.2.1 平衡常数	118
5.2.2 平衡常数的表达式	120
5.2.3 平衡常数与反应方程式写法的关系	125
5.3 平衡常数的测定和计算	126
5.3.1 平衡常数的测定	126
5.3.2 平衡常数的计算	126
5.4 温度对平衡常数的影响	128
5.5 生化反应的标准态和平衡常数	130
5.6 耦合反应	131
本章小结	132
拓展材料	133
思考题	133
习题	133
第 6 章 电解质溶液	136
6.1 电解质溶液的导电性质	136
6.1.1 电解质溶液的导电机理	136
6.1.2 Faraday 电解定律	138
6.2 离子的电迁移	139
6.2.1 离子的淌度	139

6.2.2 离子的迁移数	139
6.2.3 离子迁移数的测定	140
6.3 电导及其应用	142
6.3.1 电导、电导率及摩尔电导率	142
6.3.2 电导率、摩尔电导率与浓度的关系	144
6.3.3 离子独立运动定律和离子摩尔电导率	145
6.3.4 电导测定的应用	147
6.4 离子的平均活度和活度因子	150
6.4.1 强电解质的离子平均活度和平均活度因子	150
6.4.2 影响离子平均活度因子的因素	152
6.5 强电解质溶液理论简介	154
*6.5.1 强电解质溶液的离子互吸理论	154
6.5.2 Debye-Hückel 极限公式	155
6.5.3 Debye-Hückel-Onsager 电导公式	156
本章小结	158
阅读材料	158
拓展材料	159
思考题	160
习题	160
第7章 电化学	162
7.1 可逆电池和电池符号	163
7.1.1 可逆电池	163
7.1.2 电池符号	164
7.1.3 可逆电极的类型	164
7.1.4 可逆电池电动势测定	166
7.2 可逆电池的热力学	167
7.2.1 由电动势及其温度系数求热力学函数的变化值	167
7.2.2 由标准电动势 E^\ominus 求标准平衡常数 K^\ominus	169
7.3 电极电势和电池电动势	170
7.3.1 电池电动势产生的原理	170
7.3.2 Nernst 方程式	172
7.3.3 电池电动势的计算	175
7.4 浓差电池	176
7.5 电池电动势测定的应用	177
7.5.1 判断化学反应的方向	177
7.5.2 计算难溶盐的溶度积	178
7.5.3 离子平均活度因子 γ_\pm 的测定	179
7.5.4 pH 的测定	180

7.5.5 电池电动势测定在生物系统中的应用	181
7.6 分解电压	182
7.6.1 基本概念	182
7.6.2 分解电压的测定	183
7.6.3 理论分解电压的计算	184
7.7 极化与超电势	184
7.7.1 极化	184
7.7.2 极化曲线	185
7.7.3 超电势的测定	186
7.7.4 氢超电势	186
7.7.5 Tafel 公式	187
7.7.6 氢超电势的理论解释	187
7.8 电解时电极上的反应	188
7.8.1 析出电势与金属离子的分离	188
7.8.2 电解的应用	190
7.8.3 金属的电化学腐蚀和防腐	191
*7.9 生物电化学	192
7.9.1 生物膜模拟	193
7.9.2 电化学控释药物	193
7.9.3 在体电化学	193
7.9.4 电化学生物传感器	194
7.10 化学电源	195
7.10.1 概述	195
7.10.2 常见电池	197
本章小结	200
阅读材料	201
拓展材料	203
思考题	203
习题	204
第 8 章 化学动力学基础	207
8.1 化学反应的速率及速率方程	208
8.1.1 化学反应速率的定义	208
8.1.2 基元反应和非基元反应	209
8.1.3 反应级数和反应分子数	210
8.1.4 反应速率常数	211
8.1.5 反应速率的测定	211
8.2 简单级数反应动力学方程	211
8.2.1 零级反应	212

8.2.2	一级反应	212
8.2.3	二级反应	214
8.2.4	三级反应	216
8.2.5	反应级数的测定法	217
8.3	温度对反应速率的影响	219
8.3.1	Arrhenius 公式	220
8.3.2	基元反应的活化能	221
8.3.3	复合反应的活化能——表观活化能	222
8.4	典型的复合反应	223
8.4.1	对峙反应	223
8.4.2	平行反应	224
8.4.3	连串反应	225
8.4.4	链反应	226
8.5	复合反应的近似处理	227
8.5.1	控速步骤法	227
8.5.2	平衡态近似法	228
8.5.3	稳态近似法	228
8.6	化学反应速率理论	230
8.6.1	碰撞理论	230
8.6.2	过渡态理论	232
8.7	特殊反应的动力学分析	234
8.7.1	溶液中的反应	234
8.7.2	催化反应	236
8.7.3	光化学反应	240
*8.8	现代化学动力学研究技术	242
8.8.1	化学弛豫法	242
8.8.2	闪光光解法	243
8.8.3	交叉分子束技术	243
	本章小结	244
	阅读材料	245
	拓展材料	246
	思考题	246
	习题	247
第 9 章	表面物理化学	250
9.1	表面 Gibbs 自由能与表面张力	251
9.1.1	分散度和比表面	251
9.1.2	表面 Gibbs 自由能	252
9.1.3	表面张力	253

9.2 弯曲液面上的附加压力和蒸气压	255
9.2.1 弯曲液面上的附加压力	255
9.2.2 弯曲液面上的蒸气压	258
9.2.3 亚稳态	260
9.3 溶液表面的吸附	260
9.3.1 溶液的表面张力与溶液浓度的关系	260
9.3.2 溶液的表面吸附——Gibbs 吸附等温式	261
9.3.3 表面活性剂分子在溶液表面的定向排列	263
*9.4 表面膜	264
9.4.1 单分子表面膜——不溶性表面膜	264
9.4.2 表面压及其测定	265
9.4.3 表面膜的应用	266
9.5 液-固界面现象——润湿作用	267
9.5.1 润湿现象	267
9.5.2 接触角与润湿方程	268
9.6 表面活性剂及其作用	270
9.6.1 表面活性剂的结构特点与分类	270
9.6.2 表面活性剂的主要性能参数	271
9.6.3 表面活性剂的一些重要作用及应用	274
9.7 乳状液	277
9.7.1 乳状液的类型及其鉴别	277
9.7.2 乳状液的稳定性和乳化作用	277
9.7.3 乳状液的制备	279
9.7.4 乳状液的转型与破坏	280
9.7.5 乳状液的应用	281
9.7.6 微乳状液	281
9.8 固体表面的吸附作用	282
9.8.1 固体表面对气体的吸附作用	283
9.8.2 固体在溶液中的吸附	290
9.9 气-固表面的催化作用	293
本章小结	294
阅读材料	296
拓展材料	297
思考题	297
习题	298
第 10 章 胶体化学	301
10.1 分散系统	302
10.2 溶胶	303

10.2.1	溶胶的基本特性	303
10.2.2	溶胶的制备	304
10.2.3	溶胶的净化	306
10.2.4	胶团的结构	307
10.3	溶胶的光学性质	308
10.3.1	Tyndall 效应	308
10.3.2	Rayleigh 光散射公式	309
10.3.3	超显微镜的基本原理	310
10.4	溶胶的动力学性质	311
10.4.1	Brown 运动	311
10.4.2	扩散	312
10.4.3	沉降与沉降平衡	314
10.5	溶胶的电学性质	317
10.5.1	电动现象	317
10.5.2	双电层理论和电动电势 ζ	319
10.6	溶胶的稳定性与聚沉	321
10.6.1	溶胶的稳定性	321
10.6.2	影响溶胶聚沉的因素	322
10.7	高分子溶液	324
10.7.1	高分子溶液与溶胶的异同	324
*10.7.2	高分子化合物的平均相对分子质量	325
*10.7.3	高分子溶液的性质	328
10.7.4	Donnan 平衡	331
10.8	凝胶	334
10.8.1	凝胶的分类	334
10.8.2	凝胶的性质	335
*10.9	纳米粒子	336
10.9.1	纳米技术的发展	336
10.9.2	纳米材料的特性	337
10.9.3	纳米技术在生命科学中的应用	337
	本章小结	338
	阅读材料	339
	拓展材料	340
	思考题	340
	习题	341
	参考文献	344
	附录	347
	参考答案	360

国家自然科学基金资助项目批准通知

(预算制项目)

贾金亮 先生/女士:

根据《国家自然科学基金条例》、相关项目管理办法规定和专家评审意见,国家自然科学基金委员会(以下简称自然科学基金委)决定资助您申请的项目。项目批准号: 32572864, 项目名称: 向香蕉球茎积累的纳米咯菌腈递送载体构建及靶向传导机制, 直接费用: 50.00万元, 项目起止年月: 2026年01月至 2029年12月, 有关项目的评审意见及修改意见附后。

请您尽快登录科学基金网络信息系统(<https://grants.nsfc.gov.cn>), **认真阅读《国家自然科学基金资助项目计划书填报说明》并按要求填写《国家自然科学基金资助项目计划书》(以下简称计划书)**。对于有修改意见的项目,请您按修改意见及时调整计划书相关内容;如您对修改意见有异议,须在电子版计划书报送截止日期前向相关科学处提出。

请您将电子版计划书通过科学基金网络信息系统(<https://grants.nsfc.gov.cn>)提交,由依托单位审核后提交至自然科学基金委。自然科学基金委审核未通过者,将退回的电子版计划书修改后再行提交;审核通过者,打印纸质版计划书(一式两份,双面打印)并在项目负责人承诺栏签字,由依托单位科研、财务管理等部门审核、签章并在承诺栏加盖依托单位公章,且将申请书纸质签字盖章页订在其中一份计划书之后,一并报送至自然科学基金委项目材料接收工作组。纸质版计划书应当保证与审核通过的电子版计划书内容一致。**自然科学基金委将对申请书纸质签字盖章页进行审核,对存在问题的,允许依托单位进行一次修改或补齐。**

向自然科学基金委提交电子版计划书、报送纸质版计划书并补交申请书纸质签字盖章页截止时间节点如下:

1. **2025年9月5日16点:** 提交电子版计划书的截止时间;
2. **2025年9月12日16点:** 提交修改后电子版计划书的截止时间;
3. **2025年9月23日:** 报送纸质版计划书(一式两份,其中一份包含申请书纸质签字盖章页)的截止时间。
4. **2025年10月9日:** 报送修改后的申请书纸质签字盖章页的截止时间。

请按照以上规定及时提交电子版计划书，并报送纸质版计划书和申请书纸质签字盖章页，逾期不报计划书或申请书纸质签字盖章页且未说明理由的，视为自动放弃接受资助；未按要求修改或逾期提交申请书纸质签字盖章页者，将视情况给予暂缓拨付经费等处理。

附件：项目评审意见及修改意见表

国家自然科学基金委员会
2025年8月27日

验收项目结论及经费处理意见

序号	项目类型	项目名称	项目编号	项目负责人	承担单位	验收结论	经费处理意见	备注
1	区域联合基金-青年基金项目	复杂氧化物薄膜中氧缺陷分布的原位中子散射研究	2022A1515110596	曹磊	北京大学深圳研究生院	通过	结余经费由项目承担单位统筹安排用于后续科研活动的直接支出	
2	区域联合基金-青年基金项目	基于4D-STEM电镜技术的锂离子电池正极材料的结构演变与失效机理研究	2022A1515110816	杨婷婷	北京大学深圳研究生院	通过	结余经费由项目承担单位统筹安排用于后续科研活动的直接支出	
3	区域联合基金-青年基金项目	不同退化程度草地土壤细菌多样性对氮添加的响应及机制研究	2020A1515110110	董程程	北京大学深圳研究生院	结题	收回项目经费1.79万元	
4	区域联合基金-粤港澳研究团队项目	高性能层状锂电池正极材料结构与性能研究	2021B1515130002	潘锋	北京大学深圳研究生院	通过	结余经费由项目承担单位统筹安排用于后续科研活动的直接支出	
5	区域联合基金-重点项目	基于中子表征技术的电化学材料机理与性能研究	2022B1515120070	肖萌果	北京大学深圳研究生院	通过	结余经费由项目承担单位统筹安排用于后续科研活动的直接支出	
6	区域联合基金-青年基金项目	基于“圈-点-柱”理论在颞关节翻修术中应用颞臼牵伸技术重建慢性骨盆不连续的生物力学研究	2021A1515110726	周振春	北京大学深圳医院	通过	结余经费由项目承担单位统筹安排用于后续科研活动的直接支出	
7	省企联合基金-面上项目	肠道菌色氨酸代谢异常在2型糖尿病中的作用及其机制研究	2021A1515220012	彭佼	北京大学深圳医院	通过	结余经费由项目承担单位统筹安排用于后续科研活动的直接支出	
8	省企联合基金-面上项目	CCDC3通过WNT/ β -Catenin信号通路促进卵巢癌上皮间质转化及网膜转移的机制研究	2021A1515220143	王芬	北京大学深圳医院	通过	结余经费由项目承担单位统筹安排用于后续科研活动的直接支出	
9	区域联合基金-青年基金项目	应用热邻近共聚-质谱(TPCA-MS)技术探究宿主关键因子对SARS-CoV-2呼吸道感染性的影响及其作用机制	2022A1515110537	赵克力	北京大学深圳医院	通过	结余经费由项目承担单位统筹安排用于后续科研活动的直接支出	
10	区域联合基金-青年基金项目	m6A甲基化调控口腔颌面部骨肉瘤外泌体介导的骨破坏及机制研究	2022A1515111114	罗婷婷	北京大学深圳医院	通过	结余经费由项目承担单位统筹安排用于后续科研活动的直接支出	
11	区域联合基金-青年基金项目	CAFs亚群对非小细胞肺癌新辅助免疫治疗疗效的影响及其机制研究	2022A1515111138	陈超	北京大学深圳医院	通过	结余经费由项目承担单位统筹安排用于后续科研活动的直接支出	
12	省企联合基金-面上项目	纳米囊泡药物载体系统的构建及其在结直肠癌靶向治疗的应用研究	2022A1515220062	穆婧	北京大学深圳医院	通过	结余经费由项目承担单位统筹安排用于后续科研活动的直接支出	
13	省企联合基金-面上项目	空间取向梯度结构脱细胞SIS-丝蛋白凝胶体系的构建及其免疫调节节自噬细胞诱导关节骨软骨一体修复及机制研究	2022A1515220079	毛智南	北京大学深圳医院	通过	结余经费由项目承担单位统筹安排用于后续科研活动的直接支出	
14	省企联合基金-面上项目	小檗碱/软骨细胞/磷酸修饰甲基丙烯酸酯化壳聚糖可注射水凝胶新型仿生材料通过SIRT1/BMP信号通路修复软骨缺损的应用研究	2022A1515220111	于斐	北京大学深圳医院	通过	结余经费由项目承担单位统筹安排用于后续科研活动的直接支出	
15	省企联合基金-面上项目	仿生杂合纳米药物通过抗炎和促进软骨再生治疗OA的研究	2022A1515220165	刘朋	北京大学深圳医院	通过	结余经费由项目承担单位统筹安排用于后续科研活动的直接支出	
16	省企联合基金-面上项目	外泌体功能化的纳米水凝胶支架原位诱导促进腱骨愈合	2022A1515220168	张新涛	北京大学深圳医院	通过	结余经费由项目承担单位统筹安排用于后续科研活动的直接支出	
17	省企联合基金-面上项目	DEFB119激活精子CCR6/CatSper1在人类不明原因不孕症中的作用及机制研究	2022A1515220214	李晓峰	北京大学深圳医院	通过	结余经费由项目承担单位统筹安排用于后续科研活动的直接支出	
18	广东省自然科学基金-面上项目	CYP19A1调控前列腺间质成纤维细胞活化参与BPH进展的机制研究	2023A1515010128	李森茂	北京大学深圳医院	通过	结余经费由项目承担单位统筹安排用于后续科研活动的直接支出	
19	广东省自然科学基金-面上项目	近红外纳米光遗传系统的构建用于光控基因编辑及肿瘤动力学协同治疗	2023A1515012658	穆婧	北京大学深圳医院	通过	结余经费由项目承担单位统筹安排用于后续科研活动的直接支出	
20	区域联合基金-重点项目	多孔医用镁合金激光选区熔化增材制造关键技术及骨修复应用基础研究	2022B1515120046	曾晖	北京大学深圳医院	通过	结余经费由项目承担单位统筹安排用于后续科研活动的直接支出	
21	区域联合基金-青年基金项目	面向航空发动机叶片全生命周期的CST曲面参数化方法研究	2022A1515110055	成金鑫	北京科技大学顺德创新学院	通过	结余经费由项目承担单位统筹安排用于后续科研活动的直接支出	
22	区域联合基金-青年基金项目	高端轴承钢微缺陷控制下疲劳寿命的智能预测	2022A1515110062	顾超	北京科技大学顺德创新学院	通过	结余经费由项目承担单位统筹安排用于后续科研活动的直接支出	
23	区域联合基金-青年基金项目	面向可见光通信定位一体化系统的无资源竞争NOMA技术研究	2022A1515110154	金建力	北京科技大学顺德创新学院	通过	结余经费由项目承担单位统筹安排用于后续科研活动的直接支出	
24	区域联合基金-青年基金项目	薄膜光伏水流面的热电特性与综合节能潜力研究	2022A1515110180	柳文洁	北京科技大学顺德创新学院	通过	结余经费由项目承担单位统筹安排用于后续科研活动的直接支出	
25	区域联合基金-青年基金项目	物理模型融合工业视频的非牛顿流体仿真关键技术研究	2022A1515110350	张雅娴	北京科技大学顺德创新学院	通过	结余经费由项目承担单位统筹安排用于后续科研活动的直接支出	
26	区域联合基金-青年基金项目	注射成形TiAl合金置氧烧结细化片层组织机理	2022A1515110406	张策	北京科技大学顺德创新学院	通过	结余经费由项目承担单位统筹安排用于后续科研活动的直接支出	
27	区域联合基金-青年基金项目	基于非稳态温度场的油气水多相流流动参数反演理论与方法	2022A1515110588	郭伟	北京科技大学顺德创新学院	通过	结余经费由项目承担单位统筹安排用于后续科研活动的直接支出	
28	区域联合基金-青年基金项目	太阳能光/热耦合驱动CO ₂ 燃料转化过程质-能作用机理	2022A1515110597	方娟	北京科技大学顺德创新学院	通过	结余经费由项目承担单位统筹安排用于后续科研活动的直接支出	
29	区域联合基金-青年基金项目	基于可见光传输的传感能一体化技术及应用研究	2022A1515110770	陈丹阳	北京科技大学顺德创新学院	通过	结余经费由项目承担单位统筹安排用于后续科研活动的直接支出	
30	区域联合基金-青年基金项目	人工湿地植物根系泌氧和分泌物耦合调控反硝化过程的机制研究	2022A1515110943	孙海曙	北京科技大学顺德创新学院	通过	结余经费由项目承担单位统筹安排用于后续科研活动的直接支出	
31	区域联合基金-青年基金项目	n型碲化铋基热电材料的性能增强机理研究	2022A1515111100	裴俊	北京科技大学顺德创新学院	通过	结余经费由项目承担单位统筹安排用于后续科研活动的直接支出	
32	区域联合基金-地区培育项目	高温球磨磨形HDH钛粉激光熔凝过程中纳米尺度非均质结构的形成及其强化机理	2022A1515140006	徐伟	北京科技大学顺德创新学院	通过	结余经费由项目承担单位统筹安排用于后续科研活动的直接支出	
33	区域联合基金-地区培育项目	高效率蓝色钙钛矿量子点电致发光器件的研究	2022A1515140007	田建军	北京科技大学顺德创新学院	通过	结余经费由项目承担单位统筹安排用于后续科研活动的直接支出	
34	区域联合基金-地区培育项目	用于电催化氮氧化物还原制备氨的钌基金属间化合物催化剂	2022A1515140051	鲁启鹏	北京科技大学顺德创新学院	通过	结余经费由项目承担单位统筹安排用于后续科研活动的直接支出	
35	区域联合基金-地区培育项目	基于毫米波雷达的无扰式智能生命体征检测方法研究	2022A1515140109	肖文栋	北京科技大学顺德创新学院	通过	结余经费由项目承担单位统筹安排用于后续科研活动的直接支出	
36	海上风电联合基金-面上项目	超高压海缆聚烯烃绝缘交/直流电场调控理论和方法	2022A1515240005	查俊伟	北京科技大学顺德创新学院	通过	结余经费由项目承担单位统筹安排用于后续科研活动的直接支出	

序号	项目类型	项目名称	项目编号	项目负责人	承担单位	验收结论	经费处理意见	备注
928	广东省自然科学基金-面上项目	CYP1A1介导T-2毒素肝脏毒性的分子机制研究	2023A1515010155	蒋珺	华南农业大学	通过	结余经费由项目承担单位统筹安排用于后续科研活动的直接支出	
929	广东省自然科学基金-面上项目	E3泛素连接酶COP1介导光信号调控植物响应水淹胁迫的作用机理	2023A1515010263	谢丽娟	华南农业大学	通过	结余经费由项目承担单位统筹安排用于后续科研活动的直接支出	
930	广东省自然科学基金-面上项目	LncRNA XR-961150.1竞争miRNA-1402-X介导小菜蛾多酚氧化酶PPO1基因表达的分子机制	2023A1515010305	许小霞	华南农业大学	通过	结余经费由项目承担单位统筹安排用于后续科研活动的直接支出	
931	广东省自然科学基金-面上项目	Mxene量子点耦合分子印迹纳米材料的比率荧光传感特性及组胺可视化检测	2023A1515010338	徐小艳	华南农业大学	通过	结余经费由项目承担单位统筹安排用于后续科研活动的直接支出	
932	广东省自然科学基金-面上项目	LncRNA TAB2-AS促进TAB2基因转录影响母猪初情启动的机制研究	2023A1515010364	张豪	华南农业大学	通过	结余经费由项目承担单位统筹安排用于后续科研活动的直接支出	
933	广东省自然科学基金-面上项目	PemiR_N31参与毛竹速生分子机理解析	2023A1515010379	王凯利	华南农业大学	通过	结余经费由项目承担单位统筹安排用于后续科研活动的直接支出	
934	广东省自然科学基金-面上项目	RNA结合蛋白IGF2BP2对猪肌肉脂肪沉积的作用及转录后调控机制	2023A1515010408	吴睿帆	华南农业大学	通过	结余经费由项目承担单位统筹安排用于后续科研活动的直接支出	
935	广东省自然科学基金-面上项目	OsACL5在水稻籽粒大小调控上的作用机制研究	2023A1515010439	刘太波	华南农业大学	通过	结余经费由项目承担单位统筹安排用于后续科研活动的直接支出	
936	广东省自然科学基金-面上项目	SlARF4调控番茄果实转色的分子机理研究	2023A1515010497	关红玲	华南农业大学	通过	结余经费由项目承担单位统筹安排用于后续科研活动的直接支出	
937	广东省自然科学基金-面上项目	WRKY35转录因子在菜心糖合成代谢中的调控作用研究	2023A1515010505	钟琨	华南农业大学	通过	结余经费由项目承担单位统筹安排用于后续科研活动的直接支出	
938	广东省自然科学基金-面上项目	m6A甲基转移酶METTL3修饰lncRNA RBM39调控ALV-J促进EMT发生的分子机制	2023A1515010584	张新珩	华南农业大学	通过	结余经费由项目承担单位统筹安排用于后续科研活动的直接支出	
939	广东省自然科学基金-面上项目	γ-氨基丁酸介导米咯菌腈对香蕉枯萎病的靶向治疗	2023A1515010609	贾金亮	华南农业大学	通过	结余经费由项目承担单位统筹安排用于后续科研活动的直接支出	
940	广东省自然科学基金-面上项目	保护性耕作影响水稻秸秆向稻田有机碳转移的机制研究	2023A1515010738	祁剑英	华南农业大学	通过	结余经费由项目承担单位统筹安排用于后续科研活动的直接支出	
941	广东省自然科学基金-面上项目	光信号核心转录因子介导CsAN1调控茶树花青素合成研究	2023A1515010786	孙彬妹	华南农业大学	通过	结余经费由项目承担单位统筹安排用于后续科研活动的直接支出	
942	广东省自然科学基金-面上项目	农地确权政策如何影响政治信任？——基于基层自治组织信任的分析	2023A1515010881	胡新艳	华南农业大学	通过	结余经费由项目承担单位统筹安排用于后续科研活动的直接支出	
943	广东省自然科学基金-面上项目	呕吐毒素抑制γ-氨基丁酸信号通路促进肠道炎症的发生机制	2023A1515011044	林如琴	华南农业大学	通过	结余经费由项目承担单位统筹安排用于后续科研活动的直接支出	
944	广东省自然科学基金-面上项目	基于TLR4/NF-κB通路解析果胶寡糖缓释脂多糖引起肉鸡肠道炎症性损伤的分子机制	2023A1515011112	王伟唯	华南农业大学	通过	结余经费由项目承担单位统筹安排用于后续科研活动的直接支出	
945	广东省自然科学基金-面上项目	基于三种UMs研究槲花酸改善高脂饮食诱导小鼠非酒精性脂肪肝的差异作用及机制	2023A1515011151	杨瑞丽	华南农业大学	通过	结余经费由项目承担单位统筹安排用于后续科研活动的直接支出	
946	广东省自然科学基金-面上项目	基于区块链的数据访问控制和安全共享研究	2023A1515011194	肖媚燕	华南农业大学	通过	结余经费由项目承担单位统筹安排用于后续科研活动的直接支出	
947	广东省自然科学基金-面上项目	基于多耐药铜绿假单胞菌噬菌体耐受遗传代谢特征进行联合治疗佐剂分子的筛选	2023A1515011239	孙永学	华南农业大学	通过	结余经费由项目承担单位统筹安排用于后续科研活动的直接支出	
948	广东省自然科学基金-面上项目	基于大数据赋能的农业企业组织韧性提升机制及对策研究	2023A1515011263	林家宝	华南农业大学	通过	结余经费由项目承担单位统筹安排用于后续科研活动的直接支出	
949	广东省自然科学基金-面上项目	基于机器学习探究生物炭耦合过硫酸盐技术用于土壤有机污染原位修复的潜能	2023A1515011353	银仁莉	华南农业大学	通过	结余经费由项目承担单位统筹安排用于后续科研活动的直接支出	
950	广东省自然科学基金-面上项目	天然高效成分HXT对埃及伊蚊中肠的作用靶点和机制	2023A1515011625	黄继光	华南农业大学	通过	结余经费由项目承担单位统筹安排用于后续科研活动的直接支出	
951	广东省自然科学基金-面上项目	外泌体RNA传递介导的家蚕抗病毒免疫功能研究	2023A1515011658	张以农	华南农业大学	通过	结余经费由项目承担单位统筹安排用于后续科研活动的直接支出	
952	广东省自然科学基金-面上项目	弓形虫调控血脑屏障介导狂犬病暴露后治疗的新机制	2023A1515011795	袁子国	华南农业大学	通过	结余经费由项目承担单位统筹安排用于后续科研活动的直接支出	
953	广东省自然科学基金-面上项目	核受体NR1F的分子功能及对寄生线虫发育的调节作用	2023A1515011964	元冬娟	华南农业大学	通过	结余经费由项目承担单位统筹安排用于后续科研活动的直接支出	
954	广东省自然科学基金-面上项目	核糖体冬眠状态脑微罗诺杆菌毒力维持及巨噬细胞逃逸的分子机制	2023A1515011965	赵力超	华南农业大学	通过	结余经费由项目承担单位统筹安排用于后续科研活动的直接支出	
955	广东省自然科学基金-面上项目	杂原子掺杂杂对氧化硼基质-碳点余辉能量传递的调控机理研究	2023A1515012003	胡超凡	华南农业大学	通过	结余经费由项目承担单位统筹安排用于后续科研活动的直接支出	
956	广东省自然科学基金-面上项目	水稻条纹花叶病毒对水稻抽穗的影响及其形成症状的分子机理	2023A1515012030	陈思平	华南农业大学	通过	结余经费由项目承担单位统筹安排用于后续科研活动的直接支出	
957	广东省自然科学基金-面上项目	水稻OsUGT75A调控胚芽鞘耐淹生长的分子机制研究	2023A1515012052	赵佳	华南农业大学	通过	结余经费由项目承担单位统筹安排用于后续科研活动的直接支出	
958	广东省自然科学基金-面上项目	水稻OsNAC3基因调控种子萌发和幼苗建成的分子机制研究	2023A1515012092	何永奇	华南农业大学	通过	结余经费由项目承担单位统筹安排用于后续科研活动的直接支出	
959	广东省自然科学基金-面上项目	热-湿-力多场耦合控制的木材压缩密实化路径及调控	2023A1515012119	涂登云	华南农业大学	通过	结余经费由项目承担单位统筹安排用于后续科研活动的直接支出	
960	广东省自然科学基金-面上项目	热带边缘季雨林树木非结构性碳对高降雨的响应及调控机制	2023A1515012129	莫其锋	华南农业大学	通过	结余经费由项目承担单位统筹安排用于后续科研活动的直接支出	
961	广东省自然科学基金-面上项目	濒危植物红椿变种亲缘关系与遗传保护研究	2023A1515012137	胡新生	华南农业大学	通过	结余经费由项目承担单位统筹安排用于后续科研活动的直接支出	
962	广东省自然科学基金-面上项目	大细小病毒NS2抑制宿主蛋白翻译的分子机制研究	2023A1515012171	周沛	华南农业大学	通过	结余经费由项目承担单位统筹安排用于后续科研活动的直接支出	
963	广东省自然科学基金-面上项目	细胞色素P450酶Cyp86调控甘蔗黑粉菌侵染致病机理研究	2023A1515012440	蔡恩平	华南农业大学	通过	结余经费由项目承担单位统筹安排用于后续科研活动的直接支出	
964	广东省自然科学基金-面上项目	苏云金芽孢杆菌Bt-1降解拟除虫菊酯农药的分子机制研究	2023A1515012552	陈少华	华南农业大学	通过	结余经费由项目承担单位统筹安排用于后续科研活动的直接支出	
965	广东省自然科学基金-面上项目	荔枝类甜蛋白代谢特点及分子机制研究	2023A1515012599	赵雷	华南农业大学	通过	结余经费由项目承担单位统筹安排用于后续科研活动的直接支出	

受理编号: c23140500002865

项目编号: 2023A1515010609

文件编号: 粤基金字(2023)2号

广东省基础与应用基础研究基金项目 任务书

项目名称: γ -氨基丁酸介导纳米咯菌腈对香蕉枯萎病的靶向治疗

项目类别: 广东省自然科学基金-面上项目

项目起止时间: 2023-01-01 至 2025-12-31

管理单位(甲方): 广东省基础与应用基础研究基金委员会

依托单位(乙方): 华南农业大学

通讯地址: 广东省广州市天河区五山路483号

邮政编码: 510642

单位电话: 020-85283435

项目负责人: 贾金亮

联系电话: 020-85280319



(广东科技微信公众号)



(查看任务书信息)



(受理纸质材料二维码)

广东省基础与应用基础研究
基金委员会
二〇二〇年制

五、人员信息

项目负责人

姓名	证件号码	年龄	性别	职称	学历	在项目中承担的任务	所在单位	签名
贾金亮	422431197908301013	44	男	副教授	博士研究生	项目负责人	华南农业大学	贾金亮

项目组主要成员

姓名	证件号码	年龄	性别	职称	学历	在项目中承担的任务	所在单位	签名
朱丽	422801197806200426	45	女	高级实验师	博士研究生	抑菌活性实验	华南农业大学	朱丽
肖春霞	513022199810017405	25	女	未取得	本科	转运机理研究	华南农业大学	肖春霞
何亮亨	44020219981030031X	25	男	未取得	本科	香蕉输导性实验	华南农业大学	何亮亨
赵宁	152321199702140328	26	女	未取得	本科	纳米载体合成	华南农业大学	赵宁

工作分工及财政经费分配

承担/参与单位名称 (盖章)	工作分工	省级财政科技资金分配 (万元)
华南农业大学	华南农业大学负责	10.00
	合计	10.00

八、本任务书签约各方

管理单位（甲方）：

广东省基础与应用基础研究基金委员会（盖章）



法定代表人（或法人代理）：

曾路

（签章）

2023 年 02 月 14 日

依托单位（乙方）： 华南农业大学

（盖章）

法定代表人（或法人代理）：

刘雅红

（签章）

联系人（项目主管）姓名： 倪慧群

（签章）

Email: kjcgxk@scau.edu.cn

电话： 020-85283435 / 15920301530

开户单位名称： 华南农业大学

开户银行名称： 广东广州工行五山支行

开户银行帐号： 3602002609000310520

2023 年 3 月 1 日

联系人（项目负责人）姓名： 贾金亮

（签名）

Email: jiajinliang@scau.edu.cn

电话： 020-85280319

2023 年 2 月 24 日

附件 3:

2019 年省级乡村振兴战略专项
-农业科技创新及推广项目
(广东省现代农业产业共性关键技术研发
创新团队)

(2019—2020 年)

创新团队名称: 农业纳米共性关键技术研发创新团队

岗位名称: 纳米导向农药的创制与应用

专家姓名: 贾金亮

依托单位(公章): 华南农业大学

依托单位法定代表人: 刘雅虹

编制日期: 2019 年 7 月 4 日

一、基本情况

填表说明:

1. 组织机构代码指企事业单位国家标准代码,无组织机构代码的单位填写“000000000”; 2. 单位名称、单位公章名称及单位开户名称必须一致,如有特殊情况,需说明理由。

承担单位

单位名称	华南农业大学		
单位性质	<input type="checkbox"/> 科研机构 <input checked="" type="checkbox"/> 高等院校 <input type="checkbox"/> 推广机构 <input type="checkbox"/> 企业 <input type="checkbox"/> 其他		
单位主管部门	广东省农业厅		
单位组织机构代码	124400004554165634		
单位法人代表姓名	刘雅虹		
单位开户名称	华南农业大学		
开户银行(全称)	广东广州工行五山支行		
银行账号	3602002609000310520		
单位所属地区	广州市	(州、市、县等)	天河区
电子邮箱	kjcgxk@scau.edu.cn		
通信地址	广东省广州市五山华南农业大学	联系电话	85283435
邮政编码	510642	传真号码	85281885
岗位负责人	姓名	贾金亮	
	身份证号码	422431197908301013	
	工作单位	华南农业大学	
	电话号码	020-852850319	手机号码 13642621810
	电子邮箱	jiajinliang@scau.edu.cn	邮政编码 510642
	通信地址	广东省广州市华南农业大学材料与能源学院	
联系人	姓名	周红军	
	电话号码		手机号码 13632246809
	传真号码		
	电子邮箱	hongjunzhou@163.com	

相关责任人

二、团队人员基本情况表

填表说明:	1. 职称分类: A、正高级 B、副高级 C、中级 D、初级 E、其他;							
	2. 人员分类代码: A、首席专家 B、岗位专家 C、站长 D、团队成员							
	3. 是否有工资性收入: 是 (否)							
序号	姓名	身份证号码	工作单位	功能研究室/试验站/推广站	技术职称	是否有工资性收入	人员分类	承担任务
1	贾金亮	422431197908301013	华南农业大学	功能研究室	B	有	B	纳米导向农药设计
2	朱丽	422801197806200426	华南农业大学	功能研究室	B	有	D	纳米制剂的配制
3	吴瀚翔	510132198608240014	华南农业大学	功能研究室	E	否	D	输导性评价
4	郑烽	330621199310115914	华南农业大学	功能研究室	E	否	D	纳米导向农药合成
5	胡鹏通	142727199505163537	华南农业大学	功能研究室	E	否	D	生物活性测定
6	叶旭	342531199705262514	华南农业大学	功能研究室	E	否	D	纳米载体合成
7								
8								
9								

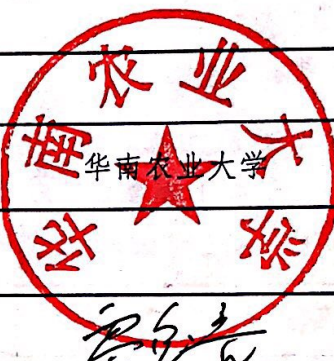
四、年度实施进度、任务内容与考核指标

实施进度	任务内容	考核指标
2019.7— 2019.12	高分子材料、无机材料与氨基酸、蛋白的偶联并进行性能表征,测定不同载体对阿维菌素、甲维盐、咯菌腈、多菌灵等的载药量、水合粒径和可控释放等性能,筛选出具有输导和积累功能的纳米载体,证实其对农药负载的普适性。参加中美华人纳米论坛。	1. 构建能够被靶标作物高效传递的纳米载体,合成具有导向功能的纳米农药1种,配制可田间使用的纳米农药悬浮剂型。
2020.1— 2020.6	优化合成工艺条件,考察不同类型表面活性剂对纳米悬浮剂型的影响,形成1套合成工艺简单的纳米导向载体制备关键技术。	2. 发表SCI论文1篇。

五、经费预算表

科目编码	预算科目名称	经费(万元)	计算依据
1	经费支出预算合计	7.5	总经费7.5万
2	(一)直接费用	7.125	按总经费95%计
3	1.设备费	0	无
4	2.材料费	3.0	主要为农药原药、化学试剂等
5	3.测试化验加工费	1.4	活性测定、材料表征分析
6	4.燃料动力费	0	无
7	5.差旅费	0.6	送样品、往返基地、会议等费用
8	6.会议费	0	无
9	7.出版/文献/信息传播/知识产权事务费	0.625	发表论文、申请专利及文献检索等

10	8. 劳务费	1.5	研究生和临工劳务费
11	9. 专家咨询费	0	无
12	(二) 间接费用	0.375	按总经费 5%计
13	1. 管理费	0.375	按总经费 5%计
合计		7.5	

六、补充内容及相关说明		
七、单位签章		
岗位依托单位	承担单位（公章）	
	负责人（签章）	
	岗位人员（签章）	
	签订日期	2019. 8. 10
	地址及邮编	广州市天河区五山路 483 号/510642
	电话及传真	020-85283435
	单位名称	华南农业大学
团队依托单位	首席专家所在单位（公章）	
	首席专家（签章）	
	签订日期	
	项目联系人	周红军
	地址和邮编	广州市海珠区仲恺路 501 号/510225
	电话及传真	020-36076118

附件 3:

2020 年省级乡村振兴战略专项
-农业科技创新及推广项目
(广东省现代农业产业共性关键技术研发
创新团队)

(2020—2024 年)

创新团队名称: 农业纳米共性关键技术研发创新团队
岗位名称: 纳米导向农药的创制与应用
专家姓名: 贾金亮
依托单位(公章): 华南农业大学
依托单位法定代表人: 刘雅红
编制日期: 2020 年 9 月 3 日

一、基本情况					
填表说明：		1. 组织机构代码指企事业单位国家标准代码，无组织机构代码的单位填写“000000000”；2. 单位名称、单位公章名称及单位开户名称必须一致，如有特殊情况，需说明理由。			
承担单位	单位名称	华南农业大学			
	单位性质	<input type="checkbox"/> 科研机构 <input checked="" type="checkbox"/> 高等院校 <input type="checkbox"/> 推广机构 <input type="checkbox"/> 企业 <input type="checkbox"/> 其他			
	单位主管部门	广东省农业厅			
	单位组织机构代码	124400004554165634			
	单位法人代表姓名	刘雅红			
	单位开户名称	华南农业大学			
	开户银行（全称）	广东广州工行五山支行			
	银行账号	3602002609000310520			
	单位所属地区	广州市	（州、市、县等）	天河区	
	电子邮箱	kjcgxk@scau.edu.cn			
	通信地址	广东省广州市五山华南农业大学	联系电话	85283435	
	邮政编码	510642	传真号码	85281885	
相关责任人	岗位负责人	姓名	贾金亮		
		身份证号码	422431197908301013		
		工作单位	华南农业大学		
		电话号码	020-852850319	手机号码	13642621810
		电子邮箱	jiajinliang@scau.edu.cn	邮政编码	510642
		通信地址	广东省广州市华南农业大学材料与能源学院		
	联系人	姓名	周红军		
		电话号码		手机号码	13632246809
		传真号码			
		电子邮箱	hongjunzhou@163.com		

二、团队人员基本情况表

填表说明:		1. 职称分类: A、正高级 B、副高级 C、中级 D、初级 E、其他;						
		2. 人员分类代码: A、首席专家 B、岗位专家 C、站长 D、团队成员						
		3. 是否有工资性收入: 是 (否)						
序号	姓名	身份证号码	工作单位	功能研究室/试验站/推广站	技术职称	是否有工资性收入	人员分类	承担任务
1	贾金亮	422431197908301013	华南农业大学	功能研究室	B	有	B	纳米导向农药设计
2	朱丽	422801197806200426	华南农业大学	功能研究室	B	有	D	纳米制剂的配制
3	吴瀚翔	510132198608240014	华南农业大学	功能研究室	E	否	D	输导性评价
4	胡鹏通	142727199505163537	华南农业大学	功能研究室	E	否	D	生物活性测定
5	叶旭	342531199705262514	华南农业大学	功能研究室	E	否	D	纳米载体合成
6	赵宁	152321199702140328	华南农业大学	功能研究室	E	否	D	靶向纳米农药合成
8								
9								

五、经费预算表			
科目编码	预算科目名称	经费（万元）	计算依据
1	经费支出预算合计	30	四年总经费 30 万（每年 7.5 万）
2	(一)直接费用	28.5	按总经费 95%计
3	1.设备费	0	无
4	2.材料费	12	主要为农药原药、化学试剂等
5	3.测试化验加工费	4.9	活性测定、材料表征分析
6	4.燃料动力费	0	无
7	5.差旅费	2.1	送样品、往返基地、会议等费用
8	6.会议费	0	无
9	7.出版/文献/信息传播/知识产权事务费	2	发表论文、申请专利及文献检索等
10	8.劳务费	7.5	研究生和临工劳务费
11	9.专家咨询费	0	无
12	(二)间接费用	1.5	按总经费 5%计
13	1.管理费	1.5	按总经费 5%计
合计		30	

六、补充内容及相关说明

七、单位签章

岗位依托单位	承担单位（公章）	华南农业大学
	负责人（签章）	刘建达
	岗位人员（签章）	李锐
	签订日期	2020.9.6
	地址及邮编	广州市天河区五山路 483 号/510642
	电话及传真	020-85283435
	单位名称	华南农业大学
团队依托单位	首席专家所在单位（公章）	仲恺农业工程学院
	首席专家（签章）	周红军
	签订日期	
	项目联系人	周红军
	地址和邮编	广州市海珠区仲恺路 501 号/510225
	电话及传真	020-36076118

广东省重点领域研发计划项目

子课题任务书

子课题名称：	高效纳米农药缓控释材料研发
所属课题	农业废弃物基缓控释农药剂型技术创新与集成
所属项目：	绿色高效农业投入品缓控释材料制备关键技术与应用
所属专项：	精准农业及生态绿色技术（农业农村污染防治）
课题承担单位：	华南农业大学
子课题承担单位：	华南农业大学
子课题负责人：	贾金亮
执行期限：	2022 年 7 月至 2025 年 7 月

课题基本信息表

子课题名称		高效纳米农药缓控释材料研发										
子课题编号		2023B0202080001-1-5										
所属课题		农业废弃物基缓控释农药剂型技术创新与集成										
所属项目		绿色高效农业投入品缓控释材料制备关键技术与应用										
所属专项		精准农业及生态绿色技术（农业农村污染防治）										
密级		■公开 □秘密 □机密		单位总数		1						
子课题类型		□基础前沿 □重大共性关键技术 ■应用示范研究 □其他										
子课题活动类型		□基础研究 ■应用研究 □试验发展										
子课题研究 所属学科		一级学科：化学工程与技术、材料与化工 二级学科：农业生物环境与能源工程										
子经费预算		总预算 30.00 万元，其中中央财政专项经费 30.00 万元										
子课题周期节点		起始时间		2022 年 07 月		结束时间		2025 年 07 月				
		实施周期		共 36 个月		预计中期时间点		2023 年 12 月				
子课题 承担 单位	单位名称		华南农业大学			单位性质		大专院校				
	单位所在地		广东省 广州市 天河区			组织机构代码		124400004554165634				
	通信地址		广东省广州市天河区五山路 483 号			邮政编码		510642				
	银行账号		3602002609000310520			法定代表人 姓名		薛红卫				
	单位开户 名称		华南农业大学									
	开户银行（全 称）		中国工商银行广州五山支行									
子课题 负责 人	姓 名		贾金亮		性 别		■男□女		出生日期		1979. 08.30	
	证件类型		身份证		证件号码		422431197908301013					
	所在单位		华南农业大学材料与能源学院									
	最高学位		☑博士 □硕士 □学士 □其他									
	职 称		□正高级 ☑副高级 □中级 □初级 □其他					职务		无		
	电子邮箱					移动电话						
子课题 参加人 数		2 人。其中：		高级职称 2 人，中级职称 0 人，初级职称 0 人，其他 0 人；								
				博士学位 2 人，硕士学位 0 人，学士学位 0 人，其他 0 人。								

八、经费预算

(一) 省财政科技资金分配金额: 30 万元。

(二) 省财政科技资金分期下达计划

第 1 期拨款: 18, 余款: 12 万元。

(三) 总经费及财政科技资金投入情况

子课题经费预算表

序号	预算科目名称	金额(万元)
1	一、省级财政科技资金	30.00
2	(一) 直接费用	27.30
3	1. 设备费	0.96
4	2. 材料费	15.96
5	3. 测试化验加工费	2.70
6	4. 燃料动力费	0.72
	5. 差旅费/会议费/国际合作交流费	2.40
	6. 出版/文献/信息传播/知识产权事务费	1.20
	7. 劳务费	2.88
	8. 专家咨询费	0.18
	9. 其他支出	0.30
7	(二) 间接费用	2.70
8	二、自筹经费	0.00
9	合计	30.00

注: 1. 甲方根据省科技厅年度拨款计划安排, 按照经费分配比例, 分批次及时将实到经费的相应部分拨付给乙方。

2. 项目经费全部根据预算按比例下拨, 未预留公共支出部分。因此, 项目考核、验收相关的专家评审、经费审计等公共事务支出, 将按照实际费用, 由各参与方按照所分配经费占总经费比例进行分摊。

3. 乙方如果同属项目管理单位(华南农业大学), 间接经费将全部用于管理费用等支出, 到账时由管理单位自动扣除。

任务书签署

甲乙双方根据有关文件规定，以及有关法律、政策和管理要求，依据项目立项通知，签署本任务书。

项目承担单位（甲方）：华南农业大学

法定代表人签字（签章）：薛红已



项目负责人签字（签章）：徐沛松

2023年10月10日

子课题承担单位（乙方）：华南农业大学

法定代表人签字（签章）：薛红已



2023年10月10日

子课题负责人签字（签章）：

费志亮

2023年10月10日

国家重点研发计划 子课题任务书

子课题名称： 纳米导向农药的减施增效技术集成与应用

子课题编号： 2018YFD020030401

子课题承担单位： 华南农业大学

子课题负责人： 贾金亮

所属课题：水稻农药与肥料协同增效减施区域性特色与共性关键技术

课题编号： 2018YFD0200304

课题承担单位： 华南农业大学

所属项目： 华南及西南水稻化肥农药减施技术集成研究与示范

项目编号： 2018YFD0200300

项目牵头承担单位： 华南农业大学

执行年限： 2018年7月-2020年12月

二〇一八年八月

为了确保国家重点研发计划“化学肥料和农药减施增效综合技术研发”项目“华南及西南水稻化肥农药减施技术集成研究与示范”(项目编号: 2018YFD0200300)顺利实施,课题牵头单位(华南农业大学)、课题承担单位(华南农业大学)与课题参加单位(华南农业大学)签订本子课题任务书。本任务书经过叁方平等协商,在真实、充分表达各自意愿的基础上,根据国家相关规定共同签署。叁方均表示,将共同恪守本任务书内容:课题承担单位按照任务书规定为课题参加单位划拨研究经费,课题参加单位按照任务书规定向课题承担单位提交研究成果。

课题承担单位与参加单位基本信息

课题承担单位: 华南农业大学

课题负责人: 徐汉虹

通讯地址: 广东省广州市天河区五山路 483 号 邮政编码: 510642

电话: 020-85285127 手机: 13802922918

电子信箱: hhxu@scau.edu.cn

开户名称: 102581000546中国工商银行股份有限公司广州五山支行

账 号: 3602002609000310520

税 号: 124400004554165634

课题参加单位: 华南农业大学

子课题负责人: 贾金亮

联系人: 贾金亮

通讯地址: 广东省广州市天河区五山路 483 号 邮政编码: 510642

电话: 020-85280319 手机: 13642621810

电子信箱: jiajinliang@scau.edu.cn

开户银行: 广州工行五山支行

账 号: 3602002609000310520

四、研究内容经费来源与支出预算

单位：万元(保留两位小数)

序号	预算科目名称	合计	专项经费	自筹经费
1	一、经费支出	17.79	17.79	0.00
2	(一) 直接经费	17.79	17.79	0.00
3	1. 设备费	2.00	2.00	0.00
4	(1) 购置设备费	2.00	2.00	0.00
5	(2) 试制设备费	0.00	0.00	0.00
6	(3) 设备改造费	0.00	0.00	0.00
7	(4) 设备租赁费	0.00	0.00	0.00
8	2. 材料费	7.10	7.10	0.00
9	3. 测试化验加工费	2.00	2.00	0.00
10	4. 燃料动力费	0.00	0.00	0.00
11	5. 差旅费/会议/国际合作与交流费	1.00	1.00	0.00
12	6. 出版/文献/信息传播/知识产权事务费	1.00	1.00	0.00
13	7. 劳务费	2.00	2.00	0.00
14	8. 专家咨询费	0.00	0.00	0.00
15	9. 其他支出	0.00	0.00	0.00
16	(二) 间接经费	1.79	1.79	0.00
	绩效	0.90	0.90	0.00
17	二、经费来源			
18	(一) 中央财政资金	17.79	17.79	0.00
19	(二) 其他来源资金	0.00	0.00	0.00
20	1、地方财政拨款	0.00	0.00	0.00
21	2、单位自有货币资金	0.00	0.00	0.00
22	3、其他资金	0.00	0.00	0.00
	其中，绩效支出	0.00	0.00	0.00

课题参加单位的经费使用应严格按照国家重点研发计划项目经费使用管理办法及课题任务书要求执行，不得挪做他用。

五、参加单位及主要研究人员

子课题承担单位：华南农业大学

子课题负责人

姓 名	性别	年龄	职务职称	业务专业	为本课题工作 时间(月)	所在单位
贾金亮	男	39	副教授	材料化学	24	材料与能源学院

主要研究人员

朱丽	女	40	高级实验师	配位化学	20	材料与能源学院
郑烽	男	25	硕士生	植物保护	24	材料与能源学院
胡鹏通	男	23	硕士生	植物保护	24	材料与能源学院

六、子课题任务书签署

项目牵头承担单位：华南农业大学（公章）

项目负责人（签字）：

徐海占

2018年8月18日

课题承担单位：华南农业大学（公章）

课题负责人（签字）：

徐海占

2018年8月18日

子课题承担单位：华南农业大学（公章）

子课题负责人（签字）：

梁晓

华南农业大学“创新强校工程”

自主创新能力提升类项目

合 同 书

(科研项目类)

项目名称： L-半胱氨酸介导鱼藤酮的输导机理及可视化研究

项目类别： 青年创新人才项目

项目子类别：

项目负责人： 贾金亮

承担单位： 华南农业大学材料与能源学院

项目起止时间： 2015 年 1 月至 2016 年 12 月

填表日期： 2015 年 3 月 25 日

华南农业大学科技处


二〇一五年制

共计：5 人。其中高级职称 3 人；中级职称 1 人；博士研究生 3 人；硕士研究生 1 人。

姓 名	性 别	年 龄	学 历	职 称	研究方向	任务分工	所在单位	签 名
贾金亮	男	36	博士	副高级	纳米生物材料	项目负责人	华南农业大 学材料与能 源学院	
周武艺	男	39	博 士	正高级	纳米生物材 料和纳米纤 维薄膜材料	纳米金偶合物 的结构解析	华南农业大 学材料与能 源学院	
朱 丽	女	37	硕 士	高级实 验师	无机生物材 料	细胞毒性及摄 入机理研究	华南农业大 学材料与能 源学院	
宋高鹏	男	35	博 士	中级	药物有机化 学	不同有机配体 的合成	华南农业大 学材料与能 源学院	
刘庆乐	男	26	学 士	初级及 以下	纳米金功能 材料	纳米金簇粒子 的合成	华南农业大 学农学院	

主要
参加
人员
情况

八、本合同签约各方

项目负责人（签名）： 

2015 年 3 月 31 日

乙方：华南农业大学材料与能源学院（公章）

负责人（签名）：



2015 年 3 月 31 日

同 意

甲方：华南农业大学科技处（公章）

代表人（签名）：


2015 年 4 月 3 日
科学技术处

合同编号：穗南农合〔2025〕107号

技术服务合同

项目名称：香蕉绿色生产关键技术集成应用与示范

委托方：广州市南沙区农业农村局

(甲方) 广州市南沙区凤凰大道1号

受托方：华南农业大学

(乙方) 广东省广州市天河区华南农业大学

签订时间：2025年7月9日

有效期限：2025年7月—2026年12月

中华人民共和国科学技术部印制

技术服务合同

委托方（甲方）： 广州市南沙区农业农村局

住 所 地： 广州市南沙区凤凰大道 1 号

法定代表人： 王青峰

项目联系人： 林亮

联系方式： 39053110

通讯地址： 广州市南沙区凤凰大道 1 号

电 话： 39053110 传真：

电子信箱： 498747665@qq.com

受托方（乙方）： 华南农业大学

住 所 地： 广东省广州市天河区五山街 483 号

法定代表人： 薛红卫

项目联系人： 贾金亮

联系方式： 13642621810

通讯地址： 广东省广州市天河区华南农业大学

电 话： 13642621810 传真：

电子信箱： jiajinliang@scau.edu.cn

本合同甲方委托乙方就 香蕉绿色生产关键技术集成应用与示范

项目进行的专项技术服务，并支付相应的技术服务报酬。双方经过平等协商，在真实、充分地表达各自意愿的基础上，根据《中华人民共和国民法典》的规定，

(4) 技术培训与推广

在建立示范基地基础上，总结形成香蕉绿色生产的技术模式，并制定相关技术规程；通过现场观摩、课题授课等形式，对蕉农进行技术指导或技术培训，进一步推广香蕉绿色生产的技术。

3. 技术服务的方式：技术示范与技术指导。

第二条：乙方应按下列要求完成技术服务工作：

1. 技术服务地点：广州市南沙区万顷沙镇

2. 技术服务期限：2025.7--2026.12

3. 技术服务进度：

2025年7月-8月：香蕉试验示范基地选址以及面上生产情况调查等。

2025年9月-2026年10月：制作展示牌2块，推广香蕉健康栽培和病虫害绿色防控技术，开展吡虫啉监测与安全替代药剂筛选，对果园农药化肥的使用以及田间各项操作等进行规范化技术指导，组织技术培训1-2场。期间，在2026年7月形成中期报告。

2026年11月-12月：总结形成香蕉绿色生产的技术模式，并制定相关技术规程，组织技术培训1-2场进行推广应用。

第三条：甲方向乙方支付技术服务报酬及支付方式为：

1. 技术服务费总额为：15万元（壹拾伍万元整）

2. 在合同签订生效后，甲方收到乙方提供有效发票5个工作日内，甲方向乙方支付合同款的50%，即¥75000.00，人民币大写：柒万伍仟元整。

3. 在2026年7月，乙方提交中期报告后，甲方收到乙方提供有效发票5个工作日内，甲方向乙方支付合同款的30%，即¥45000.00，人民币大写：肆万伍仟元整。

4. 项目完成并通过验收后，甲方收到乙方提供有效发票5个工作日内，甲

总价 1%的数额向甲方支付违约金；逾期半个月以上的，甲方有权解除合同，乙方应退还已收取的款项，并承担甲方由此产生的损失。

3.甲方无正当理由拒绝接受服务的，甲方向乙方偿付本合同总价 5%的违约金。

4.其它违约责任按《中华人民共和国民法典》处理。

第十一条：争议解决方式

因本合同引起或与本合同有关的一切争议，双方均应友好协商解决；如果不能协商解决的，可向南沙区人民法院提起诉讼，违约方应承担守约方为处理本合同项下纠纷所支出的相关费用，包括但不限于诉讼费、律师费、保全费等。

第十二条：本合同一式 4 份，双方各执 2 份，具有同等法律效力。

第十三条：本合同经双方签字盖章后生效。

甲方：广州市南沙区农业农村局（盖章）

法定代表人/委托代理人：

（签名）

2025年 7 月 9 日

乙方：华南农业大学（盖章）

法定代表人/委托代理人：

（签名）

2025年 7 月 23 日

绿色农药全国重点实验（华南农业大学）
2024 年实验室研究课题

任务合同书

课题编号：

GPLSCAU202407

课题名称：

高效纳米农药对作物隐蔽性病虫害的靶向
防控

课题联系人：

赵晨

团队成员：

张志祥、贾金亮、伍欣宙

执行期限：

2024 年 10 月 至 2026 年 12 月

2024 年 9 月

填写说明

- 一、课题任务合同书甲方即实验室，乙方即团队成员（联系人为代表）。
- 二、课题任务合同书签订后，联系人可自主决定是否与团队成员签订任务书并向实验室备案。
- 三、课题任务合同书中文字体须用宋体小四号字填写，英文字体须用 Times New Roman 号字填写，1.5 倍行距。
- 四、凡不填写内容的栏目，请用“无”表示。
- 五、乙方完成课题任务合同书填写，提交甲方审核确认后，用 A4 纸打印、装订、签章。一式两份报实验室签章，实验室和课题联系人各持一份。
- 六、《项目申报书》和《课题任务合同》是本任务合同书填报的重要依据，课题任务合同书填报不得降低考核指标，不得自行对主要研究内容作调整。《项目申报书》、和《课题任务合同》将共同作为课题过程管理、综合绩效评价（验收）和监督评估的重要依据。

课题基本信息表

所属方向		高效剂型与智慧植保					
课题编号		GPLSCAU202407					
课题名称		高效纳米农药对作物隐蔽性病虫害的靶向防控					
实验室	单位名称	绿色农药全国重点实验室（华南农业大学）					
	负责人	徐汉虹					
	通信地址	广东省广州市天河区五山路 483 号			邮政编码	510642	
	科研管理负责人	曾亮			联系方式	020-85286089	
课题联系人	姓 名	赵晨	性 别	女	出生日期	1985.07	
	国 籍	中国	身份证号码	420602198507161023			
	工作单位	华南农业大学		职 务	教师		
	最高学位	<input checked="" type="checkbox"/> 博士 <input type="checkbox"/> 硕士 <input type="checkbox"/> 学士 <input type="checkbox"/> 其他					
	职 称	<input type="checkbox"/> 正高级 <input checked="" type="checkbox"/> 副高级 <input type="checkbox"/> 中级 <input type="checkbox"/> 其他					
	电子邮箱	zhaoc@scau.edu.cn		联系方式	18819372496		
经费安排		采用“赛马制”，执行期第一年均资助申请经费 50%，第二年依据完成情况，评审其中优胜项目继续支持。					
合同周期		起始时间	2024 年 9 月 15 日		结束时间	2026 年 9 月 15 日	
		实施周期	24 个月				

课题任务书

2024 年实验室研究课题

实验室（甲方）：绿色农药全国重点实验室

课题联系人（乙方）：张志祥、贾金亮、赵晨、伍欣宙

双方就承担绿色农药全国重点实验室（华南农业大学）2024 年实验室研究课题中“高效剂型与智慧植保”方向课题“高效纳米农药对作物隐蔽性病虫害的靶向防控”，为了保证课题研究任务的完成，现就任务分工、研究经费、研究成果及知识产权归属等方面签署课题任务合同。

一、研究内容：

针对华南地区作物隐蔽性病虫害为害严重、防治难度高、常规农药制剂靶向性不足等问题，依据导向农药理论，借助新型天然源纳米材料与超分子材料作为载体，创制靶向沉积、精准传递、智能释放的纳米农药新制剂，解析其靶向传递与减量增效作用机制，并形成配适的轻简化靶向施用技术体系，实现对作物隐蔽性病虫害的靶向防治。

（1）高效靶向纳米农药制剂开发

基于隐匿性病虫害生理特性，利用天然源多糖、氨基酸基聚合物、超分子杯芳烃等功能性载体材料，综合应用绿色合成等先进工艺技术，设计、制备新型纳米农药靶向载体材料。利用靶向载体材料负载非内吸性农药分子，优化形成具备韧皮部输导性、高活性、高选择性的新型纳米农药制剂。通过对原药选择、原料配比等制备条件进行优化，开发形成农药活性成分高效负载工艺，并明确制备条件与产品性能之间的关系。以水为分散介质，探索表观水溶、热力学稳定的纳米农药的制备技术。开展纳米农药产品分散性、稀释稳定性、微粒形态与尺寸变化等质量控制指标及检测方法研究，确定纳米农药稳定性判定依据。

（2）靶向纳米农药制剂作用机制明确

对设计合成的精准纳米农药制剂在昆虫和植物体内的吸收、分布、代谢和排泄（ADME）过程进行全程可视化成像评估，充分考虑农药、作物、有害生物及非靶标生物四者之间的互作关系，利用高分辨质谱成像可视化技术等，原位监测农药及其代谢产物的时空动态变化，获得纳米农药分子轨迹并破译农药的作用机理，辅助

药物对靶和分子结构优化。在已有的基础上，进一步确定标准化检测参数，针对靶标昆虫、植物分别建立数套适用于不同农药原位质谱可视化方案，实现高灵敏度、高通量标准化快速监测系统的建设，明确纳米靶向载体材料对农药分子的靶向传递、靶向释放、联合增效机制。

(3) 靶向纳米农药随水施用技术体系构建

针对所开发精准纳米农药制剂的随水滴灌施用条件进行优化：结合药前配套施用方案，研究不同滴灌施药时间、不同温度、光照和膜下湿度条件对防治效果的影响，明确最适施用条件及作物全生育期施用次数；筛选与优化适合的土壤 pH 值调节剂、根际微生物及其它土壤微环境改良剂，合理设置其前置施用时间，随水滴灌流速、时间和用量，明确其对土壤 pH 值和微环境的影响深度、广度和时间；明确膜下滴灌施用纳米农药的防效及吸收传递效率的影响，优化形成纳米农药靶向施用技术体系及配套施用规程，

二、考核指标与考核方式：

考核指标：

计划根据 2024 年 10 月-2025 年 9 月期间的研究内容，获得以下成果：

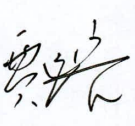
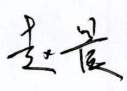

- (1) 获得靶向纳米农药增效材料 3 个；
- (2) 获得靶向纳米农药新制剂 3 个，农药有效利用率提升 15%以上；
- (3) 高水平主流期刊论文 5 篇，其中大于 10 论文 3 篇

考核方式：

- (1) 靶向纳米农药增效材料：提供材料结构与表征信息；
- (2) 纳米农药新制剂：提供材料结构、表征信息或专利信息；
- (3) 论文：提供论文全文。

三、团队人员（含联系人）：

序号	姓名	身份证号	职称/职务	工作单位	人员分类*	签名
1	张志祥	422429197403091792	教授	华南农业大学植物保护学院	负责人。负责靶向纳米农药载体材料与制剂的研发。	张志祥

2	贾金亮	422431197908301013	副教授	华南农业大学材料与能源学院	团队成员。 负责高效纳米助剂和纳米农药新制剂研发。	
3	赵晨	420602198507161023	副教授	华南农业大学植物保护学院	联系人。负责促进作物对农药吸收转运的载体材料的研发。	
4	伍欣宙	450502198612210181	副教授	华南农业大学植物保护学院	团队成员。 负责以上新研发纳米农药载体材料对农药增效机制的深度解析。	

四、经费预算：

甲方计划向乙方授权经费 25 万元。实际拨付经费甲方将根据项目概算批复结果核定，对乙方的经费进行调整。

五、双方责任

1. 甲乙双方根据华南农业大学项目管理各项规章制度等有关文件规定，及相关法律、政策和管理要求，签署本任务合同书。

根据本任务合同书和年度经费计划，甲方在合同签订 15 日内在学校财务系统授权乙方项目预算额度：

如出现课题总经费概算超出实验室获批经费，授权额度根据实际获批经费进行适当调整。

2. 课题联系人与团队成员权利责任平等，应全力以赴开展研发。课题组成员间紧密合作，相互配合完成一个明确目标，而不是各自研究内容的叠加。团队应明确围绕目标制定各成员的分工任务和目标，严格按照课题任务指标和课题任务合同书要求，按时保质保量完成研发目标。不得以任何理由降低课题目标要求，拖延子课题进展，推诿工作责任。研究结果应体现成员合作贡献，对拼凑研究结果应付目标考核的，取消实验室研究课题申报资格 3 年。

3. 课题联系人定期向实验室报送子课题进展，若经年度考核，未按课题任务合同书要求完成考核指标，实验室有权建议调整经费或终止课题的实施单位、追回已拨付资金。采用“赛马制”，执行期第一年均资助申请经费 50%，第二年依据完成情况，评审其中优胜项目继续支持。对课题所有成果产出（包括但不限于新产品、新技术、标准、专利等）的真实性、与课题的关联性等负责，落实科研作风学风和科研诚信主体责任。

4. 课题经费实行专款专用、单独核算；全部用于与本课题研究工作相关的支出，不截留、挪用、侵占，不用于与科学研究无关的支出；接受并积极配合相关部门的监督检查。如有违反，课题以及相关成果产出者愿接受项目主管单位和相关部门做出的各项处理决定，包括但不限于终止课题执行、追回课题经费，记入科研诚信严重失信行为数据库以及主要负责人接受相应党纪政纪处理等。

表 1 2024 年度课题预算支出科目表

金额单位：万元

序号	预算科目名称	金额
	(1)	(2)
1	一、中央财政资金	25.00
2	(一) 直接费用	25.00
3	1.设备费	0
4	其中：购置设备费	0
5	2.业务费	23.75
6	3.劳务费	1.25
7	(二) 间接费用	0
9	合计	25.00

2024 年度课题预算说明

1. 设备费：0 万元

2. 业务费：23.75 万元

2.1 材料费：14.00 万元

合成化合物、生物活性测定、分子生物学实验等所需试剂和耗材。

2.2 测试化验加工费：6.25 万元

化合物结构表征、活性化合物生理生化测试等费用。

2.3 会议/差旅费/国际合作交流费：3.50 万元

参加植物保护、农药学相关会议的差旅费。

3. 劳务费：1.25 万元

用于支付直接参与项目研究的研究生劳务费。

4. 间接费用：0.00 万元

六、课题任务合同书签署

甲方：绿色农药全国重点室（华南农业大学）

乙方：课题联系人（签字） 赵霞

实验室主任（签字）：

徐海

团队成员（签字）：

伍欣

张忠祥 蔡培

年 月 日

年 月 日

绿色农药全国重点实验室（华南农业大学）

GPLSCAU【2024】03号

2024 年度研究课题立项通知

根据实验室 2024 年 7 月 24 日发布的《绿色农药全国重点实验室（华南农业大学）2024 年度研究课题申报通知》，经团队申报、专家评审、实验室公示和审批等程序，对 8 个课题进行立项。具体名单及资助金额见附件。现就相关工作安排如下：

1. 各联系人根据资助资金填写签订“2024 年实验室研究课题任务书”并及时取回纸质盖章版。

2. 根据申报通知，同一研究方向资助两项，采用“赛马制”执行期第一年均资助申请经费 50%，第二年依据完成情况，评审其中优胜项目继续支持。

3. 经费预算使用及要求：请严格按照《国家重点实验室专项经费管理办法》以及华南农业大学相关财务规定使用。

绿色农药全国重点实验室（华南农业大学）

2024 年 10 月 05 日

附件 1：2024 年度研究课题立项项目信息

绿色农药全国重点实验室（华南农业大学）

2024 年度研究课题立项项目信息

指南方向	编号	题 目	成 员	资助金额 (万元)
1. 新靶标和新结构杀虫剂先导化合物研发	GPLSCAU202401	防治十字花科蔬菜重大害虫的杀虫剂创制与产业化关键技术	汤日元、徐汉虹、潘慧鹏	¥25
	GPLSCAU202402	基于 Hemocytin 蛋白的昆虫免疫抑制剂筛选与结构优化研究	胡琼波、翁群芳、刘承兰、许小霞	¥25
2. 防治稻蔬细菌性病害药剂创制与产业化关键技术研发	GPLSCAU202403	苯并稠环噻二唑/噻二唑类治疗性杀细菌剂的创制	林菲、姚光凯、曾令达、沙干	¥25
	GPLSCAU202404	靶向植物病原细菌 T3SS 的绿色农药先导创制	崔紫宁、周佳暖、王波	¥25
3. 天然源农药的生物合成与制造	GPLSCAU202405	水稻二肽 DP1 对植物线虫病和病毒病的防治作用研究	卓侃、张彤、李鹏飞	¥25
	GPLSCAU202406	天然杀菌活性分子的生物制造	田永清、廖立胜、徐泽凌、王磊	¥25
4. 高效剂型与智慧植保	GPLSCAU202407	高效纳米农药对作物隐蔽性病虫害的靶向防控	张志祥、贾金亮、赵晨、伍欣宙	¥25
	GPLSCAU202408	农药液滴在荔枝毛毡病叶片的表面沉积规律与调控机制机理研究	岳学军、兰玉彬、李震	¥25

2023 年省级涉农统筹资金 项目合作协议

甲方（承担单位）：东莞市农业科学研究中心

乙方（参与单位）：华南农业大学

丙方（参与单位）：东莞市农业技术推广管理办公室

根据《广东省财政厅关于提前下达 2023 年省级涉农统筹整合转移支付资金的通知》（粤财农〔2022〕189 号），动植物疫病防控——植物疫病防控类项目“东莞市植物重大及入侵害虫绿色监测防控技术推广示范应用”，安排 2023 年省级资金 50.0 万元。本着“优势互补、资源共享、共同发展”的原则，该项目由东莞市农业科学研究中心、华南农业大学、东莞市农业技术推广管理办公室三家单位联合开展。为保障项目的顺利开展和完成，经友好协商，三方达成如下合作协议：

一、合作关系

三方同意由甲方作为项目承担单位，乙方工作人员徐汉虹教授为项目主持人，乙方和丙方为项目参与单位。

二、任务分工

项目绩效目标为：完成推广应用植物性饵剂 1-2 种，筛选驱避性植物 3-5 种，构建以植物源为特色的驱虫隔离带 1 个，抗药性监测报告 3 份，化学农药残留动态监测报告 3 份。三方同意以分工合作的形式承担项目各项任务：

1、东莞市农业科学研究中心（甲方）

（1）甲方为项目承担单位，负责项目总结、验收、审计等，并协助乙方项目组织管理和整体实施；

（2）协助推广应用 1-2 种植物性饵剂；

（3）协助植物源驱虫隔离带的建设示范；

（4）协助抗药性监测和化学农药残留动态监测。

2、华南农业大学（乙方）

（1）因乙方为项目主持人和项目技术内容主要执行单位，需负责项目组织管理和整体实施等；

（2）负责研制提供 1-2 种植物性饵剂及推广应用；

（3）负责筛选 3-5 种驱避性植物，以及植物源驱虫隔离带的建设示范；

（4）负责组织实施抗药性监测和化学农药残留动态监测，并提供两类报告各 3 份；

（5）协助甲方完成项目总结、验收、审计等，并负责提供项目审计所需的财务资料等相关资料，提供项目验收的现场和总结报告等；

3、东莞市农业技术推广管理办公室（丙方）

（1）协助抗药性监测和化学农药残留动态监测；

（2）协助植物源驱虫隔离带的建设示范；

（3）协助推广应用 1-2 种植物性饵剂；

（4）协助完成项目总结、验收、审计等。

三、项目资助经费的分配与使用

1、项目资金由甲方按任务分工进行统筹安排、分配。其中甲方完成任务所需资金计划占立项资金 2%，即 1 万元；乙方完成任务所需资金计划占立项资金 98%，即 49 万元，支付方式如下：（1）第一期资金（20 万元）由甲方于本协议签订后 15 日内拨付给乙方；（2）在乙方完成附表 1 项目进度表序号第 1 的阶段性成果（即制备 1-2 种植物饵剂，提供试验示范效果证明），并经甲方验收合格后，由甲方拨付乙方第二期资金（29 万元）。乙方需根据单位财务管理实际情况提供财务所需的相应票据。因财政拨款问题或乙方未能提供财务所需的相应票据，甲方有权迟延安排项目经费而不视为违约。

2、乙方单位需按项目进度安排及时完成相应项目内容和资金使用，详见项目进度表（附表 1），如未及时完成，自行承担由此产生的所有责任及后果。

3、项目资金需符合省涉农资金使用的相关要求，开支专款专用，资金

预算明细表见附表 2。

四、知识产权与成果

项目实施过程中所形成的知识产权与成果归三方共同所有，具体排名顺序根据贡献大小由三方商议确定。项目实施形成的知识产权要标注由 2023 广东省省级涉农资金项目“东莞市植物重大及入侵害虫绿色监测防控技术推广示范应用”（项目编号：441900230000000001952）资金资助。未经三方一致同意，任何一方均不得转让项目实施过程中所形成的知识产权与成果，也不得许可其他第三方使用项目实施过程中所形成的知识产权与成果。

五、保密

未经对方许可，甲乙丙三方及各自参与人员（详见附表 3）不得将本项目的技术信息和材料透露给其他人员，否则，披露方应承担因此产生的全部法律及经济责任，且应承担给另两方造成的一切损失。

六、争议解决

如发生争议，三方应协商解决。协商不成的，三方同意交由甲方所在地有管辖权的人民法院诉讼管辖。

七、其他事项

1、本协议未尽事宜由三方友好协商解决，三方可另行签订补充协议，补充协议与本协议具有同等法律效力。

2、本协议附件共 3 个，分别为：附表 1 项目进度表；附表 2 资金预算明细表（单位：万元）；附表 3 项目成员基本情况表。本协议附件为本协议不可分割的重要组成部分，与本协议具有同等法律效力。

3、本协议自三方签字并盖章后生效，一式六份，甲方执贰份，乙方执贰份，丙方执贰份，具有同等法律效力。

[以下无正文，为签署页]

[本页为签署页]

甲方（公章）：东莞市农业科学研究中心

委托代理人：

项目负责人：胡珊

日期：2023年5月18日

乙方（公章）：华南农业大学

委托代理人：

项目负责人：

日期：2023年5月18日

丙方（公章）：东莞市农业技术推广管理办公室

委托代理人：

项目负责人：韩海亚

日期：2023年5月18日

附表 1 项目进度表

序	时期	主要工作内容	阶段性成果	阶段资金使用计划 (万元)
1	2023 年 4 月至 2023 年 6 月	(1) 植物性饵剂的制备及推广应用; (2) 筛选驱避性植物 3-5 种;	制备 1-2 种植物饵剂, 提供试验示范效果证明。	20
2	2023 年 7 月至 2023 年 11 月	(1) 植物源驱虫隔离带的示范建设; (2) 不同防治地点土壤及水体样本农药性监测和化学农药残留动态监测;	构建植物源驱虫隔离带 1 个; 提供抗药性监测报告和化学农药残留动态监测报告各 3 份。	29
3	2023 年 12 月	完成项目总结、验收、审计等。	项目验收报告 1 份、审计报告 1 份。	1



附表 2 资金预算明细表（单位：万元）

资金类别	甲方	乙方	合计
1.差旅费	0	3.4	3.4
2.检测费	0	7	7
3.耗材费	0	19.2	19.2
4.劳务费	0	12	12
5.水电费及其他费用支出	1	7.4	8.4
合计	1	49	50

附资金类别说明：1、差旅费：包括项目开展采样、诱饵应用调查构建植物源驱虫隔离带等工作所产生的交通（补助）费、住宿费、餐费、误餐补助费等项目相关的差旅费用；2、检测费：包括项目中化学农药残留和抗药性的检测等相关检测费用；3、耗材费：包括购置驱避性植物、检测试剂、采样工具及用品等项目相关的耗材费用；4、劳务费：包括参与项目实施的其他专家、研究生、务工人员 and 隔离带建设田间管理等的相关劳务费用；5、水电费及其他费用支出：包括项目开展过程消耗水电费，以及项目管理、审计、验收等相关的其他费用。

附表 3 项目成员基本情况表

填表说明: 1.人员分类: 负责人、骨干、其他人员; 2.职称分类: 正高级、副高级、中级、初级、其他; 3.固定人员需填写人员明细。						
序号	姓名	身份证号码	工作单位	技术职称	项目中的分工与职责	人员分工
	(1)	(2)	(3)	(4)	(5)	(6)
1	徐汉虹	440106196112061813	华南农业大学植物保护学院	教授	负责项目整体组织和实施	项目负责人
2	胡珊	522725198110090082	东莞市农业科学研究中心	正高级农艺师	负责综合监测防控技术的推广应用	项目骨干
3	张志祥	422429197403091792	华南农业大学植物保护学院	教授	负责农药的残留检测	项目骨干
4	林菲	445102197710220021	华南农业大学植物保护学院	副研究员	负责绿色监测防控技术的推广示范应用	项目骨干
5	韩海亚	130533198802280527	东莞市农业技术推广管理办公室	农艺师	负责害虫的抗性监测	项目骨干
6	田永清	422422197304254715	华南农业大学植物保护学院	副教授	绿色监测防控技术的推广示范应用	项目骨干
7	陈彦	44080219820104083X	东莞市农业科学研究中心	农业经济师	综合监测防控技术的推广应用	项目骨干
8	赵晨	420602198507161023	华南农业大学植物保护学院	副教授	害虫的抗性监测	项目骨干
9	陈生龙	421003197903010518	东莞市农业科学研究中心	农艺师	综合监测防控技术的推广应用	项目骨干
10	伍欣宙	450502198612210181	华南农业大学植物保护学院	副教授	农药的残留检测	项目骨干
11	谢志强	440583198408141111	东莞市农业技术推广管理办公室	其他	害虫的抗性监测	项目成员
12	贾金亮	422431197908301013	华南农业大学材料与能源学院	副教授	绿色监测防控技术的推广示范应用	项目成员
13	曾国玲	441900198801230200	东莞市农业科学研究中心	农艺师	综合监测防控技术的推广应用	项目成员
14	席卓君	441802198302136911	东莞市农业技术推广管理办公室	助理农艺师	综合监测防控技术的推广应用	项目成员
15	韦加奇	320982199611205013	华南农业大学植物保护学院	其他	害虫的抗性监测	项目成员
16	徐楷杰	130434199709090513	华南农业大学植物保护学院	其他	植物源饵剂	项目成员
17	刘美晨	230882199903180025	华南农业大学植物保护学院	其他	抗药性监测, 农残监测	项目成员
18	欧紫越	441226199910014320	华南农业大学植物保护学院	其他	抗药性监测, 农残监测	项目成员
19	郑溪鑫	341602199803277456	华南农业大学植物保护学院	其他	驱避植物隔离带-	项目成员
累计				19		

检索证明

根据委托人提供的论文材料，委托人华南农业大学材料与化学工程学院 贾金亮(学科类型:自然科学) 18 篇论文收录情况如下表。

序号	论文名称	发表刊物及发表的年月卷期/页码等	作者排名	论文等级	作者文中单位	收录情况	影响因子	中科院大区分区
1	Uptake and imaging of glycine functionalized gold nanoclusters inSpodoptera frugiperda(Sf9) cells	JOURNAL OF CLUSTER SCIENCE 出版年: 2021 出版日期: NOV 卷期: 32 6 页码: 1553-1561 文献类型: Article	第一作者	B类	华南农业大学	SCI	IF2-year=3.447 IF5-year=2.617 (2021)	化学 4区 Top 期刊: 否 OA 期刊: 否 (2021)
2	Enhanced intracellular uptake in vitro by glucose-functionalized nanopesticides	NEW JOURNAL OF CHEMISTRY 出版年: 2017 出版日期: OCT 7 卷期: 41 19 页码: 11398-11404 文献类型: Article	第一作者	B类	华南农业大学	SCI	IF2-year=3.201 IF5-year=3.181 (2017)	化学 3区 Top 期刊: 否 (2017)
3	Preparation, Characterization and Intracellular Imaging of 2,4-Dichlorophenoxyacetic Acid Conjugated Gold Nanorods	JOURNAL OF NANOSCIENCE AND NANOTECHNOLOGY 出版年: 2016 出版日期: MAY 卷期: 16 5 页码: 4936-	第一作者	B类	华南农业大学	SCI	IF2-year=1.483 IF5-year=1.131 (2016)	工程技术 3区 Top 期刊: 否 (2016)



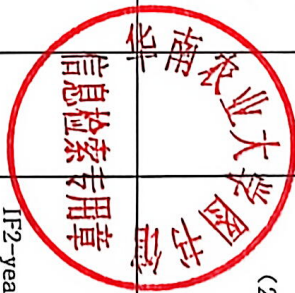
		4942 文献类型: Article						
4	Biosynthesis of Silver and Gold Nanoparticles Using Huangdan (Camellia sinensis) Leaf Extract	SYNTHESIS AND REACTIVITY IN INORGANIC METAL-ORGANIC AND NANO-METAL CHEMISTRY 出版年: 2015 卷期: 45 7 页码: 941-946 文献类型: Article	第一作者	B类	华南农业大学	SCI	IF2-year=0.493 IF5-year=0.521 (2015)	工程技术 4区 Top 期刊: 否 (2015)
5	Biosynthesis of Gold Nanoparticles Using Novel Bamboo (Bambusa chungii) Leaf Extracts	JOURNAL OF NANOSCIENCE AND NANOTECHNOLOGY 出版年: 2015 出版日期: FEB 卷期: 15 2 页码: 1674-1677 文献类型: Article	第一作者	B类	华南农业大学	SCI	IF2-year=1.338 IF5-year=1.105 (2015)	工程技术 3区 Top 期刊: 否 (2015)
6	GABA-Decorated Nanocarrier for Smart Delivery of Fludioxonil for Targeted Control of Banana Wilt Disease	JOURNAL OF AGRICULTURAL AND FOOD CHEMISTRY 出版年: 2024 出版日期: OCT 17 卷期: 72 48 页码: 26664-26676 文献类型: Article	共同通讯作者 (倒数第一)	T2类	华南农业大学	SCI	IF2-year=6.2 IF5-year=6.4 (2024)	农林科学 1区 Top 期刊: 是 OA 期刊: 否 (2025)



7	Optimized nanopesticide delivery of thiamethoxam to cowpeas (<i>Vigna unguiculata</i>) controls thrips (<i>Megalurothrips usitatus</i>) and reduces toxicity to non-target worker bees (<i>Apis mellifera</i>)	SCIENCE OF THE TOTAL ENVIRONMENT 出版年: 2024 出版日期: DEC 1 卷期: 954 页码: - 文献号: 176327 文献类型: Article	共同通讯作者 (倒数第一)	A类	华南农业大学	SCI	IF2-year=8.0 IF5-year=8.7 (2024)	环境科学与生态学 2区 Top 期刊: 是 OA 期刊: 否 标注: Mega-Journal (2025)
8	A Pyr-loaded polymer microparticle for effectively controlling <i>Solenopsis invicta</i> (Hymenoptera: Formicidae) in the nest	COLLOIDS AND SURFACES B-BIOINTERFACES 出版年: 2024 出版日期: FEB 卷期: 234 页码: - 文献号: 113675 文献类型: Article	共同通讯作者	A类	华南农业大学	SCI	IF2-year=5.6 IF5-year=5.4 (2024)	医学 2区 Top 期刊: 否 OA 期刊: 否 (2025)
9	ConA-Loaded PEGylated Graphene Oxide for Targeted Nanopesticide Carriers against <i>Magnaporthe Oryzae</i>	ACS APPLIED NANO MATERIALS 出版年: 2023 出版日期: MAY 23 卷期: 6 11 页码: 9484-9494 文献类型: Article	共同通讯作者 (倒数第一)	A类	华南农业大学	SCI	IF2-year=5.3 IF5-year=5.5 (2023)	材料科学 2区 Top 期刊: 否 OA 期刊: 否 (2023)
10	Enzyme-Responsive Lignin Nanocarriers for Triggered Delivery of Abamectin to Control Plant Root-	JOURNAL OF AGRICULTURAL AND FOOD CHEMISTRY 出版年: 2023	共同通讯作者 (倒数第一)	T2类	华南农业大学	SCI	IF2-year=5.7 IF5-year=6.0 (2023)	农林科学 1区 Top 期刊: 是 OA 期刊: 否



	Knot Nematodes (Meloitoglyne incognita)	出版日期: MAR 1 卷期: 71 8 页码: 3790-3799 文献类型: Article					(2023)
11	Targeted delivery of emamectin benzoate by functionalized polysuccinimide nanoparticles for the flowering cabbage and controlling Plutella xylostella	PEST MANAGEMENT SCIENCE 出版年: 2022 出版日期: FEB 卷期: 78 2 页码: 758-769 文献类型: Article	共同通讯作者 (倒数第一)	T2 类	华南农业大学	SCI IF2-year=4.1 IF5-year=4.4 (2022)	农林科学 1 区 Top 期刊: 是 OA 期刊: 否 (2022)
12	Graphene oxide as a pesticide carrier for enhancing fungicide activity against Magnaporthe oryzae	NEW JOURNAL OF CHEMISTRY 出版年: 2021 出版日期: FEB 7 卷期: 45 5 页码: 2649-2658 文献类型: Article	共同通讯作者 (倒数第一)	B 类	华南农业大学	SCI IF2-year=3.925 IF5-year=3.629 (2021)	化学 3 区 Top 期刊: 否 OA 期刊: 否 (2021)
13	Phloem Delivery of Fludioxonil by Plant Amino Acid Transporter-Mediated Polysuccinimide Nanocarriers for Controlling Fusarium Wilt in Banana	JOURNAL OF AGRICULTURAL AND FOOD CHEMISTRY 出版年: 2021 出版日期: MAR 10 卷期: 69 9 页码: 2668-2678 文献类型: Article	共同通讯作者	T2 类	华南农业大学	SCI IF2-year=5.895 IF5-year=6.048 (2021)	农林科学 1 区 Top 期刊: 是 OA 期刊: 否 (2021)



14	Long-lasting repellent activities of eco-friendly polyurethane system for controlled citral against melon fly	CROP PROTECTION 出版年: 2021 出版日期: OCT 卷期: 148 页码: - 文献号: 105745 文献类型: Article	共同通讯作者 (倒数第一)	A类	华南农业大学	SCI IF2-year=3.036 IF5-year=3.32 (2021)	农林科学 2区 Top 期刊: 否 OA 期刊: 否 (2021)
15	Development of Multifunctional Avermectin Poly(succinimide) Nanoparticles to Improve Bioactivity and Transportation in Rice	JOURNAL OF AGRICULTURAL AND FOOD CHEMISTRY 出版年: 2018 出版日期: OCT 31 卷期: 66 43 页码: 11244-11253 文献类型: Article	共同通讯作者 (倒数第一)	T2类	华南农业大学	SCI IF2-year=3.571 IF5-year=3.911 (2018)	农林科学 1区 Top 期刊: 是 (2018)
16	A novel water-based chitosan-La pesticide nanocarrier enhancing defense responses in rice (Oryza sativa L.) growth	CARBOHYDRATE POLYMERS 出版年: 2018 出版日期: NOV 1 卷期: 199 页码: 437-444 文献类型: Article	共同通讯作者	A类	华南农业大学	SCI IF2-year=6.044 IF5-year=5.975 (2018)	工程技术 2区 Top 期刊: 是 (2018)
17	Chitosan-based nanoparticles of avermectin to control pine wood nematodes	INTERNATIONAL JOURNAL OF BIOLOGICAL MACROMOLECULES 出版年: 2018 出版日期: JUN	共同通讯作者	A类	华南农业大学	SCI IF2-year=4.784 IF5-year=4.731 (2018)	生物 2区 Top 期刊: 否 (2018)

		卷期: 112 页码: 258-263 文献类型: Article					
18	高效编号咯菌腈纳米杀菌剂的制备及其性能研究	仲恺农业工程学院学报 出版年: 2024 卷期: 页码: - 文献号: 文献类型:	通讯作者	普刊类	华南农业大学	CNKI	无

说明: 论文等级和中科院大类分区按《华南农业大学学位论文评价方案(试行)》划分。

报告免责声明: 如未盖章, 报告无效





Uptake and imaging of glycine functionalized gold nanoclusters in *Spodoptera frugiperda* (Sf9) cells

Jinliang Jia¹ · Qingle Liu² · Xiaoyong Jin² · Hanhong Xu²

Received: 15 April 2020 / Accepted: 11 October 2020 / Published online: 21 October 2020
© Springer Science+Business Media, LLC, part of Springer Nature 2020

Abstract

Fluorescent gold nanoclusters (Au NCs) have attracted considerable interest in biological application. Here, we reported a novel Au NCs with blue fluorescence, conjugated with glycine (Gly) and rotenone (R). The structure and properties of Au-BSA-Gly-R conjugates were characterized by transmission electron microscopy (TEM), UV-visible, fluorescence spectroscopy, Fourier transform infrared spectroscopy (FTIR) and Zeta potential measurement. The results of fluorescent microscopic imaging revealed that the Au NCs with different ligands were capable of being selectively uptaken by *Spodoptera frugiperda* (Sf9) cells. Furthermore, the gold content of Au-BSA-Gly-R in Sf9 cells was 2.2 and 2.6 times higher than that of Au-BSA and Au-BSA-R, respectively. It illustrated that nanoparticles after conjugated with Gly could gain specificity to intracellular transportation. This study indicated that the Au NCs after mediated by Gly not only had great potential for applications in insect cell imaging, but also could play an important role of amino acid for agrochemicals delivery in agricultural fields.

Keywords Gold nanoclusters · Glycine · Rotenone · Cell imaging · Uptake

Introduction

Cell imaging and drug delivery by tracking technologies have been widely used for biological phenomena such as transport in cells [1–3], intracellular localization [4] and cell recognition [5]. Fluorescent quantum dots (QDs) also have attracted the attention of researchers because of their unique optical, electronic and physico-chemical

characteristics [6–9]. However, the inherent toxicity prevailing in most of the QDs limits their potential clinical application [10, 11]. In recent years, a promising approach for metal nanoclusters (NCs) as novel fluorescent markers has been widely used because of their biocompatibility, ultrasmall size and nontoxicity [12–15].

Noble metal nanoclusters composed of a few to roughly a hundred atoms, are a new type of luminescent nanomaterials which have consequently attracted a great deal of attention [16, 17]. In contrast to metal nanoparticles (NPs), Au nanoclusters (Au NCs) do not show plasmonic transitions involving surface electrons but exhibit vis-NIR fluorescence attributed to the formation of a molecular-type HOMO–LUMO bandgap opening as well as electronic transitions at subnanometer sizes smaller than the Fermi wavelength [18]. Au NCs show a lot of important properties that include enhanced catalytic activity, high fluorescence and unique electrical properties, allowing them to be applied in the biodetection [19], bioimaging [20–24], intracellular metal ion sensing [25], and so on.

Glycine (Gly) is the simplest amino acid, which has a number of important yet distinct functions in the body. It forms the essential precursors for the synthesis of proteins, nucleic acids and lipids [26]. Therefore, organisms have

Jinliang Jia and Qingle Liu are co-first authors, who contributed equally to this work.

Electronic supplementary material The online version of this article (<https://doi.org/10.1007/s10876-020-01915-3>) contains supplementary material, which is available to authorized users.

✉ Hanhong Xu
hbxu@scau.edu.cn

¹ Key Laboratory for Biobased Materials and Energy of Ministry of Education, College of Materials and Energy, South China Agricultural University, Guangzhou 510642, China

² State Key Laboratory for Conservation and Utilization of Subtropical Agro-Bioresources, South China Agricultural University, Guangzhou 510642, China

different transport systems and the associated carrier proteins for Gly that are responsible for its movement across biological membranes. Gly is also a component of the antioxidant glutathione and occupies a key place in the central nervous system. Certain cells possess a Gly transport system, which can take up the amino acid from the surrounding environment [27]. Furthermore, Gly transport is usually mediated by several carrier systems. System Gly is a Na^+ -dependent and high affinity system. This system is considered as a major route for the entry of Gly into many types of cells at physiologic concentrations of Gly in the extracellular fluid. Other systems, such as system A, take some part in the glycine transport in liver cells [28]. Gly, which was selectively transported by the glycine transport systems in cells, could be chosen as the ligand to conjugate Au NCs with prominent enhancing cellular uptake.

In agricultural fields, botanical insecticides are more environmentally friendly than chemical pesticides. Rotenone (R) has been widely used to control crop pests, which is an abundant natural product derived from the root of some leguminous plants such as *Derris* and *Lonchocarpus* [29–31]. As we known, in order to understand the action position and mechanism, it is very important that the biodistribution of pesticides inside cells can be visualized. However, the cellular uptake and transport of rotenone under the action of Gly have not been reported up to now. Therefore, we used Au NCs as fluorescence label to track and visualize rotenone. Moreover, the linking of the rotenone onto the surface of Au NCs had several advantages. Firstly, we used a simple, “green” method for the production of excellent water-soluble Au NCs [32]. The water solubility of drug could be improved by conjugating with Au NCs. Secondly, the ultrasmall size of Au NCs endowed the conjugates with the ability to enter into the cell nucleus [33].

Thus, we synthesized multifunctional conjugates based on Au NCs for cell imaging and drug delivery. To the best of our knowledge, this was the firstly to prepare both of Gly and R functionalized Au nanoparticles with fluorescence. The chemical structures and physical properties of Au-BSA-Gly-R conjugates were characterized and identified by transmission electron microscopy (TEM), UV-visible, fluorescence spectroscopy, Fourier transform infrared transmission spectroscopy (FTIR) and Zeta potential measurement. Furthermore, the cell imaging and transport ability of Au-BSA-Gly-R conjugates were investigated via laser scanning confocal microscope (LSCM), flow cytometry and inductively coupled plasma mass spectroscopy (ICP-MS) technology. This study may lead to a kind of novel fluorescence probe for applications in the imaging and delivery of agricultural chemicals, which will enhance the delivery efficacy and change application approaches of agricultural chemicals.

Materials and Methods

Materials and Characterization

The HAuCl_4 was purchased from Beijing InnoChem Science & Technology Co., Ltd. (Beijing, China). 1-(3-Dimethylaminopropyl)-3-ethylcarbodiimide hydrochloride (EDC-HCl), N-hydroxysuccinimide (NHS), 4-dimethylamino pyridine (DMAP), Glycine and albumin from bovine serum (BSA) were purchased from Aladdin (Shanghai, China). 2-O-de-methylrotenone (R-OH, MW = 380) was synthesized in our laboratory. The vessels and glassware used in the experiments were carefully cleaned with aqua regia and rinsed with deionized (DI) water.

The UV-visible absorption spectra were measured by a Shimadzu UV-2550 spectrometer. Fluorescence spectra of as-prepared samples were measured at room temperature by using a Shimadzu RF-5301PC Spectrofluorophotometer. FTIR was recorded using a Bruker Optics Vetex 70 FTIR spectrometer and KBr as a standard for back-ground correction. TEM images were performed on a FEI TECANI12 microscope operated at 120 kV. The surface charges of the samples were measured with Zeta potential measurements in water (ZetaPALS/90plus zeta potential/particle size analyzer).

Synthesis of Au-BSA Stabilized Au Clusters (Au-BSA)

Au-BSA was obtained by the method described in the literature [32]. In a typical synthesis, aqueous HAuCl_4 solution (5 mL, 10 mM, 37 °C) was added to BSA solution (5 mL, 50 mg mL^{-1} , 37 °C) under vigorous stirring for 2 min. Then, NaOH solution (0.5 mL, 1 M) was introduced, and the mixture was continuously stirred at 37 °C for 12 h. During this period, the color of the colloid gradually changed, from light yellow to dark yellowish brown. Finally, the mixture was loaded into a dialysis bag (MWCO 8000) and dialyzed against deionized water for 48 h. The product was then freeze-dried.

Synthesis of Au-BSA Conjugated with R (Au-BSA-R)

R-OH was synthesized as previously described [34, 35]. Au-BSA-R was prepared by reacting the carboxyl groups of Au-BSA with the hydroxyl group of R-OH in the presence of EDC-HCl and DMAP as the catalysts [5]. Typically, 30 mg of EDC-HCl and 15 mg of DMAP were added into 20 mL of anhydrous DMSO containing 50 mg of Au-BSA. The mixture was stirred at room temperature

for 5 h. Then, 20 mg of R-OH in 5 mL of anhydrous DMSO was added dropwise into the above mixture. This solution was stirred at room temperature for 48 h. The product was loaded into a dialysis bag (MWCO 8000) and dialyzed against deionized water. After 48 h, the product was dried in vacuum.

Synthesis of Au-BSA-Gly Conjugated with R (Au-BSA-Gly-R)

Au-BSA-Gly was prepared by the amine group of glycine coupled to the carboxyl moieties of Au-BSA through EDC·HCl and NHS [5]. Typically, 11.5 mg of EDC·HCl was added into 1.0 mL of Au-BSA clusters solution and the mixture was stirred in dark for 10 min. 6.9 mg of NHS was poured into the mixture, which was continuously stirred in dark for 2 h under the same experimental condition. After that, 7.5 mg of Gly was added into the activated Au-BSA clusters solution and the new system was incubated for 12 h. Finally, the mixture was loaded into a dialysis bag (MWCO 8000) for 48 h. The product was then freeze-dried to obtain Au-BSA-Gly.

Au-BSA-Gly (50 mg) was dissolved in anhydrous DMSO (20 mL), EDC·HCl (30 mg) and DMAP (15 mg) were added, and the mixture was stirred in dark for 5 h. R-OH (20 mg) was added into the mixture and the new system was continuously stirred in dark for 48 h. The product was desalted and purified using a dialysis bag (MWCO 8000) for 48 h and further freeze-dried to obtain Au-BSA-Gly-R.

Quantum Yield (QY) of Au-BSA-Gly-R

The QY of the as prepared Au-BSA-Gly-R was measured by a comparative method calibrated with Rhodamine 6G dissolved in ethanol (QY = 95%). According the emission peak areas and absorbances of Au-BSA-Gly-R and Rhodamine 6G, the QY of the Au-BSA-Gly-R was then calculated according to the following equation:

$$\phi_{\text{sample}} = \frac{A_{\text{std}}}{A_{\text{sample}}} \times \frac{F_{\text{sample}}}{F_{\text{std}}} \times \frac{n_{\text{sample}}^2}{n_{\text{std}}^2} \times \phi_{\text{std}}$$

where ϕ_{std} is the known QY of the referenced fluorescence dyes, F_{sample} and F_{std} are the integrated emission intensities of the sample and the reference sample, respectively. A_{std} and A_{sample} are the absorbances of the reference sample and sample at the excitation wavelength (424 nm); n is the refractive index of the solvent (1.33 for water and 1.36 for ethanol). To obtain more reliable results, all samples were prepared with concentrations adjusted to ensure the optical densities were less than 0.05 at 424 nm. Optical density

and fluorescence intensity were recorded under identical instrument settings.

Insect Cell Culture

Spodoptera frugiperda (Sf9) cells were derived from exponentially growing monolayer cultures in our laboratory. About $2\text{--}2.5 \times 10^6$ cells were seeded into sterile 25 cm² cell culture flasks (Corning Incorporated) containing 4 mL of fresh HyClone SFX-Insect culture medium (GE Healthcare Life Sciences) supplemented with 5% fetal bovine serum (Life Technologies). The cells were allowed to attach to the bottom of the flask for 4 h. Cultures were maintained at 27 °C under a humidified condition with 1% CO₂. The medium for cell culture was refreshed every day.

Cytotoxicity

The cells were cultured in 96-well tissue culture plates (Corning Incorporated) at a density of 1×10^4 cells per well. The cells were treated with varies gold concentrations of Au-BSA, Au-BSA-R and Au-BSA-Gly-R, respectively. After incubation for 24 h, 10 μ L of cell count kit-8 (CCK-8, Beyotime, China) was added into each well and incubated at humidified condition for 4 h to evaluate the cytotoxicity of Au-BSA, Au-BSA-R and Au-BSA-Gly-R in Sf9 cells. The absorbance shifts of all samples were measured at 450 nm using an iMark microplate reader (BIO-RAD) and the cell viability was calculated following the standard procedure. Five parallel replicates of each sample at each time point were prepared and each experiment was performed three times during this cell viability assay.

Transporting Ability Evaluation of Au-BSA-Gly-R

Sf9 cells were cultured in 35 mm dishes for 24 h and the cells were incubated with Au-BSA-Gly-R (gold concentration at 25 μ g mL⁻¹) for 24 h. Then, the medium was removed and the cells were washed three times with PBS solution. Fluorescence images of Sf9 cells were acquired by Zeiss LSM 7 DUO (780&7Live) confocal microscopy (ZEN Microsystems) equipped with a 40 \times objective. Confocal images were obtained by illuminating the samples with the inline Diode (425 nm) and Argon (488 nm) lasers.

Flow Cytometric Analysis

To analyze the concentration of nanoparticles in cells, flow cytometry-based detection of fluorescence was used. The cells were cultured in 6-well plates with Au-BSA, Au-BSA-R and Au-BSA-Gly-R at 25 μ g mL⁻¹ gold

concentration for 24 h at 27 °C, respectively. Followed the medium was removed and the cells were washed three times with PBS solution. The cells were then analyzed using a FACSCalibur (BD Biosciences, USA) and the data were processed with CellQuest software (BD Biosciences, USA).

Cellular Uptake of Au-BSA, Au-BSA-R and Au-BSA-Gly-R

Sf9 cells were cultured in 12-well plate with a density of 1×10^6 cells per well. After 24 h of plating, the cells were washed once with culture medium, and the solutions of Au-BSA, Au-BSA-R and Au-BSA-Gly-R were added with a final gold concentration at $25 \mu\text{g mL}^{-1}$, respectively. The cells were incubated with Au-BSA, Au-BSA-R and Au-BSA-Gly-R for 24 h and washed three times with cold PBS to remove extra nanoparticles. The cells were detached by trypsin-EDTA solution (0.25% trypsin, 1 mM EDTA). The detached cells were counted and then prepared for ICP-MS. All ICP-MS measurements were performed on a Varian 710-ES spectrometer (Varian, Santa Clara, CA). After detaching and counting of the cells, each sample was digested for 10 min at electric hot plate by adding 3 mL of aqua regia. Then the above solution was diluted to 10 mL with 1.0% HNO_3 . Cellular uptake experiments with Au-BSA, Au-BSA-R and Au-BSA-Gly-R were repeated three times, and each replicate was measured three times by ICP-MS, respectively.

Results and Discussion

Synthesis and Characterization of Au-BSA-Gly-R

The fluorescent Au-BSA NCs were obtained by using an improved procedure [32]. R-OH was synthesized as described (see Supporting Information). The synthetic routes of Au-BSA-R and Au-BSA-Gly-R were briefly summarized in Scheme 1.

The size and morphology of Au NCs were further illustrated by TEM in Fig. 1. Au NCs appeared spherical particles with high dispersion and good crystalline nature. The small size of Au NCs played a critical role in determining their biodistribution behavior. As shown in Fig. 1, the average dimensions of Au NCs and Au-BSA-Gly-R were 2.1 ± 0.4 nm and 2.9 ± 0.5 nm by analysis of at least 200 nanoparticles, respectively. It was obvious that the dimensions of Au NCs had changed after the Au NCs were modified with Gly and R, which might be attributable to the Oswald ripening process [36]. In this process, the Au NCs with small dimensions in the solution were more easily dissolved and redeposited onto the

surface of larger Au NCs. Therefore, tiny Au NPs with each other in the solution could form larger nanoparticles.

As shown in Fig. 2(a), the absorbance peaks at 278 nm and 290 nm were corresponding to Au-BSA and R-OH, respectively. No localized surface plasmon resonance (LSPR) peak of Au-BSA could be detected around 520 nm, which confirmed that the sizes of Au NCs were less than 3 nm and implied their intrinsically molecule-like properties [37]. This phenomenon was in good agreement with the results of the TEM.

Additionally, no absorption peak of pure Gly solution was observed in Fig. 2(a). The characteristic absorption peak of R-OH was stronger than the absorption peak of Au-BSA, coupled with the absorption peaks of Au-BSA and R-OH were very close. The absorption peak of the Au-BSA might be covered with the absorption peak of the R-OH. Therefore, only a wide peak at 290 nm appeared in the spectra of Au-BSA-R and Au-BSA-Gly-R, which confirmed the successful conjugation of R to Au NCs.

Inset figures showed the optical images of Au-BSA, Au-BSA-Gly, Au-BSA-R and Au-BSA-Gly-R under white light and UV light (365 nm), respectively. Au-BSA and Au-BSA-Gly showed strong red emission. However, obvious reddish brown and blue fluorescence was detected for Au-BSA-R and Au-BSA-Gly-R, respectively. Then the different true colors of four samples under UV light (365 nm) could be attributed to their different components.

In Fig. 2(b), the fluorescent of Au-BSA showed emission peak at 609 nm when the nanoclusters were excited at 492 nm. Highly fluorescent Au NCs with red emissions were successfully synthesized. However, there was 113 nm blue-shifted to 496 nm for the emission peak of Au-BSA-Gly-R (excited at 424 nm) when conjugating the Gly and R to Au NCs. For another, Au-BSA-R and Au-BSA-Gly-R increased the new C=C, C=O groups called chromophores might result in the blue-shift of the photoluminescence (PL) peak [38]. Blue shift indicated hydrophobic strengthens and polarity weakens. These results fell in line with the blue-shift of the PL peak. In addition, the QY of Au-BSA clusters was calculated to be 6%, and the QY of Au-BSA-Gly-R in aqueous solution was determined as 1.72%, using Rhodamine 6G (QY = 95% in ethanol) as a reference. Although BSA was acting as a strong stabilizing agent, the radiative transitions within the Au core were found to be affected due to the conjugation of Gly and R. This phenomenon indicated that the surface chemistry played a vital role in determining the electronic distribution and the fluorescence characteristics of Au NCs [39]. Therefore, the reduced QY of Au-BSA-Gly-R might be attributed to the change of Au NCs' electronic energy structure when Au NCs conjugated with Gly and R.

These samples of Au-BSA, R-OH and Au-BSA-Gly-R were analytically followed by FTIR spectra as shown in

Scheme 1 Synthesis routine and structures of Au-BSA-R and Au-BSA-Gly-R

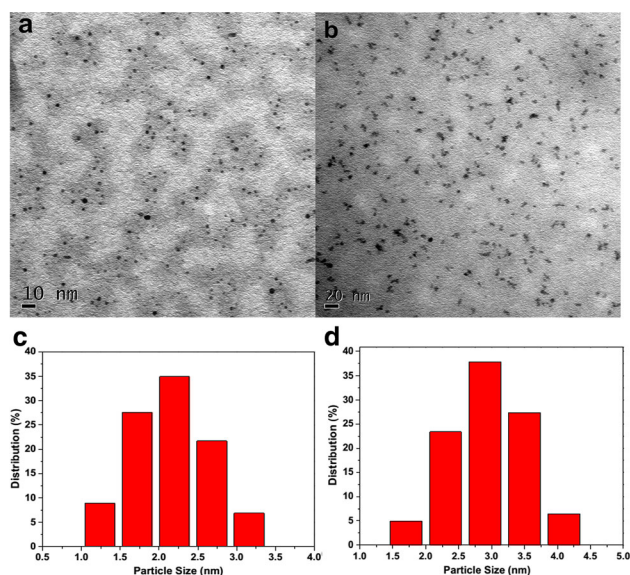
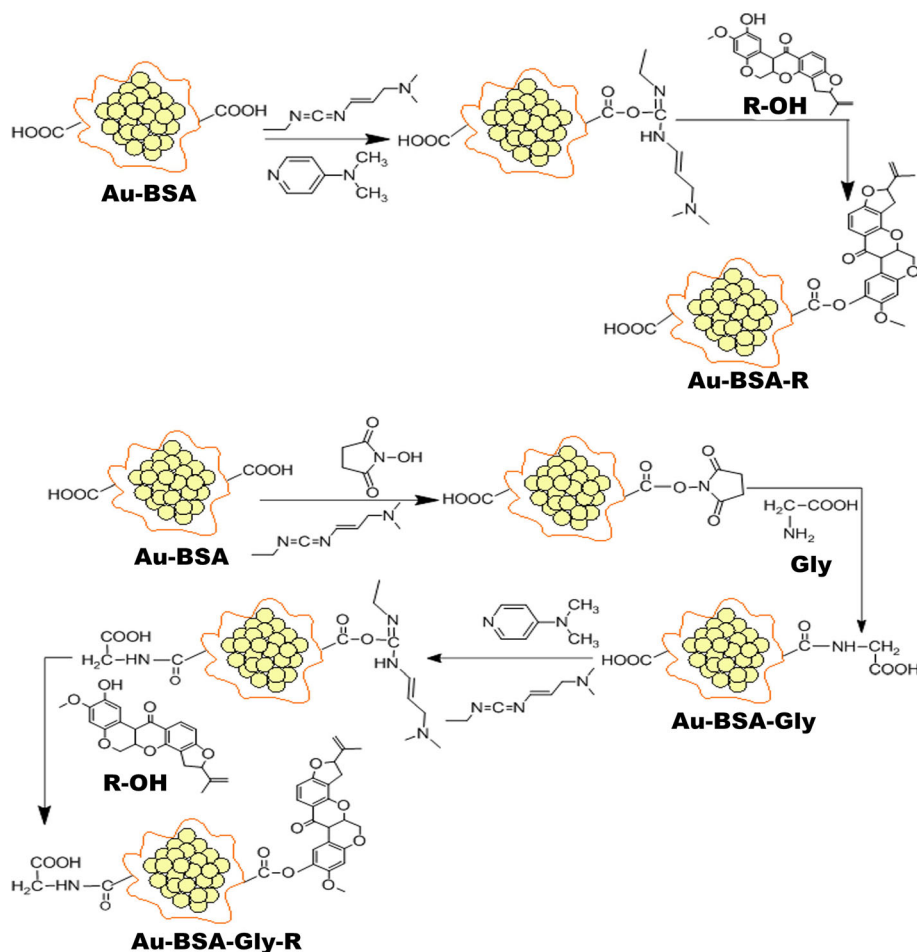


Fig. 1 TEM images and corresponding size distribution histograms of (a and c) Au-BSA and (b and d) Au-BSA-Gly-R

Fig. 3. With regard to the spectrum of Au-BSA, the characteristic absorption peaks of the C=O bond stretching

vibration and the -NH vibration of a -CONH₂ group can be observed at 1662 and 1541 cm⁻¹, respectively. There were much stronger peaks at 1662 and 1541 cm⁻¹ for Au-BSA-Gly-R after Au-BSA conjugated with Gly. Additionally, the band appearing at 1019 and 953 cm⁻¹ can be attributed to the characteristic absorption of the benzene ring of R-OH. Meanwhile, new absorption peaks of the benzene ring appeared at 1017 and 951 cm⁻¹ and there were small blue shifts for Au-BSA-Gly-R, which verified the well conjugation of R-OH with covalent linkage.

Zeta potentials of Au-BSA, Au-BSA-Gly, Au-BSA-R and Au-BSA-Gly-R were obtained in table S1 (see Supporting Information). The zeta potential of Au-BSA was -41.84 mV due to the existence of -COOH groups on the surface of Au-BSA. After conjugation with Gly and R, the zeta potential of Au-BSA-Gly-R turned into -15.54 mV because of the decrease of -COOH groups on the surface of Au-BSA. In order to verify the colloidal stability of Au-BSA-Gly-R in the cell culture medium, the stability was monitored by UV-vis spectrograph for 24 h. As shown in Fig. S1 (a), the absorbance curves of Au-BSA-Gly-R were similar. Additionally, the values of absorbance peaks remained nearly coincident at 280 and 310 nm in the

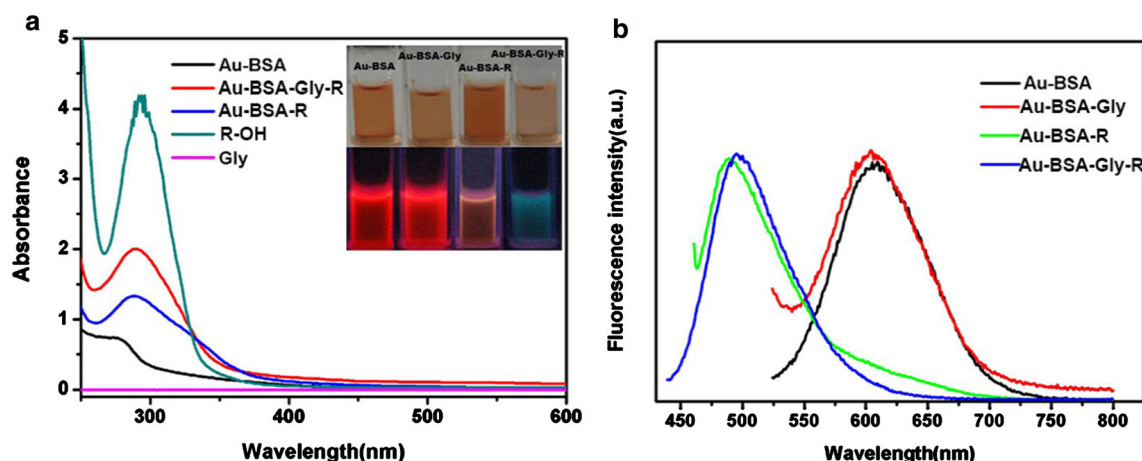


Fig. 2 **a** UV-vis absorption spectra of Gly, Au-BSA, R-OH, Au-BSA-R and Au-BSA-Gly-R. Inset: the optical images of Au-BSA, Au-BSA-Gly, Au-BSA-R and Au-BSA-Gly-R under the white

light illumination (top) and the fluorescence illumination (bottom) at 365 nm; **b** Fluorescence spectra of Au-BSA, Au-BSA-Gly, Au-BSA-R and Au-BSA-Gly-R

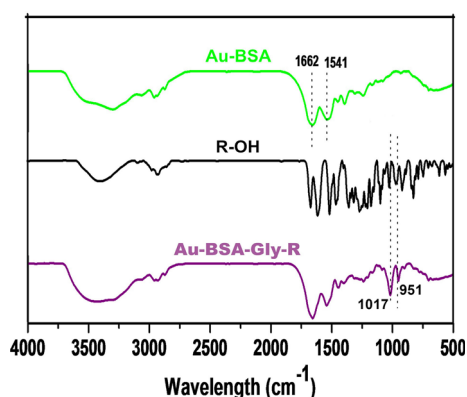


Fig. 3 FTIR spectra of Au-BSA, R-OH and Au-BSA-Gly-R

different incubation time. It stated that the absorbance of Au-BSA-Gly-R decreased slightly during first 12 h and remained essentially unchanged afterwards, which suggested that Au-BSA-Gly-R possess a very good stability in the cell culture medium within 24 h. This result was very import for biological experiments.

Cytotoxicity

To evaluate the biocompatibility of Au-BSA-Gly-R as imaging probes, the cytotoxicity of Au-BSA-Gly-R was investigated by the CCK-8 assay which relied on the mitochondrial activity of cells and represented a viable parameter for reporting metabolic activity. As shown in Fig. 4, the viability of Sf9 cells maintained above 80% when they had been incubated with Au-BSA, Au-BSA-R and Au-BSA-Gly-R up to the final gold concentration at $25 \mu\text{g mL}^{-1}$ for 24 h, respectively. In fact, the cytotoxicities of Au-BSA-R and Au-BSA-Gly-R were relatively low at the $12.5 \mu\text{g mL}^{-1}$ of gold concentration. It indicated

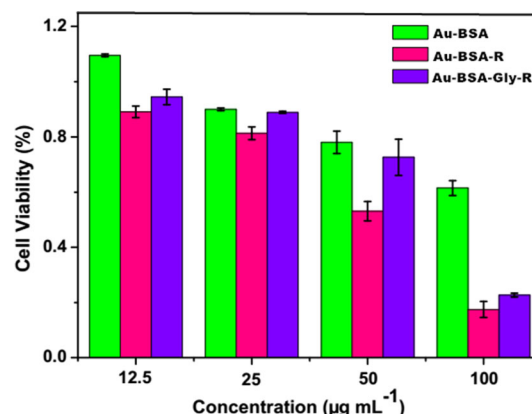


Fig. 4 The viabilities of cells after incubated with different dosages of Au-BSA, Au-BSA-R and Au-BSA-Gly-R in vitro for 24 h, respectively

that the high concentration of Au-BSA-R and Au-BSA-Gly-R could significantly reduce the cell viability because of the enhanced cytotoxicity mediated by R. In fact, R could induce to change the cell membrane potential, which led to cellular damage and reduced the cell viability [40]. Therefore, Au-BSA-R and Au-BSA-Gly-R in extracellular also did damage to the cells. Moreover, the same gold concentration of Au-BSA-R and Au-BSA-Gly-R had the same quantity of BSA capping gold clusters. Au-BSA-Gly-R was prepared by conjugating with Gly and R. In contrast, Au-BSA-R was synthesized only by the coupling of R with the BSA of Au NCs. Due to the different structures of Au-BSA-R and Au-BSA-Gly-R, Au-BSA-R contained more R molecules when compared with Au-BSA-Gly-R at the same gold concentration. The results showed that Au-BSA-R had a higher cell killing effect when the cells were treated with the same gold concentrations of Au-BSA-R and Au-BSA-Gly-R. As such, the

functionalized Au-BSA and Au-BSA-Gly-R, were further employed as optical probe for active imaging of Sf9 cells in vitro at $25 \mu\text{g mL}^{-1}$ of the concentration.

Imaging of Au-BSA-Gly-R at Cell Level

To visualize the cellular uptake of nano-conjugates, Sf9 cells were incubated with Au-BSA, Au-BSA-R and Au-BSA-Gly-R at $25 \mu\text{g mL}^{-1}$ gold concentration for 24 h, respectively. In addition, control experiments without addition of nanoclusters had been carried out to make sure that the autofluorescence from the cells at the same condition had been eliminated. As shown in Fig. 5, the cells treated with Au-BSA and Au-BSA-R did not exhibit the fluorescence by the confocal laser scanning microscopy, suggesting that the uptake of Au-BSA and Au-BSA-R were too little to find the fluorescence in the normal cells. However, strong blue fluorescence was observed in the Sf9 cell cytoplasm treated with Au-BSA-Gly-R. The dramatic difference demonstrated that the Gly on the surface of Au NCs could increase their cellular uptake inside Sf9 cells.

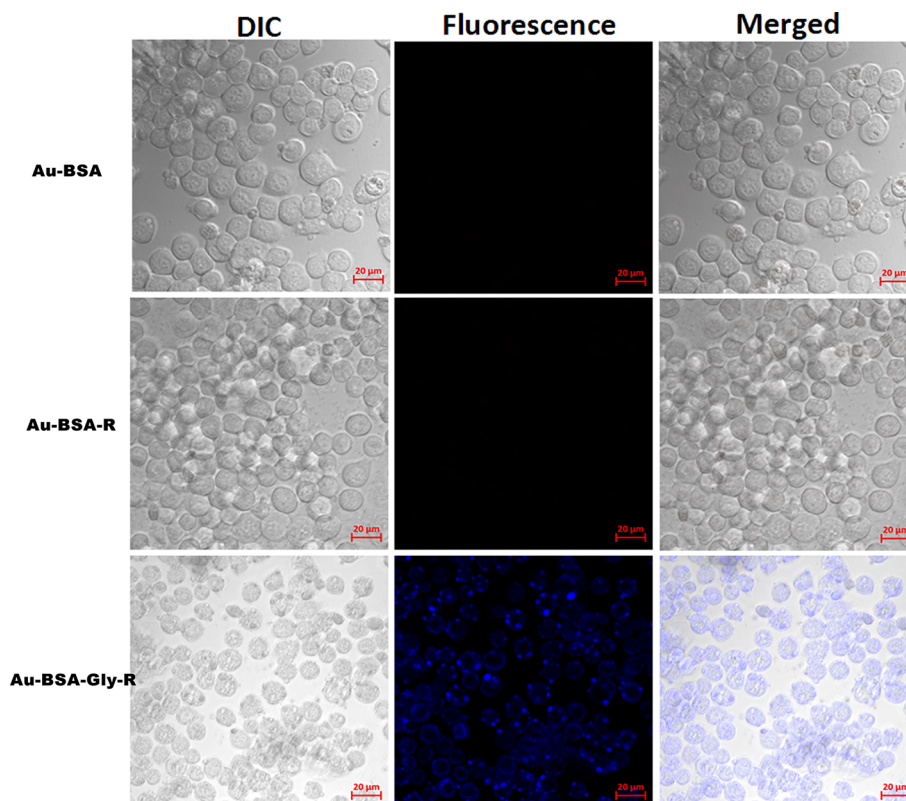
In order to evaluate the transporting ability of Au-BSA-Gly-R inside cells, we analyzed the uptakes of Au-BSA, Au-BSA-R and Au-BSA-Gly-R in Sf9 cells at the gold concentration of $25 \mu\text{g mL}^{-1}$ of 1.5×10^4 cells. Figure 6(a, b) indicated a concentration dependent uptake of Au-BSA, Au-BSA-R and Au-BSA-Gly-R, respectively.

Relative fluorescent intensity was measured by FACSCalibur and analyzed using CellQuest software. After incubation with Au-BSA, Au-BSA-R and Au-BSA-Gly-R in Sf9 cells, there was a different increase in cell-associated fluorescence. When Sf9 cells were incubated with Au-BSA-Gly-R, the value of median fluorescence intensity was 8.0 and 4.7 times higher than that incubated with Au-BSA and Au-BSA-R, respectively (Fig. 6(b)). It was obvious that the cellular uptake was significantly increased for Au-BSA-Gly-R.

Meanwhile, ICP-MS was performed after the incubation of Sf9 cells with Au-BSA, Au-BSA-R and Au-BSA-Gly-R at $25 \mu\text{g mL}^{-1}$ gold concentration for 24 h, respectively. As shown in Fig. 6(c), the gold content of Au-BSA-Gly-R in Sf9 cells was 2.2 and 2.6 times higher than that of Au-BSA and Au-BSA-R, respectively. Our results agreed with the fluorescent images examined by LSCM showing the enhanced cellular uptake of Au-BSA-Gly-R after Au NCs modified by Gly.

Cellular uptake efficiency was an important indicator of cell imaging and drug delivery capacity for Au-BSA-Gly-R. Thus, we also investigated the uptake efficiency inside *Spodoptera litura* (SL) cells to illustrate the selectivity of Au-BSA-Gly-R. ICP-MS was performed after the incubation of SL cells with Au-BSA-Gly, Au-BSA-R and Au-BSA-Gly-R at $25 \mu\text{g mL}^{-1}$ gold concentration for 24 h. As shown in Fig. S2 (see Supporting Information),

Fig. 5 The fluorescence microscopy images of Sf9 cells after incubated with Au-BSA, Au-BSA-R and Au-BSA-Gly-R



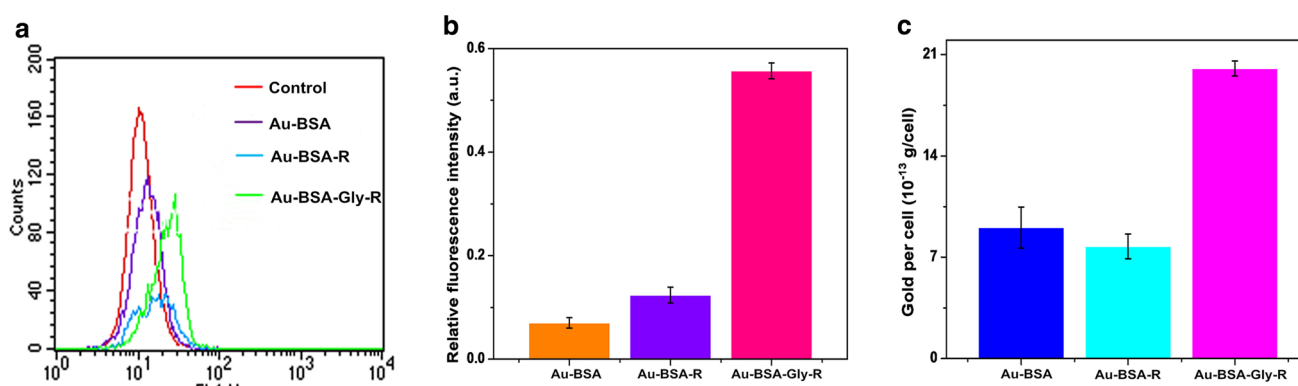


Fig. 6 **a** Fluorescent intensities of Control, Au-BSA, Au-BSA-R and Au-BSA-Gly-R in Sf9 cells analyzed by FACS. **b** Relative fluorescence intensities of Au-BSA, Au-BSA-R and Au-BSA-Gly-R in

Sf9 cells. **c** Cellular uptake of Au-BSA, Au-BSA-R and Au-BSA-Gly-R in Sf9 cells measured using ICP-MS

when SL cells were incubated with Au-BSA-Gly and Au-BSA-Gly-R, the gold content was 5.0 and 4.0 times higher than that when SL cells were incubated with Au-BSA-R, respectively. These results showed the role of Gly in cellular uptake for nanoparticles, which confirmed that Au-BSA-Gly-R was selectively uptaken by cells.

Conclusions

In summary, ultrasmall Au NCs were successfully conjugated with Gly and R, which were novel fluorescent nanoprobe selectively uptaken by Sf9 cells. In vitro cytotoxicity studies showed the normal concentration range of the new probe was low toxicity to cells. The cell imaging and transport ability of Au-BSA-Gly-R were analyzed by LSCM, flow cytometry and ICP-MS technology. These results indicated that the cellular uptake of Au-BSA-Gly-R mainly depended on Gly and the transport was significantly enhanced after Au NCs modified by Gly. The findings from this work suggest that Au NCs will be a promising nano-probe for the transport and imaging of amine acid conjugates in agricultural field.

Acknowledgements The authors are grateful for the financial support provided by the National Key R&D Program of China (2018YFD0200300), and Guangdong Provincial Innovation Team for General Key Technologies in Modern Agricultural Industry (2019KJ140).

References

1. S. Hu, B. Ye, X. Yi, Z. Cao, D. Wu, C. Shen, and J. Wang (2016). *Talanta*, **155**, 272.
2. J. Li, Y. Dai, S. Wang, C. Han, and K. Xu (2016). *Sensor. Actuat. B*, **232**, 1.
3. T. D. Fernandez, J. R. Pearson, M. P. Leal, M. J. Torres, M. Blanca, C. Mayorga, and X. L. Guevel (2015). *Biomaterials*, **43**, 1.
4. V. Venkatesh, A. Shukla, S. Sivakumar, and S. Verma (2014). *ACS Appl. Mat. Interfaces*, **6**, 2185.
5. H. Chen, B. Li, X. Ren, S. Li, Y. Ma, S. Cui, and Y. Gu (2012). *Biomaterials*, **33**, 8461.
6. A. P. Alivisatos (1996). *Science*, **271**, 933.
7. B. Xue, J. Cao, D. Den, J. Xia, Jing, Jin, Z. Qian, and Y. Gu (2012). *J. Mater. Sci. Mater. Med.*, **23**, 723.
8. A. Das, T. Li, K. Nobusada, Q. Zeng, N. L. Rosi, and R. Jin (2012). *J. Am. Chem. Soc.*, **134**, 20286.
9. C. Zeng, H. Qian, T. Li, G. Li, N. L. Rosi, B. Yoon, R. Barnett, R. Whetten, U. Landman, and R. Jin (2012). *Angew. Chem. Int. Ed.*, **51**, 13114.
10. W. Cai, A. R. Hsu, Z. B. Li, and X. Chen (2007). *Nanoscale Res. Lett.*, **2**, 265.
11. J. L. Jia, L. Zhu, X. Y. Jin, J. Wang, W. Zhang, H. X. Wu, and H. H. Xu (2014). *J. Mater. Chem. B*, **2**, 3299.
12. Z. Luo, K. Zheng, and J. Xie (2014). *Chem. Commun.*, **50**, 5143.
13. L. Zhang, and E. Wang (2014). *Mater. Sci.*, **9**, 132.
14. L. Shang, L. Yang, J. Seiter, M. Heinle, G. Brenner-Weiss, D. Gerthsen, and G. U. Nienhaus (2014). *Adv. Mater. Interfaces*, **1**, 1300079.
15. W. J. Chiu, W. Y. Chen, H. Z. Lai, C. Y. Wu, H. L. Chiang, and Y. C. Chen (2014). *J. Nanopart. Res.*, **16**, 2478.
16. K. G. Stamplecoskie, Y. S. Chen, and P. V. Kamat (2014). *J. Phys. Chem. C*, **118**, 1370.
17. K. G. Stamplecoskie, and P. V. Kamat (2014). *J. Am. Chem. Soc.*, **136**, 11093.
18. Y. Negishi, Y. Takasugi, S. Sato, H. Yao, K. Kimura, and T. Tsukuda (2004). *J. Am. Chem. Soc.*, **126**, 6518.
19. M. Hosseini, E. Ahmadi, Y. S. Borghei, and M. R. Ganjali (2017). *Methods Appl. Fluoresc.*, **5**, 015005.
20. L. Kong, X. Chu, X. Ling, G. Ma, Y. Yao, Y. Meng, and W. Liu (2016). *Microchim. Acta*, **7**, 2185.
21. S. Chattoraj, M. A. Amin, S. Mohapatra, S. Ghosh, and K. Bhattacharyya (2016). *ChemPhysChem*, **17**, 61.
22. X. L. Guevel, E. M. Prinz, R. Muller, R. Hempelmann, and M. Schneider (2012). *J. Nanopart. Res.*, **14**, 727.
23. L. Y. Chen, C. W. Wang, Z. Yuan, and H. T. Chang (2015). *Anal. Chem.*, **87**, 216.
24. J. M. Liu, J. T. Chen, and X. P. Yan (2013). *Anal. Chem.*, **85**, 3238.
25. K. Y. Pu, Z. Luo, K. Li, J. Xie, and B. Liu (2011). *J. Phys. Chem. C*, **115**, 13069.

26. A. Antonov, M. Agostini, M. Morello, M. Minieri, G. Melino, and I. Amelio, (2014). *Oncotarget*, **5**, 11004.
27. G. Tunnicliff (2003). *J. Biomed. Sci.*, **10**, 30.
28. H. N. Christensen, and M. E. Handlogten (1981). *Biochem. Biophys. Res. Commun.*, **98**, 102.
29. F. S. Sariaslani, and J. P. Rosazza (1983). *Appl. Environ. Microbiol.*, **2**, 616.
30. N. Z. Dimetry (2012). *Arch. Phytopathol. Plant. Prot.*, **10**, 1138.
31. L. Jia, X. Y. Jin, L. Zhu, Z. X. Zhang, W. L. Liang, G. D. Wang, F. Zheng, X. Z. Wu, and H. H. Xu (2017). *New J. Chem.*, **41**, 11398.
32. J. Xie, Y. Zheng, and J. Y. Ying (2009). *J. Am. Chem. Soc.*, **131**, 888.
33. X. Zhang, F. G. Wu, P. Liu, H. Y. Wang, N. Gu, and Z. Chen (2015). *J. Colloid Interface Sci.*, **455**, 6.
34. D. Carson, L. Crombie, G. W. Kilbee, F. Moffatt, and D. A. Whiting (1982). *J. Chem. Soc. Perkin Trans*, **1**, 779.
35. T. Unai, H. M. Cheng, I. Yamamoto, and J. E. Casida (1973). *J. Agric. Biol. Chem.*, **37**, 1937.
36. T. K. N. Hoang, L. Deriemaeker, V. B. La, and R. Finsy (2004). *Langmuir*, **20**, 8966.
37. H. Chen, B. Li, C. Wang, X. Zhang, Z. Cheng, X. Dai, R. Zhu, and Y. Gu (2013). *Nanotechnology*, **24**, 055704.
38. J. Pecher, and S. Mecking (2010). *Chem. Rev.*, **110**, 6260.
39. A. Retnakumari, S. Setua, D. Menon, P. Ravindran, H. Muhammed, T. Pradeep, S. Nair, and M. Koyatutty (2010). *Nanotechnology*, **21**, 055103.
40. P. Bonsi, P. Calabresi, C. D. Persis, M. Papa, D. Centonze, G. Bernardi, and A. Pisani (2004). *Exp. Neurol.*, **185**, 169.

Publisher's Note Springer Nature remains neutral with regard to jurisdictional claims in published maps and institutional affiliations.



Cite this: DOI: 10.1039/c7nj02571h

Enhanced intracellular uptake *in vitro* by glucose-functionalized nanopesticides†

 Jin-Liang Jia,^{‡ab} Xiao-Yong Jin,^{‡a} Li Zhu,^b Zhi-Xiang Zhang,^a Wen-Long Liang,^a Guo-Dong Wang,^{ab} Feng Zheng,^{ab} Xin-Zhou Wu^a and Han-Hong Xu^{ID*}

Nanopesticides have been increasingly used in agriculture. To improve the uptake of the target organisms for nanopesticides, we designed a dual-ligand nanopesticide based on gold nanoparticles (Au NPs) as a carrier. Herein, the novel structure and properties of Au NPs conjugated with D-glucose (Glc) and rotenone (R) were characterized by UV-visible and FTIR spectroscopy, transmission electron microscopy (TEM), dynamic light scattering (DLS), and zeta potential. The uptake and biodistribution of Glc-Au NPs, R-Au NPs, and Glc-Au NP-R were tested in tobacco BY-2 cells using flow cytometry, inductively coupled plasma optical emission spectroscopy (ICP-OES), confocal laser scanning microscopy (CLSM), and TEM. The cellular uptake of R-Au NP-Glc was increased by 1.8 folds as compared to that of R-Au NPs. Moreover, R-Au NPs-Glc could be actively transported into cells by hexose transporters and this uptake of the nanopesticides was an energy-dependent process. These results suggest that Glc is a promising ligand for the uptake and delivery of nanopesticides, and a well-designed system can enhance pesticidal bioavailability in agricultural scenarios.

Received 18th July 2017,
Accepted 22nd August 2017

DOI: 10.1039/c7nj02571h

rsc.li/njc

Introduction

To date, conventional pesticides as the major method for pest control have been widely used. However, some factors limit the application of agrochemical pesticides. For example, less than 0.1% of these pesticides actually reach the target area of pests.¹ Almost 99.9% of the applied pesticides move into ecosystems where they can contaminate the soil, water, nature, and the atmosphere of our environment.² Traditional technologies involve the indiscriminate use of pesticides. Recently, nanotechnology has created many opportunities for the safe application of conventional pesticides.^{3–5}

Nanodrugs, such as gold nanoparticles (Au NPs) conjugated with drugs and peptides, have been increasingly used in location, visualization, and biomedical applications^{6–8} because of their nontoxicity and biocompatibility.^{9,10} For example, Ueda *et al.* labeled the receptor for a chemical substance with a small molecular weight in plant motor cells using TEM.¹¹ Xu *et al.* used carbohydrate-binding module (CBM3a)-functionalized Au NPs to monitor the binding activity between CBM3a and plant cell wall cellulose in real time.¹² However, there have been few

reports on the uptake and imaging of nanopesticides in plant cells. In plants, plant phloem of the vascular tissue is responsible for the transport of nutrients and photosynthates.¹³ Moreover, sugar-transport proteins played a key role in long-distance transport in plants. Researchers found that the phloem mobility of monosaccharide–pesticide conjugates could be observed with the help of endogenous plant monosaccharide transporters.¹⁴ Among them, D-glucose (Glc) was better as a substrate for conferring phloem mobility than other monosaccharides.¹⁵ Therefore, small molecules, especially Glc as a basic nutrient and transported group, can be attached to the surface of Au NPs to realize drug uptake and transport.

Rotenone (R) has been used for more than 150 years to control crop pests because of its natural origin and short persistence in the environment.¹⁶ Xu *et al.* synthesized rotenone-conjugated glucose and found that the compounds could be transported into a phloem systemically type.¹⁵ To the best of our knowledge, the cellular uptake mechanism of nanopesticides by monosaccharide transporters has not been reported to date.

Therefore, it is necessary to develop dual-ligand Au NPs to understand the uptake and transport mechanism for nanopesticides inside plant cells. Herein, we synthesized a series of Au NPs with different ligands. The novel structure and properties of nanoparticles were characterized by UV-visible and FTIR spectroscopy, transmission electron microscopy (TEM), dynamic light scattering (DLS), and zeta potential analysis. The mechanism of uptake for the nanopesticides inside tobacco bright yellow 2 (BY-2) cells was reported, and the results also showed efficient

^a State Key Laboratory for Conservation and Utilization of Subtropical Agro-bioresources, South China Agricultural University, Guangzhou, Guangdong 510642, China.

E-mail: hxxu@scau.edu.cn; Fax: +86-20-38604926; Tel: +86-20-85285127

^b College of Materials and Energy, South China Agricultural University, Guangzhou, Guangdong 510642, China

† Electronic supplementary information (ESI) available. See DOI: 10.1039/c7nj02571h

‡ These two authors contributed equally.

imaging with a double-label (fluorescent, TEM) nanopesticide for a smart delivery system in agricultural scenarios.

Experimental methods

Materials

All the materials and reagents were used as purchased. Hydrogen tetrachloroaurate(III) trihydrate ($\text{HAuCl}_4 \cdot 3\text{H}_2\text{O}$, Acros, ACS reagent), ascorbic acid (AA, Beijing Chemical Reagent Company, 99%), D-glucose (Glc, Aladdin, AR), DL-thioctic acid (TA, Aladdin, 99%), 4-dimethylaminopyridine (DMAP, Aladdin, 99%), dicyclohexylcarbodiimide (DCC, Aladdin, 99%), hexamethyldisilazane (HMDS, Aladdin, 98%), trifluoroacetic acid (TFA, Aladdin, 99%), fluorescein isothiocyanate isomer (FITC, Aladdin, 95%), and trimethylchlorosilane (TMSCl, Aladdin, 98%) were used as received.

Characterization

UV-vis spectra were obtained *via* a Unico UV-2102PC spectrometer operated at a resolution of 0.5 nm using a quartz cell with a 1 cm light-path. FTIR spectra were obtained using a PE 2000 FTIR spectrometer and KBr as a standard for background correction. TEM images were obtained using a JEOL JEM-2010 microscope operated at 120 kV. Additionally, BY-2 cell sections were analyzed by TEM using well-established protocols. The ^1H and ^{13}C NMR spectra were obtained using a Bruker AVANCE III 600 (Bruker Corporation, Switzerland) spectrometer with tetramethylsilane (TMS) as the internal standard, and chemical shifts were acquired. The surface charges of the samples were measured *via* zeta potential measurements in water (a Zeta-PALS/90plus zeta potential/particle size analyzer) (Scheme 1).

Synthesis of Au NPs

Synthesis of a citrate-Au NP colloid. Citrate-Au NPs were synthesized according to earlier reports.^{17,18} Herein, 150 mL of deionized water was heated to boiling, and 30 mL (1 wt%) of aqueous trisodium citrate solution was added. When the mixture was boiling again, 20 mL (2.5 mM) of hydrogen tetrachloroaurate (trihydrate) was added to the abovementioned solution under

vigorous stirring, and the mixture was refluxed for 1 h. Finally, the mixture was cooled down to room temperature; this led to the formation of a citrate-Au NP colloid.

Synthesis of the rotenone-Au NP (R-Au NP) colloid. Herein, 10 mg of rotenone-thioctic (R-TA) was dissolved in 5 mL of tetrahydrofuran (THF), and the as-prepared solution was added dropwise to 40 mL of fresh citrate-Au NP colloid. The mixture was stirred overnight at room temperature.

Synthesis of the Glc-Au NP colloid. Typically, 10 mg of Glc-TA was dissolved in 5 mL of H_2O , and the as-prepared solution was added dropwise to 40 mL of fresh citrate-Au NP colloid. The mixture was stirred overnight at room temperature.

Synthesis of the R-Au NP-Glc colloid. Herein, 2.5 mL of THF containing R-TA (5 mg) and 2.5 mL of water containing Glc-TA (5 mg) were added dropwise to 40 mL of fresh citrate-Au NP colloid. The colloid was stirred overnight at room temperature.

Synthesis of Glc-Au NP-FITC, R-Au NP-FITC, and R-Glc-Au NP-FITC. Herein, 1.0 mg FITC-TA was added to the MeOH solution of the corresponding compounds, and the mixture was stirred.

Preparation of the samples

All the abovementioned colloids (R-Au NPs, Glc-Au NPs, Au NP-Glc, Glc-Au NP-FITC, R-Au NP-FITC, and R-Glc-Au NP-FITC) were centrifuged at 8000 rpm for 10 min. The colorless supernatant was decanted, and the solid was dispersed in deionized water. Then, the wash-centrifugation cycle was repeated 3 times. After the final washing, the functionalized Au NPs were dried in vacuum at 45 °C.

Cell culture

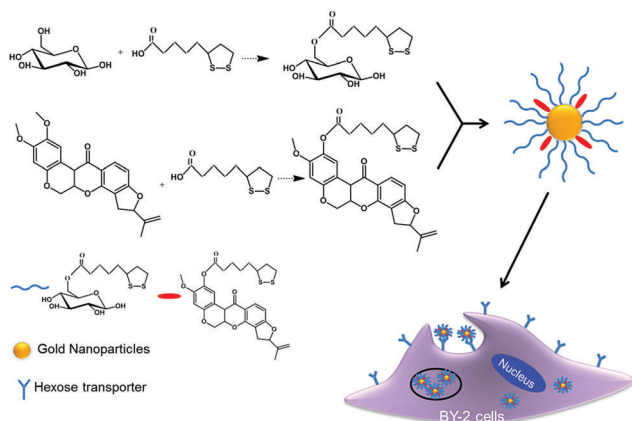
The BY-2 cells were cultured in a Murashige-Skoog medium as described by Kumagai-Sano *et al.*¹⁹ In brief, the BY-2 cells were grown in a 30 mL of culture medium (pH 5.8) containing 0.05% Tween 20 on a rotary shaker set at 130 rpm and 27 °C in the dark. Then, cell samples were obtained from 5-day-old cultures during the rapid growth phase.

ICP-OES

For quantifying these conjugations in BY-2 cells, 50 ppm of Glc-Au NPs, R-Au NPs, and R-Au NP-Glc were incubated for 6 h. Cell aliquots were obtained at the indicated times, centrifuged at 2000 rpm for 5 min, and the supernatant was discarded. Then, the pellet was washed with 1 mL of the culture medium. To remove all the unabsorbed gold nanoparticles, the washing procedure was repeated three times. After the final washing, the cells were dried in an oven at 100 °C for 24 h. The dry weight of the cells was measured. The dried cells were digested using 12 mL of HNO_3 and 6 mL of HClO_4 on a hot plate (~100 °C). The as-prepared solutions were diluted to the mark and analyzed for Au content by ICP-OES.

Flow cytometric measurement of plasma membrane potential

The protoplasts of BY-2 cells were prepared according to the method reported in literature.²⁰ Typically, 10% (v/v) BY-2 cells were added to the enzyme solution, and the mixture was incubated at 27 °C for 1 h with gentle shaking (~130 rpm).



Scheme 1 Schematic illustration for the formation of multifunctional drug-loaded Au NPs and the uptake of the R-Au NPs-Glc inside BY-2 cells by the hexose transporters.

After the cells were centrifuged at 1941 rpm for 3 min, 20 mL of enzyme solution was added to 4 mL of cells. The as-prepared solution was slightly shaken at 27 °C for 4 h in the dark. The resulting solution was then filtered into a centrifuge tube using a 75 µm nylon mesh. After separation by centrifugation at 970 rpm for 2 min, the protoplasts were obtained. This centrifugation was repeated three times by adding the culture solution.

Plasma membrane potential was measured using flow cytometric analysis of the protoplasts of BY-2 cell; bis(1,3-dibutylbarbituric acid)trimethineoxonol [DiBAC₄(3)] was used as the fluorescent membrane potential indicator dye. The membrane potential of protoplasts was estimated according to a previously described method.²¹ Herein, 50 ppm of Glc-Au NPs, R-Au NPs, and R-Au NP-Glc were added to the protoplast suspension and incubated with 2 µmol L⁻¹ DiBAC₄(3) for 30 min at 27 °C prior to the flow cytometric analysis.

TEM

Cells were incubated with Au NPs at different times. Later, the cells were obtained and fixed in glutaraldehyde-paraformaldehyde and osmium tetroxide, then washed through a graded ethanol series, and embedded in pure resin. Ultrathin sections were obtained on copper grids and stained using TEM images.

High performance liquid chromatography (HPLC) analysis

BY-2 cells were incubated with 50 ppm (gold concentration) of R-Au NPs and 10 ppm of R-OH for 6 h. Then, the wash-centrifugation cycle was repeated 3 times. The same volume of DMSO was added to the cell solution, and the as-prepared solution was sonicated for 1 min and centrifuged at 11 884 rpm for 10 min. The supernatant solution was then filtered into a centrifuge tube using a 0.22 µm nylon mesh. The samples were analyzed *via* an Agilent 1100 HPLC system using a C₁₈ reversed-phase column (5 µm; 250 × 4.6 mm i.d.; Agilent Co.) at 30 °C. The flow rate was 1.0 mL min⁻¹, and the mobile phase comprised acetonitrile and water (56/44, v/v). Recovery rate of R-OH in were

>85% conducted by adding BY-2 cells with three replicates. Additionally, R-OH was detected by UV absorption at 299 nm.

Results and discussion

Characterization of the Au NPs

The morphologies of Au NPs with different ligands were observed by TEM. As shown in Fig. 1(a–d), the average dimensions of citrate-Au NPs, R-Au NPs, Glc-Au NPs, and R-Au NP-Glc were 12.4 ± 0.9 nm, 12.6 ± 1.0 nm, 13.7 ± 1.4 nm, and 13.6 ± 1.2 nm, respectively. The mean values were slightly different depending on the type of ligands because of synthesis batch variability,²² which illustrated that the size of the exchanged ligands for Au NPs induced almost no change.

As shown in Fig. 1(e), the hydrodynamic diameters of Glc-Au NPs, R-Au NPs, and R-Au NP-Glc are 27.2, 33.4, and 35.3 nm, respectively, determined by a laser particle size analyzer (LPSA). In a water solution, the size of the Au NPs coated by two ligands was bigger than that of Au NPs coated with a single ligand; this indicated the successful formation of dual-ligand conjugations. Moreover, the mean size of Au NPs obtained by the LPSA was obviously larger as compared to the size (~13 nm) obtained by TEM. It is known that the observed size of nanoparticles under a dry condition by TEM was generally smaller than that in solution.²³ In Fig. S6 (ESI[†]), the zeta potential values of citrate-Au NPs, R-Au NPs, Glc-Au NPs, and R-Au NP-Glc were -65.87 ± 5.52 mV, -47.18 ± 3.51 mV, -42.25 ± 3.52 mV, and -35.77 ± 2.68 mV, respectively. Zeta potential is an indicator of the stability of nanoparticle suspensions. As is known, the absolute zeta potential values of about 30 mV showed good stability and the value of about 60 mV indicated excellent stability, which was valid for low molecular weight surfactants and pure electric stabilization.²⁴ Thus, these colloid solutions maintained a stable system.

As shown in Fig. 1(f), the components of the formed citrate-Au NPs, R-Au NPs, Glc-Au NPs, and R-Au NP-Glc were confirmed by

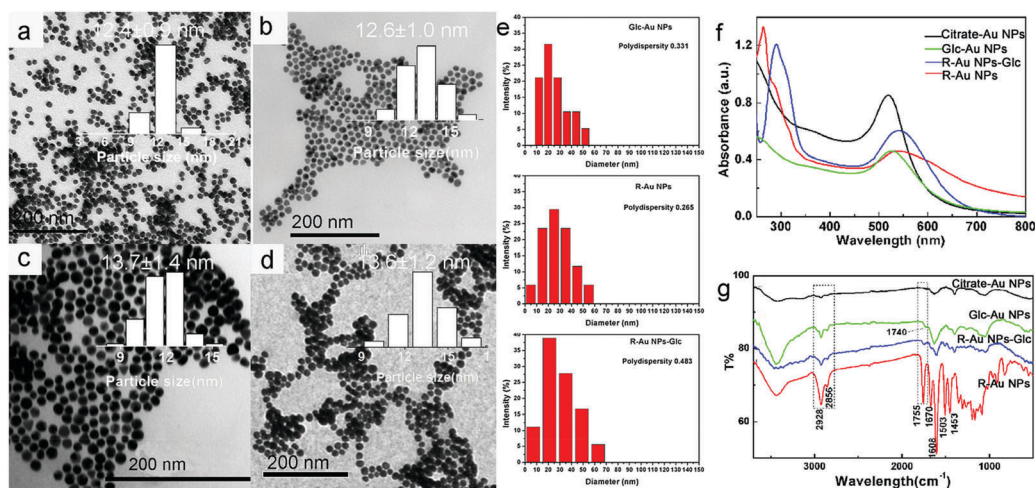


Fig. 1 TEM images of (a) citrate-Au NPs, (b) R-Au NPs, (c) Glc-Au NPs, and (d) R-Au NP-Glc. (e) Dynamic diameters of Glc-Au NPs, R-Au NPs, and R-Au NP-Glc as determined by LPSA; and the (f) UV-vis and (g) IR spectra.

UV-visible spectroscopy. The UV-visible spectrum of citrate-Au NPs showed the characteristic surface plasmon resonance (SPR) band at 520 nm. As is known, the width of the absorption band and the position of the SPR peak depend on the morphology of particles and the dielectric environment.²⁵ Owing to different solvents for different gold colloids, the peak values for other ligands of Au NPs became slightly red-shifted as compared to those of the citrate-Au NPs. Additionally, the absorption peak of Glc was very weak such that it was not obvious between 250 and 300 nm in the case of the Glc-Au NPs colloid. On the other hand, there was an obvious absorption peak at 264 nm for R-Au NPs in the THF solvent. However, the peak was observed at 290 nm for R-Au NP-Glc in THF/H₂O (V/V = 1/1), which also illustrated that the difference in the absorption peaks for R resulted from different solvents.²⁶

To confirm that the functional ligands were successfully synthesized, these samples were characterized by IR spectroscopy. On comparing the spectra of citrate-Au NPs with that of Glc-Au NPs (Fig. 1(g)), we observed that the spectrum of Glc-Au NPs showed a stretching band at 1740 cm⁻¹ that was assigned to the vibrational mode of the carbonyl group. However, the asymmetric and symmetric stretching vibration peaks at 1400 and 1620 cm⁻¹ were assigned to carboxylate ions in the citrate groups,²⁷ revealing that citrate ions were completely replaced the Glc ligands. Moreover, the spectra of R-Au NP-Glc and R-Au NPs showed the stretching band of the carbonyl groups at 1755 cm⁻¹, illustrating that there were ester groups present after the exchange reaction. The peaks of the ester group had slightly shifted because there were benzene rings conjugated with the ester group. Additionally, there were a few peaks of $\nu(\text{CH}_2)$ at 2928 and 2856 cm⁻¹. However, strong peaks were observed in the spectra of Glc-Au NPs, R-Au NP-Glc, and R-Au NPs. This suggested these Au NPs surfaces had a major stretching band of $\nu(\text{CH}_2)$. In the spectra of R-Au NP-Glc and R-Au NPs, the peaks at 1670 cm⁻¹ could be attributed to the carbonyl groups of R. The peaks at 1608, 1503, and 1453 cm⁻¹ were assigned to the aromatic ring. By contrast, the IR spectra confirmed that an exchange reaction between citrate and different ligands had occurred.

Stability of the R-Au NPs inside BY-2 cells

To examine the stability of R-Au NPs inside the BY-2 cells when the ligand of R-TA was coupled by the ester bond (Scheme S2, ESI[†]), 50 ppm of R-Au NPs (gold concentration) and 10 ppm of R-OH were individually incubated. The as-prepared solution was analyzed by HPLC to detect the potential hydrolysis products (R-OH). In Fig. 2, the peak of the R-OH position at 22.95 min could not be detected in the solution of the BY-2 cells and R-Au NPs. This indicated that there was no R-OH ingredient in the solutions of BY-2 cells or R-Au NPs. Additionally, 50 ppm of R-Au NPs was incubated for 6 h in the BY-2 cell solution. Subsequently, the peak of R-OH was detected by HPLC in the extracted solution. Moreover, 2 ppm of R-OH was calculated based on the peak area. This result indicated that the ester bond of R-Au NPs could have a certain degree of hydrolysis inside the BY-2 cells for 6 h. To investigate the degree of hydrolysis, quantitative analyses were carried out on the R-Au NP materials. Herein, 0.68 mg of R-Au

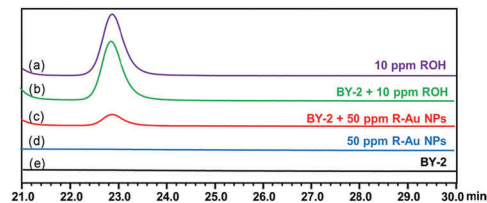


Fig. 2 HPLC chromatograms of the five samples: (a) 10 ppm of R-OH, retention time (RT) of R-OH (RT 22.95 min); (b) BY-2 cells were incubated with 10 ppm of R-OH for 6 h; (c) BY-2 cells were incubated with 50 ppm of R-Au NPs (gold concentration) for 6 h; (d) 50 ppm of R-Au NPs (gold concentration); and (e) BY-2 cells.

NPs was dispersed in 1 mL of DMSO solution. Then, 50 ppm of gold concentration in the solution was measured by ICP-OES, which indicated that there was 0.05 mg of gold in the sample of R-Au NPs (0.68 mg) if we approximated the density of the DMSO solution as 1.00 g mL⁻¹. Thus, the mass of the organic ligands for R-Au NPs was 0.63 mg. The ratio of molecular weight between R-OH of dehydrogenation and thioctic acid of dehydroxylation in organic ligands was approximately equal to 2 : 1 since their molecular weights were 380 and 189, respectively. Thus, the concentration of R-OH was 420 ppm for 50 ppm of R-Au NPs (gold concentration). Hence, the degradation ratio to R-Au NPs inside BY-2 cells for 6 h was only 0.48% because the concentration of R-OH in the extracted solution of R-Au NPs was 2 ppm, as obtained by HPLC. This result indicated that the hydrolysis process of R-Au NPs in the culture medium of BY-2 cells for 6 h was almost negligible.

Plasma membrane potential of protoplasts

Plant protoplasts without cell walls offer a versatile cell-based experimental system.²⁸ Because tobacco protoplasts are extremely fragile, they have been tested for viability with fluorescein diacetate (FDA), used to test membrane integrity. We could see that over 95% of protoplasts showed FDA-dependent fluorescence; this indicated that the cell membranes were intact and the plant protoplasts were viable. Then, plasma membrane potential was measured using flow cytometric analysis of these protoplasts. Bis(1,3-dibutylbarbituric acid) trimethine oxonol [DiBAC₄(3)] was selected as the fluorescence membrane potential indicator dye. Protoplasts in buffer with the Au NPs (50 ppm of gold concentration) were cultured for 6 h. To test the membrane potential, the DiBAC₄(3) fluorescence of 20 000 viable protoplasts was analyzed. Each treatment was repeated three times, and then, these data were analyzed by the Duncan's multiple-range test, as shown in Fig. 3. The Duncan's multiple-range test ($P > 0.05$) indicated that there were no significant differences in the relative fluorescence among treatments. Thus, these Au NP conjugates with different ligands could be used in biological experiments.

Cellular uptake of BY-2 cells for Au NPs

We quantitatively determined the cellular uptake of 50 ppm R-Au NPs in BY-2 cells to optimize the incubated time. Fig. 4(a) shows that the cellular uptake of 50 ppm R-Au NPs was

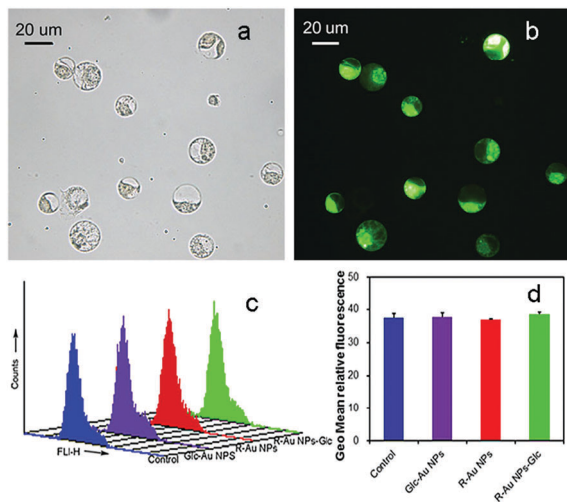


Fig. 3 Membrane potential of protoplasts treated with Au NPs with different ligands for 6 h. (a) Bright field image; (b) fluorescent image; and (c) fluorescence intensity histogram. (d) Mean relative fluorescence ($P > 0.05$).

saturated at 2 h. However, the saturation curve had a slight instability. Then, we used an incubation time of 6 h for 50 ppm R-Au NPs for full saturation.

To illustrate the role of glucose ligands, cellular uptakes of BY-2 cells for Au NPs with different ligands were investigated. In Fig. 4(b), we could see that the gold content of citrate-Au NPs was almost equal to that of R-Au NPs. However, the gold content in BY-2 cells for R-Au NPs-Glc and Glc-Au NPs was increased by 1.8 and 2.7 folds, respectively, as compared to that of R-Au NPs. The results demonstrated quantitatively that R-Au NPs conjugated with Glc could enhance the over-expression of Glc transporters.

An investigation of the cellular internalization mechanism will provide important information on the active transport for Glc. There were three critical characteristics, including energy dependence, carrier-mediation, and movement against the

concentration gradient, for active transport.²⁹ The major mode for nanomaterials entering the cells was the endocytosis process. However, it was not clear whether an energy-dependent process was involved in the uptake of R-Au NPs-Glc by the BY-2 cells. The cellular uptakes under different conditions for R-Au NPs-Glc are shown in Fig. 4(c). The uptake values decreased in the presence of the inhibitors, including Glc and carbonyl cyanide *m*-chlorophenylhydrazone (CCCP). As is known, CCCP has been widely utilized in these studies of cellular transmembrane transport because CCCP as an energy uncoupler can efficiently inhibit the membrane energy.³⁰ As shown in Fig. 4(c), CCCP inhibited the total absorption of R-Au NP-Glc by 31.14%, whereas the absorption of Glc inhibitor drastically increased by 48.35%. It suggested that the uptake of R-Au NP-Glc in BY-2 cells was an energy-dependent process. Additionally, hexose transport systems used the energy to actively transport monosaccharides into cells.³¹ Glc obviously affected the uptake of R-Au NP-Glc, as shown in Fig. 4(c); this indicated that the hexose transporters participated in the uptake of the R-Au NP-Glc. Thus, the process of R-Au NP-Glc to enter BY-2 cells was not only active transport through the hexose transporter but also an energy-dependent process.

Cell affinity evaluation of Au NPs with different ligands

The fluorescence microscopy images of Glc-Au NP-FITC, R-Au NP-FITC, and R-Glc-Au NP-FITC are shown in Fig. 5 to investigate their distribution and affinity to BY-2 protoplasts. Although there were several apoptotic cells seen by PI staining, the vast majority of protoplasts was intact. This phenomenon was in agreement with the results of the membrane potential. In addition, no fluorescence was observed for control cells. Moreover, R-Au NP-FITC provided a faint fluorescence signal during a treatment of 6 h; this indicated the low concentration of R-Au NPs in these

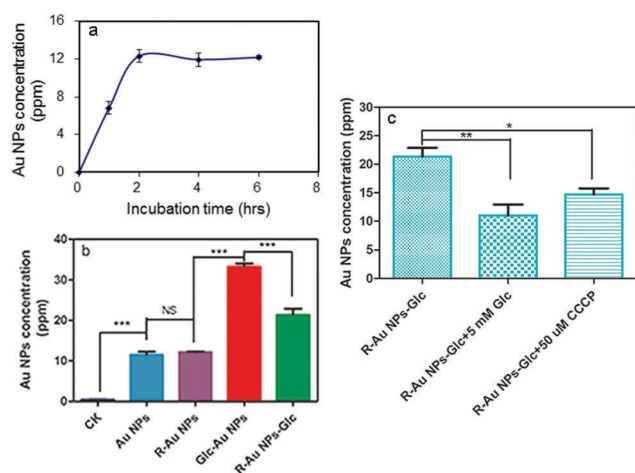


Fig. 4 (a) Optimization of incubation time in BY-2 cells for R-Au NPs; (b) cellular uptake for Au NPs with different ligands; and (c) cellular uptake under different conditions. The gold concentration in cells is 50 ppm as obtained by ICP-OES. The data represent the mean \pm standard deviation of the results obtained from three experiments. * $P < 0.05$, ** $P < 0.01$, *** $P < 0.001$.

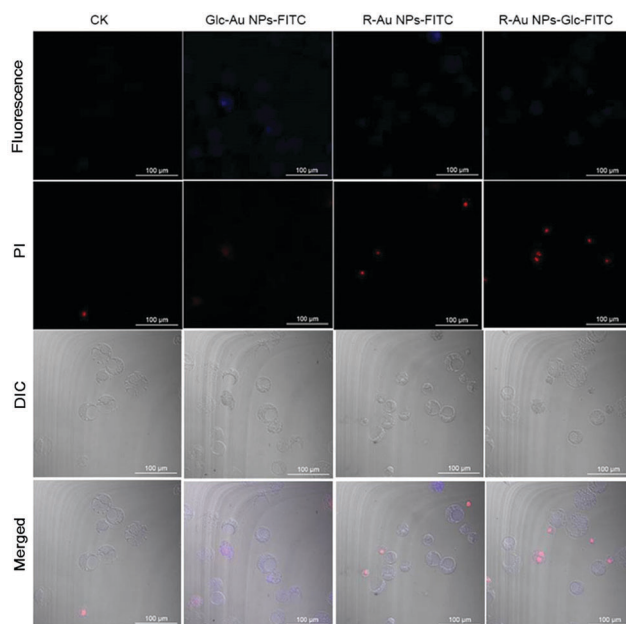


Fig. 5 Confocal laser scanning microscopy (CLSM) images of BY-2 cells after treatment with different Au NPs for 6 h. All Au NPs were labelled with FITC which had blue fluorescence. The scale bar was 100 μm.

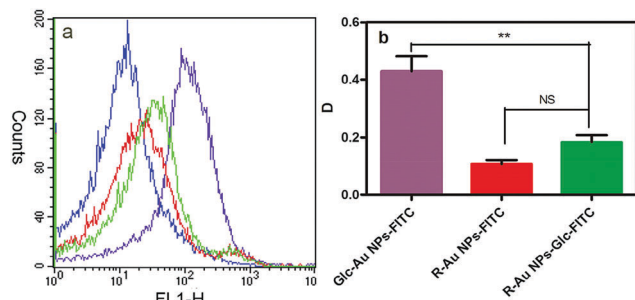


Fig. 6 Flow cytometry assay of Au NPs with different ligands in protoplasts. (a) Flow intensity of Au NPs. The blue, red, green, and purple curves represented protoplasts control, protoplasts treated with R-Au NP-FITC, R-Glc-Au NP-FITC, and Glc-Au NP-FITC, respectively; (b) the fluorescence histograms of three different Au NPs obtained using the Kolmogorov–Smirnov statistics. * $P < 0.05$, ** $P < 0.01$, *** $P < 0.001$.

protoplasts. The weak blue fluorescence in normal cells was in agreement with literature.²³ However, Glc-Au NP-FITC produced the strongest fluorescence at 6 h. This clearly demonstrated that the presence of Glc on the surface of Au NPs increased their cellular uptake; this indicated that Glc substantially enhanced R-Au NP accumulation in BY-2 cells *in vitro*.

Flow cytometry data should be more statistically reliable than CLSM data owing to the higher numbers of cells analyzed.³² Then, the quantities of FITC conjugated with Au NPs inside the cells were also evaluated, as shown in Fig. 6. Although it was difficult to precisely quantify nanoparticles uptake by fluorescence measurements using flow cytometry assay, it clearly showed that the choice of different ligands had a dramatic effect on the nanoparticles uptake of the protoplasts. The area under the curve of R-Au NP-Glc was proportional to the total number of fluorescent cells and was about twice that for R-Au NPs. The fluorescence intensity of Glc-Au NPs in protoplasts is significantly higher than those of Glc-Au NP-R and R-Au NPs, which was consistent with the ICP-OES data shown in Fig. 4(b). Moreover, this indicated that the addition of Glc enhanced the uptake of Au NPs.

TEM

To further determine the localization of the nanopesticides on the cellular compartments at different times, the uptake of R-Au NP-Glc was also visualized by TEM in time-course experiments of BY-2 cells (Fig. 7a–f). In Fig. 7(a), after 30 min of incubation, most of R-Au NP-Glc were distributed on the plasma membrane surface and the cytoplasm, which could be clearly seen in Fig. 7(b). The conjugations were at the periphery of the plasma membrane and most of the particles were found in the cytoplasm after 2 h, as shown in Fig. 7(c). Although the cellular uptake of nanoparticles was saturated at 2 h, they still could enter the inner compartments through the glucose-ligand. Next, the conjugations entered the inner vesicles and deeper cytoplasm after 4 h, as shown in Fig. 7(d). Glc was probably playing a role in membrane trafficking from the cell periphery to other compartments. Finally, the conjugations were distributed near the nucleus after 6 h, as shown in Fig. 7(e and f). Qualitative analysis showed the conjugates in

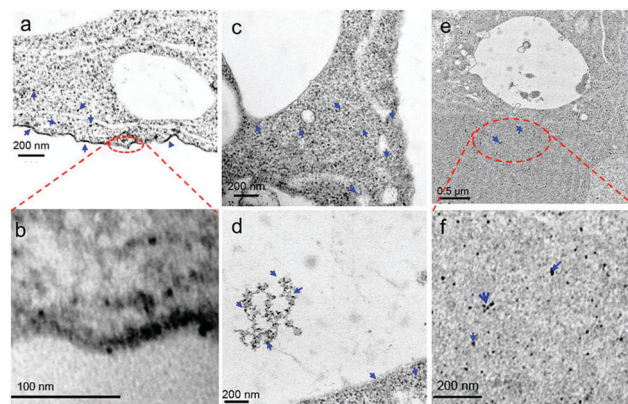


Fig. 7 Compartments labelled by 50 ppm of R-Au NPs-Glc during time-course experiments, and the time of incubation at (a) 30 min; (c) 2 h; (d) 4 h; (e) 6 h; (b and f) insets show the magnified below two images. A part of Au NPs is labelled by the blue arrows.

the different compartments during the time-course experiment, suggesting that R-Au NP-Glc could enter the inner compartments of the BY-2 cells with time, and the localization of the nanopesticides through the Glc molecules could be observed by TEM.

Conclusions

In summary, we demonstrated that Glc-coated Au NPs could efficiently deliver pesticides (Rotenone) into BY-2 cells. The uptake efficiency of R-Au NP-Glc was increased by 1.8 folds as compared to that of the R-Au NPs. Moreover, the bio-distribution of these conjugations was monitored by TEM/CFM inside the BY-2 cells. These results indicated that the internalization of R-Au NP-Glc was energy dependent and the hexose transporters participated in the uptake of the R-Au NPs-Glc. We hope that the study on the use of Glc for nanopesticides in plant cells will promote the development of a smart delivery system in the agricultural field.

Conflicts of interest

There are no conflicts to declare.

Acknowledgements

This work was financially supported by National Science Foundation of China (Grants 31401781 and 31672044), and Science and Technology Programme of Guangzhou (Grant 201510010299).

Notes and references

- 1 D. Pimentel, *J. Agric. Environ. Ethics*, 1995, **8**, 17.
- 2 D. Pimentel and H. Lenman, *In the pesticides question: environment, economics and ethics*, 1993, ch. 3, p. 47.
- 3 M. Nuruzaman, M. M. Rahman, Y. Liu and R. Naidu, *J. Agric. Food Chem.*, 2016, **64**, 1447.

- 4 J. Cao, R. H. Guenther, L. S. Tim, S. A. Lommel, C. H. Opperman and J. A. Willoughby, *ACS Appl. Mater. Interfaces*, 2015, **7**, 9546.
- 5 L. Zhao, Y. Huang, J. Hu, H. Zhou, A. S. Adeleye and A. A. Keller, *Environ. Sci. Technol.*, 2016, **50**, 2000.
- 6 A. Onoda, H. Harada, T. Uematsu, S. Kuwabata, R. Yamanaka, S. Sakurai and T. Hayashi, *RSC Adv.*, 2017, **7**, 1089.
- 7 T. Lund, M. F. Callaghan, P. Williams, M. Turmaine, C. Bachmann, T. Rademacher, I. M. Roitt and R. Bayford, *Biomaterials*, 2011, **32**, 9776.
- 8 R. Weissleder, *Science*, 2006, **312**, 1168.
- 9 L. L. Knittel, P. Schuck, C. J. Ackerson and A. A. Sousa, *RSC Adv.*, 2016, **6**, 46350.
- 10 A. Kurniawan, F. Gunawan, A. T. Nugraha, S. Ismadji and M. J. Wang, *Int. J. Appl. Pharm.*, 2017, **516**, 158.
- 11 Y. Manabe, T. Sugimoto, T. Kawasaki and M. Ueda, *Tetrahedron Lett.*, 2007, **48**, 1341.
- 12 M. Zhang, S. C. Wu, W. Zhou and B. Xu, *J. Phys. Chem. B*, 2012, **116**, 9949.
- 13 M. R. Hill, E. J. MacKrell, C. P. Forsthoefel, S. P. Jensen, M. Chen, G. A. Moore, Z. L. He and B. S. Sumerlin, *Biomacromolecules*, 2015, **16**, 1276.
- 14 Q. Xia, Y. J. Wen, H. Wang, Y. F. Li and H. H. Xu, *J. Agric. Food Chem.*, 2014, **62**, 11037.
- 15 P. W. Qin, J. Wang, H. Wang, Y. J. Wen, M. L. Lu, Y. F. Li, Y. S. Xu and H. H. Xu, *J. Agric. Food Chem.*, 2014, **62**, 4521.
- 16 M. B. Isman, *Annu. Rev. Entomol.*, 2006, **51**, 45.
- 17 G. Frens, *Nat. Phys. Sci.*, 1973, **241**, 20.
- 18 P. Nativo, I. A. Prior and M. Brust, *ACS Nano*, 2008, **2**, 1639.
- 19 F. Kumagai-Sano, T. Hayashi, T. Sano and S. Hasezawa, *Nat. Protoc.*, 2006, **1**, 2621.
- 20 S. D. Yoo, Y. H. Cho and J. Sheen, *Nat. Protoc.*, 2007, **2**, 1565.
- 21 W. Yang, H. X. Wu, H. H. Xu, A. L. Hu and M. L. Lu, *J. Agric. Food Chem.*, 2011, **59**, 12534.
- 22 C. Grabinski, N. Schaeublin, A. Wijaya, H. D' Couto, S. H. Baxamusa, K. Hamad-Schifferli and S. M. Hussain, *ACS Nano*, 2011, **5**, 2870.
- 23 H. Chen, B. Li, X. Ren, S. Li, Y. Ma, S. Cui and Y. Gu, *Biomaterials*, 2012, **33**, 8461.
- 24 S. Honary and F. Zahir, *Trop. J. Pharm. Res.*, 2013, **12**, 265.
- 25 M. Prabakaran, J. J. Grailer, S. Pilla, D. A. Steeber and S. Gong, *Biomaterials*, 2009, **30**, 6065.
- 26 J. G. Huang, H. H. Xu, L. J. Zhou, X. Y. Yang and Y. Q. Tian, *J. South China Agric. Univ., Nat. Sci. Ed.*, 2002, **3**, 46.
- 27 P. Kalimuthu and S. A. John, *Mater. Chem. Phys.*, 2010, **122**, 380.
- 28 S. D. Yoo, Y. H. Cho and J. Sheen, *Nat. Protoc.*, 2007, **2**, 1565.
- 29 A. L. Hu, W. Yang and H. H. Xu, *J. Photochem. Photobiol., B*, 2010, **101**, 215.
- 30 A. Ludwig, J. Stolz and N. Sauer, *Plant J.*, 2000, **24**, 503.
- 31 V. E. C. Stubbs, D. Standing, O. G. G. Knox, K. Killham, A. G. Bengough and B. Griffiths, *Ann. Bot.*, 2004, **93**, 221.
- 32 T. D. Fernández, J. R. Pearson, M. P. Leal, M. J. Torres, M. Blanca, C. Mayorga and X. L. Guével, *Biomaterials*, 2015, **43**, 1.

Preparation, Characterization and Intracellular Imaging of 2,4-Dichlorophenoxyacetic Acid Conjugated Gold Nanorods

Jin-Liang Jia^{1,2}, Xiao-Yong Jin¹, Qing-Le Liu¹, Wen-Long Liang¹,
Miao-Shan Lin², and Han-Hong Xu^{1,*}

¹ State Key Laboratory for Conservation and Utilization of Subtropical Agro-Bioresources,
South China Agricultural University, Guangzhou 510642, China

² College of Materials and Energy, South China Agricultural University, Guangzhou 510642, China

Visualizing the biodistribution of pesticides inside living cells is great importance for enhancing targeting of pesticides. Here we reported for the first time that gold nanorods (Au NRs) with size of 39.4 nm × 11.3 nm could be used as a fluorescent tracer to examine the distribution of a typical herbicide, 2,4-dichlorophenoxyacetic acid (2,4-D), in tobacco bright yellow 2 (BY-2) cells. The nanostructures of hybrid materials were analyzed by using Raman spectra and X-ray photoelectron spectroscopy (XPS), including spectra assignments and electronic property. These data revealed 2,4-D has successfully conjugated MP-Au NRs according to Raman and XPS. The biodistribution of the conjugates inside BY-2 cells was directly examined at 12 and 24 h by the two-photon microscopy. The intensity of two-photon luminescence (TPL) inside cells demonstrated that the conjugates could be localized and excluded by BY-2 cells. Thus, this labeling approach opens up new avenues to the facile and efficient labeling of pesticides.

Keywords: Gold Nanorods, Pesticides, Two-Photon Luminescence, BY-2 Cell, Biodistribution.

1. INTRODUCTION

Pesticides are used to ensure the food supply for the ever growing world population. It was estimated that the total amount of pesticides was applied for pest control, however, only a very small part (<0.1%) actually reached the target pests.¹ Clearly, a significant amount of applied pesticides was wasted and the eco-environment was also destroyed. Hence, it was imperative that enhancing targeting and changing traditional applying methods of pesticides. To address this problem, the imaging of the transport process for pesticides in plants was primary. Recently, radioisotopes^{2,3} or fluorescence dyes⁴⁻⁶ had been used to track pesticides in cells and plants. However, these approaches were difficultly utilized due to their radioactive risks, unstable fluorescence,^{7,8} short half-life,⁹ and so on. Given the shortcoming of conventional labeling for agricultural chemicals, the development of a new technology would fulfill a significant tracked need in plant physiology.

Au nanostructures as a promising platform for various imaging and biomedical applications were related to their spectacular physical and chemical properties, as well as low cytotoxicity.¹⁰⁻¹⁴ In biological applications, the uptake and biodistribution of Au nanostructures were analyzed inside cells and biological tissues by inductively coupled plasma mass spectrometry (ICP-MS)^{15,16} and atomic absorption spectroscopy (AAS).¹⁷ Of these, however, the methods were incapable of *in vivo* monitoring and rather time-consuming.¹⁸ In contrast, Au nanostructures as an attractive contrast agents were used in biomedical imaging through two-photon microscopy¹⁹⁻²¹ because of the longitudinal surface plasmon resonance (LSPR) peak. Among the Au nanostructures investigated for the near-infrared (NIR) photoactivated imaging, plasmon-resonant Au nanorods (NRs), were one of the most effective agents in biological tissues to date.^{18,22} For example, Park et al. reported the bright two-photon luminescence (TPL) signal for biological imaging was 140 times bright than conventional organic dyes.²³ Tong et al. stated intravital TPL

*Author to whom correspondence should be addressed.

imaging of Au NRs following through blood vessels in mice with a high signal-to-noise ratio.²⁴ Therefore, two-photon microscopy has gained popularity for imaging due to optical properties of Au NRs.

2,4-dichlorophenoxyacetic acid (2,4-D), a model herbicide, has been widely used in homes, gardens and agriculture.²⁵ To our knowledge, no research of 2,4-D conjugated Au NRs in plant cells using the two-photon microscopy has been reported in previous work. In this paper, we described the first example of 2,4-D functionalized Au NRs, which acted as a marker in tobacco bright yellow 2 (BY-2) cells. The structure of as-prepared hybrid materials was analyzed by transmission electron microscopy (TEM), Raman spectra and X-ray photoelectron spectroscopy (XPS). Furthermore, we further investigated that the two-photon induced stable luminescence of Au NRs and used the TPL intensity to evaluate the uptake and biodistribution of 2,4-D conjugated Au NRs in BY-2 cells at 12 and 24 h. The results revealed that these conjugates of Au NRs would provide a novel versatile platform for imaging of pesticides in plant physiology.

2. EXPERIMENTAL METHODS

2.1. Materials

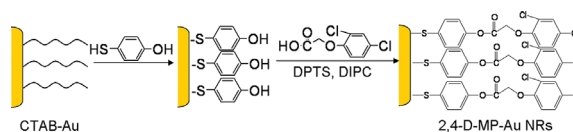
All materials and reagents were used as purchased. Hydrogen tetrachloroaurate (III) trihydrate ($\text{HAuCl}_4 \cdot 3\text{H}_2\text{O}$, Acros, ACS reagent), sodium borohydride (NaBH_4 , Sigma-Aldrich, 99%), cetyltrimethylammonium bromide (CTAB, Sigma-Aldrich, >99%), 4-mercaptophenol (MP, J&K, 99%), *N,N'*-Diisopropylcarbodiimide (DIPC, J&K, 99%), ascorbic acid (AA, Beijing Chemical Reagent Company, 99%) and silver nitrate (AgNO_3 , Beijing Chemical Reagent Company, 99.8%) were used as received. Prior to use, all glassware was cleaned with aqua regia (HCl/HNO_3) and rinsed with deionized (DI) water.

2.2. Synthesis and Purification of Au NRs

The detailed procedures for synthesis of CTAB-Au NRs can be found in earlier work^{26,27} using a seeded growth method. In order to remove a small number of nanospherical particles in the product, the home-synthesized polydisperse Au colloids (80 mL) were purified using the gradient centrifugation method.^{26,28} Then the separated Au NR colloids were collected in order to prepare the following conjugates.

2.3. Preparation of Functional MP-Au NRs

Scheme 1 shows a flowchart of the experimental procedures. To remove excess CTAB, the separated Au NRs colloid after purification was centrifuged at 8,000 rpm for 15 min, and then redispersed in DI water (15 mL). A tetrahydrofuran (THF) solution (0.11 g of MP in 1 mL of THF) was added dropwise into the above colloid.²⁶ The solution was stirred for 12 h, and the black precipitate could be collected after centrifugation (3750 rpm,



Scheme 1. The reaction scheme for the synthesis of MP-Au NRs and 2,4-D-MP-Au NRs.

10 min). The residual MP and CTAB were removed by multiple rinsing with a THF/ H_2O mixture (1:1, v/v). The total weight of the dried product was 4.4 mg.

2.4. Preparation of 2,4-D-MP-Au NRs

Firstly, 4-(*N,N*-dimethylamino)pyridinium-4-toluenesulfonate (DPTS) was synthesized according to procedures reported previously.²⁹ Secondly, 20 mg of 2,4-D and 4.4 mg of MP-Au NRs were added to the mixture of 3 mL absolute *N,N*-Dimethylformamide and 2 mL absolute dichloromethane in 50 mL flask with stirring. After 20 mg DPTS was added under vigorous stirring for 2 min, 150 μL DIPC was injected into the above solution. This mixture was stirred over night at room temperature. The resulting solution was centrifuged at 6000 rpm for 15 min, and rinsed with a THF/ H_2O mixture (1:1, v/v) at least three times. Finally, the black solid was dried in vacuo at 45 $^{\circ}\text{C}$.

2.5. BY-2 Cells Culture and Cellular Incubation with 2,4-D-MP-Au NRs

The BY-2 cells were cultured in Murashige-Skoog medium as described by Fumi et al.³⁰ In brief, the BY-2 cells were grown in 30 mL of culture medium containing 0.05% Tween 20 for 5 d with continuous agitating (120 rpm, 27 $^{\circ}\text{C}$, dark). Cell samples were obtained from 5-d-old cultures. Starved cells were prepared by transferring 5-d-old culture cells into culture medium without sucrose (starving medium) for 24 h.

Starving cells were transferred to fresh starving medium supplemented with 80 $\mu\text{g mL}^{-1}$ dimethyl sulfoxide solution of 2,4-D-MP-Au NRs, which were taken for 12 and 24 h. After incubation, the cells were rinsed three times with 2 mL starving medium by centrifuging at 4000 rpm for 10 min to remove extra 2,4-D-MP-Au NRs.

2.6. Characterization

TEM images were acquired using a JEOL JEM-2010 microscope operated at 120 kV. The samples were prepared by dropping the colloidal solution on a Formvar/carbon film coated Cu grid (3 mm, 300 mesh), followed by drying under ambient conditions. Raman spectra were taken on a Renishaw Raman System 2000 equipped with a CCD detector. The samples were irradiated at 632.8 nm line of a He-Ne laser (Spectra-Physics), with 4.7 mW laser power, with the beam 100% defocused (Renishaw software). X-ray photoelectron spectroscopy

(XPS) measurements were carried out on a PHI 5300 ESCA1610 SAM instrument equipped with Mg K α radiation.

The dimethyl sulfoxide solution of 2,4-D-MP-Au NRs was digested using a mixture 12 mL of HNO₃ and 6 mL of HClO₄ on a hot plate (~100 °C) and analyzed for Au content by inductively coupled plasma optical emission spectroscopy (ICP-OES). The cells were covered with a coverslip in order to obtain the confocal images. The 800-nm light from a Ti: sapphire laser (Mira 900, Coherent) with a duration of 130 fs and a repetition of 76 MHz was introduced into an inverted microscope (Axio Observer A1, Zeiss). The TPL emitted from Au NRs was collected by the same objective lens and analyzed in a spectrometer (SR-500i-B1, Andor) with charge-coupled device (CCD).

3. RESULTS AND DISCUSSION

3.1. TEM Images of Au NRs

Figure 1 shows the representative TEM images for some of the as-prepared Au NRs with different ligands. Au NRs dimensions were listed in Table I by counting at least 250 Au NRs for per specimen. After Au NR colloids

Table I. Averaged size and aspect ratio of different Au NRs.

Sample	Length (nm)	Width (nm)	Aspect ratio
CTAB-Au NRs	42.5 \pm 4.1	12.7 \pm 1.4	3.3
MP-Au NRs	40.1 \pm 4.8	11.9 \pm 1.2	3.4
2,4-D-MP-Au NRs	39.4 \pm 4.5	11.3 \pm 1.6	3.5

were centrifugated and purified, the CTAB-Au NRs with aspect ratio of 3.3 (length = 42.5 \pm 4.1 nm, width = 12.7 \pm 1.4 nm) are nearly monodisperse. Meanwhile, the sizes of 2,4-D-MP-Au NRs with an average width and length are 11.3 \pm 1.6 and 39.4 \pm 4.5 nm, respectively. The HRTEM image of MP-Au NRs is inserted in TEM micrograph of Figure 1(b), illustrating a perfect rod-shaped particle. MP-Au NRs and 2,4-D-MP-Au NRs exhibit similar length and width, but these values are slightly smaller for CTAB-Au NRs because of synthesis batch variability.³¹ Additionally, the aspect ratio for Au NRs is also similar in Table I, which might suggest that the conjugated method is feasible.

3.2. Raman Spectra of 2,4-D Conjugated Au NRs

In order to illustrate 2,4-D has conjugated Au NRs, the Raman spectra of MP, 2,4-D and 2,4-D-MP-Au NRs were

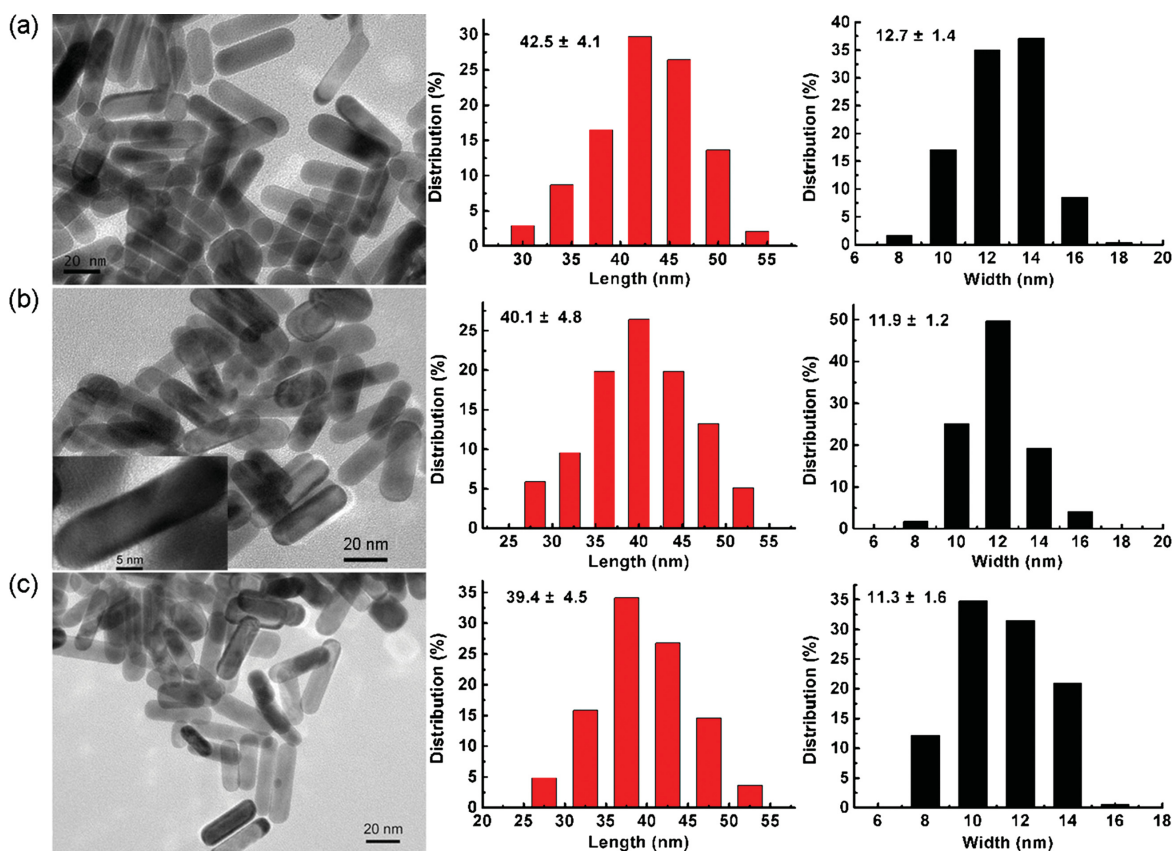


Figure 1. TEM images, length and width histograms of (a) CTAB-Au NRs, (b) MP-Au NRs, (c) 2,4-D-MP-Au NRs. The inset is the representative HRTEM image of MP-Au NRs.

examined. In Figure 2(a), the peaks at 2560 and 913 cm^{-1} are assigned to the S–H stretching and S–H bending of MP, respectively. However, these peaks are absent in Figure 2(c), indicating that Au–S bond has been formed.³² In addition, the peaks at 1079 and 1597 cm^{-1} correspond to the C–C aromatic ring stretching of MP, and ones of 2,4-D at 1109 and 1585 cm^{-1} . Meanwhile, the strongly enhanced peaks at 1078 and 1579 cm^{-1} correspond to the C–C aromatic ring stretching of 2,4-D-MP-Au NRs. It is obvious that these values of peaks have been slightly shifted when MP conjugates with Au NRs, which implies that electronic transformation between Au atom and benzene ring leads to change the polarity of this ligand.³³ In Figure 2(b), the peak at 2948 cm^{-1} is characteristic of the aliphatic C–H stretching in the CH_2 group of 2,4-D,³⁴ which can be in agreement with the band at 2911 cm^{-1} in Figure 2(c). The peaks at 1441 cm^{-1} in Figure 2(b) and 1168 cm^{-1} in Figure 2(c), respectively, are all assigned to the OC–O band of the carboxyl group. The difference of the OC–O surrounding may lead to a shift of the peaks. As a result, the ester group has been produced as expected. Additionally, the C–Cl stretching vibration of 2,4-D is observed around at 412 and 840 cm^{-1} in Table II, while the peaks of 2,4-D-MP-Au NRs at 389 and 840 cm^{-1} . The result shows the hybrid material with Cl atoms. Combined together, we conclude that 2,4-D has conjugated Au NRs according to the Raman spectra. Finally, the observed spectral frequencies and possible assignments of these samples are listed in Table II.

3.3. XPS of MP-Au NRs and 2,4-D-MP-Au NRs

To gain further insight into the surface composition and electronic property of these hybrid materials, samples were probed by XPS. Figure 3 shows XPS signals for gold (Au 4f), sulfur (S 2p) and chlorine (Cl 2p) for MP-Au NRs and 2,4-D-MP-Au NRs. In Figure 3(a), the emission of 4-f photoelectrons from Au is identified in four peaks of the XPS spectra, two of which are assigned to Au^0 (87.8 and 84.1 eV) in MP-Au NRs and two to Au^0 (88.4 and 84.8 eV) in 2,4-D-MP-Au NRs, respectively.³⁵

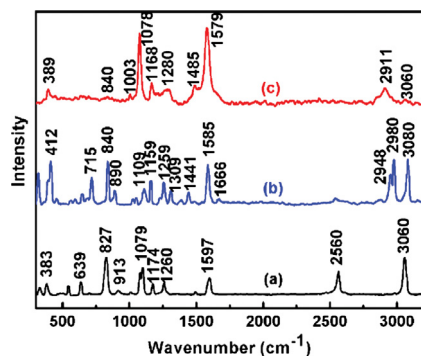


Figure 2. Raman spectra of (a) MP, (b) 2,4-D and (c) 2,4-D-MP-Au NRs.

Table II. Peak frequencies and assignments of the observed Raman bands for MP, 2,4-D and 2,4-D-MP-Au NRs.

Peak frequency (cm^{-1})		Assignments
MP	2,4-D-MP-Au NRs	
	389	δ (COC), δ (CCl)
	412	ν (CC) _{ring} , ν (CCl)
	715	δ (COO ⁻)
827	840	δ (CH) _{oop} , ν (CC) _{ring} , ν (C=O), ν (CCl)
	890	ν (C-COO ⁻)
913		δ (S–H)
	1003	δ (CH) _{oop}
	1022	ν (CC) _{ring} , ν (CO)
	1049	ν (CC) _{ring} , ν (C–O), δ (CH) _{ring}
	1078	ν (CC) _{ring} , ν (C–O)
1079		ν (CC) _{ring} , ν (CS)
	1109	ν (CC) _{ring} , ν (C–Cl)
	1159	δ (CH) _{ring}
	1168	ν (OC–O)
117		δ (C–H) _{ip}
1260		ν (C–O)
	1259	δ (CH) _{ring} , ν (C–O)
	1280	δ (CH) _{ip} , ν (C–O)
	1309	ν (CC) _{ring}
	1441	ν_s (COO ⁻), ν (CC), ω (CH ₂)
	1485	δ (CH) _{ip}
1597	1585	ν_{as} (COO ⁻), ν (CC) _{ring}
	1666	ν (C=O)
	2911	ν (CH ₂)
2560		ν (S–H)
	~2948	ν (CH ₂)
3060	3080	ν (CH) _{ring}

Notes: δ = bend or deformation; ν = stretch; ring = ring breathing mode; ip = inplane mode; oop = out of plane.

A difference between the values of two complexes indicates that there is the electron donation from Au atoms and an electron-withdrawing group has conjugated with MP-Au NRs. The thiol binding energy of MP is 164 eV according to published results.^{36,37} Photoelectron peaks with binding energies of 162.3 and 163.3 eV are assigned to the orbital doublet arising from S 2p_{3/2} and S 2p_{1/2}, respectively, which are consistent with sulfur bound to gold.^{36,38} This binding energy shift has generally been interpreted as the formation of an Au-thiolate bond. Moreover, there is no peak at 164 eV in Figure 3(b). Therefore, we can conclude that all adsorbates bind to the surface of gold through the sulfur atoms, except for a peak at 168.0 eV corresponding to small amounts oxidized sulfur species.³⁹ However, there is no oxidized sulfur species in 2,4-D-MP-Au NRs because these oxidized sulfur species on the surface of gold might be washed by centrifugation. Additionally, the detectable Cl 2p peaks are attributed to the 2,4-D-MP-Au NRs in Figure 3(c), which also indicates 2,4-D has successfully conjugated MP-Au NRs according to XPS. This result is in perfect agreement with the one obtained by Raman spectra.

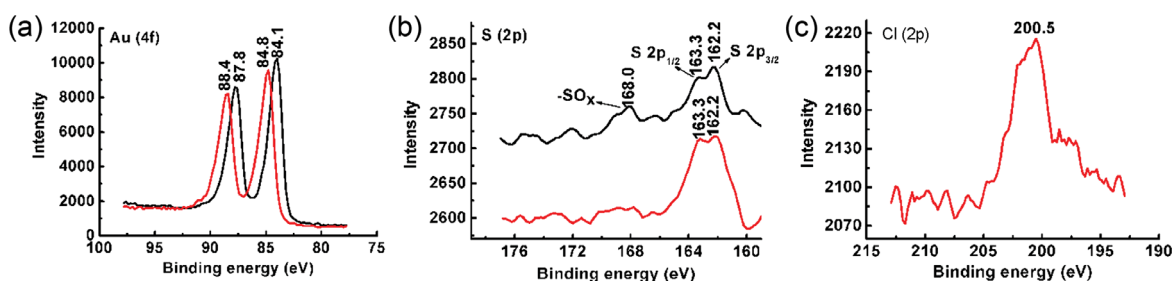


Figure 3. XPS spectra of the Au 4f (a), S 2p (b) and Cl 2p (c) of MP-Au NRs (black curve) and 2,4-D-MP-Au NRs (red curve).

3.4. TPL of 2,4-D-MP-Au NRs Inside BY-2 Cells

The TPL from the Au NRs was determined to monitor the distribution of 2,4-D-MP-Au NRs entering into the BY-2 cells. As shown in Figure 4, TPL spectra were recorded

in the time-course experiments after the switching-on of the laser light with an excitation wavelength of 800 nm. TPL images from at least three randomly selected sites of BY-2 cells, including extracellular environment, cell

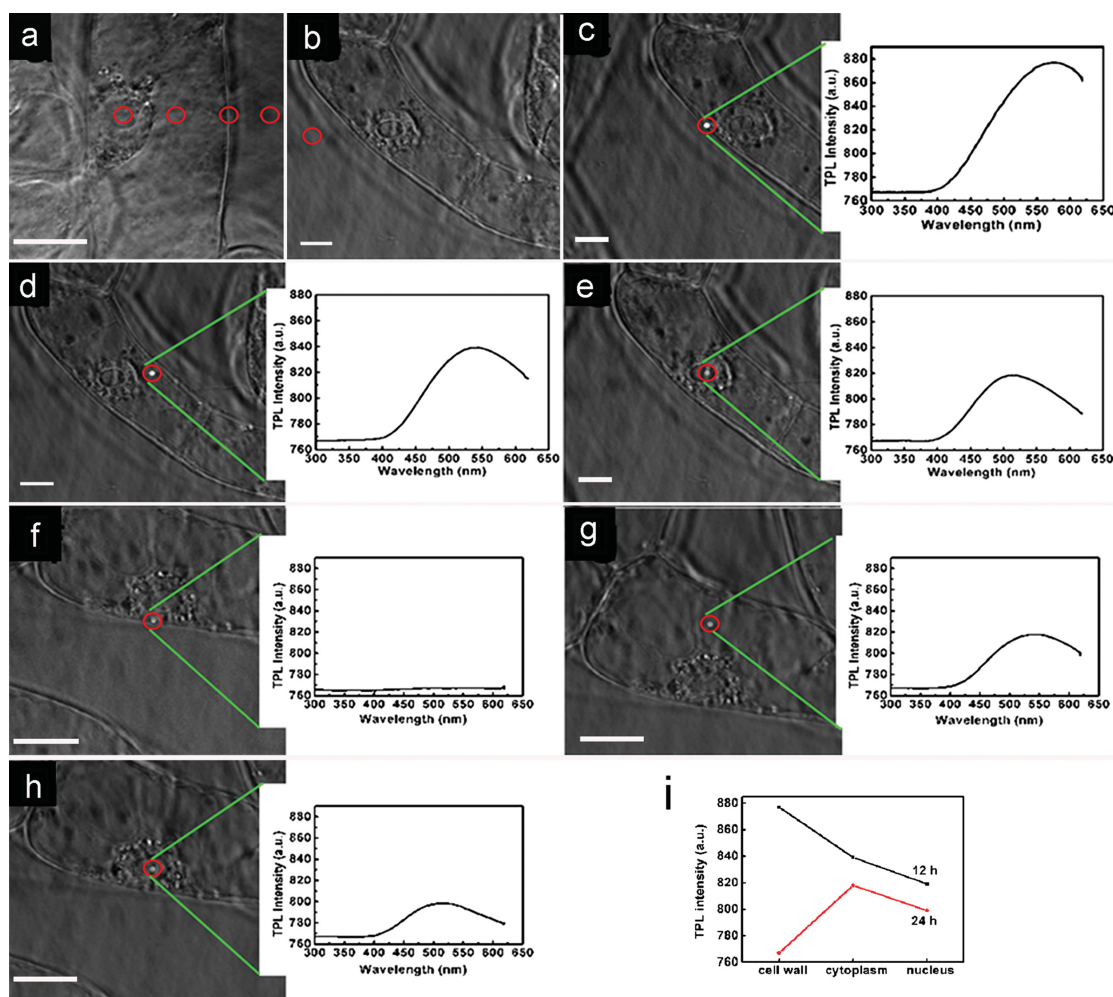


Figure 4. TPL images of BY-2 cells: (a) a control experiment; (b)–(e) treatment with 80 $\mu\text{g mL}^{-1}$ 2,4-D-MP-Au NRs for 12 h; (f)–(h) treatment with 80 $\mu\text{g mL}^{-1}$ 2,4-D-MP-Au NRs for 24 h; (i) TPL intensity versus different sites of the BY-2 cells after 12 and 24 h. For clarity, TPL positions were highlighted by red circles. Insets: the graphs of fluorescence intensity at different sites inside the BY-2 cells. The excitation wavelength was 800 nm. Scale bar = 15 μm .

wall, cytoplasm and nucleus, were acquired under identical experimental conditions. Additionally, the detector positions were highlighted by red circles. In a control experiment, no TPL signal was observed in any site of the cell that contained no Au NRs. In addition, there is also no TPL signal in the extracellular environment in Figure 4(b) because the cells were rinsed by centrifugation. However, in Figures 4(c)–(h), the bright dots of different sites inside the cells can be detected. It states that Au NRs can emit strong TPL when the fs laser waver wavelength is in resonance with their LSPR.⁴⁰ Moreover, TPL can be distinguished from tissue autofluorescence based on the specific spectral patterns, which agrees with what was reported in previous publication.⁴¹ The preliminary results show that 2,4-D-MP-Au NRs have entered into the BY-2 cells after 12 h. Additionally, TPL can be used as a reliable tool for quantitatively imaging of Au NRs.¹⁸ Therefore, we also investigated the TPL intensity from 2,4-D-MP-Au NRs in the insets of Figures 4(c)–(h). Then the TPL intensity from different sites inside the cells was plotted in Figure 4(i), indicating that the TPL intensity weakens gradually from cell wall to nucleus for 12 h. However, the TPL intensity is the highest value at the cytoplasm for 24 h. Besides, the strongest TPL intensity at 12 h was emitted at the cell wall, but almost no Au NRs could be detected anymore at 24 h. Taken together, the TPL intensity of different sites inside BY-2 cells decreases from 12 to 24 h, which illustrates the number of nanoparticles is gradually declining. It suggests that 2,4-D-MP-Au NRs have been internalized and excluded by the BY-2 cells with time. Therefore, the imaging of 2,4-D-MP-Au NRs inside BY-2 cells can be monitored by two-photon microscopy.

4. CONCLUSIONS

In this study, a novel approach toward the tracer of pesticide-Au NRs system has been described. Au NRs was firstly conjugated to 2,4-D based on powerful analytical techniques, as evidenced by TEM, Raman spectra and XPS. We reported the biodistribution of 2,4-D conjugated Au NRs inside the BY-2 cells by two-photon microscopy. The experimental results showed that 2,4-D conjugated Au NRs could enter into the BY-2 cells at 12. As a bright TPL emitter, 2,4-D conjugated Au NRs were obviously monitored at different sites of the BY-2 cells. Moreover, the TPL intensity of different sites inside BY-2 cells gradually decreased with time, suggesting the conjugates can also be excluded. These results indicate that the Au NRs conjugates may be good candidates in plant physiology for future imaging.

Acknowledgments: We thank Professor Seiichiro Hasezawa (Department of Integrated Biosciences, Graduate School of Frontier Sciences, University of Tokyo, Japan) for his kind help in the supply of the BY-2 cells. This work was financially supported by NSF (Grant

31401781) of China, the Fund of Education Department of Guangdong Province (Grant 2014KQNCX031), the Doctoral Fund of Ministry of Education of China (Grant 20114404110020 and 20134404130003).

References and Notes

1. C. J. Wang and Z. Q. Liu, *Pestic. Biochem. Phys.* 87, 1 (2007).
2. H. Alsayeda, S. Pascal-Lorber, C. Nallanthigal, L. Debrauwer, and F. Laurent, *Environ. Chem. Lett.* 6, 229 (2008).
3. A. Aajoud, M. Raveton, H. Aouadi, M. Tissut, and P. Ravel, *J. Agric. Food Chem.* 54, 5055 (2006).
4. A. L. Hu, W. Yang, and H. H. Xu, *J. Photochem. Photobiol. B* 101, 215 (2010).
5. W. Yang, H. X. Wu, H. H. Xu, A. L. Hu, and M. L. Lu, *J. Agric. Food Chem.* 59, 12534 (2011).
6. Y. S. Yin, D. W. Chen, M. X. Qiao, X. Y. Wei, and H. Y. Hu, *J. Control. Release* 123, 27 (2007).
7. L. Shang, S. J. Dong, and G. U. Nienhaus, *Nano Today* 6, 401 (2011).
8. C. Wang and J. Irudayaraj, *Small* 4, 2204 (2008).
9. A. Taylor, K. M. Wilson, P. Murray, D. G. Fernig, and R. Levy, *Chem. Soc. Rev.* 41, 2707 (2012).
10. A. Ravalli and G. Marrazza, *J. Nanosci. Nanotechnol.* 15, 3307 (2015).
11. L. Dykman and N. Khlebtsov, *Chem. Soc. Rev.* 41, 2256 (2012).
12. X. Shao, P. Schnau, W. Qian, and X. Wang, *J. Nanosci. Nanotechnol.* 15, 3834 (2015).
13. X. Li, J. Guo, J. Asong, M. A. Wolfert, and G. J. Boons, *J. Am. Chem. Soc.* 133, 11147 (2011).
14. X. Wu, L. Li, L. Zhang, T. Wang, C. Wang, and Z. Su, *J. Mater. Chem. B* 3, 2421 (2015).
15. L. Xu, Y. Liu, Z. Chen, W. Li, Y. Liu, L. Wang, Y. Liu, X. Wu, Y. Ji, Y. Zhao, L. Ma, Y. Shao, and C. Chen, *Nano Lett.* 12, 2003 (2012).
16. T. D. Fernandez, J. R. Pearson, M. P. Leal, M. J. Torres, M. Blanca, C. Mayorga, and X. L. Guevel, *Biomaterials* 43, 1 (2015).
17. J. F. Hainfeld, D. N. Slatkin, T. M. Focella, and H. M. Smilowitz, *Brit. J. Radiol.* 79, 248 (2006).
18. L. Au, Q. Zhang, C. M. Cobley, M. Gidding, A. G. Schwartz, J. Chen, and Y. Xia, *ACS Nano* 4, 35 (2010).
19. W. Lu, S. R. Arumugam, D. Senapati, A. K. Singh, T. Arbneshi, S. A. Khan, H. Yu, and P. C. Ray, *ACS Nano* 4, 1739 (2010).
20. J. L. Li and M. Gu, *Biomaterials* 31, 9492 (2010).
21. N. J. Durr, T. Larson, D. K. Smith, B. A. Korgel, K. Sokolov, and A. Ben-Yakar, *Nano Lett.* 7, 941 (2007).
22. S. Garabagiu and I. Bratu, *Appl. Surf. Sci.* 284, 780 (2013).
23. J. Park, A. Estrada, K. Sharp, K. Sang, J. A. Schwartz, D. K. Smith, C. Coleman, J. D. Payne, B. A. Korgel, A. K. Dunn, and J. W. Tunnell, *Opt. Express* 16, 1590 (2008).
24. L. Tong, W. He, Y. Zhang, W. Zheng, and J. X. Cheng, *Langmuir* 25, 12454 (2009).
25. D. H. Garabrant and M. A. Philbert, *Crit. Rev. Toxicol.* 32, 233 (2002).
26. B. P. Khanal and E. R. Zubarev, *Angew. Chem. Int. Ed.* 46, 2195 (2007).
27. J. L. Jia, H. H. Xu, G. R. Zhang, Z. Hu, and B. Q. Xu, *Nanotechnology* 23, 495710 (2012).
28. S. Li, Z. Chang, J. Liu, L. Bai, L. Luo, and X. Sun, *Nano Res.* 4, 723 (2011).
29. J. S. Moore and S. I. Stupp, *Macromolecules* 23, 65 (1990).
30. F. Kumagai-Sano, T. Hayashi, T. Sano, and S. Hasezawa, *Nat. Protoc.* 1, 2621 (2006).
31. C. Grabinski, N. Schaeublin, A. Wijaya, H. D'Couto, S. H. Baxamusa, K. Hamad-Schifferli, and S. M. Hussain, *ACS Nano* 5, 2870 (2011).

32. S. Li, D. Wu, X. Xu, and R. Gu, *J. Raman Spectrosc.* 38, 1436 (2007).
33. M. Boronat, P. Concepción, A. Corma, S. González, F. Illas, and P. Serna, *J. Am. Chem. Soc.* 129, 16230 (2007).
34. B. Karthikeyan and B. Saravanan, *Spectrochim. Acta Part A* 63, 619 (2006).
35. T. F. Jaramillo, S. H. Baeck, B. R. Cuenya, and E. W. McFarland, *J. Am. Chem. Soc.* 125, 7148 (2003).
36. D. Barriet, C. M. Yam, O. E. Shmakova, A. C. Jamison, and T. R. Lee, *Langmuir* 23, 8866 (2007).
37. P. Urchaga, M. Weissmann, S. Baranton, T. Girardeau, and C. Coutanceau, *Langmuir* 25, 6543 (2009).
38. P. E. Laibinis, G. M. Whitesides, D. L. Allara, Y. T. Tao, A. N. Parikh, and R. G. Nuzzo, *J. Am. Chem. Soc.* 113, 7152 (1991).
39. D. G. Castner, K. Hinds, and D. W. Grainger, *Langmuir* 12, 5083 (1996).
40. H. D. Deng, G. C. Li, Q. F. Dai, M. Ouyang, S. Lan, A. V. Gopal, V. A. Trofimov, and T. M. Lysak, *Opt. Express* 20, 10963 (2012).
41. T. Wang, J. Y. Chen, S. Zhen, P. N. Wang, C. C. Wang, W. L. Yang, and Q. Peng, *J. Fluoresc.* 19, 615 (2009).

Received: 10 May 2015. Accepted: 7 July 2015.



Synthesis and Reactivity in Inorganic, Metal-Organic, and Nano-Metal Chemistry

Publication details, including instructions for authors and subscription information:

<http://www.tandfonline.com/loi/lsrt20>

Biosynthesis of Silver and Gold Nanoparticles Using Huangdan (*Camellia sinensis*) Leaf Extract

Jin-Liang Jia^{ab}, Han-Hong Xu^a, Dan-Qi Li^b, Wei-Hao Ye^b & Wen-Jian Liu^b

^a State Key Laboratory for Conservation and Utilization of Subtropical Agro-bioresources, South China Agricultural University, Guangzhou, China

^b Institute of Biomaterials, College of Sciences, South China Agricultural University, Guangzhou, China

Accepted author version posted online: 13 Dec 2014.



[Click for updates](#)

To cite this article: Jin-Liang Jia, Han-Hong Xu, Dan-Qi Li, Wei-Hao Ye & Wen-Jian Liu (2015) Biosynthesis of Silver and Gold Nanoparticles Using Huangdan (*Camellia sinensis*) Leaf Extract, *Synthesis and Reactivity in Inorganic, Metal-Organic, and Nano-Metal Chemistry*, 45:7, 941-946, DOI: [10.1080/15533174.2013.862817](https://doi.org/10.1080/15533174.2013.862817)

To link to this article: <http://dx.doi.org/10.1080/15533174.2013.862817>

PLEASE SCROLL DOWN FOR ARTICLE

Taylor & Francis makes every effort to ensure the accuracy of all the information (the "Content") contained in the publications on our platform. However, Taylor & Francis, our agents, and our licensors make no representations or warranties whatsoever as to the accuracy, completeness, or suitability for any purpose of the Content. Any opinions and views expressed in this publication are the opinions and views of the authors, and are not the views of or endorsed by Taylor & Francis. The accuracy of the Content should not be relied upon and should be independently verified with primary sources of information. Taylor and Francis shall not be liable for any losses, actions, claims, proceedings, demands, costs, expenses, damages, and other liabilities whatsoever or howsoever caused arising directly or indirectly in connection with, in relation to or arising out of the use of the Content.

This article may be used for research, teaching, and private study purposes. Any substantial or systematic reproduction, redistribution, reselling, loan, sub-licensing, systematic supply, or distribution in any form to anyone is expressly forbidden. Terms & Conditions of access and use can be found at <http://www.tandfonline.com/page/terms-and-conditions>

Biosynthesis of Silver and Gold Nanoparticles Using Huangdan (*Camellia sinensis*) Leaf Extract

JIN-LIANG JIA^{1,2}, HAN-HONG XU¹, DAN-QI LI², WEI-HAO YE², and WEN-JIAN LIU²

¹State Key Laboratory for Conservation and Utilization of Subtropical Agro-bioresources, South China Agricultural University, Guangzhou, China

²Institute of Biomaterials, College of Sciences, South China Agricultural University, Guangzhou, China

Received 9 May 2013; accepted 2 November 2013

The biosynthesis of nanoparticles is in the limelight of modern nanotechnology. Biogenic Ag and Au nanoparticles were synthesized by a rapid and simple procedure using leaves extract of tea as the reducing agent. The formations of Ag and Au nanoparticles were monitored using the UV-visible spectra as a function of the reaction time and the formation process, which determined that the optimal reaction time of Ag⁺ and Au³⁺ ions was 4 and 1 h, respectively. The as-synthesized Ag (53.2 ± 7.1 nm) and Au (31.7 ± 5.2 nm) nanoparticles were characterized by transmission electron microscopy, Fourier transform infrared spectra, and thermogravimetric analysis. The X-ray diffraction spectra showed that the Ag nanoparticle was composed of two nanocrystals, while the Au nanoparticle included one nanocrystal. This rapid biosynthesis approach can be described as a green technology because of no additional chemical reagents as stabilizers or reductants.

Keywords: *Camellia sinensis*, Ag NPs, Au NPs, biosynthesis

Introduction

Nanoparticles (NPs) of noble metals, such as silver and gold, are promising because they could find wide applications in surface enhanced Raman spectroscopy (SERS),^[1–4] infrared absorbing optical coatings,^[5] protein tyrosine phosphatase 1B inhibitory activity,^[6] biosensor,^[7] cancer hyperthermia,^[8] and so on. As we all know, synthesization of nanoparticles can be used different methods. Though chemical approaches has gained popularity, some chemical approaches cannot avoid the use of toxic chemicals for environment in the synthesis process.^[9] For example, Au NPs were synthesized in a concentrated cetyl trimethylammonium bromide (CTAB) solution by chemical methods; however, the nanoparticles were limited their usefulness for many biological applications because free CTAB was highly cytotoxic.^[10] Recently, biosynthetic methods employing either plant extracts or biological microorganisms have emerged as simple and eco-friendly protocols.^[11] A great deal of effort has been put into the biosynthesis of Ag NPs and Au NPs because of their interesting properties. For instance, Lee et al.^[12] produced phytochemical-induced Au NPs with gallic acid, protocatechuic acid,

and isoflavone. These complexes showed a strong antioxidant effect. Vigneshwaran et al.^[13] demonstrated a simple route for the synthesis of stable and monodisperse silver-protein nanoparticles using spent mushroom substrate. In addition, recent advancement included a simple synthesis of nanoparticles by *Cinnamomum camphora* leaf,^[14] Neem leaf,^[15] actinobacteria *Rhodococcus* sp.,^[16] and others.^[17–19]

Tea leaf is one of the most popular beverages worldwide.^[20] In recent years, the biosynthetic method using tea leaf has received considerable attention. For example, Ag and Au NPs with highly efficient single photon-induced luminescence were synthesized using green tea extracts by Vilchis-Nestor et al.^[21] Meanwhile, Begum et al.^[22] reported the synthesis of Ag or Au NPs with black tea leaf extracts. However, the reaction time of Ag⁺ and Au³⁺ ions for complete reduction in their works was very long. To enable the biosynthesis methods of Ag and Au NPs to compete with the chemical methods, there is a need to achieve faster synthesis rates with high monodispersion.^[23]

In this paper, we reported that rapid and simple synthesis of Ag and Au NPs by the reduction of aqueous Ag⁺ and Au³⁺ using Huangdan (*Camellia sinensis*) leaf extract. To our knowledge, this is the first report on use of Huangdan leaf for the rapid synthesis of Ag and Au NPs. The nearly monodisperse Ag and Au NPs were formed at ambient conditions, without any additive protecting nanoparticles. The formation of Ag and Au NPs was recorded by the UV-visible (UV-vis) spectra. Additionally, the size, shape, stabilizer, and nanocrystals of Ag and Au NPs were analyzed by transmission electron microscopy (TEM), Fourier transform infrared

Address correspondence to Han-Hong Xu, State Key Laboratory for Conservation and Utilization of Subtropical Agro-bioresources, South China Agricultural University, Guangzhou 510642, China. E-mail: hhxu@scau.edu.cn

Color versions of one or more of the figures in the article can be found online at www.tandfonline.com/lsrt.

(FTIR) spectra, thermogravimetric analysis (TGA), and X-ray diffraction (XRD). The rapid approach using tea leaf would be suitable for developing a biological process for large-scale production.

Experimental

Materials

Tetrachloroauric acid ($\text{HAuCl}_4 \cdot 3\text{H}_2\text{O}$) was purchased from Acros Organics. Silver nitrate (AgNO_3 ; 99.8%) was purchased from Beijing Chemical Reagent Company. Fresh tea leaves (Huangdan, *Camellia sinensis*) were obtained from South China Agricultural University Arboretum, and tea leaf broth was prepared by taking 5 g of thoroughly washed and dried tea leaves in a 500 mL flask with 100 mL of deionized (DI) water, then the mixture was boiled for 5 min before finally decanting it. Prior to use, all glassware was washed with aqua regia (HCl/HNO_3) and rinsed with DI water for three times.

Synthesis of Ag and Au NPs

For reduction of Au^{3+} ions, 5 mL of tea leaf broth was added to 45 mL of 1×10^{-3} M HAuCl_4 solution. After stirring 1 min, the mixture solution was left without stirring. Similarly, 5 mL of tea leaf broth was added to 45 mL of 1×10^{-3} M AgNO_3 solution in dark for reduction of Ag^+ ions.

Characterization

The reduction processes of Ag^+ and Au^{3+} were monitored by measuring the UV-vis spectra of the colloids at regular intervals. After the colloidal solution samples were filled in a quartz cell of 1 cm light-path, UV-vis spectra were recorded as a function of the reaction time by a UV-2102PC spectrometer operated at a resolution of 1 nm.

TEM images were acquired using a Tecnai 12 operated at 100 kV. The samples were prepared by dropping the colloidal solution on a Formvar/carbon film coated Cu grid (3 mm, 300 mesh), followed by drying under ambient conditions.

For FTIR spectra measurements, dry powders of nanoparticles were obtained in the following manner. To remove excess uncoordinated biological molecules from tea leaf broth, the as-prepared Ag and Au NP colloids after optimal reaction time were centrifuged at 8,000 rpm for 15 min and rinsed with DI water at least three times. Finally, the black solid was dried *in vacuo* at 45°C. Moreover, the dried power was analyzed for the crystalline nature of Ag and Au NPs by MSAL XD-2 X-ray diffractometer (Beijing) with $\text{Cu K}\alpha$ radiation.

TGA was performed on DTG-60 Shimadzu (Japan). Samples (3.0–6.0 mg) were then heated to 850°C under a nitrogen atmosphere at a rate of 10°C/min.

Results and Discussion

UV-Vis Studies

Formation of Ag and Au NPs by reduction of the aqueous metal ions during exposure to the broth of boiled tea leaves may be easily followed by UV-vis spectra, and the optimal reaction time was recorded. All samples were diluted with the same procedure to obtain UV-vis spectra. The color of Ag and Au colloids immediately became yellowish-brown and claret after 2 min. Hence, the absorption peaks of Ag and Au NPs was exhibited quickly owing to their surface plasmon resonance (SPR).

In Figure 1a, SPR band of Ag colloids occurred at about 455 nm, and the values of absorption peaks were continually increased with the reaction time increasing. However, these values were hardly changed after 240 min. It suggested that the reduction time of Ag^+ was almost completed within 240 min in the tea leaf broth. Therefore, the optimal reaction time of Ag^+ ions is 240 min. On the other hand, SPR band of Au colloids occurred at 542 nm, and there was obvious absorption peak after the reaction took only 2 min in Figure 1b. It was obvious that the reduction time of Au^{3+} ions was almost completed within 60 min. The reduction rate of Ag^+ ions was slower than one of Au^{3+} ions, which was most likely due to the redox potential being considerably lower for Ag^+/Ag^0 than $\text{Au}^{3+}/\text{Au}^0$. This result is agreement with the earlier work.^[15] Additionally, the maximum intensity and

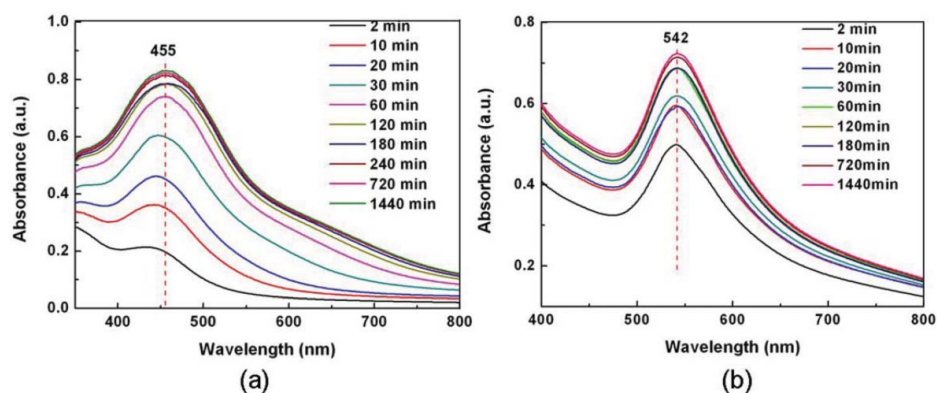


Fig. 1. UV-vis spectra recorded as a function of the reaction time (a) Ag^+ and (b) Au^{3+} aqueous solutions of with tea leaf broth.

width of Ag SPR band were obviously different. However, they are similar for Au NPs. SPR band intensity and width of NPs can be influenced by the particle shape, dielectric constant of the medium and temperature.^[7] So it suggests that the morphology of Ag and Au NPs is different and the dispersibility of Au NPs is better than one of Ag NPs. In addition, in Figure 1a, the absorption peaks of Ag NP colloids become slightly red-shifted with the reaction time increasing. However, the absorption peaks of Au NP colloids hardly shift, which implies that the yield of spherical Au NPs is higher than the one of Ag NPs. These results are agreement with the following results of TEM.

TEM Studies

The stable shape of nanoparticles is a very important aspect of nanotechnology because it plays a crucial role in modulating their physicochemical properties.^[24] The shape and size of the as-prepared NPs were characterization by TEM. As shown in Figure 2a, the average dimension of Ag NPs is 53.2 ± 7.1 nm by analyzing at least 200 Ag NPs. The largest dimension and the smallest dimensions are 86 and 33 nm for Ag NPs, respectively. Though there are a few rod and hexagon Ag NPs, the majority of Ag NPs are nearly sphere. Meanwhile, the scale of the inset is 100 nm. It was obvious that the surface of Ag NPs is coated with a skim, and the thickness of the skim is about 4 nm. So Ag NPs might be

protected by more organic compounds than Au NPs. As shown in Figure 2b, the mean size of Au NPs is 31.7 ± 5.2 nm by analyzing at least 200 nanoparticles, and Au NPs consists of almost spherical nanoparticles, which is agreement with the result of UV-vis spectra. Moreover, the largest dimension and the smallest dimension is 57 and 16 nm for Au NPs, respectively, and the size histogram of Au NPs is better than one of Ag NPs.

FTIR Studies

Figures 3a and 3b show the FTIR spectra of Ag and Au NPs, respectively. FTIR measurements were performed to identify the potential biomolecules in tea leaves responsible for reduction and then providing stability to the bioreduced Ag and Au NPs. It is well known that tea leaves are composed of polyols such as hydroxyflavones and catechins.^[22] In Figure 3, several absorption peaks are labeled in the region range of $1000\text{--}3500\text{ cm}^{-1}$. The most wide absorption peak is observed at $\sim 3400\text{ cm}^{-1}$, which is assigned to $-\text{OH}$ group of polyols such as hydroxyflavones and catechins. Comparing the 3434 cm^{-1} band in Figure 3a with the 3418 cm^{-1} band in Figure 3b, this peak of $-\text{OH}$ group is slightly shifted. It indicates that the strength of interactions between hydrogen bonding of two organic shells and water molecules is different. The same peaks are observed at 2918 and 2851 cm^{-1} , which can be

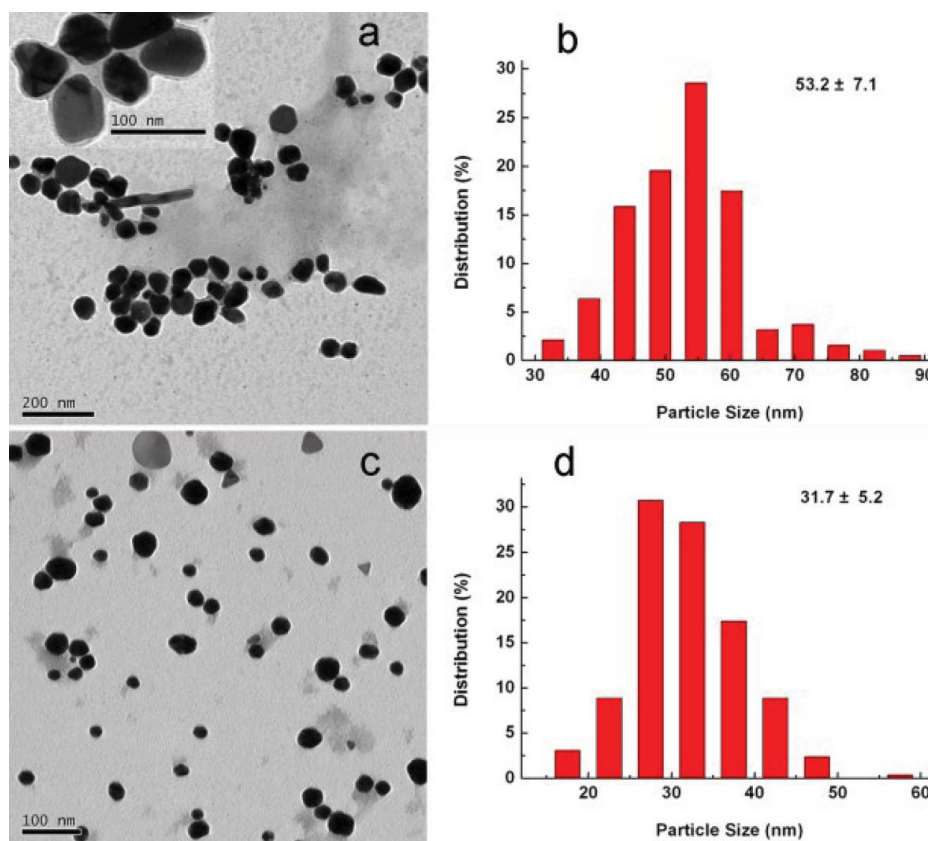


Fig. 2. Representative TEM images of as-prepared (a) Ag and (c) Au NPs after 240 and 60 min, respectively; (b) and (d) size histogram of Ag and Au NPs.

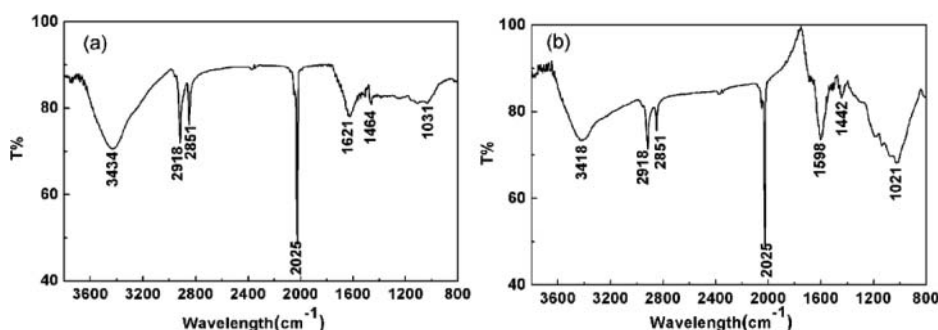


Fig. 3. FTIR spectra of (a) Ag and (b) Au NPs synthesized of tea leaf extract.

attributed to the stretching vibrations of —CH (alkane) or secondary amines. The absorbance bands at 1621, 1598, 1464, and 1442 cm^{-1} are associated with the stretching vibrations for the C—C aromatic ring stretching. In particular, the peak at 2025 cm^{-1} can correspond to —CC— or —CN stretching modes. The band at 1021 or 1031 cm^{-1} corresponds to the C—N stretching vibration of aliphatic amines or to alcohols/phenols.^[23]

TGA Studies

There were very few reports on the TGA plot of the capped Ag and Au NPs prepared using leaves extract. Therefore, the studies on the TGA curves of Ag and Au NPs are shown in Figure 4.

As shown in Figure 4, the hybrid nanoparticles reveal a weight loss in the temperature range of 100–850°C. TGA analysis of Au NPs reveals that the content of the attached organic shell as 21.2% by weight, however, the one of Ag NPs was as nearly 30.4%. The weight loss of organic shell is larger for Ag NPs, which is in good agreement with the result of TEM. The temperature and the weight loss are different from an earlier work^[19] in Au NPs synthesized using olive leaf extract, which might be resulted from the structure of the organic shell and the size of nanoparticles.

XRD Studies

As shown in Figure 5, the XRD spectra of Ag and Au NPs synthesized using the tea leaf broth were obtained.

The diffraction peaks of Bragg reflections for Ag NPs at 37.9°, 44.2°, 64.4°, and 77.5° corresponding to the (111), (200), (220), and (311) sets of lattice planes are observed, respectively, while the diffraction peaks for Au NPs are at 37.9°, 44.2°, 64.5°, and 77.6°.^[25] It is obvious that XRD patterns of Ag and Au NPs based on the face-centered-cubic structures are similar. The area of the (111) and (200) diffraction peaks is much higher than the one of the (220) and (311) peaks, suggesting that the (111) and (200) planes are the predominant orientation. As expected, the width of the diffraction peaks increases with decreasing particle size.^[26] By using the Scherrer formula, the mean size of Ag nanocrystals is 24.2 nm according to the width of the (311) peak, however, the mean size of Au nanocrystals is 30.5 nm from the width of the (311) reflection. As can be seen in Figure 2, the mean sizes of Ag and Au NPs are 53.2 ± 7.1 nm and 31.7 ± 5.2 nm, respectively, which indicates that one Ag nanoparticle may be composed of two nanocrystals and Au nanoparticle may include only one nanocrystal. Additionally, there are no the crystallizations of bioorganic phase on the surface of Ag and Au NPs according to XRD spectra. Therefore, the Ag and Au NPs formed by reduction of Ag^+ and Au^{3+} ions with the tea leaf broth.

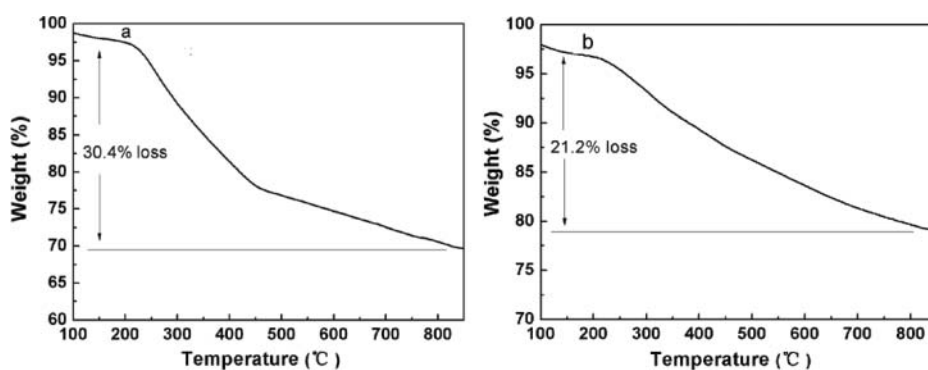


Fig. 4. TGA of capped (a) Ag and (b) Au NPs using the tea leaf broth.

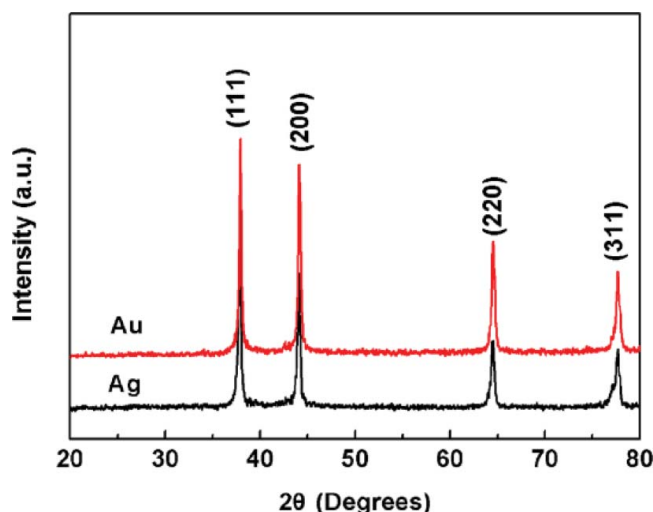


Fig. 5. X-ray diffraction patterns of Ag and Au NPs synthesized using tea leaves with Ag^+ and Au^{3+} aqueous solutions, respectively.

Conclusion

In summary, we demonstrated a rapid and simple biosynthesis method to nearly monodisperse Ag and Au NPs using Huangdan leaves. The optimal reaction time of Ag (53.2 ± 7.1 nm) and Au (31.7 ± 5.2 nm) NPs was 4 and 1 h at ambient conditions, respectively. FTIR and TGA analysis of nanoparticles indicated the capping agents from leaf extracts of tea could be hydroxyflavones and catechins, and the weight loss of organic shell was larger for Ag NPs. Moreover, Ag and Au nanoparticle may be composed of two Ag nanocrystals and one Au nanocrystal by XRD pattern, respectively. The pristine method would be applied in kinds of existing applications.

Funding

This work was financially supported by NSF (grant 31171886, 31401781) of China, the Doctoral Fund of Ministry of Education of China (grant 20114404110020), and Guangdong Provincial High Level Experts (grant 2010-79).

References

- Costa, J. C. S.; Ando, R. A.; Sant'Ana, A. C.; Rossi, L. M.; Santos, P. S.; Temperini, M. L. A.; Corio, P. High performance gold nanorods and silver nanocubes in surface-enhanced Raman spectroscopy of pesticides. *Phys. Chem. Chem. Phys.* **2009**, *11*, 7491–7498.
- Orendorff, C. J.; Gearheart, L.; Jana, N. R.; Murphy, C. J. Aspect ratio dependence on surface enhanced Raman scattering using silver and gold nanorod substrates. *Phys. Chem. Chem. Phys.* **2006**, *8*, 165–170.
- Li, J. F.; Huang, Y. F.; Ding, Y.; Yang, Z. L.; Li, S. B.; Zhou, X. S.; Fan, F. R.; Zhang, W.; Zhou, Z. Y.; Wu, D. Y.; Ren, B.; Wang, Z. L.; Tian, Z. Q. Shell-isolated nanoparticle-enhanced Raman spectroscopy. *Nature* **2010**, *464*, 392–395.
- Jia, J. L.; Xu, H. H.; Zhang, G. R.; Hu, Z.; Xu, B. Q. High quality gold nanorods and nanospheres for surface-enhanced Raman scattering detection of 2,4-dichlorophenoxyacetic acid. *Nanotechnology* **2012**, *23*, 495710.
- Shankar, S. S.; Rai, A.; Ahmad, A.; Sastry, M. Controlling the optical properties of lemongrass extract synthesized gold nanotriangles and potential application in infrared-absorbing optical coatings. *Chem. Mater.* **2005**, *17*, 566–572.
- Basha, S. K.; Govindaraju, K.; Manikandan, R.; Ahn, J. S.; Bae, E. Y.; Singaravelu, G. Phytochemical mediated gold nanoparticles and their PTP 1B inhibitory activity. *Colloid Surf. B: Biointerfaces* **2010**, *75*, 405–409.
- Ren, X.; Meng, X.; Tang, F. Preparation of Ag–Au nanoparticle and its application to glucose biosensor. *Sens. Actuators, B–Chem.* **2005**, *110*, 358–363.
- Shankar, S. S.; Rai, A.; Ankamwar, B.; Singh, A.; Ahmad, A.; Sastry, M. Biological synthesis of triangular gold nanoprisms. *Nat. Mater.* **2004**, *3*, 482–488.
- Song, J. Y.; Kim, B. S. Rapid biological synthesis of silver nanoparticles using plant leaf extracts. *Bioprocess Biosyst. Eng.* **2009**, *32*, 79–84.
- Vigderman, L.; Manna, P.; Zubarev, E. R. Quantitative replacement of cetyl trimethylammonium bromide by cationic thiol ligands on the surface of gold nanorods and their extremely large uptake by cancer cells. *Angew. Chem. Int. Ed.* **2011**, *50*, 1–7.
- Chandran, S. P.; Chaudhary, M.; Pasricha, R.; Ahmad, A.; Sastry, M. Synthesis of gold nanotriangles and silver nanoparticles using *Aloe vera* plant extract. *Biotechnol. Prog.* **2006**, *22*, 577–583.
- Lee, J.; Kim, H. Y.; Zhou, H.; Hwang, S.; Koh, K.; Han, D. W.; Lee, J. Green synthesis of phytochemical-stabilized Au nanoparticles under ambient conditions and their biocompatibility and anti-oxidative activity. *J. Mater. Chem.* **2011**, *21*, 13316–13326.
- Vigneshwaran, N.; Kathe, A. A.; Varadarajan, P. V.; Nachane, R. P.; Balasubramanya, R. H. Silver-protein (core-shell) nanoparticle production using spent mushroom substrate. *Langmuir* **2007**, *23*, 7113–7117.
- Huang, J.; Li, Q.; Sun, D.; Lu, Y.; Su, Y.; Yang, X.; Wang, H.; Wang, Y.; Shao, W.; He, N.; Hong, J.; Chen, C. Biosynthesis of silver and gold nanoparticles by novel sundried *Cinnamomum camphora* leaf. *Nanotechnology* **2007**, *18*, 105104.
- Shankar, S. S.; Rai, A.; Ahmad, A.; Sastry, M. Rapid synthesis of Au, Ag, and bimetallic Au core–Ag shell nanoparticles using Neem (*Azadirachta indica*) leaf broth. *J. Colloid Interface Sci.* **2004**, *275*, 496–502.
- Otari, S. V.; Patil, R. M.; Nadaf, N. H.; Ghosh, S. J.; Pawar, S. H. Green biosynthesis of silver nanoparticles from an actinobacteria *Rhodococcus sp.* *Mater. Lett.* **2012**, *72*, 92–94.
- Nagajyothi, P. C.; Lee, S. E.; An, M.; Lee, K. D. Green synthesis of silver and gold nanoparticles using *Lonicera japonica* flower extract. *Bull. Korean Chem. Soc.* **2012**, *33*, 2609–2612.
- Nagajyothi, P. C.; Sreekanth, T. V. M.; Lee, K. D. AgNPs: green synthesis, characterization, antimicrobial, and cytotoxicity studies of methanol and aqueous extracts of *Pseudocarya sinensis* (Chinese Quince) Fruit. *Synth. React. Inorg. Met.-Org. Nano-Met. Chem.* **2012**, *42*, 1339–1344.
- Ankamwar, B.; Chaudhary, M.; Sastry, M. Gold nanotriangles biologically synthesized using tamarind leaf extract and potential application in vapor sensing. *Synth. React. Inorg. Met.-Org. Nano-Met. Chem.* **2005**, *35*, 19–26.
- Park, S. H.; Im, N. G.; Kim, K. H. Extraction behaviors of caffeine and chlorophylls in supercritical decaffeination of green tea leaves. *LWT–Food Sci. Technol.* **2012**, *45*, 73–78.
- Vilchis-Nestor, A. R.; Sánchez-Mendieta, V.; Camacho-López, M. A.; Gómez-Espinosa, R. M.; Camacho-López, M. A.; Arenas-Alatorre, J. A. Solventless synthesis and optical properties of Au and Ag nanoparticles using *Camellia sinensis* extract. *Mater. Lett.* **2008**, *62*, 3103–3105.

22. Begum, N. A.; Mondal, S.; Basu, S.; Laskar, R. A.; Mandal, D. Biogenic synthesis of Au and Ag nanoparticles using aqueous solutions of Black Tea leaf extracts. *Colloid Surf. B: Biointerfaces* **2009**, *71*, 113–118.
23. Song, J. Y.; Jang, H. K.; Kim, B. S. Biological synthesis of gold nanoparticles using *Magnolia kobus* and *Diopyros kaki* leaf extracts. *Process Biochem.* **2009**, *44*, 1133–1138.
24. Shankar, S. S.; Ahmad, A.; Pasricha, R.; Sastry, M. Bioreduction of chloroaurate ions by geranium leaves and its endophytic fungus yields gold nanoparticles of different shapes. *J. Mater. Chem.* **2003**, *13*, 1822–1826.
25. Kannan, P.; John, S. A. Synthesis of mercaptothiadiazole-functionalized gold nanoparticles and their self-assembly on Au substrates. *Nanotechnology* **2008**, *19*, 085602.
26. Talapin, D. V.; Haubold, S.; Rogach, A. L.; Kornowski, A.; Haase, M.; Weller, H. A novel organometallic synthesis of highly luminescent CdTe nanocrystals. *J. Phys. Chem. B* **2001**, *105*, 2260–2263.

Biosynthesis of Gold Nanoparticles Using Novel Bamboo (*Bambusa chungii*) Leaf Extracts

Jin-Liang Jia^{1,2}, Han-Hong Xu^{1,*}, Li Zhu², Wei-Hao Ye², and Dan-Qi Li²

¹State Key Laboratory for Conservation and Utilization of Subtropical Agro-Bioresources,
South China Agricultural University, Guangzhou, 510642, China

²Department of Applied Chemistry, College of Sciences, Institute of Biomaterials,
South China Agricultural University, Guangzhou, 510642, China

Gold nanoparticles (Au NPs) have drawn significant interest because of their anisotropic physical properties in biomedical applications. In this paper, we reported the application of bamboo (*Bambusa chungii*) leaf extracts, previously not exploited, in the synthesis of Au NPs at ambient temperature. The average dimension of quasi-spherical Au NPs was 28.8 ± 4.5 nm by transmission electron microscopy (TEM). The UV-vis spectroscopy gave an optimal reaction time of 180 min in the process of bioreduction. The organic shell of Au NPs was characterized by Fourier transform infrared (FTIR) spectra and thermogravimetric analysis (TGA), suggesting that the main compositions of the organic shell were hydroxyflavones. The X-ray diffraction (XRD) studies indicated the Au NPs were (111) oriented. This eco-friendly method for the synthesis of Au NPs was simple, amenable for large scale commercial production and biological applications to future *in vivo* imaging and cancer therapy.

Copyright: American Scientific Publishers

Keywords: Biosynthesis, Gold Nanoparticles, Bamboo Leaf, Characterizations.

1. INTRODUCTION

In recent years, there has been growing interest in utilizing gold nanoparticles (Au NPs) as possible diagnostic probes^{1–5} and photothermal therapy⁶ because of their anisotropic physical properties. However, as-synthesized Au NPs based on the most chemical reagents, such as cetyltrimethylammonium bromide (CTAB) and sodium borohydride, are not directly useable for these applications. For example, CTAB is known to be highly cytotoxic, which makes to limit the usefulness of these Au NPs for many biomedical applications.⁷

In this case, a green approach of synthesis Au NPs is a growing need to develop clean, nontoxic chemicals, environmentally friendly solvents and renewable materials.⁸ There had been recent reports on phytosynthesis of Au NPs by employing various plant materials such as black tea leaf,⁹ *Rhodopseudomonas capsulate*,¹⁰ olive leaf,¹¹ sundried *Cinnamomum camphora* leaf,¹² *Chenopodium album* leaf,¹³ coriander leaf,¹⁴ *Cacumen platycladi* leaf,¹⁵ black seed (*Nigella sativa*),¹⁶ English

ivy (*Hedera helix*)¹⁷ and *Anacardium occidentale* leaf¹⁸ etc. Additionally, a number of microorganisms and proteins were also well-known to synthesize nanostructured composites. For instance, fungus *fusarium oxysporum*,¹⁹ bacteria,²⁰ yeast²¹ and proteins²² had been investigated. Hence, the biosynthesized method of nanoparticles becomes significant in recent years.

There are 20 million tons for the bamboo with an annual production estimated in the world, mainly in Asia and Latin America.²³ However, the bamboo leaf is as certain low cost materials and wastes. Therefore, it is very important for the bamboo leaf that exploring new applications. In this work, we explored that simple synthesis of Au NPs by the reduction of aqueous AuCl_4^- using bamboo (*Bambusa chungii*) leaf extracts. To our knowledge, this is the first report on use of bamboo leaf for the biosynthesis of Au NPs. The bioreduction process of Au NPs was investigated by the UV-visible (UV-vis) spectra. Additionally, their morphology, stabilizer and nanocrystals of Au NPs using the bamboo leaf extracts were analyzed by transmission electron microscopy (TEM), Fourier transform infrared (FTIR) spectrum, thermogravimetric analysis (TGA) and X-ray diffraction (XRD). The use

* Author to whom correspondence should be addressed.

of environmentally friendly and renewable bamboo leaf offers enormous benefits for biomaterial and biomedical applications.

2. EXPERIMENTAL METHODS

2.1. Preparation of Bamboo Leaf Broth

Tetrachloroauric acid ($\text{HAuCl}_4 \cdot 3\text{H}_2\text{O}$) was purchased from Acros Organics. Fresh bamboo (*Bambusa chungii*, China) leaf was obtained from South China Agricultural University Arboretum, and the leaf broth was prepared by taking 5 g of thoroughly washed and dried leaves in a 500 mL flask with 100 mL of deionized (DI) water or 75% (v/v) ethanol/water. The solutions were boiled for 15 min before filtration. Finally, the filter liquor was concentrated, and the concentrated solution was dissolved in 40 mL of distilled water. Prior to use, all glassware was washed with aqua regia (HCl/HNO_3) and rinsed with DI water for three times.

2.2. Synthesis Au NPs

For reduction of AuCl_4^- ions, 5 mL of as-prepared bamboo leaf broth was added to 45 mL of 1×10^{-3} M HAuCl_4 solution. After stirring 1 min, the mixture solution was left without stirring at room temperature. Then the as-prepared colloid of Au NPs was stored at 4 °C and used within 7 days.

2.3. Characterization

The bioreduction of AuCl_4^- in aqueous solution was monitored by measuring the UV-vis spectra of the colloids at regular intervals. After the periodic sampling of aliquots (0.2 mL) of the reaction solution was diluted 10-fold with distilled water, UV-vis spectra were recorded as a function of the reaction time by a UV-2102PC spectrometer operated at a resolution of 1 nm. In order to characterize the morphology of the synthesized Au NPs, TEM images were acquired using a Tecnai 12 operated at 100 kV. The samples were prepared by dropping the colloidal solution on a Formvar/carbon film coated Cu grid (3 mm,

300 mesh) and allowing water to evaporate at ambient temperature.

The structure and composition of the particle surface were analyzed by FTIR spectrum, XRD and TGA. For FTIR spectroscopy measurements, dry powders of nanoparticles were obtained using the following method. In order to make nanoparticles free from proteins or other bioorganic compounds present in the solution, the as-prepared Au NP colloids at the optimal reaction time were centrifuged at 5,000 rpm for 15 min and rinsed with DI water at least three times. Finally, the black solid was dried in vacuo at 45 °C. The dried power was analyzed for the crystalline nature of Au NPs by MSAL XD-2 X-ray diffractometer (Beijing) with Cu $K\alpha$ radiation. In addition, TGA was performed on DTG-60 Shimadzu (Japan), and the dried samples were heated under an argon atmosphere at a rate of 10 °C/min to 900 °C.

3. RESULTS AND DISCUSSION

UV-vis spectroscopy is one of the important means to explain the formation and stability of metal nanoparticles in colloidal solution. Using the ethanol/water extracts, the oxidized compounds are most probably hydroxyflavones. However, the main compositions of this bamboo leaf are the polysaccharides using DI water extracts.²⁴ During the synthesis of Au NPs with leaf extracts in different solvents, a huge difference in their total reduction time of 180 min was observed in Figure 1(a). We could see that an obviously absorbed peak at 550 nm is due to plasmon resonance absorption of Au NPs using the ethanol/water extracts, illustrating that there are a number of Au NPs in the reaction solution. However, the peak around 550 nm is lacking in the solution using the DI water extracts, suggesting that there is no particles in this solution or the formed clusters are smaller than 2 nm.²⁵ But the clusters impossibly forms through observing the color of the reaction solution using DI water extracts. Therefore, the bioreduction process may occur between AuCl_4^- and hydroxyflavones in the ethanol/water extracts.

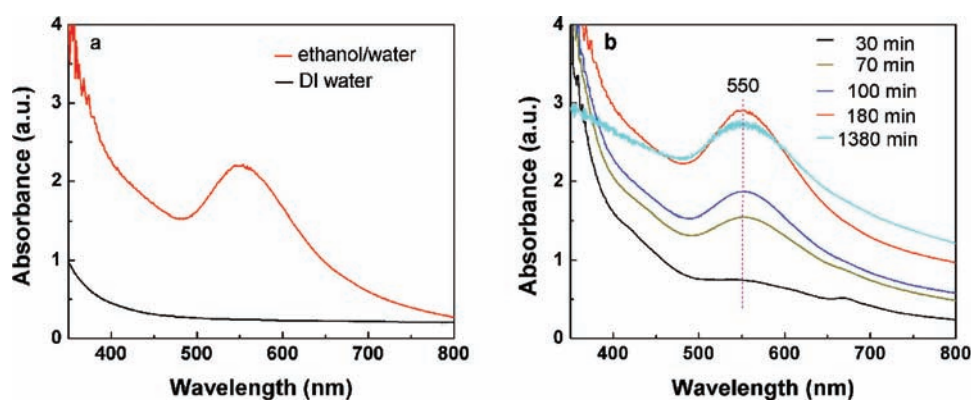


Figure 1. UV-vis spectra of Au NPs at (a) the extracts of different solvents and (b) the different bioreduction time using the ethanol/water extracts.

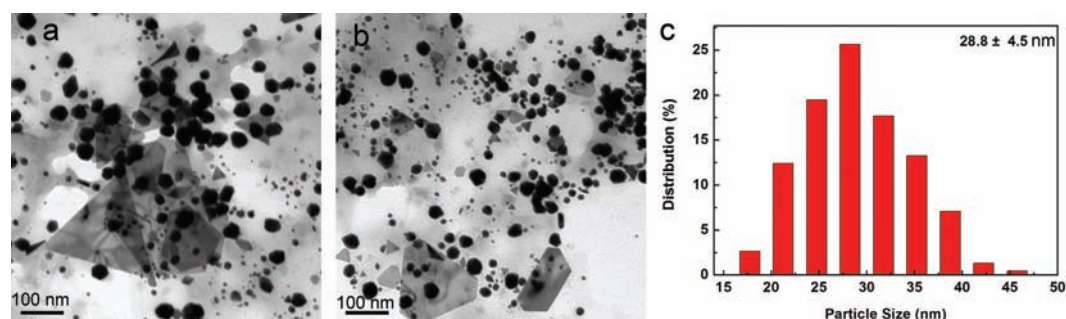


Figure 2. (a) and (b) representative TEM image of the as-prepared Au NPs at 180 min; (c) size histogram of Au NPs.

Additionally, as shown in Figure 1(b), no significant difference was observed when Au NPs were synthesized using the ethanol/water extracts, except for the intensity of the absorption peaks. The maximum absorption peak was observed to occur at ca. 550 nm, and the intensity steadily increased to saturation as a function of the reaction time. The concentrations of the Au NPs can be quantitatively monitored because the value of the absorption peak doesn't shift during the reaction.²⁶ Given the constant aqueous resolution, comparative experiments were carried out to investigate the optimal reaction time. The intensity of the absorption peaks has a slight decrease when the reaction time is longer than 180 min, which indicates that the attainment of the saturation in the bioreduction of AuCl_4^- . As a result, an optimal reaction time of 180 min is recommended.

Figures 2(a) and (b) exhibit the TEM image of typical Au NPs, and the average dimension is 28.8 ± 4.5 nm by analyzing at least 220 nanoparticles. Though there are few anisotropic nanostructures, such as big nanotriangle or nanoparticles with irregular contours, Au NPs consists of almost spherical nanoparticles. Therefore, the morphology of Au NPs is in agreement with the result of UV-vis spectra. In addition, the size histogram of Au NPs was shown in Figure 2(c). The uniform distribution of their stable shape and dimensions plays a crucial role in modulating the physical and chemical properties of nanoparticles.

The distinctive FTIR absorption peaks of the potential biomolecules in nanoparticles appeared at 400–4000 cm^{-1}

were given in Figure 3. The most wide absorption peak was about 3395 cm^{-1} , assigning to the characteristic signals for O—H. Additionally, C—H groups at 2923 cm^{-1} (asymmetrical stretching) and 2850 cm^{-1} (symmetrical stretching) were observed in Figure 3.²⁷ In particular, a band at 1722 cm^{-1} was originated from the carbonyl stretching vibration in acetyl ester groups of the flavonoids. The absorption peaks of 1649, 1509 and 1458 cm^{-1} could be attributed to the stretching vibration of $-\text{C}=\text{C}-$ (the ring of aromatic) and $-\text{C}-\text{C}-$ (the ring of aromatic). To a large extent, the weak absorption peak about 1225 cm^{-1} may be originated most probably from the stretching vibrations of $-\text{C}-\text{O}-$ group⁹ and the absorption peak at 1075 cm^{-1} can be contributed to the stretching vibrations of $-\text{C}-\text{OH}$ using the ethanol/water extracts,¹¹ which suggests the presence of flavonoids and flavones-C-glycosides in the biomass. Therefore, the Au NPs are capped by the hydroxyflavones in the bamboo leaf. Moreover, the oxygen atoms in the hydroxyflavones might facilitate the adsorption of the heterocyclic components onto the particle surface as a stabilizer, which is in good agreement with the results of UV-vis spectra.

There are few reports on the TGA of biosynthesized Au NPs in previous work. Here, the TGA curve of the hybrid Au NPs using bamboo leaf extracts was shown in

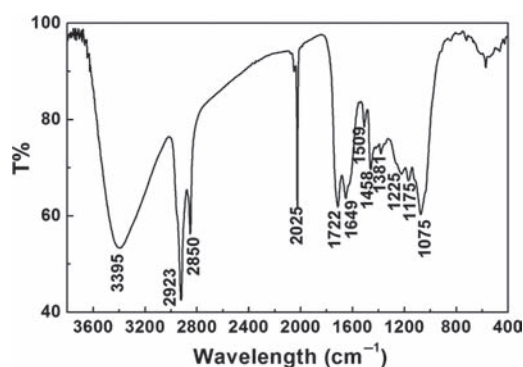


Figure 3. FTIR spectrum of Au NPs using the ethanol/water extracts.

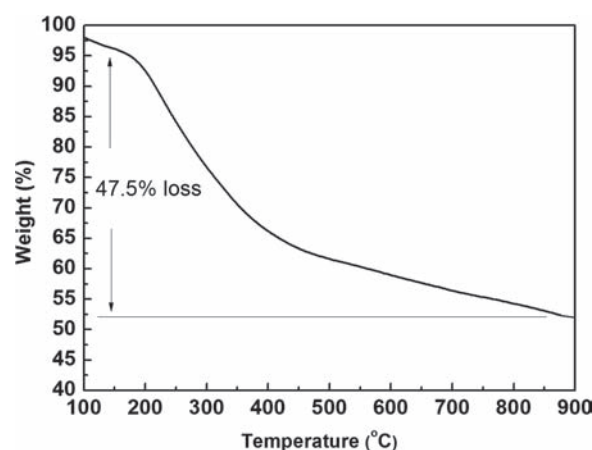


Figure 4. TGA curve of capped Au NPs using the ethanol/water extracts.

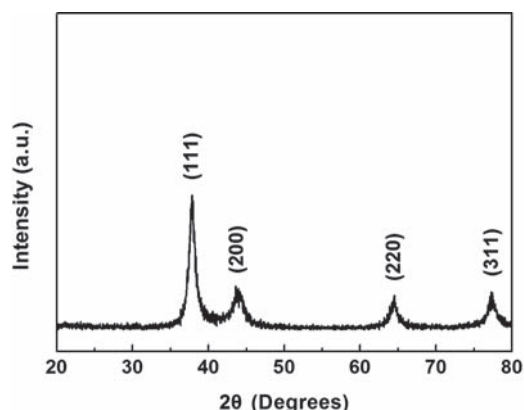


Figure 5. X-ray diffraction patterns of Au NPs using the ethanol/water extracts with AuCl_4^- aqueous solutions.

Figure 4, revealing that a steady weight loss in the temperature range of 100–850 °C. Here, the weight loss of the as-prepared nanoparticles was 47.5% because of the decomposition of bioorganic compounds. We can see that the weight of the shell as a stabilizer is less than the one of Au core. Additionally, the decomposition temperature of ca. 850 °C shows the stabilization of formed Au NPs. Hence, further studies to evaluate the invitro stabilities of bamboo leaf extracts mediated Au NPs are in progress.

The crystal structures of Au NPs were examined by XRD technique. As shown in Figure 5, the diffraction peaks of Bragg reflections for Au NPs at 37.8°, 44.1°, 64.5°, and 77.3°, which are assigned to (111), (200), (220) and (311) reflections of face-centered cubic gold lattice, respectively.²⁸ The XRD pattern shows that Au NPs formed by the reduction of AuCl_4^- by bamboo leaf extracts. Thus, it is clear that formed Au NPs are essential crystalline in nature. Additionally, the ratio between the intensity of (200) and (111) diffraction peaks of 0.3 is lower than the conventional bulk intensity ratio (0.52), suggesting that (111) plane is the predominant orientation. These results are in good agreement with those obtained by Khalil et al.¹¹

4. CONCLUSIONS

Au NPs (28.8 ± 4.5 nm) were firstly synthesized using bamboo leaf extracts, which was a simple and efficient method. The optimal time of 180 min in the bioreduction was obtained by UV-vis spectra. FTIR, TGA and XRD analysis of Au NPs with crystal structures indicated the hydroxyflavones could mostly be determined as a stabilizer from 75% (v/v) ethanol/water extracts of bamboo leaf, and the weight loss of organic shell was 47.5%. This green approach for the biosynthesis of Au NPs doesn't use any toxic reagent, which is being actively studied as a promising and large-scale commercial production.

Acknowledgments: This work was financially supported by NSF (Grant 31171886) of China, the Doctoral Fund of Ministry of Education of China (Grant 20114404110020), and Guangdong Provincial High Level Experts (Grant 2010-79).

References and Notes

1. X. M. Qian and S. M. Nie, *Chem. Soc. Rev.* 37, 912 (2008).
2. J. L. Jia, H. H. Xu, G. R. Zhang, Z. Hu, and B. Q. Xu, *Nanotechnology* 23, 495710 (2012).
3. H. M. Sun, Q. H. Yuan, B. H. Zhang, K. L. Ai, P. G. Zhang, and L. H. Lu, *Nanoscale* 3, 1990 (2011).
4. S. Shukla, A. Priscilla, M. Banerjee, R. R. Bhonde, J. Ghatak, P. V. Satyam, and M. Sastry, *Chem. Mater.* 17, 5000 (2005).
5. Y. Cui, X. S. Zheng, B. Ren, R. Wang, J. Zhang, N. S. Xia, and Z. Q. Tian, *Chem. Sci.* 2, 1463 (2011).
6. X. H. Huang, I. H. El-Sayed, W. Qian, and M. A. El-Sayed, *J. Am. Chem. Soc.* 128, 2115 (2006).
7. L. Vigderman, P. Manna, and E. R. Zubarev, *Angew. Chem. Int. Ed.* 50, 1 (2011).
8. R. S. Patil, M. R. Kokate, and S. S. Kolekar, *Spectrochim. Acta. Part A* 91, 234 (2012).
9. N. A. Begum, S. Mondal, S. Basu, R. A. Laskar, and D. Mandal, *Colloids Surf. B Biointerfaces* 71, 113 (2009).
10. S. Y. He, Y. Zhang, Z. R. Guo, and N. Gu, *Biotechnol. Prog.* 24, 476 (2008).
11. M. M. H. Khalil, E. H. Ismail, and F. El-Magdoub, *Arab. J. Chem.* 5, 431 (2012).
12. J. L. Huang, Q. B. Li, D. H. Sun, Y. H. Lu, Y. B. Su, X. Yang, H. X. Wang, Y. P. Wang, W. Y. Shao, N. He, J. Q. Hong, and C. X. Chen, *Nanotechnology* 18, 105104 (2007).
13. A. D. Dwivedi and K. Gopal, *Colloids Surf. A. Physicochem. Eng. Asp.* 369, 27 (2010).
14. K. B. Narayanan and N. Sakthivel, *Mater. Lett.* 62, 4588 (2008).
15. G. L. Zhang, M. M. Du, Q. B. Li, X. L. Li, J. L. Huang, X. D. Jiang, and D. H. Sun, *RSC Adv.* 3, 1878 (2013).
16. A. Fragoon, J. J. Li, J. Zhu, and J. W. Zhao, *J. Nanosci. Nanotechnol.* 12, 2337 (2012).
17. S. j. Yi, L. J. Xia, S. C. Lenaghan, L. M. Sun, Y. J. Huang, J. N. Burris, C. N. Stewart, Jr. and M. J. Zhang, *J. Nanosci. Nanotechnol.* 13, 1649 (2013).
18. D. S. Shen, D. Philip, and J. Mathew, *Spectrochim. Acta A. Mol. Biomol. Spectrosc.* 91, 35 (2012).
19. P. Mukherjee, S. Senapati, D. Mandal, A. Ahmad, M. I. Khan, R. Kumar, and M. Sastry, *ChemBiochem* 5, 461 (2002).
20. J. R. Stephen and S. J. Maenoughton, *Curr. Opin. Biotechnol.* 10, 230 (1999).
21. R. K. Mehra and D. R. Winge, *J. Cell. Biochem.* 45, 30 (1991).
22. P. Ravindra, *Mater. Sci. Eng. B* 163, 93 (2009).
23. M. Frías, H. Savastano, E. Villar, M. I. S. de Rojas, and S. Santos, *Cem. Concr. Compos.* 34, 1019 (2012).
24. S. S. Zhang and X. H. Zhao, *Food Sci. Technol.* 3, 167 (2008).
25. L. Shang, R. M. Dorlich, S. Brandholt, R. Schneider, V. Trouillet, M. Bruns, D. Gerthsen, and G. U. Nienhaus, *Nanoscale* 3, 2009 (2011).
26. J. Y. Song, H. K. Jang, and B. S. Kim, *Process Biochem.* 44, 1133 (2009).
27. H. Peng, M. Y. Zhou, Z. P. Yu, J. S. Zhang, R. Ruan, Y. Q. Wan, and Y. H. Liu, *Carbohydr. Polym.* 95, 262 (2013).
28. W. J. Liu, Z. N. Zhu, K. Deng, Z. T. Li, Y. L. Zhou, H. B. Qiu, Y. Gao, S. N. Che, and Z. Y. Tang, *J. Am. Chem. Soc.* 135, 9659 (2013).

Received: 18 September 2013. Accepted: 1 November 2013.

GABA-Decorated Nanocarrier for Smart Delivery of Fludioxonil for Targeted Control of Banana Wilt Disease

Liangheng He, Chunxia Xiao, Li Zhu, Wenjie Deng, Yanheng Zhang, Yang Li, Xinzhou Wu, Hanxiang Wu, Hanhong Xu,* and Jinliang Jia*



Cite This: *J. Agric. Food Chem.* 2024, 72, 26664–26676



Read Online

ACCESS |



Metrics & More



Article Recommendations



Supporting Information

ABSTRACT: Developing a targeted nanopesticide to control the vascular disease of banana in agriculture is crucial to improve pesticide utilization. In this study, according to the degree of functionalization, three γ -aminobutyric acid (GABA)-decorated nanocarriers (PSI-GABA₈, PSI-GABA₁₈, and PSI-GABA₂₈) were constructed for smart delivery of nonsystemic fungicide in banana phloem tissues. Fludioxonil (Flu) was loaded in nanocarriers to form Flu@PSI-GABA nanoparticles with a core/shell structure for control of banana wilt disease. Results demonstrated that the delivery dosage of Flu was up to 1.6 mg/L in castor phloem sap using PSI-GABA₂₈ nanocarriers. *In vitro* results showed that the EC₅₀ of Flu@PSI-GABA₂₈ was 0.0116 mg/L, and the inhibitory activity was about 8.8 times higher than that of technical-grade (TC) Flu. Flu@PSI-GABA₂₈ could be transported for long distances and accumulated to the rhizome of banana by foliar application, and the control effectiveness was about 20 times that of the conventional Flu (50% WP) for the banana wilt. This study provides a distinctive guidance for effective control of vascular diseases in precision agriculture application.

KEYWORDS: γ -aminobutyric acid, targeted, nanocarrier, fludioxonil, banana wilt disease

INTRODUCTION

Banana is the fourth most important tropical and subtropical food crop after rice, wheat, and corn, which is grown in more than 130 countries and regions of the world.^{1–3} However, banana cultivation has been affected by a worldwide soil-borne disease, wherein banana wilt is a destructive disease caused by *Fusarium oxysporum* f. sp. *Cubense* (Foc), threatening the banana industry, which is known as “banana cancer”. It destroys the function of vascular tissues and causes the plants to wilt and die. Banana wilt has spread widely and seriously threatens the sustainable development of the banana industry.³

Most of the plant foliar diseases can be effectively controlled by chemicals with osmotic and systemic properties,⁴ but the control of vascular tissue diseases such as banana wilt is still a worldwide problem. Nowadays, major management measures for banana wilt include chemical control, biological control and breeding for disease resistance, etc.,^{5–9} wherein biological control effectiveness is characterized for a longer period of time, and chemical control is still the mainstay.^{10–13} However, existing fungicides such as azoxystrobin, kresoxim-methyl, and pyraclostrobin rely mainly on xylem transportation, which will rapidly accumulate in the plant leaves and other transpiration parts. Once the pathogen invades the plant xylem, the transportation of the pesticides in the vascular tissues is blocked, which ultimately makes fungicides difficult to act on the infested parts.^{14–17} Fludioxonil (Flu) as a broad-spectrum fungicide is widely used for soil fungal control.^{18–22} Although Flu shows good activity against banana wilt *in vitro*, it is basically ineffective against the disease in banana seedlings. Therefore, the key method for chemical control of banana wilt

is to enhance the target accumulation of fungicides in the vascular tissue of the banana seedlings.

Nanotechnology is receiving more attention in precision agriculture. Many nanocarriers provided new ideas for achieving pesticide systemic absorption.²³ For example, Chen et al. synthesized iron-based metal–organic framework nanoparticles MIL-101-SL to achieve bidirectional translocation of chlorfenapyr, which enhanced insecticidal activity and persistence.²⁴ Liang et al. synthesized a zeolitic imidazolate framework-8 composite capable of transporting prochloraz to various parts of oilseed rape.²⁵ Although previous studies have shown that nanoparticles can be transported through vascular pathways, these nanoparticles passively transfer, and the design for proactive accumulation to lesion sites is still lacking.

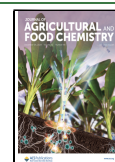
The long-distance transport of endogenous amino acid molecules in plants is transferred by amino acid transporter proteins.²⁶ When plants are stressed by pests and diseases, some plant endogenous substances are directionally transported to the lesion site such as γ -aminobutyric acid (GABA). Many studies have shown that GABA plays an important role in improving the stress resistance of plants, possibly through participation in stress.^{27–29} Threats at plants from different sources, such as salinity and drought, as well as pathogen invasion and insects, may lead to rapid accumulation of GABA

Received: August 16, 2024

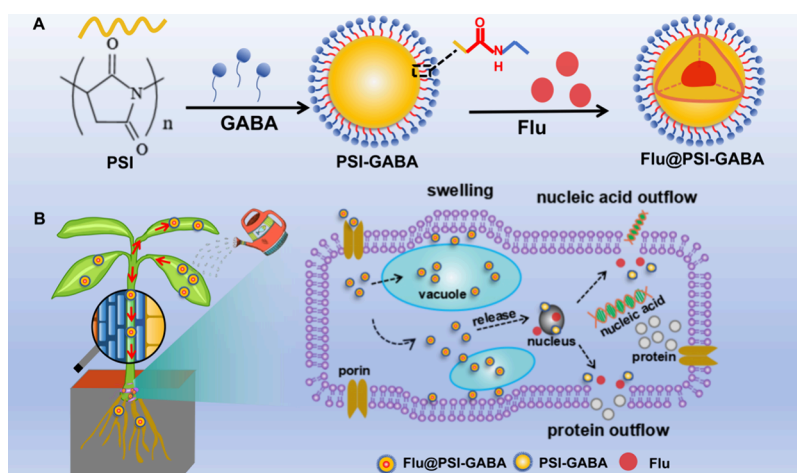
Revised: October 8, 2024

Accepted: October 9, 2024

Published: October 17, 2024



Scheme 1. (A) Schematic Illustration of the Preparation of Flu@PSI-GABA and (B) Its Application in Flu@PSI-GABA Targeted Transport and Synergistic Mechanism for Foc



in plants.^{28,29} Moreover, GABA will be stimulated during the interaction of plants with pathogenic microorganisms and promote plant self-protection against pathogenic invasion. For example, in wild xanthomonas rapeseed and pepper, the expression of arginine decarboxylase (ADC) was triggered simultaneously with an increase in GABA content.³⁰ Additionally, application of exogenous GABA suppressed the growth of pathogenic microorganisms in ADC-deficient plants, which was also able to play a role in adversity.³¹

Although previous research has successfully achieved phloem transport of pesticides using nanocarriers of glycine methyl ester in our study,^{32,33} the transport efficiency and preventive and curative effects are all low. In this study, we used simple steps to construct fungicide delivery nanocarriers by GABA and then loaded the Flu in nanocarriers to form Flu@PSI-GABA nanoparticles with a core/shell structure. Flu@PSI-GABA is transported from the leaves of banana seedlings to the rhizome, and it also shows the mechanism of activity synergism for Foc (Scheme 1). The slow-release properties, transmission dose, bacteriostatic activity and potting control effects of Flu@PSI-GABA (Flu@PSI-GABA₈, Flu@PSI-GABA₁₈, and Flu@PSI-GABA₂₈) were investigated. Finally, we detected the Flu and endogenous amino acid content in various parts of banana seedlings and evaluated the transport concentration of the pesticide delivery system. Thus, the promising application of Flu@PSI-GABA in the effective control of agricultural soil-borne diseases was revealed.

EXPERIMENTAL SECTION

Materials. Polysuccinimide (PSI) and γ -aminobutyric acid (GABA, 99%) were purchased from Shanghai Acme Biotechnology Co., Ltd. Technical-grade (TC) fludioxonil (98% purity) was obtained from Shanghai Macklin Bioengineering Co., Ltd. A 50% wettable powder (WP) formulation of Flu was purchased from Syngenta Investment Co, Ltd. Tissue-cultured Cavendish banana of the Foc race 4-susceptible cultivar “Brazilian” was used in this study. Plantlets in sealed bags were transplanted into sterile soil consisting of one part vermiculite and three parts peat (Jiffy Products Ltd., Norway) for 50 days. Castor bean (*Ricinus communis* L.) seedlings were grown for 5 days in the vermiculite, as described previously.³³ All plantlets were grown in a greenhouse at 28 ± 2 °C with a 16 h light/8 h dark photoperiod.

Preparation of Flu@PSI-GABA Nanoparticles. PSI-GABA nanoparticles were prepared according to previous publications with slight modifications.³³ At first, 0.97 g of PSI was dissolved in 10 mL of

dimethyl sulfoxide (DMSO). Then, 1.02 g of GABA was dissolved in 5 mL of water and mixed with the PSI solution under vigorous stirring for 24 h. The resulting solution was added dropwise to 500 mL of citric acid buffer at pH = 2.5. Then, the PSI-GABA nanoparticles were collected by centrifugation (10,000 rpm), washed three times with deionized water, and freeze-dried overnight.

Flu@PSI-GABA nanoparticles were synthesized as follows. PSI-GABA (100 mg) was dissolved in 10 mL of DMSO, and 100 mg of Flu (TC) was added to form a mixed organic phase. Then, the mixed solution was added to 90 mL of deionized water with vigorous stirring for 1 h. The resulting mixture was centrifuged at 10,000 rpm for 10 min and then further washed. Nanoparticles were obtained after lyophilization.

Characterization of Flu@PSI-GABA Nanoparticles. The structure of the nanoparticles was inspected by using a Fourier transform infrared spectrometry (FTIR) instrument (Nicolet IS10, Thermo Fisher, America). The hydrodynamic diameters of PSI-GABA and Flu@PSI-GABA were measured via dynamic light scattering (Zetasizer Nano ZSE, Malvern Panalytical Ltd., UK). Thermogravimetric analysis (TGA) of the nanoparticles was performed using a TG 209 F1 Libra (NETZSCH Geratebau, Germany). The morphology of the nanoparticles was characterized by transmission electron microscopy (JEOL 2100F, JEOL Co., Ltd., Japan). Also, the morphology of the Foc race 4-susceptible cultivar was characterized by scanning electron microscopy (Nova NanoSEM 450, FEI Co., USA). The elemental distribution of the Flu@PSI-GABA nanoparticles was analyzed by energy dispersive spectroscopy (EDS).

The loading efficiency of Flu was determined by the following method. Twenty milligrams of Flu@PSI-GABA was dissolved in 5 mL of ethanol, and Flu was completely released via an ultrasonic bath for 2 h. The resulting suspension was separated by centrifugation (10,000 rpm for 10 min), and the Flu was then analyzed using high-performance liquid chromatography (HPLC; Agilent Technologies 1100). An Agilent SBC18 reversed-phase column (5 μ m, 250 mm \times 4.6 mm i.d.) was used at a flow rate of 0.8 mL/min, and the injection volume was 10 μ L. The mobile phase was consisted of acetonitrile and water (1/1, V/V). The absorbance wavelength was 276 nm. The loading efficiency (LE) was calculated with the following equation:

$$LE(\%) = (M/M_0) \times 100\% \quad (1)$$

where M is the mass of Flu detected by HPLC, and M_0 is the mass of Flu@PSI-GABA.

In Vitro Release Profiles of Flu@PSI-GABA Nanoparticles. The release behavior of Flu@PSI-GABA nanoparticles was measured as described below. Twenty milligrams of the Flu@PSI-GABA nanoparticles was added to 3 mL of phosphate buffer solutions at different pH values (pH 5.0, 7.0, and 8.0) containing 50% (V/V)

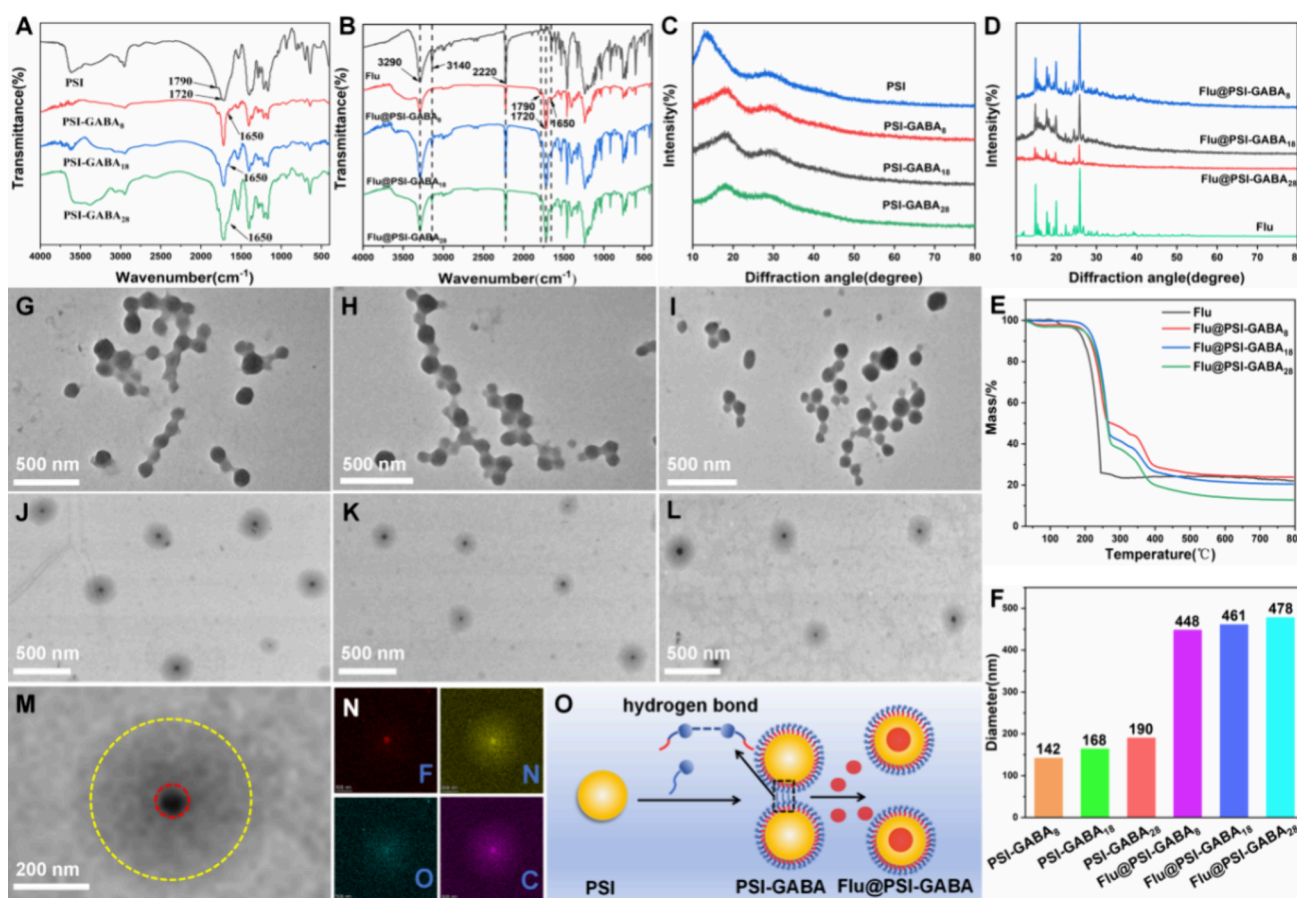


Figure 1. Infrared spectra of PSI-GABA (A) and Flu@PSI-GABA (B). XRD of PSI and PSI-GABA (C) and Flu@PSI-GABA (D). (E) TGA curves of Flu and Flu@PSI-GABA. (F) Hydrated particle sizes of PSI-GABA₈, PSI-GABA₁₈, PSI-GABA₂₈, Flu@PSI-GABA₈, Flu@PSI-GABA₁₈, and Flu@PSI-GABA₂₈. TEM images of PSI-GABA₈ (G), PSI-GABA₁₈ (H), PSI-GABA₂₈ (I), Flu@PSI-GABA₈ (J), Flu@PSI-GABA₁₈ (K), and Flu@PSI-GABA₂₈ (L). TEM of a Flu@PSI-GABA₂₈ nanoparticle (M) and its EDS mapping characterizations (N). (O) Illustration for identical interaction of two nanoparticles.

water–ethanol. The dialysis bags were submerged in 150 mL of the same phosphate buffer solution as the release medium and stirred at 120 rpm. One milliliter of release medium was collected at intervals, and then 1 mL of fresh medium was added to keep the same original volume. The Flu content in the release medium was analyzed by HPLC. The release experiments were repeated three times, and the cumulative release rate of Flu was calculated according to the following equation:

$$Q_n = C_n V_0 + (C_1 + C_2 + C_3 + \dots + C_{n-1}) \times V \quad (2)$$

where Q_n is the cumulative mass of drug released at the n th sampling time point, Q_0 is the initial drug mass of the nanofungicide, C_n is the concentration at the n th sampling time point, V_0 is the volume of the release medium, and V is the volume of each sample.

In Vivo Efficacy of Flu@PSI-GABA against Foc. Pot experiments were conducted on banana seedlings (50 days) by foliar application of Flu@PSI-GABA, Flu (TC), or Flu (50% WP) as described above. Flu (TC), Flu (50% WP), and Flu@PSI-GABA with equivalent doses of Flu were applied to leaves at final concentrations of 200, 400, and 4000 mg/L, respectively. Then, two leaves were selected from each plant for a treatment, and 1 mL of the treatment solution was used for each leaf. Controls were treated with the same solution without Flu@PSI-GABA, Flu (TC), and Flu (50% WP). The seedlings were handled with two treatments: (i) 2 days prior to inoculation and (ii) 5 days after inoculation with the pathogenic fungus. Each treatment was replicated three times with six plants per replication. Artificial inoculation of banana plants with Foc spores was described elsewhere.³³ The spore suspension was applied to the soil at a final concentration of 5000 conidia/g of soil. For disease severity 50

days after inoculation, spore suspensions were applied to the soil at a final concentration of 5000 conidia/g soil. Symptoms (grade 0–4) were described by Huang et al.³⁴ The disease severity (%) was calculated as $\sum(\text{number of plants in that rating} \times \text{rating}) / (\text{total number of plants assessed} \times \text{maximum rating}) \times 100$, while the percentage efficacy of disease control (%) was calculated as follows: $(\text{disease severity in control} - \text{disease severity in treatment}) / \text{disease severity in control} \times 100$.

Tissue Uptake in Castor Seed Seedlings. Castor seedlings were used as a plant model to assess the mobility of foreign substances. The cotyledons of seedlings were incubated in a buffered solution (pH 5.0). A solution consisting of 20 mM MES (2-morpholinoethanesulfonic acid), 0.25 mM MgCl₂, and 0.5 mM CaCl₂ was soaked for 30 min. It was then transferred to the same solution supplemented with 100 mg/L Flu@PSI-GABA or an equivalent dose of Flu (50%) for 2 h.

The bast sap was diluted with acetonitrile (bast sap/acetonitrile, V/V = 1/5). At the end of the experiment, the treated cotyledons were extracted to determine the tissue uptake of Flu. In detail, cotyledons were rinsed (3 × 2 min) in a pure water/acetone (9/1, V/V) solution. Two cotyledons of each plant were then suspended in 10 mL of acetonitrile and extracted by sonication for 10 min. Extracts were passed through a 0.22 μm pore size filter membrane. Experimental results of Flu in sap and cotyledon extracts were obtained by using an Agilent Technologies 1100 high-performance liquid chromatography (HPLC) system equipped with a UV/vis photodiode-array detector.

In Vivo Transfer and Distribution of Flu@PSI-GABA. Banana seedlings (50 days old) were treated with Flu@PSI-GABA and Flu (50% WP). To describe and quantify the movement of Flu in

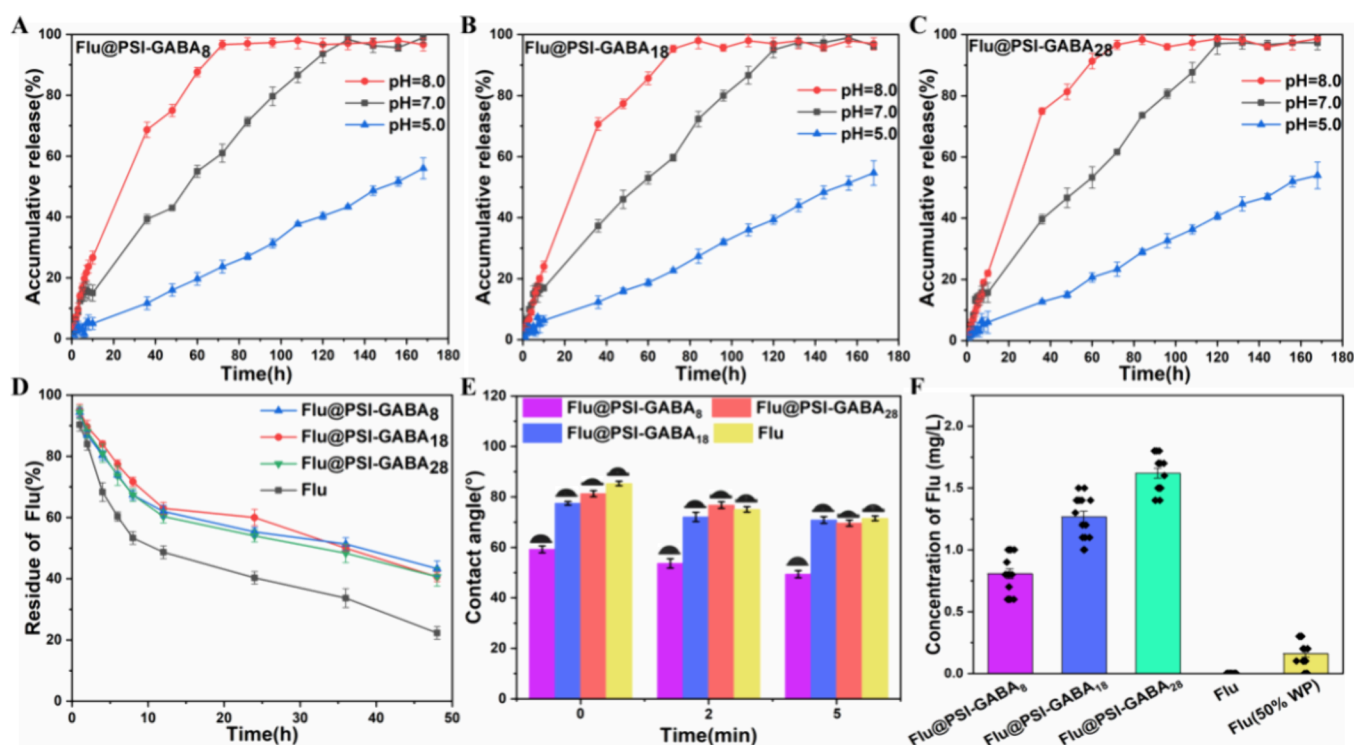


Figure 2. Cumulative release of Flu from Flu@PSI-GABA₈ (A), Flu@PSI-GABA₁₈ (B), and Flu@PSI-GABA₂₈ (C) under different pH conditions (5.0, 7.0, and 8.0). (D) UV decomposition resistance curves of Flu@PSI-GABA₈, Flu@PSI-GABA₁₈, Flu@PSI-GABA₂₈, and Flu. (E) Wetting dynamics of Flu@PSI-GABA₈, Flu@PSI-GABA₁₈, Flu@PSI-GABA₂₈, and Flu (TC) droplets on banana leaves. (F) Flu concentration in castor phloem sap of Flu@PSI-GABA₈, Flu@PSI-GABA₁₈, Flu@PSI-GABA₂₈, Flu (TC), and Flu (50% WP).

seedlings, different parts of the plant (upper leaves, treated leaves, pseudostems, rhizomes, and roots) were analyzed separately. Flu@PSI-GABA and equivalent doses of Flu (50% WP) and Flu (TC) were applied to final concentrations of 2000, 200, and 100 mg/L (1 mL/leaf and 2 leaves/plant, respectively). Flu@PSI-GABA, Flu (TC), and Flu (50% WP) were prepared in a mixed solution (acetone/water, 1:9, V/V) containing 0.15% (V/V) organosilicon surfactant (Silwet L-77).

The control group was treated with a mixed solution (acetone/water, 1:9, V/V) containing a 0.15% (V/V) organosilicon surfactant (Silwet L-77). Experiments were replicated 2 times with 24 replicates for each treatment plant. Plants were collected and extracted 5 and 10 days after foliar treatment. Plants (10 plants × 4) were collected and extracted at 5 and 10 days after foliar treatment, and each plant was analyzed individually. The analyses were performed individually. The extraction and cleaning protocols were performed according to the modified QuEChERS method. The analysis was performed using liquid chromatography–tandem mass spectrometry (LC-MS).

Mass Spectrometry Imaging (MSI) of Flu in Banana Rhizome. Banana seedlings were transplanted into sandy loam soil that had been autoclaved under the culture conditions for about 50 days, and when they grew to 3–4 leaves, banana seedlings of uniform size were selected for the experiment. Banana rhizome slices were taken and embossed on the background plate by hand and then glued to the sample plate with conductive graphite adhesive for mass spectrometry imaging analysis. In this experiment, the data obtained from the digital oscilloscope were processed by the self-written LabVIEW2014 program to obtain the information such as m/z and signal intensity. Finally, the mass spectra were obtained with Origin 9 software, and the mass spectral imaging maps were obtained with Surfer 9 software.

Statistical Analysis. All data were expressed as the mean ± SD. Each experiment was repeated at least three times. Statistical analysis was performed with Origin 9.

RESULTS AND DISCUSSION

Synthesis and Characterization of PSI-GABA and Flu@PSI-GABA. Three kinds of nanocarriers with different functionalizations of GABA were prepared in the experiment. According to the degree of functionalization by ¹H NMR spectroscopy tested, the delivery nanocarriers were named PSI-GABA₈, PSI-GABA₁₈, and PSI-GABA₂₈ (Figure S1). The three nanocarriers prepared were collectively referred to as PSI-GABA. Then, the three nanocarriers loaded with Flu were named Flu@PSI-GABA₈, Flu@PSI-GABA₁₈, and Flu@PSI-GABA₂₈, respectively, which were also collectively referred to as Flu@PSI-GABA. As shown in Figure 1A,B, the peak at 1720 cm⁻¹ represented the C=O bond within the five-membered ring of PSI.^{35,36} Also, the absorption peak at 1650 cm⁻¹ was attributed to the stretching vibration of the C=O bond during the reaction between PSI and GABA.³⁷ In addition, the peak at 2220 cm⁻¹ belonged to the C≡N of cloxynil, and the absorption peaks at 3290 and 3140 cm⁻¹ were assigned to the C–H and N–H absorption peaks of Flu, respectively. The results showed that PSI-GABA nanocarriers were synthesized, and Flu was successfully loaded by PSI-GABA. The XRD in Figure 1C,D shows that PSI had a distinct absorption peak at 9°. After the modification by GABA, three different functionalized nanocarriers with a similar peak shape, the absorption peak at 9° basically disappeared, and a new absorption peak appeared at 19°, which indicated that GABA had a chemical reaction with PSI. The characteristic peaks of Flu could still be clearly seen in the curve of Flu@PSI-GABA, illustrating that Flu existed as crystals inside the nanocarriers of PSI-GABA. Additionally, the TGA curves of Flu and Flu@PSI-GABA are shown in Figure 1E and Figure S2. It could be seen that the thermal decomposition of Flu started at 200 °C and was

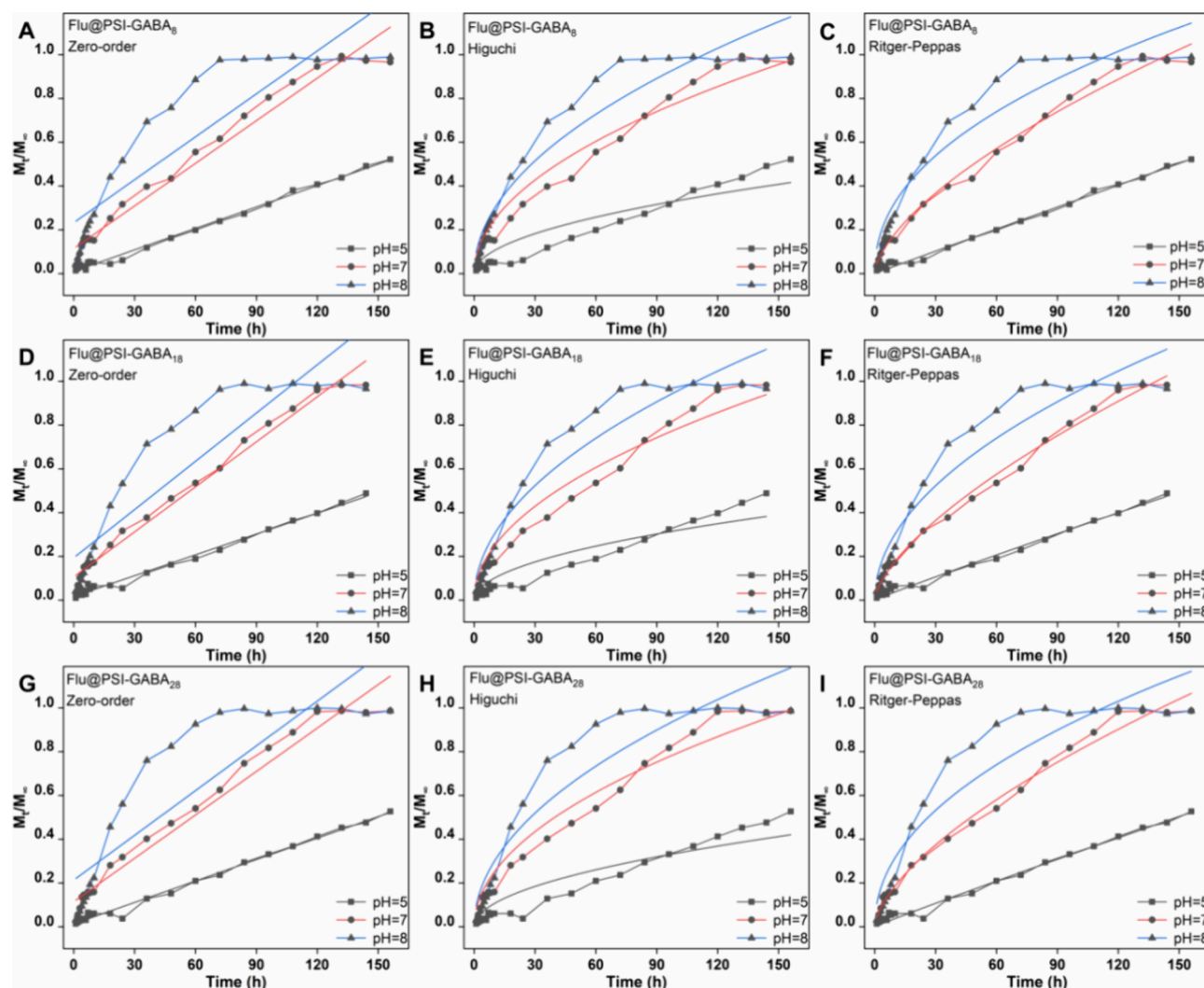


Figure 3. Fitting curves of the zero-order, Higuchi, and Ritger–Peppas models of Flu@PSI-GABA₈, Flu@PSI-GABA₁₈, and Flu@PSI-GABA₂₈ under different pH conditions.

completely decomposed at 250 °C. Also, about Flu@PSI-GABA₈, Flu@PSI-GABA₁₈, and Flu@PSI-GABA₂₈, their decomposition temperature was increased, starting from 270 °C and decomposing completely at 340 °C. At 270 °C, the unmodified intact five-membered ring started to break and the carboxyl group was decomposed to generate CO₂, losing about 58% of its mass. The amide bond generated by the modified GABA began to break at 320 °C, with a mass loss of about 20%. Thus, it can be seen that the thermal stability of Flu was significantly improved by PSI-GABA nanocarriers. The hydrated particle sizes of PSI-GABA₈, PSI-GABA₁₈, PSI-GABA₂₈, Flu@PSI-GABA₈, Flu@PSI-GABA₁₈, and Flu@PSI-GABA₂₈ were 142, 164, 190, 448, 461, and 478 nm, respectively (Figure 1F). In Figure 1G–I, the morphology of PSI-GABA₈, PSI-GABA₁₈, and PSI-GABA₂₈ was observed by TEM. The average size of the spherical PSI-GABA nanoparticles was about 160 nm. The nanoparticles were cross-linked because the multiple carboxyl groups were present in the polymer-branched chains of the nanocarriers. Therefore, they were linked together due to hydrogen bonding, as shown in Figure 1O. Spherical Flu@PSI-GABA nanoparticles with an average of about 350 nm are shown in Figure 4J–L. In Figure 1M, the center of a Flu@PSI-GABA nanoparticle showed a

clear dark dot, which was marked with a red circle, and the distribution of the fluorine element in the center of the nanoparticle was observed by EDS, which stated that the dark dot stood for Flu. Thus, Flu was encapsulated in the center by PSI-GABA, and it could be seen that the Flu@PSI-GABA nanoparticle marked with a yellow circle had a core–shell structure. Additionally, the specific surface area of Flu@PSI-GABA was less than that of PSI-GABA by the BET method (Figure S3), which also proved that Flu was loaded inside the nanocarrier.

pH-Triggered Release and Photodegradation. To study the controlled release behavior of Flu@PSI-GABA, Flu release rates of Flu@PSI-GABA₈, Flu@PSI-GABA₁₈, and Flu@PSI-GABA₂₈ were examined at pH 8.0, 7.0, and 5.0, respectively (Figure 2A–C). The Flu release rate was the fastest at pH 8.0 because Flu@PSI-GABA could decompose under alkaline conditions and the nanocarrier structure collapsed, leading to rapid drug release.³² Under acidic conditions, the hydrogen bonds between the carboxyl groups in the Flu@PSI-GABA nanoparticles were stronger, which made the structure of PSI-GABA nanocarriers more settled, and Flu was difficultly released. Therefore, before Flu@PSI-GABA nanoparticles entered the vascular phloem, the pH

value of the apoplast environment was about 5.0, and Flu was released slowly. Once inside the phloem, where the pH was alkaline (pH 8.0), the Flu@PSI-GABA nanoparticles would start to collapse and the release rate of Flu would be accelerated. To describe the kinetics of the Flu release from the test formulation, mathematical models such as zero-order, Higuchi, and Ritger–Peppas models were used in different pH conditions (Figure 3). The correlation coefficients of the simulation results for Flu@PSI-GABA₈, Flu@PSI-GABA₁₈, and Flu@PSI-GABA₂₈ were higher for all three models at pH 5.0 and 7.0, with the highest correlation coefficients for Ritger–Peppas’s model (Table 1). At pH 8.0, the correlation

Table 1. Release Kinetic Equations under Different pH Conditions

	pH	kinetic model	fitted equation	R ²
Flu@PSI-GABA ₈	5	zero-order	$y = 0.00328x + 0.01005$	0.99493
		Higuchi	$y = 0.01005x^{1/2} + 0.00655$	0.99493
		Ritger–Peppas	$y = 0.0035x^{0.9916}$	0.99341
	7	zero-order	$y = 0.00617x + 0.12345$	0.96216
		Higuchi	$y = 0.12345^{1/2} + 0.01235$	0.96216
		Ritger–Peppas	$y = 0.04521x^{0.61867}$	0.98793
	8	zero-order	$y = 0.00599x + 0.24833$	0.78458
		Higuchi	$y = 0.24833x^{1/2} + 0.01198$	0.78458
		Ritger–Peppas	$y = 0.12074x^{0.43922}$	0.93011
Flu@PSI-GABA ₁₈	5	zero-order	$y = 0.00317x + 0.01673$	0.9895
		Higuchi	$y = 0.03188x^{1/2} + 0.0029$	0.88001
		Ritger–Peppas	$y = 0.00416x^{0.95313}$	0.98365
	7	zero-order	$y = 0.00686x + 0.10614$	0.98438
		Higuchi	$y = 0.0783^{1/2} + 0.00397$	0.96504
		Ritger–Peppas	$y = 0.03857x^{0.66001}$	0.99266
	8	zero-order	$y = 0.00735x + 0.19325$	0.8172
		Higuchi	$y = 0.09556x^{1/2} + 0.00987$	0.93664
		Ritger–Peppas	$y = 0.0953x^{0.50064}$	0.9333
Flu@PSI-GABA ₂₈	5	zero-order	$y = 0.00327x + 0.0132$	0.98141
		Higuchi	$y = 0.03365x^{1/2} + 0.00359$	0.88121
		Ritger–Peppas	$y = 0.00408x^{0.96102}$	0.98869
	7	zero-order	$y = 0.00661x + 0.11427$	0.96785
		Higuchi	$y = 0.07931^{1/2} + 0.00394$	0.9689
		Ritger–Peppas	$y = 0.04298x^{0.63593}$	0.98991
	8	zero-order	$y = 0.00681x + 0.21324$	0.77199
		Higuchi	$y = 0.09477x^{1/2} + 0.01463$	0.91211
		Ritger–Peppas	$y = 0.10508x^{0.47689}$	0.90886

coefficients of three models decreased to different degrees, which was caused by the rapid release of Flu due to the collapse of the nanocarriers in the weakly alkaline environment. Additionally, the antiphotodegradation performance of nanopesticides was simulated by experimental UV lamps, and the anti-UV effects are shown in Figure 2D. After 48 h of UV irradiation, the Flu residual rates of Flu (TC), Flu@PSI-GABA₈, Flu@PSI-GABA₁₈, and Flu@PSI-GABA₂₈ were 21, 45.3, 43.2, and 43%, respectively, and the best UV-resistant effect was observed for Flu@PSI-GABA₈. After the nanocarrier coating, the photolysis resistance of Flu was increased by more

than 20%, which was favorable to prolong the holding period of field application.

Wetting State of Flu@PSI-GABA on Banana Leaves.

As shown in Figure 2E, the contact angles of Flu@PSI-GABA₈, Flu@PSI-GABA₁₈, Flu@PSI-GABA₂₈, and Flu (TC) were 49.4, 70.8, 69.6, and 71.5°, respectively. The three nanocarriers became an amphibious material by the modification of GABA. The banana leaf surface was an oily waxy layer; therefore, Flu@PSI-GABA₈ had a stronger affinity with the banana leaf surface. The structure of Flu@PSI-GABA₈ showed fewer hydrophilic and more hydrophobic functional groups, which gave a good explanation for the smallest contact angle. Flu@PSI-GABA₈ could better improve the contact area and adhesion of the agents with banana leaves through electrostatic and hydrogen bonding because the outer material had some groups such as carboxyl and amino groups.^{38–40}

Phloem Transport of Flu@PSI-GABA in Castor Bean Seedlings.

The castor as a model plant was used to test the phloem transport capacity of Flu@PSI-GABA₈, Flu@PSI-GABA₁₈, Flu@PSI-GABA₂₈, Flu (50% WP), and Flu (TC) (Figure 2F). Among them, the Flu in Flu (TC) treatment groups was not detected in the castor phloem effluent, and it was indicated that Flu (TC) itself did not possess a phloem transport ability. The Flu concentration of castor effluent treated with commercial Flu (50% WP) was 0.1 mg/L, which was because Flu (50% WP) contained a certain amount of surfactant, and it induced certain penetration of Flu. Surprisingly, the Flu concentration arrived at 0.8, 1.2, and 1.6 mg/L in the castor phloem after treatment of Flu@PSI-GABA₈, Flu@PSI-GABA₁₈, and Flu@PSI-GABA₂₈, respectively. The results showed that the Flu concentration of the treated castor effluent was 8–16 times higher than that of commercial Flu (50% WP). Flu@PSI-GABA₂₈ had the most superior phloem transport capacity, and its transport capacity was 16 times higher than that of the previously reported Flu@PGA.³³ The results stated that GABA played an important role in the transport of castor phloem.

In Vitro Fungicidal Activity. The *in vitro* inhibitory activity of Flu@PSI-GABA against banana wilt was investigated by using the mycelial growth rate inhibition method. The loading efficiencies of Flu@PSI-GABA₈, Flu@PSI-GABA₁₈, and Flu@PSI-GABA₂₈ were 6.04, 5.73, and 5.29%, respectively (Figure S4). The bacteriostatic effects of the same concentration of Flu (TC), Flu@PSI-GABA₈, Flu@PSI-GABA₁₈, and Flu@PSI-GABA₂₈ are shown in 4A. As shown in Figure 4B, at the same Flu concentration, the EC₅₀ values of Flu@PSI-GABA₂₈ and Flu (TC) were 0.0116 and 0.1015 mg/L, respectively. Also, the *in vitro* inhibitory activity of Flu@PSI-GABA₈, Flu@PSI-GABA₁₈, and Flu@PSI-GABA₂₈ was increased by 8.4–8.8 times compared with that of Flu (TC) against Foc (Figure 4B and Table S1). The effects of phloem transport and bacteriostatic activity were significantly enhanced for Flu@PSI-GABA₂₈. Therefore, Flu@PSI-GABA₂₈ was selected for the following bacterial inhibition mechanism and banana pot experiments.

Cell Membrane Permeability Test. Altered cell membrane permeability was one of the early signs of cellular damage. The relative conductivity of the mycelium was increased after treatment with Flu@PSI-GABA₈, Flu@PSI-GABA₁₈, and Flu@PSI-GABA₂₈. With the increase in Flu@PSI-GABA₈, Flu@PSI-GABA₁₈, and Flu@PSI-GABA₂₈ concentration, the changes of mycelial cell membrane were more obvious (Figure 4C and Figure S5A,B). It could be inferred

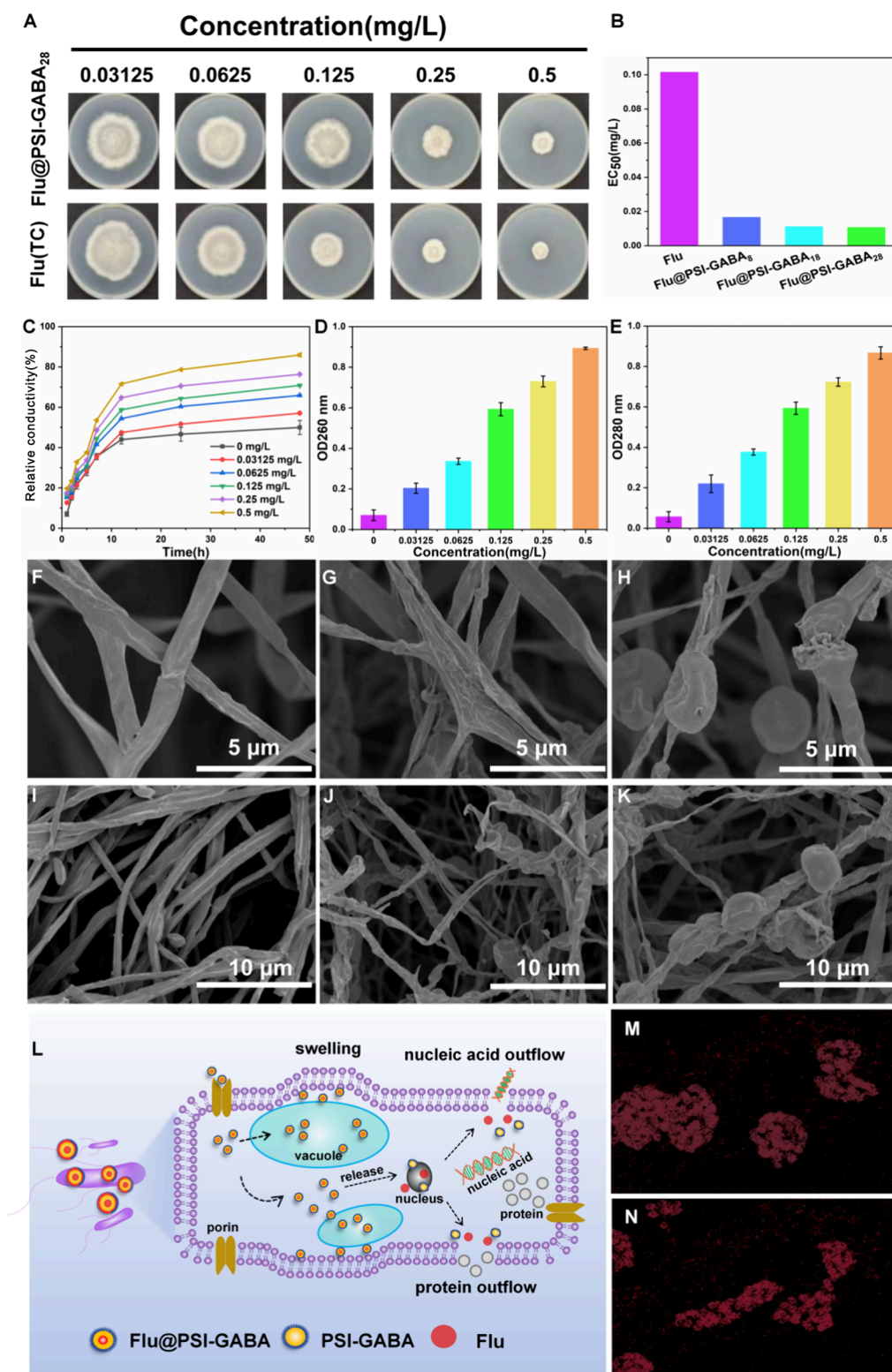


Figure 4. (A) *In vitro* fungicidal activity of Flu (TC) and Flu@PSI-GABA₂₈ for 7 days. (B) *In vitro* inhibitory activity of Flu@PSI-GABA₈, Flu@PSI-GABA₁₈, Flu@PSI-GABA₂₈, and Flu (TC) against *Foc*. Cell permeability (C) and cytoplasmic leakage (D, E) after treatment with different concentrations of Flu@PSI-GABA₂₈. SEM of mycelia of *Foc* treated with nothing (F, I), Flu (TC) (G, J), and Flu@PSI-GABA₂₈ (H, K). The distribution of the fluorine element in the mycelia shown by the EDS of Flu@PSI-GABA₂₈ is shown in panels (M) and (N), corresponding to panels (H) and (K), respectively. (L) Mechanism illustration of efficiency enhancement for Flu@PSI-GABA₂₈.

that Flu@PSI-GABA₈, Flu@PSI-GABA₁₈, and Flu@PSI-GABA₂₈ acted with the cell membrane of the mycelium.^{41,42}

Cell Content Detection. The leakage of intracellular electrolytes, thus disrupting the intracellular environment,

affected mycelial growth and even led to death.⁴³ Cells required regulation of content such as proteins and nucleic acids to maintain normal physiological functions.^{44,45} The effect of Flu@PSI-GABA₈, Flu@PSI-GABA₁₈, and Flu@PSI-

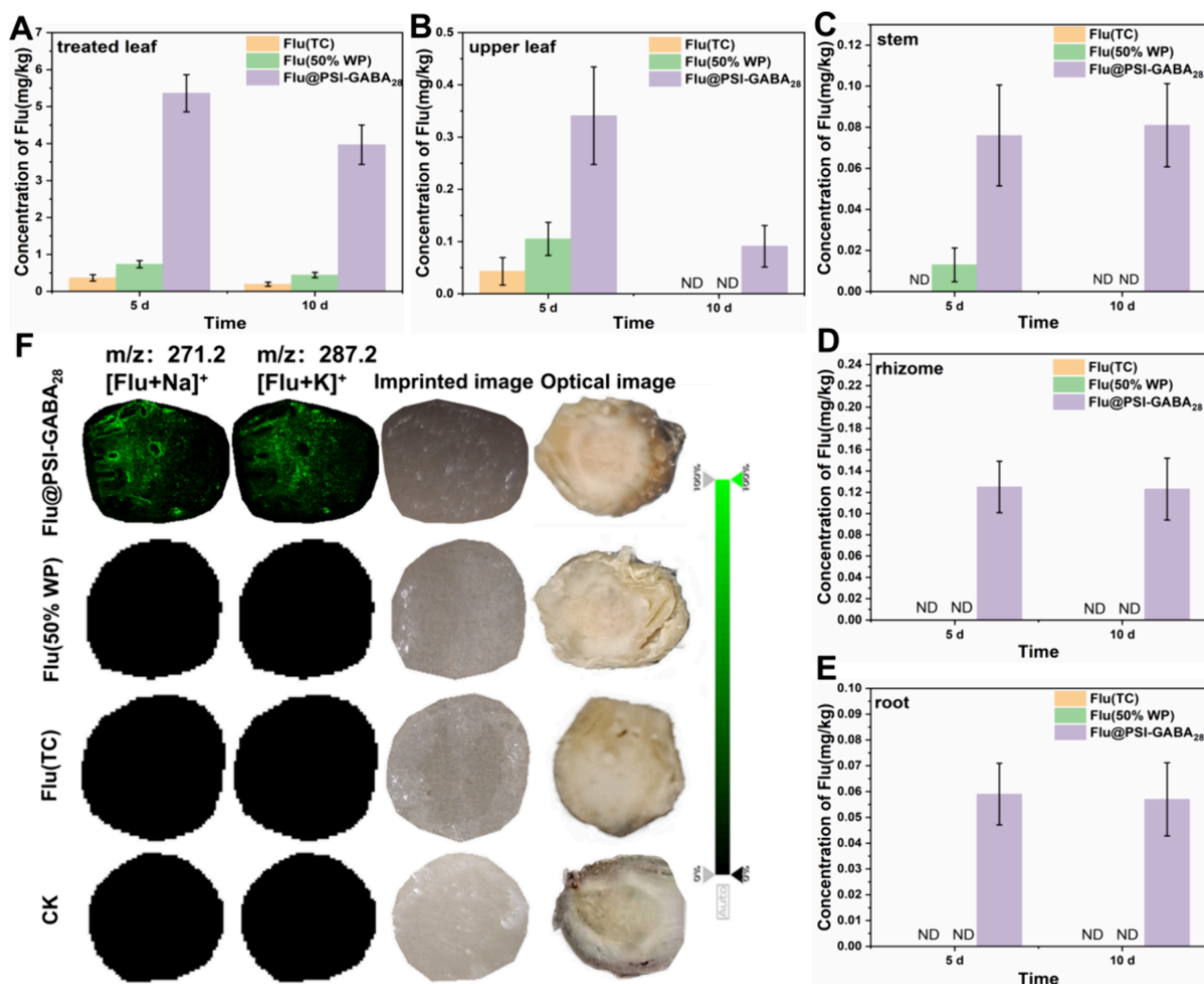


Figure 5. Concentration of Flu absorbed by the treated leaf (A), upper leaf (B), stem (C), rhizome (D), and root (E) of banana seedlings. Mass spectrometry imaging of the banana rhizome parts (F).

GABA₂₈ on mycelial cell contents was evaluated using a UV spectrophotometer at 260 and 280 nm (Figure 4D,E and Figure S5C,D). After treatment with different concentrations of Flu@PSI-GABA₈, Flu@PSI-GABA₁₈, and Flu@PSI-GABA₂₈, the absorbance values at both specific wavelengths were significantly increased. The increase in the absorbance of the blank-treated group was produced by the normal metabolism of the mycelium and destruction of the cell membrane, which seriously affected the normal growth of the mycelium. After the cell membrane was destroyed, intracellular proteins and nucleic acids flowed out, and thus, the contents were released, leading to an absorbance increase.

SEM of the Mycelial Surface. Changes in the mycelial surface of different treatment groups were observed by SEM. The mycelium without special treatment is shown in Figure 4F,I. The surface of the mycelium was complete and full. After the Flu (TC) treatment, the mycelium showed obvious withering, breakage, and abnormal growth in Figure 4G,J. It suggested that Flu had an inhibitory effect on the growth of the mycelium, which could destroy the outer membrane when contacting with the surface of the mycelium. Flu inhibited

normal physiological activities in the mycelium, which led to mycelium atrophy and necrosis.

As could be seen in Figure 3H,K, the surface of the Flu@PSI-GABA₂₈-treated mycelium appeared swollen and broken. Detecting Figure 4H,K by EDS, the red area was the distribution of the F element, representing Flu agglomeration (Figure 4M,N). It was clear that Flu@PSI-GABA₂₈ was concentrated in the enlarged area and caused the mycelium to rupture. This stated that Flu@PSI-GABA₂₈ was able to enter the interior of mycelial cells and induced the enlargement of cellular vesicles and then disrupted the cellular membrane. Finally, the nanoparticles caused the leakage loss of proteins and nucleic acids, which ultimately accelerated the death of the fungus (Figure 4L).

Long-Distance Translocation of Flu@PSI-GABA₂₈ in Banana Plants. Flu content was detected in all parts of banana seedlings after the 5th and 10th days of Flu (50% WP), Flu (TC), and Flu@PSI-GABA₂₈ by foliar application. As shown in Figure 5A–E, only a small amount of Flu was detected in the upper leaves (0.105 and 0.043 mg/kg) and stems (0.008 and 0 mg/kg) of banana after 5 days by the application of Flu (50% WP) and Flu (TC), respectively. This

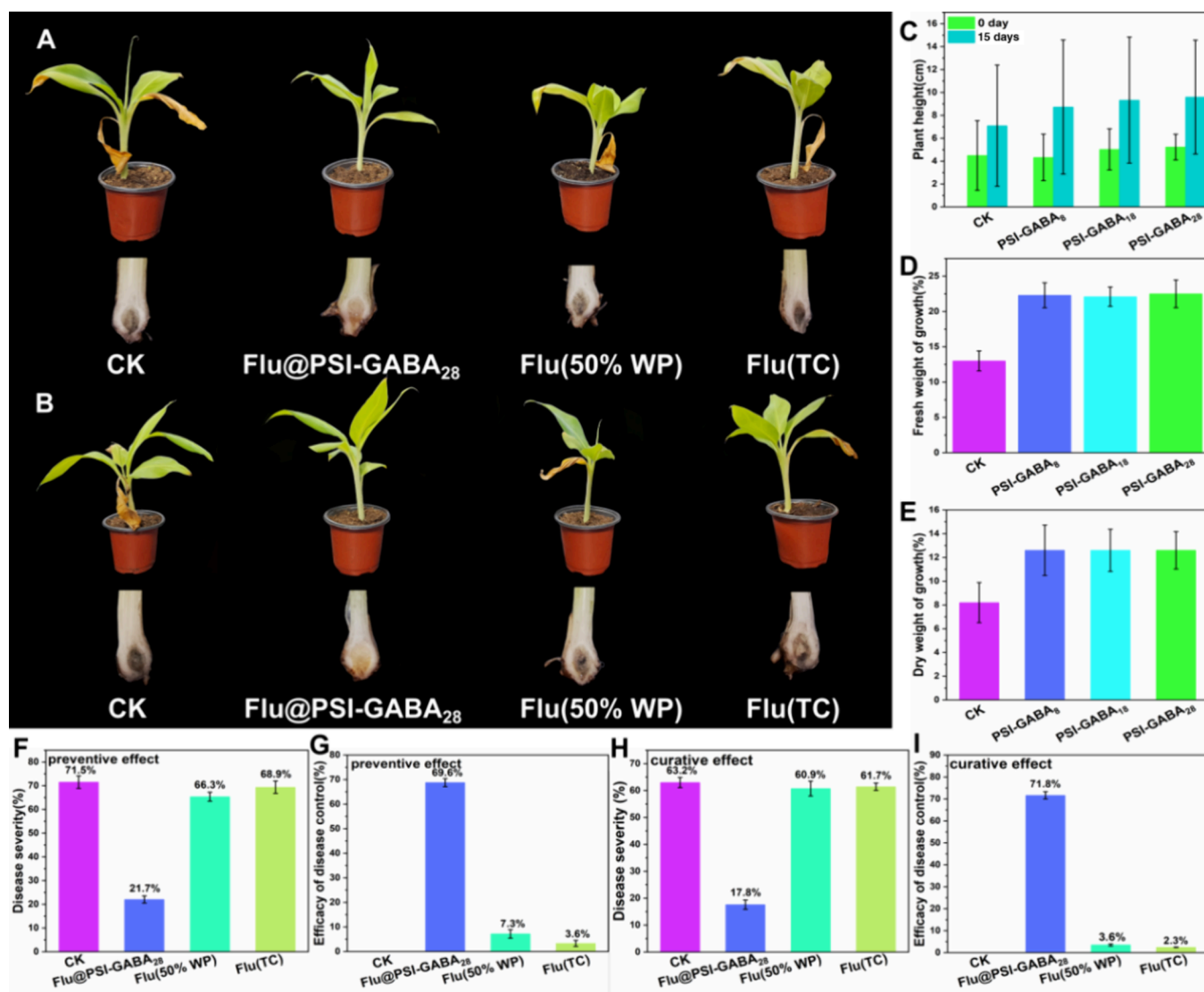


Figure 6. Effectiveness of Flu@PSI-GABA₂₈ in preventing (A–G) and curing (B–I) Foc in pot plants. Changes in plant height (C) and physiological indices (D, E) after 15 days of PSI-GABA₂₈ treatment.

indicated that the upper leaf uptake of Flu could be followed by a certain amount of transport upward through the xylem, and it was not capable of long-distance transport to other parts of the plant through the phloem. However, after application of Flu@PSI-GABA₂₈, Flu could be detected in all parts of the banana plant within 5 and 10 days, including the upper leaves and underground parts of the plant. Moreover, the Flu concentration in the rhizome reached a maximum value of 0.123 mg/kg on the 5th day (Figure 5F). After 10 days of banana leaf treatment with Flu@PSI-GABA₂₈, Flu concentrations of 0.091, 0.081, and 0.057 mg/kg were detected in upper leaves, stems, and roots, respectively (Figure 5B,C,E). However, no Flu was detected at the same sites in the Flu (50% WP) or Flu (TC) treatment groups. This suggested that Flu could achieve long-distance transport through PSI-GABA₂₈ nanocarriers. Improving the transport efficiency from the leaf to the ground was an important method to assess the effectiveness of root wilt control. Although the same doses of Flu@PSI-GABA₂₈, Flu (TC), and Flu (50% WP) were applied to the banana leaves, Flu dosage was significantly higher than that of the conventional preparation group at 5 and 10 days by PSI-GABA₂₈ nanocarrier delivery (Figure 5A). The above

result indicated that PSI-GABA₂₈ nanocarriers could significantly increase the transport efficiency of Flu in banana plants, which was expected to improve the control level of vascular tissue diseases.

Mass Spectrometry Imaging (MSI) of Flu in Banana Rhizome. MSI has emerged as label-free for spatiotemporal distribution information and simultaneous capturing of chemical recognition.⁴⁶ Therefore, it was possible to demonstrate whether unmodified Flu could be transported for long distances through the leaf to the rhizome site using the MSI method. In the experiment, the bulbous parts of banana seedlings in the four treatment groups of blank, Flu (TC), Flu (50% WP), and Flu@PSI-GABA₂₈ were sliced and imaged. Meanwhile, Flu could be detected as the ion form of [Flu + Na]⁺ and [Flu + K]⁺ in positive ion mode with highly reduced background ions. Interestingly, the Flu analyte could be clearly detected with a high signal-to-noise ratio (S/N) using Flu@PSI-GABA₂₈ by foliar application, whereas the Flu signal could not be detected for Flu (50% WP) and Flu (TC) treatment groups under the same laser energy (Figure 5F). Additionally, the location of Flu in the rhizomes for Flu@PSI-GABA₂₈-treated banana seedlings was more uniformly distributed rather

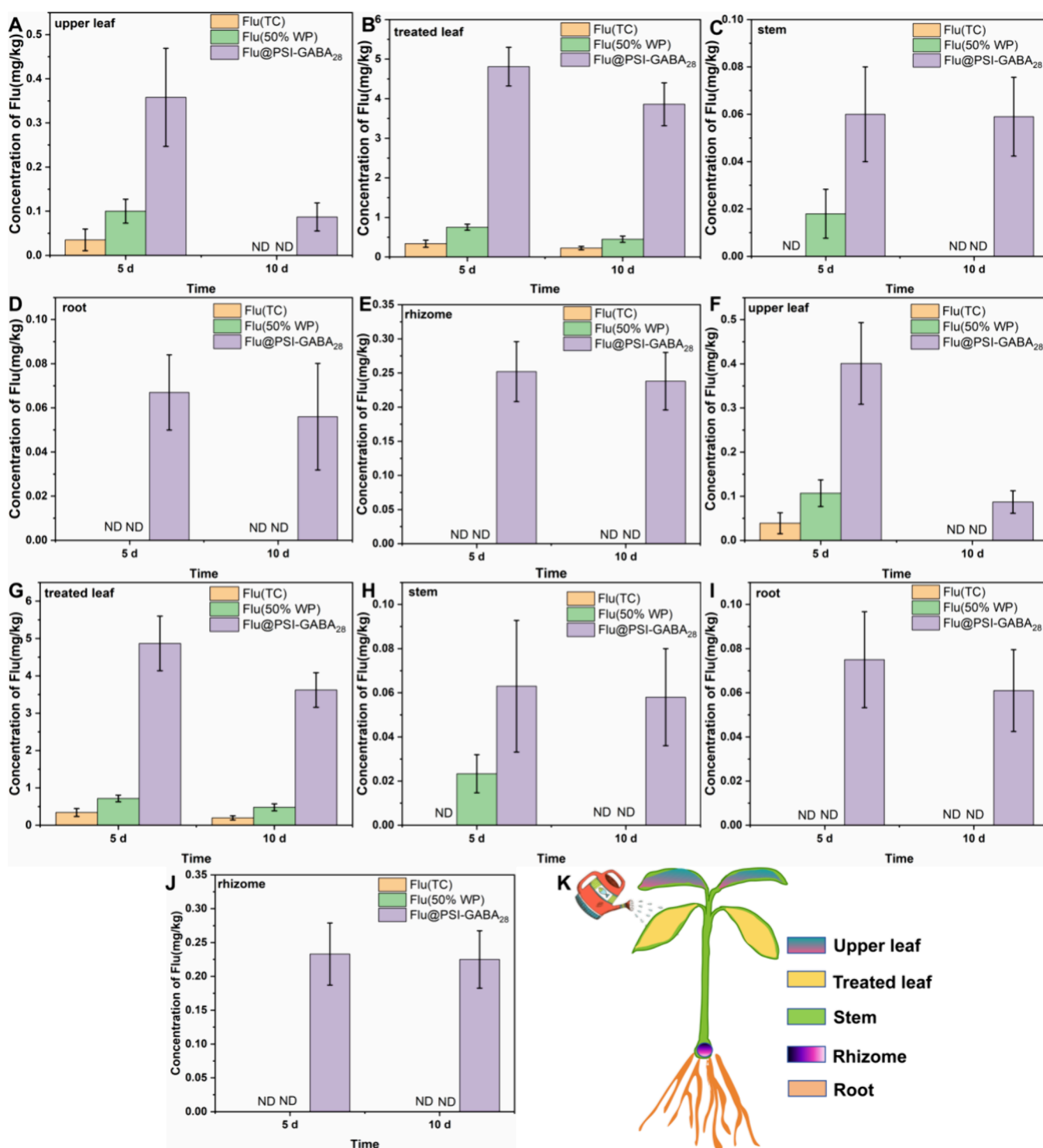


Figure 7. Flu concentration in each site in the preventive experiments (A–E) and curative experiment (F–J). Diagrammatic representation of the different parts of banana seedlings (K).

than being concentrated in the center or outer rim of the rhizome. All results illustrate that Flu@PSI-GABA₂₈ can be actively transported from leaves to banana rhizome through the phloem of vascular tissues.

In Vivo Control Effect of Flu@PSI-GABA on Foc. In pot experiments, compared with the control and the conventional 50% WP treatments, the Flu@PSI-GABA₂₈ treatment was notably more effective in reducing the disease severity of Foc after 50 days of inoculation (Figure 6A,B). The leaves of the

control, Flu (TC), and Flu (50% WP) treatment groups showed obvious symptoms of the disease, with the lower leaves wilting and the middle and upper leaves turning yellow. Cutting the rhizomes of the plant showed that the control, Flu (TC), and Flu (50% WP) treatment groups had large black-brown lesions, which were indicative of severe Foc infections. Surprisingly, only small areas of discoloration were present in the Flu@PSI-GABA₂₈-treated plantlets. The preventive and curative effects were evaluated through the disease index

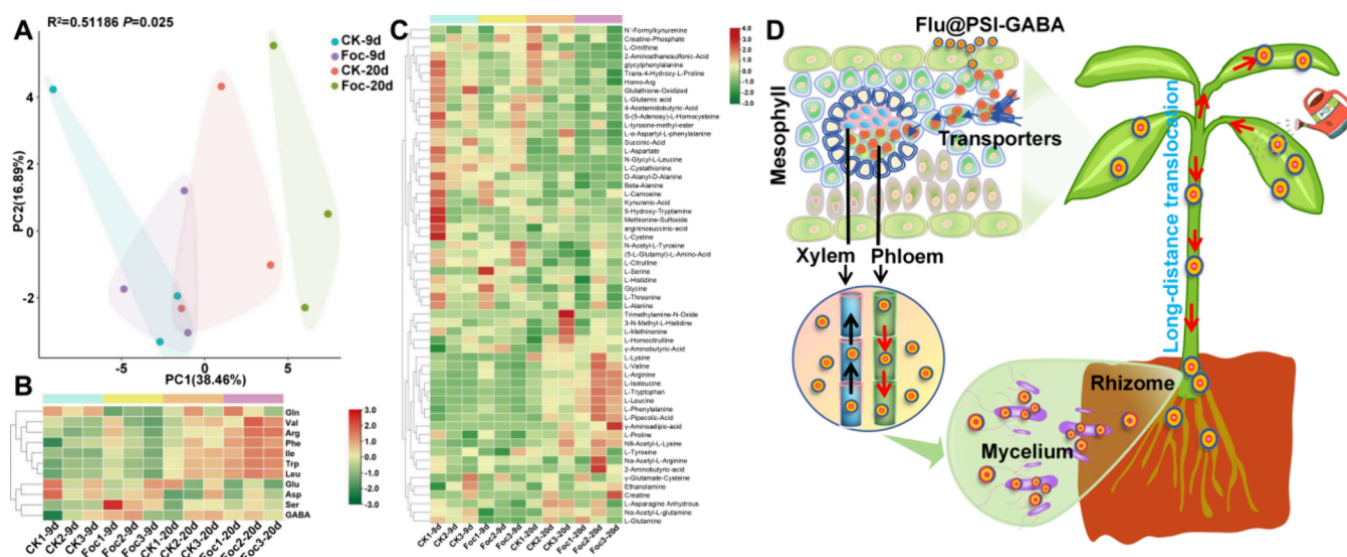


Figure 8. (A) Ellipses correspond to Gaussian distributions fitted to each cluster (95% confidence interval). (B) Expression patterns of amino acids and their metabolites in banana corm before and after Foc treatment. (C) Expression patterns of partial amino acids and their metabolites in banana rhizomes before and after Foc treatment. (D) Schematic diagram of banana phloem transport for Flu@PSI-GABA₂₈ by foliar application.

(Figure 6F,H and Tables S2 and S3). In Figure 6G, the preventive effects of Flu@PSI-GABA₂₈, Flu (TC), and Flu (50% WP) were 69.6, 3.3, and 7.1%, respectively. In addition, the curative effect of 71.6% was recorded for the Flu@PSI-GABA₂₈-treated plants, which was about 20 times that observed for the conventional Flu (50% WP)-treated plants (Figure 6I). At the same time, the control effect of 71.6% on banana seedlings was higher for Flu@PSI-GABA₂₈ than that of 50.4% previously reported for Flu@PGA nanoparticles.³³ The Flu concentrations in each site in the preventive and curative experiments are shown in Figure 7. Among others, treating with Flu@PSI-GABA₂₈, the rhizome of diseased banana seedlings had higher Flu content compared to healthy banana seedlings (Figures 5D and 7E,J). It was widely known that none of the systemic fungicides had shown low effects on banana Fusarium wilt in the field by foliar spray application. Thus, the results indicated that the PSI-GABA₂₈ nanocarriers provided a promising chemical control method against banana wilt.

Safety Evaluation of PSI-GABA Nanoparticles. To verify the effect of nanocarriers on the growth of banana seedlings, physiological indices of the treated and blank groups were tested after 15 days. Compared with the control group, the average plant height increased by 20.2% and fresh and dry weights increased by 10.1 and 4.3%, respectively (Figure 6C–E). The nanocarriers might be degraded to aspartic acid in the plant phloem,^{47,48} together with GABA that acted on plant growth.⁴⁹ Therefore, GABA nanocarriers had some positive effects on the growth of the banana seedlings.

Principal Component Analysis. To verify whether GABA accumulated in banana rhizomes after the onset of the disease, we analyzed the differences in the amino acid content of banana seedlings before and after disease. Changes of amino acid content in the rhizomes of healthy and diseased banana seedlings were detected by metabolomic approaches on the 9th and 20th days, respectively. As could be seen from Figure 8A, the distribution of the results of each experimental group had a high degree of intragroup reproducibility. Except for the results on the 20th day of diseased banana seedlings, the distribution

areas for the other experimental groups overlapped partially. This indicated that the amino acid content of the rhizomes did not change much when banana seedlings were infected for 9 days compared with healthy seedlings. At 20 days of infection, the amino acid content of the banana rhizomes was changed significantly. In Figure 8B,C, the content of GABA in the rhizomes increased after the infection of banana seedlings. This was caused by the self-defense of banana seedlings when they were stressed by the pathogen, and then GABA could be transported to banana rhizomes by transporter proteins. Therefore, PSI-GABA₂₈ nanocarriers may be transported using the GABA group to deliver Flu into infested rhizomes through the phloem of vascular tissues (Figure 8D), which can realize targeted control of banana wilt disease.

In summary, core-shell Flu@PSI-GABA₂₈ nanoparticles with long-distance transport were successfully constructed. In this process, PSI-GABA nanocarriers could deliver and release Flu in the environment of the banana phloem by foliar application. Flu@PSI-GABA₈, Flu@PSI-GABA₁₈, and Flu@PSI-GABA₂₈ increased the *in vitro* antifungal efficacy against the pathogen by 8.4–8.8 times compared with Flu (TC). Especially, the effects of prevention and control were significantly enhanced for Flu@PSI-GABA₂₈. In addition, Flu@PSI-GABA₂₈ nanoparticles were able to accumulate toward the rhizome at the onset of banana disease, which realized the targeted long-distance transport of Flu and improved the utilization of pesticides. The nanocarriers also promoted the growth and development of banana seedlings for a short period of time, but the long-term impact of plants required further studies to prove its environment safety. Nonetheless, these results could provide a good idea for designing smart pesticide formulations for controlling vascular or soil-borne pathogens in sustainable agriculture.

■ ASSOCIATED CONTENT

Supporting Information

The Supporting Information is available free of charge at <https://pubs.acs.org/doi/10.1021/acs.jafc.4c07549>.

Characterization of PSI-GABA and Flu@PSI-GABA, including ^1H NMR spectra, BET curves, TG, and DTG curves; loading efficiency of Flu@PSI-GABA; cell permeability and content release of Flu@PSI-GABA (PDF)

AUTHOR INFORMATION

Corresponding Authors

Hanhong Xu – National Key Laboratory of Green Pesticide, South China Agricultural University, Guangzhou 510642, P. R. China; Email: hbxu@scau.edu.cn

Jinliang Jia – National Key Laboratory of Green Pesticide and Key Laboratory for Biobased Materials and Energy of Ministry of Education, College of Materials and Energy, South China Agricultural University, Guangzhou 510642, P. R. China; orcid.org/0000-0002-6974-904X; Email: jiajinliang@scau.edu.cn

Authors

Liangheng He – National Key Laboratory of Green Pesticide and Key Laboratory for Biobased Materials and Energy of Ministry of Education, College of Materials and Energy, South China Agricultural University, Guangzhou 510642, P. R. China

Chunxia Xiao – National Key Laboratory of Green Pesticide, South China Agricultural University, Guangzhou 510642, P. R. China

Li Zhu – National Key Laboratory of Green Pesticide and Key Laboratory for Biobased Materials and Energy of Ministry of Education, College of Materials and Energy, South China Agricultural University, Guangzhou 510642, P. R. China

Wenjie Deng – National Key Laboratory of Green Pesticide and Key Laboratory for Biobased Materials and Energy of Ministry of Education, College of Materials and Energy, South China Agricultural University, Guangzhou 510642, P. R. China

Yanheng Zhang – National Key Laboratory of Green Pesticide and Key Laboratory for Biobased Materials and Energy of Ministry of Education, College of Materials and Energy, South China Agricultural University, Guangzhou 510642, P. R. China

Yang Li – Key Laboratory for Biobased Materials and Energy of Ministry of Education, College of Materials and Energy, South China Agricultural University, Guangzhou 510642, P. R. China

Xinzhou Wu – National Key Laboratory of Green Pesticide, South China Agricultural University, Guangzhou 510642, P. R. China; orcid.org/0000-0001-5079-4994

Hanxiang Wu – State Key Laboratory for Biology of Plant Disease and Insect Pests, Institute of Plant Protection, Chinese Academy of Agricultural Sciences, Beijing 100193, P. R. China

Complete contact information is available at:

<https://pubs.acs.org/10.1021/acs.jafc.4c07549>

Notes

The authors declare no competing financial interest.

ACKNOWLEDGMENTS

This work was supported by the Guangdong Provincial Key Research and Development Program (2023B0202080001), Guangdong Basic and Applied Basic Research Foundation

(2023A1515010609), and Research Fund of National Key Laboratory of Green Pesticide (GPLSCAU202407).

REFERENCES

- (1) Staver, C.; Pems, D. E.; Scheerer, L.; Perez, V. L.; Dita, M. Ex ante assessment of returns on research investments to address the impact of Fusarium wilt tropical race 4 on global banana production. *Front. Plant Sci.* **2020**, *11*, 844.
- (2) Blomme, G.; Dita, M.; Jacobsen, K. S.; Pérez Vicente, L.; Molina, A.; Ocimati, W.; Poussier, S.; Prior, P. Bacterial diseases of bananas and enset: current state of knowledge and integrated approaches toward sustainable management. *Front. Plant Sci.* **2017**, *8*, No. 1290.
- (3) Ploetz, R. C. Fusarium wilt of banana. *Phytopathology* **2015**, *105*, 1512–1521.
- (4) Ismail, A. A.; Ahmad, K.; Siddique, Y.; Wahab, M. A. A.; Kutawa, A. B.; Abdullahi, A.; Zobir, S. A. M.; Abdu, A.; Abdullah, S. N. A. Fusarium wilt of banana: current update and sustainable disease control using classical and essential oils approaches. *Hortic. Plant J.* **2023**, *9*, 1–28.
- (5) Zheng, S.; Hu, H.; Li, Y.; Chen, J.; Li, X.; Bai, T. Editorial: microbial interaction with banana: mechanisms, symbiosis, and integrated diseases control. *Front. Microbiol.* **2024**, *15*, No. 1390969.
- (6) Geberewold, A. Z.; Yildiz, F. Review on impact of banana bacterial wilt (*Xanthomonas campestris* pv. *Musacerum*) in east and central africa. *Cogent Food Agr.* **2019**, *5*, 1586075.
- (7) Tripathi, J. N.; Ntui, V. O.; Tripathi, L. Precision genetics tools for genetic improvement of banana. *Plant Genome* **2023**, *17*, No. e20416.
- (8) Zou, N.; Zhou, D.; Chen, Y.; Lin, P.; Chen, Y.; Wang, W.; Xie, J.; Wang, M. A novel antifungal actinomycete *streptomyces* sp. Strain H3–2 effectively controls banana Fusarium wilt. *Front. Microbiol.* **2021**, *12*, No. 706647.
- (9) Bubici, G.; Kaushal, M.; Prigigallo, M. I.; Gómez-Lama Cabanás, C.; Mercado-Blanco, J. Corrigendum: biological control agents against Fusarium wilt of banana. *Front. Microbiol.* **2019**, *10*, No. 1290.
- (10) Belgrove, A.; Steinberg, C.; Viljoen, A. Evaluation of nonpathogenic Fusarium oxysporum and pseudomonas fluorescens for banana disease control. *Plant Dis.* **2011**, *95*, 951–959.
- (11) Hong, S.; Jv, H.; Lu, M.; Wang, B.; Zhao, Y.; Ruan, Y. Significant decline in banana fusarium wilt disease is associated with soil microbiome reconstruction under chilli pepper-banana rotation. *Eur. J. Soil. Biol.* **2020**, *97*, No. 103154.
- (12) Shen, Z.; Ruan, Y.; Xue, C.; Zhong, S.; Li, R.; Shen, Q. Soils naturally suppressive to banana Fusarium wilt disease harbor unique bacterial communities. *Plant Soil* **2015**, *393*, 21–33.
- (13) Shen, Z.; Ruan, Y.; Wang, B.; Zhong, S.; Su, L.; Li, R.; Shen, Q. Effect of biofertilizer for suppressing Fusarium wilt disease of banana as well as enhancing microbial and chemical properties of soil under greenhouse trial. *Appl. Soil Ecol.* **2015**, *93*, 111–119.
- (14) Li, C.; Chen, S.; Zuo, C.; Sun, Q.; Ye, Q.; Yi, G.; Huang, B. The use of GFP-transformed isolates to study infection of banana with *Fusarium oxysporum* f. sp. *cubense* race 4. *Eur. J. Plant Pathol.* **2011**, *131*, 327–340.
- (15) Li, C.; Yang, J.; Li, W.; Sun, J.; Peng, M. Direct root penetration and rhizome vascular colonization by *Fusarium oxysporum* f. sp. *cubense* are the key steps in the successful infection of brazil cavendish. *Plant Dis.* **2017**, *101*, 2073–2078.
- (16) Liao, T.; Chen, Y.; Tsai, J.; Chao, C.; Huang, T.; Hong, C.; Wu, Z.; Tsai, I. J.; Lee, H.; Klopfenstein, N. B.; Kim, M.; Stewart, J. E.; Atibalentja, N.; Brooks, F. E.; Cannon, P. G.; Farid, A. M.; Hattori, T.; Kwan, H.; Ching Lam, R. Y.; Ota, Y.; Sahashi, N.; Schlub, R. L.; Shuey, L. S.; Tang, A. M. C.; Chung, C. Translocation of fungicides and their efficacy in controlling phellinus noxius, the cause of brown root rot disease. *Plant Dis.* **2023**, *107*, 2039–2053.
- (17) Lehocski-Krsjak, S.; Varga, M.; Szabó-Hevér, Á.; Mesterházy, Á. Translocation and degradation of tebuconazole and prothioconazole in wheat following fungicide treatment at flowering. *Pest Manag. Sci.* **2013**, *69*, 1216–1224.

- (18) Brandhorst, T. T.; Klein, B. S. Uncertainty surrounding the mechanism and safety of the post-harvest fungicide fludioxonil. *Food Chem. Toxicol.* **2019**, *123*, 561–565.
- (19) Zhang, J. The potential of a new fungicide fludioxonil for stem-end rot and green mold control on florida citrus fruit. *Postharvest Biol. Technol.* **2007**, *46*, 262–270.
- (20) Li, X.; He, L.; Pang, X.; Gao, Y.; Liu, Y.; Zhang, P.; Wei, G.; Mu, W.; Li, B.; Liu, F. Tank-mixing adjuvants enhanced the efficacy of fludioxonil on cucumber anthracnose by ameliorating the penetration ability of active ingredients on target interface. *Colloid Surf. B-Biointerfaces* **2021**, *204*, No. 111804.
- (21) Chen, Y. W.; Luo, S. Y.; Xin, H. W.; Xiong, Z.; Liu, S. M.; Zheng, W.; Xu, J. Q. Effect of fludioxonil on morphological characteristics of *Fusarium pseudograminearum* and wheat crown rot control. *Phytoparasitica* **2024**, *52*, 34.
- (22) Errampalli, D.; Northover, J.; Skog, L.; Brubacher, N. R.; Collucci, C. A. Control of blue mold (*Penicillium expansum*) by fludioxonil in apples (cv Empire) under controlled atmosphere and cold storage conditions. *Pest Manag. Sci.* **2005**, *61*, 591–596.
- (23) Xu, Z.; Tang, T.; Lin, Q.; Yu, J.; Zhang, C.; Zhao, X.; Kah, M.; Li, L. Environmental risks and the potential benefits of nanopesticides: a review. *Environ. Chem. Lett.* **2022**, *20*, 2097–2108.
- (24) Chen, H.; Yang, L.; Wu, P.; Liu, P.; Xu, H.; Zhang, Z. Combined application of surfactants and iron-based metal-organic framework nanoparticles for targeted delivery of insecticides. *Chem. Eng. J.* **2024**, *488*, No. 151193.
- (25) Liang, W.; Cheng, J.; Zhang, J.; Xiong, Q.; Jin, M.; Zhao, J. pH-responsive on-demand alkaloids release from core-shell ZnO@ZIF-8 nanosphere for synergistic control of bacterial wilt disease. *ACS Nano* **2022**, *16*, 2762–2773.
- (26) Tegeder, M. Transporters for amino acids in plant cells: some functions and many unknowns. *Curr. Opin. Plant Biol.* **2012**, *15*, 315–321.
- (27) Li, L.; Dou, N.; Zhang, H.; Wu, C. The versatile gaba in plants. *Plant Signal. Behav.* **2021**, *16*, 1862565.
- (28) Ramesh, S. A.; Tyerman, S. D.; Gilliam, M.; Xu, B. γ -aminobutyric acid (GABA) signalling in plants. *Cell. Mol. Life Sci.* **2017**, *74*, 1577–1603.
- (29) Seifkhalhor, M.; Aliniaieifard, S.; Hassani, B.; Niknam, V.; Lastochkina, O. Diverse role of gamma-aminobutyric acid in dynamic plant cell responses. *Plant Cell Rep.* **2019**, *38*, 847–867.
- (30) Kim, N. H.; Kim, B. S.; Hwang, B. K. Pepper arginine decarboxylase is required for polyamine and γ -aminobutyric acid signaling in cell death and defense response. *Plant Physiol.* **2013**, *162*, 2067–2083.
- (31) Dabravolski, S. A.; Isayenkov, S. V. The role of the γ -aminobutyric acid (GABA) in plant salt stress tolerance. *Horticulturae* **2023**, *9*, 230.
- (32) Ye, X.; Liu, M.; Zhao, N.; Xiao, C.; Xu, H.; Jia, J. Targeted delivery of emamectin benzoate by functionalized polysuccinimide nanoparticles for the flowering cabbage and controlling *plutella xylostella*. *Pest Manag. Sci.* **2022**, *78*, 758–769.
- (33) Wu, H.; Hu, P.; Xu, Y.; Xiao, C.; Chen, Z.; Liu, X.; Jia, J.; Xu, H. Phloem delivery of fludioxonil by plant amino acid transporter-mediated polysuccinimide nanocarriers for controlling *Fusarium* wilt in banana. *J. Agric. Food Chem.* **2021**, *69*, 2668–2678.
- (34) Huang, Y. H.; Wang, R. C.; Li, C. H.; Zuo, C. W.; Wei, Y. R.; Zhang, L.; Yi, G. J. Control of *Fusarium* wilt in banana with chinese leek. *Eur. J. Plant Pathol.* **2012**, *134*, 87–95.
- (35) Chen, J.; Xu, L.; Han, J.; Su, M.; Wu, Q. Synthesis of modified polyaspartic acid and evaluation of its scale inhibition and dispersion capacity. *Desalination* **2015**, *358*, 42–48.
- (36) Yeh, J.; Yang, H.; Hsu, Y.; Su, C.; Lee, T.; Lou, S. Synthesis and characteristics of biodegradable and temperature responsive polymeric micelles based on poly(aspartic acid)-g-poly(n-isopropylacrylamide-co-n,n-dimethylacrylamide). *Colloid Surf. A-Physicochem. Eng. Asp.* **2013**, *421*, 1–8.
- (37) Migahed, M. A.; Rashwan, S. M.; Kamel, M. M.; Habib, R. E. Synthesis, characterization of polyaspartic acid-glycine adduct and evaluation of their performance as scale and corrosion inhibitor in desalination water plants. *J. Mol. Liq.* **2016**, *224*, 849–858.
- (38) He, L.; Xi, S.; Ding, L.; Li, B.; Mu, W.; Li, P.; Liu, F. Regulating the entire journey of pesticide application on surfaces of hydrophobic leaves modified by pathogens at different growth stages. *ACS Nano* **2022**, *16*, 1318–1331.
- (39) Zhang, Y.; Fu, L.; Li, S.; Yan, J.; Sun, M.; Giraldo, J. P.; Matyjaszewski, K.; Tilton, R. D.; Lowry, G. V. Star polymer size, charge content, and hydrophobicity affect their leaf uptake and translocation in plants. *Environ. Sci. Technol.* **2021**, *55*, 10758–10768.
- (40) Xu, C.; Cao, L.; Cao, C.; Chen, H.; Zhang, H.; Li, Y.; Huang, Q. Fungicide itself as a trigger to facilely construct hymexazol-encapsulated polysaccharide supramolecular hydrogels with controllable rheological properties and reduced environmental risks. *Chem. Eng. J.* **2023**, *452*, No. 139195.
- (41) Hammoudi Halat, D.; Younes, S.; Mourad, N.; Rahal, M. Allylamines, benzylamines, and fungal cell permeability: a review of mechanistic effects and usefulness against fungal pathogens. *Membranes* **2022**, *12*, 1171.
- (42) De Oliveira, H. C.; Rossi, S. A.; García-Barbazán, I.; Zaragoza, Ó.; Trevijano-Contador, N. Cell wall integrity pathway involved in morphogenesis, virulence and antifungal susceptibility in *cryptococcus neoformans*. *J. Fungi* **2021**, *7*, 831.
- (43) Somero, G. N. The cellular stress response and temperature: function, regulation, and evolution. *J. Exp. Zool. Part. A-Ecol. Integr. Physiol.* **2020**, *333*, 379–397.
- (44) Jeppesen, D. K.; Zhang, Q.; Franklin, J. L.; Coffey, R. J. Extracellular vesicles and nanoparticles: emerging complexities. *Trends Cell Biol.* **2023**, *33*, 667–681.
- (45) Yates, A. G.; Pink, R. C.; Erdbrügger, U.; Siljander, P. R. M.; Dellar, E. R.; Pantazi, P.; Akbar, N.; Cooke, W. R.; Vatsish, M.; Dias Neto, E.; Anthony, D. C.; Couch, Y. In sickness and in health: the functional role of extracellular vesicles in physiology and pathology *in vivo*. *J. Extracell. Vesicles* **2022**, *11*, No. e12151.
- (46) Wu, X.; Qin, R.; Wu, H.; Yao, G.; Zhang, Y.; Li, P.; Xu, Y.; Zhang, Z.; Yin, Z.; Xu, H. Nanoparticle-immersed paper imprinting mass spectrometry imaging reveals uptake and translocation mechanism of pesticides in plants. *Nano Res.* **2020**, *13*, 611–620.
- (47) Molnar, K.; Voniatis, C.; Feher, D.; Szabo, G.; Varga, R.; Reiniger, L.; Juriga, D.; Kiss, Z.; Krisch, E.; Weber, G.; Ferencz, A.; Varga, G.; Zrinyi, M.; Nagy, K. S.; Jedlovsky-Hajdu, A. Poly(amino acid) based fibrous membranes with tuneable *in vivo* biodegradation. *PLoS One* **2021**, *16*, No. e0254843.
- (48) Lavoignat, M.; Cassan, C.; Petriacq, P.; Gibon, Y.; Heumez, E.; Duque, C.; Momont, P.; Rincet, R.; Blancon, J.; Ravel, C.; Le Gouis, J. Different wheat loci are associated to heritable free asparagine content in grain grown under different water and nitrogen availability. *Theor. Appl. Genet.* **2024**, *137*, 46.
- (49) Alsmairat, N.; Engelgau, P.; Beaudry, R. Changes in free amino acid content in the flesh and peel of “cavendish” banana fruit as related to branched-chain ester production, ripening, and senescence. *J. Am. Soc. Hortic. Sci.* **2018**, *143*, 370–380.



Optimized nanopesticide delivery of thiamethoxam to cowpeas (*Vigna unguiculata*) controls thrips (*Megalurothrips usitatus*) and reduces toxicity to non-target worker bees (*Apis mellifera*)

Wenjie Deng^{a,b}, Yanheng Zhang^{a,b}, Liangheng He^{a,b}, Li Xu^b, Xulang Ye^a, Hanhong Xu^a, Li Zhu^{a,b,*}, Jinliang Jia^{a,b,*}

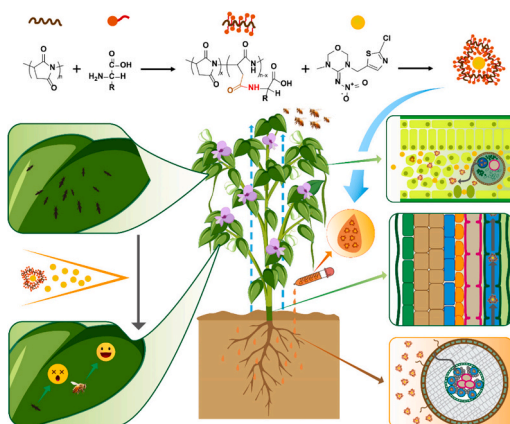
^a National Key Laboratory of Green Pesticide, South China Agricultural University, Guangzhou 510642, China

^b Key Laboratory for Biobased Materials and Energy of Ministry of Education, College of Materials and Energy, South China Agricultural University, Guangzhou 510642, China

HIGHLIGHTS

- Pesticide delivery system of amino acid-functionalized polymers was constructed for high foliar transport.
- PSI-GLU nanocarrier increased the thiamethoxam content in the leaves of cowpea plants by 2.3 times.
- Compared with thiamethoxam, the LC₅₀ of THX@PSI-GLU for thrips was reduced by nearly 32 %.
- THX@PSI-GLU significantly reduced the acute toxicity to worker bees and promoted the growth of cowpea plants.

GRAPHICAL ABSTRACT



ARTICLE INFO

Editor: Yi Yang

Keywords:

Cowpea thrips
Nano-delivery systems
Nanopesticide
Thiamethoxam
Worker bees

ABSTRACT

Thrips [*Megalurothrips usitatus* (Bagnall)] (Thysanoptera: Thripidae) is a pest that poses a serious challenge to global crop production and food supply, especially to the cowpea industry. Nano-delivery systems have broad application prospects in the prevention and control of pests in agriculture. Herein, three types of amino acid (AA) modified polysuccinimide nano-delivery carriers (PSI-GABA, PSI-ASP and PSI-GLU) were constructed with a diameter of approximately 150 nm to load thiamethoxam (THX), which enhanced THX effective distribution and use with cowpea plants. Significantly, the PSI-GLU nanocarrier effectively delivered THX to cowpea plant tissues following 6 h of soil application. Compared with commercial THX suspension (SC), the THX content in the leaves of cowpea plants was increased by 2.3 times. Confocal laser scanning microscopy revealed that the FITC-labeled PSI-GLU nanocarrier reached the leaves through the vascular system after being absorbed by the roots of cowpea plants. The PSI-GLU nanocarrier decreased the LC₅₀ of THX from 11.45 to 7.79 mg/L and significantly enhanced

* Corresponding authors at: National Key Laboratory of Green Pesticide, South China Agricultural University, Guangzhou 510642, China.

E-mail addresses: zhuli2008@scau.edu.cn (L. Zhu), jiainliang@scau.edu.cn (J. Jia).

<https://doi.org/10.1016/j.scitotenv.2024.176327>

Received 3 July 2024; Received in revised form 14 September 2024; Accepted 14 September 2024

Available online 17 September 2024

0048-9697/© 2024 Elsevier B.V. All rights are reserved, including those for text and data mining, AI training, and similar technologies.

the insecticidal effect. The PSI-GLU nanocarrier also improved the safety of THX to worker bees at 48 h, and moreover showed a growth-promoting effect on cowpea seedlings. These results demonstrated that the PSI-GLU nano-delivery carrier has promising uses on improving the effective utilization of THX for the sustainable control of thrips and reducing the risk to non-target pollutions.

1. Introduction

With the rapid growth of the global population, ensuring food security has become one of the primary tasks of agricultural production (Boliko, 2019; Kah et al., 2019). Cowpea (*Vigna unguiculata* (L.) Walp.) is an important vegetable crop with a global planting area of >15 million

hectares. It is rich in plant proteins and amino acids, providing special nutritional value for humans and livestock (Gitonga et al., 2022; Omo-Ikerodah et al., 2008). However, cowpea growth is often affected by diseases and pests, especially bean flower thrips [*Megalurothrips usitatus* (Bagnall)] (Thysanoptera: Thripidae) (Kusi et al., 2019; Tang et al., 2023). Cowpea thrips feed on the sap of the leaves and flowers, leading

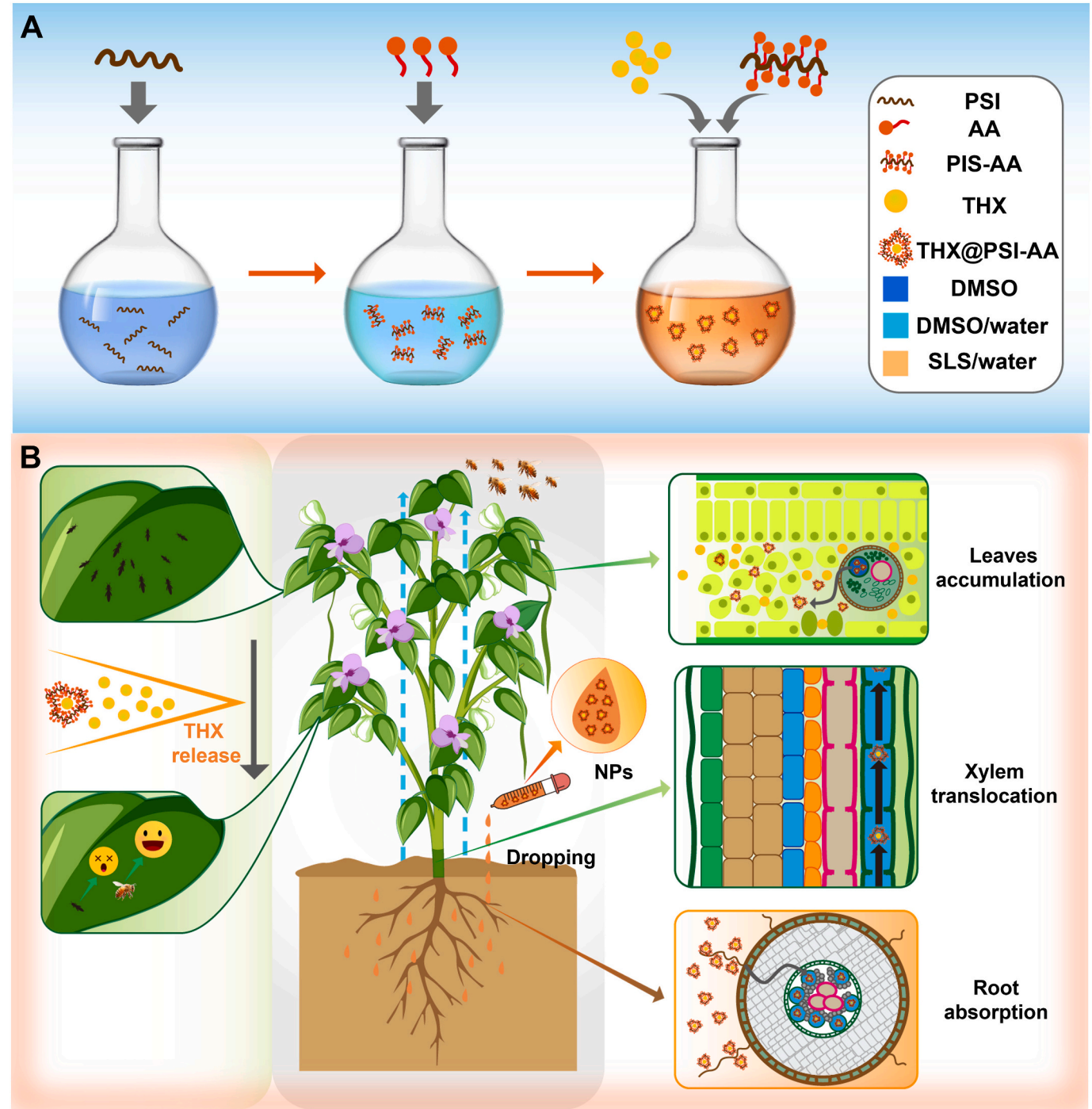


Fig. 1. (A) Illustration for the synthesis of THX@PSI-AA nanoparticles and (B) their applications in the cowpea thrips smart control.

to deformation, drying, and premature dropping of flower buds, endangering seriously the yield of cowpea. It has been reported that pest thrip induced damage can cause 20–80 % loss of cowpea yield, and up to 100 % in severe cases (Agbahoungba et al., 2021; Nabirye et al., 2003; Ngakou et al., 2008). At present, using chemical pesticides remains the main means of cowpea thrip control (Yu et al., 2023). Nevertheless, thrips are often hidden in the heart leaves and flowers because of their small size, resulting in the inability of pesticides to contact thrips through traditional foliar spraying methods, thus causing a waste of pesticides and poor insect control (Liu et al., 2020; Tang et al., 2022). Therefore, improving the directional accumulation of pesticides in the damaged parts of cowpea plants has become a key technical challenge for the thrip prevention and control.

In the past decade, with the development of nanotechnology in the field of agricultural science, nanopesticides have been developed as innovative formulations that use nanotechnology in attempts to improve pest management in agriculture (Shangguan et al., 2024). Nanopesticides can enhance the effectiveness of traditional pesticides through better absorption, targeted delivery, and controlled release (Wu et al., 2023). Nanocarriers have become a mechanism for targeting pest control challenges due to their better versatility, lower cost, and easier control of physical and chemical properties (Chaud et al., 2021). These nano-delivery carriers have received significant attention and are being applied for plant protection (Jiang et al., 2022; Usman et al., 2020; Xu et al., 2020). The targeted delivery of chemical substances and biomolecules by nanocarriers is made possible because of their adjustable physical and chemical properties, such as size, surface charge, lipophilic hydrophilicity, biomolecular coating and multiple chemical modifications (Liang et al., 2021; Xiao et al., 2022a). For example, (Zhang et al., 2022a) constructed a nanocarrier-based transdermal delivery system which improved the penetrability and contact toxicity of an insect growth regulator (IGR). (Xiong et al., 2024) also reported that tebuconazole could be transported to all parts of tomato seedlings faster by using esterified dextran as a nanocarrier, achieving long-distance material transport. Accordingly, functional nanocarriers are a promising method for delivering chemicals to specific parts of plants (Gan et al., 2023; Shangguan et al., 2024; Zakeri et al., 2018). However, the directional transport capacity of polymer-based nanomaterials in plants has rarely been reported. Conducting environmental risk assessments and implementing proper safety measures to mitigate potential risks are essential steps when developing, testing and applying nanomaterials (Mariyam et al., 2024). Nanoparticles pose several environmental risks, primarily due to their small size and high reactivity. They can easily enter ecosystems, potentially affecting soil health, water quality, and biodiversity. Their interaction with non-target organisms may lead to toxic effects on beneficial insects, aquatic life, and plants (Kah and Hofmann, 2014). Moreover, nanoparticles can persist in the environment, accumulating in food chains and leading to long-term ecological consequences (He et al., 2019).

Polysuccinimide (PSI) is an environmentally friendly material with excellent biocompatibility and biodegradability (Su et al., 2021), having broad application as a new nanomaterial for the delivery of chemical and biological molecules in plants (Hernández-González et al., 2017; Xin et al., 2018). Besides, modifying nanomaterial with endogenous substances (such as sugars, proteins and amino acids) can enhance the absorption and transport of compounds in plants, which has been proven to be feasible (Jiang et al., 2018; Mariyam et al., 2024; Zhong et al., 2024). It has been reported that γ -aminobutyric acid (GABA) is a non-protein amino acid and an endogenous regulator that promotes the accumulation of GABA in plants under the defense system against various biotic and abiotic stresses (Islam et al., 2024). In addition, the concentration of aspartic acid (ASP) and glutamic acid (GLU) in most cowpea varieties are much higher than those of other amino acids (Tekla et al., 2020; Xiong et al., 2013). Thus, the above amino acids (ASP, GLU and GABA) to modify PSI (PSI-GABA, PSI-ASP and PSI-GLU) were selected as nano-delivery carriers.

In this study, nanocarriers were designed by ring-opening induced amide reaction, and THX was loaded into different nanocarriers to obtain nanoparticles (THX@PSI-GABA, THX@PSI-ASP and THX@PSI-GLU) for the control of cowpea thrips (Fig. 1). The nanoparticles were characterized in detail, and the properties of THX after encapsulation were systematically researched, including release properties, thermal stability and insecticidal activity against thrips. The transport efficiency and behavior of these nanoparticles in cowpea plants were investigated by QuEChERS and fluorescence labeling methods, respectively (Zhang et al., 2022b). In addition, plant growth of cowpea seedlings and toxicity to bees were investigated. Thus, this study demonstrated that the amino acid functionalized nano-delivery system is an efficient strategy, which provides the feasible idea for scientific control of thrips.

2. Materials and methods

2.1. Materials

Polysuccinimide (PSI, M_w : 5600 Da) was procured from Hubei YuanChen SaiChuang Technology Co., Ltd. (Hubei, China). D-Glutamic acid (GLU, 97 %), D-Aspartic acid (ASP, 97 %), γ -Aminobutyric acid (GABA, 98 %), Sodium dodecane-1-sulfonate (SLS, 98 %) were purchased from Shanghai Acme Biochemical Co., Ltd. (Shanghai, China). Fluorescein isothiocyanate (FITC, 90 %) was obtained from Aladdin Biochemical Technology Co., Ltd. (Shanghai, China). Sodium hydroxide, hydrochloric acid, ethanol and dimethyl sulfoxide (DMSO) were purchased from Guangdong Guanghua Chemical Factory Co., Ltd. (Shantou, China). Primary secondary amine sorbent (PSA, 40–60 μ m) was purchased from Shanghai Yuexu Technology Co., Ltd. (Shanghai, China). Acetonitrile and methanol (HPLC grade) were purchased from Beijing DingGuoChangsheng Biotechnology Co., Ltd. (Beijing, China). Technical-grade Thiamethoxam (THX, 98 %) was provided by Guangdong Yuantian Bioengineering Co., Ltd. (Guangzhou, China). Thiamethoxam suspension (THX SC, 30 %) was provided by Beijing Green Agricultural Science and Technology Group Co., Ltd. (Beijing, China).

Nutrient soil and vermiculite were purchased from Beijing Huiqi Weiye Flower Co., Ltd. (Beijing, China). The worker bees were provided by the National State Key Laboratory of Green Pesticides (South China Agricultural University).

2.2. Synthesis of amino acid modified PSI nanocarriers

PSI-GLU was synthesized by condensation polymerization according to previous studies with slight modifications (Torma et al., 2007). First, PSI (30 mmol of succinimide repeating unit, 2.91 g) was dissolved in 20 mL of DMSO. Subsequently, a total of 0.44 g of GLU and 0.24 g of sodium hydroxide were dissolved in 30 mL of water, and PSI solution was added slowly while stirring continuously with a magnetic stirrer. After sufficient reacting, the mixture was added dropwise to 500 mL of citric acid buffer (pH = 2.5). Eventually, the reaction mixture was centrifuged at 11090 RCF for 10 min to get rid of the aggregates and excess reagents. The final products were washed three times, freeze-dried overnight, thus, the PSI-GLU nanocarriers were produced. The synthesis methods of PSI-GABA and PSI-ASP nanocarriers were similar to that of PSI-GLU nanocarriers.

2.3. Preparation of THX-loaded nanoparticles

THX-loaded PSI-GLU nanoparticles were prepared by the solvent exchange method (Liang et al., 2022). THX (0.5 g) and PSI-GLU (0.5 g) were ultrasonically dissolved in 3 mL of DMSO. Then, the mixed solution was added drop-by-drop into 5 mL of 0.2 wt% aqueous solution of sodium dodecane-1-sulfonate (SLS) and stirred for 90 min. The resulting mixture was centrifuged at 11090 RCF for 10 min, washed three times, freeze-dried overnight, and THX@PSI-GLU nanoparticles was obtained. The preparation methods of THX@PSI-ASP and THX@PSI-GABA

nanoparticles were similar to the THX@PSI-GLU nanoparticles described.

2.4. Synthesis of FITC@PSI-GLU

Briefly, PSI-GLU (1.0 g) and FITC (0.1 g) were ultrasonically dissolved in 10 mL of DMSO, and were stirred for 2 h in the dark. The reaction mixture was subjected to the same impurity removal step as washing to obtain PSI-GLU until the supernatant had no obvious fluorescence characteristic color. Finally, the FITC@PSI-GLU was obtained by freeze-drying.

2.5. Characterizations

The characteristics and amide-derived functional groups of nanoparticles were recorded on a FTIR spectrophotometer (Nicolet IS10, USA) using KBr pellets with a wavenumber range of 400 to 4000 cm^{-1} at room temperature. The hydration particle size and zeta potentials were determined by dynamic light scattering (DLS, Zetasizer Nano ZSE, UK). Thermogravimetric analysis (TGA) of nanoparticles was determined by thermogravimetric analyzer (TG209F1LibraTM, Germany) with temperature changes between 40 and 800 $^{\circ}\text{C}$ under a N_2 atmosphere at a heating rate of 10 $^{\circ}\text{C}/\text{min}$. The crystal structure was characterized by X-ray diffractometry (XRD, Bruker D8 Focus, German). The chemical composition and surface properties were identified by X-ray photoelectron spectroscopy (XPS, Thermo Scientific Escalab 250Xi, USA) using the binding energy of C 1 s 284.80 eV as the energy standard. Scanning electron microscope (SEM, Hitachi SU8010, Japan), energy dispersive spectroscopy (EDS) and transmission electron microscope (TEM, Talos L120C, Czech) were used to observe the structures and morphologies of nanoparticles.

2.6. In vitro release of THX

The dialysis bag method at room temperature was used to investigate the release behavior of THX-loaded nanoparticles under different pH conditions (Xiao et al., 2022b). The THX (10 mg) and nanoparticles containing the same mass of THX were added to 3 mL of phosphate buffer/absolute ethanol mixed solution (1:1, V/V) at three pH values (pH 5.0, 7.0 and 9.0) respectively. Then, the dialysis bag (3500 Mw) was immersed in 100 mL of phosphate buffer solution, while continuously stirring with a magnetic stirrer at room temperature. At each specific time, 1 mL of the supernatant was extracted, and the same volume of fresh phosphate buffer/absolute ethanol was added to ensure the total volume unchanged. The collected supernatant was centrifuged at 11090 RCF for 6 min. Finally, the centrifuged liquid analyzed by high performance liquid chromatography (HPLC, Agilent 1260, USA). The experiment was carried out in three replicates.

The cumulative release ratio of THX was calculated with the following Eq. (1)

$$\text{Cumulative release rate (\%)} = \frac{C_n \times V_0 + \sum_{i=1}^{n-1} C_n \times V}{M_0} \times 100 \quad (1)$$

where C_n is the concentration of THX at the n th sampling time point; V_0 is the total volume of the release medium; V is the volume of each sampling at different times; and M_0 is the initial THX mass of THX-loaded nanoparticles.

In addition, the cumulative release data were fitted by zero-order, first-order, Higuchi and Ritger–Peppas models to investigate the release mechanism of THX-loaded nanoparticles, according to Eqs. (2)–(5), respectively (Ma et al., 2023).

$$\text{Zero – order model : } M_t/M_0 = kt + b \quad (2)$$

$$\text{First – order model : } \ln(1 - M_t/M_0) = -kt + b \quad (3)$$

$$\text{Higuchi model : } M_t/M_0 = kt^{1/2} + b \quad (4)$$

$$\text{Ritger–Peppas model : } M_t/M_0 = kt^n + b \quad (5)$$

where M_t/M_0 is the release ratio of THX at time t , k is the kinetic constant and n is the diffusion exponent: Fickian diffusion ($n \leq 0.43$), cooperation of drug diffusion and dissolution ($0.43 < n < 0.89$), and dissolution control ($n \geq 0.89$).

2.7. In vivo uptake of THX in cowpea plant

In the case of the drip irrigation method, the cowpea seeds were grown in a seedling tray and watered once every two days. The soil was a mixture of sterilized nutrient soil and vermiculite (mass ratio = 3:1). After the seeds germinated, the seedlings were transferred to a flowerpot with a diameter of 12 cm. After 1 month of growth, 100 mL of THX SC, THX@PSI-GLU, THX@PSI-ASP and THX@PSI-GABA solutions were added to each pot, respectively, in which the THX contents were 300 mg/L. Water was used as control treatments. Eventually, each cowpea seedling was cut into 3 parts of root, stem and leaf after absorbing THX solution for 6 h. Three repeated pot experiments were set up for each treatment. Each sample (0.5 g) was added to 5 mL of acetonitrile and steel balls to break the sample. After breaking the sample tissue, the sample was sonicated for 15 min, then added NaCl (1 g), centrifuged at 990 RCF for 15 min. Subsequently, 1 mL supernatant was extracted and mixed with anhydrous MgSO_4 (25 mg) and Primary secondary amine sorbent (PSA, 50 mg) for 30 s in a centrifuge tube, and centrifuged at 11090 RCF for 15 min. The resulting supernatant was filtered through 0.22 μm nylon syringe filters membrane into a vial for HPLC detection and quantification. Each treatment was conducted with three replicates.

In addition, the upward transport of THX could be defined as transfer factor (TF) (Wu et al., 2023), and the TF was used to express the transport efficiency of THX in cowpea plant. The TF of THX on cowpea was calculated with the following Eqs. (6)–(7)

$$TF_1 = C_{\text{stem}}/C_{\text{root}} \quad (6)$$

$$TF_2 = C_{\text{leaves}}/C_{\text{stem}} \quad (7)$$

where TF_1 and TF_2 indicate the ability of THX to transport from roots to stems and from stems to leaves, respectively. C is the concentration of THX in each part of the cowpea plants.

2.8. Distribution and translocation of PSI-GLU nanocarriers

The roots of cowpea seedlings were soaked in 0.1 mg/mL of FITC@PSI-GLU solution by hydroponics for 6, 12 and 24 h, respectively. The roots, stems and leaves of cowpea were cut into 30 μm thick sections using a freezing microtome (CM1950, Lecia EM UC7/FC7 Germany). The distribution of FITC@PSI-GLU in roots, stems, and leaves of cowpea plants was observed by confocal laser scanning microscope (CLSM, Lecia TCS SP8 STED 3 \times , Germany) with a laser excitation wavelength of 488 nm.

2.9. Insecticidal activity of THX@PSI-GLU

To determine insecticidal activity of THX@PSI-GLU, we evaluated the LC_{50} of THX@PSI-GLU to thrips collected in Guangzhou by leaf dipping method (Zhang et al., 2023). Briefly, the THX and THX@PSI-GLU were dissolved in DMSO, so that the concentration of the stock solution was 1 mg/mL, respectively. Then the above solution was diluted to 5, 7.5, 10, 12.5 and 15 mg/L with 0.1 % of Tween-80. Subsequently, cowpea was soaked in various concentrations of solution, natural air-dried after soaking 10 min, and placed in a petri dish with a moisturizing filter paper. Soaking the cowpeas in water without pesticide was designated as the CK group. At the same time, fifteen thrips

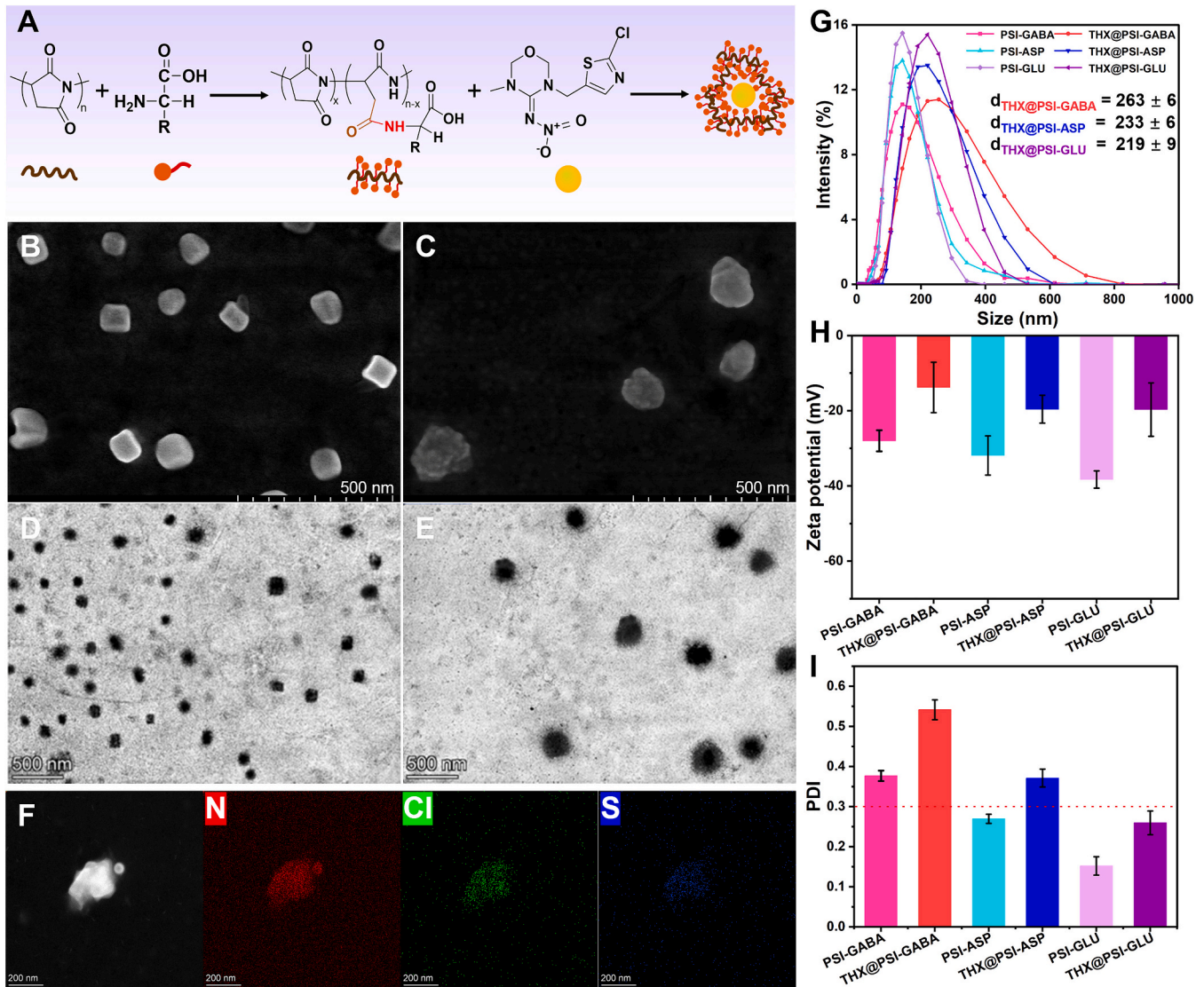


Fig. 2. (A) Synthetic steps for THX@PSI-AA. SEM images of (B) PSI-GLU, and (C) THX@PSI-GLU and TEM images of (D) PSI-GLU, and (E) THX@PSI-GLU. (F) EDS analysis of THX@PSI-GLU. (G) Average particle diameter distributions, (H) Zeta potential and (I) PDI of PSI-ASP, PSI-GABA, PSI-GLU, THX@PSI-GABA, THX@PSI-ASP, and THX@PSI-GLU.

adults were placed in each petri dish and maintained under suitable conditions (temperature 26 ± 1 °C, relative humidity 65 ± 5 %, and photoperiod 14 L:10 D) for 24 h. After 24 h, the death number of thrips was observed and the LC_{50} was calculated. The thrips that did not move when gently pushed with a brush were recorded as dead. Three repeated experiments were set up in each treatment.

2.10. Effect of THX@PSI-GLU on cowpea seedling growth

Cowpea seedling culture is the same as the above THX absorption test in cowpea plants. After the cotyledons of cowpea seedlings grow out, 100 mL THX@PSI-GLU and PSI-GLU solutions were added to each pot of cowpea seedlings by drip irrigation, respectively, in which the contents were 100 mg/L. After 7 days of treatment, the plant height, leaf width, root weight, shoot weight, fresh weight and dry weight of cowpea seedlings were measured, and the fresh leaves were collected for chlorophyll content measurement. The experiment was repeated three times. Chlorophyll content measurement was performed and modified (Huang et al., 2023). Leaves (0.5 g) were immersed in a test tube containing acetone/absolute ethanol mixed solution (1:1, V/V) and placed in darkness. When the leaves were completely whitened, the test tube was

shaken and the supernatant was taken. The absorbance at 645, 663 and 440 nm was measured by UV-Vis spectrophotometer, respectively.

Chlorophyll a, chlorophyll b and carotenoid were calculated with the following Eqs. (8)–(10)

$$C_a = 13.95 \times A_{663} - 6.88 \times A_{645} \quad (8)$$

$$C_b = 24.96 \times A_{645} - 7.32 \times A_{663} \quad (9)$$

$$C_{x,c} = (1000 \times A_{440} - 2.05 \times C_a - 114.8 \times C_b) / 245 \quad (10)$$

where C_a , C_b and $C_{x,c}$ represent the concentrations of chlorophyll A, chlorophyll B and carotene in cowpea leaves, respectively.

2.11. Acute toxicity of THX@PSI-GLU to worker bees (*Apis mellifera*)

The acute oral toxicity test of worker bees (*Apis mellifera*) was performed to measure the lethal dose of pesticides according to the method we previously reported (Yang et al., 2023). THX SC and THX@PSI-GLU were diluted with 500 g/L sucrose solution to the desired concentration. The worker bees were transferred to cages (size: $20 \times 20 \times 20$ cm³) with about 12 worker bees per cage. The worker bees were starved for 2 h,

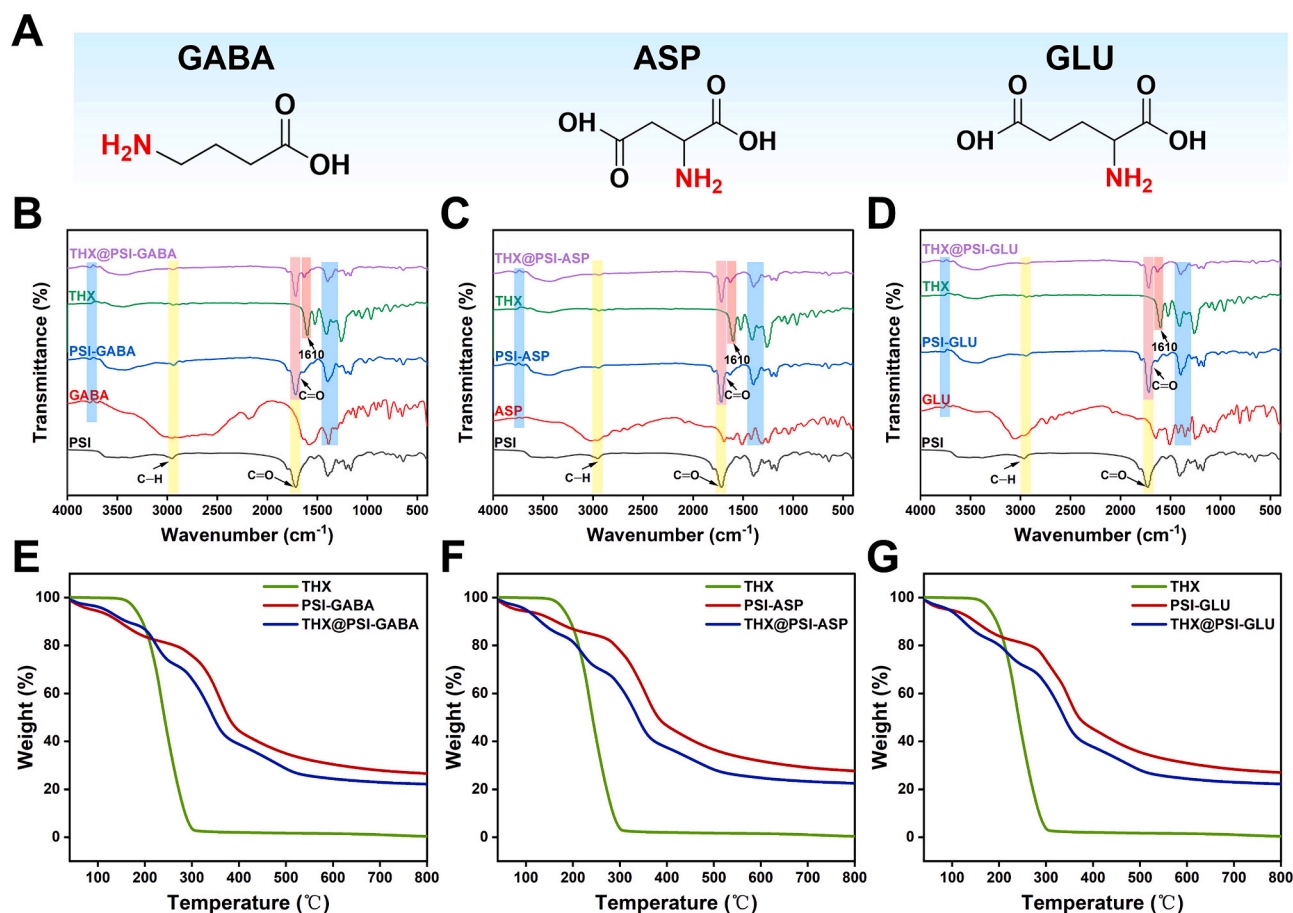


Fig. 3. (A) Molecular structures of three amino acids. FTIR spectra of (B) THX@PSI-GABA, (C) THX@PSI-ASP, and (D) THX@PSI-GLU. TGA patterns of (E) THX@PSI-GABA, (F) THX@PSI-ASP, and (G) THX@PSI-GLU.

and then fed with sucrose solution containing the tested compound. Each concentration of the tested compound was repeated 3 times, and 500 g/L sucrose solution was used as negative control. The cages were kept in darkness at 25 ± 2 °C and 75 ± 2 % relative humidity, and fresh sucrose solution was replaced every 6 h. The mortality of worker bees at 24 and 48 h was recorded and the LD₅₀ was calculated.

2.12. Statistical analysis

Statistical analysis of all data was performed using Microsoft Office Excel 2021 and SPSS 26.0 software. Graphs were made with the help of Origin 2021, Microsoft Office PowerPoint 2019 software. The difference between the two groups was tested by independent sample test. The results were expressed as the mean \pm standard error. "Slope \pm SE" in table represents the slope of the dose-response curve and its standard error. One-way ANOVA was first used and then the Duncan test was used for comparison between multiple groups.

3. Results and discussion

3.1. Preparation and characterization of nanoparticles

In this study, THX-loaded nanoparticles were prepared by condensation polymerization and solvent exchange method (Liang et al., 2022; Torma et al., 2007), and the detailed synthetic procedure was presented in Fig. 2A. SEM and TEM revealed that PSI-GLU exhibited a square appearance with uniform particle size, clear edge and smooth surface (Fig. 2B, D). THX@PSI-GLU was approximately spherical in shape, but the edge was not clear. It appeared rough and not smooth (Fig. 2C, E).

With the encapsulation of THX, the particle size also increased. The chlorine and sulfur were unique components of THX, and EDS analysis (Fig. 2F) exhibited that chlorine and sulfur were evenly distributed in the range of nanoparticles, which demonstrated the presence of THX in the PSI-GLU nanocarriers. Furthermore, as shown in Fig. 2G, the hydrated particle sizes of the nanocarriers were basically about 150 nm. After loading THX, the hydrated particle sizes of THX@PSI-GABA, THX@PSI-ASP and THX@PSI-GLU were 262.7, 232.3 and 218.6 nm, respectively. In Fig. 2H, the zeta potentials of PSI-GABA, PSI-ASP, PSI-GLU, THX@PSI-GABA, THX@PSI-ASP and THX@PSI-GLU were -28.0 , -31.9 , -38.3 , -13.8 , -19.6 and -19.7 mV, respectively. The loading of THX reduced the potential of the nanoparticles, which was due to the electrostatic interaction between the nanocarriers and THX. The polymer dispersity index (PDI) is a measure used in polymer chemistry to describe the distribution of molecular weights in a given polymer sample. A low PDI (< 0.3) indicates a uniform molecular weight distribution, meaning most polymer molecules in the sample have a similar size. Conversely, a high PDI suggests a broader distribution, with significant variation in molecular weights among the polymer molecules in the sample (Ahmad et al., 2019; Hu et al., 2017). The PDI of all nanoparticles increased after loading THX, only the PDI of THX@PSI-GLU was in the range of (< 0.3) (Fig. 2I). Thus, THX@PSI-GLU nanoparticles are considered to be more stable in water.

Fourier transform infrared (FTIR) spectra of THX-loaded nanoparticles were shown in Fig. 3B-D. For PSI nanocarriers modified by different amino acids (Fig. 3A), the absorption bands of PSI-GABA, PSI-ASP and PSI-GLU at 1300 – 1500 cm⁻¹ had different degrees of stretching vibration due to the difference in the combination of C–H groups, and the absorption peak at 3750 cm⁻¹ was the characteristic peak of the

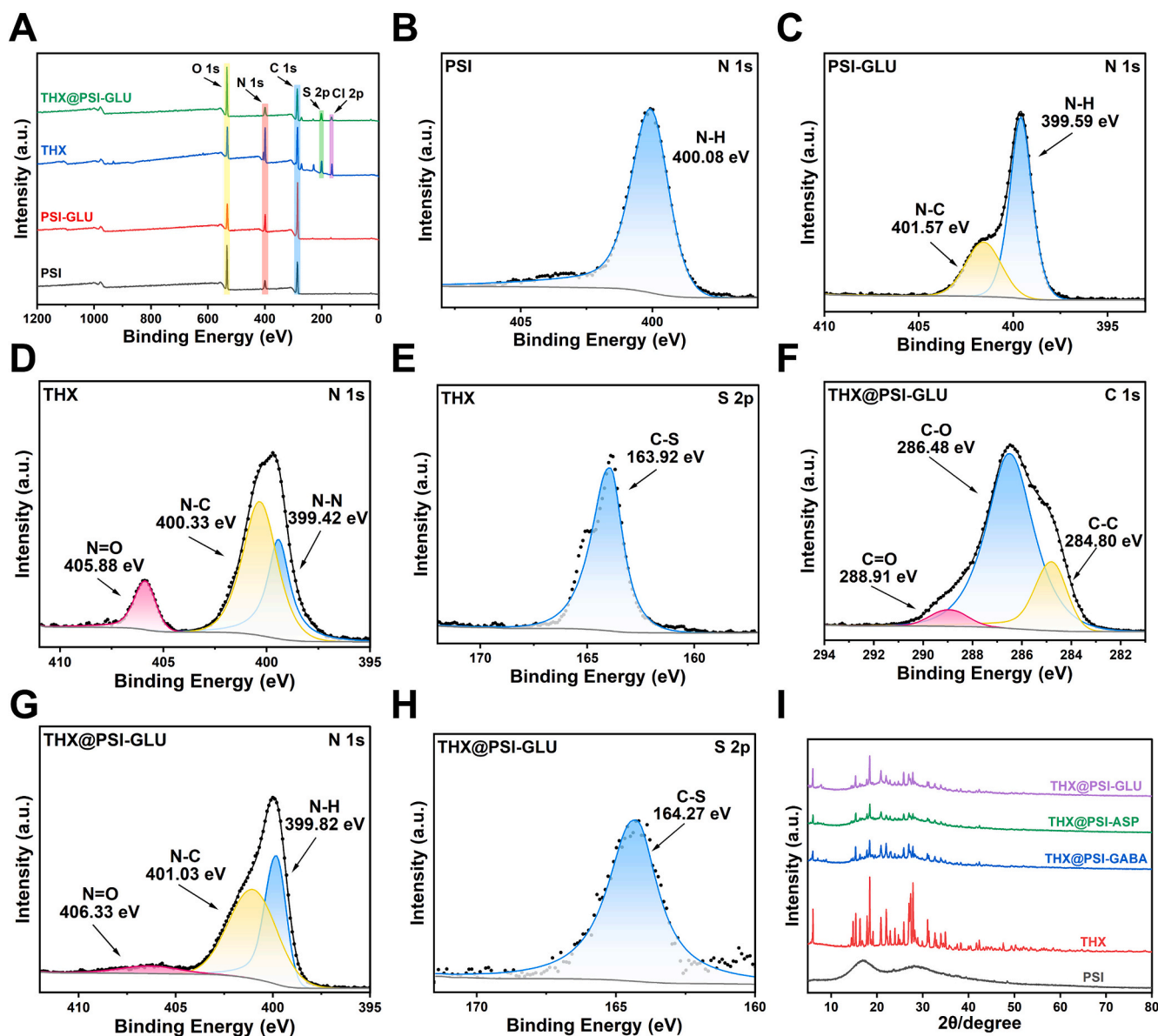


Fig. 4. (A) XPS analyses of PSI, PSI-GLU, THX, and THX@PSI-GLU. (B) N 1s XPS spectra of PSI. (C) N 1s XPS spectra of PSI-GLU. (D) N 1s XPS spectra, and (E) S 2p XPS spectra of THX. (F) C 1s XPS spectra, (G) N 1s XPS spectra, and (H) S 2p XPS spectra of THX@PSI-GLU. (I) XRD patterns of PSI, THX, THX@PSI-GABA, THX@PSI-ASP, and THX@PSI-GLU.

carboxyl group of amino acids. Moreover, a new characteristic peak appeared at 1690 cm^{-1} , which was the C=O stretching vibration of the amide II region (Yang et al., 2021). The characteristic absorption bands of C=O stretching vibration at 1720 cm^{-1} and C—H stretching vibration at 2950 cm^{-1} of succinimide were also observed on the nanocarriers (Wu et al., 2021). This indicated that the successful synthesis of PSI-GABA, PSI-ASP and PSI-GLU nanocarriers. For THX-loaded nanoparticles, the characteristic peaks of the above nanocarriers were retained. Moreover, the C=C stretching vibration band of THX was observed at 1610 cm^{-1} (Wu et al., 2022), which proved that THX existed in the nanocarriers and the structure was not altered.

As shown in Fig. 3E-G, the thermal stability of THX-loaded nanoparticles was studied by the thermogravimetric analyses (TGA). THX began to degrade at about 120°C and completely decomposed at 300°C approximately. In the curves of all nanoparticles, when the temperature was below 100°C , there was a small amount of weight loss (5 %), which was due to the evaporation of water absorbed during the synthesis of nanoparticles. In the curves of PSI-GABA, PSI-ASP and PSI-GLU

nanocarriers, the first weight loss occurred between 100°C and 220°C , which was caused by the cleavage of the amide bond between amino acids and PSI. It has been in a state of weightlessness after 220°C , which was caused by the degradation of PSI-GABA, PSI-ASP and PSI-GLU. In the curves of THX@PSI-GABA, THX@PSI-ASP and THX@PSI-GLU nanoparticles, the first weight loss occurred between 100 and 180°C , which was lower than the temperature of the nanocarriers. This difference between before and after THX loading in the first weight loss was because the bond position was weakened after loading THX, and the amide bond was more easily broken (Fig. S2). This result was consistent with the conclusion of Zeta potential. Different from the nanocarriers, the curves of THX-loaded nanoparticles exhibited an additional weight loss interval of THX at $400\text{--}540^\circ\text{C}$ approximately, and the weight loss rate was about 15 %, which was consistent with the mass fraction of THX loaded (Fig. S1). The results indicated that the nanocarriers could improve the thermal stability of THX, which was conducive to the long-term preservation of pesticides in practical applications.

The XRD curve of THX-loaded nanoparticles showed that the

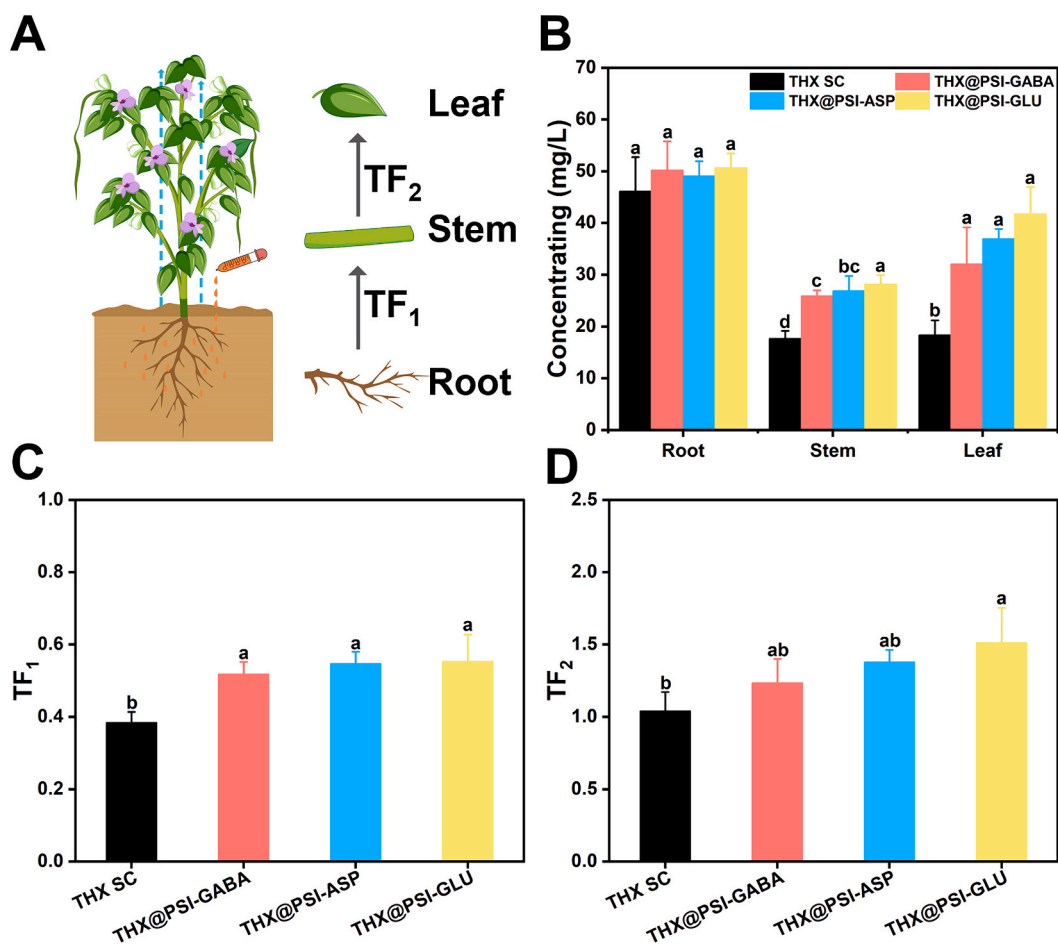


Fig. 5. (A) Schematic diagram of cowpea plants absorbing THX. (B) The content of THX in roots, stems and leaves of cowpea plants treated with THX SC, THX@PSI-GABA, THX@PSI-ASP, and THX@PSI-GLU for 6 h. (C) Transfer factor from roots to stems (TF₁) and (D) Transfer factor from stems to leaves (TF₂) values of THX absorbed by cowpea seedlings.

characteristic peaks of THX and PSI could be clearly seen in Fig. 4I. The elemental composition and interaction mechanism of the nanoparticles were studied using XPS in Fig. 4A–H and Fig. S3, 4. There was no significant difference between PSI and PSI-GLU except for an additional N–C peak at 401.57 eV, which was the amide bond formed by the reaction of PSI and GLU (Fig. 4B, C). The binding energy of Cl (Cl 2p) and S (S 2p) in THX@PSI-GLU increased after loading THX (Fig. 4A, H), which was a unique characteristic of THX, indicating that THX was successfully loaded. Compared with THX, the high-resolution characterization of THX@PSI-GLU showed that the peaks of N–H, N–C and N=O in the XPS spectrum of N1s were blue-shifted, corresponding to 399.82, 401.03 and 406.33 eV, respectively (Fig. 4D, G) (Liang et al., 2021). This was because the interaction between THX and PSI-GLU reduced the electron density of the N atom, thereby increasing the binding energy. These results indicated the successful modification of PSI, and THX were encapsulated in nanocarriers through physical methods.

3.2. Uptake and translocation of THX in cowpea plants

To verify whether the THX-loaded nanoparticles can successfully transfer THX from roots to stems and leaves, we used a modified QuEChERS method to measure the content of THX in the roots, stems and leaves of cowpea (Zhang et al., 2022b). HPLC results demonstrated that after 6 h of drip irrigation, the content of THX in the roots, stems and leaves of THX SC, THX@PSI-GABA, THX@PSI-ASP and THX@PSI-GLU were 46.2, 50.3, 49.1, 50.7, 17.7, 25.9, 26.9, 28.2, 18.4, 32.1, 37.0 and 41.8 mg/L, respectively (Fig. 5B). Compared with THX SC,

THX-loaded nanoparticles had higher THX content in roots, stems and leaves, and THX content in stems and leaves of THX-loaded nanoparticles increased significantly. This confirmed that amino acid-functionalized nanocarriers could enhance the transport capacity of THX in cowpea plants. Transfer factor (TF) was introduced to evaluate the efficiency of nanocarriers in transferring THX after root irrigation. The TF₁ and TF₂ of THX SC, THX@PSI-GABA, THX@PSI-ASP and THX@PSI-GLU were 0.38, 0.51, 0.54, 0.55, 1.04, 1.23, 1.38 and 1.51, respectively (Fig. 5C, D). The TF₁ and TF₂ of amino acid functionalized nanocarriers were higher than THX SC. This demonstrated that the amino acid functionalized nanocarriers were directionally transported through plant identification to increase the content of thiamethoxam in leaves. This phenomenon may be due to the fact that after the amino acid functionalized nanocarriers entered the vascular system through the symplastic pathway of the passage cells, the amino acid structure was recognized as a nutrient substance, thereby entering the xylem and transporting it to the top of the plant. In conclusion, amino acid functionalized nanocarriers could deliver THX to various parts of cowpea plants faster and significantly improve the utilization rate of THX.

Interestingly, the TF₁ and TF₂ of THX@PSI-GLU was the highest among the amino acid functionalized nanocarriers in cowpea plants. Particularly, compared with THX SC, the TF₂ of THX@PSI-GLU was increased by nearly 50 %. It had been reported that the distribution of nanoparticles in plant cells was regulated by their size and charge (Avellan et al., 2019; Hu et al., 2020). The size of nanoparticles ≤ 340 nm can pass through the pit membranes of xylem of most plant (Su et al., 2019) and the absolute value of the potential of nanoparticles ≥ 20 mV is

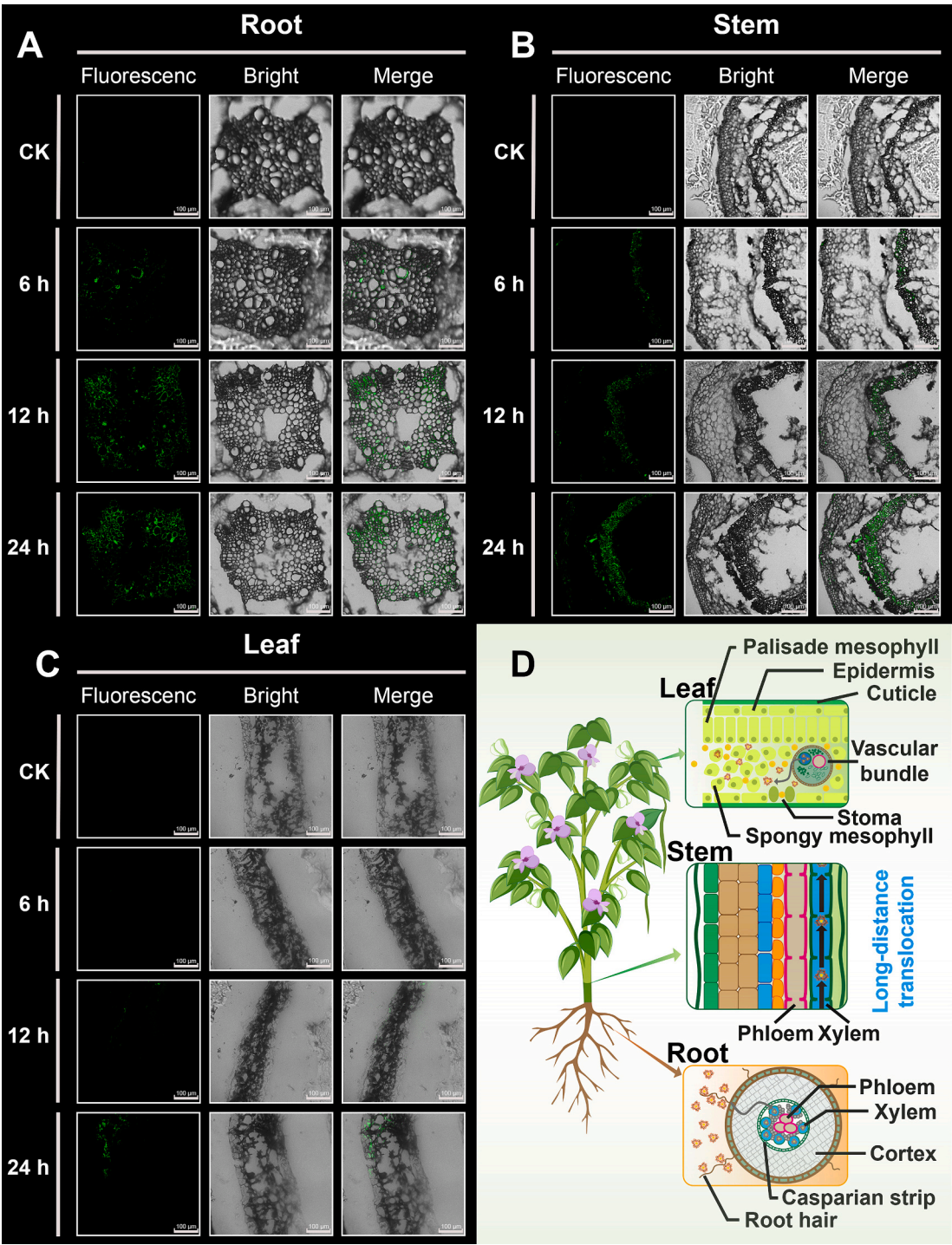


Fig. 6. Confocal imaging of FITC@PSI-GLU nanoparticles in (A) roots, (B) stems, and (C) leaves of cowpea plants at 6,12, and 24 h. (D) Schematic illustration of the root uptake pathway after treatment with THX@PSI-GLU nanoparticles in cowpea plants. Plants treated with water served as the “CK” group.

beneficial to absorption through plant lipid membranes (Jeon et al., 2024). Combined with the characterization of hydrated particle size, zeta potential and PDI, this may be the reason why the transport efficiency of THX@PSI-GLU was highest in amino acid functionalized nanocarriers. Based on the excellent comprehensive characterization and transportation efficiency, PSI-GLU nanocarrier was selected as the research object.

To further determine the distribution of amino acid functionalized nanocarriers in cowpea plants, the transport mode of nanocarriers was observed by fluorescence labeling method. The quenching response was

caused by the reaction of FITC with PSI-GLU (Jeon et al., 2024), indicating that FITC successfully labeled PSI-GLU (Fig. S5). Fig. 6A-C were confocal microscope images of roots, stems and leaves of cowpea plants treated with FITC@PSI-GLU for 6,12 and 24 h, and no FITC fluorescence signals were observed in the roots, stems and leaves of cowpea plants in the CK group. The fluorescence absorption image of the roots showed that the fluorescence migrated inward, reached the vascular system and accumulated in the vascular tissue over time, indicating that PSI-GLU could be absorbed by the roots and then reached the vascular tissue. The fluorescence absorption image of the stems showed that the

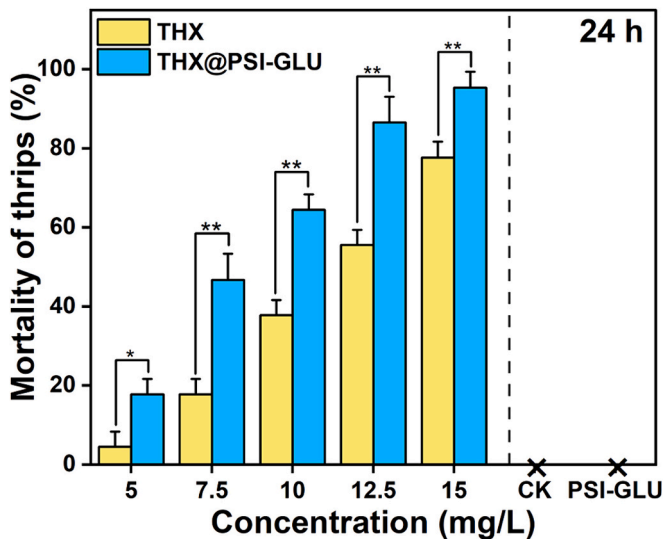


Fig. 7. The mortality of thrips (*Megalurothrips usitatus*) exposed to different concentrations of THX and THX@PSI-GLU at 24 h. When $p < 0.05$, there was a significant difference between the groups, represented by an asterisk (*) and when $p < 0.01$, there was a highly significant difference between the groups, represented by two asterisks (**). The “CK” group refers to the mortality of thrips exposed to cowpea soaked in water without pesticides. Each group of experiments was 15 thrips, and the experiment was repeated three times. Data marked with (×) indicate that mortality for this treatment was 0 %.

Table 1
Lethal concentration values of THX@PSI-GLU and THX to thrips (*Megalurothrips usitatus*) at 24 h.

Formulation	LC ₅₀ (μg/mL)	Slope ± SE	95 % confidence interval	χ ² (df)
THX	11.45	5.03 ± 0.69	10.51–12.66	4.88 (13)
THX@PSI-GLU	7.80	5.19 ± 0.63	7.06–8.49	4.49 (13)

fluorescence of the xylem in the stem deepened with time, indicating that PSI-GLU was delivered through the xylem of the stem after reaching the root vascular tissue. Moreover, slight fluorescence can be observed in the leaves image at 12 h, whereas clear fluorescence is visible in mesophyll cells of leaves image at 24 h. These results indicated that the PSI-GLU nanocarrier can be absorbed by the root hairs of cowpea plants, pass through the root cortex and the Casparian strip, and reach the vascular system, and then transport upward through the xylem of the stem and finally reach the mesophyll cells, thus realizing the long-distance material transport inside the plant.

In addition, these results were also consistent with the absorption experiment of THX in cowpea plants, which further proved that the PSI-GLU delivery system could optimize the translocation of active substances from roots to leaves in cowpea plants.

3.3. Insecticidal activity of THX@PSI-GLU against thrips (*Megalurothrips usitatus*)

The biological activity of THX@PSI-GLU against thrips was studied by a feeding method. In the insecticidal activity tests, thrips adults were fed with cowpea treated with PSI-GLU, THX and THX@PSI-GLU, respectively. No thrips adult was found dead after 24 h of treatment with CK and PSI-GLU, indicating that the nanocarrier had no insecticidal activity (Fig. S6). Moreover, as shown in Fig. 7, the 24 h mortality rates after treatment with THX and THX@PSI-GLU were positively correlated with the concentration, and compared with the THX treatment group, the mortality from each concentration in the THX@PSI-GLU treatment

group was significantly increased. The mortality rates of 12.5 mg/L THX@PSI-GLU treatment and 15 mg/L THX treatment were 86.56 % and 77.67 %, respectively, with the former being higher than the latter. In addition, as shown in Table 1, the LC₅₀ values of THX and THX@PSI-GLU calculated from the corresponding toxicity regression equation were 11.45 and 7.80 mg/L, respectively. Compared with THX, the LC₅₀ of THX@PSI-GLU to thrips was reduced by nearly 1.32 times (Table 1). These results indicated that the THX@PSI-GLU only needed a lower level of THX to kill thrips at the same active ingredient dose and time.

3.4. Safety of THX@PSI-GLU on cowpea plants

When nanocarriers are applied to plants, their biosafety and effects on seedling growth are crucial (Xiang et al., 2023; Zhu et al., 2018). Hence, we studied the effect of PSI-GLU and THX@PSI-GLU on the growth of cowpea plants and the change of chlorophyll in leaves for 7 days. Fig. 8A, B showed that PSI-GLU and THX@PSI-GLU promoted the development of cowpea seedlings within 7 days of drip irrigating treatment. Furthermore, the plant height, leaf width, root weight, stem weight, fresh weight and dry weight of cowpea seedlings were measured as growth indexes. As shown in Fig. 8C–E, except for plant height and root weight, other indicators increased significantly, especially fresh weight, with an increase of 40 % and 54 %. These results indicated that the vector PSI-GLU had a significant promoting effect on plant growth. In addition, as shown in Fig. 8F, the chlorophyll A, chlorophyll B and carotene in the leaves of the treatment group were significantly higher than those of the control group, which indicated that PSI-GLU could enhance the photosynthesis of cowpea plants and accelerate the growth of cowpea plants. Overall, PSI-GLU as a nanocarrier could promote plant growth.

3.5. Safety of THX@PSI-GLU on worker bees (*Apis mellifera*)

The honeybees are important global pollinators of crops and flowering plants (Zhang et al., 2021). It has been reported that neonicotinoid insecticides, especially THX, presents a sizeable hazard to honeybees (Kessler et al., 2015). Therefore, the toxicity of THX SC and THX @ PSI-GLU to worker bees was evaluated. Fig. 9A, B showed the mortality of worker bees in THX SC and THX@PSI-GLU solutions at different times and concentrations. Whether at 24 h or 48 h, there was no significant difference in the mortality of worker bees treated with 25, 50 and 75 ng/L THX SC concentrations compared with the THX@PSI-GLU group, but the mortality of worker bees treated with 100 and 125 ng/L THX SC was significantly higher than THX@PSI-GLU group. In addition, according to the corresponding toxicity regression equation, the LD₅₀ of THX SC and THX@PSI-GLU treated worker bees was 1.47, 1.28, 1.92 and 1.69 ng a. i./bee at 24 and 48 h, respectively (Table 2). The THX@PSI-GLU nanoparticles exhibited lower levels of toxicity when exposed to worker bees.

3.6. Controlled release kinetics

Environmental pH is a key influencing factor that regulates the structure and function of an ecosystem by biological, chemical and physical processes (Naz et al., 2022). For understanding and managing environmental issues, pH is an important factor that must be considered. As shown in Fig. 10A–C, the drug release rates of THX@PSI-GABA, THX@PSI-ASP, and THX@PSI-GLU were detected at pH = 5, 7 and 9, respectively. The results showed the release behavior of THX was rapid, and the cumulative release rates of THX@PSI-GABA, THX@PSI-ASP, and THX@PSI-GLU at pH = 9 were 88.76, 86.39 and 76.36 (72 h), respectively. In contrast to THX alone, THX encapsulated in these three nanoparticles was slowly released over time in different pH environments and the release rate of THX was the fastest under alkaline conditions. This was because THX was encapsulated in the nanocarriers, and the nanocarriers retained the carboxyl group after being modified by the

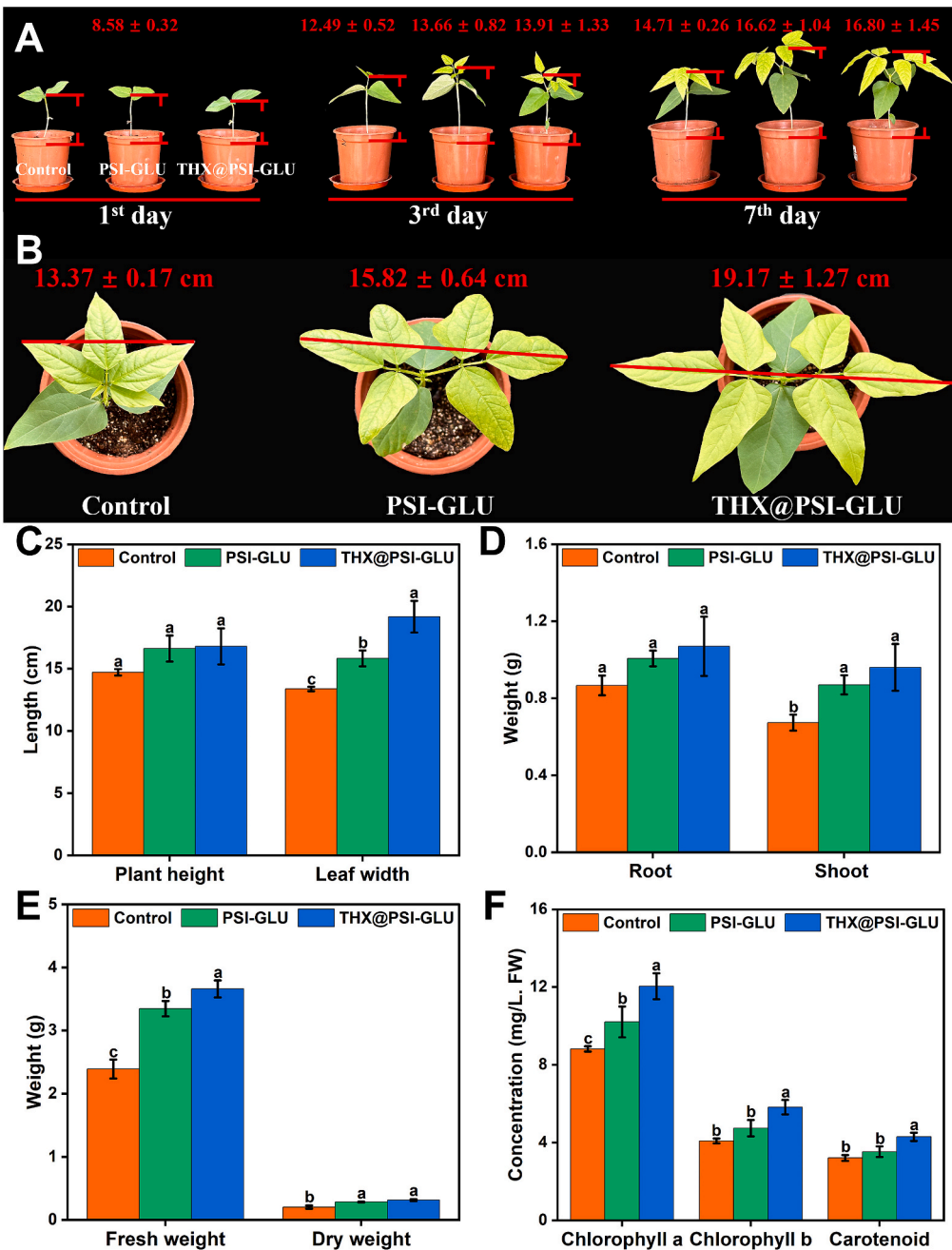


Fig. 8. (A) Representative images of plant height of cowpea plants on the 1st, 3rd, and 7th day after exposure to PSI-GLU and THX@PSI-GLU (Unit: cm), and (B) Representative images of leaf width of cowpea plants on the 7th day after exposure to PSI-GLU and THX@PSI-GLU. (C) Plant height and leaf width, (D) root and shoot weight, and (E) fresh and dry weight of control, PSI-GLU, and THX@PSI-GLU NPs treated cowpea plants. (F) Chlorophyll content of the treated plants. Significant differences ($p < 0.05$) among the various treatment groups are indicated by different letters over the SE bars. “Control” plants were treated with water. All experiments were repeated 3 times.

amino acid, which would be decomposed under alkaline conditions and more stable under acidic conditions. Moreover, the cumulative release rate of THX@PSI-GLU (72 h) was lowest in the same release environment, which indicated the THX@PSI-GLU was more capable of slow release.

To further explore the potential release mechanism of THX@PSI-GABA, THX@PSI-ASP, and THX@PSI-GLU under different pH conditions, the cumulative release rates of drugs were fitted by zero-order, first-order, Higuchi and Ritger-Peppas models, respectively (Fig. S8–10). The release behavior of the three nanoparticles was more in line with the first-order model, based on the correlation coefficient analysis of the fitted equations (R^2) shown in Table S1–3. The results showed that

the release rate of THX in nanocarriers was proportional to its content, and the higher the content of THX, the faster the release rate. Previous studies have indicated that the midgut of honeybees is generally acidic (Zheng et al., 2017), and release experiments have shown that THX@PSI-GLU releases more slowly than THX, particularly in acidic environments (Fig. 10C). Thus, PSI-GLU nanocarriers could significantly reduce the oral toxicity of THX to worker bees.

4. Conclusion

In summary, a nano-delivery system of amino acid modified carriers was successfully prepared, and THX was physically encapsulated in

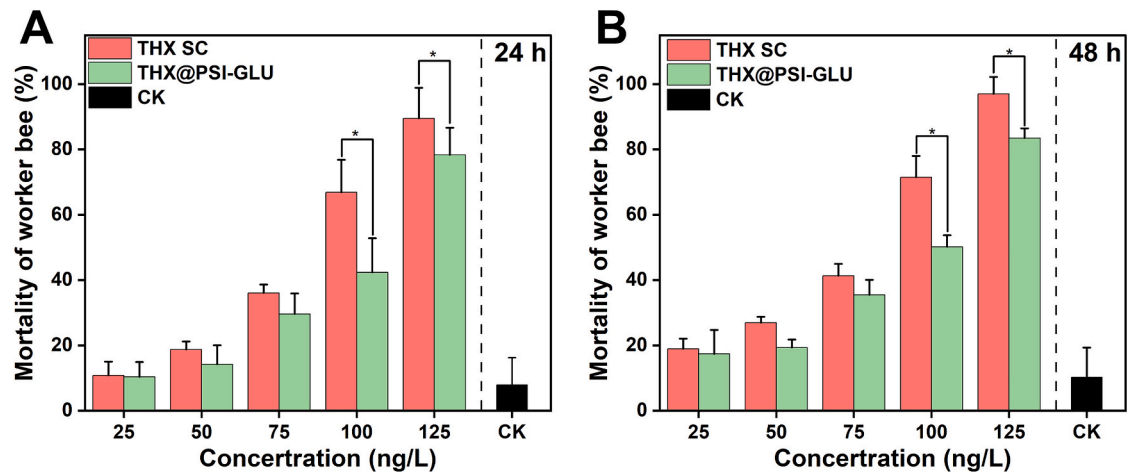


Fig. 9. The mortality of worker bees (*Apis mellifera*) treated with different concentrations of THX SC and THX@PSI-GLU (A) 24 h, and (B) 48 h. The data marked with an asterisk (*) indicate that the two treatments are significantly different ($p < 0.05$). The “CK” group was treated with sucrose water.

Table 2
Acute toxicity of different analytes against worker bees (*Apis mellifera*) at 24 and 48 h, respectively.

Formulation	Time	LD ₅₀ (ng a.i. /bee)	Slope ± SE	95 % confidence interval	χ ² (df)
THX SC	24 h	1.47	3.56 ± 0.50	1.29–1.69	13.29 (13)
	48 h	1.28	3.20 ± 0.45	1.10–1.48	18.07 (13)
THX@PSI-GLU	24 h	1.92	2.89 ± 0.48	1.64–2.36	14.85 (13)
	48 h	1.69	2.47 ± 0.43	1.39–2.06	14.23 (13)

these nanocarriers. These nanoparticles (THX@PSI-GABA, THX@PSI-ASP, and THX@PSI-GLU) demonstrated effective absorption and transport of THX within cowpea plants. Interestingly, the PSI-GLU nano-carrier exhibited exceptional performance in delivering THX, which could be rapidly accumulated to the leaves after drip irrigation. Compared with the THX SC formulation, the THX content in the leaves treated with THX@PSI-GLU was 2.3 times higher. Additionally, the THX@PSI-GLU nanoparticles not only enhanced the insecticidal efficacy against cowpea thrips but also reduced acute toxicity to bees. Moreover, THX@PSI-GLU was found to be harmless to cowpea plants and even promoted plant growth. This study provides strategies for improving the effective utilization of pesticides, sustainable control of thrips and reducing the risk to non-target organisms and the environment, all within the context of the target ecological risks of nanotechnological delivery of pesticides in plants meant for consumption.

Abbreviations

PSI	Polysuccinimide
AA	Amino acid
GLU	D-Glutamic acid
ASP	D-Aspartic acid
GABA	γ-Aminobutyric acid
SLS	Sodium dodecane-1-sulfonate
FITC	Fluorescein isothiocyanate
DMSO	Dimethyl sulfoxide
NPs	Nanoparticles

CRediT authorship contribution statement

Wenjie Deng: Writing – review & editing, Writing – original draft, Validation, Methodology, Investigation. **Yanheng Zhang:** Validation, Methodology, Investigation. **Liangheng He:** Methodology, Investigation, Conceptualization. **Li Xu:** Supervision, Editing. **Xulang Ye:** Validation, Methodology, Investigation. **Hanhong Xu:** Supervision, Resources, Methodology. **Li Zhu:** Supervision, Resources, Methodology. **Jinliang Jia:** Supervision, Resources, Project administration, Methodology, Funding acquisition.

Declaration of competing interest

The authors declare that they have no known competing financial interests or personal relationships that could have appeared to influence the work reported in this paper.

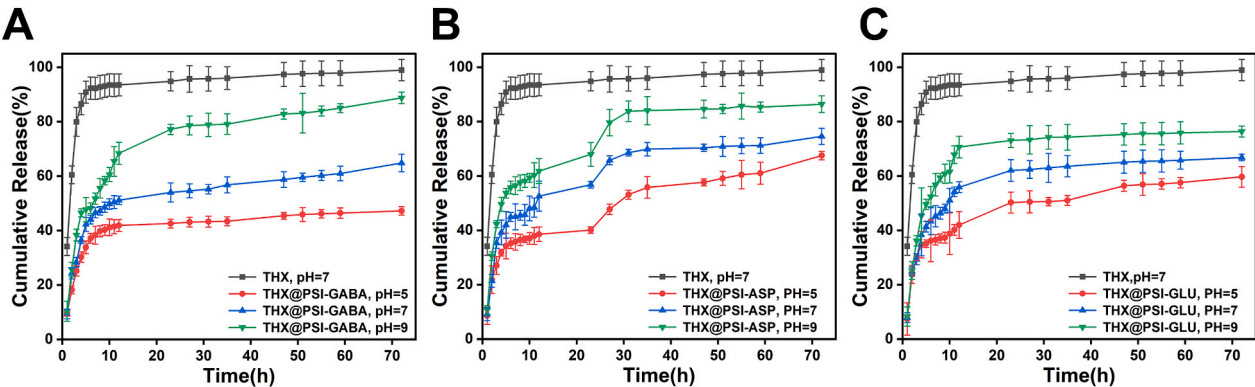


Fig. 10. Cumulative release of THX from (A) THX@PSI-GABA, (B) THX@PSI-ASP, and (C) THX@PSI-GLU at pH of 5, 7, and 9, respectively.

Data availability

Data will be made available on request.

Acknowledgments

This work was supported by the Guangdong Provincial Key Research and Development Program (2023B0202080001), Guangdong Basic and Applied Basic Research Foundation (2023A1515010609) and Research Fund of National Key Laboratory of Green Pesticide (GPLSCAU202407).

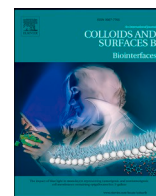
Appendix A. Supplementary data

Supplementary data to this article can be found online at <https://doi.org/10.1016/j.scitotenv.2024.176327>.

References

- Agbahoungba, S., Datinon, B., Billah, M., Tossou, H.T., Agoyi, E.E., Kpoviessi, A.D., Assogbadjo, A.E., Sinsin, B., 2021. Flower bud thrips (*Megalurothrips sjostedti* Trybom) population diversity and sources of resistance among Benin cowpea germplasm. *Ann. Appl. Biol.* 179 (3), 395–404. <https://doi.org/10.1111/aab.12713>.
- Ahmad, M., Mudgil, P., Gani, A., Hamed, F., Masoodi, F.A., Maqsood, S., 2019. Nano-encapsulation of catechin in starch nanoparticles: characterization, release behavior and bioactivity retention during simulated *in-vitro* digestion. *Food Chem.* 270, 95–104. <https://doi.org/10.1016/j.foodchem.2018.07.024>.
- Avellan, A., Yun, J., Zhang, Y.L., Spielman-Sun, E., Unrine, J.M., Thieme, J., Li, J.R., Lombi, E., Bland, G., Lowry, G.V., 2019. Nanoparticle size and coating chemistry control foliar uptake pathways, translocation, and leaf-to-rhizosphere transport in wheat. *ACS Nano* 13 (5), 5291–5305. <https://doi.org/10.1021/acs.nano.8b09781>.
- Boliko, M.C., 2019. FAO and the situation of food security and nutrition in the world. *J. Nutr. Sci. Vitaminol.* 65 (Supplement), S4–S8. <https://doi.org/10.3177/jnsv.65.S4>.
- Chaud, M., Souto, E.B., Zielinska, A., Severino, P., Batain, F., Oliveira, J., Alves, T., 2021. Nanopesticides in agriculture: benefits and challenge in agricultural productivity, toxicological risks to human health and environment. *Toxics* 9 (6), 19. <https://doi.org/10.3390/toxics9060131>.
- Gan, W., Kong, X.B., Fang, J.X., Shi, X., Zhang, S.F., Li, Y.X., Qu, L.J., Liu, F., Zhang, Z., Zhang, F.B., Zhang, X.Y., 2023. A pH-responsive fluorescent nanopesticide for selective delivery and visualization in pine wood nematode control. *Chem. Eng. J.* 463, 13. <https://doi.org/10.1016/j.cej.2023.142353>.
- Gitonga, H.W., Kyamanywa, S., Arusei, P., Lukanda, M.M., Edema, R., Dramadri, I.O., 2022. Genotype x environment interaction influence secondary metabolite in cowpea infested by flower bud thrips. *Agronomy-Basel* 12 (12), 22. <https://doi.org/10.3390/agronomy12123210>.
- He, X.J., Deng, H., Hwang, H.M., 2019. The current application of nanotechnology in food and agriculture. *J. Food Drug Anal.* 27 (1), 1–21. <https://doi.org/10.1016/j.jfda.2018.12.002>.
- Hernández-González, M., Berumen, C.M.P., Ruiz, H.S., Salazar, C.V.R., Paz, J.F.H., Olivas-Armendáriz, I., Martel-Estrada, S.A., González, C.A.R., 2017. Polysuccinimide functionalized with oregano's essential oil extracts, an antimicrobial extended release bio-material. *Mater. Lett.* 191, 73–76. <https://doi.org/10.1016/j.matlet.2017.01.035>.
- Hu, P.G., An, J., Faulkner, M.M., Wu, H.H., Li, Z.H., Tian, X.L., Giraldo, J.P., 2020. Nanoparticle charge and size control foliar delivery efficiency to plant cells and organelles. *ACS Nano* 14 (7), 7970–7986. <https://doi.org/10.1021/acsnano.9b09178>.
- Hu, Y.Q., Wu, T.T., Wu, C.H., Fu, S.L., Yuan, C.H., Chen, S.G., 2017. Formation and optimization of chitosan-nisin microcapsules and its characterization for antibacterial activity. *Food Control* 72, 43–52. <https://doi.org/10.1016/j.foodcont.2016.06.013>.
- Huang, Y.Q., Yang, Y.L., Liang, B., Lu, S.H., Yuan, X.Y., Jia, Z., Liu, J., Liu, Y.A., 2023. Green nanopesticide: pH-responsive eco-friendly pillar 5 arene-modified selenium nanoparticles for smart delivery of carbendazim to suppress sclerotinia diseases. *ACS Appl. Mater. Interfaces* 15 (13), 16448–16459. <https://doi.org/10.1021/acsaami.2c23241>.
- Islam, S.N.U., Kouser, S., Hassan, P., Asghar, M., Shah, A.A., Khan, N.A., 2024. Gamma-aminobutyric acid interactions with phytohormones and its role in modulating abiotic and biotic stress in plants. *Stress Biol.* 4 (1), 36. <https://doi.org/10.1007/s44154-024-00180-y>.
- Jeon, S.J., Zhang, Y.L., Castillo, C., Nava, V., Ristroph, K., Therrien, B., Meza, L., Lowry, G.V., Giraldo, J.P., 2024. Targeted delivery of sucrose-coated nanocarriers with chemical cargoes to the plant vasculature enhances long-distance translocation. *Small* 20 (7), 15. <https://doi.org/10.1002/sml.202304588>.
- Jiang, Q.H., Peng, M., Yin, M.Z., Shen, J., Yan, S., 2022. Nanocarrier-loaded imidaclothiz promotes plant uptake and decreases pesticide residue. *Int. J. Mol. Sci.* 23 (12), 16. <https://doi.org/10.3390/ijms23126651>.
- Jiang, X.Y., Xie, Y., Ren, Z.F., Ganeteg, U., Lin, F., Zhao, C., Xu, H.H., 2018. Design of a new glutamine-fipronil conjugate with α -amino acid function and its uptake by *A-thaliana* lysine histidine transporter 1 (*AtLHT1*). *J. Agric. Food Chem.* 66 (29), 7597–7605. <https://doi.org/10.1021/acs.jafc.8b02287>.
- Kah, M., Hofmann, T., 2014. Nanopesticide research: current trends and future priorities. *Environ. Int.* 63, 224–235. <https://doi.org/10.1016/j.envint.2013.11.015>.
- Kah, M., Tufenkji, N., White, J.C., 2019. Nano-enabled strategies to enhance crop nutrition and protection. *Nat. Nanotechnol.* 14 (6), 532–540. <https://doi.org/10.1038/s41565-019-0439-5>.
- Kessler, S.C., Tiedeken, E.J., Simcock, K.L., Derveau, S., Mitchell, J., Softley, S., Stout, J. C., Wright, G.A., 2015. Bees prefer foods containing neonicotinoid pesticides. *Nature* 521 (7550), 74–U145. <https://doi.org/10.1038/nature14414>.
- Kusi, F., Nboyine, J.A., Abudulai, M., Seidu, A., Agyare, Y.R., Sugri, I., Zakaria, M., Owusu, R.K., Nutsugah, S.K., Asamoah, L., 2019. Cultivar and insecticide spraying time effects on cowpea insect pests and grain yield in northern Ghana. *Ann. Agric. Sci.* 64 (1), 121–127. <https://doi.org/10.1016/j.aaoas.2019.03.001>.
- Liang, W.L., Xie, Z.G., Cheng, J.L., Xiao, D.X., Xiong, Q.Y., Wang, Q.W., Zhao, J.H., Gui, W.J., 2021. A light-triggered pH-responsive metal-organic framework for smart delivery of fungicide to control sclerotinia diseases of oilseed rape. *ACS Nano* 15 (4), 6987–6997. <https://doi.org/10.1021/acsnano.0c10877>.
- Liang, W.L., Zhang, J.D., Wurm, F.R., Wang, R., Cheng, J.L., Xie, Z.A., Li, X.B., Zhao, J. H., 2022. Lignin-based non-crosslinked nanocarriers: a promising delivery system of pesticide for development of sustainable agriculture. *Int. J. Biol. Macromol.* 220, 472–481. <https://doi.org/10.1016/j.ijbiomac.2022.08.103>.
- Liu, P.P., Qin, Z.F., Feng, M.Y., Zhang, L., Huang, X.Z., Shi, W.P., 2020. The male-produced aggregation pheromone of the bean flower thrips *Megalurothrips usitatus* in China: identification and attraction of conspecifics in the laboratory and field. *Pest Manag. Sci.* 76 (9), 2986–2993. <https://doi.org/10.1002/ps.5844>.
- Ma, Y.J., Wang, Y.M., Zhao, R., Wang, Z.J., Li, S., Yu, M., Pang, S., Guo, X.Y., Xu, Y., Wu, X.M., 2023. pH-responsive ZIF-8 film-coated mesoporous silica nanoparticles for clean, targeted delivery of fungicide and environmental hazard reduction. *J. Environ. Chem. Eng.* 11 (6), 11. <https://doi.org/10.1016/j.jece.2023.111513>.
- Mariyam, S., Upadhyay, S.K., Chakraborty, K., Verma, K.K., Duhan, J.S., Muneer, S., Meena, M., Sharma, R.K., Ghodake, G., Seth, C.S., 2024. Nanotechnology, a frontier in agricultural science, a novel approach in abiotic stress management and convergence with new age medicine-a review. *Sci. Total Environ.* 912, 15. <https://doi.org/10.1016/j.scitotenv.2023.169097>.
- Nabirye, J., Nampala, P., Kyamanywa, S., Ogenga-Latigo, M.W., Wilson, H., Adipala, E., 2003. Determination of damage-yield loss relationships and economic injury levels of flower thrips on cowpea in eastern Uganda. *Crop Prot.* 22 (7), 911–915. [https://doi.org/10.1016/s0261-2194\(03\)00086-3](https://doi.org/10.1016/s0261-2194(03)00086-3).
- Naz, M., Dai, Z.C., Hussain, S., Tariq, M., Danish, S., Khan, I.U., Qi, S.S., Du, D.L., 2022. The soil pH and heavy metals revealed their impact on soil microbial community. *J. Environ. Manage.* 321, 8. <https://doi.org/10.1016/j.jenvman.2022.115770>.
- Ngakou, A., Tamò, M., Parh, I.A., Nwaga, D., Ntonifor, N.N., Korie, S., Nebane, C.L.N., 2008. Management of cowpea flower thrips, *Megalurothrips sjostedti* (Thysanoptera, Thripidae). *Cameroon. Crop Prot.* 27 (3–5), 481–488. <https://doi.org/10.1016/j.cropro.2007.08.002>.
- Omo-Ikerodah, E.E., Fawole, I., Fatokun, C.A., 2008. Genetic mapping of quantitative trait loci (QTLs) with effects on resistance to flower bud thrips (*Megalurothrips sjostedti*) identified in recombinant inbred lines of cowpea (*Vigna unguiculata* (L.) Walp). *Afr. J. Biotechnol.* 7 (3), 263–270. <https://doi.org/10.5897/AJB07.222>.
- Shangquan, W.J., Huang, Q.L., Chen, H.P., Zheng, Y.Y., Zhao, P.Y., Cao, C., Yu, M.L., Cao, Y.S., Cao, L.D., 2024. Making the complicated simple: a minimizing carrier strategy on innovative Nanopesticides. *Nano-Micro Lett.* 16 (1), 16. <https://doi.org/10.1007/s40820-024-01413-5>.
- Su, S.C., Chen, L., Hao, L., Chen, H.Y., Zhou, X.H., Zhou, H.J., 2021. Preparation of p-amino salicylic acid-modified polysuccinimide as water-based nanocarriers for enhancing pesticide stability and insecticidal activity. *Coll. Surf. B Biointerf.* 207, 10. <https://doi.org/10.1016/j.colsurfb.2021.111990>.
- Su, Y.M., Ashworth, V., Kim, C., Adeleye, A.S., Rolshausen, P., Roper, C., White, J., Jassby, D., 2019. Delivery, uptake, fate, and transport of engineered nanoparticles in plants: a critical review and data analysis. *Environ. Sci.-Nano.* 6 (8), 2311–2331. <https://doi.org/10.1039/c9en00461k>.
- Tang, L.D., Guo, L.H., Ali, A., Desneux, N., Zang, L.S., 2022. Synergism of qdjuvants mixed with spinetoram for the management of bean flower thrips, megalurothrips usitatus (Thysanoptera: Thripidae) in cowpeas. *J. Econ. Entomol.* 115 (6), 2013–2019. <https://doi.org/10.1093/jeet/toac149>.
- Tang, L.D., Guo, L.H., Wu, J.H., Zang, L.S., 2023. Thrips in genus *Megalurothrips* (Thysanoptera: Thripidae): biodiversity, bioecology, and IPM. *J. Integr. Pest Manag.* 14 (1), 11. <https://doi.org/10.1093/jipm/pmad006>.
- Teka, T.A., Retta, N., Bultosa, G., Admassu, H., Astatkie, T., 2020. Protein fractions, *in vitro* protein digestibility and amino acid composition of select cowpea varieties grown in Ethiopia. *Food Biosci.* 36, 9. <https://doi.org/10.1016/j.fbio.2020.100634>.
- Torma, V., Gyenes, T., Szakács, Z., Noszá, B., Némethy, A., Zrínyi, M., 2007. Novel amino acid-based polymers for pharmaceutical applications. *Polym. Bull.* 59 (3), 311–318. <https://doi.org/10.1007/s00289-007-0774-9>.
- Usman, M., Farooq, M., Wakeel, A., Nawaz, A., Cheema, S.A., Rehman, H.U., Ashraf, I., Sanaullah, M., 2020. Nanotechnology in agriculture: current status, challenges and future opportunities. *Sci. Total Environ.* 721, 16. <https://doi.org/10.1016/j.scitotenv.2020.137778>.
- Wu, H.X., Hu, P.T., Xu, Y., Xiao, C.X., Chen, Z.B., Liu, X.J., Jia, J.L., Xu, H.H., 2021. Phloem delivery of fludioxonil by plant amino acid transporter-mediated polysuccinimide nanocarriers for controlling fusarium wilt in banana. *J. Agric. Food Chem.* 69 (9), 2668–2678. <https://doi.org/10.1021/acs.jafc.0c07028>.
- Wu, T.Y., Zhao, K.F., Zhang, C.H., Zhong, T.J., Li, Z.L., Bao, Z.P., Gao, Y.X., Du, F.P., 2022. Promising delivery platform for smart pest control with high water-retaining capacity. *ACS Appl. Mater. Interfaces* 14 (49), 55062–55074. <https://doi.org/10.1021/acsaami.2c15737>.

- Wu, T.Y., Zhao, K.F., Liu, S.Y., Bao, Z.P., Zhang, C.H., Wu, Y.L., Song, R.D., Gu, Y.C., Gao, Y.X., Du, F.P., 2023. Promising nanocarriers endowing non-systemic pesticides with upward translocation ability and microbial community enrichment effects in soil. *Chem. Eng. J.* 474, 14. <https://doi.org/10.1016/j.cej.2023.145570>.
- Xiang, H.M., Meng, J., Shao, W.B., Zeng, D., Ji, J., Wang, P.Y., Zhou, X., Qi, P.Y., Liu, L.W., Yang, S., 2023. Plant protein-based self-assembling core-shell nanocarrier for effectively controlling plant viruses: evidence for nanoparticle delivery behavior, plant growth promotion, and plant resistance induction. *Chem. Eng. J.* 464, 15. <https://doi.org/10.1016/j.cej.2023.142432>.
- Xiao, D.X., Wu, H.X., Zhang, Y.L., Kang, J., Dong, A., Liang, W.L., 2022a. Advances in stimuli-responsive systems for pesticides delivery: recent efforts and future outlook. *J. Control. Release* 352, 288–312. <https://doi.org/10.1016/j.jconrel.2022.10.028>.
- Xiao, S.T., Shoaib, A., Xu, J., Lin, D.H., 2022b. Mesoporous silica size, charge, and hydrophobicity affect the loading and releasing performance of lambda-cyhalothrin. *Sci. Total Environ.* 831, 10. <https://doi.org/10.1016/j.scitotenv.2022.154914>.
- Xin, X.P., He, Z.L., Hill, M.R., Niedz, R.P., Jiang, X.J., Sumerlin, B.S., 2018. Efficiency of biodegradable and pH-responsive polysuccinimide nanoparticles (PSI-NPs) as smart nanodelivery systems in grapefruit: in vitro cellular investigation. *Macromol. Biosci.* 18 (7), 8. <https://doi.org/10.1002/mabi.201800159>.
- Xiong, Q.Y., Liang, W.L., Shang, W.X., Xie, Z.A., Cheng, J.L., Yu, B., Fang, Y., Sun, L., Zhao, J.H., 2024. Bidirectional uptake, transfer, and transport of dextran-based nanoparticles in plants for multidimensional enhancement of pesticide utilization. *Small* 20 (8), 14. <https://doi.org/10.1002/sml.202305693>.
- Xiong, S.L., Yao, X.L., Li, A.L., 2013. Antioxidant properties of peptide from cowpea seed. *Int. J. Food Prop.* 16 (6), 1245–1256. <https://doi.org/10.1080/10942912.2011.582976>.
- Xu, C.L., Shan, Y.P., Bilal, M., Xu, B., Cao, L.D., Huang, Q.L., 2020. Copper ions chelated mesoporous silica nanoparticles via dopamine chemistry for controlled pesticide release regulated by coordination bonding. *Chem. Eng. J.* 395, 13. <https://doi.org/10.1016/j.cej.2020.125093>.
- Yang, L.P., Kaziem, A.E., Lin, Y.G., Li, C., Tan, Y.T., Huang, S.Q., Cheng, D.M., Xu, H.H., Zhang, Z.X., 2021. Carboxylated β -cyclodextrin anchored hollow mesoporous silica enhances insecticidal activity and reduces the toxicity of indoxacarb. *Carbohydr. Polym.* 266, 10. <https://doi.org/10.1016/j.carbpol.2021.118150>.
- Yang, S., Tang, J.H., Li, B.J., Yao, G.K., Peng, H.X., Pu, C.M., Zhao, C., Xu, H.H., 2023. Rational design of insecticidal isoxazolines containing sulfonamide or sulfonamide structure as antagonists of GABA receptors with reduced toxicities to honeybee and zebrafish. *J. Agric. Food Chem.* 71 (39), 14211–14220. <https://doi.org/10.1021/acs.jafc.3c03459>.
- Yu, X.R., Tariq, T., Guo, L.H., Wu, S.Y., Tang, L.D., Zang, L.S., 2023. Assessing the effectiveness of imidacloprid and thiamethoxam via root irrigation against *Megalurothrips usitatus* (Thysanoptera: Thripidae) and its residual effects on cowpea. *J. Econ. Entomol.* 116 (5), 1767–1775. <https://doi.org/10.1093/jeet/toad166>.
- Zakeri, A., Kouhbanani, M.A.J., Beheshtkhoo, N., Beigi, V., Mousavi, S.M., Hashemi, S.A.R., Karimi Zade, A., Amani, A.M., Savardashtaki, A., Mirzaei, E., Jahandideh, S., Movahedpour, A., 2018. Polyethylenimine-based nanocarriers in co-delivery of drug and gene: a developing horizon. *Nano Rev. Exp.* 9 (1), 1488497. <https://doi.org/10.1080/20022727.2018.1488497>.
- Zhang, L., Yan, S., Li, M.J., Wang, Y., Shi, X.Y., Liang, P., Yin, M.Z., Shen, J., Gao, X.W., 2022a. Nanodelivery system alters an insect growth regulator's action mode: from oral feeding to topical application. *ACS Appl. Mater. Interfaces* 9. <https://doi.org/10.1021/acsami.2c08239>.
- Zhang, Q., Ma, C., Duan, Y., Wu, X.P., Lv, D.Z., Luo, J.H., 2022b. Determination and dietary intake risk assessment of 35 pesticide residues in cowpea (*Vigna unguiculata* L. Walp) from Hainan province, China. *Sci. Rep.* 12 (1), 11. <https://doi.org/10.1038/s41598-022-09461-w>.
- Zhang, X.Q., He, Y., Yuan, Z.T., Shen, G.M., Zhang, Z., Niu, J.Z., He, L., Wang, J.J., Qian, K., 2023. A pH- and enzymatic-responsive nanopesticide to control pea aphids and reduce toxicity for earthworms. *Sci. Total Environ.* 861, 8. <https://doi.org/10.1016/j.scitotenv.2022.160610>.
- Zhang, Y., Chen, D., Du, M.Y., Ma, L.L., Li, P., Qin, R., Yang, J.R., Yin, Z.B., Wu, X.Z., Xu, H.H., 2021. Insights into the degradation and toxicity difference mechanism of neonicotinoid pesticides in honeybees by mass spectrometry imaging. *Sci. Total Environ.* 774, 11. <https://doi.org/10.1016/j.scitotenv.2021.145170>.
- Zheng, H., Powell, J.E., Steele, M.I., Dietrich, C., Moran, N.A., 2017. Honeybee gut microbiota promotes host weight gain via bacterial metabolism and hormonal signaling. *Proc. Natl. Acad. Sci.* 114 (18), 4775–4780. <https://doi.org/10.1073/pnas.1701819114>.
- Zhong, X.M., Su, G.F., Hao, L., Chen, H.Y., Li, C., Xu, H., Zhou, H.J., Zhou, X.H., 2024. Foliar application of glycine-functionalized nanopesticides for effective prevention and control of root-knot nematodes via a targeted delivery strategy. *Pest Manag. Sci.* 80 (4), 2120–2130. <https://doi.org/10.1002/ps.7948>.
- Zhu, F., Liu, X.G., Cao, L.D., Cao, C., Li, F.M., Chen, C.J., Xu, C.L., Huang, Q.L., Du, F.P., 2018. Uptake and distribution of fenoxanil-loaded mesoporous silica nanoparticles in rice plants. *Int. J. Mol. Sci.* 19 (10), 13. <https://doi.org/10.3390/ijms19102854>.



A Pyr-loaded polymer microparticle for effectively controlling *Solenopsis invicta* (Hymenoptera: Formicidae) in the nest

Meichen Liu^{a,b}, Kaijie Xu^{a,b}, Ning Zhao^{a,c}, Chi Yao^{a,b}, Xixin Zheng^{a,b}, Jinliang Jia^{a,c,*}, Hanhong Xu^{a,b,*}

^a National Key Laboratory of Green Pesticide, South China Agricultural University, Guangzhou, China

^b Key Laboratory of Natural Pesticide and Chemical Biology, Ministry of Education, South China Agricultural University, Guangzhou, China

^c Key Laboratory for Biobased Materials and Energy of Ministry of Education, College of Materials and Energy, South China Agricultural University, Guangzhou, China

ARTICLE INFO

Keywords:

Microparticles
Solenopsis invicta Buren
Polysuccinimide
Releasing

ABSTRACT

Human interference and incorrect use of pesticides are easy to induce red imported fire ant (RIFA) escape and migrate from a nest, resulting in ineffective control of RIFA. In order to avoid RIFA alert, we designed an amphiphilic PSI-mPEG-Boc-DAH loaded Pyr to make the microparticles with effective controlled release. The investigation showed that the quantity of Pyr released by Pyr@PSI-mPEG-Boc-DAH under acidic environment was only $36.40 \pm 1.90\%$ at 48 h, whereas the release rate of original Pyr was $75.23 \pm 5.71\%$. And the RIFA mortality rate of 1 ppm Pyr in Pyr@PSI-mPEG-Boc-DAH microparticles at 48 h was only 7.78%, which was significantly lower than that of the Pyr (47.78%). Furthermore, the death rate increased sharply after 48 h, and reached 95.84% within a week after using Pyr@PSI-mPEG-Boc-DAH microparticles. Moreover, PSI-mPEG-Boc-DAH carriers could be absorbed and even transported to crop of the RIFA for subsequent trophallaxis by using fluorescence tracking. In the field experiment, the reduction rate of Pyr@PSI-mPEG-Boc-DAH treatment was achieved 99.89% after 7 d. Pyr@PSI-mPEG-Boc-DAH didn't cause RIFA to be alarmed within 48 h and could kill nearly all of ants in the nest after 7 d, which showed a very good control effect in the field experiment. This work provided a new idea and guidance for the effective control RIFA and the development of sustainable agriculture.

1. Introduction

Solenopsis invicta Buren, commonly known as the red imported fire ant (RIFA), is included in the list of dangerous biological species as a quarantine object [1]. The ant stings humans, pets, farm animals, and wildlife, as well as damaging farm, electrical equipments and irrigation systems. Due to its ferocious habits, high fecundity, mixed diet, strong competitiveness and easy formation of high-density populations in newly invaded areas, RIFA is listed as one of the 100 most destructive invasive species by the International Union for Conservation of Nature (IUCN) [2,3]. According to monitoring by the Ministry of Agriculture and Rural Affairs, RIFA have spread to 435 counties (cities and districts), and 191 new RIFA have occurred in county-level administrative regions in the past five years [4]. In addition, the geographical range that may be suitable for its survival is very wide, so it has become a serious and dangerous pest of high concern [5–8].

Chemical control is the most widely used method, which can rapidly

control the spread of RIFA. At present, there are mainly pharmaceutical nesting and poison bait methods. However, the rapid effect of traditional agents and inappropriate use will immediately cause RIFA to be alert, resulting in the death of only a small number of RIFA. The most RIFA nest relocation and spread, which brings great problems for controlling the whole nest annihilation of RIFA. Besides, the excessive use of chemical pesticide has caused various environmental problems [9,10]. Thus, there is an urgent need to develop new agents to control RIFA.

In recent years, microparticles as a new type of drug carriers, have attracted more and more researchers' active attention. Microparticles have the advantages of molecular designability, stability, and strong permeability, which also provides new scientific methods for modern agriculture, significantly increasing the effectiveness of pesticides and agricultural yields. For example, Ye *et al.* reported that polysuccinimide (PSI) conjugated with glycine methylester nanoparticles could internalize into the intestinal wall of *Plutella xylostella*, thus increasing the penetration of the drug and enhancing the insecticidal activity [11]. Xin

* Corresponding authors at: National Key Laboratory of Green Pesticide, South China Agricultural University, Guangzhou, China.

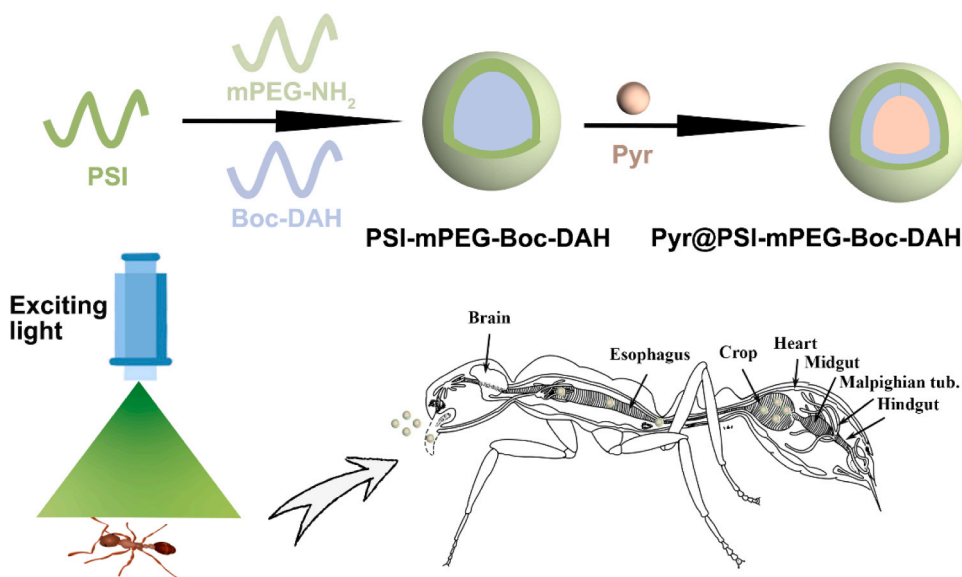
E-mail addresses: jiajinliang@scau.edu.cn (J. Jia), hxxu@scau.edu.cn (H. Xu).

<https://doi.org/10.1016/j.colsurfb.2023.113675>

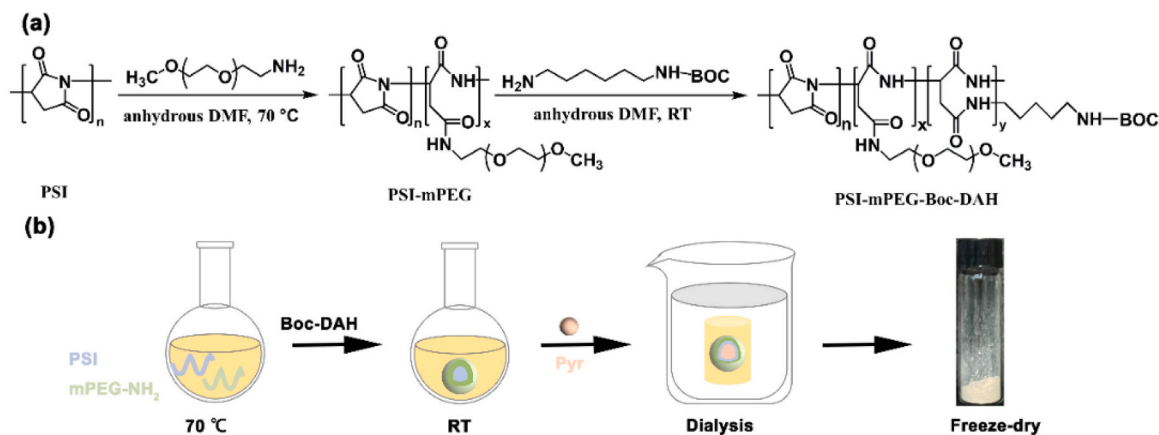
Received 7 October 2023; Received in revised form 14 November 2023; Accepted 25 November 2023

Available online 30 November 2023

0927-7765/© 2023 Elsevier B.V. All rights reserved.



Scheme 1. Illustration for the synthesis of Pyr@PSI-mPEG-Boc-DAH microparticles and their feeding mechanism of RIFA.



Scheme 2. (a) Synthesis route of PSI-mPEG-Boc-DAH. (b) Schematic illustration of preparation procedure of Pyr@PSI-mPEG-Boc-DAH.

et al. reported that biodegradable pH-responsive polysuccinimide nanoparticles (PSI-NPs) had potential of application in agriculture for mitigating phloem-limited diseases, such as citrus huanglongbing [12]. Su *et al.* reported that water-dispersible functionalized polysuccinimide nanoparticles (PAD) could potentially and effectively promote drug stability and biological activity in agriculture [13].

PSI has the characteristic of natural degradability, which doesn't cause environmental pollution. And methoxypolyethylene glycol amine (mPEG-NH₂) was conjugated to improve its hydrophilic [14]. We also introduced *N*-Boc-1,6-diaminohexane (Boc-DAH) because its relatively long alkyl side chains in polyaspartamide were preferred for microparticles formation [15,16]. Pyraquinil (Pyr) was a new pesticide independently developed in our laboratory, which had high activity against *Plutella xylostella* and *Spodoptera frugiperda*, and it had not been reported to control RIFA [17,18]. So, in this study, an amphiphilic copolymer was designed using PSI (Scheme 1), mPEG-NH₂ and Boc-DAH to encapsulate Pyr for the sustainable control of RIFA. Hence, the use of the amphiphilic microparticles loaded Pyr to control RIFA were significant strategies for killing all of ants in the nest. The obtained microparticle was characterized roundly, and the slowly release performance, thermogravimetric analysis, release power curves were investigated in detail. Moreover, the insecticidal activity of RIFA and control efficacy in field, as well as the imaging of PSI-mPEG-Boc-DAH in RIFA were investigated. This study

proved that Pyr@PSI-mPEG-Boc-DAH could be used as a promising platform for the sustainable control of pest in agriculture.

2. Materials and methods

2.1. Materials

Polysuccinimide (PSI: Mw = 5.6 kDa, 99%) was supplied by Hubei YuanChengSaichuang Technology Co., Ltd. (Wuhan, China). Methoxypolyethylene glycol amine (mPEG-NH₂) (Mw = 2000), *N*-Boc-1,6-diaminohexane (Boc-DAH) and anhydrous N, N-Dimethylformamide (DMF) were obtained from Shanghai Acme Biochemical Co., Ltd. (Shanghai, China). Pyraquinil was synthesised by the National Key Laboratory of Green Pesticide, South China Agricultural University [17]. Tween 80 was procured from Tianjin Fuyu Fine Chemical Co., Ltd. (Tianjin, China). Acetonitrile at high-performance liquid chromatography (HPLC) grade were obtained from Beijing DingGuoChangsheng Biotechnology Co., Ltd. (Beijing, China). All other reagents and chemicals were commercially available and used without any purification.

2.2. Synthesis of PSI-mPEG-Boc-DAH

To synthesize PSI-mPEG-Boc-DAH, some modifications were made

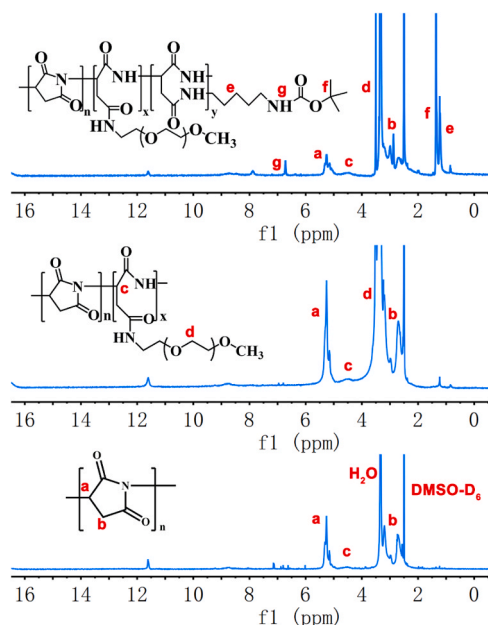


Fig. 1. ^1H NMR spectra of PSI, PSI-mPEG and PSI-mPEG-Boc-DAH in DMSO-D_6 .

according to previous methods [19,20], PSI (240 mg) and mPEG-NH₂ (98.8 mg) were dissolved in anhydrous DMF (10 mL). The mixture was heated at 70 °C for 48 h under nitrogen gas. Then the solution was cooled to room temperature, and Boc-DAH (165 μL) was added dropwise to the solution. The solution was stirred at room temperature overnight. After reaction, the residual monomers and solvents were removed using a dialysis membrane (molecular weight cut-off 3500 Da) under room temperature for 3 d, and then freeze-dried.

2.3. Synthesis of Pyr@PSI-mPEG-Boc-DAH

After PSI-mPEG-Boc-DAH was synthesized, 100 mg Pyr was added to the above 10 mL of reaction product, then stirred at room temperature for 30 min. After mixed evenly, the residual monomers and solvents were removed using a dialysis membrane for 3 d, and then freeze-dried.

2.4. Loading capacity of Pyr@PSI-mPEG-Boc-DAH

Pyr@PSI-mPEG-Boc-DAH (10 mg) was dispersed in 4 mL of acetonitrile and transferred to an ultrasonic bath for 2 h to completely disassociate the Pyr. The resulting suspension was centrifuged (10,000 rpm, 10 min), and the supernatant collected. The amount of Pyr in the supernatant was determined by high-performance liquid chromatography (HPLC) with the help of a Pyr calibration curve ($y = 10.84x - 8.01$, $R^2 = 0.99967$) (Fig. S1). Agilent 1100 HPLC system equipped with a reversed phase column (ZORBAX SB-C₁₈, 3.5 μm , 50 \times 2.1 mm; Agilent Technologies, Santa Clara, CA, USA) for HPLC. The mobile phase consisted of acetonitrile and water (60:40, v/v) flowing at a rate of 1 mL/min. Analysis was performed at 210 nm, the maximum absorption wavelength of Pyr, and each measurement was analyzed in triplicate. The Pyr loading capacity (LC) was calculated by using the following equation:

$$\text{LC} = \frac{\text{weight of pyraquinil loaded}}{\text{weight of Pyr@mPEG - Boc - DAH - PSI}} \times 100\%$$

2.5. Characterization

The PSI-mPEG-Boc-DAH was centrifuged by a table model high speed centrifuge (TG-16, China) and measured by a nuclear magnetic resonance spectrometer (AV III 600; Bruker, Berlin, Germany). The

structural changes of microparticles were characterized by a Fourier transform infrared spectrometry (FTIR) (Nicolet IS10; Thermo Fisher Scientific GmbH, Dreieich, Germany) with quantitative means. Scanning electron microscopy (SEM) (Hitachi SU-8010, Japan) and (TEM) (FEI/Talos L120C, USA) was used to observe the morphological characteristics of the microparticles. XPS was carried out by using Thermo Scientific K-Alpha Nexsa X-ray photoelectron spectrometer (K-Alpha, USA). Thermogravimetric analysis (TGA) was performed on a TGA system (TG209F1LibraTM, Germany) under N₂ from 30° to 800°C at a heating rate of 10 °C/min.

2.6. In Vitro Release at Acid pH Conditions

According to the method of Liang *et al.* to assess the pH-responsive release properties of the drug-loaded nanoparticles [21]. 5 mg of Pyr and Pyr@PSI-mPEG-Boc-DAH containing 5 mg of Pyr was respectively added to 3 mL 50% PBS ethanol-water solution (50:50, v/v), and the suspension were moved into the dialysis bags (DWCO = 3500 Da), which was submerged into 97 mL of release medium in 200 mL reagent bottles. The release system was under slow magnetic stirring at room temperature. Periodically, 1 mL of the release medium was taken, followed by the addition of the same volume of fresh medium to maintain the total volume. The cumulative release amount of Pyr was analyzed using HPLC.

2.7. Release kinetics investigation

The release kinetics of Pyr from Pyr@PSI-mPEG-Boc-DAH were analyzed using zero-order, first-order and Higuchi models as follows [22]:

Zero-order model: $M_t/M_\infty = kt$

First-order model: $M_t/M_\infty = 1 - \exp^{-kt}$

Higuchi model: $M_t/M_\infty = kt^{1/2}$

where M_t amount of Pyr released at time t , M_∞ the maximal amount of the released Pyr at infinite time, k was the rate constant of Pyr.

The correlation coefficient (R^2) in each case was obtained after fitting the pure data to each equation.

2.8. Bioactivity against RIFA

The biological toxicity test of RIFA was conducted according to previous reported method with slight modifications [23,24]. The medium-size RIFA were placed in a 250 mL beaker, the vertical wall was coated with Teflon emulsion, and cut off the supply of water and food. After 6 h of starvation, 1 mL of the sample solution in the centrifuge tube was placed at the bottom of the beaker, compared to 1 mL of water in the control group. All treatments were repeated three times, with 30 worker ants for each treatment. The worker ants were maintained at 25 ± 2 °C and the relative humidity was $70 \pm 10\%$. The number of dead ants was recorded at different times after treatment.

2.9. Distribution of PSI-mPEG-Boc-DAH-FITC-cad

To investigate if PSI-mPEG-Boc-DAH carriers could be absorbed by RIFA and its distribution after absorption, PSI-mPEG-Boc-DAH-FITC-cad was synthesized for experiment. FITC-cad was added to the solution which the PSI-mPEG-Boc-DAH reacted. After one day of room temperature reaction, the residual monomers and solvents were removed using a dialysis membrane for 3 d, and then freeze-dried. The PSI-mPEG-Boc-DAH-FITC-cad was fed to RIFA in the same way with bioactivity treatment. The RIFA were sectioned at 40 μm thickness using a freezing microtome (CM1950, Lecia Microsystem Inc., Wetzlar, Germany) at -20 °C after 6, 12, 24 h. The distribution of PSI-mPEG-Boc-DAH-FITC-

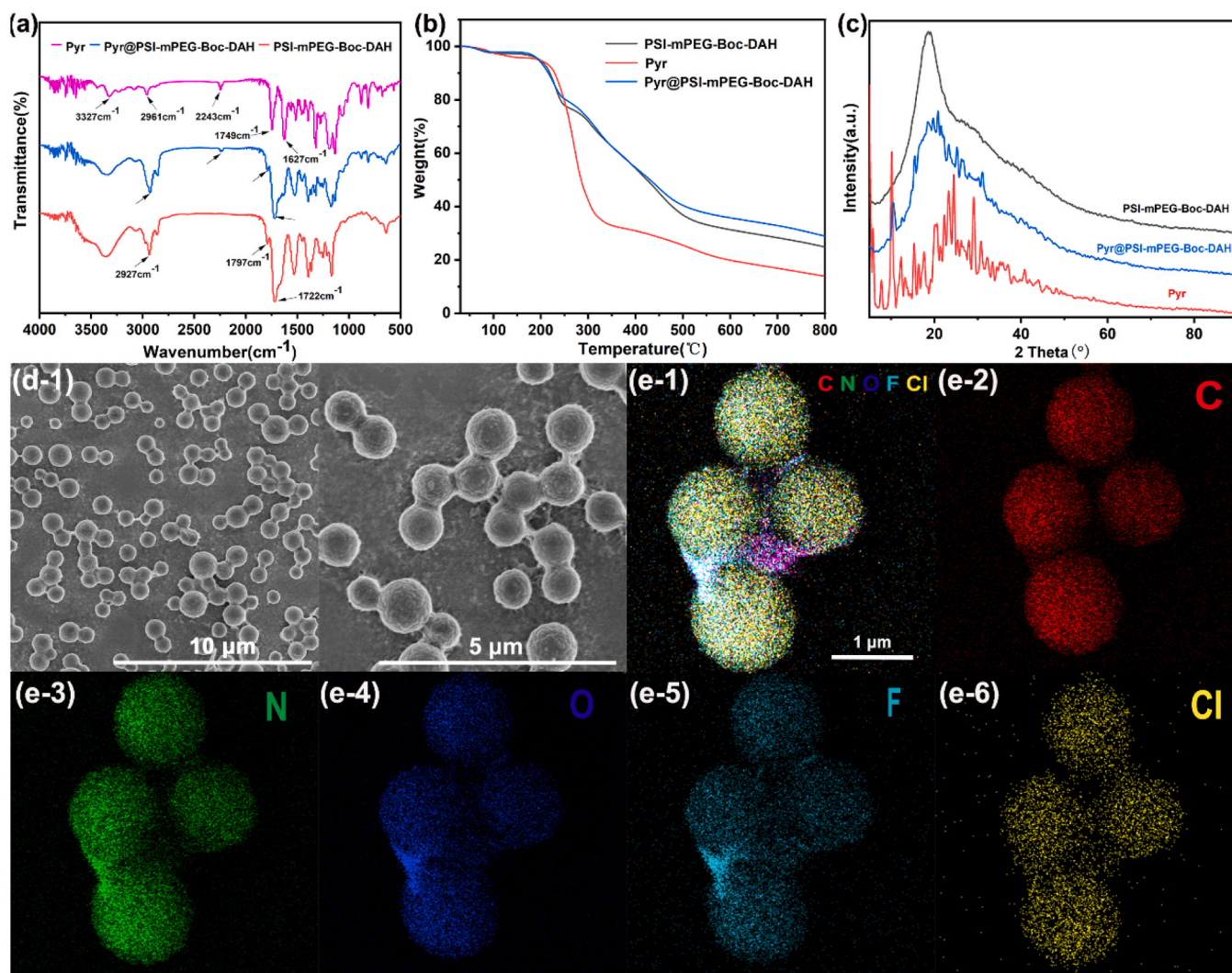


Fig. 2. (a) FTIR, (b) TGA, and (c) XRD characterizations of Pyr, PSI-mPEG-Boc-DAH and Pyr@PSI-mPEG-Boc-DAH, (d) SEM of Pyr@PSI-mPEG-Boc-DAH microparticles, (e) EDS mapping characterizations of Pyr@PSI-mPEG-Boc-DAH microparticles.

cad in various parts (head, thorax and abdomen) of RIFA was observed using a confocal laser scanning microscopy (CLSM) (Zeiss, LSM710, German).

2.10. Evaluation of edible effect of RIFA on materials

One blank bait and three baits containing 0.25%, 0.5% and 1% mass fraction PSI-mPEG-Boc-DAH were used for evaluation, respectively. Each dish was placed with 1 g different bait, and the number of RIFA attracted by different bait was observed 30 min later. The experiment was repeated three times.

2.11. Field control effect of RIFA

The treatments were divided into baits containing Pyr and Pyr@PSI-mPEG-Boc-DAH, respectively. Baits were sprayed artificially at a distance of 0.3 m from the centre of the ant nest. The control effect of worker ants was investigated by bait method [25]. Thin slices of fresh ham sausage were used as baits. From 16:00–18:00, 10 mL transparent plastic bottles containing ham sausage slices were placed with the bottle mouth close to the ground, and placed for about 30 min. After that, they were taken back into the room soaked in ethanol to record the number of worker ants in each bait bottle.

The reduction rate of RIFA was calculated as:

$$\text{Reduction Rate} = \left(1 - \frac{W_0 * TW_1}{TW_0 * W_1}\right) \times 100\%$$

TW_1 : average number of RIFA on bait in post-treatment area; W_0 : average number of RIFA on bait in control area before drug treatment; W_1 : average number of RIFA on bait in control area after treatment; TW_0 : average number of RIFA on bait in pre-treated area.

3. Results and discussion

3.1. Synthesis and Characterization of Pyr@PSI-mPEG-Boc-DAH

In this study, the resulting polymers were partially functionalized by reaction with N-alkyl primary amines to yield amphiphilic PSI derivatives and the synthesis route of the PSI-mPEG-Boc-DAH was shown in Scheme 2a. The detailed synthetic procedure was presented in Scheme 2b. The chemical structure of PSI-mPEG-Boc-DAH was confirmed by ^1H NMR spectra. From the ^1H NMR spectrum of PSI-mPEG-Boc-DAH (Fig. 1), the successful conjugation was confirmed by the methylene proton peak d (3.52 ppm) for conjugated mPEG [26,27]. And the methylene proton peak e (1.23 ppm), the Boc group peaks (f, g) (1.36 ppm, 6.72 ppm) proved for conjugated Boc-DAH [16]. The GPC spectra of PSI and PSI-mPEG-Boc-DAH were showed in Fig. S2 and S3, the Mw of PSI was 5742 Da, whereas the Mw of PSI-mPEG-Boc-DAH was

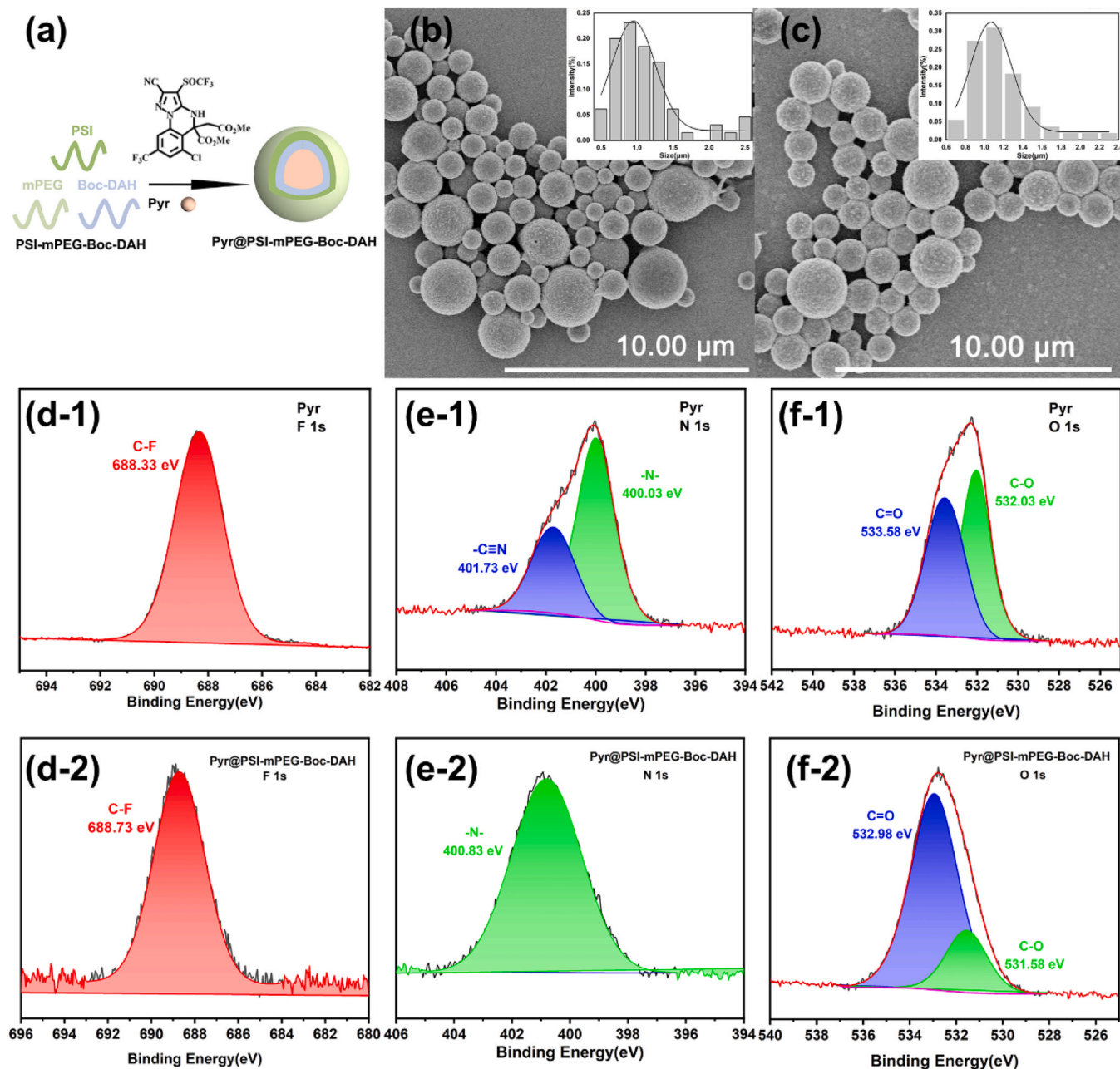


Fig. 3. (a) Schematic of Pyr-loading mechanism. (b, c) SEM and size of Pyr@PSI-mPEG-Boc-DAH on dialysis for two and three days. (d) F 1 s XPS spectra, (e) N 1 s XPS spectra, and (f) O 1 s XPS spectra of Pyr and Pyr@PSI-mPEG-Boc-DAH.

7992 Da, which demonstrated the successful conjugation of microparticles by their molecular weight differences.

The FTIR spectra of PSI-mPEG-Boc-DAH, Pyr and Pyr@PSI-mPEG-Boc-DAH were shown in Fig. 2a. The spectrum for PSI-mPEG-Boc-DAH showed a band at 2927 cm^{-1} corresponding to the stretching vibration of $-\text{CH}_2$, a band caused by the coupling effect of adjacent carbonyl groups at 1797 cm^{-1} , and a band at 1722 cm^{-1} indicating the presence of $\text{C}=\text{O}$. These indicated that the structure contains five-membered cyclic imides [28–31]. The bands at 3327 cm^{-1} , 2961 cm^{-1} and 2243 cm^{-1} corresponded to the stretching vibration of the $-\text{CH}_2$, $-\text{NH}$, and $-\text{C}\equiv\text{N}$ in Pyr structure, respectively. And, bands at 1749 cm^{-1} and 1627 cm^{-1} indicated the presence of $\text{C}=\text{O}$ in Pyr. Moreover, the peaks of $-\text{C}\equiv\text{N}$ of Pyr were distinctly observed in Pyr@PSI-mPEG-Boc-DAH, which indicated that Pyr was successfully loaded by the PSI-mPEG-Boc-DAH. To further confirm thermal stability of PSI-mPEG-Boc-DAH, Pyr and Pyr@PSI-mPEG-Boc-DAH, TGA curves

were shown in Fig. 2b and DTG curves were shown in Fig. S4. The thermal degradation of PSI started at 270°C , which could potentially be due to the condensation reaction between $-\text{OH}$ and $-\text{NH}_2$ groups caused by dehydration of PSI. Another main degradation peak occurred at 390°C , was because the fracture of $\text{C}-\text{C}$ bonds in the main chain of PSI [32]. The result exhibited a rapid weight-loss step of 80% from ca. $200\text{--}300^\circ\text{C}$, indicating that the structures of Pyr were unstable at temperatures higher than 200°C . In contrast, a gradual weight loss occurred in Pyr@PSI-mPEG-Boc-DAH from 200°C to 500°C was attributed to the slow decomposition of Pyr. The results indicated that PSI-mPEG-Boc-DAH improved the thermal stability of Pyr. XRD measurements were performed to investigate crystal changes during the loading process (Fig. 2c). The strong crystallinity of Pyr was confirmed by the presence of strong and sharp peaks in XRD pattern, such as those at 5.12° , 7.68° , 10.02° , 16.32° , 22.18° , 24.16° , and 28.92° . Those peaks were also observed in the pattern of Pyr@PSI-mPEG-Boc-DAH which

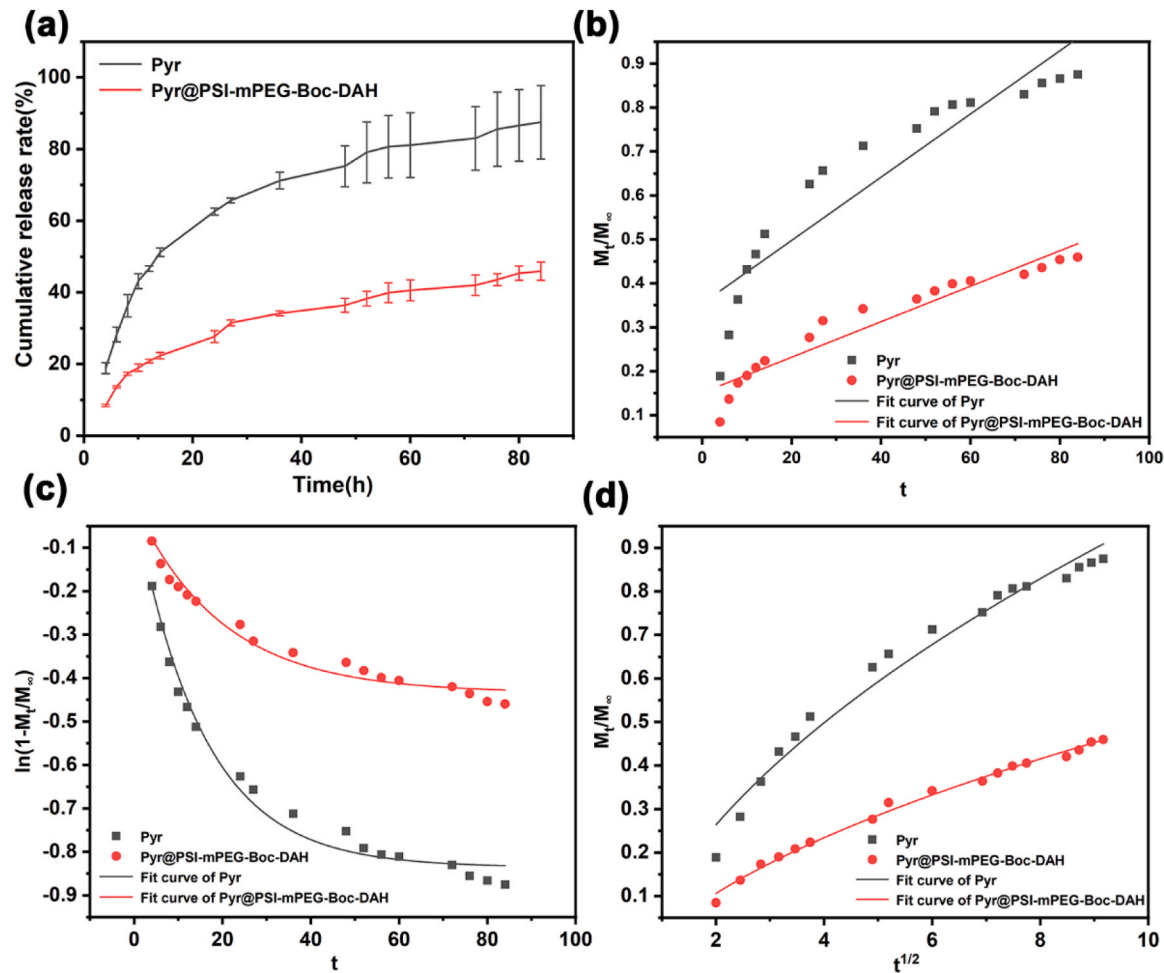


Fig. 4. (a) Release behavior of Pyr and Pyr@PSI-mPEG-Boc-DAH. (b, c, d) Fitting curves of Zero-order model, First-order model and Higuchi model for the release of Pyr from Pyr@PSI-mPEG-Boc-DAH.

Table 1
 R^2 for different fitted equations of sustained release curves.

Sample	Zero-order	First-order	Higuchi
Pyr	0.8460	0.9829	0.9735
Pyr@PSI-mPEG-Boc-DAH	0.9144	0.9694	0.9934

indicated that Pyr was successfully loaded by the PSI-mPEG-Boc-DAH. The above conclusions collectively showed that the crystal form of Pyr remained unchanged during encapsulation. The morphology and size of Pyr@PSI-mPEG-Boc-DAH were observed and analyzed by SEM. In Fig. 2d, the Pyr@PSI-mPEG-Boc-DAH was regular spheric morphology and the particle size was homogeneous. The microparticle size was about 1 μm and the loading capacity was between 27%–29%. In addition, energy dispersive spectroscopy (EDS) mappings exhibited a uniform distribution in the microparticles of C, N, O, F and Cl, which demonstrated the presence of Pyr in the PSI-mPEG-Boc-DAH microparticles, as shown in Fig. 2e.

3.2. Study of Interaction Mechanism

In order to study the formation of microparticles in the dialysis process, SEM observation and drug loading rate detection experiments were carried out. The morphology of Pyr@PSI-mPEG-Boc-DAH was observed at different times during dialysis and the drug loading rate was measured simultaneously. As shown in Fig. 3b, on the second day of

dialysis, the size of the microparticles was not uniform, but on the third day (Fig. 3c), the size of the microparticles became uniform, which indicated that regular polymer micellar particles were gradually formed during dialysis. This phenomenon indicated that the material completed self-assembly and gradually became uniform during the dialysis process. Moreover, the drug loading rate was about the same, the first day was 27.5% and the second day was 28.4%, indicating that the Pyr was packed at first.

X-ray photoelectron spectroscopy (XPS) survey spectra (Fig. S5) showed that there was no significant difference between PSI-mPEG-Boc-DAH and Pyr@PSI-mPEG-Boc-DAH except the peak of Cl 2p observed at 201.14 eV in the spectra of Pyr@PSI-mPEG-Boc-DAH, demonstrating that Pyr was successfully loaded by PSI-mPEG-Boc-DAH. To study the interaction mechanism of Pyr and PSI-mPEG-Boc-DAH, the samples were characterized by F 1 s, O 1 s, and N 1 s high resolution. All binding energies were referenced to the C 1 s peak at 284.80 eV to compensate for any possible charging-up effect. As shown in Fig. 3d, the F 1 s peak was shifted to 688.73 eV, after the loading of Pyr, indicating that there may be interaction forces between Pyr and PSI-mPEG-Boc-DAH. The N 1 s XPS spectrum (Fig. 3e) yielded two peaks at 400.03 and 401.73 eV in Pyr, which corresponded to -N- and -C≡N, respectively. However, the peak of -N- in Pyr@PSI-mPEG-Boc-DAH was shifted to 400.83 eV, and the peak of -C≡N appeared. The -C≡N in Pyr formed hydrogen bonds with PSI-mPEG-Boc-DAH, which caused this peak to disappear. Furthermore, the spectra of O 1 s (Fig. 3f) yielded the peaks at 532.03 and 533.58 eV in Pyr, corresponding to the binding of C-O and C=O, respectively, and the peaks at 531.58 and 532.98 eV in Pyr@PSI-mPEG-

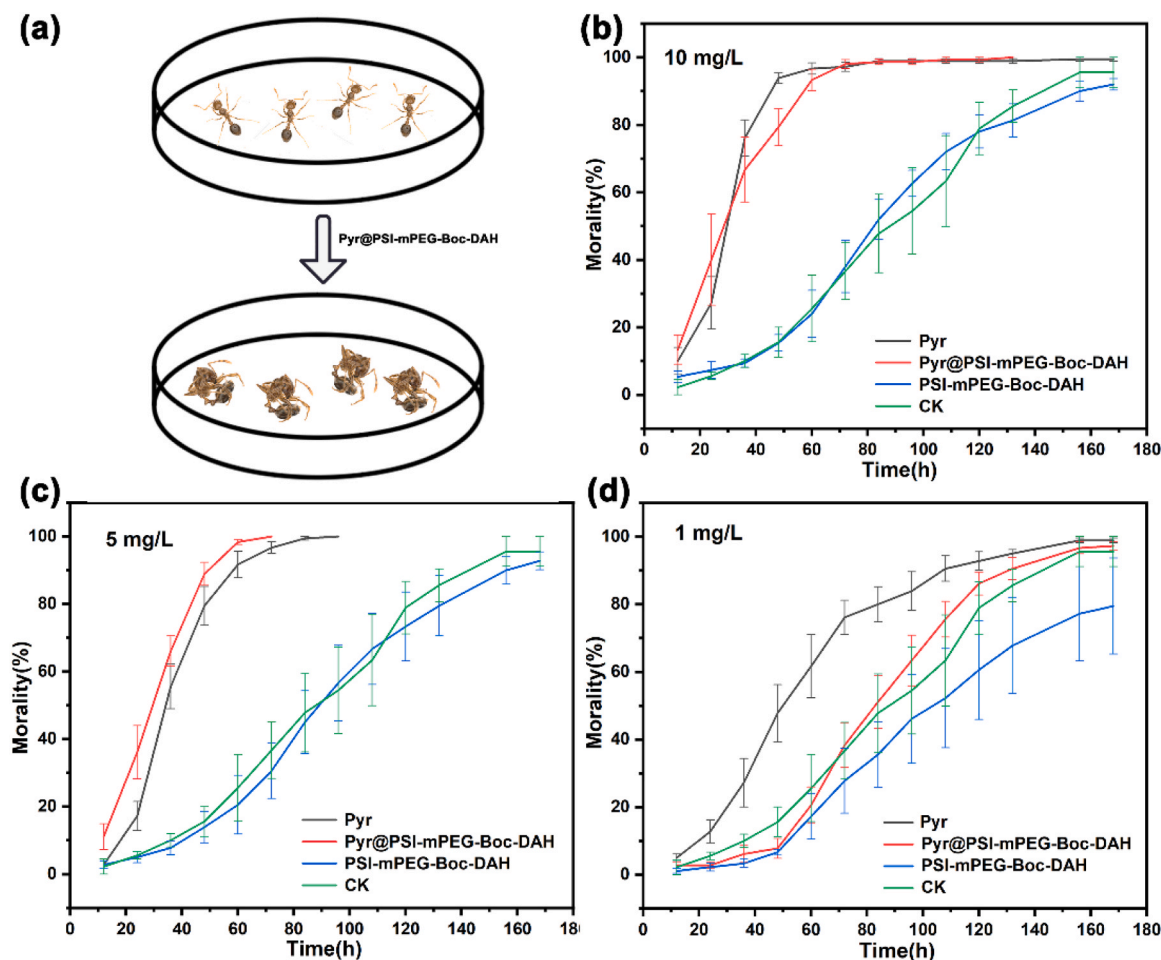


Fig. 5. (a) Schematic of toxicity bioassays process. (b, c, d) Insecticidal activities of Pyr and Pyr@PSI-mPEG-Boc-DAH against RIFA.

Boc-DAH were attributed to C-O and C=O, respectively. Two peaks shifted after the Pyr loading also indicated that O may play a role in the process of Pyr loading.

3.3. *In vitro* release of Pyr@PSI-mPEG-Boc-DAH

In order to simulate the release of microparticles in the gut of RIFA, a sustained release experiment was conducted. According to the midgut of RIFA was acidic (pH 4.6–6.8), the release experiment of Pyr@PSI-mPEG-Boc-DAH microparticles was studied in a weakly acid environment [23]. As shown in Fig. 4a, from 4 h on, the release rate of Pyr was about 10% more than the Pyr from Pyr@PSI-mPEG-Boc-DAH. After 24 h, the release rate of Pyr was $62.59 \pm 0.96\%$, while it was only $27.67 \pm 1.64\%$ of Pyr from Pyr@PSI-mPEG-Boc-DAH. After 84 h, Pyr was almost completely released, which was nearly twice than that from the Pyr@PSI-mPEG-Boc-DAH ($45.95 \pm 2.55\%$). These results showed that the Pyr@PSI-mPEG-Boc-DAH could slowly release Pyr in a slightly acidic environment.

The release mechanism of Pyr was described using zero-order (Fig. 4b), first-order (Fig. 4c), and Higuchi (Fig. 4d) models. According to the R^2 of the fitted equations (Table 1), the data of Pyr release was best fitted with the first-order model. This indicated that there was a certain relationship between the drug release speed and the drug content. When the drug content was high, the drug release rate was faster. The data of Pyr released from Pyr@PSI-mPEG-Boc-DAH was best fitted with the Higuchi model. The Higuchi model could be used to fit the drug release process based on Fick's diffusion theorem. Therefore, the Fick

diffusion theorem was followed when Pyr@PSI-mPEG-Boc-DAH released Pyr in acidic solution, which indicated that Pyr was mainly released by swelling and diffusion, and could be affected by carrier permeability without any structural collapse [33].

3.4. Laboratory toxicity bioassays

The toxicity biological activities of Pyr and Pyr@PSI-mPEG-Boc-DAH with 10, 5 and 1 mg/L against RIFA were shown in Fig. 5a. The treatment with 10 mg/L Pyr was effectively, but not significantly higher than that treatment with Pyr@PSI-mPEG-Boc-DAH (Fig. 5b). 5 mg/L Pyr@PSI-mPEG-Boc-DAH treatment had higher mortality rate of RIFA than Pyr treatment (Fig. 5c). The mortality of the RIFA could be significantly decreased by the 1 mg/L Pyr@PSI-mPEG-Boc-DAH (Fig. 5d). At the concentration of 1 mg/L Pyr@PSI-mPEG-Boc-DAH, the mortality rate of RIFA in 48 h was only 7.78%, which was significantly lower than that of the Pyr (47.78%). This showed that the Pyr@PSI-mPEG-Boc-DAH could kill ants slowly, and didn't cause RIFA to alert within two days. During this time, the Pyr@PSI-mPEG-Boc-DAH would be passed between different grades of RIFA, eventually killing all of them. Although the activity of Pyr@PSI-mPEG-Boc-DAH was low in two days, the active ingredients accumulated gradually over time, and could eventually kill the RIFA within 7 d. Feeding the Pyr@PSI-mPEG-Boc-DAH didn't cause RIFA to react with alarm, which achieved the purpose of slowly killing more and more ants.

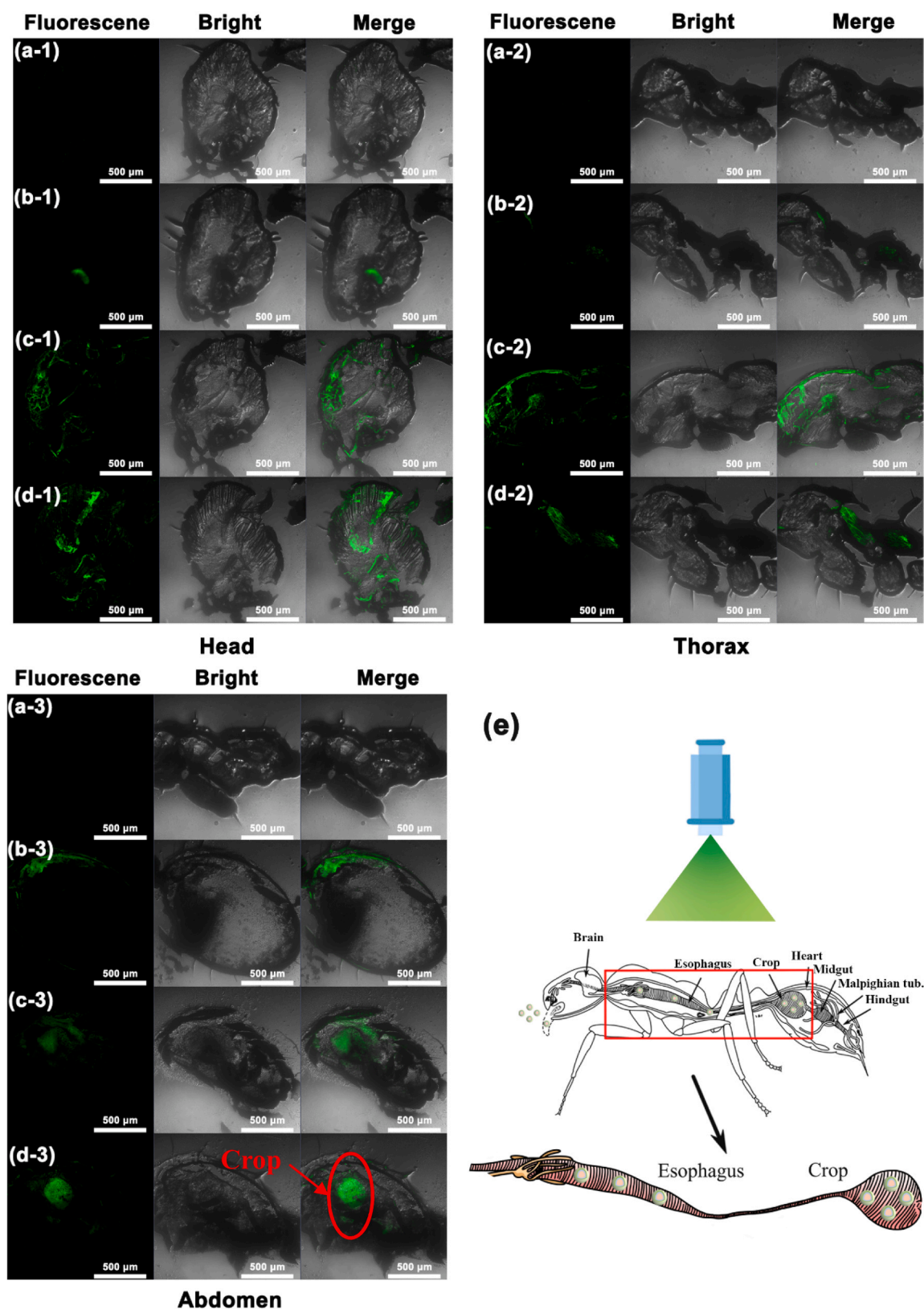


Fig. 6. Confocal imaging of different parts of RIFA (head, thorax, and abdomen). (a) FITC-cad control and (b, c, d) after 6, 12, 24 h of treatment with PSI-mPEG-Boc-DAH-FITC-cad. (e) Schematic illustration of the uptake pathway in RIFA after treatment by PSI-mPEG-Boc-DAH-FITC-cad.

Table 2
Reduction rate (%) of worker ants.

Treatment	5 d after application	7 d after application
Pyr	45.16	70.50
Pyr@PSI-mPEG-Boc-DAH	38.90	99.89

3.5. *In Vivo* Imaging of PSI-mPEG-Boc-DAH-FITC-cad

To determine the absorption and distribution of PSI-mPEG-Boc-DAH in RIFA, PSI-mPEG-Boc-DAH-FITC-cad was used to treat RIFA to make its distribution visible under CLSM. FITC-cad was a fluorescent substance, which attached to PSI-mPEG-Boc-DAH for tracing. In the blank control (Fig. 6a), there were no fluorescence signal was observed. Fig. 6b, c, d showed that fluorescence signals were observed at the head, thorax and abdomen after 6, 12, 24 h PSI-mPEG-Boc-DAH-FITC-cad treatment, respectively. The results indicated that the PSI-mPEG-Boc-DAH-FITC-cad could undergo long-distance transport via the gut reached the crop. After 6 h treatment (Fig. 6b), only subtle fluorescence was observed in the head. Similarly, almost no fluorescence was seen in the thorax. Some fluorescence could be seen in the abdominal margin. With the extension of time, clear fluorescence could be seen in head, thorax and abdomen after 12 h (Fig. 6c). After 24 h (Fig. 6d), the head was almost full of fluorescence. And the fluorescence was distributed in the back part of the thorax. Additionally, in the abdomen, fluorescence was concentrated in the crop. It was worth noting that movement of food through trophallaxis played important roles in ants. While crop was where the ant stored food for trophallaxis. This suggested that the PSI-mPEG-Boc-DAH-FITC-cad could be absorbed by worker ants and through trophallaxis to feed larvae and even the queen. This was a strong indication that Pyr@PSI-mPEG-Boc-DAH had the potential to kill an entire colony of ants.

3.6. Edible effect of RIFA

In order to determine whether the addition of PSI-mPEG-Boc-DAH will affect RIFA feeding of baits, this feeding selection experiment was conducted. Results showed that the baits containing 0.25% and 0.5% mass fraction PSI-mPEG-Boc-DAH could attract more ants than the blank bait, indicating that added a small amount of PSI-mPEG-Boc-DAH to the bait had an attractive effect on RIFA. Although the 1% baits attracted fewer ants than the blank baits, the difference was not significant. The experimental results showed that the addition of PSI-mPEG-Boc-DAH in the bait did not affect the feeding of RIFA.

3.7. Control effect of RIFA in the field

The Pyr and Pyr@PSI-mPEG-Boc-DAH were mixed into the bait individually and conducted field experiments to evaluate the control effect. All treatments could obtain good control effect in reducing the number of worker ants. However, the reduction degree of worker ants was different in different treatments. After 5 d of treatment, the decreasing speed of worker ant population was in the order of Pyr@PSI-mPEG-Boc-DAH > Pyr (Table 2). After 7 d of treatment, the reduction rate of Pyr@PSI-mPEG-Boc-DAH treatment was achieved 99.89%, which showed a very good control effect.

4. Conclusion

In summary, an effective controlled release Pyr@PSI-mPEG-Boc-DAH microparticles was successfully constructed by physical encapsulation. During this process, Pyr@PSI-mPEG-Boc-DAH microparticles could release Pyr slowly in the gut of RIFA. Moreover, compared with the Pyr, Pyr@PSI-mPEG-Boc-DAH used in the RIFA exhibited better duration and insecticidal activity. It could realize kill the whole nest ants slowly without causing RIFA to be alert. In addition, the RIFA stored the

Pyr@PSI-mPEG-Boc-DAH in its crop and feed it to other ants. In the control of RIFA, it was very important to have the opportunity to kill the ants without causing nest migration. Furthermore, these results could provide a future design for formulating pesticides and promote the development of sustainable agriculture.

Declaration of Competing Interest

The authors declare that they have no known competing financial interests or personal relationships that could have appeared to influence the work reported in this paper.

Data Availability

Data will be made available on request.

Acknowledgment

This work was supported by the Guangdong Provincial Key Research and Development Program (2023B0202080001), Guangdong Basic and Applied Basic Research Foundation (2023A151010609) and Guangdong Provincial Innovation Team for General Key Technologies in Modern Agricultural Industry (2019KJ140).

Appendix A. Supporting information

Supplementary data associated with this article can be found in the online version at doi:10.1016/j.colsurfb.2023.113675.

References

[1] S. Jiang, D. Liu, G. Li, A review: the biology of red imported fire ant (*Solenopsis invicta* Buren), J. Southwest Agric. Univ. 27 (3) (2005) 312–315, 318.

[2] Y. Lu, L. Zeng, Ten years after red imported fire ant found to invade china: history, current situation and trend of its infestation, Plant Quar. 29 (2) (2015) 1–6.

[3] S. Vinson, Invasion of the red imported fire ant (Hymenoptera: Formicidae): spread, biology and impact, J. Am. Entomol. 439 (1) (1997) 23–39.

[4] T. Chen, S. Tan, J. Wen, Z. Xiao, X. Chen, The occurrence and control measures of *Solenopsis invicta* Buren in Guangdong Province, Plant Quar. 36 (2) (2022) 78–81.

[5] L. Morrison, Long-term impacts of an arthropod-community invasion by the red imported fire ant, *Solenopsis invicta*, Ecology 83 (8) (2022) 2337–2345.

[6] K. Jetter, J. Hamilton, J. Klotz, Red imported fire ants threaten agriculture, wildlife and homes, Calif. Agr. 56 (1) (2002) 26–34.

[7] Ni Gotell, A. Arnett, Biogeographic effects of red imported fire ant invasion, Ecol. Lett. 3 (4) (2000) 257–261.

[8] L. Zeng, Y. Lu, X. He, W. Zhang, G. Liang, Identification of red imported fire ant *Solenopsis invicta* to invade mainland China and infestation in Wuchuan, Guangdong, Chin. Bull. Entomol. 42 (2) (2005) 144–148, 230–231.

[9] S. Yan, Q. Hu, J. Li, Z. Chao, C. Cai, M. Yin, X. Du, J. Shen, A star polycation acts as a drug nanocarrier to improve the toxicity and persistence of botanical pesticides, ACS Sustain Chem. Eng. 7 (20) (2019) 17406–17413.

[10] A. Kazem, L. Yang, Y. Lin, A. Kazem, H. Xu, Z. Zhang, Pathogenic invasion responsive carrier based on mesoporous silica/β-glucan nanoparticles for smart delivery of fungicides, ACS Sustain Chem. Eng. 9 (27) (2021) 9126–9138.

[11] X. Ye, M. Liu, N. Zhao, C. Xiao, H. Xu, J. Jia, Targeted delivery of emamectin benzoate by functionalized polysuccinimide nanoparticles for the flowering cabbage and controlling *Plutella xylostella*, Pest Manag. Sci. 78 (2) (2022) 758–769.

[12] X. Xin, Z. He, M. Hill, R. Niedz, X. Jiang, B. Sumerlin, Efficiency of biodegradable and pH-responsive polysuccinimide nanoparticles (PSI-NPs) as smart nanodelivery systems in grapefruit: in vitro cellular investigation, Macromol. Biosci. 18 (7) (2018), 1800159.

[13] S. Su, L. Chen, L. Hao, H. Chen, H. Zhou, Preparation of p-amino salicylic acid-modified polysuccinimide as water-based nanocarriers for enhancing pesticide stability and insecticidal activity, Colloid. Surf. B 207 (2021), 111990.

[14] H. Xing, L. Cheng, M. Lu, H. Liu, L. Lang, T. Yang, X. Zhao, H. Xu, L. Yang, P. Ding, A biodegradable poly (Amido Amine) based on the antimicrobial polymer polyhexamethylene biguanide for efficient and safe gene delivery, Colloid. Surf. B 182 (2019), 110355.

[15] M. Hill, E. MacKrell, C. Forsthoefel, S. Jensen, M. Chen, G. Moore, Z. He, B. Sumerlin, Biodegradable and pH-responsive nanoparticles designed for site-specific delivery in agriculture, Macromolecule 16 (4) (2015) 1276–1282.

[16] B. Kim, S. Chuanoi, T. Suma, Y. Anraku, K. Hayashi, M. Naito, H. Kim, I. Kwon, K. Miyata, A. Kishimura, K. Kataoka, Self-assembly of siRNA/PEG-b-cationer at integer molar ratio into 100 nm-sized vesicular polyion complexes (siRNAsomes) for RNAi and codelivery of cargo macromolecules, J. Am. Chem. Soc. 141 (8) (2019) 3699–3709.

- [17] X. Jiang, Y. Xie, Z. Ren, U. Ganeteg, F. Lin, C. Zhao, H. Xu, Design of a new glutamine–fipronil conjugate with α -amino acid function and its uptake by *A. thaliana* Lysine histidine transporter 1 (*AtLHT1*), J. Agric. Food Chem. 66 (29) (2018) 7597–7605.
- [18] S. Huang, Z. Zhang, X. Jiang, H. Xu, The bioactivity of fused heterocyclic compounds of pyraquinil against *Spodoptera frugiperda*, Chin. J. Appl. Entomol. 56 (4) (2019) 780–787.
- [19] C. Gong, M. Shan, B. Li, G. Wu, A pH and redox dual stimuli-responsive poly (Amino Acid) derivative for controlled drug release, Colloid Surf. B 146 (2016) 396–405.
- [20] T. Le, D. Kim, Folate-PEG/Hyd-curcumin/C18-g-PSI micelles for site specific delivery of curcumin to colon cancer cells via Wnt/ β -catenin signaling pathway, Mat. Sci. Eng. C. 101 (2019) 464–471.
- [21] W. Liang, Z. Xie, J. Cheng, D. Xiao, Q. Xiong, Q. Wang, J. Zhao, W. Gui, A light-triggered pH-responsive metal–organic framework for smart delivery of fungicide to control sclerotinia diseases of oilseed rape, ACS Nano 15 (4) (2021) 6987–6997.
- [22] D. Xiao, J. Cheng, W. Liang, L. Sun, J. Zhao, Metal-phenolic coated and prochloraz-loaded calcium carbonate carriers with pH Responsiveness for Environmentally-safe Fungicide Delivery, Chem. Eng. J. 418 (2021) 12927.
- [23] Q. Zheng, R. Wang, D. Qin, L. Yang, S. Lin, D. Cheng, S. Huang, Z. Zhang, Insecticidal efficacy and mechanism of nanoparticles synthesized from chitosan and carboxymethyl chitosan against *Solenopsis invicta* (Hymenoptera: Formicidae), Carbohydr. Polym. 260 (2021), 117839.
- [24] Q. Zheng, L. Yang, S. Lin, Q. Ma, Z. Zhang, Insecticidal activity of the leaf and stem water extract of gelsemium elegans against *Solenopsis invicta*, Sociobiology 67 (2) (2020) 232.
- [25] J. Huang, Y. Lu, Y. Xu, L. Zeng, Control effect of 0.045% indoxacarb on the red imported fire ant *Solenopsis invicta*, Plant Prot. 35 (3) (2009) 145–148.
- [26] N. Liu, B. Li, C. Gong, Y. Liu, Y. Wang, A pH and thermo-responsive Poly (Amino Acid)-based drug delivery system, Colloid Surf. B 136 (2015), 562–529.
- [27] K. Cherukula, S. Uthaman, I. Park, Design of an amphiphilic poly (Aspartamide)-mediated self-assembled nanoconstruct for long-term tumor targeting and bioimaging, Molecules 24 (5) (2019) 885.
- [28] B. Li, M. Shan, X. Di, C. Gong, L. Zhang, Y. Wang, G. Wu, A dual pH and reduction-responsive anticancer drug delivery system based on PEG–SS–Poly (Amino Acid) block copolymer, RSC Adv. 7 (48) (2017) 30242–30249.
- [29] D. Zhao, B. Li, J. Han, Y. Yang, X. Zhang, G. Wu, pH responsive polypeptide based polymeric micelles for anticancer drug delivery, J. Biomed. Mater. Res. A 103 (9) (2015) 3045–3053.
- [30] J. Chen, L. Xu, J. Han, M. Su, Q. Wu, Synthesis of modified polyaspartic acid and evaluation of its scale inhibition and dispersion capacity, Desalination 358 (2015) 42–48.
- [31] J. Yeh, H. Yang, Y. Hsu, C. Su, T. Lee, S. Lou, Synthesis and characteristics of biodegradable and temperature responsive polymeric micelles based on poly (Aspartic Acid)-g-Poly (N-Isopropylacrylamide-co-N, N-dimethylacrylamide), Colloid Surf. A 421 (2013) 1–8.
- [32] J. Velazco-de-la-Garza, L. Avérous, G. Sosa-Santillán, E. Pollet, A. Zugasti-Cruz, C. Sierra-Rivera, N. Pérez-Aguilar, E. Oyervides-Muñoz, Biological properties of novel polysuccinimide derivatives synthesized via quaternary ammonium grafting, Eur. Polym. J. 131 (2020), 109705.
- [33] M. Pooremaeil, H. Namazi, Facile preparation of pH-sensitive chitosan microspheres for delivery of curcumin, characterization, drug release kinetics and evaluation of anticancer activity, Int. J. Biol. Macromol. 162 (2020) 501–511.

ConA-Loaded PEGylated Graphene Oxide for Targeted Nanopesticide Carriers against *Magnaporthe Oryzae*

Pengtong Hu, Li Zhu, Wenjie Deng, Weirou Huang, Hanhong Xu,* and Jinliang Jia*



Cite This: *ACS Appl. Nano Mater.* 2023, 6, 9484–9494



Read Online

ACCESS |



Metrics & More



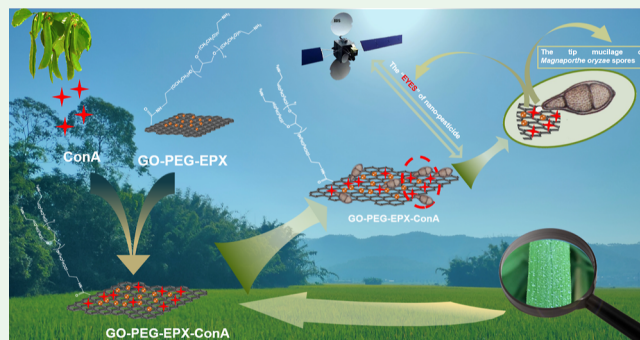
Article Recommendations



Supporting Information

ABSTRACT: Rice blast is a destructive rice disease that is rapidly spread by the drift of *Magnaporthe oryzae* spores. Conidial attachment to the rice leaf surface is the most crucial step in the rapid spread of rice blast. Therefore, blocking the chance of contact between spores and the rice leaf surface is extremely vital for controlling rice blast. In this study, based on the strong affinity between the lectin protein-ConA and *M. oryzae* spores, we successfully constructed ConA-loaded PEGylated graphene oxide (GO-PEG-ConA) as targeted nanopesticide carriers to load epoxiconazole (EPX) against *M. oryzae*. The ConA loading capacity of the GO-PEG-EPX-ConA nanocarrier was 14.7% by the sodium dodecyl sulfate–polyacrylamide gel electrophoresis assay. The GO-PEG-ConA nanocarrier could obviously inhibit the germination of *M. oryzae* spores by 41.7% and showed 2.4-fold higher inhibitory activity than the inhibition ratio (17.4%) of GO-PEG nanocarriers, which was mainly due to the higher affinity between the GO-PEG-ConA nanocarrier and *M. oryzae* spores. Moreover, the greenhouse experiment indicated that the GO-PEG-EPX-ConA nanopesticide could significantly reduce rice blast lesions in rice seedlings, fundamentally settling the transmission of rice blast. Therefore, GO-PEG-ConA could be a targeted nanopesticide carrier to realize precise release of pesticides, which would offer an important reference value for improving pesticide utilization efficiency.

KEYWORDS: graphene oxide, fungus control, spore germination, synergistic effect, rice blast



1. INTRODUCTION

Rice blast, as one of the most destructive worldwide diseases of rice crops, is called “rice cancer”, which is caused by the filamentous ascomycete fungus *Magnaporthe oryzae*.^{1,2} It ravages various rice-producing areas all year round, causing a substantial reduction in rice production or even no harvest. Rice blast has become a major hidden danger to global grain security and could be rapidly spread by the drift of *M. oryzae* spores.^{3,4} When *M. oryzae* spores, a three-celled conidium, land on the rice leaf, the teardrop-shaped conidium could generate tip mucilage to attach itself to the hydrophobic rice leaf and promote germination. Then, the germ tube emerges and forms an appressorium, generating turgor through the leaf cuticle and resulting in disease lesions. The disease lesion will generate plenty of fungal spores to spread rapidly to adjacent rice under the influence of wind and dewdrop splashing.^{5,6} Currently, rice blast is controlled primarily by chemical prevention in the field. However, the agents acting on the site of action are only 0.1%,⁷ and a large mass of agents are released into the Earth’s environment, leading to severe environmental pollution.^{8–11} Epoxiconazole (EPX), a demethylation inhibitor (DMI) fungicide, is significantly effective against rice blast by disrupting the biosynthesis of ergosterol and hindering the

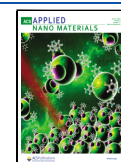
synthesis of the germ cell wall.¹² However, EPX, as a triazole fungicide, is widely applied in fields, causing serious pesticide residues which generate enormous risks for human health.¹³ Therefore, in the case of ensuring the effect of pesticide application, it is particularly momentous to reduce the application of EPX by precise release of pesticides.

The lectin protein ConA, isolated from jack bean, with a size of approximately 8 nm, has been in the limelight due to its strong affinity with the carbohydrate structure on the surface of cancer cells.^{14,15} Therefore, ConA is widely applied in the biomedical field. It was reported that the spore tip mucilage at the conidial apex was a critical point of the mechanism of *M. oryzae* conidial attachment.¹⁶ When *M. oryzae* spores land on the rice leaf surface, the conidial apex can generate mucilage that has a strong affinity and combines with lectin concanavalin (ConA) before germ tube emergence to attach to the plant

Received: March 15, 2023

Accepted: May 14, 2023

Published: May 23, 2023



surface. Conidial attachment, in the life cycle of *M. oryzae* spores, is the most crucial step. Therefore, it is vital to block the chance of contact between spores and the leaf surface of rice to control rice blast.

Graphene, a monolayer carbon atom two-dimensional nanomaterial, was first prepared by Novoselov and Geim et al. through mechanical stripping in 2004.¹⁷ Along with its appearance, graphene has brought new development opportunities to the field of nanotechnology and nanoscience.^{18,19} Graphene oxide (GO), as a derivative of graphene, has attracted increasing attention in numerous fields because of its extraordinary hydrophilic and colloidal stability compared to graphene.^{20–22} Moreover, GO has been intensively explored in biomedical aspects, such as cancer drug loading and delivery.²² For example, graphene oxide-based hydrogels could be used as nanocarriers for anticancer drug delivery.¹⁸ Also, the combination of GO and fruit preservation could extend the fruit's shelf life.²³ He et al. demonstrated that GO could be an antimicrobial agent to extend the vase life of cut flowers.²⁴ GO has become highly appreciated for agricultural applications. In addition, poly(ethylene glycol) (PEG), with minimal toxicity, favorable biocompatibility, and water solubility, has been used to modify nanoparticles in drug delivery systems.^{25,26} PEG-functionalized graphene oxide could load water-insoluble anticancer drugs via noncovalent van der Waals interactions.^{27,28}

Therefore, considering that the spore tip mucilage at the conidial apex of *M. oryzae* has an affinity and combination with lectin protein-ConA, we attempted to synthesize ConA-loaded PEGylated graphene oxide as targeted nanopesticide carriers against *M. oryzae*. In the present study, (1) EPX, destroying the synthesis of germ cell walls, was loaded on nanocarriers; (2) the ConA loading capacity of nanosheets was assessed by SDS–PAGE; (3) the antifungal activity of nanosheets against *M. oryzae* was studied in vitro; and (4) the spore germination assay and synergistic mechanism of nanosheets against *M. oryzae* were investigated in vivo and in vitro. In the future, we will continue to study the actual effects of this targeted nanopesticide in field experiments.

2. EXPERIMENTAL SECTION

2.1. Materials. Graphene oxide (GO) was purchased from Chengdu Organic Chemicals Co., Ltd. (China). EPX at a purity of 97% (the original fungicide) was provided by Jiangsu Ruibang Pesticide Factory Co., Ltd. (China). 8-arm PEG-NH₂ (MW = 20,000) was obtained from Shanghai Ponsure Biotechnology Co., Ltd. (China). Concanavalin A from *Canavalia ensiformis* (jack bean) was purchased from Sigma-Aldrich (USA). 3-(3-Dimethylaminopropyl)-1-ethylcarbodiimide hydrochloride (EDC·HCl) was provided by Adamas Reagent Co., Ltd. (China). Dimethyl sulfoxide (DMSO) was obtained from Shanghai Titan Scientific Co., Ltd. (China). Fluorescein-5-isothiocyanate (FITC) was purchased from Hangzhou Xinqiao Biotechnology Co., Ltd. (China). *M. oryzae* (08719) was preserved in our laboratory by the filter paper method.

2.2. Preparation of GO-PEG, GO-PEG-EPX, and GO-PEG-EPX-ConA. The surfaces of GO nanosheets were modified with 8-arm PEG-NH₂ to synthesize GO-PEG nanoparticles according to a previous method with a title modification.^{29–31} Briefly, 100 mg of GO nanosheets were dissolved in 80 mL of H₂O with 200 mg of 8-arm PEG-NH₂, followed by ultrasonic treatment for 5 min. Then, 20 mg of EDC·HCl was added to the solution under ultrasonic treatment for 40 min. Next, 60 mg of EDC·HCl was added to the above mixture solution under vigorous stirring at room temperature for 18 h. The resulting solution was purified by dialysis against distilled water for 3 days, and the distilled water was changed every 8 h. The obtained

GO-PEG was handled by freeze-drying overnight. Then, EPX and ConA were loaded on the surface of GO-PEG. In brief, 0.5 mL of EPX solution (40 mg mL⁻¹ in DMSO) was added dropwise to 20 mL of GO-PEG aqueous solution (1 mg mL⁻¹) under vigorous stirring at room temperature for 24 h. Then, the resulting solution was centrifuged at 10,000 rpm for 5 min and further purified by centrifugation in the mixed solution (DMSO/H₂O = 1:40) three times. Finally, the sediment in the centrifuge tube was lyophilized in a vacuum freeze dryer. In addition, for the synthesis of GO-PEG-EPX-ConA, when EPX and GO-PEG were stirred in the reaction solution for 23 h, 5 mg of ConA was added into the above mixed solution under stirring at room temperature for 1 h. After the reaction was completed, the resulting solution was handled by centrifugation at 4 °C, and the above cleaning operation was repeated.

2.3. Preparation of GO-PEG-FITC and GO-PEG-FITC-ConA.

To visualize the nanosheets acting on the spores of *M. oryzae*, the GO-PEG nanosheets were modified by FITC to form GO-PEG-FITC, and then ConA was loaded on GO-PEG-FITC. Briefly, 1 mL of FITC aqueous solution (1 mg mL⁻¹) was added to 20 mL of GO-PEG aqueous solution (2 mg mL⁻¹) under vigorous stirring at room temperature for 1 h. Next, the resulting solution was separated by centrifugation, followed by thorough washing with water three times. For the synthesis of GO-PEG-FITC-ConA, 10 mg of GO-PEG-FITC was redispersed in 10 mL of water, and then 2.5 mg of ConA was added into the above solution under stirring for 1 h. The excess ConA was washed away with water three times.

2.4. Characterization and the EPX-Loading Capacity of Nanomaterials.

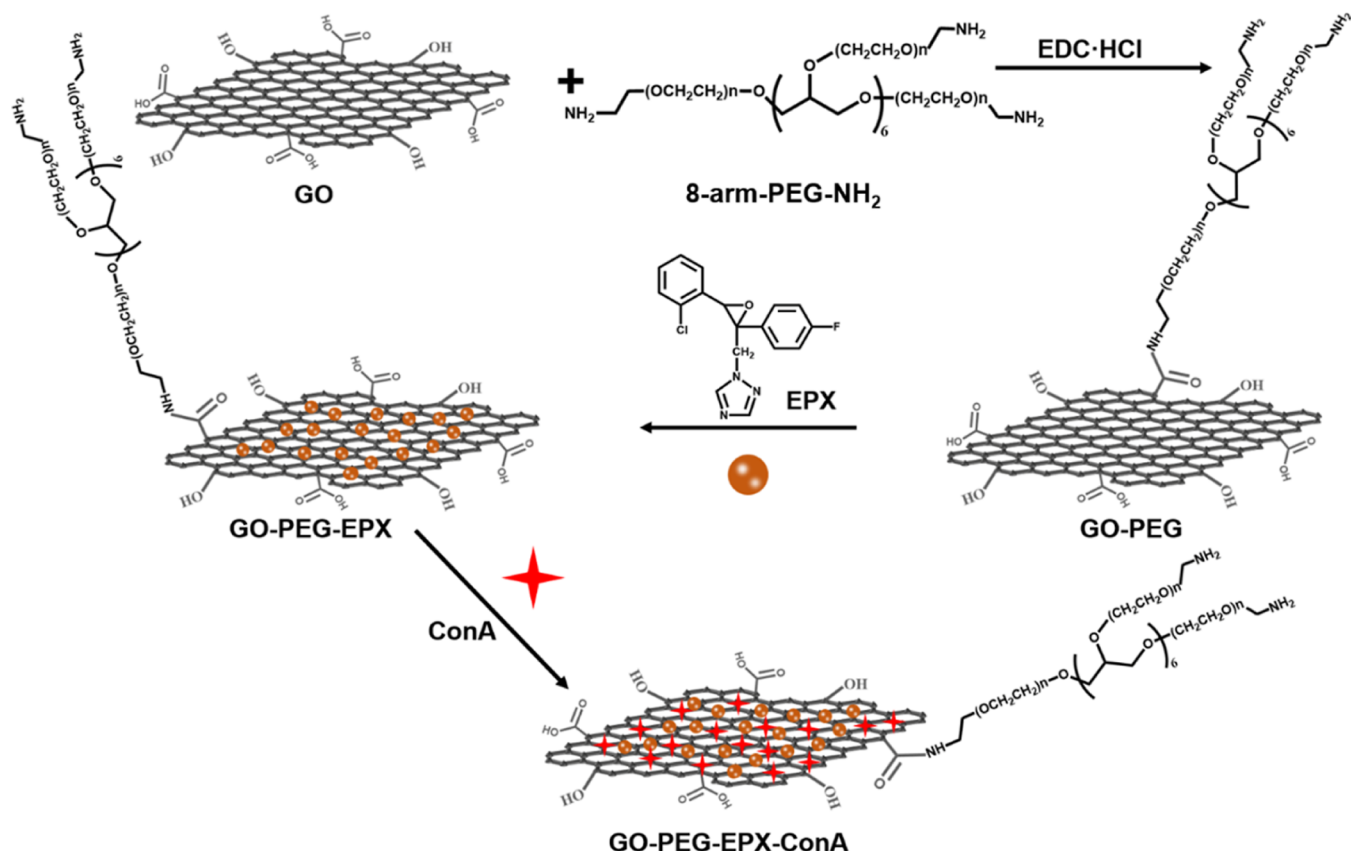
Fourier transform infrared (FTIR) spectra were obtained via a Vertex 70 spectrometer (Bruker Co., Germany) in the wavenumber range of 4000–400 cm⁻¹. UV–vis spectra were obtained using a UV–vis spectrophotometer (UV 2550, Shimadzu Co., Japan). The hydrodynamic diameter and zeta potential of nanosheets in an aqueous solution were characterized by dynamic light scattering (Zetasizer Nano ZSE, Malvern Panalytical Ltd., UK). To observe the morphology of nanosheets, the assay was accomplished by a scanning electron microscopy (SEM) instrument (Nova Nano 450, FEI Co., U.S.A.). Thermogravimetric (TG) analysis was inspected by a TG209F1 instrument. X-ray photoelectron spectroscopy (XPS) was conducted on a Thermo Scientific K-Alpha⁺ spectrometer equipped with a monochromatic Al K α X-ray source (1486.6 eV) operating at 100 W. All peaks were calibrated with a C 1s peak binding energy at 284.8 eV for adventitious carbon. The experimental peaks were fitted with XPSPEAK software.

Note that 5 mg of GO-PEG-EPX or GO-PEG-EPX-ConA nanomaterials was dissolved in 3 mL of methanol and then transferred into an ultrasonic bath for 2 h to thoroughly disassociate the EPX. Subsequently, the resulting suspension was centrifuged at 10,000 rpm for 10 min, and the supernatant was filtered and detected using HPLC. The mobile phase was acetonitrile–water (60:40). The flow rate was 1 mL min⁻¹, and 10 μ L of sample was injected into HPLC with a detector wavelength of 225 nm. The EPX loading capacity (LC) was calculated based on the following equation

$$LC = \frac{\text{weight of EPX loaded}}{\text{weight of nanomaterials}} \times 100\%$$

2.5. Sodium Dodecyl Sulfate–Polyacrylamide Gel Electrophoresis Assay.

The ConA loading capacity of nanosheets was assessed by sodium dodecyl sulfate–polyacrylamide gel electrophoresis (SDS–PAGE). SDS–PAGE running buffer (1 \times Tris–glycine) was prepared, and the protein standard (10–250 kDa) was used as the protein marker. 1 mg of ConA was dissolved in 3 mL of PBS buffer at pH 6.5, which was used as a standard solution of ConA. The other nanomaterials (GO-PEG, GO-PEG-EPX, GO-PEG-EPX-ConA, GO-PEG-FITC, and GO-PEG-FITC-ConA) were also suspended in PBS buffer at pH 6.5. Ten microliters of 5 \times protein loading buffer were added to 40 μ L of nanomaterial suspension liquid and ConA solution. All samples were heated in boiling water for 5 min to denature proteins, and then centrifuged at 10,000 rpm and 5 °C for 5 min. The supernatant (10 μ L) was loaded onto each well of a 12% polyacrylamide gel and subjected to electrophoresis at 100 V for 1 h.

Scheme 1. Diagram of the Preparation of the GO-PEG-EPX-ConA Nanopesticide^a

^aGO will react with multiple 8-arm-PEG-NH₂, and multiple arms will react with GO. The drawn scheme is the simplest structure among possible structures.

The gel was washed with water, followed by observation in a gel imager.

2.6. Mycelial Growth of *M. oryzae* In Vitro. The inhibitory effect of nanosheets on the mycelial growth of *M. oryzae* in vitro was assessed according to a previously described method.³² To determine the EC₅₀ values, the antifungal activities of EPX (the original fungicide), GO-PEG-EPX, and GO-PEG-EPX-ConA were tested using a series of concentrations (0.1–0.5 μg mL⁻¹). EPX, GO-PEG-EPX, and GO-PEG-EPX-ConA were dissolved in DMSO (0.2% final concentration in PDA medium) and then added to molten PDA medium. The mixtures were shaken and poured into 9 cm plastic Petri dishes. The control check was composed of PDA with 0.2% DMSO. Mycelial discs (5 mm in diameter) with *M. oryzae* from the margin of an actively growing colony were placed on the center of the PDA plates. All plates were incubated at 28 °C for 9 days in the dark, and then the average fungal colony diameters were measured by the cross method. The inhibition effect of mycelia (I, %) was calculated based on the formula below

$$I(\%) = (d_c - d_t)/d_c \times 100$$

where d_c refers to the diameter of the fungal colony in the control check and d_t refers to the diameter of the fungal colony in the treatment.

2.7. Spore Germination Assay. For the spore germination assay, *M. oryzae* spores were prepared using the following method.³³ The mycelial discs of *M. oryzae* were incubated on rice stalk corn flour agar (RCA) medium. All plates were incubated at 28 °C in a light incubator with alternating light and dark conditions. The spores were harvested by gently scraping off the hyphae with sterile water, and then the resulting suspension liquid was filtered through a double layer of sterile lens cleaning paper. The spore suspensions were adjusted to a concentration of 2×10^6 spores mL⁻¹ by centrifugation

at 3000 rpm for 10 min. Next, 500 μL of spore suspensions were mixed with 500 μL of nanosheets (GO-PEG or GO-PEG-ConA) in a 1.5 mL tube to obtain a nanosheet suspension at a final concentration of 50 μg mL⁻¹. The control check consisted of 500 μL of spore suspensions with 500 μL of sterile water. The mixed solutions were incubated in a shaker at 150 rpm and 28 °C for 6 h. 40 μL of the mixture was transferred onto a hydrophobic slide in a sterile Petri dish with wet filter paper for further incubation at 28 °C for 12 h. Each treatment was made up of three hydrophobic slides, and the mean values were compared. The spore germination rate (%) was calculated according to the following formula: spore germination rate (%) = (the number of germinated spores)/(the total number of spores). The remaining spore mixture in the centrifuge tube was centrifuged at 3000 rpm for further structural and morphological observation of spores with SEM (SU-8010. Hitachi, Japan). The collected spores were fixed overnight with 2.5% glutaraldehyde.

2.8. Visualization of Spores by Confocal Laser Scanning Microscopy. To identify the effect of ConA loaded on the GO-PEG nanosheets, the nanosheets were labeled by FITC. 100 μL of the GO-PEG-FITC and GO-PEG-FITC-ConA nanosheets were mixed with 100 μL of spore suspension to obtain nanosheet suspensions at a final concentration of 50 μg mL⁻¹. The mixtures were incubated in a shaker at 150 rpm and 28 °C for 6 h. Then, the resulting solution was centrifuged at 3000 rpm to collect spores. Then, the spores were dispersed in PBS buffer at pH 6.5 with 20% glycerol, which was observed through a Nikon Eclipse Ti-E A1 laser-scanning confocal system (Nikon Instruments Inc., Japan).

2.9. Greenhouse Experiment. A greenhouse study was conducted on rice seedlings to evaluate the effect of nanosheets against rice blast. Rice seedlings were grown in the greenhouse with alternating light and dark for 30 days and then sprayed with an equal volume of different nanosheet suspensions with 0.1% Silwet L-77

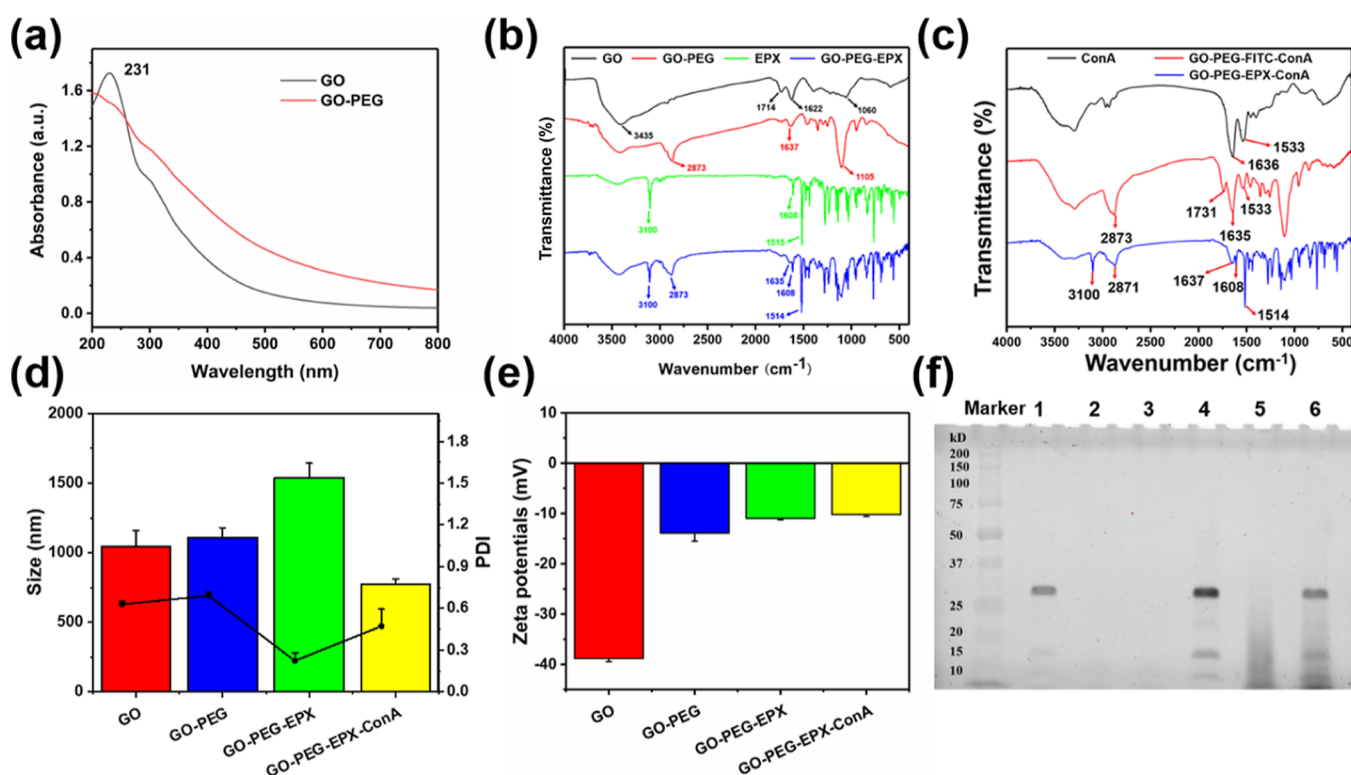


Figure 1. Characterization of nanosheets. (a) UV-vis spectra of GO and GO-PEG; (b,c) FTIR spectra of different nanosheets; (d,e) hydrodynamic size and zeta potential of GO, GO-PEG, GO-PEG-EPX, and GO-PEG-EPX-ConA in the water. The hydrodynamic sizes represent the average hydrodynamic diameters of nanomaterials. (f) SDS-PAGE of nanosheets and ConA: (1) ConA; (2) GO-PEG; (3) GO-PEG-EPX; (4) GO-PEG-EPX-ConA; (5) GO-PEG-FITC; (6) GO-PEG-FITC-ConA to explore the protein loading capacity on nanosheets.

containing a uniform drug concentration of $50 \mu\text{g mL}^{-1}$. In addition, seedlings treated with $50 \mu\text{g mL}^{-1}$ EPX and 0.1% Silwet L-77 were used to compare the control effect. The control check consisted of sterile water with 0.1% Silwet L-77. After 3 hours, the rice seedlings were infected by spraying the *M. oryzae* spore suspension at 2×10^6 spores mL^{-1} . These rice seedlings were incubated under greenhouse conditions to further observe disease severity after 5 days.

3. RESULTS AND DISCUSSION

3.1. Characterization of Nanoparticles. The GO-PEG-EPX-ConA nanopesticide was prepared as shown in Scheme 1. First, GO was modified with 8-arm PEG-NH₂ by a covalent amide bond between the -NH₂ group on the PEG branched arm and the -COOH group on the GO nanosheets. Second, EPX and ConA were loaded on the GO-PEG nanosheets by absorption and π - π interactions.

The UV-vis spectra of GO and GO-PEG are shown in Figure 1a. The characteristic absorption peak of GO appeared at 231 nm, representing the π -electron plasmon excitation of carbon.³⁴ However, the spectrum of GO-PEG, in which carboxyl groups on the surface of GO sheets reacted with 8-arm PEG-NH₂ via amidation reaction, was a smooth curve without any distinct absorption peak. To affirm whether nanocomposites were synthesized successfully, the FTIR spectra are depicted in Figure 1b,c. There were characteristic peaks at 1714, 1622, and 1060 cm^{-1} , representing C=O stretch vibrations, the vibrations of undried water molecules, and C-O-C functional groups in GO.^{23,28} After the amidation reaction, a new signal appeared at 1637 cm^{-1} in the FTIR spectrum of GO-PEG, originating from the amide group (-NH-CO-). Meanwhile, the strong peaks at 2873 and 1105 cm^{-1} , which represented -CH₂- and -C-O-

stretch vibrations of the PEG chains, also sufficiently illustrated the covalent grafting between PEG chains and the carboxyls on the surface of GO sheets. The spectrum of GO-PEG-EPX contained the characteristic peaks of EPX, including the unsaturated =C-H of the triazole ring (3100 cm^{-1}) and the benzene ring stretch vibrations (1608 and 1514 cm^{-1}). In particular, the peak of the amide group appeared at 1635 cm^{-1} in the spectrum curve of GO-PEG-EPX because of the interaction between GO-PEG and EPX. These results demonstrated that EPX was loaded successfully on the GO-PEG nanocarriers. With regard to FITC in Figure S1, the strong absorption peak at 1735 cm^{-1} was assigned to the stretching vibrations of C=O. Compared to the spectrum of GO-PEG-FITC, the same peak appeared at 1735 cm^{-1} , which belonged to the stretching vibration of FITC, and the stretching vibrations of -CO-NH- showed a shift in the band maxima toward lower wavenumbers, from 1637 to 1630 cm^{-1} . For the spectrum of GO-PEG-FITC-ConA, the stretching vibration of -CO-NH- appeared at 1635 cm^{-1} due to the interaction between GO-PEG-FITC and ConA, and the same peak at 1533 cm^{-1} appeared, belonging to the characteristic peak of ConA. With respect to GO-PEG-EPX-ConA, the strong absorption peaks at 3100, 1608, and 1514 cm^{-1} belonged to the characteristic peak of EPX. In particular, the peak of the -CO-NH- stretching mode in GO-PEG-EPX-ConA appeared at 1652 cm^{-1} due to the existence of ConA. Thus, the results confirmed that EPX and ConA were successfully loaded on the GO-PEG nanocarriers.

The hydrodynamic size and zeta potential of nanocomposites were studied by dynamic light scattering. As shown in Figure 1d, the hydrodynamic sizes of GO, GO-PEG,

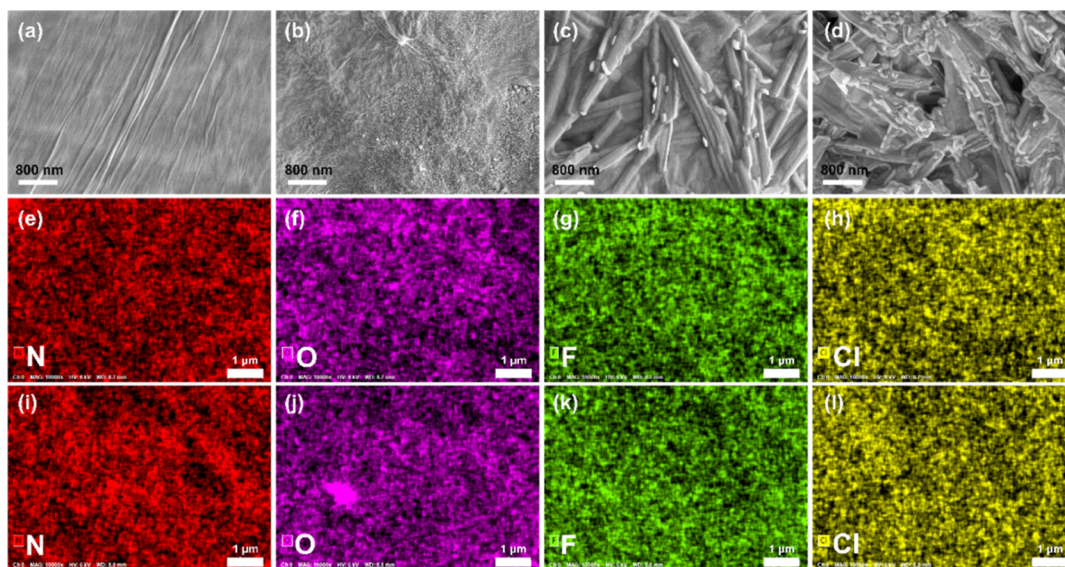


Figure 2. SEM of nanoparticles: (a) GO; (b) GO-PEG; (c) GO-PEG-EPX; (d) GO-PEG-EPX-ConA. EDS analysis of nanosheets: mapping images of GO-PEG-EPX (e–h) and GO-PEG-EPX-ConA (i–l).

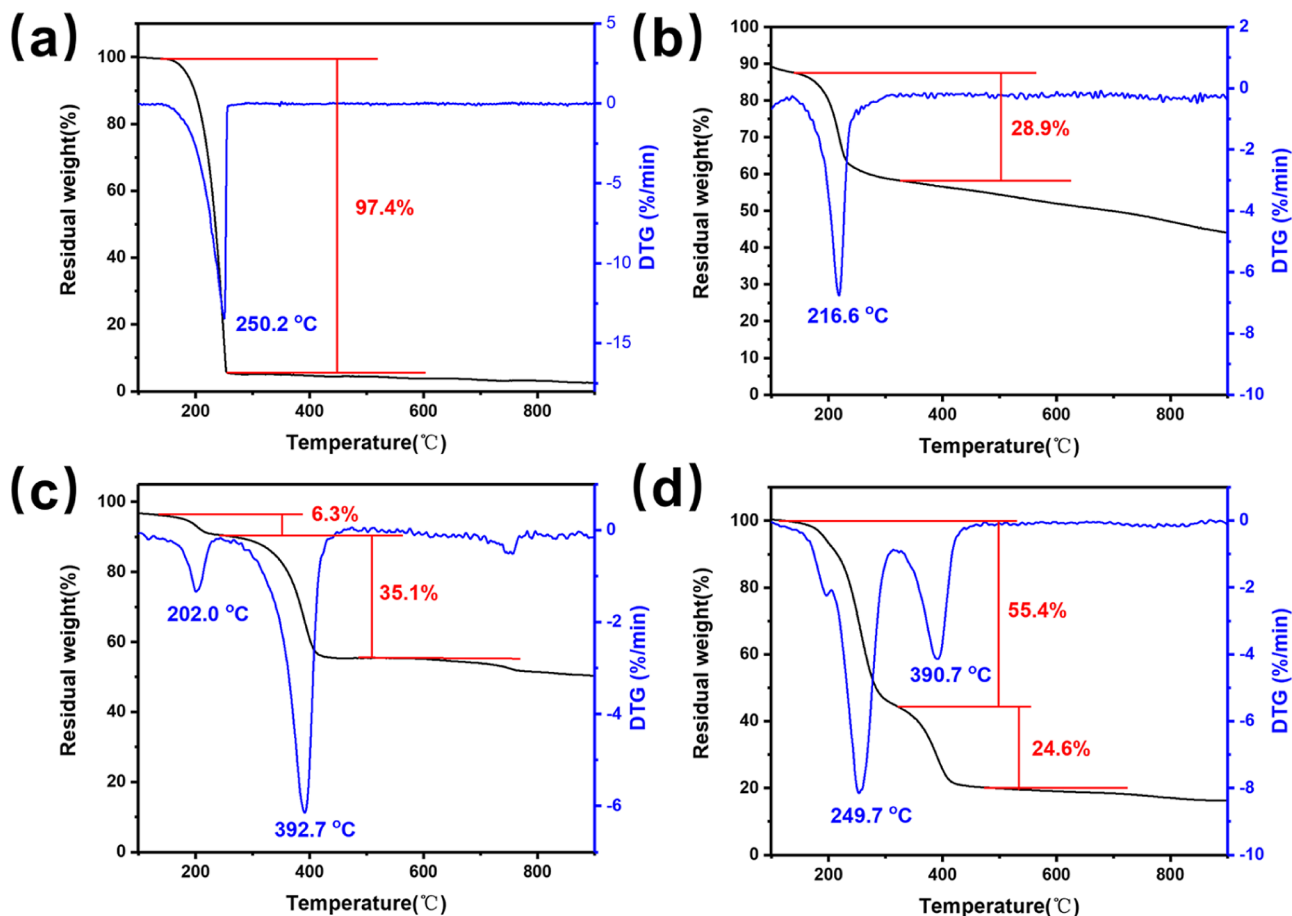


Figure 3. TG profiles and DTG analysis of (a) EPX, (b) GO, (c) GO-PEG, and (d) GO-PEG-EPX. The black and blue lines correspond to mass fraction and DTG, respectively.

and GO-PEG-EPX were 981, 1138, and 1549 nm, respectively. After the amidation reaction, the hydrodynamic size of GO-PEG increased to 1138 nm due to the presence of PEG chains on the surface of GO sheets. Compared to empty GO-PEG nanocarriers, the hydrodynamic size of GO-PEG-EPX nano-

particles increased to 1549 nm, which may be caused by the existence of an organic layer on the surface of GO-PEG.⁸ GO will react with multiple 8-arm-PEG-NH₂, and multiple arms will react with GO. The amino group not reacted may react with EPX by the nucleophilic ring-opening reaction. The

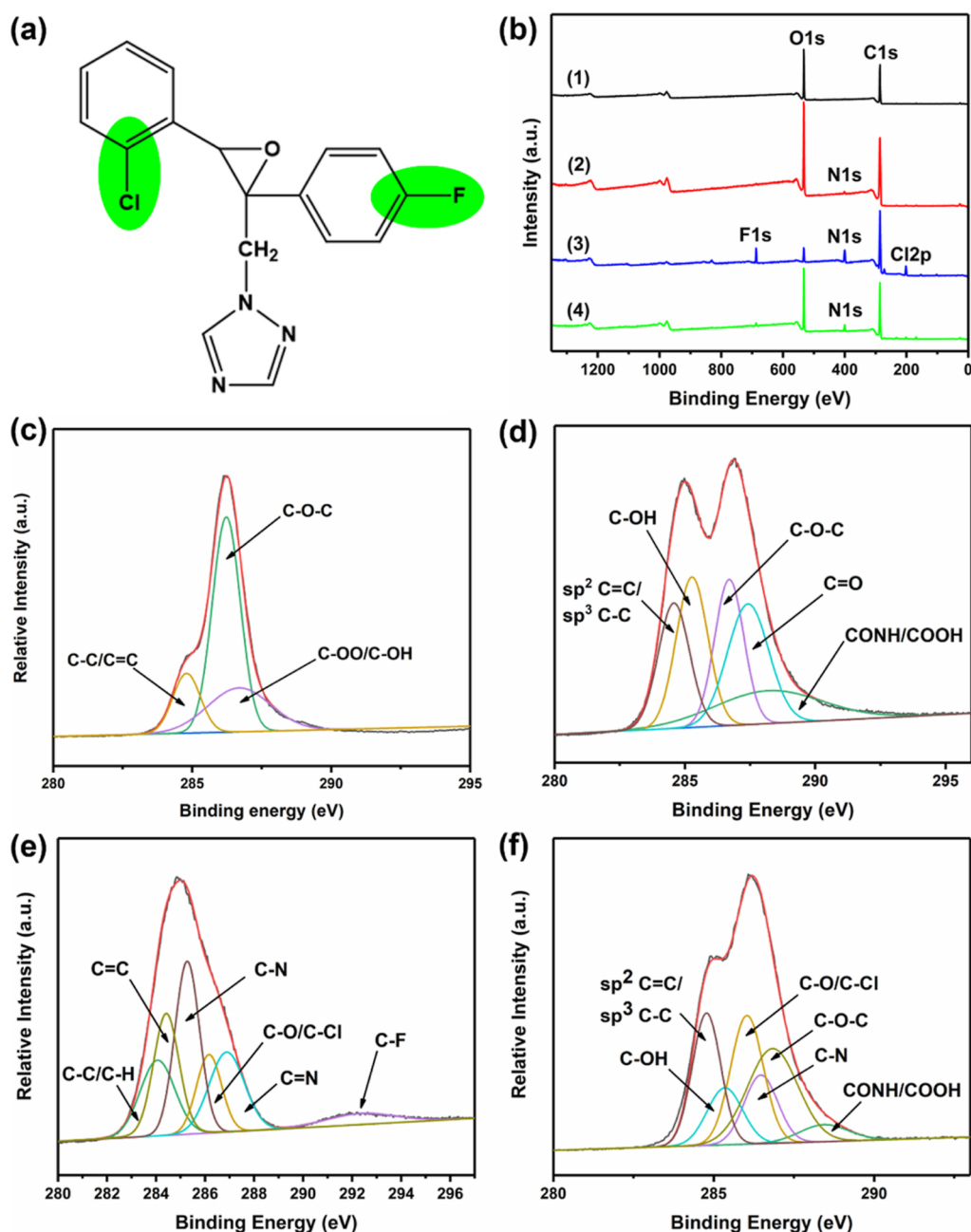


Figure 4. XPS survey curves of samples. (a) Chemical structural formula of EPX. (b) XPS survey curves of (1) GO, (2) GO-PEG, (3) EPX, and (4) GO-PEG-EPX-ConA. Deconvoluted C 1s XPS spectra of (c) GO, (d) GO-PEG, (e) EPX, and (f) GO-PEG-EPX-ConA.

interactions between EPX and GO-PEG include non-covalent and covalent binding. In particular, when ConA was loaded on the nanocarriers, the hydrodynamic size of GO-PEG-EPX-ConA decreased to 793 nm due to the excellent water solubility of ConA. With regard to the surface charge of nanoparticles, GO showed the most negative charge (-39.5 mV) in Figure 1e, indicating that the GO aqueous solution was relatively stable. Compared to the zeta potentials of GO, GO-PEG had less surface charge (-12.4 mV) because of the presence of amino acids. In addition, compared with the zeta potential of GO-PEG, there was a slight decrease in the zeta potentials (-10.7 and -10.6 mV) of GO-PEG-EPX and GO-PEG-EPX-ConA after loading drugs and proteins, presumably due to the electrostatic interactions between nanocarriers and other molecules.

3.2. SDS-PAGE Assay. As shown in Figure 1f, SDS-PAGE showed extensive ConA on nanosheets. Lane 1 represented the strip of ConA at 0.333 mg mL $^{-1}$, and its monomeric molecular weight corresponded to 25,500 Da. Lanes 2, 3, and 5 had no strips, indicating that these nanosheets had no influence on the movement of the ConA protein. The ConA loading capacities of GO-PEG-EPX and GO-PEG-FITC were 14.7 and 37.5%, respectively, based on strip analysis. Compared to GO-PEG-EPX, GO-PEG-FITC had a higher ConA loading capacity due to the stronger affinity between FITC and ConA.

3.3. Structure and Morphology Analysis of Nanomaterials. The morphologies of the GO, GO-PEG, GO-PEG-EPX, and GO-PEG-EPX-ConA nanoparticles were observed by SEM. As shown in Figure 2a, the GO sheets were smooth

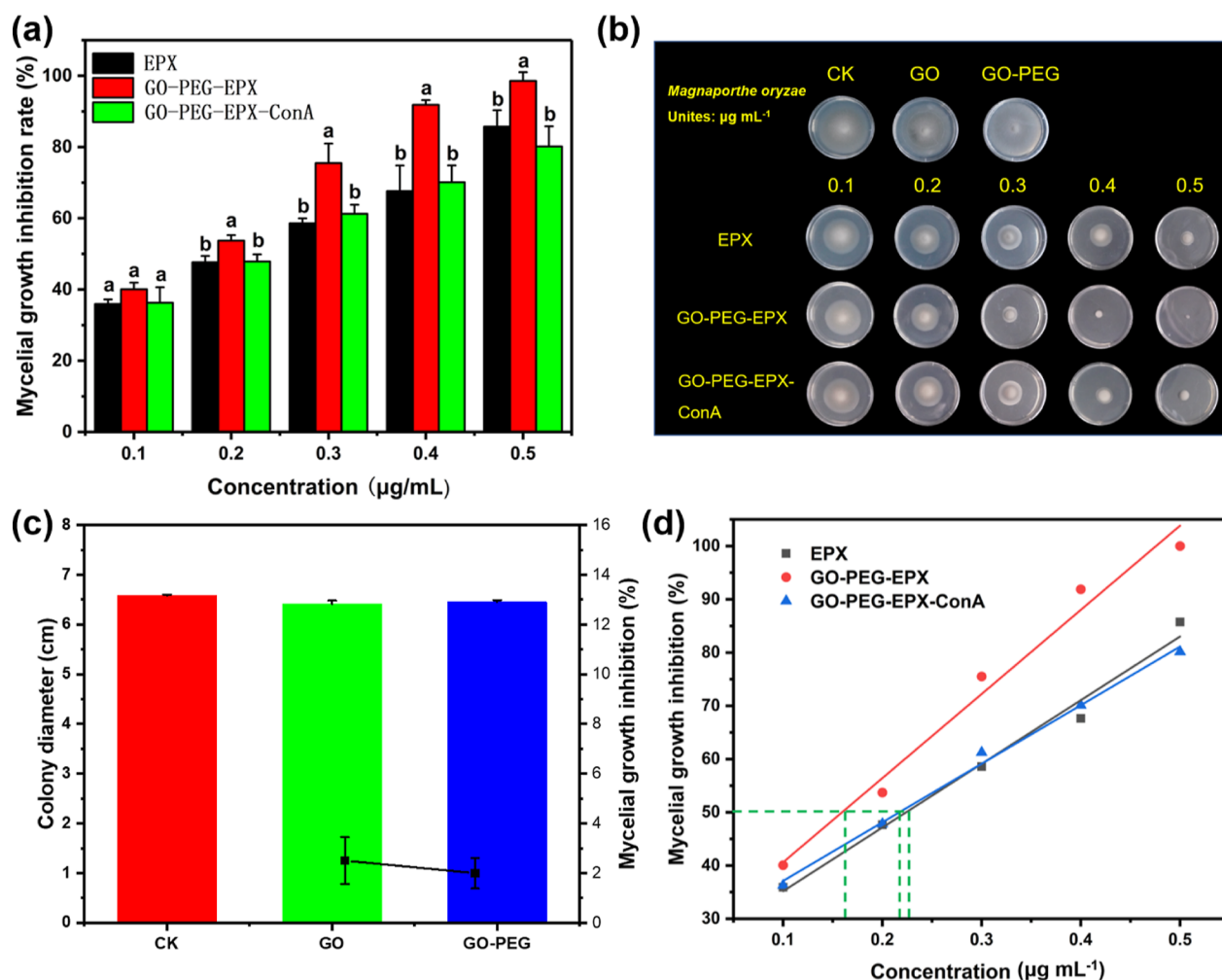


Figure 5. (a) Mycelial growth rate of *M. oryzae* on PDA media containing different concentrations of EPX. Graph represents mean \pm SE followed by the same letter is not significantly different at $p \leq 0.05$ as determined by Duncan. (b) Photos of *M. oryzae* incubated with nanocomposites. (c) Mycelial growth rate of *M. oryzae* on PDA media for GO and GO-PEG at $0.5 \mu\text{g mL}^{-1}$. (d) EC₅₀ fitting curves of EPX, GO-PEG-EPX, and GO-PEG-EPX-ConA regarding mycelial growth inhibition.

with some small wrinkles, similar to silk. However, after the amidation reaction, some defects were observed on the surface of GO-PEG. After loading EPX, drug molecules were absorbed on the surface of GO-PEG via electrostatic attraction, hydrophobic interactions, and π - π stacking.^{35–37} Moreover, the nanoparticles in Figure 2c, after the loading of the drug, showed more stereoscopic wrinkles on the surface of GO-PEG-EPX compared to the morphologies of GO and GO-PEG. When EPX and ConA were loaded simultaneously on the surface of GO-PEG, the surface of GO-PEG-EPX-ConA became slightly smooth compared to GO-PEG-EPX because of the addition of ConA. ConA may act as a dispersion stabilizer due to its excellent water solubility, which was shown by the hydrodynamic size results. In addition, as shown in Figure S2, strong signals of fluorine and chlorine were detected in the energy dispersive spectroscopy (EDS) point scan spectra of GO-PEG-EPX and GO-PEG-EPX-ConA, which confirmed the existence of EPX. Furthermore, it was demonstrated that EPX was evenly distributed on the GO-PEG nanosheets by elemental mapping of fluorine and chlorine.

3.4. TG Analysis of Nanomaterials. Figure 3 shows the TG and derivative thermogravimetry (DTG) profiles of EPX, GO, GO-PEG, and GO-PEG-EPX. There was only one peak

from 138 to 258 °C in the DTG curve of EPX, corresponding to weight loss in the TG profile. The TG curve of GO revealed a step at 138–324 °C because of the decomposition of oxygen-containing groups in GO.³⁸ After grafting PEG, the TG curve of GO-PEG exhibited two steps corresponding to weight loss. The first peak between 133 and 242 °C appeared due to degradation of the organic functional groups. The second peak in the range of 242–445 °C appeared, which could be caused mainly by the decomposition of GO-PEG. PEGylated GO seemed to have higher thermal stability than GO.³⁹ Compared with the observed curves of GO, the maximum weight loss temperatures of GO-PEG and GO-PEG-EPX were increased to 392.7 and 390.7 °C, respectively. Similarly, GO-PEG-EPX also showed two distinct steps of weight loss. The first stage emerged in the range of 133–320 °C owing to the decomposition of EPX and organic functional groups. Compared to the first one of GO-PEG, the weight losses of GO-PEG-EPX were approximately 55.4%; thus, the loading rate of EPX was approximately 48.1%, which was roughly consistent with the results (46.9%) of HPLC analysis (Figure S3). The second stage arose between 320 and 474 °C because of the degradation of GO-PEG. Simultaneously, GO-PEG-EPX nanosheets had less final residue than GO and GO-PEG

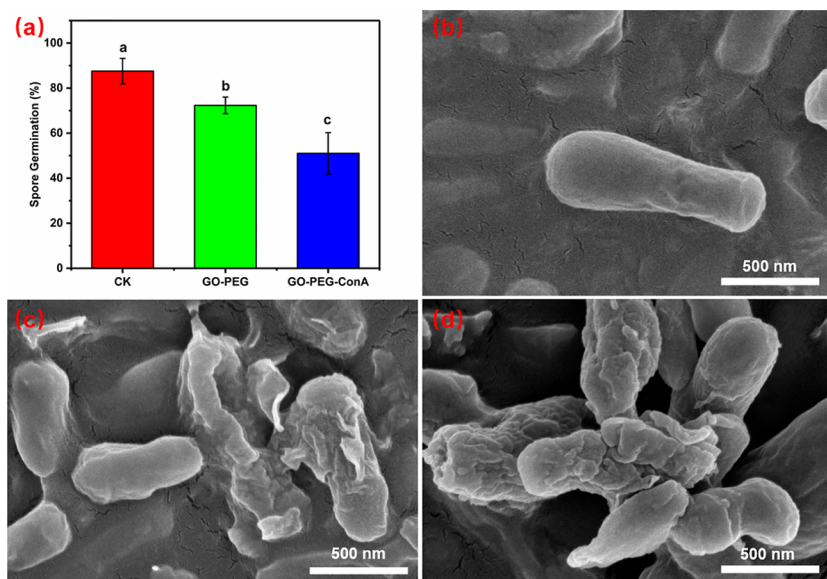


Figure 6. Effect of GO-PEG and GO-PEG-ConA on spore germination and SEM analysis of spores after incubation with nanosheets. (a) Spores were germinated on hydrophobic slides at 28 °C in darkness at different nanosheets for 12 h. Significant statistical analysis was performed by one-way ANOVA with Duncan's post-hoc multiple range test. (b) CK: normal *M. oryzae* spores. The structure and morphology of spores cultivated with GO-PEG (c) and GO-PEG-ConA (d). Scale bar = 500 nm.

because of the existence of EPX. Taken together, these abovementioned results confirmed that GO-PEG and GO-PEG-EPX nanoparticles were successfully synthesized.

3.5. XPS Spectroscopy. XPS survey spectra revealed that the surface components and structural changes were caused by shifts in the binding energy (BE) values. As shown in Figure 4b, there was no characteristic peak of N 1s in the survey curve of GO. However, the survey curve of PEGylated GO had an obvious N 1s band belonging to the amine group of PEG.³⁹ Meanwhile, obvious bands of F 1s and Cl 2p were observed in the survey of GO-PEG-EPX-ConA. For the C 1s XPS spectra of GO, oxygen-containing functional groups were observed, including C–OH, C–OO, and C–O–C.⁴⁰ The C 1s XPS spectrum of GO-PEG showed significant shifts for all groups, and a new characteristic peak at 288.5 eV appeared to originate from –CONH/COOH, which was caused by chemical modification. In addition, after loading EPX and ConA, the binding energy of CONH/COOH was basically unchanged at 288.4 eV, which may be due to the noncovalent bonding force between GO-PEG nanosheets and drugs. The binding energy of C–O/C–Cl in GO-PEG-EPX-ConA was 286.8, which was consistent with the C–O/C–Cl of EPX, indicating that no chemical reaction took place between nanocarriers and drugs. The XPS results indicated that the combination of GO and 8-arm PEG–NH₂ was covalently bonded, whereas EPX and ConA were loaded on the surface of GO-PEG carriers by physical interaction.

3.6. In Vitro Antifungal Activity against *M. oryzae*. As shown in Figure 5, the fungicidal activity of GO-PEG-EPX and GO-PEG-EPX-ConA was studied through the mycelial growth rate method on PDA medium. The GO and GO-PEG nanosheets had almost no inhibitory effect. The EC₅₀ (50% of maximal effect) values of GO-PEG-EPX, GO-PEG-EPX-ConA, and EPX were 0.148, 0.184, and 0.187 μg mL^{−1}, respectively, based on the virulence regression equation, which showed the linear correlation in Table S1. Moreover, GO-PEG-EPX could significantly inhibit the mycelial growth of rice blast compared with EPX and GO-PEG-EPX-ConA, indicating

a synergistic effect between GO-PEG nanocarriers and EPX drugs.³⁷ GO-PEG-EPX nanomaterials showed concentration dependence, and the synergistic effect was stronger with increasing concentration. As shown in Figure 5a, when the concentration was 0.2–0.5 μg mL^{−1}, the fungicidal activity of the GO-PEG-EPX nanomaterial showed a significant difference compared with the other two treatment groups, according to Duncan analysis. However, it should be noted that EPX and GO-PEG-EPX-ConA showed almost equal antifungal activity against *M. oryzae*, which might be due to the existence of ConA. The main purpose of ConA in GO-PEG-EPX-ConA nanosheets was to enhance the combination between nanocarriers and spores, whereas ConA might provide nitrogen source nutrition for mycelial growth to weaken the synergistic effect between nanocarriers and drugs. All the results above indicated that GO-PEG nanosheets could be an excellent pesticide carrier for the control of *M. oryzae* hyphae.

3.7. Effect of Nanomaterials on Spore Germination of *M. oryzae*. Considering that the lectin protein ConA was inclined to combine with spores, a spore germination assay was designed to observe the effect of nanocarriers on spores. As shown in Figure 6a, the spore germination rate of normal *M. oryzae* spores was 87.6%. There was a significant difference after incubation with GO-PEG and GO-PEG-ConA. Compared with the normal *M. oryzae* spores, after 12 h of incubation with GO-PEG or GO-PEG-ConA, the spore germination rates were 72.3 and 51.0%, respectively, which might be caused by the strong combination between GO-PEG-ConA and spores. Simultaneously, the structure and morphology of spores after coincubation with nanocarriers were observed by SEM. The structure of spores was severely destroyed after incubation with GO-PEG and GO-PEG-ConA, as shown in Figure 6c,d, due to the nanometer effect of GO.^{41,42} However, compared to GO-PEG, GO-PEG-ConA nanocarriers could extremely damage the structure of *M. oryzae* spores. These results demonstrated that GO-PEG-ConA nanocarriers could seriously inhibit the germination of *M. oryzae* spores.

3.8. Visualization of Spores. To investigate the mutual effect between nanocarriers and *M. oryzae* spores, FITC-labeled nanosheets (GO-PEG-FITC and GO-PEG-FITC-ConA) were prepared. The maximum emission (EM) wavelengths of GO-PEG-FITC and GO-PEG-FITC-ConA were 523 and 520 nm, respectively, as shown in Figure S4, corresponding to the maximum EM wavelength of FITC, which indicated that GO-PEG-FITC and GO-PEG-FITC-ConA nanomaterials showed green fluorescence with excitation at 488 nm. There was a significant distinction between Figure 7b,d. After 6 h of cocultivation with spores, GO-PEG-

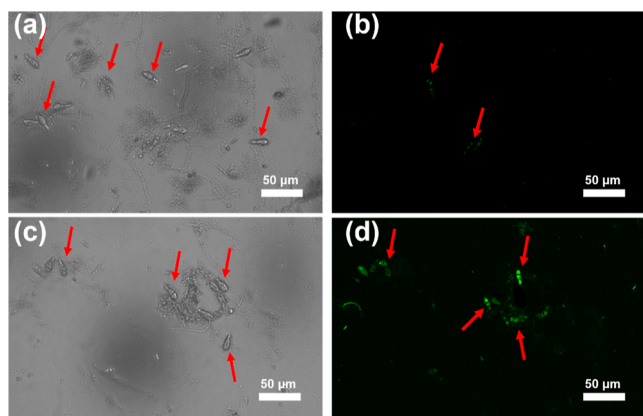


Figure 7. Confocal fluorescence microscopy images of GO-PEG-FITC (a,b) and GO-PEG-FITC-ConA (c,d) after incubation with spores at 28 °C for 6 h. Green channel for FITC with $\lambda_{\text{ex}} = 488$ nm and $\lambda_{\text{em}} = 500\text{--}550$ nm. Scale bar = 100 μm . The red arrowheads represent *M. oryzae* spores.

FITC-ConA showed stronger green fluorescence than GO-PEG-FITC, indicating that GO-PEG-FITC-ConA was more liable to combine with spores. When *M. oryzae* spores were cultivated with nanocarriers, the addition of ConA increased the chance of contact between spores and nanocarriers. From the spore assay results shown in Figures 6 and 7, the GO-PEG-ConA nanocarriers can be prone to close bonds with spores and cause greater damage to spores to inhibit germination. These consequences laid a theoretical foundation for the practical application of nanomaterials.

3.9. Control Effect of Rice Blast on Rice. To further investigate practical efficiency, different nanosheets containing a uniform pesticide concentration of 50 $\mu\text{g mL}^{-1}$ were applied to rice seedlings to control rice blast. Taking into consideration the characteristics of the spread of rice blast by spores, all rice

plants were infected by spraying the spore suspension. As shown in Figure 8a, the CK group had no symptoms, which indicated that the experimental environment was qualified and free of other pests and diseases. In addition, the CK- showed severe symptoms of rice blast, in which almost all leaves turned yellow and there were plenty of dark spots on the leaves. However, after applying different treatments, the incidence of rice blast showed a decreasing trend: EPX > GO-PEG-EPX > GO-PEG-EPX-ConA. For the GO-PEG-EPX treatment groups, there were some dark spots on the leaf. The EPX treatment groups had a mass of dark spots, and the rice leaves also turned slightly yellow. There were almost no rice blast lesions for GO-PEG-EPX-ConA. This result coincided with the consequences of spore germination. After the spore was sprayed on the rice leaf, the high affinity of GO-PEG-EPX-ConA with spores led to these spores failing to attach to rice leaves. As shown in Figure 8b, the presence of ConA was equivalent to the eyes of nanopesticides to catch spores and then killed spores by the superior synergistic effect between GO and EPX to protect rice plants from rice blast, which indicated that the nanomaterials had a Global Position System (GPS). It was concluded that the addition of ConA could generate distinct antifungal activity for rice seedlings.

4. CONCLUSIONS

In conclusion, GO-PEG-EPX and GO-PEG-EPX-ConA nanomaterials were prepared successfully. The GO-PEG-EPX nanosheets could significantly increase the antifungal activity of EPX against the mycelial growth of rice blast due to the synergistic effect between nanocarriers and drugs. In addition, the GO-PEG-ConA nanosheets could specifically identify the spores of *M. oryzae* to inhibit their germination. The FITC-labeled assay demonstrated that the addition of ConA made the spores more prone to combine with nanomaterials. Furthermore, in vivo experiments on rice plants indicated that the GO-PEG-EPX-ConA nanomaterial could obviously reduce rice blast lesions in rice seedlings. More importantly, the design of GO-PEG-EPX-ConA nanomaterials fundamentally settled the transmission of rice blast. All results demonstrate that GO-PEG-ConA can be a targeted nanopesticide carrier to realize precise release of drugs, which will have immense potential to improve the utilization efficiency of pesticides and protect the ecological environment.

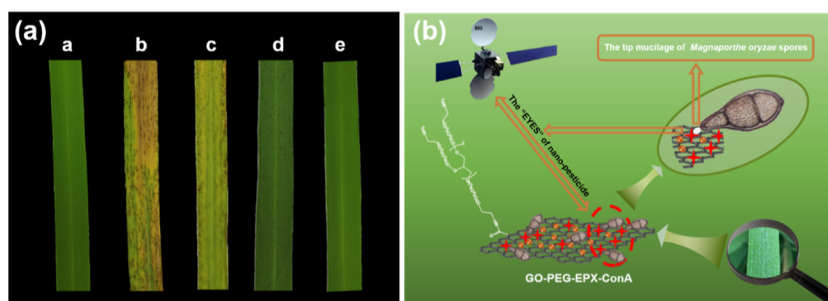


Figure 8. (a) Control effect of nanosheets on rice blast in pot experiments. (a) CK, normal rice leaf without treating anything; (b) CK-, *M. oryzae* spore-infected rice without applying any pesticide; (c–e) after applying EPX, GO-PEG-EPX, and GO-PEG-EPX-ConA, *M. oryzae* spore-infected rice. (b) Schematic diagram in which GO-PEG-EPX-ConA captured *M. oryzae* spores.

■ ASSOCIATED CONTENT

SI Supporting Information

The Supporting Information is available free of charge at <https://pubs.acs.org/doi/10.1021/acsanm.3c01170>.

FTIR spectra of FITC and GO-PEG-FITC; EDS point scan analysis of GO-PEG-EPX and GO-PEG-EPX-ConA; standard curve of EPX detected by HPLC; fluorescence spectra of FITC, GO-PEG-FITC, and GO-PEG-FITC-ConA; and virulence regression equation of EPX, GO-PEG-EPX, and GO-PEG-EPX-ConA regarding mycelial growth inhibition (PDF)

■ AUTHOR INFORMATION

Corresponding Authors

Hanhong Xu – National Key Laboratory of Green Pesticide, South China Agricultural University, Guangzhou 510642, China; orcid.org/0000-0001-7841-2396; Email: hwxu@scau.edu.cn

Jinliang Jia – National Key Laboratory of Green Pesticide, South China Agricultural University, Guangzhou 510642, China; Key Laboratory for Biobased Materials and Energy of Ministry of Education, College of Materials and Energy, South China Agricultural University, Guangzhou, Guangdong 510642, China; orcid.org/0000-0002-6974-904X; Email: jiajinliang@scau.edu.cn

Authors

Pengtong Hu – National Key Laboratory of Green Pesticide, South China Agricultural University, Guangzhou 510642, China; Key Laboratory for Biobased Materials and Energy of Ministry of Education, College of Materials and Energy, South China Agricultural University, Guangzhou, Guangdong 510642, China

Li Zhu – Key Laboratory for Biobased Materials and Energy of Ministry of Education, College of Materials and Energy, South China Agricultural University, Guangzhou, Guangdong 510642, China

Wenjie Deng – National Key Laboratory of Green Pesticide, South China Agricultural University, Guangzhou 510642, China; Key Laboratory for Biobased Materials and Energy of Ministry of Education, College of Materials and Energy, South China Agricultural University, Guangzhou, Guangdong 510642, China

Weirou Huang – Key Laboratory for Biobased Materials and Energy of Ministry of Education, College of Materials and Energy, South China Agricultural University, Guangzhou, Guangdong 510642, China

Complete contact information is available at: <https://pubs.acs.org/doi/10.1021/acsanm.3c01170>

Notes

The authors declare no competing financial interest.

■ ACKNOWLEDGMENTS

The authors are thankful for financial support of the Guangdong Basic and Applied Basic Research Foundation (grant no. [2023A1515010609](https://doi.org/10.1021/acsanm.3c01170)) and the Innovation Team of Modern Agricultural Industry Technology System of Guangdong Province (grant no. 2019KJ140).

■ REFERENCES

- (1) Kim, S.; Kim, C.-Y.; Park, S.-Y.; Kim, K.-T.; Jeon, J.; Chung, H.; Choi, G.; Kwon, S.; Choi, J.; Jeon, J.; Jeon, J.-S.; Khang, C. H.; Kang, S.; Lee, Y.-H. Two nuclear effectors of the rice blast fungus modulate host immunity via transcriptional reprogramming. *Nat. Commun.* **2020**, *11*, 5845.
- (2) Wu, C.; Lin, Y.; Zheng, H.; Abubakar, Y. S.; Peng, M.; Li, J.; Yu, Z.; Wang, Z.; Naqvi, N. I.; Li, G.; Zhou, J.; Zheng, W. The retromer CSC subcomplex is recruited by MoYpt7 and sequentially sorted by MoVps17 for effective conidiation and pathogenicity of the rice blast fungus. *Mol. Plant Pathol.* **2021**, *22*, 284–298.
- (3) Liu, J.; Wang, X.; Mitchell, T.; Hu, Y.; Liu, X.; Dai, L.; Wang, G.-L. Recent progress and understanding of the molecular mechanisms of the rice-Magnaporthe oryzae interaction. *Mol. Plant Pathol.* **2010**, *11*, 419–427.
- (4) Mentlak, T. A.; Kombrink, A.; Shinya, T.; Ryder, L. S.; Otomo, I.; Saitoh, H.; Terauchi, R.; Nishizawa, Y.; Shibuya, N.; Thomma, B. P. H. J.; Talbot, N. J. Effector-Mediated Suppression of Chitin-Triggered Immunity by Magnaporthe oryzae Is Necessary for Rice Blast Disease. *Plant Cell* **2012**, *24*, 322–335.
- (5) Skamnioti, P.; Gurr, S. J. Against the grain: safeguarding rice from rice blast disease. *Trends Biotechnol.* **2009**, *27*, 141–150.
- (6) Wilson, R. A.; Talbot, N. J. Under pressure: investigating the biology of plant infection by Magnaporthe oryzae. *Nat. Rev. Microbiol.* **2009**, *7*, 185–195.
- (7) Liang, W.; Xie, Z.; Cheng, J.; Xiao, D.; Xiong, Q.; Wang, Q.; Zhao, J.; Gui, W. A Light-Triggered pH-Responsive Metal-Organic Framework for Smart Delivery of Fungicide to Control Sclerotinia Diseases of Oilseed Rape. *ACS Nano* **2021**, *15*, 6987–6997.
- (8) Sharma, S.; Singh, S.; Ganguli, A. K.; Shanmugam, V. Anti-drift nano-stickers made of graphene oxide for targeted pesticide delivery and crop pest control. *Carbon* **2017**, *115*, 781–790.
- (9) Shen, Z.; Wen, H.; Zhou, H.; Hao, L.; Chen, H.; Zhou, X. Coordination bonding-based polydopamine-modified mesoporous silica for sustained avermectin release. *Mater. Sci. Eng., C* **2019**, *105*, 110073.
- (10) Tong, Y.; Shao, L.; Li, X.; Lu, J.; Sun, H.; Xiang, S.; Zhang, Z.; Wu, Y.; Wu, X. Adhesive and Stimulus-Responsive Polydopamine-Coated Graphene Oxide System for Pesticide-Loss Control. *J. Agric. Food Chem.* **2018**, *66*, 2616–2622.
- (11) Xu, C.; Shan, Y.; Bilal, M.; Xu, B.; Cao, L.; Huang, Q. Copper ions chelated mesoporous silica nanoparticles via dopamine chemistry for controlled pesticide release regulated by coordination bonding. *Chem. Eng. J.* **2020**, *395*, 125093.
- (12) Chen, Y.; Yao, J.; Wang, W.-X.; Gao, T.-C.; Yang, X.; Zhang, A.-F. Effect of epoxiconazole on rice blast and rice grain yield in China. *Eur. J. Plant Pathol.* **2013**, *135*, 675–682.
- (13) Kaziem, A. E.; He, Z.; Li, L.; Wen, Y.; Wang, Z.; Gao, Y.; Wang, M. Changes in soil and rat gut microbial diversity after long-term exposure to the chiral fungicide epoxiconazole. *Chemosphere* **2021**, *272*, 129618.
- (14) Dutta Chowdhury, A.; Ganganboina, A. B.; Tsai, Y.-c.; Chiu, H.-c.; Doong, R.-a. Multifunctional GQDs-Concanavalin A@Fe₃O₄ nanocomposites for cancer cells detection and targeted drug delivery. *Anal. Chim. Acta* **2018**, *1027*, 109–120.
- (15) Zhang, J.-T.; Cai, Z.; Kwak, D. H.; Liu, X.; Asher, S. A. Two-Dimensional Photonic Crystal Sensors for Visual Detection of Lectin Concanavalin A. *Anal. Chem.* **2014**, *86*, 9036–9041.
- (16) Hamer, J. E.; Howard, R. J.; Chumley, F. G.; Valent, B. A mechanism for surface attachment in spores of a plant pathogenic fungus. *Science* **1988**, *239*, 288–290.
- (17) Novoselov, K. S.; Geim, A. K.; Morozov, S. V.; Jiang, D.; Zhang, Y.; Dubonos, S. V.; Grigorieva, I. V.; Firsov, A. A. Electric field effect in atomically thin carbon films. *Science* **2004**, *306*, 666–669.
- (18) Ghawanmeh, A. A.; Ali, G. A. M.; Algarni, H.; Sarkar, S. M.; Chong, K. F. Graphene oxide-based hydrogels as a nanocarrier for anticancer drug delivery. *Nano Res.* **2019**, *12*, 973–990.

- (19) Goenka, S.; Sant, V.; Sant, S. Graphene-based nanomaterials for drug delivery and tissue engineering. *J. Controlled Release* **2014**, *173*, 75–88.
- (20) Bidram, E.; Sulistio, A.; Amini, A.; Fu, Q.; Qiao, G. G.; Stewart, A.; Dunstan, D. E. Fractionation of graphene oxide single nano-sheets in water-glycerol solutions using gradient centrifugation. *Carbon* **2016**, *103*, 363–371.
- (21) Carrales-Alvarado, D. H.; Rodriguez-Ramos, I.; Leyva-Ramos, R.; Mendoza-Mendoza, E.; Villela-Martinez, D. E. Effect of surface area and physical-chemical properties of graphite and graphene-based materials on their adsorption capacity towards metronidazole and trimethoprim antibiotics in aqueous solution. *Chem. Eng. J.* **2020**, *402*, 126155.
- (22) Cheng, L.; Wang, X.; Gong, F.; Liu, T.; Liu, Z. 2D Nanomaterials for Cancer Theranostic Applications. *Adv. Mater.* **2020**, *32*, 1902333.
- (23) Sharma, S.; Biswal, B. K.; Kumari, D.; Bindra, P.; Kumar, S.; Stobdan, T.; Shanmugam, V. Ecofriendly Fruit Switches: Graphene Oxide-Based Wrapper for Programmed Fruit Preservative Delivery To Extend Shelf Life. *ACS Appl. Mater. Interfaces* **2018**, *10*, 18478–18488.
- (24) He, Y.; Qian, L.; Liu, X.; Hu, R.; Huang, M.; Liu, Y.; Chen, G.; Losic, D.; Zhu, H. Graphene oxide as an antimicrobial agent can extend the vase life of cut flowers. *Nano Res.* **2018**, *11*, 6010–6022.
- (25) Hao, L.; Gong, L.; Chen, L.; Guan, M.; Zhou, H.; Qiu, S.; Wen, H.; Chen, H.; Zhou, X.; Akbulut, M. Composite pesticide nanocarriers involving functionalized boron nitride nanoplatelets for pH-responsive release and enhanced UV stability. *Chem. Eng. J.* **2020**, *396*, 125233.
- (26) Leung, H.-W.; Ballantyne, B.; Hermansky, S. J.; Frantz, S. W. Peroral subchronic, chronic toxicity, and pharmacokinetic studies of a 100-kilodalton polymer of ethylene oxide (Polyox N-10) in the Fischer 344 rat. *Int. J. Toxicol.* **2000**, *19*, 305–312.
- (27) Liu, Z.; Robinson, J. T.; Sun, X.; Dai, H. PEGylated nanographene oxide for delivery of water-insoluble cancer drugs. *J. Am. Chem. Soc.* **2008**, *130*, 10876–10877.
- (28) Xu, Z.; Wang, S.; Li, Y.; Wang, M.; Shi, P.; Huang, X. Covalent Functionalization of Graphene Oxide with Biocompatible Poly(ethylene glycol) for Delivery of Paclitaxel. *ACS Appl. Mater. Interfaces* **2014**, *6*, 17268–17276.
- (29) Miao, W.; Shim, G.; Lee, S.; Lee, S.; Choe, Y. S.; Oh, Y.-K. Safety and tumor tissue accumulation of pegylated graphene oxide nanosheets for co-delivery of anticancer drug and photosensitizer. *Biomaterials* **2013**, *34*, 3402–3410.
- (30) Sun, X.; Liu, Z.; Welsher, K.; Robinson, J. T.; Goodwin, A.; Zaric, S.; Dai, H. Nano-Graphene Oxide for Cellular Imaging and Drug Delivery. *Nano Res.* **2008**, *1*, 203–212.
- (31) Zhao, R.; Lv, M.; Li, Y.; Sun, M.; Kong, W.; Wang, L.; Song, S.; Fan, C.; Jia, L.; Qiu, S.; Sun, Y.; Song, H.; Hao, R. Stable Nanocomposite Based on PEGylated and Silver Nanoparticles Loaded Graphene Oxide for Long-Term Antibacterial Activity. *ACS Appl. Mater. Interfaces* **2017**, *9*, 15328–15341.
- (32) Sawangphruk, M.; Srimuk, P.; Chiochan, P.; Sangsri, T.; Siwayaprahm, P. Synthesis and antifungal activity of reduced graphene oxide nanosheets. *Carbon* **2012**, *50*, 5156–5161.
- (33) Lee, K.; Singh, P.; Chung, W. C.; Ash, J.; Kim, T. S.; Hang, L.; Park, S. Light regulation of asexual development in the rice blast fungus, *Magnaporthe oryzae*. *Fungal Genet. Biol.* **2006**, *43*, 694–706.
- (34) Sun, X.; Luo, D.; Liu, J.; Evans, D. G. Monodisperse Chemically Modified Graphene Obtained by Density Gradient Ultracentrifugal Rate Separation. *ACS Nano* **2010**, *4*, 3381–3389.
- (35) Gao, Y.; Wu, J.; Ren, X.; Tan, X.; Hayat, T.; Alsaedi, A.; Cheng, C.; Chen, C. Impact of graphene oxide on the antibacterial activity of antibiotics against bacteria. *Environ. Sci.: Nano* **2017**, *4*, 1016–1024.
- (36) Maliyekkal, S. M.; Sreeprasad, T. S.; Krishnan, D.; Kouser, S.; Mishra, A. K.; Waghmare, U. V.; Pradeep, T. Graphene: A Reusable Substrate for Unprecedented Adsorption of Pesticides. *Small* **2013**, *9*, 273–283.
- (37) Wang, X.; Xie, H.; Wang, Z.; He, K.; Jing, D. Graphene oxide as a multifunctional synergist of insecticides against lepidopteran insect. *Environ. Sci.: Nano* **2019**, *6*, 75–84.
- (38) Sun, H.; Liu, S.; Liu, S.; Wang, S. A comparative study of reduced graphene oxide modified TiO₂, ZnO and Ta₂O₅ in visible light photocatalytic/photochemical oxidation of methylene blue. *Appl. Catal., B* **2014**, *146*, 162–168.
- (39) Chen, M.-L.; Wang, H.; Mao, Q.-X.; Chen, X.-W.; Wang, J.-H. Hydrous-ferric oxide nanorods grown on PEGylated graphene oxide with superior capacity for selective adsorption of albumin. *Carbon* **2015**, *85*, 335–343.
- (40) Lu, Y.-J.; Wang, Y.-H.; Sahu, R. S.; Chen, J.-P.; Dash, B. S.; Chung, P.-J.; Yang, H.-W.; Chuang, E.-Y.; Hwang, T.-L. Mechanism of Nanoformulated Graphene Oxide-Mediated Human Neutrophil Activation. *ACS Appl. Mater. Interfaces* **2020**, *12*, 40141–40152.
- (41) Liu, S.; Zeng, T. H.; Hofmann, M.; Burcombe, E.; Wei, J.; Jiang, R.; Kong, J.; Chen, Y. Antibacterial Activity of Graphite, Graphite Oxide, Graphene Oxide, and Reduced Graphene Oxide: Membrane and Oxidative Stress. *ACS Nano* **2011**, *5*, 6971–6980.
- (42) Tu, Y.; Lv, M.; Xiu, P.; Huynh, T.; Zhang, M.; Castelli, M.; Liu, Z.; Huang, Q.; Fan, C.; Fang, H.; Zhou, R. Destructive extraction of phospholipids from *Escherichia coli* membranes by graphene nanosheets. *Nat. Nanotechnol.* **2013**, *8*, 594–601.

Enzyme-Responsive Lignin Nanocarriers for Triggered Delivery of Abamectin to Control Plant Root-Knot Nematodes (*Meloidogyne incognita*)

Ning Zhao, Li Zhu, Meichen Liu, Liangheng He, Hanhong Xu,* and Jinliang Jia*



Cite This: *J. Agric. Food Chem.* 2023, 71, 3790–3799



Read Online

ACCESS |

Metrics & More

Article Recommendations

ABSTRACT: Intelligently responsive nanoparticles can improve insecticidal activity against target organisms and reduce the use of pesticides in agriculture. In this study, enzymatic hydrolysis lignin (EHL) nanocarriers with enzyme responsiveness were successfully prepared by electrostatic interaction, and abamectin (Abm)-loaded EHL-based nanoparticles (Abm@L-CL) were investigated. The release behavior of Abm@L-CL nanoparticles showed that Abm was released rapidly in the presence of cellulase and pectinase but slowly under natural conditions. The insecticidal activity of Abm@L-CL treatment ($LC_{50} = 0.68 \mu\text{g/mL}$) against nematodes (*Meloidogyne incognita*) was significantly more effective than that of original Abm treatment ($LC_{50} = 1.32 \mu\text{g/mL}$). The mortality rate of Abm@L-CL was more than 90% by applying the same dose of Abm after 12 h. The bioactivity of Abm@L-CL against root-knot nematodes was 1.7-fold greater than that of Abm. The result of fluorescence indicated that nanoparticles could enter the intestinal tract through the oral cavity of nematodes and achieve obvious gastric toxicity. Furthermore, the enzyme-controlled lignin-based Abm nanocarriers could penetrate the tomato root near the elongation zone. This study provided intelligent enzyme-responsive nanocarriers for efficient management of soil-borne diseases and pests in green agricultural inputs.

KEYWORDS: enzyme stimulus-responsive, enzymatic hydrolysis lignin, *Meloidogyne incognita*, abamectin

1. INTRODUCTION

Tomato (*Solanum Lycopersicon* L.) is one of the most popular edible crops in the world, with the global tomato production reaching 43.8 million tons in 2020.^{1–3} However, pests, soil-borne fungal pathogens, and bacterial wilt can have a momentous impact on crop failure and economic damage.⁴ Among them, root-knot nematodes (RKNs) (*Meloidogyne incognita*) are considered to be the most detrimental.⁵ The infective second-stage juveniles (J2s) of the RKN arrive at the root and destroy lignin to enter the root by secreting cell wall decomposition enzymes and cellulases.^{6,7} Cell wall decomposition enzymes include pectinase, cellulase, hemicellulase, and so forth. Then, they migrate to the vascular cylinder; nematodes establish specific interactions with their hosts by using their protractile stylets to pierce plant cells and extract nutrients.^{8,9} Crop nematode diseases cause an annual economic loss of more than 157 billion dollars.¹⁰ Thus, it is urgent to develop an effective method to control nematodes.

Although there are many ways to control nematodes, such as crop rotation, flooding treatment, predatory fungi, and so forth, chemical control is still the most common method.¹¹ Abamectin (Abm) is a biogenic pesticide with high activity against nematodes; however, it is easily adsorbed by organic matter near the soil surface and Abm cannot effectively reach the tomato roots to control the nematodes. Abm modified with phenyl isocyanate could significantly enhance the migration ability of Abm in the soil and the field control effect of RKN disease.¹² But it is hard for the pesticide to reach the target accurately to exert its effects, so the problems of low pesticide

utilization and aggravating environmental pollution get highlighted. Nano-based intelligent pesticide delivery systems can solve this problem through targeted or controlled release. Nanotechnology has shown promising potential in promoting sustainable agriculture. By wrapping pesticides with different carriers, nanopesticides get the ability for pH-, temperature-, and other intelligent-responsive release.^{13–16} Among them, the enzymes' response shows good performance in intelligent controlled release because of its specificity.¹⁷

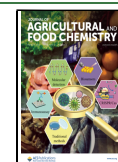
Lignin being a low-cost and environment-friendly material attracts much attention. Lignin is a polycyclic aromatic hydrocarbon polymer composed of phenylpropionate units and is the second abundant plant biopolymer on earth after cellulose.^{18,19} Compared with lignin sulfonate and alkali lignin, enzymatic hydrolysis lignin (EHL) is obtained without harsh process technology; it can retain the active functional groups of natural lignin to a greater extent and is closer to natural materials. EHL has been widely used as the appropriate carrier for drug molecules.²⁰ Acetylated lignin and benzoyleated lignin were used as shell materials to encapsulate Abm; the nanospheres showed good anti-photolysis properties.²¹ In

Received: October 25, 2022

Revised: January 30, 2023

Accepted: February 7, 2023

Published: February 17, 2023



Zhang's work, anionic lignosulfonate was combined with epoxy resin to establish novel negatively charged pesticide nano-carriers loaded with Abm. Polymer nanocarriers could prevent the premature release of Abm and protect active ingredients from degradation by microbial degradation.²² Chen et al. pioneered a new and facile method to synthesize lignin nanoparticles, with the encapsulated efficiency of up to 90%.²³ The results showed that lignin could be used as a nano-carrier to coat pesticides, but the carrier had no specific response and could not release pesticides according to the characteristics of the insect to achieve the desired insecticidal effect. At the same time, in the research of nanopesticides, there were some studies on enzyme-controlled release. Kaziem et al. had prepared α -amylase-responsive carriers based on anchored hollow mesoporous silica.²⁴ Abdelrahman et al. prepared pectinase-responsive carriers as a fungicide.²⁵ However, it is difficult to degrade silica in the natural environment and would remain in the environment. The use of lignin as the nanocarrier would reduce this risk also.

In this work, enzyme stimulus-responsive nanoparticles were designed using EHL as the nanocarrier loaded with Abm (Abm@L-CL). EHL and modified cationic lignin (CL) were cross-linked to form the lignin nanocarrier (L-CL). A series of experiments were designed to study the interaction between Abm@L-CL and nematodes as well as plants. At the same time, the insecticidal mechanism of Abm@L-CL was revealed. The chemical and physical properties of Abm@L-CL were studied by Fourier transform infrared (FTIR) spectroscopy, scanning electron microscopy (SEM), X-ray photoelectron spectroscopy (XPS), and so forth.

2. EXPERIMENTAL SECTION

2.1. Materials. EHL was obtained from Jinzhou Ling Yu Chemical Co., Ltd. The weight-average molecular weight of EHL was 1123 g/mol by GPC. Abamectin (Abm, original pesticide) with a purity of 96% was provided by Zhejiang Hebei Technology Co., Ltd. (China). 5% Abm emulsifiable concentrate (EC) was provided by Beijing Green Agricultural Science and Technology Group Co., Ltd. Cellulase and pectinase were purchased from Shanghai Macklin Biochemical Technology Co., Ltd. Glycidyl-trimethylammonium chloride (GTMAC), sodium hydroxide, sulfuric acid, and ethanol were purchased from Guangdong Guanghua Chemical Factory Co., Ltd (China). All other reagents were used without extra purification. The RKN was obtained from State Key Laboratory for Conservation and Utilization of Subtropical Agro-bioresources.

Eggs of *M. incognita* were obtained from infected tomato roots and soaked in a NaClO solution. The eggs were incubated at 25 °C in darkness, and second-stage juveniles (J2s) were collected daily and temporarily stored at 15 °C.

2.2. Preparation of Abm@L-CL. EHL (1 g) was dissolved in water and then 0.5 M NaOH solution was gradually added into the solution to adjust the initial pH to 12.5. When the temperature of the system reached 70 °C, GTMAC (2 g) was added and reacted for 1 h. After completion, the round-bottom glass flask was immersed in cold water for 20 min, and sulfuric acid was used to adjust the pH to 7.²⁶ After dialysis and drying, pure cationic EHL was obtained.

First, EHL (1 g) and cationic lignin CL (0.1 g) were dissolved in 20 mL of ethanol, and 50 mL of distilled water was added dropwise with continuous magnetic stirring. After reacting, the mixture was washed with ethanol and deionized water by centrifugation twice, deionized water for once, and the purified lignin carrier (L-CL) was collected. Then, L-CL (0.1 g) and Abm (0.05 g) were dissolved in 10 mL of ethanol. The mixture was dispersed ultrasonically for 5 min, and 100 mL of distilled water was added dropwise into the mixture. After reacting, the mixture was washed with ethanol and deionized

water by centrifugation twice, deionized water for once, and the lignin drug-loading material (Abm@L-CL) was prepared.

2.3. Characterizations. Morphological inspection of the Abm@L-CL was done by SEM (Hitachi SU8010, Japan) and transmission electron microscopy (TEM, FEI/Talos L120C). The variation in the functional groups on the samples were recorded on a FTIR spectrophotometer (Nicolet IS10 USA) using KBr pellets with a wavenumber range of 400 to 4000 cm⁻¹. The sample stability was determined by thermogravimetric analysis with a Pyris TGA system (TG209F1LibraTM, Germany). The distribution of Abm@L-CL in nematodes and tomato roots was observed using confocal laser scanning microscopy (CLSM, Zeiss LSM710, Germany). Elemental analyses (EA) were performed on an elemental analyzer (Vario EL cube, Germany). The surface elemental distributions of L-CL and Abm@L-CL were measured by XPS using a Thermo Scientific K-Alpha Nexsa X-ray photoelectron spectrometer with Al K α radiation (1486.6 eV), taking the binding energy of C 1s 284.80 eV as the energy standard.

2.4. Determination of Abm Loading Efficiency of Abm@L-CL. Abm@L-CL (20 mg) was dissolved in 10 mL of ethanol, placed in an ultrasonic bath for 2 h, and centrifuged (8000 rpm, 10 min); then, the supernatant was filtered and analyzed using the Agilent Technologies 1100 HPLC system equipped with an ultraviolet detector and an Agilent SB-C₁₈ column (4.6 × 250 mm, 5 μ m, Agilent Technologies) with methanol–water (93:7, v/v) as the mobile phase. The flow rate was 1 mL/min, and 10 μ L of the sample was injected into HPLC with a detector wavelength of 245 nm. All the samples were filtered with a 0.22 μ m membrane filter; the organic solvent and water used for HPLC were all filtered by a vacuum extraction filter bottle with a membrane.

The Abm loading efficiency was calculated via eq 1

$$\text{Abm loading (\%)} = \left(\frac{\text{weight of Abm loaded}}{\text{weight of Abm@L-CL}} \right) \times 100\% \quad (1)$$

2.5. Controlled Release of Abm. In order to determine the intelligent response and controlled release of Abm@L-CL, the cumulative release of nanoparticles at different times was determined using the dialysis method at room temperature. Specifically, 20 mg of Abm@L-CL, 20 mg of Abm@L-CL with 5 mg of cellulase and 5 mg of pectinase were weighed accurately, then dissolved with 3 mL of 50% ethyl alcohol and put in a processed dialysis bag. The dialysis bags were suspended in a brown reagent bottle containing 97 mL of 50% ethyl alcohol solution. 1 mL of the solution was taken at regular intervals, and 1 mL of fresh 50% ethyl alcohol solution was added to ensure that the total volume was stable at 100 mL. The cumulative release of Abm@L-CL was computed by analyzing the concentration of Abm dissolved in the release medium at different points in time using HPLC. The results were reported as the mean of three replicates.

The cumulative release rate of Abm was calculated according to eq 2

$$\text{cumulative release rate (\%)} = \frac{C_n \times V_0 + \sum_{i=1}^{n-1} C_i \times V}{Q_0} \times 100\% \quad (2)$$

where Q_0 is the initial Abm mass of Abm@L-CL; C_n is the concentration at the n th sampling time point; V_0 is the volume of the release medium; and V is the volume of each sampling.

Moreover, three mathematical models were adopted to analyze the release mechanism of pesticides from Abm@L-CL, including zero-order, first-order, and Higuchi models, according to eqs 3–5, respectively.²⁷

Zero-order model

$$M_t/M_\infty = kt + b \quad (3)$$

First-order model

$$\ln(1 - M_t/M_\infty) = -kt + b \quad (4)$$

Scheme 1. Schematic Diagram of Abm@L-CL Synthesis Steps

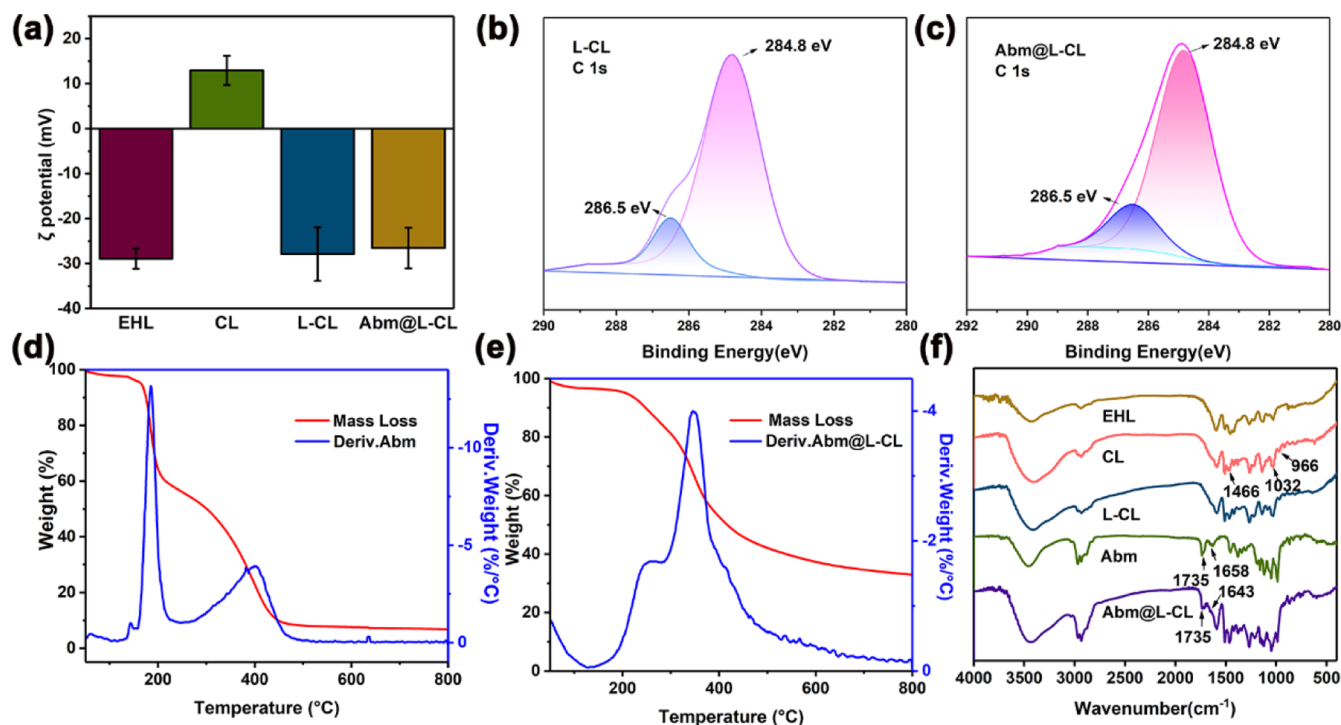
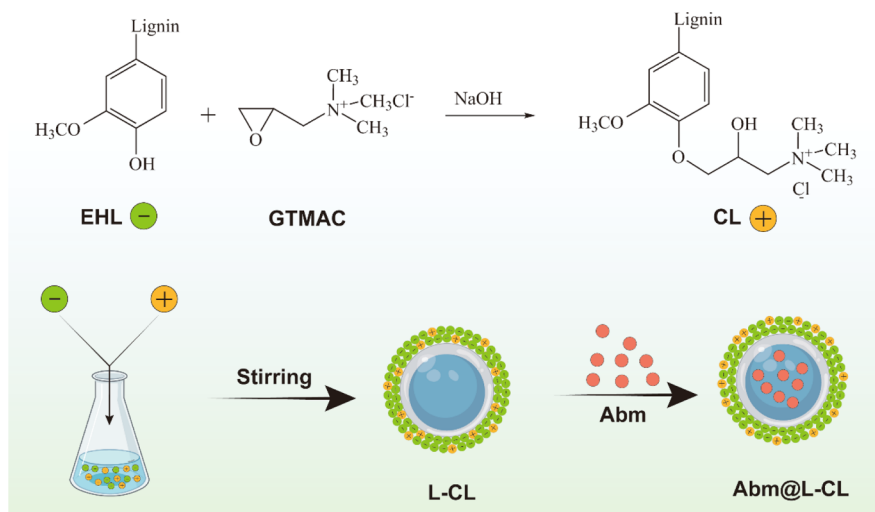


Figure 1. Zeta potential measurements of EHL, CL, L-CL, and Abm@L-CL (a); XPS C 1s spectra of L-CL (b) and Abm@L-CL (c); DTG curves of Abm (d) and Abm@L-CL (e); and FTIR spectra of EHL, CL, L-CL, Abm, and Abm@L-CL (f).

Higuchi release model

$$M_t/M_\infty = kt^{0.5} + b \quad (5)$$

where M_t and M_∞ represent the cumulative release at time t and ∞ , respectively. M_t/M_∞ is the pesticide release ratio at time t , and k is the kinetic constant.

2.6. Insecticidal Activity of Abm@L-CL. 1 mg of Abm original pesticide was accurately weighed and Abm@L-CL containing an equal amount of Abm was weighed. They were each dispersed in 1 mL of absolute ethanol to prepare stock solutions of 1000 $\mu\text{g/mL}$ for further experiments. The stock solutions were then diluted to 1.2, 1.4, 1.8, 2, and 6 $\mu\text{g/mL}$ using distilled water containing 0.1% Tween-80, and 80 μL of each was pipetted into 96-well plates. 20 μL of nematode suspension (a total of approximately 30 ± 5 *M. incognita* J2) was mixed with 80 μL of diluted solutions, and this was repeated three times for each concentration. Deionized water and 1 $\mu\text{g/mL}$ of

L-CL nanocarriers as CK groups. Subsequently, the plates were placed in a 25 $^\circ\text{C}$ incubator (dark treatment). J2 mortality was assessed after 12 h.

2.7. Distribution of FITC@L-CL in Nematodes and Tomato Roots. Preparation of FITC@L-CL: L-CL (0.1 g) and FITC (0.01 g) were dissolved in 10 mL of ethanol. The mixture was dispersed ultrasonically for 5 min, and 100 mL of distilled water was added dropwise into the mixture. After reacting, the mixture was washed with ethanol and deionized water by centrifugation twice, with deionized water once, and the lignin FITC-loading material (FITC@L-CL) was prepared.

To further explore the nematicidal mechanism of the nanoparticles, the nanocarriers were labeled with FITC (FITC@L-CL), and the main distribution of FITC@L-CL in RKNs and tomato roots were observed by laser confocal microscopy.

10 mg of FITC@L-CL was accurately weighed and dispersed in 1 mL of ethanol to prepare a solution of 10,000 $\mu\text{g/mL}$, and diluted to 100 $\mu\text{g/mL}$ with 0.1% Tween 80 water. Nematodes and the roots of tomato were exposed to the solutions for a period of time. Then, the nematodes and roots were washed with distilled water and placed on a glass slide. The roots were sectioned at 40 μm thickness using a freezing microtome (CM1950, Lecia Microsystem Inc., Wetzlar, Germany) at $-20\text{ }^{\circ}\text{C}$.

2.8. Acute Toxicity of Abm@L-CL to Zebrafish. The acute toxicity of Abm EC and Abm@L-CL against adult blue zebrafish with a length of 2–3 cm was tested by using a static test. Tap water was subject to solarization for 2 d to remove chlorine. According to the concentration range determined in the pre-experiment, five concentration groups were set up at the same time. Additionally, one solvent control group, one L-CL particle control group, and one blank control group were set up at the same time. All zebrafish remained unfed during the test. The symptoms of fish poisoning and the number of deaths in each group were observed and recorded after 48 h. The dead fish were removed on time. Each treatment was performed in triplicate.

2.9. Statistical Analysis. The experiments were repeated three times to ensure consistency and reliability of the results. The data was collected by Origin 2019 software (Origin Lab Corp., USA). Data analyses were performed using the SPSS software (SPSS Inc., USA) for ANOVA. The statistical significance p -value was determined to be $p < 0.05$.

3. RESULTS AND DISCUSSION

3.1. Synthesis and Characterization of Abm@L-CL. In this experiment, Abm@L-CL was prepared using the

Table 1. Elemental Distributions of L-CL, Abm, and Abm@L-CL Detected by EA and Elemental Distributions of L-CL and Abm@L-CL Detected by XPS

method	samples	element content (%)				
		N	C	O	N/O	O/C
EA	L-CL	1.50	59.93	32.82	0.05	0.56
	Abm	0	62.90	27.02		0.43
	Abm@L-CL	1.19	59.18	31.64	0.04	0.53
XPS	L-CL	6.68	63.81	29.52	0.23	0.46
	Abm@L-CL	3.84	72.07	24.10	0.16	0.33

amphiphilicity of lignin. EHL was negatively charged, and after modification, it became positively charged. Nanocarriers can be formed between EHL and cationic EHL by electrostatic interaction. Scheme 1 shows the schematic diagram of Abm@L-CL synthesis steps. The modified CL and EHL were cross-linked to form nanocarriers and loaded with Abm.

From Figure 1a the initial potential of EHL was -26.3 mV , and the potential after modification was 11.5 mV ; this testified the successful preparation of the CL. We noticed that the potential absolute value of Abm@L-CL was smaller than that of L-CL. This was because during the formation of Abm@L-CL, the CL containing quaternary ammonium groups had better hydrophilicity and could turn outward. The CL neutralized some of the negative charge, making the absolute value of the charge smaller.

In the XPS spectra, 284.8 eV was the value of the C–C characteristic peak, and 286.5 eV was the ester characteristic peak's value. From Figure 1b,c, it can be seen that no new peaks appear before and after the Abm was loaded, indicating that the Abm was loaded through physical action. Also, the loading process did not change the chemical properties of Abm. XPS was a good method to test the elemental

distribution on the surface of the samples, while EA tested the total element content in the samples. In Table 1, to confirm that Abm was encapsulated in the nanocarriers, we investigated the elemental distribution both on the surface and in the whole microsphere.

To research thermodynamic properties of Abm and Abm@L-CL, TG and DTG analyses were performed, and the results are shown in Figure 1d,e, respectively. For Abm, two distinct regions of weight loss could be clearly observed at $123\text{--}253$ and $253\text{--}663\text{ }^{\circ}\text{C}$. Abm@L-CL was pyrolyzed from $176\text{ }^{\circ}\text{C}$. The weight loss of Abm@L-CL was much slower than that of Abm. At $800\text{ }^{\circ}\text{C}$, the residual mass of Abm was 6.76%, while that of Abm@L-CL was 32.91%. Encapsulation of L-CL nanocarriers could delay the weight loss of Abm.

In Figure 1f, FTIR spectra of the samples are shown. As for lignin, obvious peaks at 3400 cm^{-1} (the stretching vibrations of the hydroxyl group) and 1700 cm^{-1} ($\text{C}=\text{O}$ stretching) were assigned. The C–H stretching vibration of the methyl and benzene ring skeleton were at 2900 and 1460 cm^{-1} , respectively.^{28,29} As for CL, an intensity peak at 1032 cm^{-1} was assigned to the C–O–C bond of CL.³⁰ The characteristic peaks for GTMAC could be observed for CL, including the CH_2 (1466 cm^{-1}) and methyl group (966 cm^{-1}) of GTMAC, further demonstrating the successful incorporation of GTMAC into EHL. The absorption peaks of L-CL were similar to those of EHL and CL because the preparation process was spontaneous self-assembly without the breaking and bonding of chemical bonds. Abm exhibited two characteristic peaks of $\text{C}=\text{O}$ stretching vibration in 16-membered ring macrolides (1735 cm^{-1}) and $\text{C}=\text{C}$ stretching vibration in conjugated diene (1658 cm^{-1}).³¹ When Abm was loaded, similar absorption bands at 1735 and 1643 cm^{-1} appeared again. The red shifts of the two peaks resulted from the formation of a hydrogen bond between lignin and Abm.

Nitrogen was unique in L-CL, so we selected nitrogen as the marker and employed the elemental ratio of N/O to determine the microsphere's structure by scientific calculation. The EA's N/O ratio of the whole microsphere was 0.04, while the N/O ratio of the microsphere surface was 0.16 by XPS. The N/O ratio on the surface of the microsphere was 4 times of that in the whole microsphere separately, which demonstrated that the content of nitrogen on the surface was tremendously higher than that in the whole microsphere. It is noteworthy that the nitrogen proportion on the surface of Abm@L-CL was higher than that on the whole microsphere in L-CL. First, EHL was an amphiphilic compound, and L-CL was a mixture of EHL and CL with different hydrophilicity properties. The CL containing quaternary ammonium groups had better hydrophilicity and tended to turn outward. Second, the formation of Abm@L-CL was a process of self-assembly, the hydrophilic L-CL was more likely to move outward, while hydrophobic Abm tended to transfer inward. Then, the hydrophobic pesticide Abm was encapsulated inside. It was further shown that Abm@L-CL was a core-shell structure, and Abm was successfully loaded inside the nanocarriers.

The morphology and size of Abm@L-CL were observed and analyzed by TEM. In Figure 2, Abm@L-CL had a solid, spherical shape without a pore structure on the surface. The particle size distribution measured by TEM (Figure 2c) showed that the average particle was 315 nm. Moreover, Abm@L-CL had a dark inner center, confirming the successful loading of the Abm, and the conclusion also corroborated the results of XPS and EA. In order to see the internal

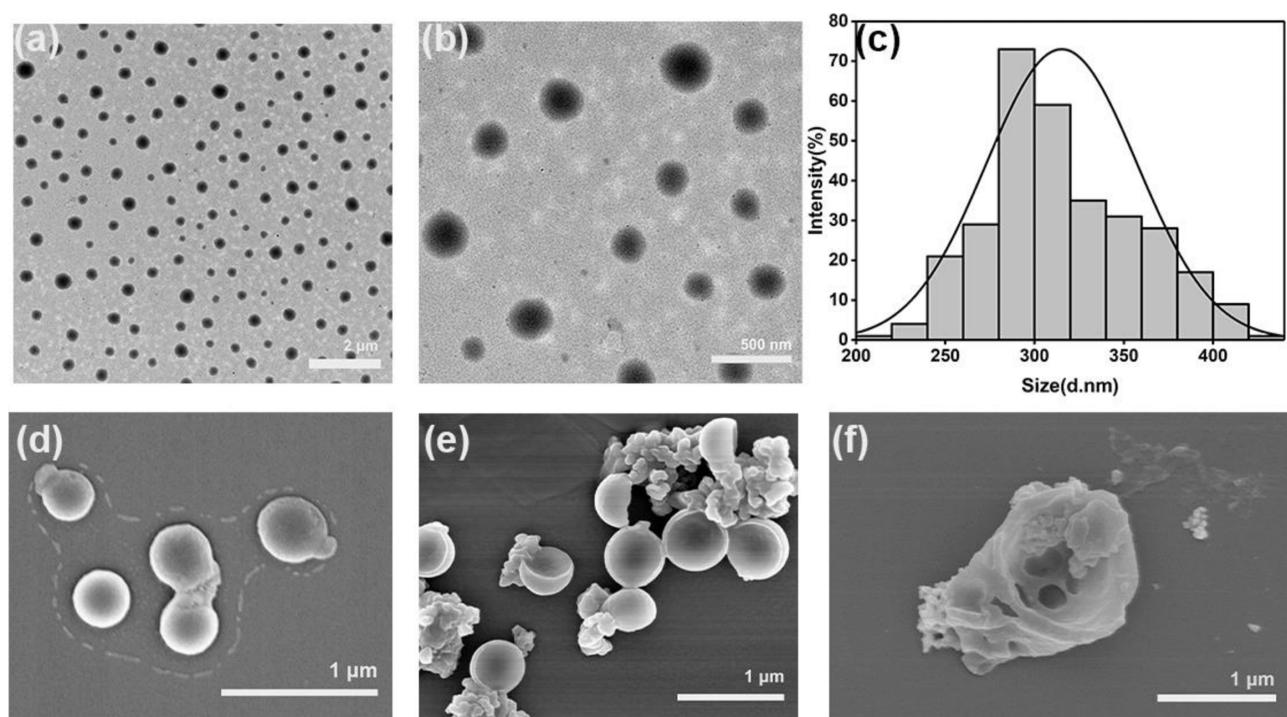


Figure 2. TEM of Abm@L-CL (a,b); particle size analysis of Abm@L-CL (c); and SEM of Abm@L-CL (d), after ultrasonication for 10 min (e), and after 72 h of controlled release (f).

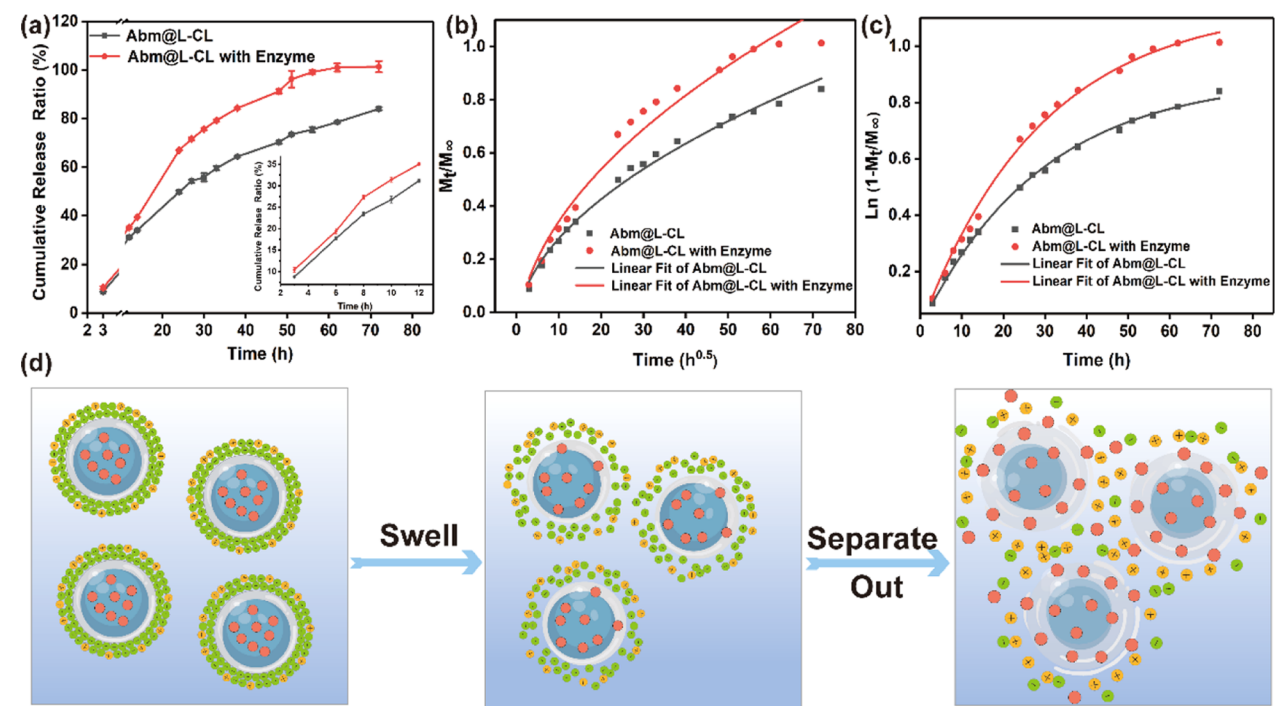


Figure 3. Release behavior (a), Higuchi release model (b), first-order kinetics model (c), and schematic diagram of Abm@L-CL release mechanism (d). Data are displayed as means \pm SE.

Table 2. Fitting Results for the Data of Sustained Release Curves with the Enzyme

kinetic model	fitting formula	k	b	R^2
zero-order	$M_t/M_\infty = kt + b$	0.01	0.18	0.93
first-order	$\ln(1 - M_t/M_\infty) = -kt + b$	0.03	0.89	0.99
Higuchi	$M_t/M_\infty = kt^{0.5} + b$	0.11	−0.08	0.99

Table 3. Fitting Results for the Data of Sustained Release Curves without the Enzyme

kinetic model	fitting formula	k	b	R^2
zero-order	$M_t/M_\infty = kt + b$	0.01	0.21	0.89
first-order	$\ln(1 - M_t/M_\infty) = -kt + b$	0.03	1.15	0.99
Higuchi	$M_t/M_\infty = kt^{0.5} + b$	0.15	−0.13	0.97

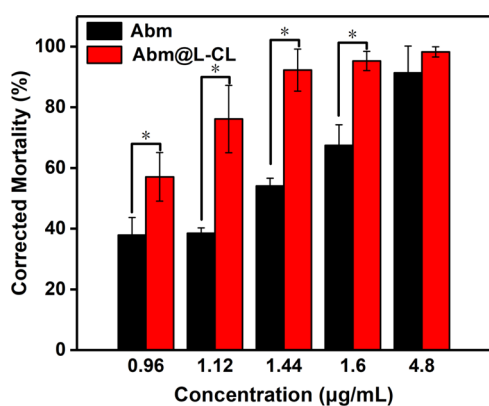


Figure 4. Corrected mortality of *M. incognita* treated by the original Abm and Abm@L-CL after 12 h. Data in the figure are means \pm SD of three replications ($n = 3$); the data marked with an asterisk (*) indicates a significant difference between the two treatments (ANOVA, $p < 0.05$).

Table 4. Lethal Concentration Values of Abm@L-CL and Original Abm at 12 h

analytes	LC ₅₀ (µg/mL)	95% confidence interval	slope \pm SE	χ^2 (df)
Abm@L-CL	0.68	0.01–0.99	2.76 \pm 0.38	28.49 (5)
original Abm	1.32	0.82–1.80	2.78 \pm 0.28	9.57 (3)

microstructure of the nanoparticles, Abm@L-CL was ultrasonically processed. After sonication for 10 min, the nanocarrier shells were broken, and the Abm was exposed (Figure 2e); the core–shell structure of Abm@L-CL can be clearly seen. At the end of the sustained release, the Abm@L-CL size became larger, the external carrier was destroyed by the enzyme, and the Abm was released freely.

The experiment measured the loading efficiency of Abm@L-CL which was 10.73% by HPLC. Through the previous series of experiments, we found that Abm was loaded with L-CL by the physical method of oil-in-water; the physical binding was weaker than the chemical bonds. However, the physical binding did not change the chemical properties of the pesticide and retained the biological activity of the pesticide to a great extent. Abm and the nanocarriers were negative, and they had some electrostatic repulsion. Therefore, the loading efficiency of Abm@L-CL was not very high.

3.2. Controlled Release and Release Kinetics Analysis. **3.2.1. Effect of Enzymes.** Nematodes secreted cellulase and pectinase when they fed on the roots of crops. The controlled release experiment was conducted at the room temperature, which was close to the temperature of the tomato planting soil. From Figure 3a, it can be seen that there was little difference between the two samples in the first 12 h. It was probably because the enzymes needed a period of time to activate in vitro before they played a role. With the progress of the experiment, the release amount of Abm gradually appeared to be different. In the presence of enzymes, the cumulative release rate reached 96% after 51 h. In the absence of the enzyme, Abm@L-CL was released more slowly, with a cumulative release of 73%. Over the same period, the cumulative release rate increased by 33%. In the presence of nematode enzymes, a lot of Abm was rapidly released, so we thought that the enzyme was the main reason for the

accelerated release, rather than the increase of osmotic pressure.

3.2.2. Release Kinetics of Abm from Abm@L-CL. The kinetics models could reveal the underlying mechanism of the release behavior. To further understand the Abm@L-CL release behavior, zero-order, first-order, and Higuchi kinetic models were used to fit the sustained release data of Abm. Tables 2 and 3 show the release behavior of Abm@L-CL. The release of Abm was more suited to the first-order and Higuchi kinetic models because correlation coefficient R^2 was higher. The release rate of Abm was related to the content of Abm. The higher the content of Abm in the nanocarrier, the faster the cumulative release rate of Abm. It was consistent with the sudden release effect of Abm in the first 12 h. Figure 3b is the fitting diagram of the Higuchi drug release model. After controlled release, Abm@L-CL became larger in size. Under the action of the enzyme, inhomogeneous folds appeared on the surface of the carrier shell and Abm precipitates were observed externally.

Combining the SEM picture and the two models, we obtained the release mechanism of Abm shown in Figure 3d. The lignin nanocarriers expanded in solution and were destroyed by enzymes, and then Abm was released.

3.3. Biological Activity Analysis. In the experiment, J2s were selected for the biological activity determination. Throughout the experiment, no nematode mortality occurred in the L-CL empty carriers and CK group, indicating that the empty materials had no insecticidal activity against the nematodes. From Figure 4, RKNs showed a dose-dependent response to the original Abm and Abm@L-CL. The mortality rate of Abm@L-CL for the J2s at 1.44 µg/mL was over 90% and that for the original Abm was only 54%. It was obvious that at 1.44 µg/mL, the insecticidal effect of Abm@L-CL was 1.7 times that of original Abm. The lethal concentration 50 (LC₅₀) of Abm@L-CL was 0.68 µg/mL and that of the original Abm was 1.32 µg/mL. The tiny size and hydrophilic segment of Abm@L-CL was evenly distributed in the water. Then, the J2s ingested the Abm@L-CL into the oral cavity, the nematodes secreted enzymes that destroyed the lignin carrier of Abm@L-CL, which significantly increased the speed of Abm entry into the nematode's intestine and expanded the distribution of Abm in the nematode. The insecticidal activity of Abm@L-CL treatment against the nematodes was significantly more effective than that of original Abm treatment (Table 4).

3.4. Fluorescence Imaging. Considering that Abm was non-fluorescent, we loaded FITC with L-CL nanocarriers. CLSM was used to visualize the distribution of nanoparticles in nematodes and tomato roots. Nematodes without treatment were non-fluorescent at 488 nm (Figure 5a); it could reduce the interference of nematode self-luminescence. After cocultivation with FITC@L-CL, green fluorescence could be seen in the intestinal tract of nematodes (Figure 5b). It was possible that enzymes secreted by the nematode oral cavity destroyed the FITC@L-CL lignin nanocarriers, allowing FITC to enter the intestine directly. The distribution of fluorescence in nematodes also clustered over time, providing indirect evidence that the drug content was proportional to the time of exposure to nematodes. At 12 h, it could be clearly seen that the fluorescence was enriched in the intestinal tract (Figure 5c). At 24 h, the fluorescence was distributed throughout the nematodes (Figure 5d). This may be due to intersystem crossover behavior or enhanced drug absorption by continuous

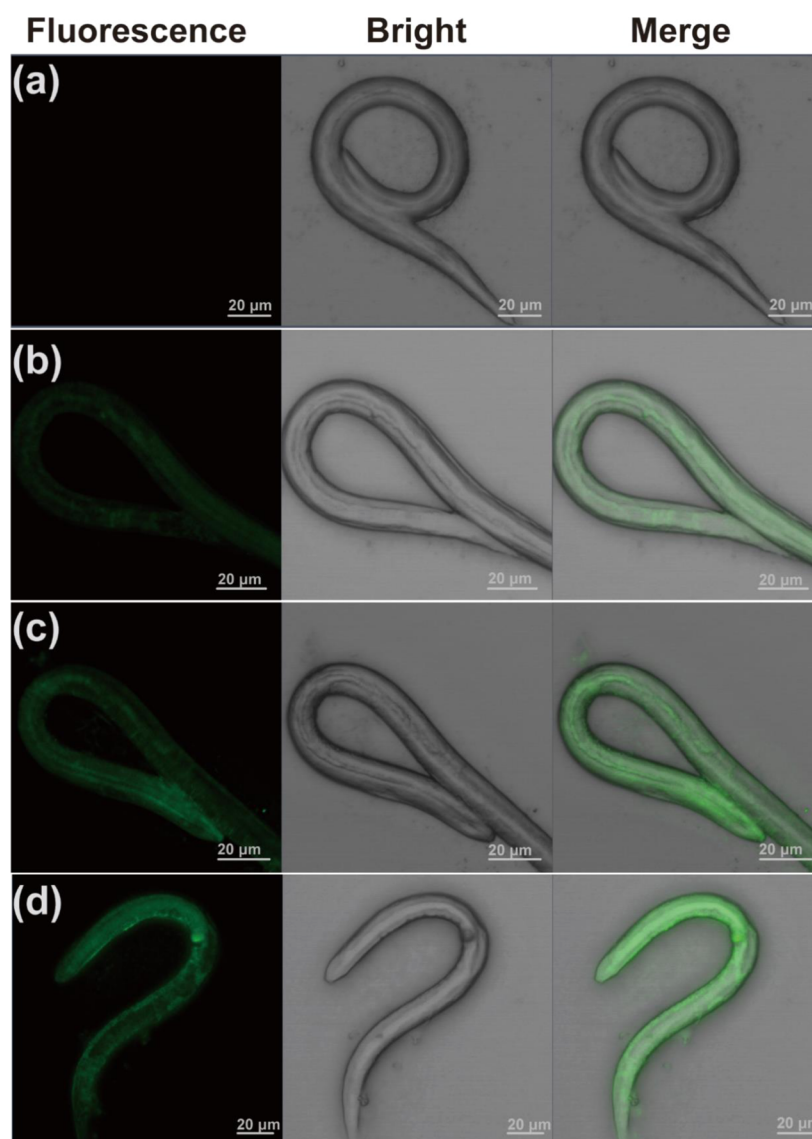


Figure 5. CLSM images of *M. incognita* treated by CK (a) and treated by FITC@L-CL at 6 h (b), 12 h (c), and 24 h (d).

drug release,^{32,33} which made the nanoparticles enhance the gastric toxicity of Abm.

This work investigated the interaction between nanoparticles and tomato roots. We visualized the way how nanoparticles entered the tomato roots via CLSM. Figure 6a shows a cross-sectional photograph of untreated roots, and no fluorescence was observed. A distinct fluorescence was observed in the root treated with FITC@L-CL. From Figure 6b,c, it is obvious that FITC@L-CL entered the vascular bundles from the root cortex through the apoplast pathway after root cocultivation. Scheme 2 shows the pathways of nematodes and Abm@L-CL into the tomato roots. When J2 RKN invaded the tomato root, RKN secreted cell wall decomposition enzymes, cellulase and other enzymes, to degrade the cell wall, and the nematodes would form giant cells after reaching the tomato root, resulting in slow growth and abnormal leaf color of tomato over-ground parts. When eating tomato roots treated with Abm@L-CL, nematodes secreted enzymes that destroyed the nanocarriers of Abm@L-CL, releasing Abm on demand to kill nematodes. Notably, the J2s invaded from the cortex and extended to the vicinity of the vascular bundles to damage crops, which was consistent with the distribution of FITC@L-CL in roots.

Figure 6b,c shows that FITC@L-CL still remained in tomato roots before and after washing. However, the FITC attached to the root was significantly reduced after washing (Figure 6d,e). The results stated clearly that the nanoparticles had eximious adhesion on the roots of crops and could help kill nematodes invading the root system.

3.5. Biosafety Assessment. Adult zebrafish, as a typical model organism to evaluate the biosafety of pesticides, were selected to assess the acute toxicity of Abm@L-CL. In order to investigate the toxicity of Abm@L-CL in practical applications, we chose the commercially available EC for comparison. Throughout the experiment, no zebrafish mortality occurred in the CK, solvent, and the empty L-CL particle control groups, proving that the acute contact toxicity of the L-CL particles to zebrafish was very low. The LC_{50} of the Abm@L-CL at 48 h was 87.96 $\mu\text{g/L}$, while that of the Abm EC was 25.90 $\mu\text{g/L}$ (Table 5). The acute toxicity of Abm to zebrafish was reduced by 3.4 times after being loaded with L-CL carriers. These data showed that Abm@L-CL had a high activity toward nematodes and low toxicity to aquatic organisms. This was because the lignin carriers had a good encapsulation effect

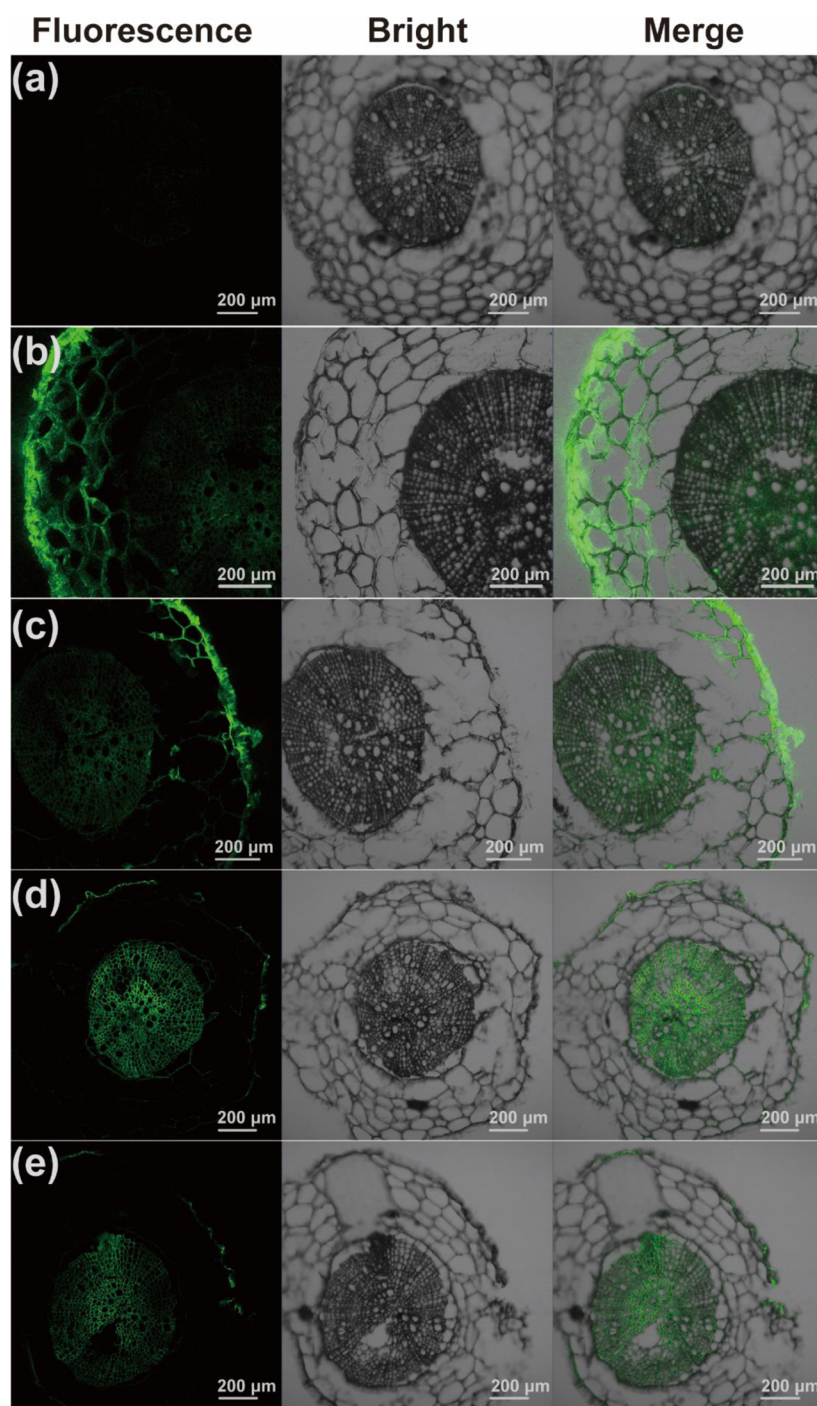


Figure 6. CLSM images of tomato roots treated by CK (a) and treated by FITC@L-CL before washing (b) and after washing (c), and FITC retained in the root before washing (d) and after washing (e) at 24 h.

on Abm and had a specific response to the enzymes secreted by nematodes.

4. CONCLUSIONS

In this work, newly designed green Abm nanoparticles were formulated using EHL as the loading carrier. Abm@L-CL had a nano-size range and showed excellent enzymatic control characteristics. Abm@L-CL was effective in controlling *M. incognita*. At 1.44 $\mu\text{g/mL}$, the mortality of Abm@L-CL was 38% higher than that of Abm. In addition to this, Abm@L-CL was less toxic to zebrafish than Abm EC. The ability of Abm@

L-CL to enter tomato roots was of considerable significance for nematode control. It not only realized the precise and controlled release of pesticide active ingredients in nematode feeding but also provided new ideas and potential applications for reducing the dosage and improving the effect of agricultural pesticides.

AUTHOR INFORMATION

Corresponding Authors

Hanhong Xu — State Key Laboratory for Conservation and Utilization of Subtropical Agro-bioresources, South China

Scheme 2. Pathways of Nematodes and Abm@L-CL into Tomato Roots

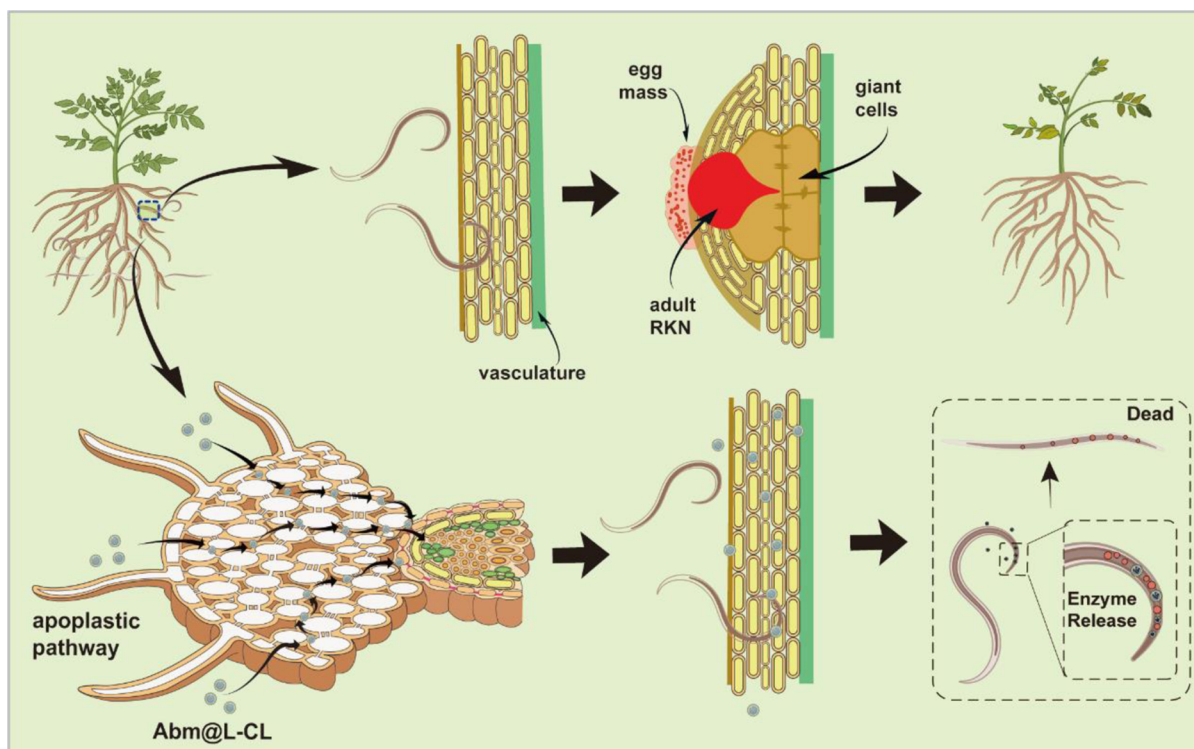


Table 5. Acute Toxicity of Different Analytes against Zebrafish at 48 h

analytes	LC ₅₀ (mg/L)	95% confidence interval	slope ± SE	χ ² (df)
Abm@L-CL	87.96 × 10 ⁻³	76.13–99.42	8.66 ± 1.99	0.75 (3)
Abm EC	25.90 × 10 ⁻³	23.83–27.93	10.82 ± 1.71	1.29 (3)

Agricultural University, Guangzhou 510642, China;
 orcid.org/0000-0001-7841-2396; Email: hbxu@scau.edu.cn

Jinliang Jia – State Key Laboratory for Conservation and Utilization of Subtropical Agro-bioresources, South China Agricultural University, Guangzhou 510642, China; Key Laboratory for Biobased Materials and Energy of Ministry of Education, College of Materials and Energy, South China Agricultural University, Guangzhou 510642, China;
 orcid.org/0000-0002-6974-904X; Email: jiajinliang@scau.edu.cn

Authors

Ning Zhao – State Key Laboratory for Conservation and Utilization of Subtropical Agro-bioresources, South China Agricultural University, Guangzhou 510642, China; Key Laboratory for Biobased Materials and Energy of Ministry of Education, College of Materials and Energy, South China Agricultural University, Guangzhou 510642, China

Li Zhu – Key Laboratory for Biobased Materials and Energy of Ministry of Education, College of Materials and Energy, South China Agricultural University, Guangzhou 510642, China

Meichen Liu – State Key Laboratory for Conservation and Utilization of Subtropical Agro-bioresources, South China Agricultural University, Guangzhou 510642, China

Liangheng He – State Key Laboratory for Conservation and Utilization of Subtropical Agro-bioresources, South China Agricultural University, Guangzhou 510642, China; Key Laboratory for Biobased Materials and Energy of Ministry of Education, College of Materials and Energy, South China Agricultural University, Guangzhou 510642, China

Complete contact information is available at:
<https://pubs.acs.org/10.1021/acs.jafc.2c07466>

Funding

This work was supported by the Guangdong Provincial Innovation Team for General Key Technologies in Modern Agricultural Industry (2019KJ140).

Notes



The authors declare no competing financial interest.

REFERENCES

- (1) Tieman, D.; Zhu, G. T.; Resende, M. F. R.; Lin, T.; Nguyen, M.; Bies, B.; Rambla, H.; Beltran, Z. Y.; Taylor, J.; Zhang, L.; Ikeda, A. J.; Liu, D.; Fisher, A.; Zemach, M.; Monforte, S.; Zamir, H.; Granell, C.; Kirst, D.; Huang, J. L.; Klee, K. S. O. A chemical genetic roadmap to improved tomato flavor. *Science* **2017**, *355*, 391–394.
- (2) Yue, L.; Feng, Y.; Ma, C. X.; Wang, C. X.; Chen, F. R.; Cao, X. S.; Wang, J.; White, I. C.; Wang, Z. Y.; Xing, B. S. Molecular Mechanisms of Early Flowering in Tomatoes Induced by Manganese Ferrite (MnFe₂O₄) Nanomaterials. *ACS Nano* **2022**, *16*, 5636–5646.
- (3) Quinet, M.; Angosto, T.; Yuste-Lisbona, F. J.; Blanchard-Gros, R.; Bigot, S.; Martinez, J. P.; Lutts, S. Tomato fruit development and metabolism. *Front. Plant Sci.* **2019**, *10*, 1554.
- (4) Ghareeb, R. Y.; Shams El-Din, N. G. E. S.; Maghraby, D. M.; Ibrahim, D. S. S.; Abdel-Megeed, A.; Abdelsalam, N. R. Nematicidal activity of seaweed-synthesized silver nanoparticles and extracts against *Meloidogyne incognita* on tomato plants. *Sci. Rep.* **2022**, *12*, 3841.
- (5) Mejias, J.; Chen, Y. P.; Bazin, J.; Truong, N. M.; Mulet, K.; Noureddine, Y.; Jaubert-Possamai, S.; Ranty-Roby, S.; Soulé, S.; Abad,

- P.; Crespi, M. D.; Favory, B.; Quentin, M. Silencing the conserved small nuclear ribonucleoprotein SmD1 target gene alters susceptibility to root-knot nematodes in plants. *Plant Physiol.* **2022**, *189*, 1741–1756.
- (6) Smant, G.; Stokkermans, J. P. W. G.; Yan, Y. T.; de Boer, J. M.; Baum, T. J.; Wang, X. H.; Hussey, R. S.; Gommers, F. J.; Henrissat, B.; Davis, E. L.; Helder, J.; Schots, A.; Bakker, J. Endogenous cellulases in animals: Isolation of β -1,4-endoglucanase genes from two species of plant-parasitic cyst nematodes. *Proc. Natl. Acad. Sci. U.S.A.* **1998**, *95*, 4906–4911.
- (7) Przybylska, A.; Obrępańska-Stęplowska, A. Plant defense responses in monocotyledonous and dicotyledonous host plants during root-knot nematode infection. *Plant Soil* **2020**, *451*, 239–260.
- (8) Martínez-Medina, A.; Mbaluto, C. M.; Maedicke, A.; Weinhold, A.; Vergara, F.; van Dam, N. M. Leaf herbivory counteracts nematode-triggered repression of jasmonate-related defenses in tomato roots. *Plant Physiol.* **2021**, *187*, 1762–1778.
- (9) Vieira, P.; Gleason, C. Plant-parasitic nematode effectors - insights into their diversity and new tools for their identification. *Curr. Opin. Plant Biol.* **2019**, *50*, 37–43.
- (10) Cao, J.; Guenther, R. H.; Sit, T. L.; Lommel, S. A.; Opperman, C. H.; Willoughby, J. A. Development of abamectin loaded plant virus nanoparticles for efficacious plant parasitic nematode control. *ACS Appl. Mater. Interfaces* **2015**, *7*, 9546–9553.
- (11) Li, B. X.; Ren, Y. P.; Zhang, D. X.; Xu, S. Y.; Mu, W.; Liu, F. Modifying the Formulation of Abamectin to Promote Its Efficacy on Southern Root-Knot Nematode (*Meloidogyne incognita*) under Blending-of-Soil and Root-Irrigation Conditions. *J. Agric. Food Chem.* **2018**, *66*, 799–805.
- (12) Jing, T. F.; Zhang, D. X.; Pan, S. H.; LiuPan, G.; Mu, W.; Hou, Y. M.; Liu, F. Phenyl Isocyanate-Modified Avermectin B1a Improves the Efficacy against Plant-Parasitic Nematode Diseases by Facilitating Its Soil Mobility. *ACS Sustainable Chem. Eng.* **2020**, *8*, 2310–2319.
- (13) Zhao, X.; Cui, H. X.; Wang, Y.; Sun, C. J.; Cui, B.; Zeng, Z. H. Development strategies and prospects of nano-based smart pesticide formulation. *J. Agric. Food Chem.* **2018**, *66*, 6504–6512.
- (14) Usman, M.; Farooq, M.; Wakeel, A.; Nawaz, A.; Cheema, S. A.; Rehman, H. U.; Ashraf, I.; Sanaullah, M. Nanotechnology in agriculture: Current status, challenges and future opportunities. *Sci. Total Environ.* **2020**, *721*, 137778.
- (15) Chen, H. Y.; Lin, Y. S.; Xu, H.; Cheng, D. M.; Gong, S.; Liu, Q. H.; Zhou, X. H.; Zhou, H. J. Preparation of sustained-release chlorpyrifos particles via the emulsification coacervation method and their sustained-release performance. *J. Macromol. Sci., Part A: Pure Appl. Chem.* **2017**, *54*, 91–96.
- (16) Xie, Z. A.; Liang, W. L.; Xiong, Q. Y.; Zhao, Y. Y.; Cheng, J. L.; Li, X. B.; Zhao, J. H. Acetalated dextran microparticles for the smart delivery of pyraclostrobin to control Sclerotinia diseases. *Carbohydr. Polym.* **2022**, *291*, 119576.
- (17) Yan, S.; Hu, Q.; Jiang, Q. H.; Chen, H. T.; Wei, J.; Yin, M. Z.; Du, X. G.; Shen, J. Simple osthole/nanocarrier pesticide efficiently controls both pests and diseases fulfilling the need of green production of strawberry. *ACS Appl. Mater. Interfaces* **2021**, *13*, 36350–36360.
- (18) Qian, Y.; Deng, Y. H.; Qiu, X. Q.; Li, H.; Yang, D. J. Formation of uniform colloidal spheres from lignin, a renewable resource recovered from pulping spent liquor. *Green Chem.* **2014**, *16*, 2156–2163.
- (19) Tortora, M.; Cavalieri, F.; Mosesso, P.; Ciuffardini, F.; Melone, F.; Crestini, C. Ultrasound driven assembly of lignin into microcapsules for storage and delivery of hydrophobic molecules. *Biomacromolecules* **2014**, *15*, 1634–1643.
- (20) Irvani, S.; Varma, R. S. Greener synthesis of lignin nanoparticles and their applications. *Green Chem.* **2020**, *22*, 612–636.
- (21) Zhou, M. S.; Wang, D. P.; Yang, D. J.; Qiu, X. Q.; Li, Y. X. Avermectin loaded nanosphere prepared from acylated alkali lignin showed anti-photolysis property and controlled release performance. *Ind. Crops Prod.* **2019**, *137*, 453–459.
- (22) Zhang, X. Q.; Tang, X. Y.; Zhao, C. C.; Yuan, Z. T.; Zhang, D.; Zhao, H.; Yang, N.; Guo, K. Y.; He, K.; He, Y.; Hu, J.; He, L.; He, L.; Qian, K. A pH-responsive MOF for site-specific delivery of fungicide to control citrus disease of Botrytis cinerea. *Chem. Eng. J.* **2022**, *431*, 133351.
- (23) Chen, L. H.; Zhou, X. Y.; Shi, Y. F.; Gao, B.; Wu, J. P.; Kirk, T. B.; Xu, J. K.; Xue, W. Green synthesis of lignin nanoparticle in aqueous hydrotropic solution toward broadening the window for its processing and application. *Chem. Eng. J.* **2018**, *346*, 217–225.
- (24) Kaziem, A. E.; Gao, Y. H.; Zhang, Y.; Qin, X. Y.; Xiao, Y. Y.; Zhang, Y. H.; You, H.; Li, J. H.; He, S. α -Amylase triggered carriers based on cyclodextrin anchored hollow mesoporous silica for enhancing insecticidal activity of avermectin against Plutella xylostella. *J. Hazard. Mater.* **2018**, *359*, 213–221.
- (25) Abdelrahman, T. M.; Qin, X. Y.; Li, D. L.; Senosy, I. A.; Mmby, M.; Wan, H.; Li, J. H.; He, S. Pectinase-responsive carriers based on mesoporous silica nanoparticles for improving the translocation and fungicidal activity of prochloraz in rice plants. *Chem. Eng. J.* **2021**, *404*, 126440.
- (26) Kong, F. G.; Parhiala, K.; Wang, S. J.; Fatehi, P. Preparation of cationic softwood kraft lignin and its application in dye removal. *Eur. Polym. J.* **2015**, *67*, 335–345.
- (27) Dredan, J.; Antal, I.; Racz, I. Evaluation of mathematical models describing drug release from lipophilic matrices. *Int. J. Pharm.* **1996**, *145*, 61–64.
- (28) Casas, A.; Alonso, M. V.; Oliet, M.; Rojo, E.; Rodríguez, F. FTIR analysis of lignin regenerated from *Pinus radiata* and Eucalyptus globulus woods dissolved in imidazolium-based ionic liquids. *J. Chem. Technol. Biotechnol.* **2012**, *87*, 472–480.
- (29) Xiong, F. Q.; Han, Y. M.; Li, G. Y.; Qin, T. F.; Wang, S. Q.; Chu, F. X. Synthesis and characterization of renewable woody nanoparticles fluorescently labeled by pyrene. *Ind. Crops Prod.* **2016**, *83*, 663–669.
- (30) Liu, Z. H.; Ni, Y. H.; Fatehi, P.; Saeed, A. Isolation and cationization of hemicelluloses from pre-hydrolysis liquor of kraft-based dissolving pulp production process. *Biomass Bioenergy* **2011**, *35*, 1789–1796.
- (31) Shen, W.; Zhang, G. H.; Guo, N.; Li, Y. T. Study on the inclusion compound of avermectin by infrared spectroscopy. *Spectrosc. Spectral Anal.* **2014**, *34*, 1201–1205.
- (32) Lossbroek, T. G.; Ouden, H. Tests with a solid solution of permethrin in a degradable polymer formulation as stomach and contact poison on *Mamestra brassicae* (Lep., Noctuidae) and *Calandra granaria* (Col., Curculionidae). *J. Appl. Entomol.* **1988**, *105*, 355–359.
- (33) Yang, D.; Cui, B.; Wang, C. X.; Zhao, X.; Zeng, Z. H.; Wang, Y.; Sun, C. J.; Liu, G. Q.; Cui, H. X. Preparation and characterization of emamectin benzoate solid nanodispersion. *J. Nanomater.* **2017**, *2017*, 6560780.

Targeted delivery of emamectin benzoate by functionalized polysuccinimide nanoparticles for the flowering cabbage and controlling *Plutella xylostella*

Xu Ye,^{a,b} Meichen Liu,^b Ning Zhao,^{a,b} Chunxia Xiao,^b Hanhong Xu^{b*}  and Jinliang Jia^{a,b*} 



Abstract

BACKGROUND: *Plutella xylostella*, one of the most destructive and cosmopolitan pests of cruciferous crops, is especially harmful to the young tissues of the flowering cabbage (*Brassica campestris* L.). Although emamectin benzoate (EB) has high insecticidal activity against *P. xylostella*, one major reason of low utilization for EB is the lack of internal transport in the young plants.

RESULTS: In this study, four kinds of functional EB/polysuccinimide (PSI) with glycine methylester nanoparticles (EB@PGA NPs) were prepared. The obtained EB@PGA NPs could effectively protect EB from photolysis, and the degradation rate of EB@PGA NPs was <30% in 24 h. Simulating the intestinal pH = 9 of *P. xylostella*, the highest cumulative release rate of EB@PGA NPs could reach 89.61% in 24 h. Furthermore, EB@PGA NPs could deliver EB into the young tissues of the flowering cabbage through the nanocarrier, and the highest transport efficiency of EB@PGA₂₅ reached 1.437%. The bioactivity of EB@PGA₂₅ against *P. xylostella* larvae (LC₅₀ = 0.34 µg mL⁻¹) was 1.6-fold higher than that of EB (LC₅₀ = 0.53 µg mL⁻¹). EB@PGA could easily become 'internalized' into the intestinal wall of *P. xylostella*, thus increasing the penetration of the drug and enhancing the insecticidal activity.

CONCLUSION: The accurate delivery of insecticides by PGA nanocarriers into young tissues of plants could be a promising new method for the efficient management of field pests and diseases.

© 2021 Society of Chemical Industry.

Supporting information may be found in the online version of this article.

Keywords: nanopesticides; *plutella xylostella*; emamectin benzoate; target accumulation; delivery

1 INTRODUCTION

By 2050, the world's population is expected to exceed 9 billion, and food demand will increase rapidly as a result.¹ At the same time, there is a growing demand for fresh and healthy vegetables. The flowering cabbage is rich in various essential vitamins, and is deeply loved by the Chinese people.² Nevertheless, the threat posed by *Plutella xylostella* pests and diseases to the flowering cabbage has become extremely serious. *Plutella xylostella* causes widespread damage to the flowering cabbage annually, as well as an estimated annual economic loss of >US\$4 billion worldwide.^{3–5} At present, chemical prevention is the main control method to control *P. xylostella*. However, few insecticides with phloem transport can achieve targeted accumulation in tissues of plants, and most pesticides sprayed run off causing environmental pollution and a significant waste of money and resources.

Emamectin benzoate (EB) is a highly effective semisynthetic antibiotic pesticide against *P. xylostella*.⁶ The insecticidal activity of EB against *P. xylostella* is ≈400-fold greater than other traditional pesticides such as terbufenozide, and its efficacy is three orders of magnitude greater than abamectin (AVM).⁷ In addition, EB has low toxicity to humans and other mammals,⁸ and easily

degrades under ultraviolet (UV) light.⁹ Currently, commercial EB pesticides are emulsions and microemulsions because of the poor water solubility of EB, which is not friendly to the environment.^{10,11} Moreover, *P. xylostella* prefers to feed on young leaves of the flowering cabbage,¹² and the planting period of the flowering cabbage overlaps with the outbreak period of *P. xylostella*.¹¹ Thus, chemical control of *P. xylostella* using EB will be difficult without its transport and accumulation in young leaves.

In recent years, nanotechnology has been increasingly applied in agriculture. In particular, much attention has been given to

* Correspondence to: H Xu or J Jia, State Key Laboratory for Conservation and Utilization of Subtropical Agro-bioresources, South China Agricultural University, Guangzhou, Guangdong 510642, China. E-mail: hxxu@scau.edu.cn (Xu); E-mail: jiajinliang@scau.edu.cn (Jia)

a Key Laboratory for Biobased Materials and Energy of Ministry of Education, College of Materials and Energy, South China Agricultural University, Guangzhou, China

b State Key Laboratory for Conservation and Utilization of Subtropical Agro-bioresources, South China Agricultural University, Guangzhou, China

improving the utilization rate of pesticides, with the general aim of developing green agriculture.^{13–18} Asem Elabasy *et al.*¹⁹ prepared nano-delivery systems loading EB successfully through combining cellulose nanocrystals (CNCs) and silicon dioxide nanoparticles (SNPs), which could effectively protect EB from photolysis under UV radiation. Huang *et al.*²⁰ used nonsystemic cellulose ester cellulose acetate butyrate (CAB) to obtain microcapsules with good controlled release drug properties. Although nanotechnology already has improved the performance of EB, there remain few studies on the use of nanotechnology to solve the targeted accumulation of EB in plants.

In preliminary work in our laboratory, we incorporated nanotechnology into plant transport. Wang *et al.*²¹ modified polysuccinimide (PSI) with methyl glycine ester to obtain polyglycerol adipate (PGA) nanocarriers, and found that the nonsystemic AVM could be transported in rice by PGA nanocarriers. However, it has not yet been investigated whether PGA nanocarriers can deliver EB via the phloem of the flowering cabbage in order to protect the young leaves. Furthermore, the mechanism of enhancing the insecticidal activity by PGA nanocarriers against *P. xylostella* remains unclear.

In this study, the functionalization degree of glycine methyl ester was adjusted to obtain different functionalized PGA nanoparticles (NPs), which were loaded with EB to prepare EB@PGA NPs. The hydration particle size of the NPs, thermal stability and stimulus response slow-release behavior were studied. In addition, the phloem accumulation and transport efficiency of different functionalized EB@PGA NPs in young tissues of the flowering cabbage were investigated. EB@PGA NPs with the strongest transport efficiency were selected to compare the bioactivity of *P. xylostella* with the original form of EB, and a fluorescence method was used to elucidate the synergistic mechanism of PGA on the bioactivity of the *P. xylostella*.

2 MATERIALS AND METHODS

2.1 Materials

Polysuccinimide (PSI; Mw = 5.6 k Da, 99%) was supplied by Hubei YuanChengSaichuang Technology Co., Ltd. (Wuhan, China). Glycine methyl ester hydrochloride (HGlyOMe, 99%) was purchased from Shanghai Hanhong Scientific Co., Ltd. (Shanghai, China). Dibutylamine (DBA) and dimethyl sulfoxide (DMSO) were provided by Shanghai Lingfeng Scientific Co., Ltd. (Shanghai, China). Tween 80 was procured from Tianjin Fuyu Fine Chemical Co., Ltd. (Tianjin, China). Fluorescein-5-isothiocyanate cadaverine (FITC-cad) was purchased from Hangzhou Xinqiao Biotechnology Co., Ltd. (Hangzhou, China). Triethylamine (TEA) was procured from Xilong Chemical Co., Ltd. (Shantou, China). EB with a purity of 96% was purchased by Zhejiang Heben Technology Co., Ltd.

(Wenzhou, China). EB micro-emulsion was purchased by Guangzhou Jinnong Technology Development Co., Ltd. (Guangdong, China). Acetonitrile and methanol at high-performance liquid chromatography (HPLC) grade were obtained from Beijing DingGuoChangsheng Biotechnology Co., Ltd. (Beijing, China). All other reagents and chemicals were commercially available and used without any purification.

Third instar larvae of *P. xylostella* were supplied by South China Agricultural University, Guangdong, China. The larvae were cultivated with the flowering cabbage. The *P. xylostella* larvae were reared in a pest house at 26 °C, with a relative humidity of 80% and 16 h:8 h, light:dark photoperiod.

2.2 Synthesis of different functionalized PGA nanocarriers

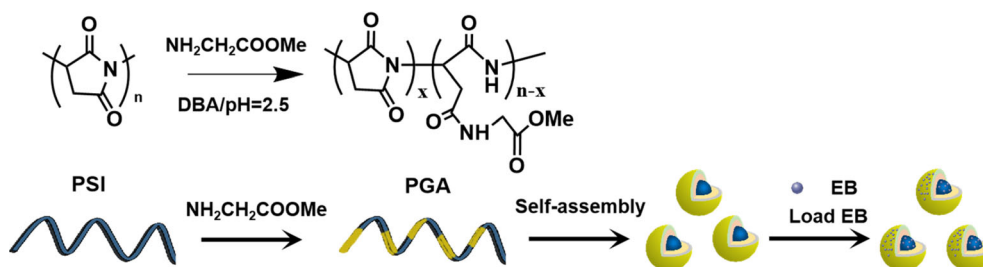
The synthesis path was executed according to previous methods in the literature with minor modifications.²² First, 0.485 g PSI (0.005 mol succinimide repeating units) was dissolved into 5 mL DMSO. Then 0.75 g (0.006 mol) HGlyOMe and 0.755 g (0.006 mol) DBA were dissolved in 5 mL DMSO and added to PSI solution under vigorous stirring at room temperature for 6, 10, 18 and 24 h, respectively. Different functionalized PGA nanocarriers were precipitated after adding 150 mL citric acid buffer (pH = 2.5). Eventually, different functionalized PGA nanocarriers were obtained by centrifugation (10 000 rpm), washed three times with distilled water and freeze-dried overnight.

2.3 Preparation of EB@PGA NPs

A total of 50 mg PGA nanocarriers were dissolved in 5 mL DMSO. Then, 50 mg EB were added into the above solution and stirred evenly to form a mixed solution. Subsequently, the mixed solution was added into 23 mL distilled water and stirred fiercely at RT for 2 h. After centrifugation (10 000 rpm), the obtained precipitate was washed three times with the mixed reaction solution (DMSO:H₂O = 5:23) and washed once with distilled water to remove the residual EB and DMSO. The synthetic schematic diagram of EB@PGA NPs is shown in Scheme 1.

2.4 Synthesis of FITC-cad-PGA NPs

PSI (50 mg) was dissolved in 2 mL DMSO; after adding 77 mg HGlyOMe, 5 mg FITC-cad and 100 µL DBA were added to form a mixed organic phase. Then, the mixed solution was stirred in the dark for 18 h at RT. The FITC-cad-PGA NPs were precipitated after adding 60 mL citric acid buffer (pH = 2.5). Subsequently, the FITC-cad-PGA NPs were collected by centrifugation (10 000 rpm), washed three times with distilled water and freeze-dried overnight.



Scheme 1. Synthetic schematic diagram of EB@PGA NPs.

2.5 Loading capacity of EB@PGA NPs

A total of 3 mg EB@PGA NPs were dissolved in 3 mL ethanol for ultrasonic treatment and all of the wrapped EB was dissolved into ethanol. Subsequently, the supernatant was centrifuged at 10 000 rpm for 10 min and collected in a brown liquid bottle to avoid any degradation by light. Determination of EB concentration by an Agilent 1100 HPLC system equipped with a reversed phase column (ZORBAX SB-C₁₈, 3.5 µm, 50 × 2.1 mm; Agilent Technologies, Santa Clara, CA, USA) at 30 °C. Methanol and 0.1% TEA aqueous solution (90:10, v/v) were used as mobile phase, with flow rate 1.0 mL min⁻¹ and 10 µL injected volume. The excitation and emission wavelengths were 245 and 470 nm, respectively. The following equation was used to calculate EB loading capacity (LC):

$$LC = \frac{\text{weight of EB loaded}}{\text{weight of EB@PGA}} \times 100\%$$

2.6 Characterization

The PGA NPs were measured by a nuclear magnetic resonance spectrometer (AV III 600; Bruker, Berlin, Germany). The structural changes of NPs were characterized by a Fourier transform infrared spectrometry (FTIR) (Nicolet IS10; Thermo Fisher Scientific GmbH, Dreieich, Germany) with quantitative means. Scanning electron microscopy (SEM) (Nova Nano 450; FEI Co., Hillsboro, OR, USA) was used to observe the morphological characteristics of the NPs. Thermogravimetric analysis (TGA) of the NPs was operated on a TG209F1 Iris thermobalance (NETZSCH-Gerätebau GmbH, Selb, Germany). The hydration particle size and Zeta potentials of NPs were determined by laser particle size analyzer (Zetasizer Nano ZSE, Malvern Panalytical Ltd, UK). Agilent 1290 HPLC was used to determine EB content levels in the newly grown leaves of flowering cabbage. The system was equipped with a fluorescence detector (FLD) and configured with a reversed phase column (ZORBAX SB-C₁₈, 3.5 µm, 50 × 2.1 mm; Agilent) at 30 °C. Elemental analysis (EA) was characterized by an elemental analyzer (Vario EL cube; Elementar, Langenselbold, Germany). X-ray photoelectron spectroscopy (XPS, Thermo ESCALAB 250 Xi; Thermo Fisher Scientific) was used to verify the combination method between PGA NPs and EB.

2.7 In vitro release investigation

The sustained release experiments of EB for different functional nanocarriers were carried out via a dialysis-based experiment. A total of 15 mg different functional EB@PGA NPs were suspended in 3 mL ethanol-water medium (30:70, v/v) in a dialysis membrane (molecular weight cut-off 3500 Da). The dialysis bag was immersed in 150 mL ethanol-water mixture (30:70, v/v) with pH 9.0 under slow magnetic stirring. At regular intervals, 1 mL medium was fetched out and the same volume of fresh medium added to keep the total volume constant. The collected samples were analyzed by an Agilent 1290 HPLC equipped with a reversed phase column (ZORBAX SB-C₁₈, 3.5 µm, 50 × 2.1 mm) at 30 °C. In detail, the solution of methanol and 0.1% TEA aqueous solution (90:10, v/v) was used as a mobile phase at a 0.8 mL min⁻¹ flow rate with 10-µL injection volume. The excitation wavelength and emission wavelengths were 365 and 470 nm, respectively. Each treatment was repeated three times at RT.

2.8 Phloem translocation of EB@PGA

The flowering cabbage seeds were provided by South China Agricultural University. The flowering cabbage was cultivated for

20 days with the living conditions of 25 °C, 16 h:8 h, light:dark photoperiod, and watering every 2 days. After treatment with EB@PGA NPs or EB, the newly grown young tissues of the flowering cabbage were removed and the EB content in the samples was detected by HPLC.^{23,24} To depict and quantify the transport of EB in the leaves, selected upper leaves were analyzed by applying the same dose of original EB and different functionalized EB@PGA NPs. For example, EB@PGA₃₃ NPs or an equivalent dose of EB was applied to the leaves at a final concentration of 200 or 37 mg·L⁻¹, respectively (0.2 mL per leaf and two leaves per plant). Leaves treated with distilled water containing 0.1% (v/v) organo-silicone surfactant (Silwet L-77) and 0.1% (v/v) Tween 80 were kept as controls. The experiment was repeated three times with 30 replicate plants per treatment. The newly grown upper leaves were collected at 24, 48, 72 h post-treatment. The efficiency of transport was calculated as follows:

The efficiency of transport

$$= \frac{\text{The quality of EB detected in the upper leaves}}{\text{The quality of EB coated on treated leaves}} \times 100\%$$

2.9 Insecticidal activity investigation

The EB@PGA NPs, original EB and a commercial EB micro-emulsion were dissolved in DMSO and diluted with distilled water containing Tween 80 (0.1%, v/v) to obtain desired concentrations. The leaves of the flowering cabbage (cabbage with two cotyledons) were immersed in test solution for 30 s before drying. The control group was treated with Tween 80 (0.1%, v/v). After air-drying, the treated leaves and 12 3rd instar larvae of *P. xylostella* were placed into lucid cylindrical culture bottles lined with filter paper to co-culture. The instar larvae were cultivated at 26 °C and 85% relative humidity for 16 h in light conditions. The mortality (%) of *P. xylostella* larvae and the median lethal concentration (LC₅₀) values were calculated after 24 h of treatment. All treatments were repeated three times.

2.10 Fluorescence distribution of nanocarriers

The 3rd instar larvae of *P. xylostella* were fed with an artificial diet mix containing 20 µg FITC-cad-PGA NPs. Larvae fed with 1 µg free FITC-cad solution were used as control. After 24 h cultivation at RT, *P. xylostella* larvae were dissected and their guts were imaged under fluorescent microscopy. In particular, the fluorescent images were obtained under the same conditions.

3 RESULTS AND DISCUSSION

3.1 ¹H NMR analysis

In order to verify the degree of functionalization of the PGA nanocarriers, the ¹H NMR spectra in (CD₃)₂SO are shown in Fig. 1. The curve illustrates that the signal at 3.2 ppm was attributed to —CH₂— of PSI. The signal in the shift range 3.73–3.89 ppm was ascribed to —CH₂— in HGlyOMe. The peaks of H₂O and (CD₃)₂SO appeared at 3.34 and 2.50 ppm, respectively. In addition, a new peak ranged from 8.42–8.73 ppm was ascribed to —N—H— in —CONH— group, which further testified that PSI was modified by HGlyOMe successfully. The signal of —CH₃— appeared at 3.66 ppm in —COOCH₃— and the signal of —CH— ranged from 5.07 to 5.31 ppm in the PSI main chain.^{25–27} The ratio of the modified PSI could be calculated by comparing the integrated intensity of —CH₃— with the thrice integrated intensity of —CH—.

With increasing reaction time, four kinds of PGA nanocarriers with different functionalization degree (11%, 18%, 25% or 33%) were obtained.

3.2 FTIR analysis

FTIR spectra of different functionalized PGA and EB@PGA NPs are shown in Fig. 2(a),(b). As for HGlyOMe, the absorption bands at 2628 and 2682 cm^{-1} were attributed to the stretching vibration N—H, and the absorption band at 1259 cm^{-1} was ascribed to C—O—C stretching vibration.^{27, 28} Besides the characteristic absorption band at 2950 cm^{-1} corresponding to $-\text{CH}_2-$ stretching vibration, two strong additional bands at 1790 and 1728 cm^{-1} were due to the C=O and the cyclic imide of succinimide group stretching vibration, respectively. Comparing with PSI, the coupling of N—H bending vibration and C—N stretching vibration among amide absorption band II in the newly formed

$-\text{CONH}-$ appeared at 1540 cm^{-1} .^{29, 30} As the degree of functionalization increased, the characteristic peak intensity of N—H and C—N stretching vibration that appeared at 1540 cm^{-1} became increasingly stronger. Furthermore, the absorption band at 1036 cm^{-1} was associated to the stretching vibration of C—C and C—N, which indicated that HGlyOMe was grafted on the PSI successfully.²⁹

With respect to EB, the specific peaks at 2967 and 2932 cm^{-1} were attributed to C—H stretching vibrations of an aromatic ring corresponding to the benzoate fraction or conjugated olefins.¹⁹ The specific absorbance peak at 1730 cm^{-1} was attributed to bending vibration of C=O in the benzene skeleton. The peaks at 1555 and 1599 cm^{-1} were ascribed to C=C stretching vibrations of an aromatic ring or conjugated olefins. The special band at 1120 cm^{-1} was identified as skeleton vibration of O—H, which belonged to the characteristic peaks of EB.^{19, 31} As for the spectra

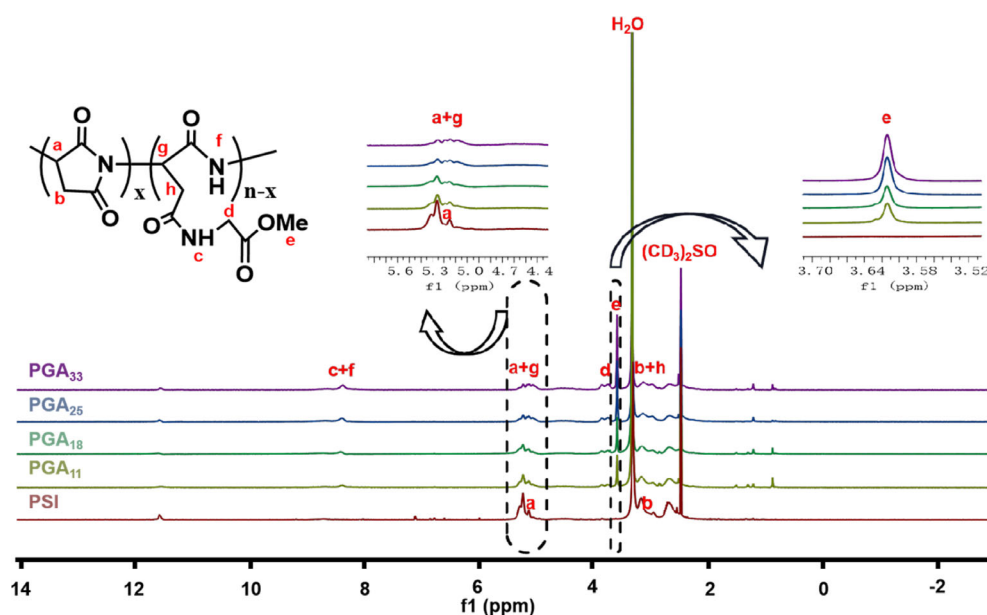


Figure 1. ^1H NMR spectra of different functional PGA nanocarriers.

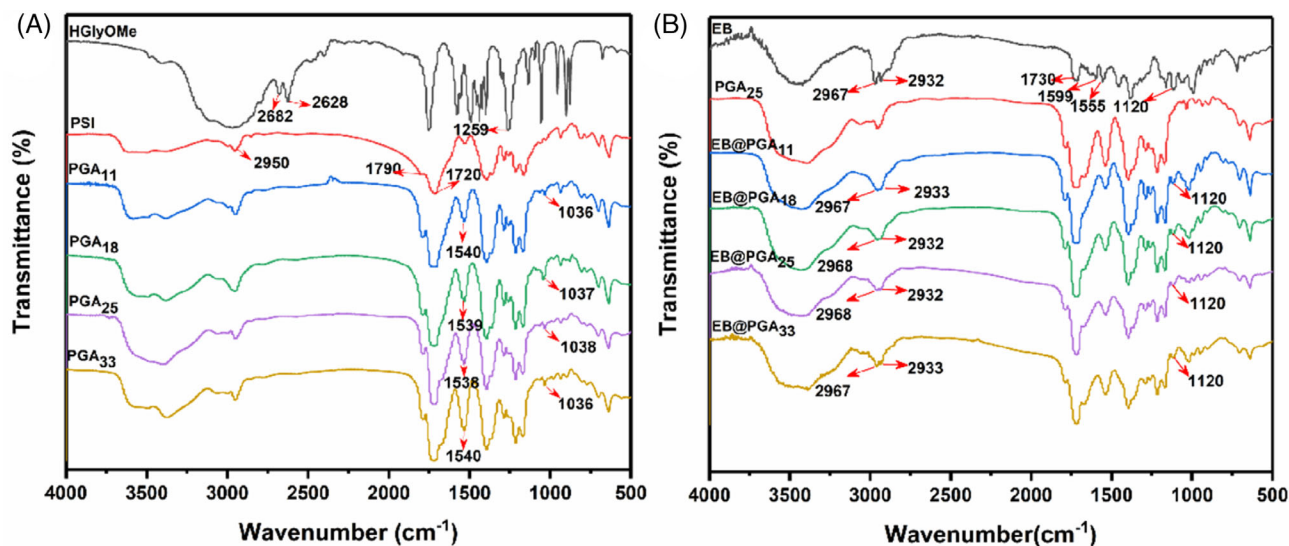


Figure 2. FTIR spectra of (a) PSI, HGlyOMe, PGA₁₁, PGA₁₈, PGA₂₅, PGA₃₃, (b) EB, PGA₂₅, EB@PGA₁₁, EB@PGA₁₈, EB@PGA₂₅ and EB@PGA₃₃.

of EB@PGA₁₁, EB@PGA₁₈, EB@PGA₂₅ and EB@PGA₃₃, the peaks at 2967, 2933 and 1120 cm⁻¹ were exactly like the spectra of EB, which indicated that PGA NPs were successfully loaded with EB. The LC of different functionalized EB@PGA NPs was listed in Supporting Information, Table S1. With the increase of the degree of functionalization, the LC increased slowly, a result that was consistent with the previous literature.²¹ The highest LC of EB@PGA₃₃ NPs reached 18.5% among the different functionalized PGA NPs.

3.3 Morphology and zeta potential analysis

The representative morphological characteristics of PGA and EB@PGA NPs were compared by SEM in Fig. 3(a) and (b). We chose EB@PGA₃₃ NPs with the highest drug loading rate for comparison. In Fig. 3(a), the appearance of PGA₃₃ NPs with a porous network structure was basically spherical; this shape could be attributed to self-assembly of the hydrophilic part and the hydrophobic part in water. Furthermore, there was no individual NP arranged in parallel in the field of vision. The results indicated that PSI molecules functionalized by methyl glycinate not only self-assembled within the molecules, but also participated with adjacent PSI molecules in the formation of particles in water. In Fig. 3(b), EB@PGA₃₃ NPs appear to have larger, plumper overall particle size and reduced size of voids between the NPs.

The hydrodynamic size and zeta potentials of the nanocomposites were measured by the dynamic light scattering in Fig. 3 (c) and (d). The hydrodynamic size of different functionalized EB@PGA NPs decreased gradually with increase of the degree of functionalization from 367.35 ± 0.15 nm of EB@PGA₁₁ to 261.33 ± 0.24 nm of EB@PGA₃₃. The hydrated particle size of PGA nanocarriers increased slightly after EB loading; the average hydrodynamic size of EB was in the large micron scale at 3954.18 ± 0.87 nm. The slightly high polymer dispersity index (PDI = 0.680) of EB indicated that it had poor stability and poor dispersion in water. However, the PDI values of different functionalized EB@PGA NPs were >0.6, indicating that the dispersion and stability of EB in water were improved after nanocrystallization. Consequently, the PGA nanocarriers could improve the water dispersibility and stability of the hydrophobic EB, and contribute to change from micron-scale to nanocrystalline EB. PGA₁₁, PGA₁₈, PGA₂₅ and PGA₃₃ NPs showed negative charges in water (-31.50 ± 1.22, -36.81 ± 0.89, -35.72 ± 1.76 and -28.21 ± 1.02 mV, respectively), confirming that the amide bond had negatively charged groups which formed after functionalization. Zeta potentials reflected the stability of NPs in water,²⁵ as EB@PGA₁₁, EB@PGA₁₈, EB@PGA₂₅ and EB@PGA₃₃ NPs held less negative charge (-19.51 ± 0.69, -20.80 ± 1.10, -20.01 ± 0.96 and -18.67 ± 2.51 mV, respectively). It might be

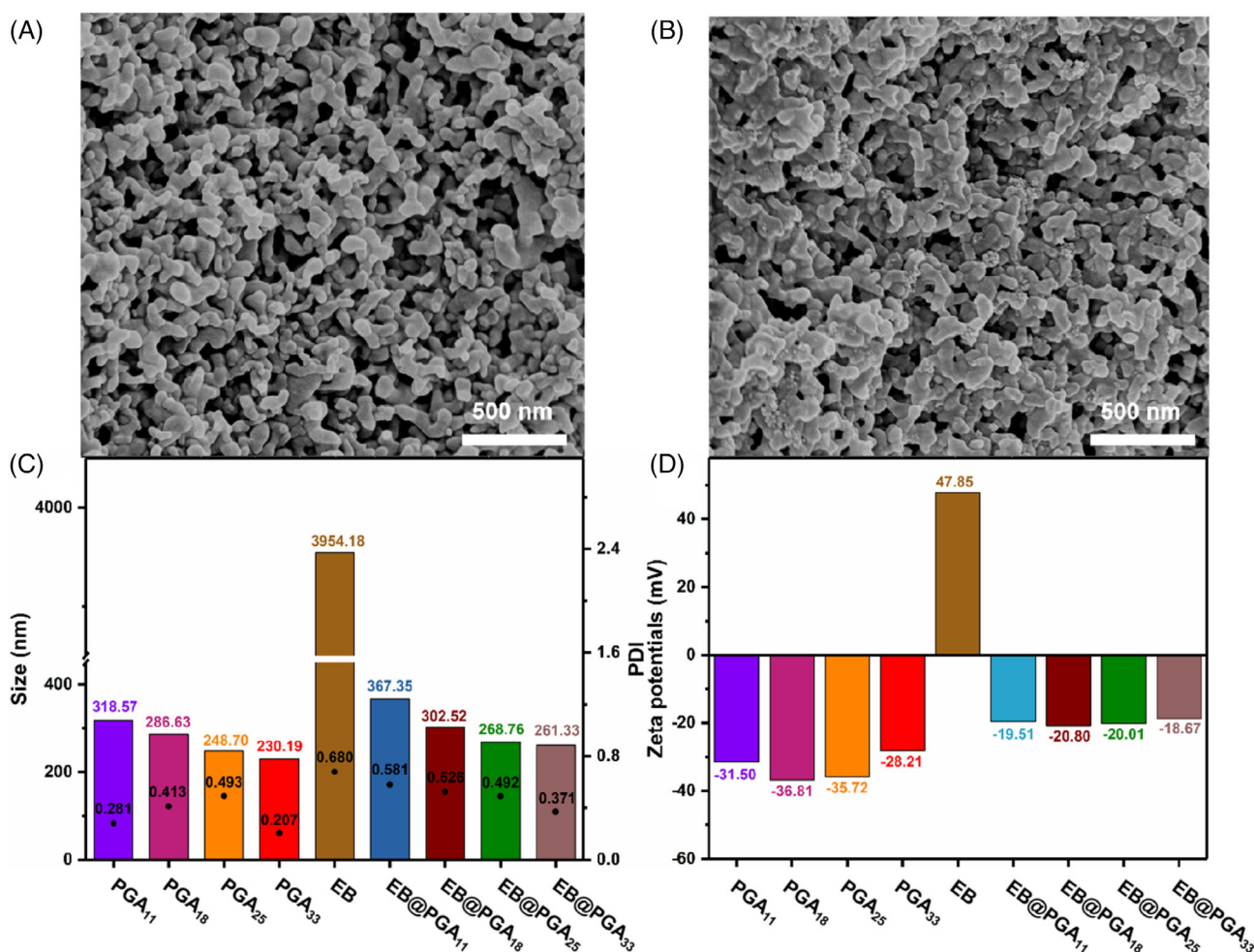


Figure 3. SEM images of PGA₃₃ NPs (a) and EB@PGA₃₃ NPs (b). (c) Hydrated particle size of different functionalized PGA and EB@PGA NPs with their PDI. (d) Zeta potentials of different functionalized PGA and EB@PGA NPs.

the electrostatic interactions of PGA and EB neutralized the negative charges on the surface of the nanocarriers. Taken together, PGA nanocarriers could enhance the stability and dispersion of EB in water.

3.4 Surface element and spectra analysis

In order to further confirm the relationship between PGA nanocarriers and EB, EA and XPS methods were used, with PGA₃₃ again the focal research formulation. It is well-known that EA could be used to illustrate the total element content in the samples,³² and XPS is a good means of accounting for the elemental distribution on the surface of samples (Fig. S1).³³ In Table 1, the contents of nitrogen (N) in the surface and whole of EB@PGA₃₃ were 9.964% and 9.235%, respectively. The N content of EB of 1.389% accounted for a very small part of the total content. In addition, the N content of the whole NPs was $\approx 10\%$ which was similar to that of the surface. Therefore, we assumed that N was evenly distributed on the surface and inside the EB@PGA NPs simultaneously. Then we calculated the element ratios of carbon (C):N and oxygen (O):N to elaborate the structure of microsphere. The C:N and O:N ratios of the whole NPs manifested by EA were 4.685 and 3.512, respectively, whereas the C:N and O:N ratios on the surface of NPs obtained by XPS were 6.634 and 2.315, respectively. As the proportion of C content in EB was as high as 66.667%. The reason why the C:N ratio in EB@PGA₃₃ increased 1.42-fold was that a part of EB was bound on the surface of PGA nanocarriers. Combined with the results of Fig. 3(d) zeta potentials, the zeta potential of EB in water was ≈ 48 mV. Nevertheless, the different functionalized PGA nanocarriers had exhibited negative charge in aqueous solution of around -30 mV. After loading EB, the zeta potentials of different functionalized EB@PGA NPs were approximately -20 mV, which further indicated that EB and PGA had positive and negative electrostatic attraction, probably on the surface of the EB@PGA NPs.

In order to further investigate whether drugs were encapsulated in NPs, we adjusted the ratio of PGA₃₃ NPs to EB added in the reaction. The zeta potentials obtained by the reaction are shown in Table S2. The zeta potentials of these NPs were approximately -19 mV. As the amount of EB increased, the zeta potentials no longer increased appreciably, which indicated that the EB adsorbed on the surface of PGA₃₃ NPs by electrostatic interaction had reached saturation. As the ratio of EB to PGA₃₃ increased, the drug LC of PGA₃₃ nanocarriers strengthened gradually. It was obvious that a part of EB was encapsulated inside the PGA₃₃ nanocarriers. To sum up, a part of the EB was bound to the surface of the PGA₃₃ nanocarriers by electrostatic interaction, and the other part of the EB was wrapped in the PGA nanocarriers.

3.5 Thermal property analysis

In order to research thermodynamic properties of nanocomposites, the TG and DTG analysis of EB, functionalized PGA and EB@PGA were performed. The TGA and DTG data of PGA₂₅, EB and EB@PGA₂₅ are shown in Fig. 4(a) and (b), respectively. For the thermal degradation curve of EB, the initial weight loss happened at ≈ 180 °C. The most severe degradation moment appeared at 248.5 °C, and weight loss continued to the point of disappearance at 440 °C.¹⁹ As for PGA₂₅, an original mass loss at 5% appeared among in the temperature range 0–120 °C as a consequence of the loss of water of crystallization and physically adsorbed water on the PGA₂₅ surface. The second stage of thermal degradation temperature ranged from 260 to 420 °C with the peak at 359.7 °C being a result of the degradation of amide bonds. With regard to EB@PGA₂₅, the main thermal degradation temperature range happened at 180–430 °C with the peak at 351.7 °C preceded by a tiny peak at 225.1 °C. A broad thermal degradation temperature for EB@PGA₂₅ probably demonstrated the initial destruction of the electrostatic attraction of EB and PGA.^{34,35} Furthermore, with the increase of functionalization degree, the main degradation temperature of PGA nanocarriers decreased gradually. The thermal degradation peaks of each functional PGA nanocarriers shifted to the left, ranging from 384.1 °C for PGA₁₁ to 345.5 °C for PGA₃₃. The thermostability of PGA decreased with enhanced degree of functionalization to a certain extent. Because the unopened polysuccinimide unit was a stable five-membered ring structure, the thermal stability decreased when the five-membered ring was opened. In addition, the TG and DTG curves of different functionalized EB@PGA NPs are shown in the Fig. 4(e) and (f), respectively. Three distinct stages of different functionalized EB@PGA can be observed in the TG curve. The thermal degradation of other different functionalized EB@PGA NPs was similar to that of EB@PGA₂₅. As the degree of functionalization increased, the slope of the TGA curve in the third stage flattened. This was attributed to increased ring-opening of polysuccinimide units, which led to a decrease in thermal stability. In conclusion, PGA nanocarriers could significantly improve the thermal stability of EB. With the increase of functionalization degree, the thermal stability showed a slightly decreasing trend.

3.6 Sustained release of EB@PGA

It is notable that the pH value of the midgut of *P. xylostella* is weakly alkaline at ≈ 9 .³⁶ Therefore, we studied the release behavior of different functionalized EB@PGA NPs in a weakly alkaline environment. As shown in Fig. 5, all EB@PGA NPs underwent sudden release in the sustained-release solution within 24 h initially.³⁷ The released amount of EB@PGA NPs was $>50\%$, possibly with preferential release of EB wrapped around the PGA nanocarriers. EB was released in large numbers, too, with

Table 1. Composition of elements of PGA₃₃, EB, and EB@PGA₃₃ NPs detected by EA and the elemental distribution of EB@PGA₃₃ NPs detected by XPS

Method	Samples	Element content (%)				
		C	O	N	C:N	O:N
EA	PGA ₃₃	44.254	37.997	12.998	3.405	2.923
	EB	66.667	23.810	1.389	47.996	17.142
	EB@PGA ₃₃	46.684	35.073	9.964	4.685	3.512
XPS	EB@PGA ₃₃	61.268	21.380	9.235	6.634	2.315

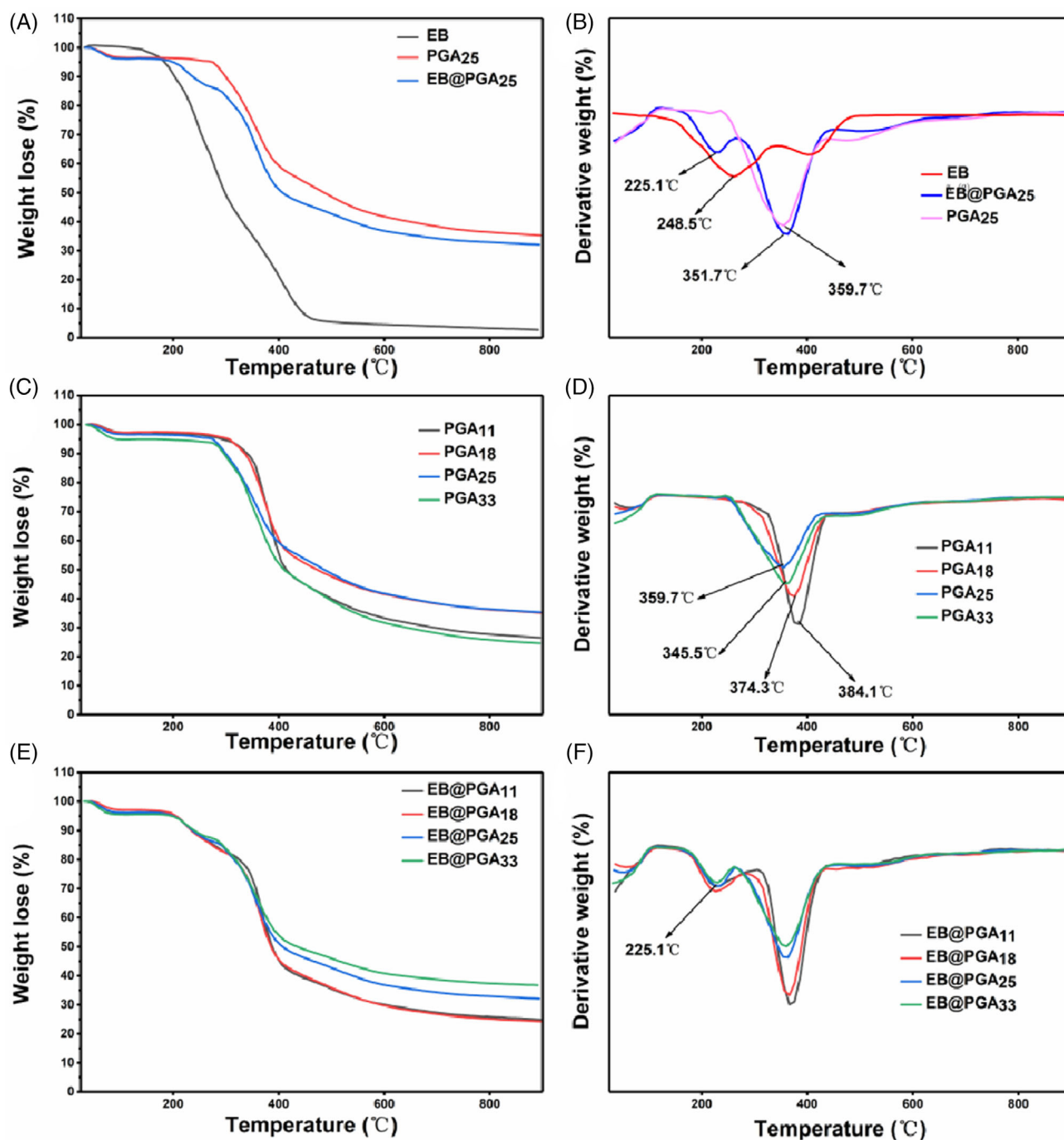


Figure 4. (a) TGA and (b) DTG curves of PGA₂₅, EB and EB@PGA₂₅. (c) TGA and (d) DTG curves of PGA₁₁, PGA₁₈, PGA₂₅ and PGA₃₃. (e) TGA and (f) DTG curves of EB@PGA₁₁, EB@PGA₁₈, EB@PGA₂₅ and EB@PGA₃₃.

95% cumulative released value. The high release efficiency in a short time could make the drug release quickly and achieve a favorable insecticidal effect. The rate of release slowed down over time, which might because the amide bond of the PGA nanocarriers broke down in the alkaline environment and released the encased EB.²⁴ The release rate of different functionalized EB@PGA slowed down and the EB released completely after 144 h. The final cumulative release rates of EB@PGA₁₁, EB@PGA₁₈, EB@PGA₂₅ and EB@PGA₃₃ reached up to $86.15 \pm 0.21\%$, $86.84 \pm 1.02\%$, $88.36 \pm 0.89\%$ and $89.61 \pm 1.33\%$, respectively. Comparatively, the sustained release ability of the four EB@PGA NPs was close,

and the highest value of the release efficiency was $89.61 \pm 1.33\%$ for EB@PGA₃₃. These results suggested that the greater the number of degradable amide bonds, the more completely degradation of the PGA, and the more completely release of EB in the alkaline environment. The release mechanism of EB@PGA NPs is shown in Scheme 2.

3.7 Phloem transport

Plutella xylostella was more likely to harm the young leaves of the flowering cabbage. In Fig. 6(a), we designed an experiment to elucidate the transportation of PGA in flowering cabbage. A

schematic diagram of the treatment is shown in Fig. 6(b). The detection of the drug in the newly growing leaves after application on the old leaves was confirmed to be the result of phloem transport.^{23,24} In Fig. 6(c), after one day of treatment with EB, there was no detectable effect of EB in the newly growing leaves of the flowering cabbage by HPLC. Moreover, a tiny minority of EB was detected on the second and third days, which indicated that the flowering cabbage could hardly transport EB *in vivo*. However, EB could be detected in the newly growing leaves of the treated with EB@PGA, and the contents of EB were different for the four functionalized PGA nanocarriers. Taking the leaves after one day's treatment as an example, the content of EB in the newly growing leaves after different functionalized EB@PGA treatments were all $>0.2 \text{ mg kg}^{-1}$. By horizontal contrast, the amount of EB transported by EB@PGA₂₅ was the largest after one day's treatment, and the content of EB in newly grown leaves was $\approx 0.8 \text{ mg kg}^{-1}$. With the increase of functionalization, the transport volume of EB decreased overall, except for EB@PGA₂₅. By longitudinal comparison, the phloem transport content of EB@PGA₂₅ and EB@PGA₁₈ decreased gradually as time went on, whereas that of EB@PGA₁₁ and EB@PGA₃₃ increased first and then decreased over time. These results indicated that PGA nanocarriers were used to help the phloem transportation of nonsystemic drugs and delivered EB to the new leaves (targets). To further explore the transport efficiency of different functionalized EB@PGA in the flowering cabbage, the transport efficiency of EB for newly growing leaves after one day treatment was investigated as shown in Fig. 6(d). EB@PGA₂₅ NPs had the highest transport efficiency reaching up to 1.437% with the corresponding effective transport concentration was $0.8 \mu\text{g mL}^{-1}$. Nevertheless, there was no direct

correlation between the transport efficiency of EB@PGA and the degree of functionalization. The results illustrated that NPs with 260–360 nm could be transported through phloem tissue, a size consistent with those reported in the literature.³⁸ PGA nanocarriers could effectively improve phloem transport of EB in the flowering cabbage.

3.8 Bioactivity against *Plutella xylostella*

EB@PGA₂₅ with the highest phloem transport ability was selected to test the bioactivity of the 3rd instar larvae of *P. xylostella*. For comparison, bioactivity tests at 24 h on EB, PGA₂₅ and EB@PGA₂₅ are shown in Fig. 7. PGA₂₅ nanocarriers were basically nontoxic to the 3rd instar larvae of *P. xylostella*. It could be observed that the *P. xylostella* larvae mortality of EB@PGA₂₅ was significantly higher than that of the EB group at the any concentration of the assay. The *P. xylostella* larvae mortality of the EB group varied from 24.6% to 72.1% for corresponding concentrations from 0.125 to $2 \mu\text{g mL}^{-1}$. Additionally, the insecticidal activity of EB@PGA₂₅ showed a gradual increase ranging from 34.0% to 80.1% at the corresponding concentration.

In Table S3, the LC_{50} of EB@PGA₂₅ NPs to the 3rd instar *P. xylostella* larvae is $0.34 \mu\text{g mL}^{-1}$. This was less than that of EB ($\text{LC}_{50} = 0.53 \mu\text{g mL}^{-1}$), and was basically consistent with the bioactivity of the commercial EB micro-emulsion ($\text{LC}_{50} = 0.33 \mu\text{g mL}^{-1}$). The result indicated the bioactivity of EB@PGA₂₅ against *P. xylostella* larvae was 1.6-fold greater than that of EB. The effective phloem delivery concentration of EB@PGA₂₅ within 24 h in Fig. 6(c) was $0.8 \mu\text{g mL}^{-1}$, which was higher than that of EB ($\text{LC}_{50} = 0.53 \mu\text{g mL}^{-1}$). In combination with the sustained-release analysis (Fig. 5), the results indicated that EB@PGA NPs released the encapsulated EB in a burst release behavior within 24 h in a weakly alkaline gut. PGA nanocarriers increased the phloem accumulation of EB in young tissue of the flowering cabbage, so that it could control *P. xylostella* larvae through targeted delivery of EB. Therefore, the young tissues of the flowering cabbage could be effectively protected.

3.9 Distribution of FITC-cad-PGA *in vivo*

In order to explain the bioactivity synergistic mechanism of EB@PGA nanocarriers, FITC-cad-PGA fluorescent NPs were prepared (Fig. S2). Hence, the obtained FITC-cad-PGA NPs were fed to 3rd instar *P. xylostella* larvae. As shown in Fig. 8(b) and (e), the sample slices of the 3rd instar larvae after treatment for 4 and 8 h showed very low fluorescence intensity. Figure 8(b) shows a faint green light in the intestinal position of *P. xylostella* larvae, which illustrated that a part of the fluorescent NPs was attached to the intestines. According to the fluorescence intensity, there was low accumulation of NPs in the gut. Lengthening the feeding time to 8 h resulted in the spread of the fluorescence to the outside of the intestine, illustrating how the FITC-cad-PGA NPs could penetrate the intestine, whereas the accumulation of NPs was

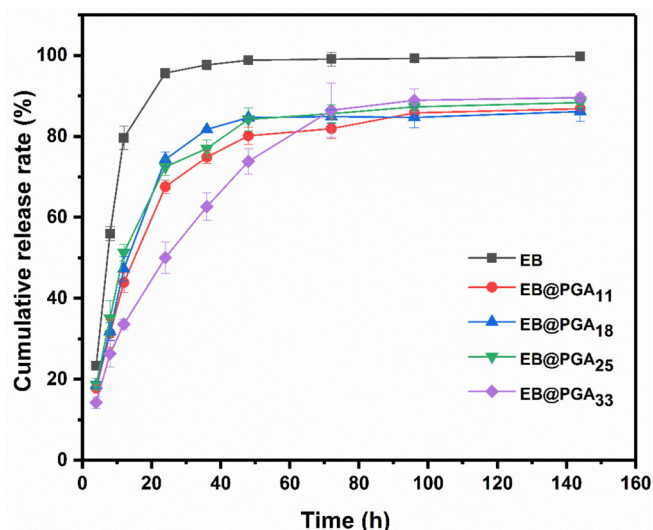
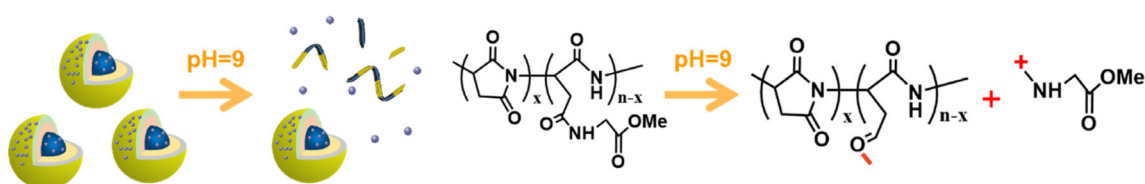


Figure 5. Sustained release of different functionalized EB@PGA at pH 9.



Scheme 2. Mechanism of sustained release for EB@PGA NPs.

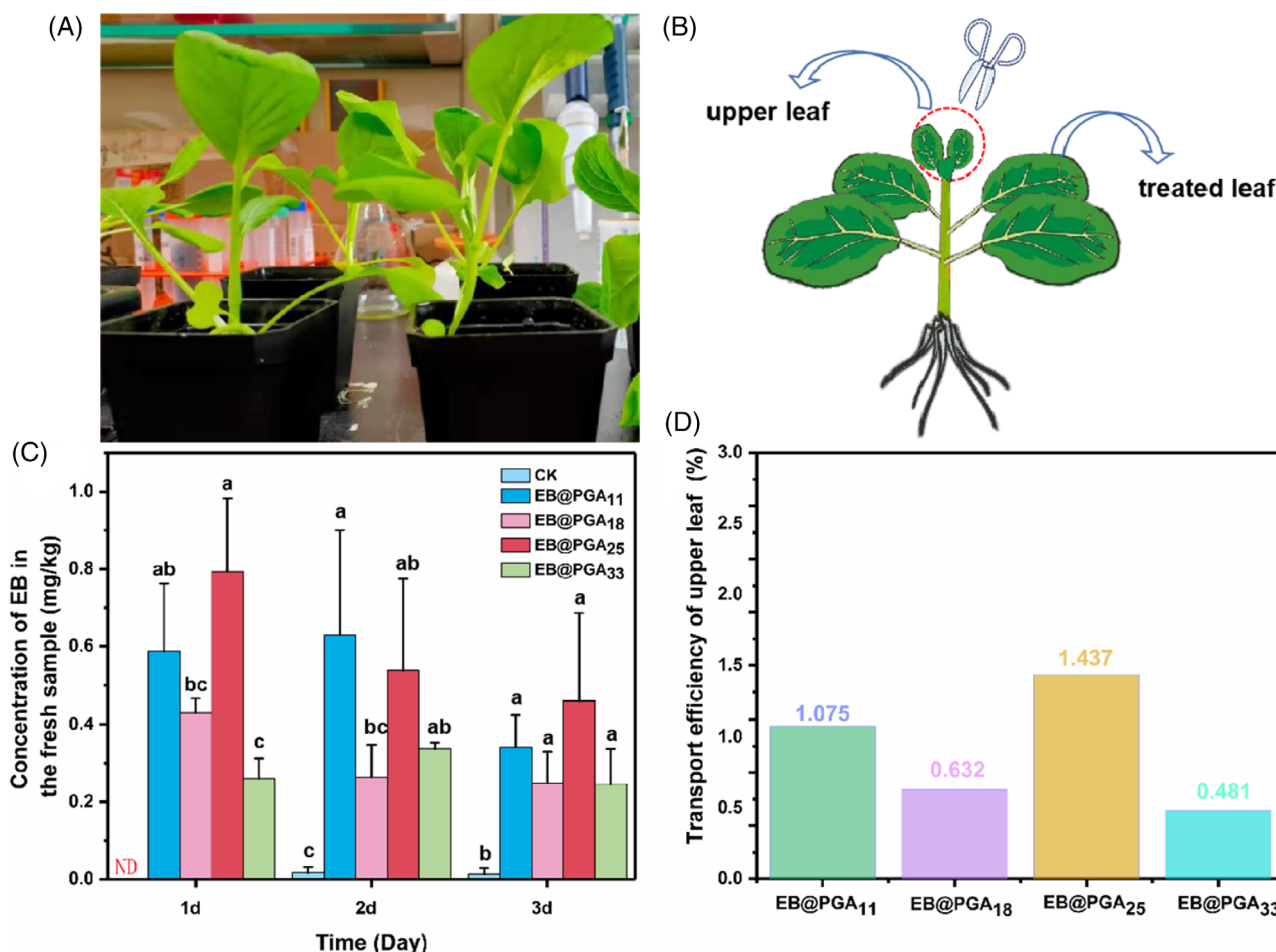


Figure 6. (a) Growing status of the flowering cabbage with EB@PGA NPs application after one day. (b) Schematic diagram of the treatment of the flowering cabbage. (c) The content of EB in upper leaves after treatment with different functionalized EB@PGA for one day. (d) Transport efficiency of EB after treatment with different functionalized EB@PGA for one day. ND, not detected.

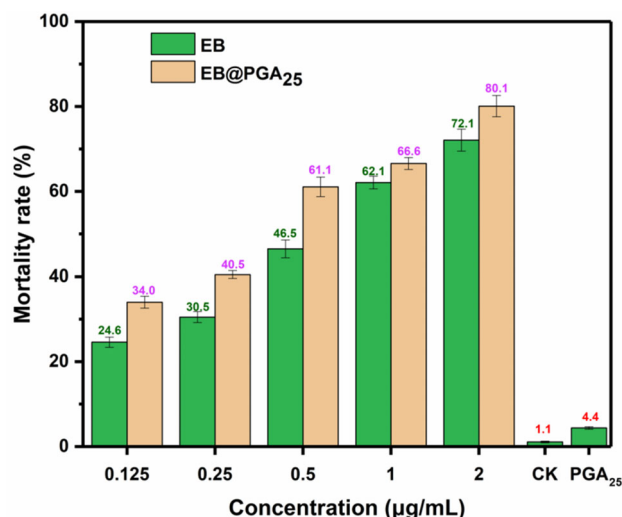


Figure 7. Insecticidal activities of EB@PGA₂₅ and EB against the 3rd instar larvae of *P. xylostella* after 24 h treatment.

minimal. After 24 h treatment, a large amount of fluorescence appeared in the gut cavity of *P. xylostella* larvae. The fluorescence intensity of larval slices after 24 h treatment met the requirements

of visualization. Thus, *P. xylostella* larvae fed for 24 h were selected for further research.

3.10 Synergistic mechanism of EB@PGA NPs

We further explored the synergistic mechanism of EB@PGA NPs from the perspective of the nanocarriers acting on intestinal cells. Rapid cell internalization of nanocarriers was an important prerequisite for *in vivo* application.³⁹ After 24 h treatment, the larvae were dissected and their intestines were removed for frozen sectioning. As shown in Fig. 9(b), the blue dotted lines indicated the peritrophic membrane of *P. xylostella* larvae intestine, the red dotted line represented the outer membrane of the larva intestine. It could be observed that the fluorescence of FITC-cad was concentrated mainly in the peritrophic membrane; only a small amount of fluorescence existed in the intestinal wall of the control group, indicating that the fluorescence molecules did not leave the peritrophic membrane after ingestion. Moreover, the fluorescence intensity was relatively weak. The large size of free fluorescent dyes was not absorbed easily by gut cells as a consequence of aggregation.³⁹ Combined with the conclusion of particle size in Fig. 3(c), EB appeared as a large micron-sized particle in water that could not penetrate the peritrophic membrane quickly to reach the target site. Excitingly, in Fig. 9(e), the intestinal wall indicated by the white arrow emitted bright green fluorescence, suggesting

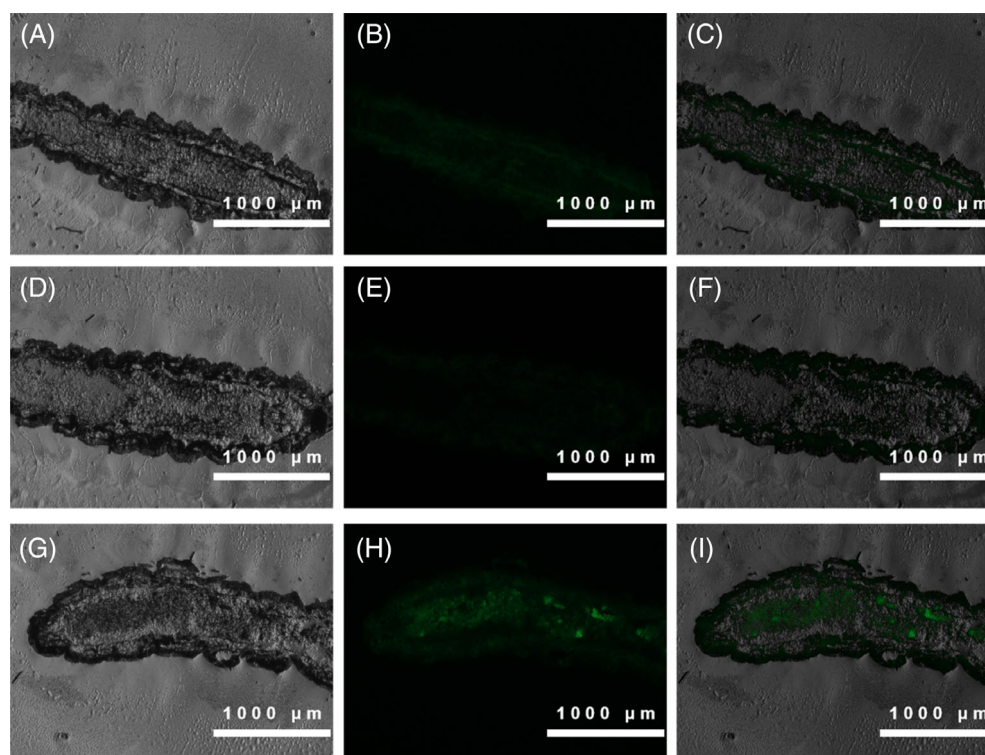


Figure 8. Fluorescence images showing FITC-cad-PGA distribution in *P. xylostella* larvae at 4 h (a, b, c), 8 h (d, e, f) and 24 h (g, h, i).

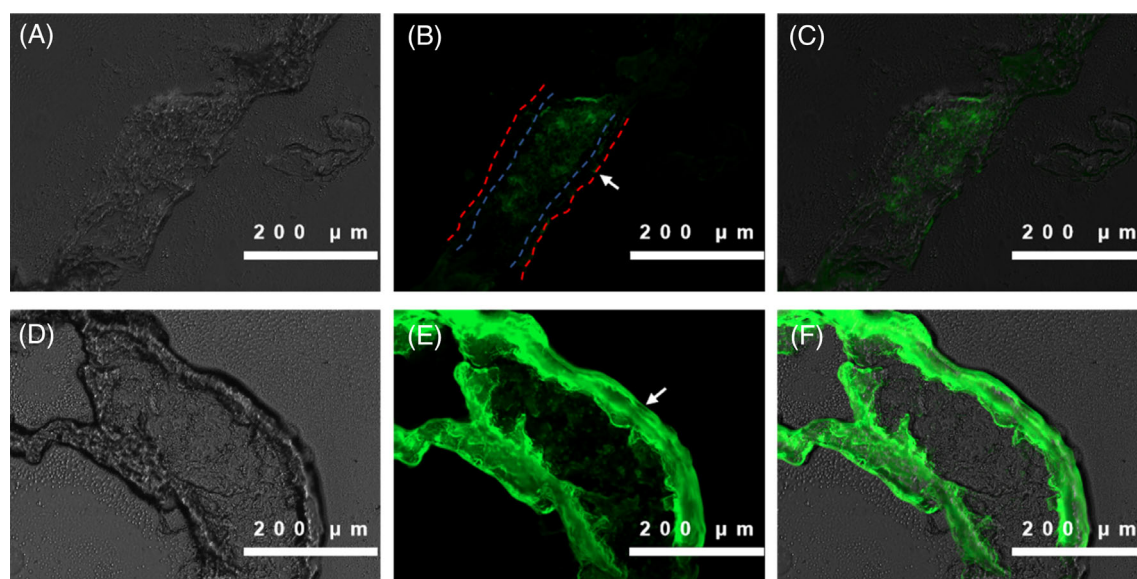


Figure 9. Fluorescence images of the dissected *P. xylostella* larvae intestine: (a,b,c) fed with FITC-cad diet as negative control and (d,e,f) larvae fed with FITC-cad-PGA.

that the great mass of FITC-cad-PGA NPs were internalized in the intestinal wall. Meanwhile, the negative charge on the surface of PGA nanocarriers could improve penetration and absorption of the NPs by the gut cells.

According to the above results, the synergistic mechanism of EB@PGA NPs is proposed as follows (Fig. 10). First, EB@PGA NPs

carries EB to the intestine of *P. xylostella* larvae. Secondly, PGA nanocarriers with surface charge prevent EB from aggregating and improve penetration of the peritrophic membrane. Thirdly, EB is released accurately in the intestinal wall, which caused a large number of drug reacting with the target cells. As a result, the insecticidal activity of EB increases significantly.

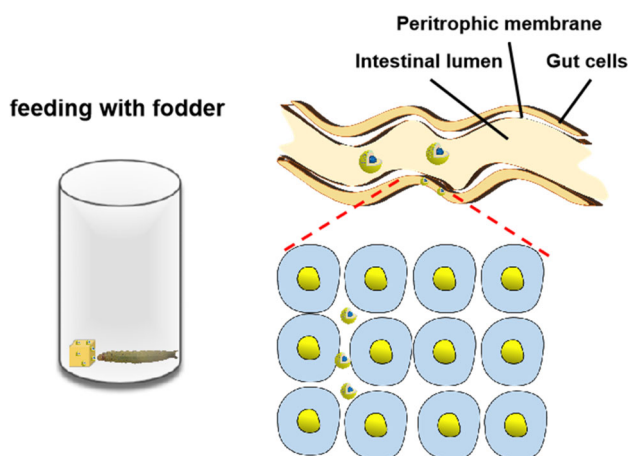


Figure 10. Schematic diagram of the behavioral pathway of EB@PGA NPs into *P. xylostella* larvae.

4 CONCLUSIONS

In brief, functionalized EB@PGA NPs for phloem transportation were successfully prepared in this study. The chemical structure results showed that EB could be bound to the surface of the PGA nanocarriers by electrostatic interaction, and also could be wrapped inside the PGA nanocarriers. The EB@PGA NPs could achieve controlled release in a weakly alkaline buffer solution (pH = 9), and achieved insecticidal effect within 24 h. In addition, different functionalized EB@PGA NPs showed phloem transport ability in the flowering cabbage, which obviously increased the accumulation of EB in young tissues. Biological activity tests showed that EB@PGA NPs were more likely to penetrate the intestinal wall of *P. xylostella* larvae and enhanced the insecticidal activity. This work demonstrates broad possibilities for a novel strategy by which nonsystemic insecticides can accumulate in young tissues in plants via the phloem, and improve the utilization efficiency of agrochemicals.

ACKNOWLEDGEMENTS

The authors are grateful for the financial support provided by the Guangdong Provincial Innovation Team for General Key Technologies in Modern Agricultural Industry (2019KJ140), and the National Key R&D Program of China (grant no. 2018YFD0200300).

SUPPORTING INFORMATION

Supporting information may be found in the online version of this article.

REFERENCE

- Isobel T, Doubling food production to feed the 9 billion: a critical perspective on a key discourse of food security in the UK. *J Rural Stud* **29**:81–90 (2013).
- Ishita A, Jens R and Atle M, Defence mechanisms of Brassicaceae: implications for plant-insect interactions and potential for integrated pest management. A review. *Agron Sustain* **30**:311–348 (2010).
- Furlong MJ, Wright DJ and Dossall LM, Diamondback moth ecology and management: problems, progress, and prospects. *Annu Rev Entomol* **58**:517–541 (2013).
- Ratnasinghe G and Hague N, The invasion, development and reproduction of *Steinernema carpocapsae* (Rhabditida: Steinernematidae) in the diamondback moth, *Plutella xylostella* (Lepidoptera: Yponomeutidae). *Nematropica* **28**:1–6 (1998).

- Lu JH, Liu SS and Shelton A, Laboratory evaluations of a wild crucifer *Barbarea vulgaris* as a management tool for the diamondback moth *Plutella xylostella* (Lepidoptera: Plutellidae). *Bull Entomol Res* **94**:509–516 (2004).
- Tariq SR, Rafique N, Kiran S and Khan AM, Photo-induced degradation of emamectin benzoate: effect of iron amendments and solvent system. *Environ Earth Sci* **72**:983–988 (2014).
- White SM, Dunbar DM, Brown R, Cartwright B, Cox D, Eckel C *et al.*, Emamectin benzoate: a novel avermectin derivative for control of lepidopterous pests in cotton. *Beltwide Cotton Conf*:171–177 (1997).
- Willis KJ and Ling N, The toxicity of emamectin benzoate, an aquaculture pesticide, to planktonic marine copepods. *Aquaculture* **221**:289–297 (2003).
- Zhu J, He Y, Gao M, Zhou W, Hu J, Shen J *et al.*, Photodegradation of emamectin benzoate and its influence on efficacy against the rice stem borer, *Chilo suppressalis*. *Crop Prot* **30**:1356–1362 (2011).
- Yoshii K, Kaihara A, Tsumura Y, Ishimitsu S and Tonogai Y, Liquid chromatographic determination of emamectin, milbemectin, ivermectin and abamectin in crops and confirmation by liquid chromatography-mass spectrometry. *J Chromatogr A* **896**:75–85 (2000).
- Cheng X, Liu X, Wang H, Ji X, Wang K, Wei M *et al.*, Effect of emamectin benzoate on root-knot nematodes and tomato yield. *PLoS One* **10**:e0141235 (2015).
- Sarfraz M, Keddie AB, Dossall LM, Biological control of the diamondback moth, *Plutella xylostella*: a review. *Biocontrol Sci Technol* **15**:763–789 (2007).
- Shah M, Ullah N and Choi MH, Amorphous amphiphilic P(3HV-co-4HB)-b-mPEG block copolymer synthesized from bacterial copolyester via melt transesterification:nanoparticle preparation, cisplatin-loading for cancer therapy and in vitro evaluation. *Eur J Pharm Biopharm* **80**:518–527 (2012).
- Mura S, Nicolas J and Couvreur P, Stimuli-responsive nanocarriers for drug delivery. *Nat Mater* **12**:991–1003 (2013).
- He Z, Su Y, Yang S, Wu L, Liu S, Ling C *et al.*, Hierarchical structure engineering of brookite TiO₂ crystals for enhanced photocatalytic and external antitumor property. *Sci Bull* **61**:1818–1825 (2016).
- Shang Q, Shi Y, Zhang Y, Zheng T and Shi H, Pesticide-conjugated polyacrylate nanoparticles: novel opportunities for improving the photostability of emamectin benzoate. *Polym Adv Technol* **24**:137–143 (2013).
- Kulkarni AR, Soppimath KS, Aminabhavi TM, Dave AM and Mehta MH, Glutaraldehyde crosslinked sodium alginate beads containing liquid pesticide for soil application. *J Control Release* **63**:97–105 (2000).
- Guo M, Zhang W, Ding G, Guo D, Zhu J, Wang B, Preparation and characterization of enzyme-responsive emamectin benzoate microcapsules based on a copolymer matrix of silica-epichlorohydrin-carboxymethylcellulose. *RSC Adv* **5**:93170–93179 (2015).
- Elabasy A, Shoaib A, Waqas M, Jiang MX and Shi ZH, Synthesis, characterization, and pesticidal activity of emamectin benzoate nanoformulations against *phenacoccus solenopsis tinsley* (Hemiptera: Pseudococcidae). *Molecules* **24**:2801–2010 (2019).
- Huang A, Li XH, Liang XT, Zhang YJ, Hu HY, Yin YZ *et al.*, Solid-phase synthesis of cellulose acetate butyrate as microsphere wall materials for sustained release of emamectin benzoate. *Polymers* **10**:1381–1390 (2018).
- Wang GD, Xiao YY, Xu HH, Hu PT, Liang WL, Xie LJ *et al.*, Development of multifunctional avermectin poly(succinimide) nanoparticles to improve bioactivity and transportation in rice. *J Agric Food Chem* **66**:11244–11253 (2018).
- Viktória T, Tamás G, Zoltán S, Béla N, Árpád N and Miklós Z, Novel amino acid-based polymers for pharmaceutical applications. *Polym Bull* **59**:311–318 (2007).
- Hsu FC, Kleier DA and Melander WR, Phloem mobility of xenobiotics. *Plant Physiol* **86**:1265–1271 (1988).
- Szabolcs LK, Mónika V, Ágnes SH and Ákos M, Translocation and degradation of tebuconazole and prothioconazole in wheat following fungicide treatment at flowering. *Pest Manag Sci* **69**:1216–1224 (2013).
- Chitsiga T, Daramola MO, Wagner N and Ngoy J, Effect of the presence of water-soluble amines on the carbon dioxide (CO₂) adsorption capacity of amine-grafted poly-succinimide (PSI) adsorbent during CO₂ capture. *Energy Procedia* **86**:90–105 (2016).
- Gong C, Shan M, Li BQ and Wu GL, A pH and redox dual stimuli-responsive poly(amino acid) derivative for controlled drug release. *Colloid Surf B* **146**:396–405 (2016).

- 27 Yang Z, Yu M, Liu Y, Chen X and Zhao Y, Synthesis and performance of an environmentally friendly polycarboxylate superplasticizer based on modified poly (aspartic acid). *Construct Build Mater* **202**:154–161 (2019).
- 28 Yeh JC, Yang HH, Hsu YT, Su CM, Lee TH and Lou SL, Synthesis and characteristics of biodegradable and temperature responsive polymeric micelles based on poly(aspartic acid)-g-poly(N-isopropylacrylamide-co-N, N- dimethylacrylamide). *Colloid Surf A* **421**:1–8 (2013).
- 29 Migahed MA, Rashwan SM, Kamel MM and Habib RE, Synthesis, characterization of polyaspartic acid-glycine adduct and evaluation of their performance as scale and corrosion inhibitor in desalination water plants. *J Mol Liq* **224**:849–858 (2016).
- 30 Nita T and Chiriac AP, TGA/FTIR/MS study on thermal decomposition of poly(succinimide) and sodium poly(aspartate). *Polym Test* **30**:397–407 (2011).
- 31 Shen Y, Wang Y, Zhao X, Sun CJ, Cui B, Gao F *et al.*, Preparation and physicochemical characteristics of thermo-responsive emamectin benzoate microcapsules. *Polymers* **9**:418–429 (2017).
- 32 Dong XM, Revol JF and Gray DG, Effect of microcrystallite preparation conditions on the formation of colloid crystals of cellulose. *Cellul* **5**:19–32 (1998).
- 33 Hong NL, Li Y and Qiu XQ, A highly efficient dispersant from black liquor for carbendazim suspension concentrate: preparation, self-assembly behavior and investigation of dispersion mechanism. *J Appl Polym Sci* **133**:43067–43068 (2016).
- 34 Li J, Liu Y, Shi J, Wang Z, The investigation of thermal decomposition pathways of phenylalanine and tyrosine by TG-FTIR-science direct. *Thermochim Acta* **467**:20–29 (2008).
- 35 Marcilla AG and Menargues S, TGA/FTIR study of the catalytic pyrolysis of ethylene–vinyl acetate copolymers in the presence of MCM-41. *Polym Degrad Stabil* **89**:145–152 (2005).
- 36 Wakisaka S, Tsukuda R and Nakasuji F, Life tables of the diamondback moth, *Plutella xylostella* (L.) (Lepidoptera: Yponomeutidae) and effects of rainfall, temperature and host plants on survival and reproduction. *Jpn J Appl Entomol Z* **35**:115–122 (1991).
- 37 Tan J, Karthivashan G and Arulselvan P, Characterization and in vitro studies of the anticancer effect of oxidized carbon nanotubes functionalized with betulonic acid. *Drug Des Dev Ther* **8**:2333–2343 (2014).
- 38 Luo J, Huang X, Jing T, Zhang D, Li B and Liu F, Analysis of particle size regulating the insecticidal efficacy of phoxim polyurethane microcapsules on leaves. *ACS Sustain Chem Eng* **6**:17194–17203 (2018).
- 39 Yao Q, Zheng Y, Cheng W and Shen J, Difunctional fluorescent HSA modified CoFe₂O₄ magnetic nanoparticles for cell imaging. *J Mater Chem B* **4**:6344–6349 (2016).

PAPER



Cite this: *New J. Chem.*, 2021, 45, 2649

Graphene oxide as a pesticide carrier for enhancing fungicide activity against *Magnaporthe oryzae*†

Pengtong Hu,^{ab} Li Zhu,^{ac} Feng Zheng,^{ab} Jingyun Lai,^a Hanhong Xu^{id} *^{bc} and Jinliang Jia^{id} *^{abc}

The fungus *Magnaporthe oryzae* causes disastrous consequences for rice growth. Carbendazim (CBZ) has been extensively used for disease management. However, because of the heavy use of traditional CBZ, a majority of CBZ is wasted, resulting in an extremely low utilization rate and severe pollution problems. In this work, carbendazim–graphene oxide (CBZ–GO) and carbendazim–ultrasonic graphene oxide (CBZ–UGO) were synthesized for use against rice blast. The EC₅₀ of CBZ–GO and CBZ–UGO on the mycelium of *Magnaporthe oryzae* was 0.28 and 0.41 µg mL^{−1}, which showed 2.29- and 1.56-fold higher antifungal activity than the EC₅₀ (0.64 µg mL^{−1}) of CBZ, respectively. GO can destroy mycelia and compromise cell integrity as confirmed from the SEM images of mycelia. Nanocomposites can damage glutathione on the cell membrane through an electron transfer to weaken the fungus cell activity. Moreover, the application of nanocomposites on rice seedlings significantly reduced the severity of rice blast compared to other processing groups in a greenhouse experiment. Therefore, GO as a high-efficiency carrier would offer an important opportunity for managing fungal diseases.

Received 25th September 2020,
Accepted 16th December 2020

DOI: 10.1039/d0nj04721j

rsc.li/njc

1. Introduction

As the staple diet of human beings, rice plays an irreplaceable role in human life.¹ While rice blast is the most devastating plant disease affecting rice growth^{2–4} and has been accepted as the most prominent fungus among the top 10 fungal plant pathogen based on scientific/economic importance,⁵ which poses a serious threat to global food security. Due to the ravages of rice blast, annual rice production is reduced by 30%, which can be enough to feed 60 million people.⁶ Rice blast control that is consistent with the strategy of sustainable development is urgently required. Currently, in the field, chemical agents are the primary prevention and control measure for rice blast. However, only 0.1% of agents can actually act on the site of the action, and a majority of the agent will flow into the soil and waters through runoffs, leaching, and volatilization, causing

serious environmental pollution.^{7–9} Carbendazim (CBZ), a type of broad-spectrum benzimidazole fungicide, is extensively used to protect crops from various diseases, for instance, rice blast.^{10–12} Unfortunately, as a result of the abuse of CBZ, it is seriously over-standard on certain crops, causing severe environmental pollution. In addition, when it is applied in the environment, CBZ may induce health hazards due to its long metabolic period and toxicity.¹³ Therefore, it is imperative to improve the effective utilization rate of CBZ and reduce the amount of pesticide.

Graphene is a 2D nanomaterial composed of a single-atom-thick layer of carbon atoms, which has attracted extensive attention in all types of fields over the past decade due to its extraordinary physicochemical properties.^{14,15} However, because of the huge van der Waals forces between layers, graphene is more inclined to aggregation and does not readily dissolve in common solvents, resulting in limited applications.¹⁶ In contrast, graphene oxide (GO), a derivative of graphene, exhibits excellent hydrophilic and colloid stability as a result of a great deal of oxygen-containing functional groups on its edges and defective sites.¹⁷ Moreover, GO nanosheets show enormous advantages on high drug loading and excellent biological activity due to π – π stacking, hydrophobic interaction and 2D structure, compared to starch-based hydrogels carriers¹⁸ and also polymeric and solid lipid nanoparticles,¹⁹ which have been widely studied in biomedicine and chemistry.^{20,21} For example, graphene oxide, with its distinguished

^a Key Laboratory for Biobased Materials and Energy of Ministry of Education, College of Materials and Energy, South China Agricultural University, Guangzhou, Guangdong 510642, China. E-mail: jiajinliang@scau.edu.cn

^b Key Laboratory of Natural Pesticide & Chemical Biology, Ministry of Education, South China Agricultural University, Guangzhou, 510642, China. E-mail: hhxu@scau.edu.cn

^c Guangdong Laboratory for Lingnan Modern Agricultural Science and Technology, Guangzhou, Guangdong 510642, China

† Electronic supplementary information (ESI) available. See DOI: 10.1039/d0nj04721j

performance, has been a new nanotherapeutic drug delivery platform to carry small drug molecules, antibodies, DNA and genes.²² Zhu *et al.* reported that GO can promote seed germination by retaining moisture in the soil and extending the vase life of flowers.¹⁶ Wang *et al.* demonstrated that the combination of GO and insecticides may contribute to stronger insecticidal effects against lepidopteran insect.²³ The application of GO in agriculture has become more and more extensive. While very little is known on the use of GO for the control of fungus. Therefore, GO as pesticide carriers for enhancing the fungicide activity is a new exploration for the application of GO in the field of agriculture.

Here, we attempted to select two different types of GO to load CBZ, forming CBZ-GO and CBZ-UGO (GO was subjected to sonication for 6 h) nanocomposites. In the present study, (1) the CBZ loading of the two types of nanocomposites was investigated, and the release mechanism was studied *in vitro*; (2) the antifungal activity and synergistic mechanism of the two nanocomposites against *Magnaporthe oryzae* were investigated *in vivo* and *in vitro*. To our knowledge, we are the first to investigate the activity of GO and fungicides against *Magnaporthe oryzae*, and the experimental results will form the basis of further research about the synergistic mechanism of GO as a nano-carrier for tackling rice fungi.

2. Experimental

2.1. Materials

Graphene oxide (GO) was obtained from Chengdu Organic Chemicals Co., Ltd (China). CBZ at a purity of 98% (the original fungicide) was obtained from Jiangsu Ruibang Pesticide Factory Co., Ltd (China). *N,N*-Dimethylformamide (DMF) and 5,5'-dithiobis-(2-nitrobenzoic acid) (DTNB) at a purity of 98% was provided by Hanghai Acme Biochemical Co., Ltd (China). Dimethyl sulfoxide (DMSO) was purchased from Shanghai Titan Scientific Co., Ltd (China). Methanol (HPLC grade) was obtained by Guangdong Guanghua Chemical Factory Co., Ltd (China). L-Glutathione reduced of 97% purity was supplied by Alfa Aesar Chemicals Co., Ltd (China). Tris(hydroxymethyl)aminomethane was obtained from Sinopharm Chemical Reagent Co., Ltd (China).

2.2. Characterization

X-Ray diffraction analysis of graphene oxide, ultrasonic graphene oxide was carried out using a Rigaku D/Max-III diffractometer. UV-vis spectra were obtained *via* a UV-vis spectrophotometer (UV 2550, Shimadzu Co., Japan). The structure of the nanocomposite was characterized by a Fourier transform infrared spectrometer (FTIR) (Vertex 70, Bruker Co., Germany). The morphology of CBZ-GO and CBZ-UGO was inspected by using a scanning electron microscope (SEM) (Nova Nano 450, FEI Co., USA). The hydrodynamic diameter and zeta potential of nanocomposites in solution were measured by Dynamic Light Scattering (Zetasizer Nano ZSE, Malvern Panalytical Ltd, UK). Thermogravimetric (TG) analysis was performed on a TG209F1 instrument. Typically, 6.5 mg of the sample was heated from 100 to 900 °C at a heating rate of 10 °C min⁻¹ under a constant nitrogen flow rate

(20 mL min⁻¹). X-Ray photoelectron spectroscopy (XPS) was conducted on a Thermo Scientific™ K-Alpha™ spectrometer equipped with a monochromatic Al K α X-ray source (1486.6 eV) operating at 100 W. Samples were analyzed under vacuum ($P < 10^{-8}$ mbar) with a pass energy of 150 eV (survey scans) or 25 eV (high-resolution scans). The experimental peaks were fitted with XPSPEAK.

2.3. Preparation of CBZ-GO and CBZ-UGO

CBZ was loaded on the surface of GO by adsorption and π - π interactions. Briefly, 8 mL of CBZ DMF solution (2.5 mg mL⁻¹) was added dropwise to the 40 mL of GO aqueous solution (0.5 mg mL⁻¹) under vigorously stirring at room temperature for 48 h. The resulting mixture was then separated by centrifugation at 10 000 rpm for 10 min and further washed in the reaction solution (DMF:H₂O = 1:5) thrice to remove residual CBZ, followed by freeze-drying overnight. In addition, in the interest of the synthesis of the CBZ-UGO, GO was subjected to 6 h sonication and the above procedure was repeated.

2.4. Determination of the CBZ-loading capacity of GO and UGO

Note that 5 mg of CBZ-GO or CBZ-UGO was dissolved in 3 mL of methanol and transferred into an ultrasonic bath for 2 h to thoroughly disassociate the CBZ. The resulting suspension was centrifuged (10 000 rpm, 10 min), and the supernatant was filtered and analyzed using the Agilent Technologies 1100 HPLC system equipped with an ultraviolet detector and an Agilent C18 column (4.6 \times 250 mm, 5 μ m, Agilent Technologies) with methanol-water (50:50, v/v) as the mobile phase. The flow rate was 0.8 mL min⁻¹, and 10 μ L of the sample was injected into HPLC with a detector wavelength of 286 nm. The CBZ loading capacity (LC) was calculated using the following equation:

$$LC = \frac{\text{weight of CBZ loaded}}{\text{weight of CBZ - GO or CBZ - UGO}} \times 100\%$$

2.5. Antifungal activity

To explore the antifungal activities of CBZ-GO, CBZ-UGO and CBZ, growth inhibition of the rice blast fungus was carried out as described previously.²⁴ Mycelial discs (5 mm in diameter) covered by the rice blast fungus, which were grown on potato dextrose agar (PDA) plates, were aseptically cut from the margins of colonies and placed on the center of the PDA plates containing different concentrations of CBZ, CBZ-GO and CBZ-UGO (0–10 μ g mL⁻¹). All plates were incubated at 28 °C for nine days, at which point the average fungal colony diameters were determined by the cross method. The inhibition effect of mycelia (I , %) was calculated using the formula below:

$$I (\%) = \frac{d_c - d_t}{d_c} \times 100$$

where d_c is the diameter of the fungal colony in control and d_t is the diameter of the fungal colony in the treatment sample.

After the above antifungal assay was completed, the antifungal activity of GO, CBZ/GO, CBZ/UGO (the physical blending

of CBZ and GO or UGO) was performed. The CBZ/GO and CBZ/UGO solutions were prepared based on their EC₅₀ values and then the above operation was repeated.

2.6. Oxidative stress measurements

The oxidative stress experiment was performed according to previous methods from literature with a bit of modification.^{25,26} To investigate the possibility of superoxide radical anion (O₂^{•-}) generation by GO and UGO, the absorption of 2,3-bis(2-methoxy-4-nitro-5-sulphophenyl)-2*H*-tetrazolium-5-carboxanilide (XTT) was measured by UV-vis spectroscopy. Note that 4 mL of GO or UGO dispersion in PBS (pH 7.4) was mixed with 4 mL of the XTT solution (0.4 mM), and the XTT solution was used as the control sample. The mixture was placed in the dark for 2, 4, 6 h, and GO or UGO was removed using a 0.22 μm syringe filter. The filtrate was analyzed using the UV-vis spectrometer at 470 nm, and XTT could be reduced to water-soluble XTT-formazan.

GSH oxidation was performed according to Ellman's assay to analyze the ROS-independent oxidative stress pathway. Note that 5 mL of 0.8 mM GSH in 50 mM bicarbonate buffer (pH 8.6) was mixed with 5 mL of 100 μg mL⁻¹ GO or UGO dispersion in 50 mM bicarbonate buffer, and the mixture was incubated in dark for 2, 6, 10, and 14 h. Simultaneously, the mixture of H₂O₂ and GSH solutions was used as a positive control; GSH solution without nanosheets, however, was used as a negative control. After the reaction, 900 μL solution is filtered using 0.22 μm syringe filter was mixed with 157 mL of Tris-HCl and 40 μL of 10 mM DTNB, and the mixture solution was analyzed by UV-vis at 412 nm. The loss of GSH (*I*, %) was calculated using the following equation:

$$I(\%) = \frac{OD_y - OD_s}{OD_y} \times 100$$

where OD_y is the absorbance of the negative and OD_s is the absorbance of the sample.

2.7. Structural and morphological changes

To observe the morphology and structure of *Magnaporthe oryzae*, after exposure to GO (40 μg mL⁻¹), *Magnaporthe oryzae* was incubated at 28 °C on the PDA plates in a digital biochemical incubator. After 8 days, the collected *Magnaporthe oryzae* was fixed overnight with 2.5% glutaraldehyde.²⁷ The fixed samples were examined under a scanning electron microscope (SEM, SU-8010, Hitachi, Japan).

2.8. In vitro release experiment

To measure the release behavior of CBZ from CBZ-GO and CBZ-UGO, a dialysis method was designed as follows: 5 mg of CBZ-GO and CBZ-UGO were added to 3 mL of DMF-H₂O medium (40:60, v/v), and then the suspension was moved into the dialysis bags (DWCO = 3500 Da), which was submerged into 100 mL of release medium in 200 mL reagent bottles. The release system was placed onto a magnetic stirrer at a stirring speed of 300 rpm at room temperature. Periodically, 1 mL of the release medium was taken, followed by the addition of the same volume of fresh medium to maintain the total volume.

The cumulative release amount of CBZ was analyzed using HPLC.

2.9. Adhesion performance assay

The adhesion performance of nanocomposites was investigated according to earlier reports with minor changes.⁷ All the experimental rice uniformly grew in the field. First, the rice seedlings were laid down on the experiment table, then the CBZ-GO or CBZ-UGO nanocomposite that had 200 μg of CBZ was added evenly on the rice leaves and maintained for 1 h until the liquid naturally dried. After that, 7 mL of distilled water was evenly sprayed on the treated rice to simulate the rainwater scour. Then, the sprayed rice seedlings were cut into pieces that were placed into a mortar and ground with liquid nitrogen. To measure the remaining CBZ that have resisted the given drift, the above-treated samples were extracted with 25 mL of acetonitrile by sonication, and the mixture was centrifuged at 5000 rpm for 5 min. In addition, the supernatant liquid was condensed by a vacuum rotary evaporator, followed by analysis on HPLC. A similar process was repeated for the CBZ suspending agent at the same concentration. All treatments were performed with three replicates.

2.10. Greenhouse experiment

To evaluate the control effect of nanocomposites on the rice blast in rice, an *in vivo* study was performed on rice seedling. Blast-susceptible seedlings of rice (CO39) were grown in a greenhouse. After 30 days, the equal volume of CBZ-GO and CBZ-UGO with 0.5% Silwet-77, which contained a uniform drug concentration of 0.64 μg mL⁻¹ were sprayed onto seedlings.^{28,29} Plants treated with 0.64 μg mL⁻¹ of CBZ and sterile water with 0.5% Silwet-77 were maintained as controls. Each treatment was repeated four times. Three hours after treatment, the seedlings were infected by spraying, and then the disease severity was observed after 5 days.

3. Results and discussion

3.1. Characterization of CBZ-GO and CBZ-UGO

The UV-vis spectra of GO and UGO are shown in Fig. 1a. The maximum optical absorption peak at ~230 nm was observed, which was caused by the π-electron plasmon excitation of carbon.¹⁵ In addition, the special peak of GO, a shoulder peak at 300 nm, was observed representing n → π* electronic transition of C=O bonds.³⁰ The absorbance spectra between GO and UGO were similar, which indicated that the ultrasonic processing for GO did not influence its optical absorption. Further characterization of different graphene oxide was performed using X-ray diffraction wherein a sharp diffraction peak at 2θ = 26.5° (002), corresponding to an interplanar spacing of crude graphite³¹ was observed. When graphite was oxidized, the (002) peak disappeared and a typical diffraction peak at 9.7° (001), in agreement with graphene oxide was observed. These results revealed that both graphene oxides were highly crystalline, and there was no influence on their crystalline nature. To

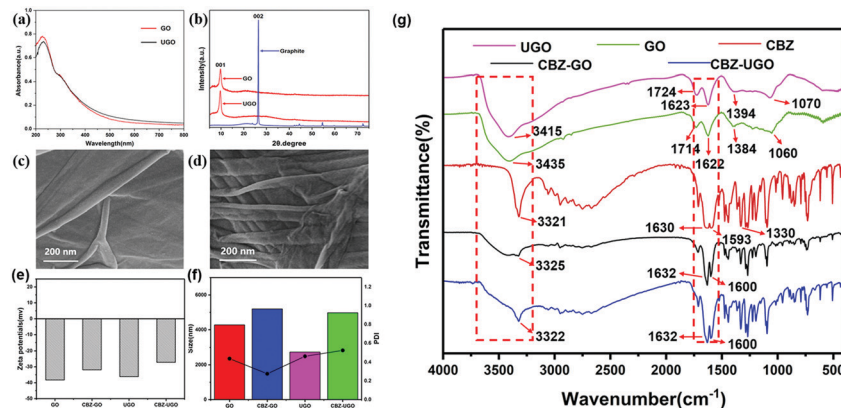


Fig. 1 (a) UV-vis of GO; (b) XRD pattern of graphite, GO, UGO; (c and d) SEM images of GO and UGO. (e) Hydrodynamic size of GO, CBZ-GO, UGO, CBZ-UGO; (f) zeta potential of GO, CBZ-GO, UGO, CBZ-UGO. (g) FTIR spectra of UGO, GO, CBZ, CBZ-GO, CBZ-UGO.

further visualize the morphology of the UGO and GO, an SEM study was undertaken and the results are shown in Fig. 1c. Compared with the smooth surface of GO, the UGO possessed more wrinkles on its surface and more curly shapes on the edges.

Nanocomposites were studied using FTIR and hydrodynamic size change and Zeta potential measurements. FTIR spectra of nanocomposites are depicted in Fig. 1g. A strong and broad absorption band between 3200 and 3600 cm^{-1} was seen, which was assigned to -OH in the GO. Moreover, the characteristic peaks at 1714, 1622, 1384 and 1060 cm^{-1} represented C=O stretching vibration, C=C stretching vibration, the vibration of -OH and C-O-C functional groups, respectively, which are consistent with those on graphene oxide.³² There were similar characteristic peaks in the FTIR spectra of UGO, indicating that the oxygen-containing functional groups on the surface of GO were not destroyed after the ultrasonication treatment. The spectra of CBZ-GO and CBZ-UGO were similar. However, there was some distinction compared with the spectra of CBZ, the broad absorption band between 3200 and 3600 cm^{-1} was attributed to the -N-H stretching vibration of CBZ, which overlapped with the vibrations of the -OH groups of graphene oxide.³³ The peak at 1630 and 1593 cm^{-1} in the spectra of CBZ represented C=C stretching vibration of the aromatic ring and those at 1330 cm^{-1} (C-N) were also observed. Especially, the peak of the C=C stretching mode in CBZ-GO and CBZ-UGO appeared at 1632 and 1600 cm^{-1} , respectively, which could have been caused by C=C of GO. These results confirmed that CBZ had been successfully loaded onto the graphene oxide sheet.

3.2. Size distribution analysis of GO sheets

The hydrodynamic size of nanocomposites was measured using dynamic light scattering. The hydrodynamic sizes of GO and UGO were 4331 and 2551 nm, respectively, which indicated that the size of GO subjected to 6 h sonication became smaller. The sizes of CBZ-GO and CBZ-UGO increased to 4660 and 5838 nm, respectively, which may have been caused by the presence of an organic layer on graphene oxide.⁷ The surface charge of the nanocomposites is given in Fig. 1e. The GO and UGO

nanosheets showed a negative charge (-38.3 and -36.2 mV, respectively), indicating that the nanocomposites were relatively stable in the aqueous medium.³⁴ Alternatively, the CBZ-GO and CBZ-UGO held less negative charge (-31.9 and -27.2 mV, respectively), probably due to the electrostatic interactions of GO and CBZ. Moreover, the loading of CBZ was detected using HPLC and the drug loading capacity of CBZ-GO and CBZ-UGO was 43.57% and 53.75%, respectively (Fig. S2, ESI†). It is worth noting that antibiotics rich in the aromatic rings and multiple functional groups may be easily interacting with GO by π - π stacking, H-bonding, van der Waals forces, and electrostatic interactions.²⁰ The corresponding CBZ, which comprises the benzene ring, amidogen, and ester groups can be easily absorbed on GO. This performance further indicated that UGO had higher loading for the drug due to more wrinkles.

3.3. TG analysis of nanocomposites

To research thermodynamic properties of nanocomposites, the TG and DTG analysis of GO, CBZ, CBZ-GO and CBZ-UGO were performed. As seen in Fig. 2a, there was a significant weight loss of 29.53% at 209 $^{\circ}\text{C}$, presumably due to the decomposition of oxygen-containing groups in GO.³⁵ In addition, the TG curve of UGO showed a significant weight loss of 26.14% at 218.6 $^{\circ}\text{C}$ in Fig. S3 (ESI†), which indicated that ultrasonic processing did not influence the thermodynamic properties of GO. For the TG curve of CBZ, the initial weight loss occurred around 186 $^{\circ}\text{C}$, and the temperature of the complete oxidative decomposition was 548.5 $^{\circ}\text{C}$. Interestingly, the thermogravimetric profiles shown in Fig. 2c and d showed lower starting decomposition temperatures around 115.3 $^{\circ}\text{C}$ and 109.3 $^{\circ}\text{C}$ for nanocomposites than those of pure CBZ, which can be assigned to the thermal degradation and decomposition of GO.³⁶ However, the complete weight loss was observed for nanocomposites at 605.4 $^{\circ}\text{C}$ and 514.6 $^{\circ}\text{C}$, respectively, presumably due to the higher drug loading of CBZ-UGO. In addition, the residue of nanocomposites was decreased from 40.99% for CBZ-GO to 36.41% for CBZ-UGO. Compared with the TG profile of CBZ, nanocomposites had lower starting decomposition temperature and more residue.

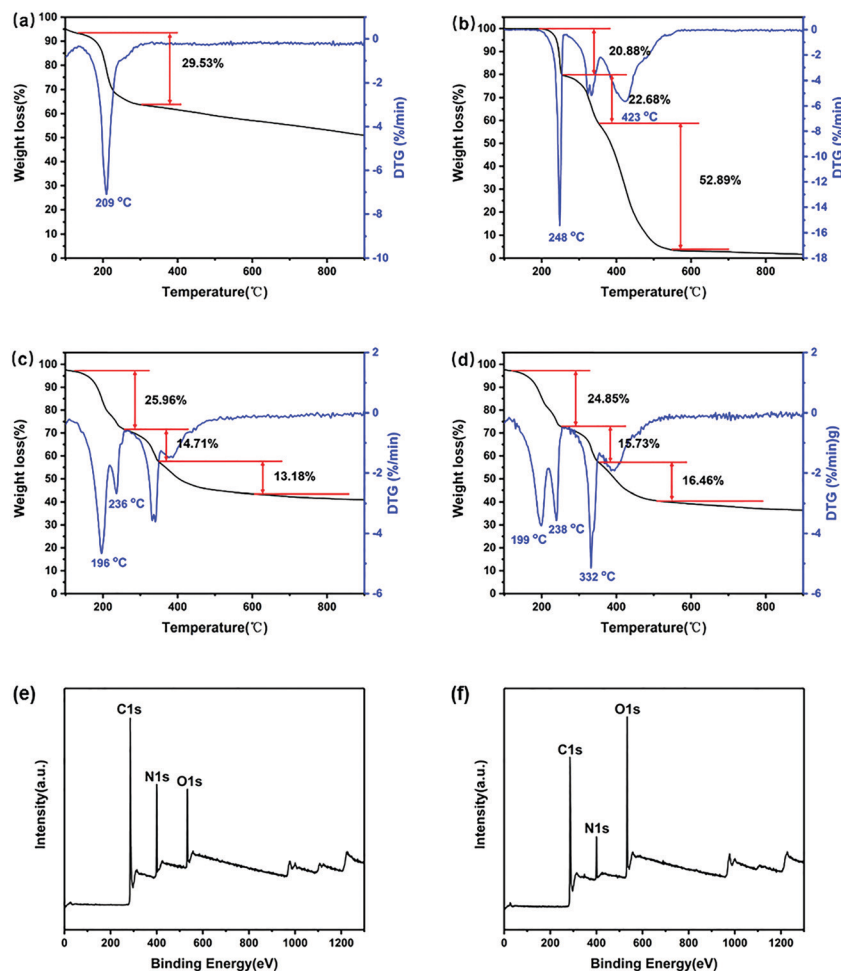


Fig. 2 TGA profiles and DTG analysis of (a) GO, (b) CBZ, (c) CBZ-GO, (d) CBZ-UGO. XPS survey scan of (e) CBZ and (f) CBZ-GO.

3.4. XPS spectroscopy

XPS analysis was performed to identify the chemical states of CBZ and CBZ-GO nanocomposite. We can verify the nature of bonding between elements by analysis of binding energy (BE) values. As shown in Fig. 2e and f, the survey spectra clearly indicated the existence of C, N, O in CBZ and CBZ-GO nanocomposite. Table 1 showed the atomic percentages of carbon, nitrogen and oxygen in CBZ and CBZ-GO. There was 10.84% of N in the CBZ-GO, which was mainly attributed to N on CBZ. By calculation, the CBZ-GO drug content was approximately 40% that was in agreement with the HPLC results of the nanocomposite. In addition, in the CBZ-GO, the atomic percentage of nitrogen was higher than that in CBZ, which proved that GO contained a large number of oxygen-containing functional groups.

Table 1 Atomic concentration of C, N, and O of CBZ and CBZ-GO was analyzed by XPS survey scan

Sample	C 1s (%)	N 1s (%)	O 1s (%)
CBZ	52.53	29.34	18.13
CBZ-GO	67.29	10.84	21.87

The C 1s and N 1s core-level spectra of CBZ-GO are shown in Fig. 3d and e. The C 1s core level XPS spectrum can be deconvoluted into four components with binding energies at 284.8 eV (C=C/C-C in aromatic ring), 285.7 eV (C-N), 287.4 eV (C-O-C), 289 eV (HO-C=O).^{37,38} As shown in Fig. 3e, XPS spectra clearly showed the elemental status of N (1s). The binding energies of N 1s peaks were 398.7 eV (C-N=C) and 400.4 eV (C-N-H), respectively, which was in agreement with the BE values of CBZ in Fig. 3b. In addition, according to the anastomotic BE values of N 1s in CBZ and CBZ-GO, it indicated that the combination of CBZ molecules and GO nanosheets was physically bound rather than covalent bonding.

3.5. Release property and adhesion-performance investigation

The release profiles of CBZ from CBZ-GO and CBZ-UGO were investigated by using HPLC and dialysis methods. The corresponding results are shown in Fig. 4a. Compared with the values of CBZ-GO, the CBZ-UGO presented more excellent slow-release behavior, which could arise from the presence of more wrinkles and curly shapes on the CBZ-UGO. Again, their release corresponded to biphasic behavior, including an initial sharp release

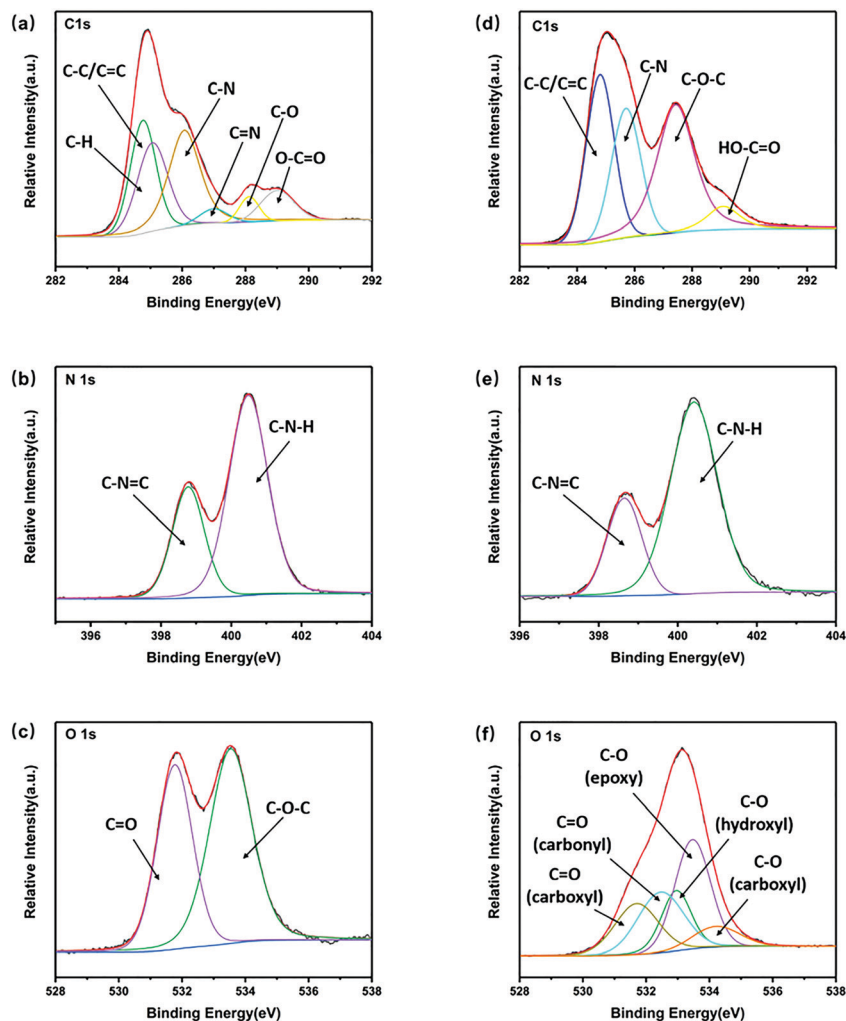


Fig. 3 XPS spectra of CBZ and CBZ-GO (a) C 1s, (b) N 1s, (c) O 1s spectra of CBZ, and (d) C 1s, (e) N 1s, (f) O 1s spectra of CBZ-GO.

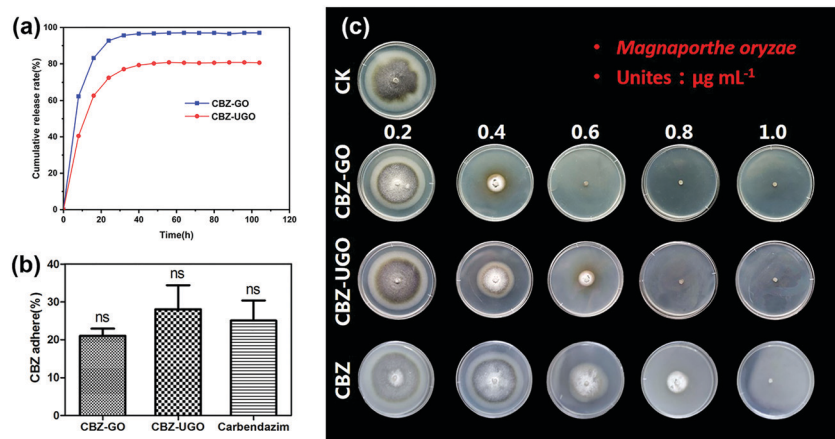


Fig. 4 Release profiles and adhesion performance of nanocomposites: (a) release profiles of CBZ-GO (blue line), CBZ-UGO (red line); (b) percent CBZ adhered to rice leaves, sprayed in the form of CBZ-GO, CBZ-UGO and CBZ suspension agent. A significant statistical analysis was performed through one-way ANOVA with *post hoc* Duncan's multiple range test compared with CBZ suspension agent. Error bars represent the standard error of the mean. (c) Mycelial growth of *Magnaporthe oryzae* on PDA media containing different concentrations of CBZ.

for 16 h, followed by a slow-release, which lasted more than 100 h.^{39–41} Eventually, 97.1% of CBZ was released from the CBZ-GO nanocomposite after 104 h; while for the CBZ-UGO, the final accumulative release rate was 77.8%. In addition, the

results of the release investigation indicated that it was in accordance with the first-order model due to the highest R^2 value^{42,43} (Fig. S1 and Table S1 of the ESI†). To investigate the adhesion performance of nanocomposites, a simulated rain wash assay was designed. There was no significant difference between nanocomposites and CBZ suspension agent from the market on the adhesion-performance investigation, which was analyzed by the Duncan method as shown in Fig. 4b. These results indicated that the nanocomposites had similar adhesion performance on the rice leaves with CBZ suspension agent. Note that compared to the CBZ suspension agent containing a large amount of surfactant, the aqueous dosage form of nanocomposites was more environmentally friendly.

3.6. *In vitro* antifungal test

As shown in Fig. 4c, nanocomposites can significantly inhibit the mycelial growth of rice blast, compared with the inhibition effect of the CBZ alone. It can be seen that the concentrations of CBZ-GO and CBZ-UGO thoroughly inhibiting the mycelia growth of rice blast were $0.6 \mu\text{g mL}^{-1}$ and $0.8 \mu\text{g mL}^{-1}$, respectively. Moreover, when the concentration of CBZ was at $1 \mu\text{g mL}^{-1}$, the rice blast was thoroughly inhibited, which was obviously not as good as the nanocomposites. The concentration for 50% of

maximal effect (EC_{50}) was calculated by plotting the concentration of the nanocomposites *versus* mycelial growth inhibition (%), which showed a linear correlation as shown in Fig. 5a. The EC_{50} values of CBZ-GO, CBZ-UGO, and CBZ against rice blast were 0.28 , 0.41 , and $0.64 \mu\text{g mL}^{-1}$, respectively. Compared with the EC_{50} of CBZ, the CBZ-GO and CBZ-UGO exhibited 2.29- and 1.56-fold higher antifungal activity, respectively.

To further investigate the effect of GO carriers, and the simple physical blending of CBZ and GO or UGO was executed to observe the inhibition effect of *Magnaporthe oryzae* mycelial. As shown in Fig. 5b, GO had a weak impact on the growth of mycelium, and the mycelial growth inhibition of CBZ/GO and CBZ/UGO were 0.86% and 8.17%, respectively, which were far below the 50% inhibition rate of nanocomposites. In addition, to investigate the influence of GO on the structure of *Magnaporthe oryzae*, SEM observations were undertaken. Obvious differences between the control groups and GO exposed group were observed as seen from the data in Fig. 5c and d. Compared with normal mycelium in Fig. 5c, when it was exposed to GO, the structure of *Magnaporthe oryzae* was severely destroyed as shown in Fig. 5d, whereas these damages were not enough to inhibit the growth of the mycelium as seen from Fig. 5d. Interestingly, it was enough that GO could cause these injuries.

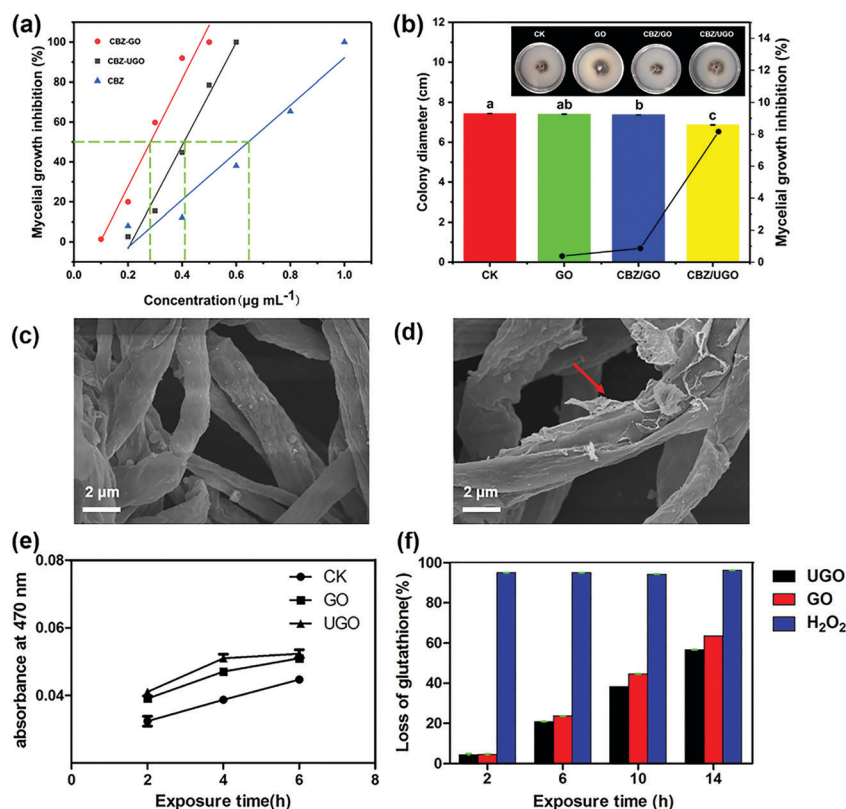


Fig. 5 EC_{50} fitting curves of CBZ-GO, CBZ-UGO and CBZ regarding mycelial growth inhibition (a) and the antifungal activities of GO, CBZ/GO, CBZ/UGO (the physical blending of CBZ and GO or UGO) (b). The insets in (b) are the photos of *Magnaporthe oryzae* mycelial incubated with nanocomposites. Column means labeled with different letters are statistically-significantly different at $p < 0.05$ based on one-way ANOVA with *post hoc* Duncan's multiple range test. Error bars represent the standard error of the mean. SEM images of *Magnaporthe oryzae*: (c) control; (d) *Magnaporthe oryzae* exposed to GO of $40 \mu\text{g mL}^{-1}$. Oxidative stress-mediated by GO and UGO: (e) ROS-dependent oxidative stress at exposure times of 2–6 h by XTT test; (f) *in vitro* glutathione oxidation using Ellman's assay.

These damages may be due to the cutting of mycelia by the two-dimensional sheet structure of GO.^{44,45} The SEM results demonstrated that GO was able to destroy the structure of *Magnaporthe oryzae* to impair cell viability. All the above results indicated that the nanocomposites had superior antifungal properties, compared with those of CBZ.

3.7. Oxidative stress-mediated antifungal activity

Generally, oxidative stress is a state where the concentration of ROS in the body is increased. Therefore, there are two main possibilities for causing oxidative stress: ROS-dependent oxidative stress, in which the ROS will be increased to disrupt microbial viability; ROS-independent oxidative stress, in which the nanocomposite will interact with antioxidants in cells to induce oxidative stress by reducing the antioxidant function of the antioxidant defense system without any ROS production.²⁵ Therefore, the GSH and XTT test was used to illuminate the antifungal mechanisms of materials. As shown in Fig. 5e, there was no dramatic difference between GO and UGO. In addition, compared with the control (CK), the GO and UGO had almost not generated any superoxide anions, which indicated that the ROS-dependent oxidative stress may not be the primary antifungal mechanism.

To further investigate the antifungal mechanism, the GSH test was executed to confirm ROS-independent oxidative stress through Ellman's assays. As shown in Fig. 5f, GO and UGO induced GSH oxidation, whereas GO nanosheets showed higher oxidation capacity than that by UGO nanosheets, which was in agreement with the results of the antifungal test. As the duration of exposure was extended, GSH oxidation increased in all samples. Moreover, recent studies have indicated that the GO-induced oxidation of glutathione occurs through a direct electron-transfer mechanism, while the smaller GO sheets possessed a higher antimicrobial effect due to oxidative mechanisms associated with the higher defect density of smaller sheets.¹⁴ Our assays monitored the hydrodynamic size of UGO, subjected to 6 h sonication, which became smaller compared with GO, which demonstrated lower oxidation of GSH attributed to the less negative charge for charge transfer to compromise cell integrity. Note that compared with the CBZ-GO, CBZ-UGO nanocomposite showed lower antifungal effects for rice blast, which can be attributed to the blunt edges and lower cumulative release rate of CBZ-UGO. From XTT and GSH results shown in Fig. 5e and f, the GO and UGO can show different GSH oxidation capacities, and the ROS-independent played a primary role in antifungal effects.

In comparison, nanocomposites improved antifungal effects dramatically than that by the original drug, which is caused by the "carrier effect".²⁰ That is to say that the GO can cause cell damage by the cutting of mycelia and GSH oxidation, thereby the drug-loaded on the surface of GO was released precisely to attack *Magnaporthe oryzae*. As shown in Fig. 6, when GO caused these damages to the mycelium, the drug-loaded on the surface of GO was more inclined to attack the mycelium, thereby inhibiting the growth of the mycelium. In brief, when fungi were exposed to the nanocomposites, it would generate a superior synergistic effect between graphene oxide and the drug to attack fungi.

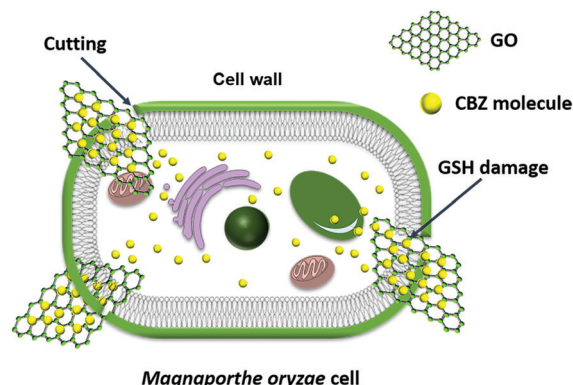


Fig. 6 The antifungal model of CBZ-GO nanocomposite against *Magnaporthe oryzae*.

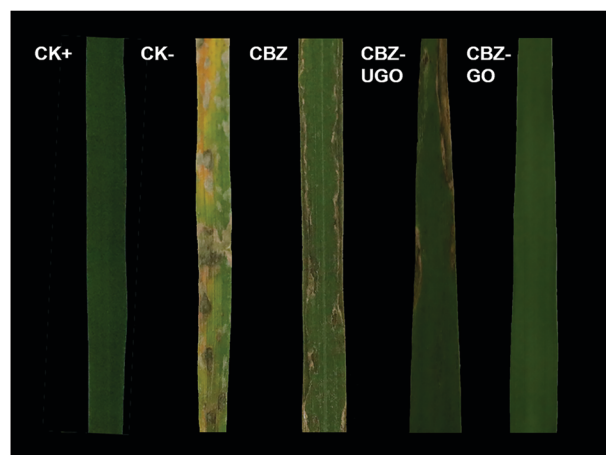


Fig. 7 Effect of nanocomposites on suppressing blast disease of rice in a pot experiment. CK+: normal rice leaf without any treatment; CK-: rice blast-infected rice.

3.8. The suppression of rice blast on rice

To investigate the practical efficiency, CBZ-GO and CBZ-UGO nanocomposites, which had a uniform drug concentration of $0.64 \mu\text{g mL}^{-1}$ were applied to rice transplants to control rice blast. As shown in Fig. 7, CK- had severe symptoms of rice blast on the leaf after 5 days of fungal inoculation. The incidence of rice blast in other treatments showed a decreasing trend. The CBZ treatment group was the most severe, followed by CBZ-UGO and CBZ-GO. Compared with the original drug, the CBZ-UGO nanocomposites showed fewer disease spots on the leaf, and there were almost no lesions for CBZ-GO. This result was consistent with the *in vitro* mycelial growth inhibition experiment. It is concluded that the CBZ-GO nanocomposites have better antibacterial activity than that of CBZ for rice transplants.

4. Conclusions

In summary, CBZ-GO and CBZ-UGO nanocomposites were successfully prepared. These nanocomposites were characterized

by UV-vis, XRD, FTIR, DLS, TG, XPS and SEM measurements. The bioassay on the inhibition of *Magnaporthe oryzae* demonstrated that the nanocomposites had remarkable bioactivity. Investigation of the antifungal mechanism showed that CBZ-GO nanocomposites led to damaging the cell structure, causing GSH oxidative stress, *i.e.*, there was a superior synergistic effect between GO and CBZ. The *in vivo* test on rice plants indicated that CBZ-GO reduced the severity of rice blast. All results indicated that GO as a pesticide carrier has enormous potential in improving pesticide utilization efficiency and reducing pesticide use.

Author contributions

P. Hu conceived the project and wrote the manuscript with the help of H. Xu and J. Jia L. Zhu conducted the bioassay experiments. F. Zheng performed the rice experiment. J. Lai completed the adhesion performance assay of nanocomposites. All authors have approved the final version of the manuscript.

Conflicts of interest

The authors declare that there is no conflict of interest associated with this study.

Acknowledgements

The authors are grateful for the financial support provided by the National Key R&D Program of China (2018YFD0200300), and Guangdong Provincial Innovation Team for General Key Technologies in Modern Agricultural Industry (2019KJ140).

References

- 1 P. Skamnioti and S. J. Gurr, *Trends Biotechnol.*, 2009, **27**, 141–150.
- 2 R. A. Wilson and N. J. Talbot, *Nat. Rev. Microbiol.*, 2009, **7**, 185–195.
- 3 J. Liu, X. Wang, T. Mitchell, Y. Hu, X. Liu, L. Dal and G. Wang, *Mol. Plant Pathol.*, 2010, **11**, 419–427.
- 4 T. A. Mentlak, A. Kombrink, T. Shinya, L. S. Ryder, I. Otomo, H. Saitoh, R. Terauchi, Y. Nishizawa, N. Shibuya, B. P. H. J. Thomma and N. J. Talbot, *Plant Cell*, 2012, **24**, 322–335.
- 5 R. Dean, J. A. L. V. Kan, Z. A. Pretorius, K. E. Hammond-Kosack, A. D. Pietro, P. D. Spanu, J. J. Rudd, M. Dickman, R. Kahmann, J. Ellis and G. D. Foster, *Mol. Plant Pathol.*, 2012, **13**, 414–430.
- 6 Y. F. Dagdas, K. Yoshino, G. Dagdas, L. S. Ryder, E. Bielska, G. Steinberg and N. J. Talbot, *Science*, 2012, **336**, 1590–1595.
- 7 S. Sharma, S. Singh, A. K. Ganguli and V. Shanmugam, *Carbon*, 2017, **115**, 781–790.
- 8 Y. Tong, L. Shao, X. Li, J. Lu, H. Sun, S. Xiang, Z. Zhang, Y. Wu and X. Wu, *J. Agric. Food Chem.*, 2018, **66**, 2616–2622.
- 9 Z. Shen, H. Wen, H. Zhou, L. Hao, H. Chen and X. Zhou, *Mater. Sci. Eng., C*, 2019, **105**, 110073.
- 10 X. Chen, M. Lin, L. Sun, T. Xu, K. Lai, M. Huang and H. Lin, *Food Chem.*, 2019, **293**, 271–277.
- 11 C. A. Razzino, F. Sgobbi Livia, T. C. Canevari, J. Cancino and S. A. S. Machado, *Food Chem.*, 2015, **170**, 360–365.
- 12 Y. Yang, D. Huo, H. Wu, X. Wang, J. Yang, M. Bian, Y. Ma and C. Hou, *Sens. Actuators, B*, 2018, **274**, 296–303.
- 13 Y. Guo, S. Guo, J. Li, E. Wang and S. Dong, *Talanta*, 2011, **84**, 60–64.
- 14 X. Lu, X. Feng, J. R. Werber, C. Chu, I. Zucker, J. H. Kim, C. O. Osuji and M. Elimelech, *Proc. Natl. Acad. Sci. U. S. A.*, 2017, **10996**, E9793–E9801.
- 15 X. Sun, D. Luo, J. Liu and D. G. Evans, *ACS Nano*, 2010, **4**, 3381–3389.
- 16 Y. He, R. Hu, Y. Zhong, X. Zhao, Q. Chen and H. Zhu, *Nano Res.*, 2017, **11**, 1928–1937.
- 17 E. Bidram, A. Sulistio, A. Amini, Q. Fu, G. G. Qiao, A. Stewart and D. E. Dunstan, *Carbon*, 2016, **103**, 363–371.
- 18 C. Bai, S. Zhang, L. Huang, H. Wang, W. Wang and Q. Ye, *Carbohydr. Polym.*, 2015, **125**, 376–383.
- 19 E. V. R. Campos, J. L. D. Oliveira, C. M. G. D. Silva, M. Pascoli, T. Pasquoto, R. Lima, P. C. Abhilash and L. F. Fraceto, *Sci. Rep.*, 2015, **5**, 13809.
- 20 Y. Gao, J. Wu, X. Ren, X. Tan, T. Hayat, A. Alsaedi, C. Cheng and C. Chen, *Environ. Sci.: Nano*, 2017, **4**, 1016–1024.
- 21 Y. Tu, M. Lv, P. Xiu, T. Huynh, M. Zhang, M. Castelli, Z. Liu, Q. Huang, C. Fan, H. Fang and R. Zhou, *Nat. Nanotechnol.*, 2013, **8**, 594–601.
- 22 X. Wang, A. Cai, X. Wen, D. Jing, H. Qi and H. Yuan, *Sci. China Mater.*, 2017, **60**, 258–268.
- 23 X. Wang, H. Xie, Z. Wang, K. He and D. Jing, *Environ. Sci.: Nano*, 2019, **6**, 75–84.
- 24 M. Sawangphruk, P. Srimuk, P. Chiochan, T. Sangsri and P. Siwayaprahm, *Carbon*, 2012, **50**, 5156–5161.
- 25 T. I. Kim, B. Kwon, J. Yoon, I. J. Park, G. S. Bang, Y. K. Park, Y. S. Seo and S. Y. Choi, *ACS Appl. Mater. Interfaces*, 2017, **9**, 7908–7917.
- 26 C. D. Vecitis, K. R. Zodrow, S. Kang and M. Elimelech, *ACS Nano*, 2010, **4**, 5471–5479.
- 27 J. Xie, Z. Ming, H. Li, H. Yang, B. Yu, R. Wu, X. Liu, Y. Bai and S. Yang, *Chemosphere*, 2016, **151**, 324–331.
- 28 W. Liang, A. Yu, G. Wang, F. Zheng, P. Hu, J. Jia and H. Xu, *Carbohydr. Polym.*, 2018, **199**, 437–444.
- 29 Y. Li, D. Yang and J. Cui, *RSC Adv.*, 2017, **7**, 38853–38860.
- 30 J. I. Paredes, S. Villar-Rodil, A. Martínez-Alonso and J. M. D. Tascón, *Langmuir*, 2008, **24**, 10560–10564.
- 31 C. Li, X. Wang, F. Chen, C. Zhang, X. Zhi, K. Wang and D. Cui, *Biomaterials*, 2013, **34**, 3882–3890.
- 32 S. Sharma, B. K. Biswal, D. Kumari, P. Bindra, S. Kumar, T. Stobdan and V. Shanmugam, *ACS Appl. Mater. Interfaces*, 2018, **10**, 18478–18488.
- 33 C. Bai, S. Zhang, L. Huang, H. Wang, W. Wang and Q. Ye, *Carbohydr. Polym.*, 2015, **125**, 376–383.
- 34 F. Zheng, Y. Li, Z. Zhang, J. Jia, P. Hu, C. Zhang and H. Xu, *J. Cleaner Prod.*, 2020, **264**, 121685.
- 35 Y. Xue, Y. Liu, F. Lu, J. Qu, H. Chen and L. Dai, *J. Phys. Chem. Lett.*, 2012, **3**, 1607–1612.

- 36 M. Ionita, M. A. Pandele and H. Iovu, *Carbohydr. Polym.*, 2013, **94**, 339–344.
- 37 W. Shao, X. Liu, H. Min, G. Dong, Q. Feng and S. Zuo, *ACS Appl. Mater. Interfaces*, 2015, **7**, 6966–6973.
- 38 K. Krishnamoorthy, M. Veerapandian, K. Yun and S. J. Kim, *Carbon*, 2013, **53**, 38–49.
- 39 G. Wang, Y. Xiao, H. Xu, P. Hu, W. Liang, L. Xie and J. Jia, *J. Agric. Food Chem.*, 2018, **66**, 11244–11253.
- 40 R. N. Sindhura, S. Sowmya, J. D. Bumgardner, K. P. Chennazhi, R. Biswas and R. Jayakumar, *Biochim. Biophys. Acta, Gen. Subj.*, 2014, **1840**, 2080–2090.
- 41 L. Cao, Y. Liu, C. Xu, Z. Zhou, P. Zhao, S. Niu and Q. Huang, *Mater. Sci. Eng., C*, 2019, **102**, 134–141.
- 42 J. Xu, B. Xu, D. Shou, X. Xia and Y. Hu, *Polymers*, 2015, **7**, 1850–1870.
- 43 Z. Shen, H. Zhou, H. Chen, H. Xu, C. Feng and X. Zhou, *Nanomaterials*, 2018, **8**, 317.
- 44 S. Liu, T. H. Zeng, M. Hofmann, E. Burcombe, J. Wei, R. Jiang, J. Kong and Y. Chen, *ACS Nano*, 2011, **5**, 6971–6980.
- 45 J. Xie, Z. Ming, H. Li, H. Yang, B. Yu, R. Wu, X. Liu, Y. Bai and S. Yang, *Chemosphere*, 2016, **151**, 324–331.

Phloem Delivery of Fludioxonil by Plant Amino Acid Transporter-Mediated Polysuccinimide Nanocarriers for Controlling Fusarium Wilt in Banana

Hanxiang Wu,[†] Pengtong Hu,[†] Ye Xu, Chunxia Xiao, Zhibin Chen, Xiaojing Liu, Jinliang Jia,*
and Hanhong Xu*



Cite This: *J. Agric. Food Chem.* 2021, 69, 2668–2678



Read Online

ACCESS |



Metrics & More



Article Recommendations



Supporting Information

ABSTRACT: Fusarium wilt disease poses a serious threat to the global production of bananas. The targeted delivery of fungicides to banana phloem tissues may offer new hope for controlling this hard-to-treat vascular disease. In this study, fludioxonil (FLU)-loaded glycine methyl ester-conjugated polysuccinimide nanoparticles (PGA) were prepared with a loading efficiency (LE) of 27.9%. The obtained nanoparticles (FLU@PGA) exhibited pH-sensitive controlled release, specifically under an alkaline pH in plant phloem. *In vivo* experiments in potted bananas demonstrated that FLU@PGA can achieve the downward delivery of FLU to banana rhizomes and roots after foliar application, reducing disease severity by 50.4%. The phloem transport studies showed that the phloem loading of FLU@PGA was involved in an active transport mechanism at the organ level (castor bean seedlings). The observation of fluorescein-5-isothiocyanate cadaverine-labeled PGA nanocarriers showed that they could be absorbed by mesophyll cells and loaded into vascular tissues through the symplastic pathway. Furthermore, the interaction of FLU@PGA with the plant amino acid transporter AtLHT1 was observed to enhance transmembrane uptake at the cellular level (*Xenopus* oocytes). These results suggested that the phloem-targeted delivery of fungicide by transporter-mediated nanocarriers could be a promising new strategy for the management of Fusarium wilt in bananas.

KEYWORDS: nanopesticide, vascular wilts, panama disease, pH-responsive release, carrier-mediated transport, amino acid transporter

INTRODUCTION

Banana (*Musa* spp.) is the most important fruit crop in the world and is also a major staple food for 400 million people in many developing countries in Africa, Asia, and Latin America.^{1,2} Since the 1900s, global banana production has been seriously threatened by a destructive disease, Fusarium wilt, and no sustainable control strategy is available for its management to date.^{2–4} This vascular disease is caused by the soil-borne fungus *Fusarium oxysporum* f. sp. *cubense* (Foc), which can penetrate the banana root endodermis and cortex, reach the xylem vessels, and then grow fastidiously inside the vascular system (both the xylem and phloem).^{4–6} As the pathogenic fungus lives inside the vascular tissues once the penetration process is completed, it can easily escape from contact with control agents.⁷ Several fungicides from different chemical groups have shown good *in vitro* fungicidal activities against the pathogen.⁸ However, none of these compounds has been practically applied for Foc management in the field to date.

Nanotechnology has promoted new concepts and solutions for the agrochemical industry to face the challenges of food safety and security.^{9,10} Among these, nanodelivery systems provide a feasible approach for the delivery of agrochemicals to specific sites in plants.¹¹ Bioinspired mussel nanoparticles highly improved the adhesive property and retention time of avermectin on hydrophilic plant foliage.¹² Lignin nanocarriers were developed as an enzyme-responsive fungicide delivery

system for controlling fungal trunk infections in grapevine.¹³ Thus, developing nanocarriers for the vascular delivery of agrochemicals may offer new hope for the effective chemical control of Fusarium wilt in bananas.

Phloem-mobile fungicides with downward movement properties are considered more promising to control soil-borne vascular diseases because they can be applied to leaves and then be transported to the roots for new growth.^{14–16} Several types of nanoparticles have been reported to enter the plant vascular system and then be transported downward through the phloem, that is, mesoporous silica nanoparticles and poly(acrylic acid)-block-poly(N-isopropylacrylamide) star polymers.^{17,18} However, the phloem-loading mechanism and pathway of nanoparticles in plants remain largely unclear, and there is no sophisticated strategy for the development of phloem-targeting nanocarriers.

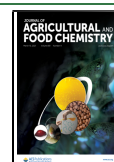
Phloem loading and unloading of many endogenous substances are regulated by plasma membrane transporters.^{19,20} Phloem delivery of nanocarriers may be further improved by conjugating the substrates of these transporters,

Received: November 6, 2020

Revised: January 26, 2021

Accepted: January 27, 2021

Published: February 25, 2021



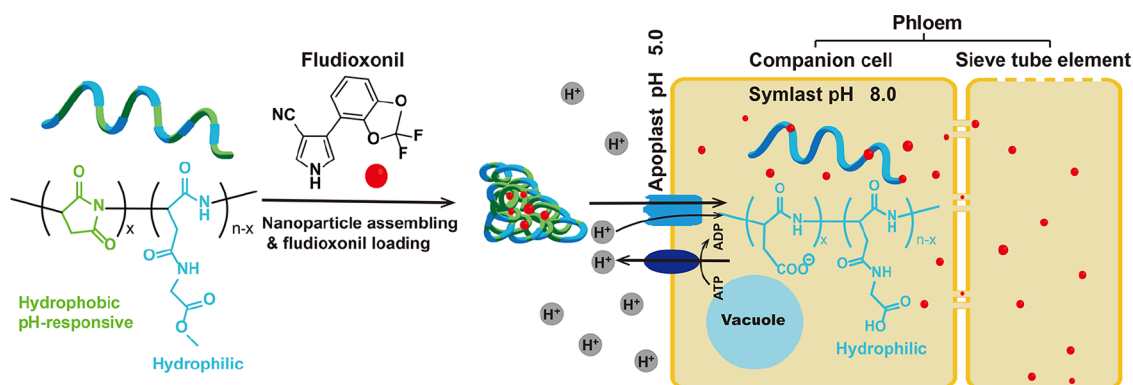
ACS Publications

© 2021 American Chemical Society

2668
第230页,共289页

<https://dx.doi.org/10.1021/acs.jafc.0c07028>
J. Agric. Food Chem. 2021, 69, 2668–2678

Scheme 1. Schematic Illustration of the PGA Nanoparticles as Targeted Nanocarriers of the Fungicide FLU and the Proposed Carrier-Mediated Transport to Plant Phloem



thereby allowing for binding to the transporter protein. This strategy to target specific membrane transporters has already been applied to mediate the targeted delivery of drugs and medicinal nanoparticles.^{21,22} By the use of large amino acid transporter 1 at the blood–brain barrier, L-valine-conjugated chitosan nanoparticles were prepared and observed to be an excellent drug carrier system for brain delivery.²³ In plants, amino acid transporters have also been demonstrated to enhance the uptake and phloem transport of amino acid–pesticide conjugates.^{24–27} Thus, the introduction of amino acid side chains may be a reasonable strategy to enhance phloem targeting of manufactured nanocarriers.

Polysuccinimide (PSI) has been used to design biodegradable and pH-responsive nanoparticles for agrochemical delivery systems in plants.^{28,29} Because of their remaining succinimidyl groups, *in vitro* studies showed that PSI nanoparticles could be hydrolyzed in phosphate-buffered solution under a pH of 8.5 (similar to that of plant phloem), thereby releasing the encapsulated drug and reducing the risk to the plant.²⁸ In our previous study, the amino acid glycine was selected as a functional group for conjugating to polysuccinimide (PGA), and *in vivo* studies showed that PGA nanocarriers can improve the bioactivity and absorption of avermectin in rice.³⁰ However, the phloem transport properties of PSI-based nanocarriers in plants have not been directly investigated. The mechanism of phloem loading of PGA and further applications of nanocarriers for fungicide delivery are worthy of study.

To investigate the phloem delivery capability of functionalized PGA nanocarriers in banana plants, nonsystemic phenylpyrrole fungicide fludioxonil (FLU), which exhibited good *in vitro* fungicidal activity against Foc in a preliminary experiment, was selected as a model compound (Scheme 1). The nonsystemic properties can also make the active ingredient remain in target tissues after release from the nanocarriers, thus reducing potential contamination of new growth tissues such as flowers and fruits. In the present study, (1) fludioxonil-loaded PGA (FLU@PGA) nanoparticles were prepared, and their controlled release profiles were studied *in vitro*; (2) long-distance delivery of FLU by FLU@PGA in banana plants and their control efficiency against Fusarium wilt of banana were evaluated in greenhouse trials; (3) and the transporter-mediated mechanisms of transmembrane uptake and phloem transport of PGA nanocarriers at the cellular and organ levels were investigated using *Xenopus* oocytes and castor bean seedlings, which are powerful heterologous

expression systems and widely used plant models for phloem exudate collection, respectively.

EXPERIMENTAL SECTION

Materials. Polysuccinimide was purchased from Hubei YuanChen SaiChuang Technology Co., Ltd. (China). Glycine methyl ester hydrochloride (HGlyOMe, 99%) was purchased from Shanghai Hanhong Scientific Co., Ltd. (China). Technical-grade (TC) fludioxonil (98% purity) was obtained from Guangdong Yuantian Bioengineering Co., Ltd. (China). A 50% wettable powder (WP) formulation of FLU under the trade name Huiyou was purchased from Syngenta Investment Co., Ltd. (China). Fluorescein-5-isothiocyanate cadaverine (FITC-cad) was purchased from Hangzhou Xinqiao Biotechnology Co., Ltd. (China). Carbonyl cyanide 3-chlorophenylhydrazone (CCCP) was purchased from Sigma-Aldrich (Saint Louis, USA).

Tissue-cultured Cavendish banana of the Foc race 4-susceptible cultivar ‘Brazilian’ was used in this study. Plantlets in sealed bags were transplanted into sterile medium consisting of one part vermiculite and three parts peat (Jiffy Products Ltd. Norway) for 50 days. Mature female African clawed frogs (*Xenopus laevis*) were purchased from the Shanghai Institute of Biochemistry and Cell Biology (China). Castor bean (*Ricinus communis* L.) seedlings were grown for 6 days in vermiculite, as described previously.³¹ All plantlets were grown in a greenhouse at 28 ± 2 °C with a 16 h light/8 h dark photoperiod.

Preparation and Characterization of FLU@PGA Nanoparticles. PGA nanoparticles were prepared according to previous publications with slight modifications.^{30,32} Briefly, 0.97 g of PSI was dissolved in 10 mL of dimethyl sulfoxide (DMSO). Then, 1.5 g of HGlyOMe and 1.55 g of dibutylamine were dissolved in 5 mL of DMSO and then added to the PSI solution under vigorous stirring for 24 h. The resulting solution was added dropwise to 300 mL of citric acid buffer at pH 2.5. Subsequently, the PGA nanoparticles were collected by centrifugation (10,000 r/min), washed three times with deionized water, and freeze-dried overnight.

After obtaining PGA nanoparticles, FLU@PGA nanoparticles were synthesized as previously described.³⁰ PGA (100 mg) was dissolved in 5 mL of dimethylformamide (DMF), after which 100 mg of FLU (TC) was added to form a mixed organic phase. Then, the mixed solution was added to 45 mL of deionized water under vigorous stirring for 1 h. The resulting mixture was transferred to a centrifuge tube for centrifugation at 10000 rpm for 10 min and was further washed in a solution of DMF and H₂O (DMF/H₂O = 2/9). The cleaning procedure was repeated three times to remove residual FLU, after which the precipitate was lyophilized overnight.

The structure of the nanoparticles was inspected using a Fourier transform infrared spectrometry (FTIR) instrument (Vertex 70, Bruker Co., Germany). The hydrodynamic diameter and zeta potential of PGA and FLU@PGA were measured via dynamic light scattering (Zetasizer Nano ZSE, Malvern Panalytical Ltd., UK). Thermogravimetric analysis (TGA) of the nanoparticles was

performed using a TG209F1 Iris thermobalance (NETZSCH-Gerätebau, Germany). The morphology of the nanoparticles was characterized by scanning electron microscopy (SEM; Nova Nano-SEM 450, FEI Co., USA) and transmission electron microscopy (TEM; JEOL 2100F, JEOL Co., Ltd., Japan). In addition, the distribution of FLU in the PGA nanocarriers was analyzed by energy-dispersive spectroscopy (EDS).

To determine the FLU LE, 10 mg of FLU@PGA was dissolved in 5 mL of ethanol and transferred into an ultrasonic bath for 2 h to completely disassociate the FLU. The resulting suspension was separated by centrifugation (10,000 r/min for 10 min), and the supernatant was then analyzed using an Agilent Technologies 1100 high-performance liquid chromatography (HPLC) system equipped with a UV/vis photodiode-array detector. An Agilent C18 reversed-phase column (5 μ m, 250 mm \times 4.6 mm i.d.) was used at a flow rate of 0.8 mL/min, and the injection volume was 10 μ L. The mobile phase consisted of acetonitrile and water (65/35, V/V). The absorbance wavelength was 212 nm. The LE was calculated with the following equation:³³

$$\text{LE (\%)} = (M/M_0) \times 100\% \quad (1)$$

where M is the mass of FLU detected by HPLC and M_0 is the mass of the FLU@PGA nanocarriers.

In Vitro Release Profiles of FLU@PGA Nanoparticles. The release behavior of FLU from the FLU@PGA nanoparticles was measured as follows: 10 mg of the FLU@PGA nanoparticles or equivalent dose of FLU (TC) was added to 3 mL of phosphate buffer solutions at different pH values (pH 5.0 and 8.0) containing 30% (V/V) ethanol, after which the suspensions were transferred to dialysis bags (molecular weight cut-off of 3500 Da). Then, the dialysis bags were submerged in 100 mL of the same phosphate buffer solution as the release medium and stirred at 120 r/min. Periodically, 1 mL of release medium was collected, after which 1 mL of fresh medium was added to maintain the original volume. The FLU content in the release medium was analyzed by the abovementioned HPLC method. The release experiments were repeated three times, and the cumulative release rate of FLU was calculated according to the following equation:¹⁷

$$E_r = \frac{V_e \sum_{i=1}^n C_i}{M_p} \times 100\% \quad (2)$$

Here, E_r is the accumulative release (%) of FLU from the FLU@PGA nanoparticles; V_e is 1 mL, the volume of the release medium taken during a time interval; C_i is the FLU concentration in the release medium at sampling time n ; and M_p is the total amount of FLU entrapped in the nanoparticles.

In Vivo Translocation and Distribution of FLU@PGA in Banana Plants. Banana seedlings (50 day old) were treated with FLU@PGA or FLU (50% WP) by foliar application with a small brush. To characterize and quantify the FLU movement in the seedlings, the different plant parts (upper leaf, treated leaves, pseudostem, rhizome, and roots) were analyzed separately (Figure 1). FLU@PGA or an equivalent dose of FLU (50% WP) was applied to the leaves at a final concentration of 200 or 111.6 mg/L, respectively (1 mL/leaf and two leaves/plant). FLU@PGA and FLU were prepared in a mixture solution (acetone/water, 1:9, V/V) containing 0.15% (V/V) organosilicone surfactant (Silwet L-77). The control group was treated with the same solution without FLU@PGA or FLU. The experiment was repeated two times with 24 replicate plants per treatment. The plants were collected and extracted 2, 5, 7, and 10 days after foliar treatment (6 plants \times 4), and each plant was analyzed individually.

The extraction and clean-up protocols were performed according to a modified QuEChERS method, as previously described.³⁴ The analyses were performed using a liquid chromatography–tandem mass spectrometry (LC–MS/MS) system (Waters Acquity UPLC system equipped with a Xevo TQD Triple Quadrupole Mass Spectrometer, Waters Corp., USA). Quantification was performed by multiple reaction monitoring (MRM), and the retention time, cone

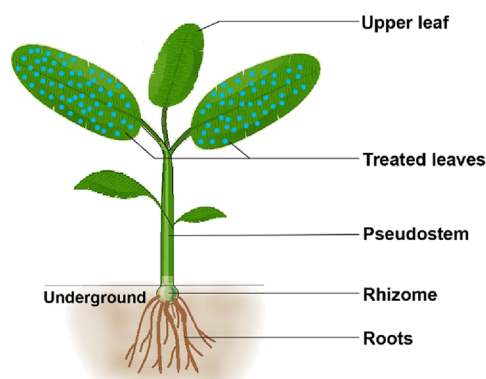


Figure 1. Diagrammatic representation of the different parts of banana seedlings that were individually analyzed by LC–MS/MS. The FLU@PGA nanoparticles were applied to two mature leaves (blue points).

voltage, MRM transition, and collision energy for all analytes are listed in Table S2. The quantification of FLU in the banana plant samples was conducted using different external matrix-matched standard calibration curves (Table S3 and Figure S5). The limit of detection (LOD) obtained was 0.001 mg/kg for both leaf and root samples (Table S3). Satisfactory recovery rates were achieved for the leaf and root samples at three spiking levels (between 89 and 111%, Table S4).

Fungicidal Activity of FLU@PGA Nanoparticles against Foc in Vitro. The pathogenic fungus Foc used in this study was the wild-type tropical race 4 (Foc TR4). The isolation and identification of this strain from Guangdong Province in China have been described previously.⁵ The inhibitory effect of FLU@PGA on the mycelial growth was assessed according to a previously described method.⁸ The FLU@PGA nanoparticles and FLU (50% WP) were tested with a range of concentrations to determine the EC_{50} values (effective concentration of the active ingredient that could reduce mycelial growth by 50%). FLU@PGA nanoparticles and FLU (50% WP) were dissolved in DMSO (0.5% final concentration) and diluted in sterile water containing 0.1% Tween 80. The solution was then added to 55 °C molten potato dextrose agar (PDA) media at a 1/9 proportion (V/V), and the mixtures were then poured into 9 cm plastic Petri dishes. The control consisted of PDA with 0.5% DMSO and 0.1% Tween 80. The plates were inoculated with agar plugs (0.5 mm in diameter) from the margin of an actively growing colony and incubated for 5 days at 28 °C in the dark. EC_{50} values were calculated as described in detail elsewhere.¹⁷

In Vivo Efficacy of FLU@PGA against Foc under Greenhouse Conditions. Pot experiments were performed on banana seedlings (50 days old) by foliar application of FLU@PGA or FLU (50% WP), as described above. FLU@PGA or an equivalent dose of FLU was applied to the leaf at a final concentration of 800 or 446 mg/L, respectively (1 mL/leaf and two leaves/plant). The control group was treated with the same solution without FLU@PGA or FLU. Treatments were applied twice, 2 days before and 5 days after inoculation with pathogenic fungi. Each treatment was replicated three times, with six plants per replication. The artificial inoculation of banana plants with Foc TR4 spores is described elsewhere.⁵ The spore suspension was applied to the soil at a final concentration of 5000 conidia/g soil. After 50 days of inoculation, disease severity assessments were performed according to the rating system for leaf symptoms (0–4 scale) described by Huang et al.³⁵ The disease severity (%) was calculated as the $\sum(\text{number of plants in that rating} \times \text{rating}) / (\text{total number of plants assessed} \times \text{maximum rating}) \times 100$, while the percentage efficacy of disease control (%) was calculated as follows: $(\text{disease severity in control} - \text{disease severity in treatment}) / (\text{disease severity in control} \times 100)$.

Phloem Exudation and Tissue Uptake of FLU@PGA in Castor Bean Seedlings. Castor bean seedlings are often used as a plant model to evaluate the phloem mobility of xenobiotics.^{31,36} The cotyledons of seedlings were incubated in buffered solution (pH 5.0)

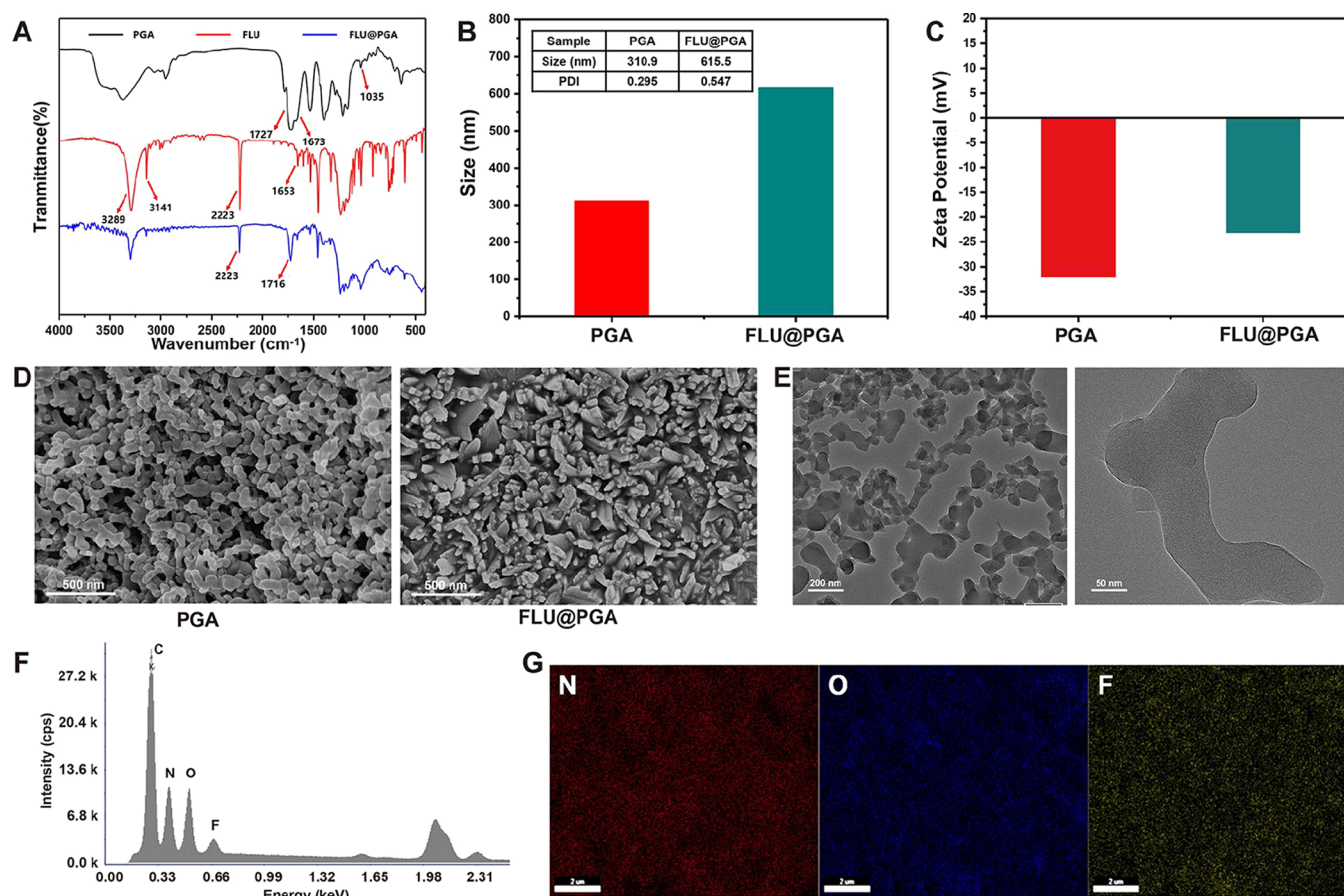


Figure 2. Characterization of the PGA and FLU@PGA nanoparticles. (A) FTIR spectra of PGA nanoparticles (PGA), FLU, and FLU-loaded PGA nanoparticles (FLU@PGA). (B) Hydrodynamic size and (C) zeta potential of PGA and FLU@PGA. (D) SEM images of PGA and FLU@PGA. (E) TEM images of FLU@PGA. (F) EDS spectrum of FLU@PGA nanoparticles and (G) SEM mapping of FLU@PGA nanoparticles for the following specific elements: nitrogen (N), oxygen (O), and fluorine (F).

consisting of 20 mM MES, 0.25 mM MgCl_2 , and 0.5 mM CaCl_2 for 30 min before being transferred to the same solution supplemented with 100 mg/L FLU@PGA (with or without 50 μM CCCP) or an equivalent dose of FLU (50% WP) for 2 h. The phloem sap was collected for the following 2 h using a previously described method.³¹ The phloem sap was diluted with acetonitrile (phloem sap/ acetonitrile, 1/5, V/V). At the end of the experiment, the treated cotyledons were extracted to determine the tissue uptake of FLU. In detail, the cotyledons were rinsed (3×2 min) in a solution of pure water/acetone (9/1, V/V). After they were ground in liquid nitrogen, two cotyledons from each plant were then suspended in 10 mL of acetonitrile and ultrasonically extracted for 10 min. The extracts were passed through a 0.22 μm pore-sized filter membrane. The quantification of FLU in phloem sap and the cotyledon extracts was performed using the abovementioned HPLC method.

Visualization of the PGA Movement by Confocal Laser Scanning Microscopy. To visualize the distribution of the PGA nanocarriers in plants, the nanocarriers were labeled by FITC-cad. The preparation of FITC-cad-labeled PGA (PGA-FITC) was performed in a manner similar to that described above. The structure of the PGA-FITC nanoparticles was inspected via FTIR, and fluorescence spectra were obtained using an F-7000 fluorescence spectrometer (Hitachi, Japan).

The uptake and translocation of the PGA-FITC nanoparticles in castor bean seedlings were visualized, as described previously.³⁷ The cotyledons were incubated in the abovementioned buffer solution with (test) or without (control) 100 mg/mL of PGA-FITC nanoparticles. After 2 h of treatment, the cotyledons were washed with the incubation solution (3×1 min). Then, the cotyledon midvein cross sections were observed using a Nikon Eclipse Ti-E A1

laser scanning confocal system (Nikon Instruments, Inc., Japan) through two fluorescence channels with time-separated collection. FITC-cad signals were collected in the channel with excitation at 488 nm and emission at 500–550 nm. Plant autofluorescence signals were collected in the second channel with excitation at 405 nm and emission at 417–477 nm.

Xenopus Oocyte Uptake of FLU@PGA. cRNA of the amino acid transporter AtLHT1 was prepared using an mMessage mMachine T7 Transcription kit (Thermo Fisher Scientific, Vilnius, Lithuania), as described previously.²⁵ For the uptake experiments, the oocytes were preincubated for 30 min in modified Kulori solution (90 mM NaCl, 1 mM KCl, 1 mM CaCl_2 , 1 mM MgCl_2 , and 5 mM MES adjusted to pH 5.0) at 25 $^\circ\text{C}$, after which each oocyte was transferred to 0.5 mL of the same Kulori solution supplemented with 20 mg/L FLU@PGA or an equivalent dose of FLU (50% WP). After 1 h of uptake, the oocytes were washed five times with ice-cold Kulori solution (1 mL \times 5) in separate microcentrifuge tubes (10 oocytes for each treatment).

Each oocyte was separately homogenized in 100 μL of acetonitrile using a pipette, and the solutions were then ultrasonically extracted for 10 min. Before being filtered by 0.22 μm pore-sized filter membranes, the extracts were analyzed with the same system as described above. The linearity for FLU was satisfactory, with a correlation coefficient (R^2) = 0.9942, and the LOD was 0.001 mg/kg (Table S3).

Statistical Analysis. For the translocation test, the Mann–Whitney U test was used to assess significant differences between the FLU@PGA and FLU (50% WP) treatment groups ($P < 0.05$). The disease severity data were submitted to one-way analysis of variance, and Tukey's test was used to compare means at the $P = 0.05$ level. For the castor bean experiments, the Kruskal–Wallis test was used to

determine significant differences among treatments ($P < 0.05$). The statistical calculations were performed via SPSS software.

RESULTS AND DISCUSSION

Characterization of the Nanoparticles. The FTIR spectra of the PGA nanocarriers, FLU, and FLU@PGA are shown in Figure 2A. For PGA, the peak at 1727 cm^{-1} was attributed to C=O, and the absorption band at 1673 cm^{-1} was assigned to C=O stretching vibration in the newly formed -CONH-. In addition, the peak at 1035 cm^{-1} was attributed to the stretching vibration of C-N mixed with C-C, which indicated the presence of HGlyOMe. These results demonstrated that the PGA nanocarriers were successfully prepared. With regard to FLU, the strong absorption peak at 2223 cm^{-1} was contributed to by $\text{N}\equiv\text{C}$ stretching vibrations, and the peaks at 3089 and 3141 cm^{-1} were assigned to N-H and C-H stretching vibrations, respectively. Compared with that of FLU, the spectrum of FLU@PGA exhibited the same peak at 2223 cm^{-1} , which belonged to the characteristic peak of FLU. In particular, the C=O stretching peak in FLU@PGA appeared at 1716 cm^{-1} because of the interaction between PGA and FLU. Thus, the results confirmed that FLU was successfully loaded into the PGA nanocarriers.

The hydrodynamic size and zeta potential of the nanoparticles were measured by dynamic light scattering. As shown in Figure 2B, the hydrodynamic sizes of PGA and FLU@PGA were 310.9 and 615.5 nm, respectively. Compared with that of the empty PGA nanocarriers, the hydrodynamic size of the FLU@PGA nanoparticles increased by approximately twofold, which may be due to the presence of an organic layer on the nanoparticles.³⁸ The slightly high polymer dispersity index (0.547) of FLU@PGA was caused by the uncontrolled self-assembling and cross-linking that occurred during the formation process without the addition of other auxiliaries (Figure 2B).³³ As shown in Figure 2C, the PGA and FLU@PGA nanoparticles showed negative charge (-32.1 and -23.1 mV, respectively), indicating that the nanoparticles were relatively stable in aqueous medium. In addition, FLU@PGA had less negative potential, possibly because of the electrostatic interactions of PGA and FLU.

The morphologies of the PGA and FLU@PGA nanoparticles were observed by SEM and TEM. As shown in Figure 2D,E, there were slight morphological differences between the PGA and FLU@PGA nanoparticles, which could be due to changes in the internal electric field caused by the interaction between FLU and the nanocarriers (relatively less negative charge for the zeta potential). After FLU was loaded onto the PGA nanocarriers, the morphology of FLU@PGA was approximately bone-shaped. In addition, the incompletely unified morphology of the nanoparticles was caused by the overlapping layers of nanoparticles as previously demonstrated.³⁰ The amphiphilic PSI-based copolymers are self-assembled systems consisting of hydrophobic and hydrophilic components that can form core-shell nanoparticles.²⁸ The observed morphology of the FLU@PGA nanoparticles was probably due to the self-assembling properties of the long polymer chain. Additionally, the EDS spectrum of FLU@PGA nanoparticles showed strong signals from fluorine, which demonstrated the presence of FLU (Figure 2F). Moreover, mapping of elemental nitrogen, oxygen, and fluorine (Figure 2G) clearly demonstrated that there was even distribution within the framework of the FLU@PGA nanoparticles.

To further determine the amount of FLU loaded on the nanoparticles, TGA was implemented over the temperature range $25\text{--}900\text{ }^{\circ}\text{C}$. The TGA results and DTG analysis of FLU, PGA, and FLU@PGA are shown in Figure S1. The maximum weight loss of FLU occurred at approximately $300\text{ }^{\circ}\text{C}$, and total weight losses of PGA and PGA@FLU at $300\text{ }^{\circ}\text{C}$ were approximately 19.0 and 48.0%, respectively (Figure S1). After the weight loss between PGA and PGA@FLU was subtracted, the loading rate of FLU was approximately 29%. This was further confirmed by the HPLC analysis, and the result showed that the LE was 27.9%. Taken together, the abovementioned results confirmed that the FLU@PGA nanoparticles were successfully prepared.

In Vitro Controlled Release. It is well known that pH gradients exist between the inside ($\text{pH} \approx 8.0$) and outside ($\text{pH} \approx 5.0$) of plant phloem,³⁹ which can be used as a physiological basis to design pH-responsive nanoparticles for phloem delivery.²⁸ The release behaviors of FLU@PGA at two plant physiological pH values were investigated in buffered solutions. In Figure 3, the release of FLU (TC) into the medium was not

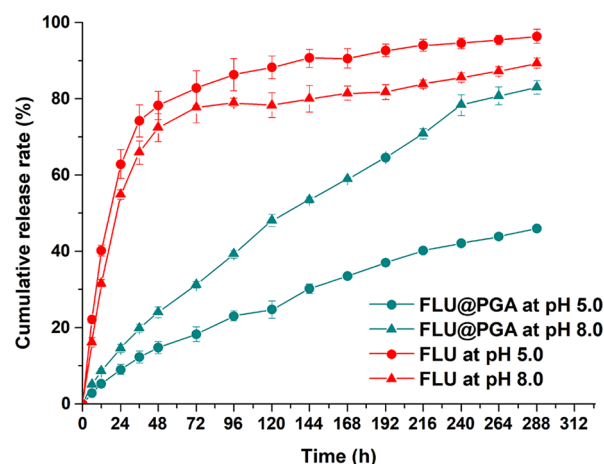


Figure 3. *In vitro* release profiles of FLU from the FLU@PGA nanoparticles at different pH values.

pH-dependent, as it occurred rapidly and reached a plateau of approximately 80% after 72 h. In contrast, the FLU@PGA nanoparticles showed the desired pH-sensitive controlled release of FLU during the 288 h measuring period. The cumulative release rate of these nanoparticles at pH 8.0 was 83% after 288 h, which was almost 2 times higher than that observed at pH 5.0 (Figure 3). Consistent with our previous work, the avermectin-loaded PGA nanoparticles showed a maximum cumulative release rate of 85.1% at pH 8.5.³⁰ The greater cumulative release rate of the PGA nanoparticles under an alkaline pH was due to the hydrolysis of the succinimidyl primary chain of PSI units.²⁸ To investigate the release mechanism of FLU@PGA, the cumulative release rates were curve-fitted using three different mathematical models (zero-order, first-order, and Higuchi, Figure S2). As shown in Table S1, the cumulative release rates could best be described by the Higuchi model, which had the highest correlation coefficients (R^2). The results of this study suggested that the release of FLU from FLU@PGA nanoparticles occurred primarily through the diffusion effect, satisfying Fick's law. Thus, the PGA nanoparticles exhibited pH-responsive properties and controlled release behaviors, especially at an alkaline pH in plant phloem.

In Vitro Antifungal Activity of FLU@PGA against Foc TR4. A filter paper method was used to initially evaluate the effect of the PGA nanocarriers alone on Foc TR4 growth. As shown in Figure S4A, 200 mg/L of the PGA nanocarriers did not reduce the mycelial growth of Foc TR4, whereas both FLU alone (55.8 mg/L, TC) and FLU-loaded nanocarriers (200 mg/L) notably inhibited mycelial growth. Then, the fungicidal activity of FLU@PGA was studied using the mycelial growth rate method on PDA (Figure S4B). The results indicated that the PGA nanocarriers have no direct antifungal activity even at a concentration of 800 mg/L (Figure S4C and Figure S5C). FLU@PGA and the conventional formulation of FLU (WP) showed almost equal antifungal activity against Foc TR4 in the same concentration range (0.125 to 2 mg/L). As shown in Table 1, the EC_{50} values of FLU@PGA and FLU (50% WP)

Table 1. In Vitro Fungicidal Activities of the FLU@PGA Nanoparticles and FLU against *Fusarium oxysporum* f. Sp. cubense on the 5th Day

treatment	regression equation	correlation coefficient (r)	$EC_{50} \pm SE$ (mg/L)
FLU@PGA ^a	$y = 1.9956x + 5.5445$	0.9621	0.533 ± 0.054
FLU (WP) ^b	$y = 2.3305x + 5.7337$	0.9458	0.484 ± 0.044

^aFLU@PGA nanoparticles with 27.9% FLU loading. ^b50% WP.

were 0.533 and 0.484 mg/L, respectively. However, the FLU content of the nanobased formulation (27.9%) was much lower than that of the conventional formulation (0.149 vs 0.242 mg/L) when reaching the 50% reduction in mycelial growth (EC_{50}). Therefore, the nanobased formulation could increase the antifungal efficiency of the active ingredient against Foc TR4 by 38.6% compared with that observed using the conventional formulation under *in vitro* conditions. Similarly, nanocarriers could increase the antifungal activity of the encapsulated fungicides, which might be explained by the higher availability of active ingredient in the nanocarrier dispersions, as well as the better solubility in aqueous media.⁴⁰

Long-Distance Translocation of FLU@PGA in Banana Plants. The long-distance translocation and distribution of FLU@PGA was evaluated in potted banana plants by LC–MS/MS. As shown in Figure 4A,C, when the conventional formulation of FLU (WP) was applied to the leaves, only a small amount of FLU was observed in the upper leaves and pseudostems in the 2- and 5-d samples. In addition, FLU was not detected in the underground tissues (Figure 4D,E), suggesting that limited systemicity within plants was a hindering factor for FLU to exert its biological activity *in vivo*, although it displayed good antifungal activity in the *in vitro* bioassays. In contrast, after foliar treatment of FLU@PGA, FLU was detected in all parts of the plant, both above and below the application site, during the 2 to 10 day period. The maximum concentration of FLU in rhizomes and roots was observed at 7 days (Figure 4D,E). The results indicated that the PGA nanocarriers significantly improved the uptake and translocation performance of FLU in banana plants. Furthermore, when an equivalent dose of FLU was applied to the treated leaves in both treatments, the final concentration of FLU detected in the FLU@PGA-treated group was significantly higher than that observed in the group treated with the conventional WP at 5 and 7 days (Figure 4B). These results

may be due to the improved photostability of FLU@PGA (Figure S3).

The biological activities of pesticides against their targets can be significantly influenced by their systemicity within plants, especially for root and vascular diseases.¹⁶ Our results indicated that the PGA nanocarriers could successfully enhance the downward translocation of the fungicide to the rhizomes and roots of banana plants, which confirmed the results of the previous study reporting that the PGA nanocarriers achieved transportation of avermectin from treated rice leaves to the stem.³⁰ This basipetal translocation is a typical phloem transport characteristic. However, it should be noted that the final concentration of FLU in the underground tissues (rhizomes and roots) was much lower than the EC_{50} value at the assayed application dose of FLU@PGA. The aim of this translocation experiment was to investigate the efficacy of FLU@PGA in delivering FLU into banana plants. To further evaluate their activity *in vivo* in greenhouse tests, the application dose should be increased.

Biological Control Effect of FLU@PGA on Foc *In Vivo*.

In pot experiments, compared with the control and the conventional WP treatments, the FLU@PGA treatment was notably more effective in reducing the disease severity of Foc TR4 (Figure 5 and Table 2). On the basis of the *in vivo* translocation experiment results, the application dose of FLU@PGA was increased from 200 to 800 mg/L, and the treatment was administered two times. After 50 days of inoculation, banana plantlets in the control and FLU (WP)-treated groups showed notable symptoms of Fusarium wilt, such as yellowing of the bottom leaves and upper leaf chlorosis (Figure 5A). However, the banana plantlets treated with FLU@PGA showed no visible symptoms or slight yellowing of the bottom leaves (Figure 5A). In addition, reddish-brown discoloration was observed on more than half of the entire rhizome in the control and FLU (WP)-treated plantlets, which was indicative of severe Foc TR4 infections (Figure 5B). In contrast, only small areas of discoloration were present in the FLU@PGA-treated plantlets (Figure 5B). The control and conventional WP-treated plants showed 66.7 and 61.1% disease severity, respectively, while 33.3% disease severity was observed in the FLU@PGA-treated plants (Table 2). In addition, a control efficacy of 50.4% was recorded for the FLU@PGA-treated plants, which was 6 times higher than that observed for the conventional WP-treated plants.

Several systemic fungicides such as propiconazole and azoxystrobin have been used to control banana leaf spot diseases for a long time,⁴¹ and both propiconazole and azoxystrobin have previously been reported to significantly reduce the mycelial growth of Foc *in vitro*.⁸ However, none of them have shown any effects on Fusarium wilt in banana in the field by foliar spray application. In contrast with current systemic fungicides, the FLU@PGA nanoparticles exhibited *in vivo* biological activity after foliar application under our experimental conditions, which suggests that the phloem delivery of fungicide could markedly improve the control efficacy against Foc TR4, although the Foc TR4 infection in FLU@PGA-treated plantlets was not completely suppressed. Further improvement of the delivery efficacy of FLU@PGA is required, which can be realized by the identification of targeted amino acid transporters as well as the optimization of the surface chemistry of nanoparticles with transported substrates. Regardless, our results indicate that the PGA nanocarriers provide a promising chemical control approach for Fusarium

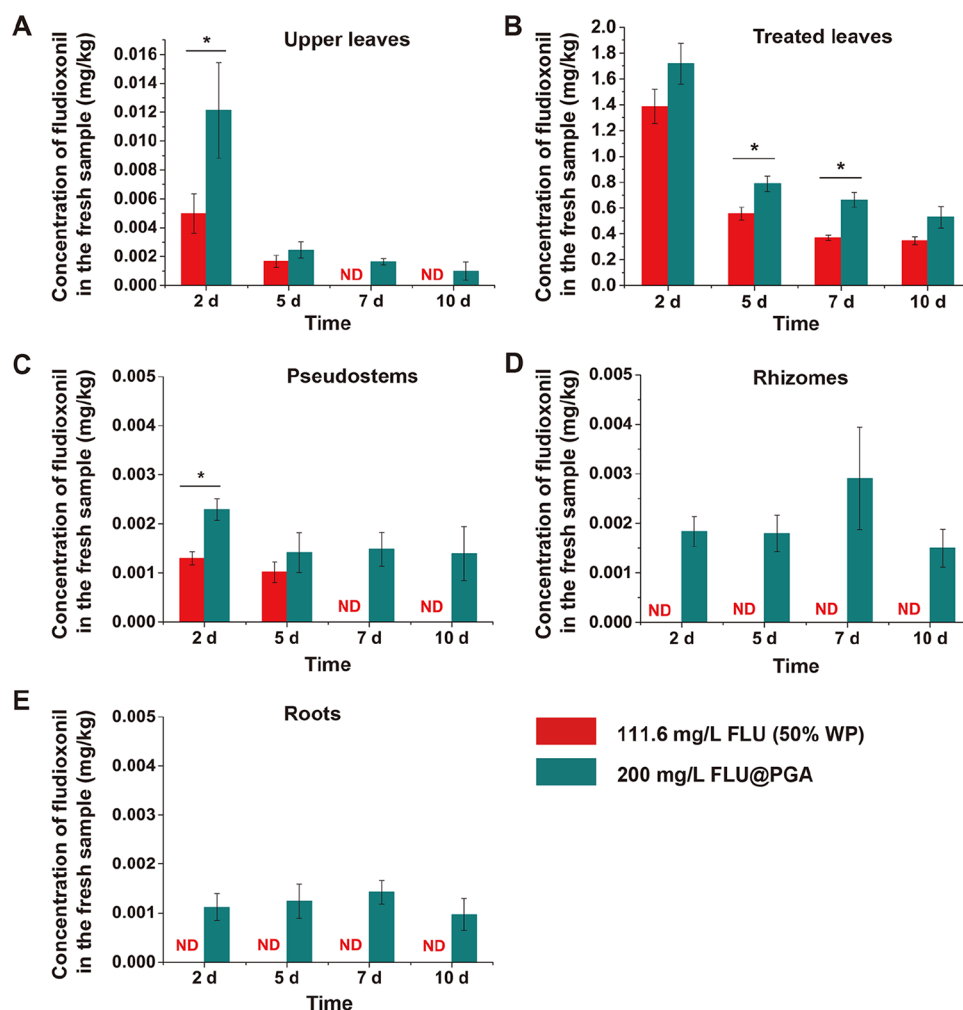


Figure 4. Distribution of FLU in the following different parts of banana plants after foliar application of FLU@PGA (loading rate 27.9%) or an equivalent dose of FLU (50% WP): (A) upper leaves; (B) treated leaves; (C) pseudostems; (D) rhizomes; and (E) roots. The data are presented as the mean \pm SEs ($n = 6$). The Mann–Whitney U test was used to assess significant differences; P values < 0.05 were considered significant (*). ND: not detected.



Figure 5. Symptoms of potted banana plantlets after artificial inoculation with Foc TR4 under greenhouse conditions. FLU@PGA or an equivalent dose of FLU (50% WP) was applied to the leaf at a final concentration of 800 or 446 mg/L, respectively. The control group was treated with the same application solution without FLU@PGA or FLU. (A) External symptoms 50 days post-inoculation and (B) rhizome tissue 50 days post-inoculation. The red arrows indicate the reddish-brown discoloration caused by Foc TR4 infection.

wilt in bananas because the most prevalent fungicides are unable to access infection sites.

Phloem Transport of FLU@PGA in Castor Bean Seedlings. After proving the effectiveness of FLU@PGA against Foc, further studies were performed to determine

Table 2. Control Effect of FLU@PGA Treatment on the Severity of Fusarium Wilt Caused by Foc TR4 under Greenhouse Conditions

treatment	disease severity (%) ^a	percent efficacy of disease control (%)
Control ^b	66.7 \pm 2.4 a	
800 mg/L FLU@PGA	33.3 \pm 4.8 b	50.4 \pm 5.4
446 mg/L FLU ^c	61.1 \pm 2.8 a	8.3 \pm 2.1

^aMean \pm SEs of three replications; the different letters for each treatment indicate significant differences at $P = 0.05$, as determined by Tukey's test. ^bFoliar treatment with an application solution (acetone/water, 1/9, V/V) consisting of 0.15% (V/V) organosilicone surfactant (Silwet L-77). ^cFLU (50% WP) was dissolved in the application solution at the equivalent dose level of FLU@PGA (loading rate of 27.9%).

whether the PGA nanoparticles can enter the plant phloem and to investigate the mechanism of their phloem loading. Because the collection of pure phloem sap is experimentally challenging, there is no feasible method to obtain the phloem sap from bananas. Thus, a specialized model plant, castor bean seedlings,³¹ was chosen to evaluate the uptake and phloem delivery of FLU@PGA.

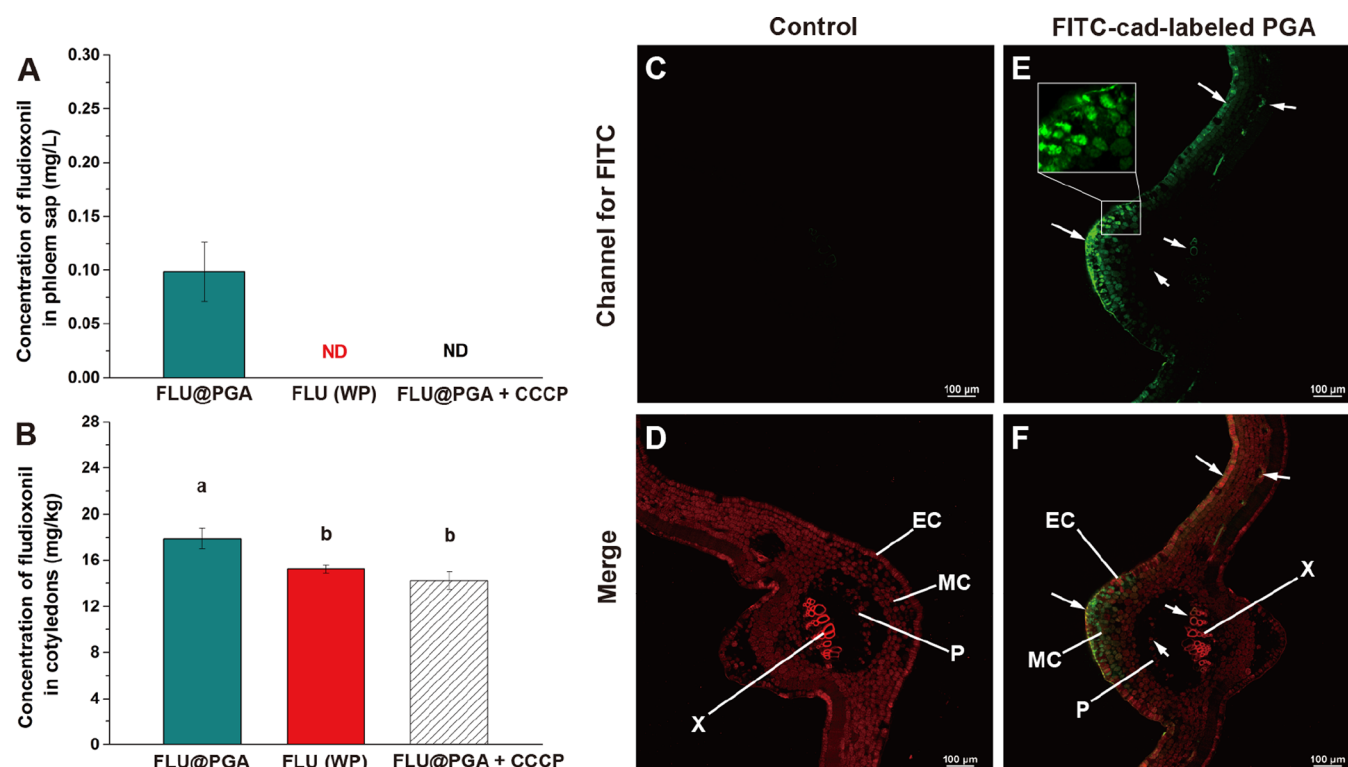


Figure 6. Uptake and phloem transport of the PGA nanoparticles in the castor bean model. **A:** Concentration of FLU in phloem sap. The data are presented as the mean \pm SE with 8 plants for each treatment ($n = 8$). **B:** Concentration of FLU in cotyledon tissues at the end of the experiment represented as mean \pm SE ($n = 8$). The Kruskal–Wallis test was used to assess significant differences at the $P = 0.05$ level, and different letters indicated significant differences. ND, not detected. **C** and **D:** Cross sections of midveins were taken from cotyledons that were incubated without (control) 100 mg/L FITC-cad-labeled PGA nanoparticles. The images were taken with a confocal laser scanning microscope through the following two fluorescence channels with time-separated collection: the green channel for FITC with $\lambda_{\text{ex}} = 488$ nm and $\lambda_{\text{em}} = 500$ –550 nm and the red (pseudocolor) channel for plant autofluorescence with $\lambda_{\text{ex}} = 405$ nm and $\lambda_{\text{em}} = 417$ –477 nm. The images of two channels were merged (**D**, **F**). **E** and **F:** Cotyledons that were incubated with 100 mg/L of FITC-cad-labeled PGA nanoparticles. The arrowheads indicate the presence of FITC-cad-labeled PGA nanoparticles. EC: epidermal cells; MC: mesophyll cells; P: phloem; X: xylem. Scale bar = 100 μm .

After treatment with the conventional formulation (WP), FLU was not detected in the phloem sap of castor bean seedlings, suggesting that it has no phloem mobility (Figure 6A). In contrast, when the cotyledons were treated with the FLU@PGA nanoparticles, FLU could be detected in the phloem sap at a concentration of approximately 0.1 mg/L (Figure 6A), indicating that the PGA nanocarriers could promote the phloem delivery of a nonsystemic fungicide. However, after adding the proton-gradient uncoupler CCCP (50 μM) to the FLU@PGA incubation solution, the phloem loading of FLU was significantly inhibited (Figure 6A). In addition, the concentration of FLU in the FLU@PGA-treated cotyledon tissues was 15 and 20% higher than that observed in the cotyledons treated with the conventional formulation and FLU@PGA + CCCP, respectively (Figure 6B). The majority of plant amino acid transporters use the proton motive force created by H^+ -ATPases to move amino acids across the plasma membrane.⁴² CCCP can dissipate this proton motive force, resulting in a strong inhibition of active transporter-mediated uptake and phloem loading of amino acids.³⁶ In our experiments, 50 μM CCCP significantly inhibited the uptake and phloem loading of FLU@PGA, suggesting the occurrence of FLU@PGA active transport. Although transporter-mediated transport (CCCP-sensitive) contributed to only 20% of the total uptake, it was shown to be crucial for phloem loading of PGA nanocarriers.

To visualize the phloem delivery of the PGA nanocarriers, FITC-cad-labeled PGA (PGA-FITC) was prepared and assembled by covalent bonding (Figure S6). The phloem loading of PGA-FITC nanoparticles was observed by confocal laser scanning microscopy using two fluorescence channels (Figure 6C–F). High levels of plant autofluorescence were collected in one channel and displayed in red pseudocolor (Figure 6D). After 2 h of treatment, the strong green fluorescence of FITC was observed in epidermal and mesophyll cells of the castor bean cotyledon (Figure 6E), indicating that the PGA nanocarriers could be rapidly absorbed by plant cells. In addition, green fluorescence was observed in the phloem and xylem of the midvein as well as the minor vein, suggesting that the PGA-FITC nanoparticles were gradually loaded into the vascular tissues. As castor bean is a symplastic-apoplastic loader,³⁶ there are two possible pathways for the phloem loading of PGA-FITC nanoparticles, namely, the symplastic and apoplastic pathways. No notable fluorescence was observed in the cell wall and intercellular space, suggesting that the phloem loading of PGA-FITC primarily occurred through the symplastic pathway.

Uptake of FLU@PGA Nanoparticles by *Xenopus* Oocytes. The castor bean test showed that the transporter-mediated mechanism may play an important role in PGA transport. However, further identification and characterization of targeted amino acid transporters involved in PGA transport is also very challenging. In our previous study, a plasma

membrane-localized amino acid transporter expressed in the rhizodermis and leaf mesophyll cells of *Arabidopsis thaliana*, AtLHT1, was shown to significantly improve the uptake of a glycine-chlorantraniliprole conjugate (CAP-Gly) by leaf mesophyll protoplasts,²⁵ which has the same amino acid moiety as PGA. Therefore, the possible interaction of AtLHT1 and FLU@PGA was investigated using a *Xenopus* oocyte expression system, which is a powerful system for studying the transport activity of plant membrane transporters.⁴³

As shown in Figure 7, the oocyte uptake of the FLU@PGA nanoparticles was almost 2 times higher than that observed

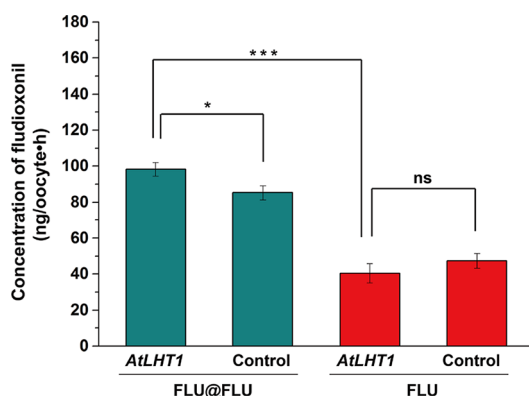


Figure 7. Oocyte uptake of 20 mg/L of the FLU@PGA nanoparticles and an equivalent dose of FLU (50% WP). *Xenopus* oocytes were injected with amino acid transporter AtLHT1 cRNA or water (control). Quantification of FLU levels in each oocyte was performed by LC–MS/MS. The data are presented as the mean \pm SEs, and 10 oocytes were assayed for each treatment ($n = 10$). The Mann–Whitney U test was used to assess significant differences between the two treatments; *, $P < 0.05$; ***, $P < 0.001$; and ns = not significantly different ($P > 0.05$).

using the conventional formulation (WP) of FLU, indicating that the PGA nanocarriers distinctly enhanced the cellular uptake and transmembrane transport of the loaded FLU. Moreover, unlike for FLU uptake, there was a significant difference in FLU@PGA uptake between AtLHT1-expressing oocytes (98.13 ng/oocyte-h) and the water-injected control oocytes (85.14 ng/oocyte-h). Although only a 13% increase in total absorption was observed, the results revealed that the amino acid transporter AtLHT1 was involved in the uptake process of FLU@PGA in addition to passive diffusion.

Our results in *Xenopus* oocytes showed that the same transporter could also stimulate the transmembrane transport of amino acid conjugated nanoparticles at the cellular level. Taken together with the results of the phloem transport according to the castor bean model, the amino acid transporter-mediated mechanism significantly improved the uptake and transport of the PGA nanoparticles from the cellular to the organ level. These findings suggested that our previous strategy for phloem targeting based on a carrier-mediated transport mechanism was also applicable for designing targeted nanocarriers.^{16,26,44} Further investigations should be performed to identify the amino acid transporters involved in the transport of the PGA nanoparticles, specifically in bananas.

According to the abovementioned results, the mechanisms of the phloem loading and pH-sensitive release of the PGA nanocarriers in plants are proposed in Figure 8. The PGA nanocarriers are first absorbed by epidermal and mesophyll

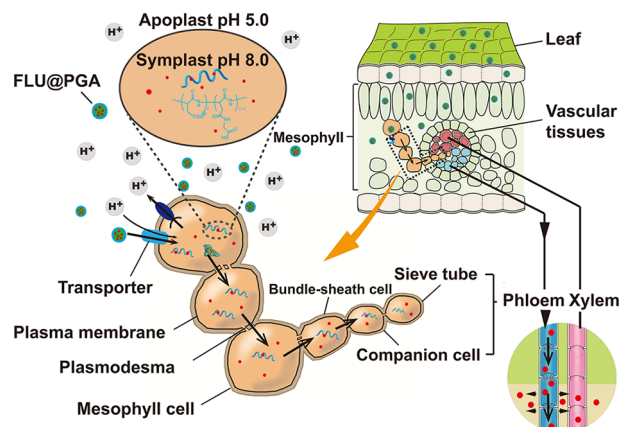


Figure 8. Schematic diagrams depicting the transport pathway and transporter-mediated phloem loading of the PGA nanocarriers and their pH-sensitive controlled release in plants.

cells through amino acid transporters and then may move cell-to-cell through the plasmodesmata to the vascular tissues. After crossing the plasma membrane to reach the symplast ($pH \approx 8.0$), the PGA nanocarriers are hydrolyzed and the encapsulated FLU is substantially released in the symplast. Finally, FLU can symplastically move to the sieve tubes through plasmodesmata.

The plant plasma membrane is one of the most important barriers preventing systemic agrochemicals from reaching the vascular tissues because molecules must cross the cell plasma membrane at least once to enter xylem- and/or phloem-conducting cells.¹⁶ Many attempts have been made to design nanodelivery systems for improving the transmembrane permeation of pesticides.^{29,45} However, those studies primarily focused on the optimization of key physicochemical properties of nanoparticles, such as their size and shape. For example, nanoparticles with a diameter less than 30 nm were considered ideal for passing through specific plant cell wall pores to reach the plasma membrane.²⁹ How the nanoparticles cross the plant cell membrane, including whether they use transporters/channels, remains largely unknown.⁴⁶ Our results demonstrated a new mechanism to further improve the transmembrane transport and phloem loading of nanoparticles in plants.

In conclusion, glycine methyl ester-modified polysuccinimide nanoparticles were selected as nanocarriers for the phloem-targeted delivery of the fungicide fludioxonil to control Fusarium wilt in banana. The PGA nanocarriers showed pH-sensitive controlled release, especially under alkaline pH in plant phloem. The FLU@PGA nanoparticles increased the antifungal efficacy of FLU against the pathogen by approximately 40% compared with that of the conventional WP formulation. *In vivo* experiments in banana plants demonstrated that the PGA nanocarriers can successfully achieve the downward delivery of FLU to the plant rhizomes and roots after foliar application, allowing it to exert its biological activity against the pathogen Foc. More importantly, the PGA nanocarriers were observed to interact with a plant amino acid transporter, enhancing their cellular uptake and phloem loading. This is the first time that the phloem-targeted delivery of fungicide using transporter-mediated nanocarriers has been reported, which provides a new promising strategy to further improve phloem targeting of manufactured nanoparticles. This strategy can also be extended to improve the

biological performance of pesticides against other plant vascular diseases, as well as phloem-sucking insects. Furthermore, these controlled and targeted pesticide delivery systems have great potential to further improve the utilization efficiency of agrochemicals and reduce environmental risks.

■ ASSOCIATED CONTENT

Supporting Information

The Supporting Information is available free of charge at <https://pubs.acs.org/doi/10.1021/acs.jafc.0c07028>.

Thermogravimetric analysis, release mechanism, photostability and *in vitro* antifungal activity of FLU@PGA nanoparticles, LC–MS/MS method validation procedures, LC–MS/MS chromatograms of fludioxonil in banana samples, and FTIR spectra of PGA-FITC nanoparticles (PDF).

■ AUTHOR INFORMATION

Corresponding Authors

Jinliang Jia – State Key Laboratory for Conservation and Utilization of Subtropical Agro-bioresources, South China Agricultural University, Guangzhou, Guangdong 510642, China; Key Laboratory of Natural Pesticide and Chemical Biology, Ministry of Education and Key Laboratory for Biobased Materials and Energy of Ministry of Education, South China Agricultural University, Guangzhou, Guangdong 510642, China; Guangdong Laboratory for Lingnan Modern Agricultural Science and Technology, Guangzhou, Guangdong 510642, China; Email: jjiajinliang@scau.edu.cn

Hanhong Xu – State Key Laboratory for Conservation and Utilization of Subtropical Agro-bioresources, South China Agricultural University, Guangzhou, Guangdong 510642, China; Key Laboratory of Natural Pesticide and Chemical Biology, Ministry of Education, South China Agricultural University, Guangzhou, Guangdong 510642, China; Guangdong Laboratory for Lingnan Modern Agricultural Science and Technology, Guangzhou, Guangdong 510642, China; orcid.org/0000-0001-7841-2396; Email: hxxu@scau.edu.cn

Authors

Hanxiang Wu – State Key Laboratory for Conservation and Utilization of Subtropical Agro-bioresources, South China Agricultural University, Guangzhou, Guangdong 510642, China; Key Laboratory of Natural Pesticide and Chemical Biology, Ministry of Education, South China Agricultural University, Guangzhou, Guangdong 510642, China

Pengtong Hu – Key Laboratory of Natural Pesticide and Chemical Biology, Ministry of Education and Key Laboratory for Biobased Materials and Energy of Ministry of Education, South China Agricultural University, Guangzhou, Guangdong 510642, China

Ye Xu – Key Laboratory of Natural Pesticide and Chemical Biology, Ministry of Education and Key Laboratory for Biobased Materials and Energy of Ministry of Education, South China Agricultural University, Guangzhou, Guangdong 510642, China

Chunxia Xiao – Key Laboratory of Natural Pesticide and Chemical Biology, Ministry of Education, South China Agricultural University, Guangzhou, Guangdong 510642, China

Zhibin Chen – Key Laboratory of Natural Pesticide and Chemical Biology, Ministry of Education, South China Agricultural University, Guangzhou, Guangdong 510642, China

Xiaojing Liu – Key Laboratory of Natural Pesticide and Chemical Biology, Ministry of Education, South China Agricultural University, Guangzhou, Guangdong 510642, China

Complete contact information is available at: <https://pubs.acs.org/doi/10.1021/acs.jafc.0c07028>

Author Contributions

[†]H.W. and P.H. contributed equally to this work.

Notes

The authors declare no competing financial interest.

■ ACKNOWLEDGMENTS

We thank Dr. Chunyu Li at the Institution of Fruit Tree Research, Guangdong Academy of Agricultural Sciences for kindly providing Foc TR4. This work was supported by the Key Research and Development Project of Guangdong Province (2019B020217003), the National Natural Science Foundation of China (31801777), the Guangdong Provincial Innovation Team for General Key Technologies in Modern Agricultural Industry (2019KJ140), and the China Postdoctoral Science Foundation (2018M643104).

■ REFERENCES

- (1) Ploetz, R. C. Fusarium Wilt of Banana. *Phytopathology* **2015**, *105*, 1512–1521.
- (2) Dita, M.; Barquero, M.; Heck, D.; Mizubuti, E. S. G.; Staver, C. P. Fusarium Wilt of Banana: Current Knowledge on Epidemiology and Research Needs Toward Sustainable Disease Management. *Front. Plant Sci.* **2018**, *9*, 1468.
- (3) Stokstad, E. Banana Fungus Puts Latin America on Alert. *Science* **2019**, *365*, 207–208.
- (4) Guo, L.; Yang, L.; Liang, C.; Wang, G.; Dai, Q.; Huang, J. Differential Colonization Patterns of Bananas (*Musa* Spp.) by Physiological Race 1 and Race 4 Isolates of *Fusarium Oxysporum* f.sp. *Cubense*. *J. Phytopathol.* **2015**, *163*, 807–817.
- (5) Li, C.; Chen, S.; Zuo, C.; Sun, Q.; Ye, Q.; Yi, G.; Huang, B. The Use of GFP-Transformed Isolates to Study Infection of Banana with *Fusarium Oxysporum* f. sp. *Cubense* Race 4. *Eur. J. Plant Pathol.* **2011**, *131*, 327–340.
- (6) Li, C.; Yang, J.; Li, W.; Sun, J.; Peng, M. Direct Root Penetration and Rhizome Vascular Colonization by *Fusarium Oxysporum* f. sp. *Cubense* Are the Key Steps in the Successful Infection of Brazil Cavendish. *Plant Dis.* **2017**, *101*, 2073–2078.
- (7) Bubici, G.; Kaushal, M.; Prigigallo, M. I.; Cabanás, C. G.-L.; Mercado-Blanco, J. Biological Control Agents Against Fusarium Wilt of Banana. *Front. Microbiol.* **2019**, *10*, 616.
- (8) Nel, B.; Steinberg, C.; Labuschagne, N.; Viljoen, A. Evaluation of Fungicides and Sterilants for Potential Application in the Management of Fusarium Wilt of Banana. *Crop Prot.* **2007**, *26*, 697–705.
- (9) Camara, M. C.; Campos, E. V. R.; Monteiro, R. A.; do Espírito Santo Pereira, A.; de Freitas Proença, P. L.; Fraceto, L. F. Development of Stimuli-Responsive Nano-Based Pesticides: Emerging Opportunities for Agriculture. *J. Nanobiotechnol.* **2019**, *17*, 100.
- (10) Zhao, X.; Cui, H.; Wang, Y.; Sun, C.; Cui, B.; Zeng, Z. Development Strategies and Prospects of Nano-Based Smart Pesticide Formulation. *J. Agric. Food Chem.* **2018**, *66*, 6504–6512.
- (11) Kumar, S.; Nehra, M.; Dilbaghi, N.; Marrazza, G.; Hassan, A. A.; Kim, K.-H. Nano-Based Smart Pesticide Formulations: Emerging Opportunities for Agriculture. *J. Controlled Release* **2019**, *294*, 131–153.

- (12) Liang, J.; Yu, M.; Guo, L.; Cui, B.; Zhao, X.; Sun, C.; Wang, Y.; Liu, G.; Cui, H.; Zeng, Z. Bioinspired Development of P(St-MAA)-Avermectin Nanoparticles with High Affinity for Foliage To Enhance Folia Retention. *J. Agric. Food Chem.* **2018**, *66*, 6578–6584.
- (13) Fischer, J.; Beckers, S. J.; Yiamsawas, D.; Thines, E.; Landfester, K.; Wurm, F. R. Targeted Drug Delivery in Plants: Enzyme-Responsive Lignin Nanocarriers for the Curative Treatment of the Worldwide Grapevine Trunk Disease Esca. *Adv. Sci.* **2019**, *6*, No. 1802315.
- (14) Augusto, J.; Brennen, T. B. Assessing Systemicity of Peanut Fungicides Through Bioassay of Plant Tissues with *Sclerotium Rolfsii*. *Plant Dis.* **2012**, *96*, 330–337.
- (15) Tjamos, E. C. Problems and Prospects in Controlling Verticillium Wilt. In *Vascular wilt diseases of plants: Basic Studies and Control*; Tjamos, E. C., Beckman, C. H., Eds.; Springer Berlin Heidelberg, 1989; 441–456.
- (16) Wu, H.; Xu, H.; Marivingt-Mounir, C.; Bonnemain, J.-L.; Chollet, J.-F. Vectorizing Agrochemicals: Enhancing Bioavailability via Carrier-Mediated Transport. *Pest Manag. Sci.* **2019**, *75*, 1507–1516.
- (17) Zhao, P.; Cao, L.; Ma, D.; Zhou, Z.; Huang, Q.; Pan, C. Translocation, Distribution and Degradation of Prochloraz-Loaded Mesoporous Silica Nanoparticles in Cucumber Plants. *Nanoscale* **2018**, *10*, 1798–1806.
- (18) Zhang, Y.; Yan, J.; Avellan, A.; Gao, X.; Matyjaszewski, K.; Tilton, R. D.; Lowry, G. V. Temperature- and pH-Responsive Star Polymers as Nanocarriers with Potential for *in Vivo* Agrochemical Delivery. *ACS Nano* **2020**, *14*, 10954–10965.
- (19) Hennion, N.; Durand, M.; Vriet, C.; Doidy, J.; Maurousset, L.; Lemoine, R.; Pourtau, N. Sugars En Route to the Roots. Transport, Metabolism and Storage within Plant Roots and towards Microorganisms of the Rhizosphere. *Physiol. Plant.* **2019**, *165*, 44–57.
- (20) Tegeder, M. Transporters for Amino Acids in Plant Cells: Some Functions and Many Unknowns. *Curr. Opin. Plant Biol.* **2012**, *15*, 315–321.
- (21) Suter, F. M.; De Caro, V.; Giannola, L. I. Small Endogenous Molecules as Moieties to Improve Targeting of CNS Drugs. *Expert Opin. Drug Deliv.* **2017**, *14*, 93–107.
- (22) Saraiva, C.; Praça, C.; Ferreira, R.; Santos, T.; Ferreira, L.; Bernardino, L. Nanoparticle-Mediated Brain Drug Delivery: Overcoming Blood–Brain Barrier to Treat Neurodegenerative Diseases. *J. Controlled Release* **2016**, *235*, 34–47.
- (23) Fernandes, J.; Ghate, M. V.; Mallik, S. B.; Lewis, S. A. Amino Acid Conjugated Chitosan Nanoparticles for the Brain Targeting of a Model Dipeptidyl Peptidase-4 Inhibitor. *Int. J. Pharm.* **2018**, *547*, 563–571.
- (24) Yao, G.; Wen, Y.; Zhao, C.; Xu, H. Novel Amino Acid Ester–Chlorantraniliprole Conjugates: Design, Synthesis, Phloem Accumulation and Bioactivity. *Pest Manag. Sci.* **2017**, *73*, 2131–2137.
- (25) Yan, C.; Ying, Y.; Li, J.; Tian, Y.; Lin, F.; Xu, H. AtLHT1 Transporter Can Facilitate the Uptake and Translocation of a Glycineric–Chlorantraniliprole Conjugate in *Arabidopsis thaliana*. *J. Agric. Food Chem.* **2018**, *66*, 12527–12535.
- (26) Wu, H.; Marhadour, S.; Lei, Z. W.; Yang, W.; Marivingt-Mounir, C.; Bonnemain, J. L.; Chollet, J. F. Vectorization of Agrochemicals: Amino Acid Carriers Are More Efficient than Sugar Carriers to Translocate Phenylpyrrole Conjugates in the *Ricinus* System. *Environ. Sci. Pollut. Res.* **2018**, *25*, 14336–14349.
- (27) Wu, X.; Qin, R.; Wu, H.; Yao, G.; Zhang, Y.; Li, P.; Xu, Y.; Zhang, Z.; Yin, Z.; Xu, H. Nanoparticle-Immersed Paper Imprinting Mass Spectrometry Imaging Reveals Uptake and Translocation Mechanism of Pesticides in Plants. *Nano Res.* **2020**, *13*, 611–620.
- (28) Hill, M. R.; MacKrell, E. J.; Forsthoefel, C. P.; Jensen, S. P.; Chen, M.; Moore, G. A.; He, Z. L.; Sumerlin, B. S. Biodegradable and pH-Responsive Nanoparticles Designed for Site-Specific Delivery in Agriculture. *Biomacromolecules* **2015**, *16*, 1276–1282.
- (29) Xin, X.; He, Z.; Hill, M. R.; Niedz, R. P.; Jiang, X.; Sumerlin, B. S. Efficiency of Biodegradable and pH-Responsive Polysuccinimide Nanoparticles (PSI-NPs) as Smart Nanodelivery Systems in Grapefruit: *In Vitro* Cellular Investigation. *Macromol. Biosci.* **2018**, *18*, No. 1800159.
- (30) Wang, G.; Xiao, Y.; Xu, H.; Hu, P.; Liang, W.; Xie, L.; Jia, J. Development of Multifunctional Avermectin Poly (Succinimide) Nanoparticles to Improve Bioactivity and Transportation in Rice. *J. Agric. Food Chem.* **2018**, *66*, 11244–11253.
- (31) Marhadour, S.; Wu, H.; Yang, W.; Marivingt-Mounir, C.; Bonnemain, J. L.; Chollet, J. F. Vectorisation of Agrochemicals via Amino Acid Carriers: Influence of the Spacer Arm Structure on the Phloem Mobility of Phenylpyrrole Conjugates in the *Ricinus* System. *Pest Manag. Sci.* **2017**, *73*, 1972–1982.
- (32) Torma, V.; Gyenes, T.; Szakács, Z.; Noszál, B.; Némethy, Á.; Zrínyi, M. Novel Amino Acid-Based Polymers for Pharmaceutical Applications. *Polym. Bull.* **2007**, *59*, 311–318.
- (33) Liang, W.; Yu, A.; Wang, G.; Zheng, F.; Hu, P.; Jia, J.; Xu, H. A Novel Water-Based Chitosan-La Pesticide Nanocarrier Enhancing Defense Responses in Rice (*Oryza Sativa* L) Growth. *Carbohydr. Polym.* **2018**, *199*, 437–444.
- (34) González-Curbelo, M. Á.; Hernández-Borges, J.; Ravelo-Pérez, L. M.; Rodríguez-Delgado, M. A. Insecticides Extraction from Banana Leaves Using a Modified QuEChERS Method. *Food Chem.* **2011**, *125*, 1083–1090.
- (35) Huang, Y. H.; Wang, R. C.; Li, C. H.; Zuo, C. W.; Wei, Y. R.; Zhang, L.; Yi, G. J. Control of Fusarium Wilt in Banana with Chinese Leek. *Eur. J. Plant Pathol.* **2012**, *134*, 87–95.
- (36) Delétage-Grandon, C.; Chollet, J. F.; Faucher, M.; Rocher, F.; Komor, E.; Bonnemain, J. L. Carrier-Mediated Uptake and Phloem System of a 350-Dalton Chlorinated Xenobiotic with an α -Amino Acid Function. *Plant Physiol.* **2001**, *125*, 1620–1632.
- (37) Wang, J.; Lei, Z.; Wen, Y.; Mao, G.; Wu, H.; Xu, H. A Novel Fluorescent Conjugate Applicable to Visualize the Translocation of Glucose-Fipronil. *J. Agric. Food Chem.* **2014**, *62*, 8791–8798.
- (38) Sharma, S.; Singh, S.; Ganguli, A. K.; Shanmugam, V. Anti-Drift Nano-Stickers Made of Graphene Oxide for Targeted Pesticide Delivery and Crop Pest Control. *Carbon* **2017**, *115*, 781–790.
- (39) Wu, H.; Marhadour, S.; Lei, Z.-W.; Dugaro, É.; Gaillard, C.; Porcheron, B.; Marivingt-Mounir, C.; Lemoine, R.; Chollet, J.-F.; Bonnemain, J.-L. Use of D-Glucose–Fenpiclonil Conjugate as a Potent and Specific Inhibitor of Sucrose Carriers. *J. Exp. Bot.* **2017**, *68*, 5599–5613.
- (40) Machado, T. O.; Beckers, S. J.; Fischer, J.; Müller, B.; Sayer, C.; de Araújo, P. H. H.; Landfester, K.; Wurm, F. R. Bio-Based Lignin Nanocarriers Loaded with Fungicides as a Versatile Platform for Drug Delivery in Plants. *Biomacromolecules* **2020**, *21*, 2755–2763.
- (41) De Bellaire, L. D. L.; Fouré, E.; Abadie, C.; Carlier, J. Black Leaf Streak Disease Is Challenging the Banana Industry. *Fruits* **2010**, *65*, 327–342.
- (42) Ortiz-Lopez, A.; Chang, H.-C.; Bush, D. R. Amino Acid Transporters in Plants. *Biochim. Biophys. Acta* **2000**, *1465*, 275–280.
- (43) Larsen, B.; Xu, D.; Halkier, B. A.; Nour-Eldin, H. H. Advances in Methods for Identification and Characterization of Plant Transporter Function. *J. Exp. Bot.* **2017**, *68*, 4045–4056.
- (44) Jiang, X.; Xie, Y.; Ren, Z.; Ganeteg, U.; Lin, F.; Zhao, C.; Xu, H. Design of a New Glutamine–Fipronil Conjugate with α -Amino Acid Function and Its Uptake by *A. thaliana* Lysine Histidine Transporter 1 (AtLHT1). *J. Agric. Food Chem.* **2018**, *66*, 7597–7605.
- (45) Jia, J.-L.; Zhu, L.; Jin, X.-Y.; Wang, J.; Zhang, W.; Wu, H.-X.; Xu, H.-H. 2,4-Dichlorophenoxyacetic Acid Functionalized Gold Nanoparticles: Synthesis, Characterization and Biological Effects. *J. Mater. Chem. B* **2014**, *2*, 3299–3305.
- (46) Tripathi, D. K.; Shweta; Singh, S.; Singh, S.; Pandey, R.; Singh, V. P.; Sharma, N. C.; Prasad, S. M.; Dubey, N. K.; Chauhan, D. K. An Overview on Manufactured Nanoparticles in Plants: Uptake, Translocation, Accumulation and Phytotoxicity. *Plant Physiol. Biochem.* **2017**, *110*, 2–12.



Long-lasting repellent activities of eco-friendly polyurethane system for controlled citral against melon fly

Feng Zheng^{a,b}, Tiantian Li^b, Hanhong Xu^b, Pengtong Hu^{a,b}, Ruifei Wang^b, Zhixiang Zhang^{b,*}, Jinliang Jia^{a,b,**}

^a Key Laboratory for Biobased Materials and Energy of Ministry of Education, College of Materials and Energy, South China Agricultural University, Guangzhou, 510642, China

^b Key Laboratory of Natural Pesticide & Chemical Biology, Ministry of Education, South China Agricultural University, Guangzhou, 510642, China

ARTICLE INFO

Keywords:

Eco-friendly
Waterborne polyurethane
Citral
Melon fly control
Plant protection

ABSTRACT

Using plant essential oil instead of chemical pesticides to control melon fly (*Bactrocera cucurbitae* (Coquillett)) is still a great challenge in agricultural practices, which must effectively slow down the volatility rate of plant essential oil. In this study, citral as a natural plant essential oil was blended with environmentally friendly castor oil based waterborne polyurethane (PU). The interaction, chemical resistance, adhesion property and sustained release behavior of the composites with different citral content were clarified, and the efficacies against the melon fly under field conditions were explored. The results indicated that the composites prepared exhibited excellent adhesion behavior on bitter gourds (*Momordica charantia* L.) even under rainfall washing, meanwhile the chemical resistance of composites could be tailored via controlling citral content. Low citral content composite films could be washed off by alcohol without worrying about the safety of that on crops. The composite prepared exhibited long-lasting repellent behavior against melon fly. The composite can be prepared via a simple technology and low cost, which has great value for plant essential oil applied in agriculture and can provide a new approach for melon fly control.

1. Introduction

Melon fly, *Bactrocera cucurbitae* (Coquillett) (Diptera: Tephritidae) is widely distributed in more than 30 countries and regions of the world, mainly damaging cucurbits (Dhillon et al., 2005; Kandakoor et al., 2019), amongst these melon fly damage of bitter gourds (*Momordica charantia* L.) has become a major limiting factor to obtain high yield and good quality fruits. Several management strategies have been developed and usually applied to control the damage by melon fly. Bagging of fruit minimizes melon fly infestation; field sanitation can break the reproduction cycle (Klungness et al., 2005) and other strategies, such as par-pheromone lures/cue-lure traps, host plant resistance are effective to control melon fly (Prokopy et al., 2003; Sen et al., 2019). However, these strategies are not sufficient to widely apply due to high labor cost and time requirements, especially for farmers in China, which is unacceptable. In addition, chemical control is the most common and effective practices in agricultural ascribe to its efficient, handy and economic

characteristics. Such as deltamethrin and malathion were widely used to control melon fly resulting in minimum fruit infestation (Gupta et al., 2012; Sunil et al., 2016). Even so, limitations of chemical control are existed that bitter gourds need to be picked up at short intervals for self-consumption and marketing. It is necessary to rely on safer pesticides with reasonable waiting periods and low residual toxicity to ensure environment friendly and human health (Dhillon et al., 2005).

The development of botanical pesticides has attracted widely attention due to lower environmental and biological impact. Citral extracts from the plant essential oil, has been found as an efficient natural botanical pesticide to repel many pests (Ju et al., 2020; Yang et al., 2014), such as *Rhopalosiphum padi* L. (Pascual-Villalobos et al., 2017), *Megalurothrips sjostedti* (Diabate et al., 2019), *Aedes albopictus* (Wu et al., 2013). However, volatile nature of citral limited its further application under field conditions (Oyedele et al., 2002). In order to improve the effective utilization of plant essential oil, several techniques had been developed (Gao et al., 2020; Yang et al., 2018). For example, previous

* Corresponding author.

** Corresponding author. Key Laboratory for Biobased Materials and Energy of Ministry of Education, College of Materials and Energy, South China Agricultural University, Guangzhou, 510642, China.

E-mail addresses: zdsys@scau.edu.cn (Z. Zhang), jiajinliang@scau.edu.cn (J. Jia).

<https://doi.org/10.1016/j.cropro.2021.105745>

Received 9 January 2021; Received in revised form 15 June 2021; Accepted 17 June 2021

Available online 19 June 2021

0261-2194/© 2021 Published by Elsevier Ltd.

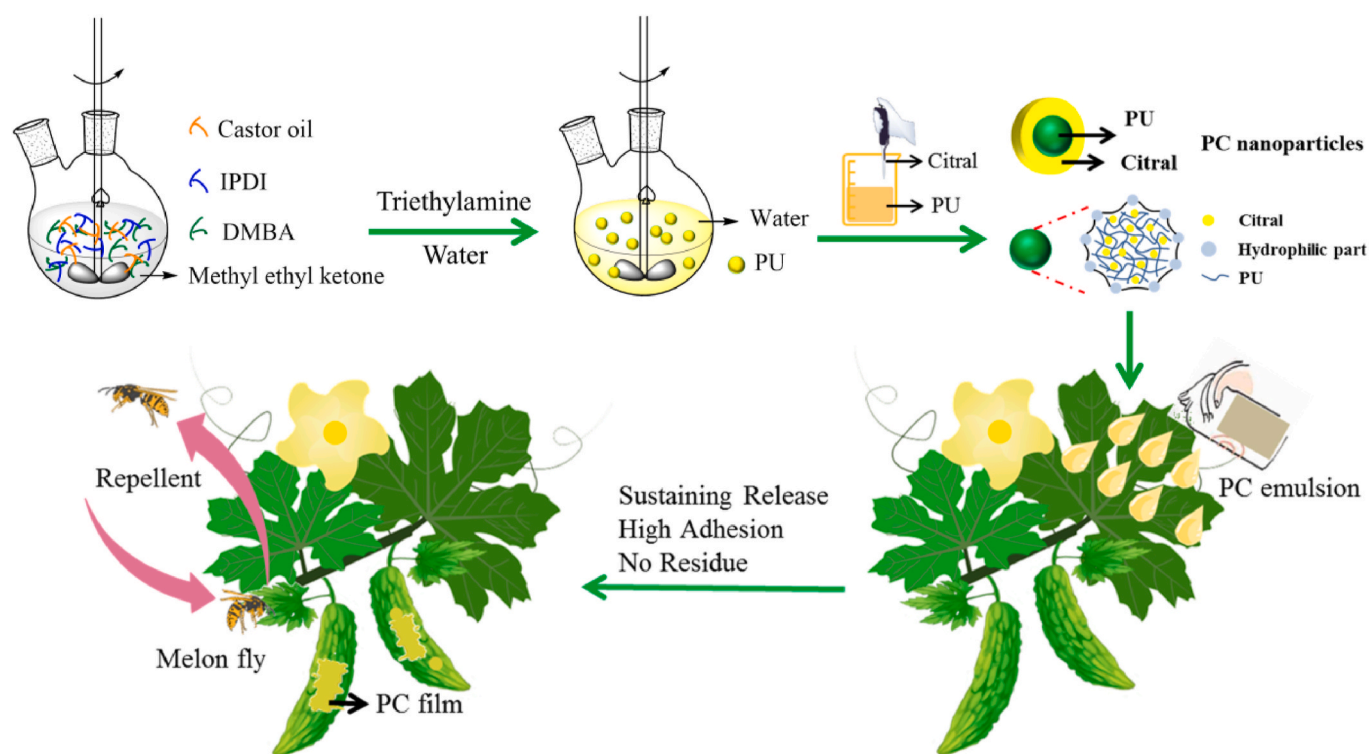


Fig. 1. Schematic illustration of the preparation of composites and its application for long-lasting repellent behavior against melon fly.

research had suggested that different content clove bud essential oil was incorporated into citrus pectin to prepare an antimicrobial film, which had continuous antibacterial activities against many bacteria (Nisar et al., 2018). Wu et al. reported a Herba Schizonepetae oil microcapsule with gelatin and gum Arabic as wall materials. It was found that the microcapsule could effectively repelled *Aedes (Stegomyia) albopictus* in rearing cage for 4–5 h (Wu et al., 2013). Although there has been much progress in slowing the volatility rate of plant essential oil, these technologies usually suffer from high cost and complicated technology, which greatly restricts their application. Therefore, developing an efficient, facile and environment friendly application method for controlling melon fly is a major challenge for agricultural production.

Castor oil-based waterborne polyurethanes are versatile polymers with environment friendly and degradability (Zhang et al., 2017; Zheng et al., 2020), which are already widely used in agriculture (Gurunathan et al., 2013). For example, the existed research showed that avermectin nano-emulsions with castor oil-based polyurethane as the carrier were prepared via emulsion solvent evaporation, which had a controlled release effect and decreased of photolysis rate on avermectin (Zhang et al., 2018). In addition, the hydrogen bonding were able to form between urea and urethane groups of castor oil-based waterborne polyurethane and hydroxyl, carboxyl and aldehyde groups of foliage surface, which could promote a longer pesticide retention (Qin et al., 2017). Although these studies demonstrate excellent sustained release and adhesion performances of castor oil-based waterborne polyurethane, significant slowing down the volatility rate of plant essential oil for controlling melon fly has been less studied in agricultural production.

This work attempted to develop a sustained release composite with citral as active constituent to control melon fly on bitter gourd. In detail, citral was mixed into environmentally friendly castor oil based waterborne polyurethane by blending, resulting in citral imbedded in polyurethane films. The chemical resistance, wettability, adhesion and sustained-release behavior of the composites were investigated. Besides, efficacies against melon fly under field conditions were explored. The schematic illustration of the preparation of composites and its

application for long-lasting repellent behavior against melon fly was shown in Fig. 1. This work obtains desirable properties and provides a potential approach with simple technology and low cost to control melon fly.

2. Materials and methods

2.1. Materials

Castor oil (OH number: 164 mg KOH/g) was obtained from Fuyu Chemical Co. Ltd. (Tianjin, China). Dimethylol butanoic acid (DMBA) was obtained from Bailingwei Technology Co. Ltd. (Beijing, China). Isophorone diisocyanate (IPDI) was obtained from Wengjiang Chemical Reagent Co. Ltd. (Guangdong, China). Dibutyltin dilaurate (DBTDL) was obtained from Fuchen Chemical Reagent Factory. (Tianjin, China). Triethylamine (TEA) and citral were obtained from Aladdin reagent. Methyl ethyl ketone (MEK) was obtained from Hongda Chemical reagent. (Tianjin, China). All chemical reagents were used without further purification. Bitter gourd (*Momordica charantia* L.) and melon fly (*Bactrocera cucurbitae*) were supplied by Key Laboratory of Natural Pesticide & Chemical Biology, Ministry of Education at South China Agricultural University (Guangzhou, China). Sexually mature female adults were selected for bioassay experiments, bitter gourds were grown in the field without being exposed to any chemicals.

2.2. Preparation of castor oil-based anionic waterborne polyurethane emulsion

Castor oil-based anionic waterborne polyurethane (PU) was synthesized by the previously reported method (Liang et al., 2018a). 15 g Castor oil, 3.84 g DMBA and 9.68 g IPDI were mixed and continuously stirred at 78 °C for 10 min to obtain uniformly distributed mixture. Then, 25 μ L DBTDL as catalyst was added into the double neck flask, 40 mL MEK were added into mixture to reduce the viscosity after the mixture almost can't flow. After homogenizing the mixture for 4 h at

Table 1
Repellent effect of free citral and PC-0.5 against melon fly female adults.

Time (min)	Percentage repellency (%)	
	Citral	PC-0.5
5	69.53 ± 2.23	67.49 ± 3.49
10	77.75 ± 2.86	73.84 ± 4.12
15	86.09 ± 2.82	76.62 ± 2.19
20	88.99 ± 2.50	82.30 ± 0.70
25	86.10 ± 5.55	85.80 ± 3.33
30	69.30 ± 3.38	88.25 ± 2.84
45	58.41 ± 4.47	91.15 ± 0.35
60	47.17 ± 3.00	91.15 ± 0.35

78 °C, the mixture was cooled to room temperature and TEA was added to neutralize free COOH under high-speed stirring for 30 min. Finally, an appropriate amount of distilled water was introduced in reaction, stirred for another 2 h and evaporated MEK to obtain PU.

2.3. Preparation of PU/citral composite emulsions (PC-R)

Designated volumes of citral were added in PU dispersions to prepare a series of PU/citral mixtures with different percentages of citral. The mixtures were vortexed continuously with a turbine mixer for 5–10 min and sonicated for 5 min to obtain a PC-R composite emulsion, where R represented the volume percentage of citral in composite emulsions (R = 0, 0.5, 1.0, 1.5, 2.0). PC-R emulsions were casted in a silicon mold to obtain corresponding composite films at room temperature and the specific compositions of PC-R films showed in Table 1. Noteworthy was that no additional organic solvent was needed to add in the preparation.

2.4. Characterization

The average particle size, size distribution and zeta potential of the PC samples were recorded on a laser particle sizer (Nano ZSE, Malvern Instruments, UK). The morphology of the dried samples was observed using transmission electron microscope (TEM, JEM-1200EX, JEOL, Japan) and the samples were obtained with phosphor-tungstic acid as stain agent. The stability of waterborne PU dispersion was evaluated by visual inspection, no obvious layered structures were observed in emulsions after storage for over 3 months at ambient temperature, which were considered stable. The wettability of samples was obtained by contact angle and surface tension via the contact angle measurement (Powereach JC2000C1 goniometer, Zhongchen Science & Technology Co., Ltd., China).

The gel content (G) of film samples was measured based on the Soxhlet extraction method (Feng et al., 2018). The specific operation steps were as follows: First, samples of a known weight (M_0) wrapped in filter paper and weighted (M_1). Then, tetrahydrofuran as the extracting agent was used to adequately extract the film samples for 6 h. After that, the residual samples were vacuum dried to a constant weight M_2 . In the end, the gel content (G) was calculated by equation:

$$G (\%) = \frac{M_0 - (M_1 - M_2)}{M_0} \times 100$$

For the chemical resistance of film samples, the dried films were accurately weighed as M_0 and immersed in distilled water or alcohol. The weights of the films after immersion were measured as M_1 . Average values of three replicates of each sample were taken. The swelling of the films in alcohol was recorded with a camera and the water absorption (W) was calculated by equation:

$$W (\%) = \frac{(M_1 - M_0)}{M_0} \times 100$$

2.5. Adhesion property of the PC compound emulsion

The bitter gourds were used to test the adhesion behavior of the PC composite emulsions, and the sample PC-0.5 was chosen due to its security which could be washed off by alcohol. The PC-0.5, PU emulsions were diluted for 30 times with distilled water, and as a comparison, a free citral suspension with the same citral concentration was prepared through distilled water and Tween-80. All samples were sprayed evenly on the bitter gourds and allowed to dry for 2 h. Water was uniformly sprayed on the treated bitter gourds to simulate rainwater. The surface of the bitter gourds with or without washing was characterized using a scanning electron microscope (SEM, Merlin Compact, Zeiss, Germany). Each experiment was conducted in triplicates.

2.6. Repellent bioassay

The repellent activity of PC emulsions against melon fly was subjected using a Y-tube olfactometer according to the methods previously reported (Wu et al., 2013). The head of the Y-tube was 24 cm long, the arms were 26 cm long and the diameter was 4 cm. The Y-tube olfactometer consisted of sample chambers, vacuum pumps, water towers, drying towers and tasteless silicone tubes. The purified external air was led into the Y-tube olfactometer at a gas flow rate of 150 mL/min.

Female adult melon flies were subjected to the repellent bioassay of PC emulsions. 10 μ L of PC emulsion was added to a filter strip and putted it on the one of the sample chamber, another filter paper as a blank control was placed on the other side of the sample chamber, as a comparison, a free citral suspension with the same citral concentration was subjected to the same repellent bioassay. The numbers of female adult melon flies were recorded at 5, 10, 15, 20, 25, 30, 45 and 60 min to calculate repellency (R) (Yang et al., 2012).

$$R (\%) = \frac{N_c - N_t}{N_c + N_t} \times 100$$

Where N_c and N_t were the numbers of melon flies in the control and treated arms, respectively.

2.7. Release properties of PC composite

In order to investigate the release properties of PC composite in the field, Bitter gourd plants with similar age containing fruits were selected and tagged. PU emulsions were diluted for 30 times and sprayed to bitter gourd with similar growth, as a comparison, citral suspensions with the same citral concentration were tested simultaneously. Five bitter gourd fruits of treatments were collected 0.5, 1, 2, 3, 5, 7, 12, 24, 36, 60, 72, 84 and 96 h after spraying. The residual citral content of bitter gourd surface was analyzed through HPLC. Each treatment included 3 bitter gourds, and the experiment was repeated three times.

2.8. Field experiment

The field experiment was conducted at Guangzhou (China) to test the repellent effect of PC composite emulsions and citral suspension which had the same citral concentration. Bitter gourd plots were spaced by a completely randomized design to ensure no interference between treatments. All the plots were received the same field management measures without used any other pesticides.

Bitter gourd plants with similar age containing fruits were selected and tagged. PU emulsions were diluted for 30 times with distilled water and sprayed for these Bitter gourds. The control received the same amount of water as treatment. Each treatment included 30 bitter gourds, and the experiment was repeated three times. Bitter gourds with obvious spawning micropyles were considered spoilt. The damages of the tagged bitter gourds were recorded at 1, 3, 5, 7, 10 d to calculate bitter gourd damage rate and melon fly control effect. The damage rate of bitter

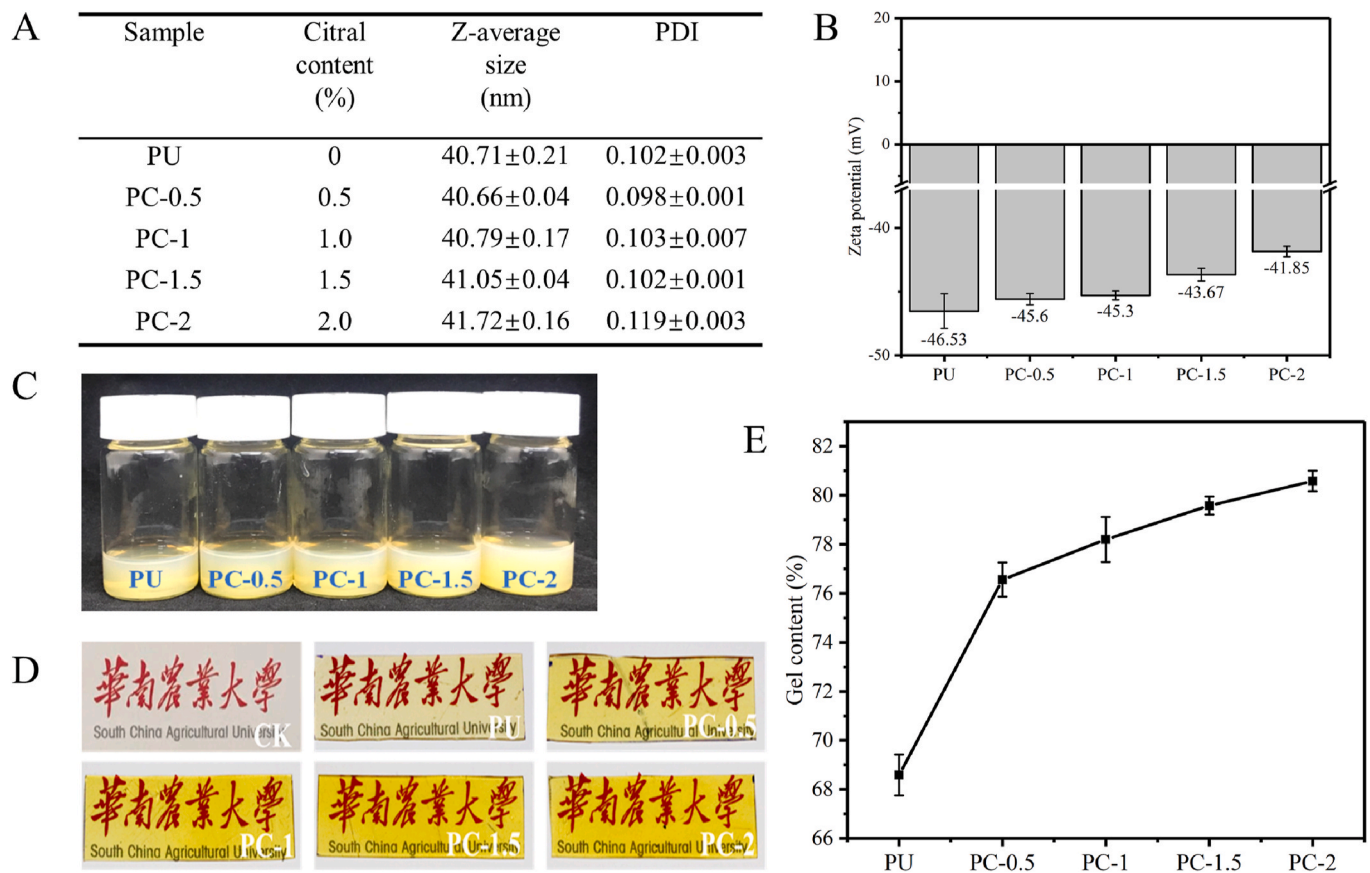


Fig. 2. The average particle sizes (A) and zeta potentials (B) of the emulsions prepared, photographs of PC emulsions (C) and films (D), Gel content of film samples (E).

gourd (D) and the control effect against melon fly (C) were calculated using the following equation.

$$D(\%) = \frac{PT}{PR} \times 100$$

Where PT was the number of spoilt bitter gourds and PR was the total number of tagged bitter gourds.

$$C(\%) = \frac{CK - CT}{CK} \times 100$$

Where CT was the bitter gourd damage rate of treatment and CK was the bitter gourd damage rate of control group.

2.9. Sample preparation and HPLC analysis

In order to detect the residual citral content of bitter gourd, 1 g bitter gourd peel was placed into a centrifuge tube by addition of added 2 mL of methanol and homogenized for 1 min. Then, the mixture was sonicated for 30 min to extract citral. 0.3 g sodium chloride was added and centrifuged for 5 min at 3000 rpm to remove precipitate. Subsequently, 1 mL supernatant was collected and filtered with 0.22 µm organic phase membrane filters. The citral residue was analyzed by HPLC. Each sample was repeated 3 times.

The content of citral was analyzed using an HPLC system (LC-20A, Shimadzu, Japan) with Agilent Zorbax SB-C18 column (250 mm × 4.6 mm × 5 µm). Methanol/water (60/40, v/v) was used as the mobile phase with a flow rate of 1 mL/min, and the detection wavelength was 234 nm. The column temperature was 30 °C and the sample size was 10 µL. Under these conditions, the chromatogram of citral had two peaks represented two isomers of citral, which were neral and geranial,

respectively. Standard solutions of citral were dissolved with chromatographic-grade methanol to the following concentrations: 0.1, 0.5, 1.0, 5.0, 10.0 mg/L to chart the calibration curve.

2.10. Statistical analysis

The dissipation dynamics of citral was governed by first-order kinetic equation.

$$C_t = C_0 e^{-KT}$$

Where T was the time after the drug, C_t was the citral content at T, C_0 was the initial citral content, K was the rate constant.

Half-life ($T_{1/2}$) was calculated by $T_{1/2} = \ln 2/k$. All data processing was performed through Excel 2010 and Origin 2017. If significance occurred, means were separately compared using one-way ANOVA tests followed by Tukey's HSD method ($P < 0.05$) for each time and all data represent means ± S.E. ($n = 3$).

3. Results and discussion

3.1. Interaction between citral and PU

The effect of different contents of citral on average sizes and zeta potentials of PC samples was assessed through the DLS technique. The particle size of PU was 40.71 nm and the result of PDI demonstrated that the particle was dispersed uniformly. The average particle size of the PC emulsions was around 40 nm (Fig. 2A) with the introduction of citral and the emulsions remained yellowish, clear and transparent (Fig. 2C). The zeta potentials of PC samples increased from −46.53 mV to −41.85 mV as the content of citral increased from 0% to 2% (Fig. 2B). This

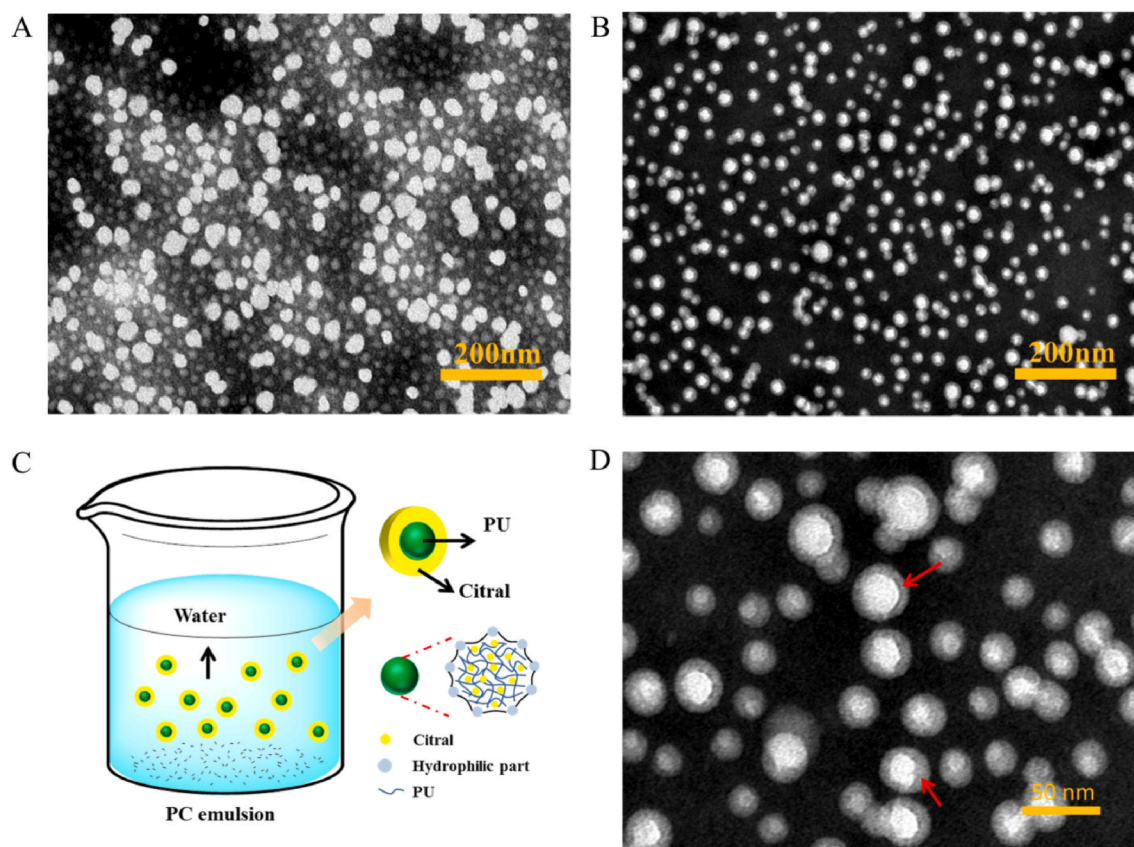


Fig. 3. 200 nm TEM images of the samples: (A) PU; (B) PC-2; (C) schematic representation of PC emulsion particle; (D) 50 nm TEM images of PC-2.

behavior proved to electrostatic interaction between PU and citral (Schultz et al., 2008). All composite emulsions demonstrated excellent storage stability simultaneously. No obvious layered structures were observed in emulsions after storage for over 3 months at ambient temperature. Composite films were transparent and color uniformly (Fig. 2D), which indicated that citral was uniformly dispersed in the PU emulsion. The color of films turned gradually dark yellow with the citral content increased, though the appearance of emulsions did not change obviously.

The impact of citral on gel content of PC films was detailed

investigated as shown in Fig. 2E. Gel fraction of PC films was greater than PU sample in tetrahydrofuran and obviously increased with increasing the citral content. Among them, the gel fraction of PC-2 was up from 68.59% of PU to 80.58%. This gel fraction was related to the crosslink density, i.e., high crosslink density gave great gel content (Ahn et al., 2008; Rolere et al., 2016). In this study, the introduction of citral enhanced the physical crosslink density of the composites via electrostatic interaction.

The dispersion capacity of pesticide aqueous formulations was vital for their application in practice. As indicated in Fig. 3A, the PU

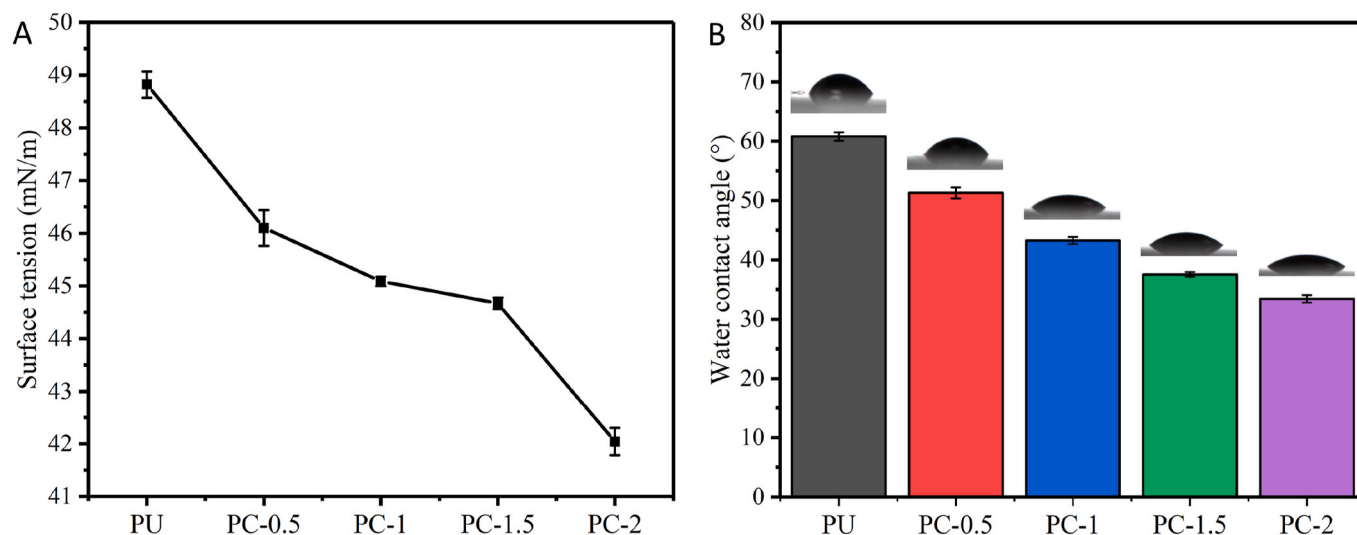


Fig. 4. Wettability of composites: (A) surface tension; (B) water contact angle.

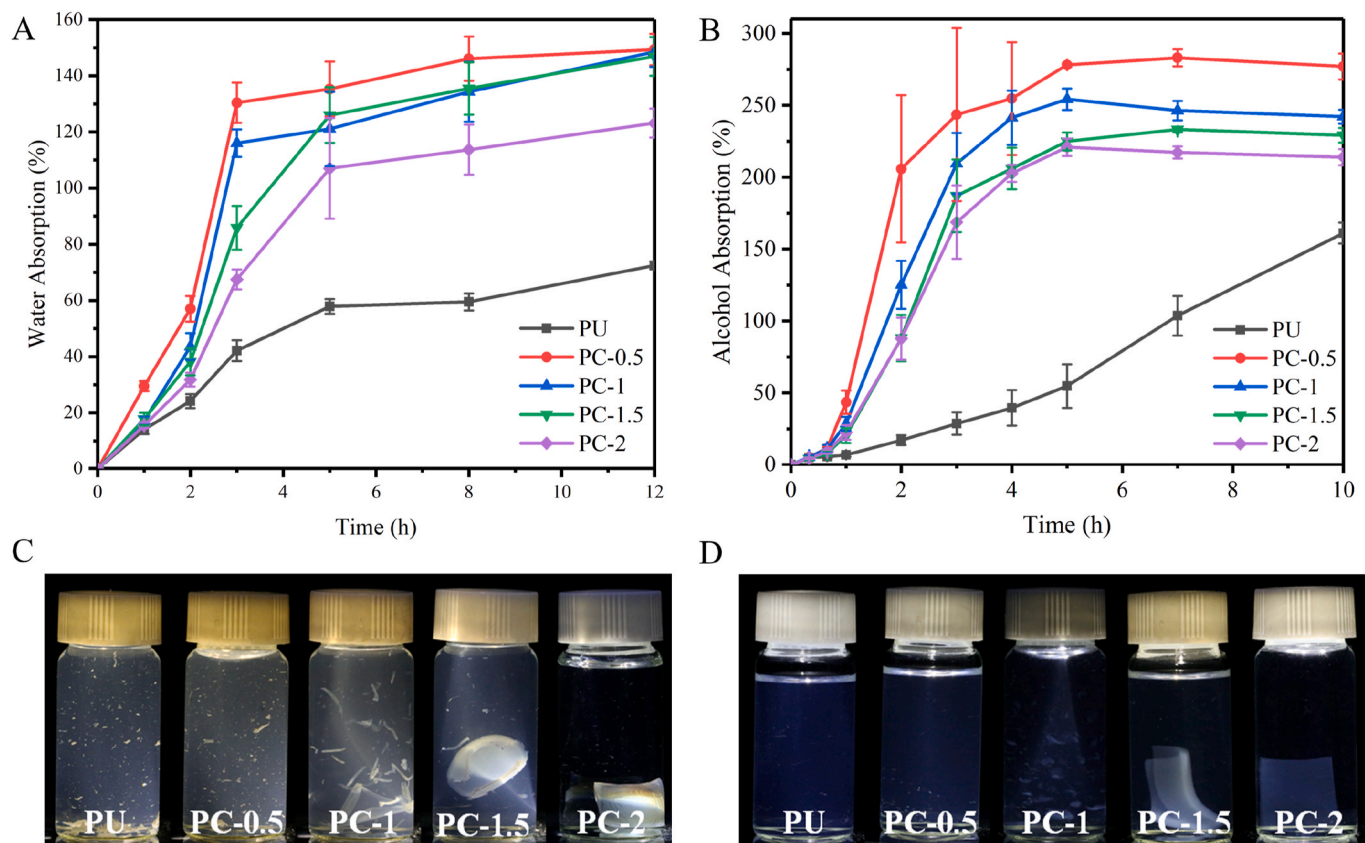


Fig. 5. Solvent absorption of composites: (A) water; (B) alcohol (10/90, v/v), optical photos of composites: (C) alcohol (40/60, v/v); (D) absolute ethanol.

nanoparticles were approximately uniform with the number-average diameter of about 40 nm, which was close to the corresponding Z-average size in Fig. 2A. PC-2 nanoparticles with high citral content exhibited more uniform spheres than PU emulsion and dispersed uniformly (Fig. 3B). The uniform spherical morphology and nanoscale of the PC emulsions were favorable to improve its adhesion on crop (Zhang et al., 2018). As shown in Fig. 3D, compared with the TEM image of PU, the edges of PC-2 nanoparticles became blurred and gray shades appeared, which were considered to be caused by the introduction of citral. Moreover, since the electrostatic interaction and increasing crosslink density, the structure schematic representation of PC-2 nanoparticles as showed in Fig. 3C. The experimental results showed that two factors mainly influence the particle size of emulsion. On the one hand, the citral introduction could cause an increase in particle size. On other hand, with citral content increased, PC exhibited greater crosslink density, which could greatly decrease particle size of nanoparticles. Obviously, both dominated the influence, resulting in the particle size remained virtually unchanged.

3.2. Wettability of composites

The wettability of emulsion samples had important influence on its application in agriculture (Liang et al., 2018c). As shown in Fig. 4A, it was obvious that the surface tension of PC emulsions was decreased compared with PU. The surface tension of PU was 48.82 mN/m and the surface tension of PC-0.5 after adding 0.5% of citral was 46.1 mN/m. As the citral content continued to increase to 2%, the contact angle tended to decrease until 42.04 mN/m. The result indicated that citral obviously decreased the surface tension of the PC composites. The impact of citral on the contact angle of PC emulsions was investigated as shown in Fig. 4B. With an increasing of citral content, the contact angle of emulsion samples decreased from 60.8° to 33.41°. The decrease of the contact angle was caused by the change of the surface tension. It was

clear that the wettability of emulsion samples was increased with the addition of citral content. Because excellent wettability could improve the adhesion of composites on crop surface (Kalin and Polajnar, 2014), PC samples were more conducive to spreading on the crop surface, droplets were not easy to bounce and roll off.

3.3. Chemical resistance of composites

The water absorption in water of the films prepared was presented in Fig. 5A. All the film samples demonstrated two stages of water absorption within 12 h: a fast absorption stage and a slow absorption stage, respectively. Firstly, the water absorption of the film samples increased rapidly and then the absorption rate slowed down with immersion time. In this study, two factors mainly influence the water absorption of film samples. First of all, the hydrophilic group increased with the citral introduction, which led to film water absorption raised (Liang et al., 2018b). In detail, the water absorption of the PU film was 72.48% after immersion for 12 h, while that of PC-0.5 film was 149.36%. On the other hand, the greater cross-linking density made the molecular chains more compacted, which led to water more difficult entering the interior of the films (Yu et al., 2016). Therefore, the water absorption of PC-2 decreased from 149.36% of PC-0.5 to 123.16% with the citral content increased.

As shown in Fig. 5B, three stages of alcohol absorption were observed for the PC films within 10 h: a fast absorption, a slow absorption and an equilibrium absorption stage, which was different from the PC film water absorption. Simultaneously, PU film was observed two stages of alcohol absorption, increased slowly firstly and then increased faster with immersion time. Similar to the film water absorption, the alcohol absorption of PC film was increased ascribed to the citral introduction, while greater cross-linking density led to an increase in hydrophobicity (Gao et al., 2017). In detail, the alcohol absorption of PU was 161.18% at 10 h, however that of PC-0.5 already reached maximum 283.03%

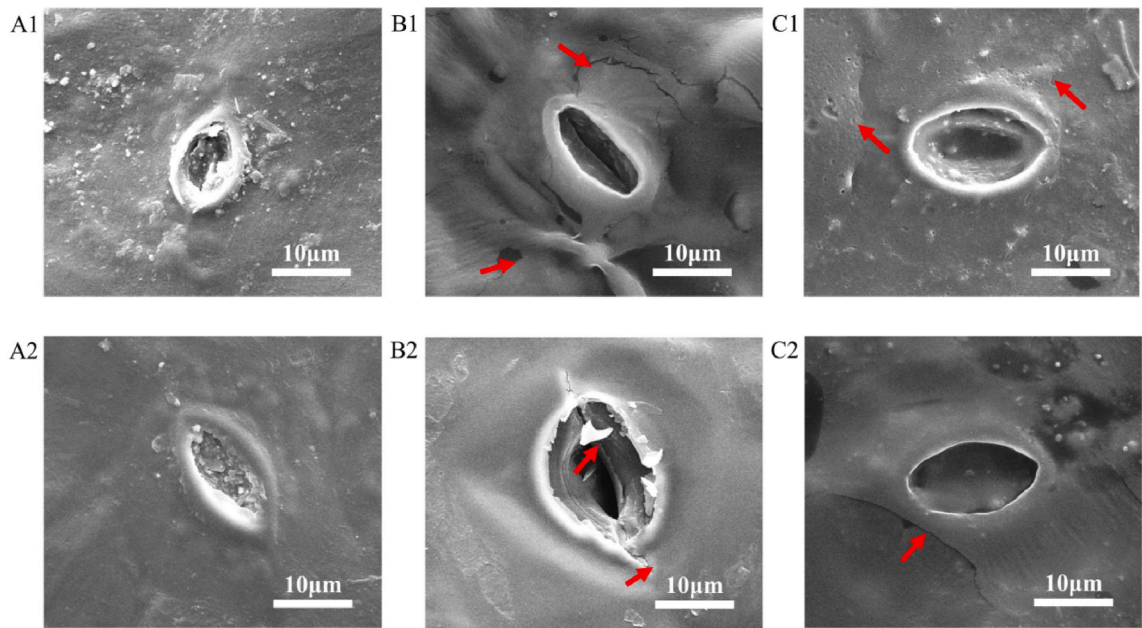


Fig. 6. SEM images of the different samples around stoma of bitter melon: free citral before (A1) and after (A2) washing; PU emulsion before (B1) and after (B2) washing; PC emulsion before (C1) and after (C2) washing.

before 7 h and then decreased to 276.98% at 10 h, which was due to the partly dissolution of the small molecular material made the weight loss of the PU film. With the citral content increased from 0.5% to 2%, the alcohol absorption of PC films decreased from 276.98% to 213.93%.

The morphology of film samples was clearly observed via optical photos in 40% alcohol or absolute ethanol. As shown in Fig. 5C, PU and PC-0.5 were broken into pieces and partly film dissolved in 40% alcohol before 2 h. The film samples became complete as the citral content increased, which was due to the increase of cross-linking densities caused by citral, resulting in an increase in chemical resistance (Azeredo and Waldron, 2016). Obviously PC-2 film was only swelled and still intact. For absolute ethanol treatment, PU and PC-0.5 were dissolved almost in absolute ethanol (Fig. 5D). PC-1 had undissolved molecular material, but PC-1.5 and PC-2 still intact.

Experiments showed that PC-0.5 film with reasonable citral content had water resistance, but residual film sample could be washed off by alcohol. Compared with other drug delivery systems, PC-0.5 had the

potential for highly efficient control of insect pests, which was unnecessary to worry about the composite residue on the crop surface. PC-0.5 composite was further studied in the following experiments.

3.4. Adhesion property of the emulsions

A high adhesion was always desired for drug delivery systems, which increased the pesticide retention on crop and decrease the loss. To prove the adhesion property of PC emulsion, experimented according to the method previously reported (Jia et al., 2014). The results showed that for the free citral, many particles remained around stoma of bitter melon at first (Fig. 6A1), and most of these particles were washed away after washing (Fig. 6A2). However, for the PU and PC-0.5 emulsions, formed film on bitter melon, which could be obviously demonstrated via cracks, pieces and pores of composites around stoma (Fig. 6B1 and 6C1). After being washed with water, films still remained on bitter melon (Fig. 6B2 and 6C2), which was ascribed to the hydrogen bonding formed between

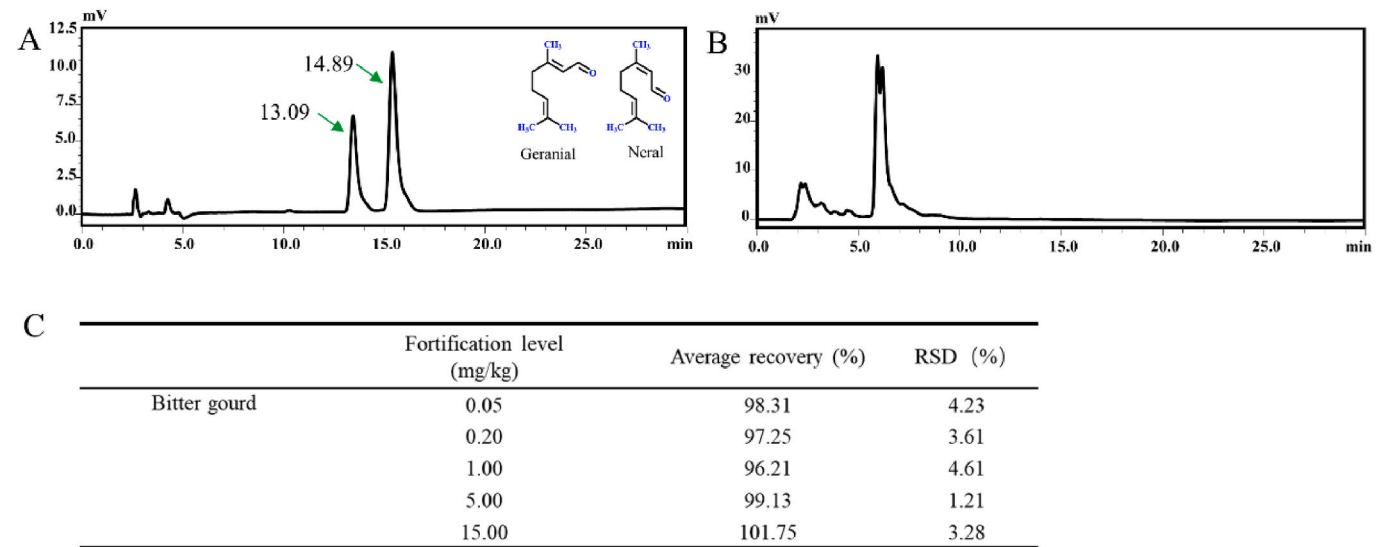


Fig. 7. HPLC chromatograms of citral standard (A), bitter melon blank (B); (C) Recoveries and relative standard deviation (RSDs) in sample.

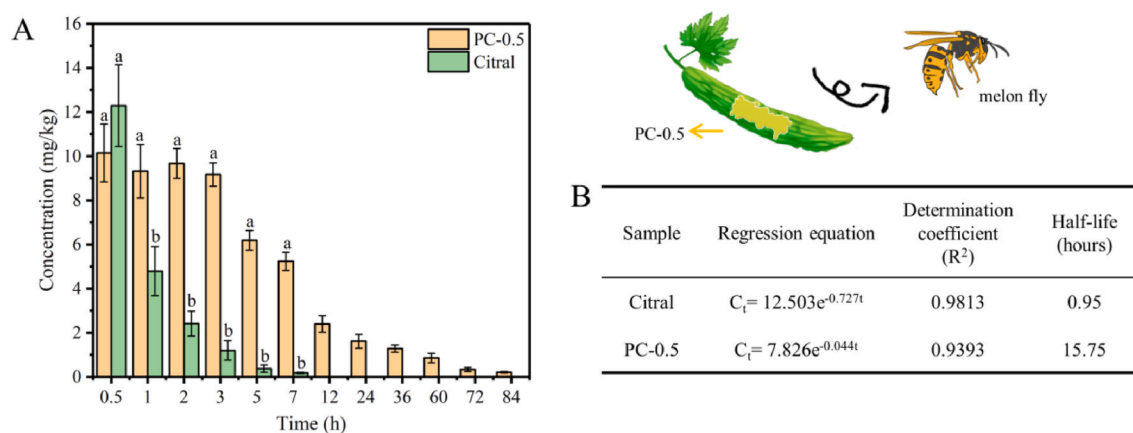


Fig. 8. (A) Citral content on bitter gourd surface, (B) Dissipation parameters of composite.

PU chains bitter gourd surface (Qin et al., 2017). These results indicated that PC-0.5 emulsion had stronger adhesion than free citral. Compared with PU treatment, some particles were vaguely found on bitter gourd in Fig. 6C1 and 6C2, which represented citral. However, citral particles were far less than free citral treatment (Fig. 6A1), which was due to more citral was embedded in PU film. It was clear that this behavior could improve the crop citral retention.

3.5. Repellent effect of PC-0.5 prepared

Citral and some plant essential oil with citral as the main constituent were reported to have an obvious repellent effect against housefly and mosquito (Chauhan et al., 2018). The repellency potential of citral and PC-0.5 composite were evaluated against melon fly female adults via Y-tube olfactometer with suitable laboratory conditions (Table 1). The results showed that for the free citral, the repellent effect reached maximum 88.99% before 20 min and then decreased to 47.17% with testing time, which was ascribed to strong volatility of citral. For PC-0.5 treatment, the repellency percentage was continuous improved to 91.15% before 45 min, and retained to 60 min, which was significantly higher than free citral. It was clear that long-lasting repellent effect for melon fly female adults was obtained via embedded citral into PU film.

3.6. Method validation of HPLC

A calibration curve was charted via the peak area in the citral concentration range ($y = 52746x - 5943.3$, $R^2 = 0.9994$). Fig. 7C showed the average recovery rate of citral on bitter gourd peel at five concentrations (0.05, 0.20, 1.00, 5.00 and 15.00 mg/kg). The average recovery of five replicates for bitter gourd peel ranged from 96.21% to 101.75%, and the relative standard deviation ranged from 1.21% to 6.61%. The average recovery fulfilled the range (70%–120%), which was specified via the European Commission. Fig. 7A and B showed the HPLC chromatograms of the citral standard with cis- and trans-Isomers, neral and geraniol, respectively. Bitter gourd peel blank had no interference with the peak time of the citral standard.

3.7. Sustained-release property of the composite

In order to investigate the sustained-release property of PC-0.5, the content of citral on bitter gourd surface was determined via HPLC to evaluate citral volatile rate (Fig. 8A), PC-0.5 and free citral with the same citral concentration were sprayed to similar bitter gourd. As expected, for free citral treatment, the concentration of citral rapidly decreased from 12.29 mg/kg before 0.5 h to 4.79 mg/kg at 1 h, which was due to the rapid volatilization of citral. The concentration of citral was only 0.18 mg/kg at 7 h, and this behavior was consistent with the

Table 2

Terminal residues of citral on bitter gourd surface.

Sample	Dilution factor	The sampling interval (hours)	Residues (mg/kg) ^a
Free Citral	15	84	< LOD
		96	< LOD
	30	84	< LOD
		96	< LOD
PC-0.5	15	84	0.27 ± 0.05
		96	< LOD
	30	84	0.21 ± 0.03
		96	< LOD

results in Table 1. Unlike free citral, the citral concentration of PC-0.5 was 10.15 mg/kg before 0.5 h, and retained to 9.17 mg/kg at 3 h, while the citral concentration of free citral treatment was only 1.20 mg/kg at the same stage. The concentration of citral between the two treatments was significantly different except for 0.5 h. The result showed that PC-0.5 could effectively slow down the volatile rate of citral via embedded citral into PU film. The citral concentration of PC-0.5 could be detected to 0.21 mg/kg until 84 h, and the detected time was 12 times that of free citral treatment. It was clear that PC-0.5 sample had a sustained citral release behavior and therefore enhanced the efficiency of citral application. Fig. 8B presented the half-life and regression equations of citral in different samples under field conditions. The citral half-life of free citral treatment was only 0.95 h and that of PC-0.5 was 15.75 h. The difference in the half-life of citral between treatments was ascribed to sustained-release effect of PU on citral, which was consistent with the results in Fig. 8A.

3.8. Terminal residues of citral on bitter gourd surface

^aLOD: limit of detection.

As indicated in Table 2, the terminal residues of citral on bitter gourd surface were detected under different dilution factor and sampling intervals. Citral residues of free citral treatment were not detected on bitter gourd surface at 84 h. For PC-0.5 with 30 times diluted, the terminal residues of citral was 0.21 mg/kg at 84 h, and not detected at 96 h, as a comparison, PC-0.5 with 15 times diluted had the same residual behavior. The result showed that no citral residue of all samples could be detected after 96 h. Compared with other polymer drug delivery systems, PC-0.5 composite could be washed off via low concentration alcohol, simultaneously citral residue remained no exceed 96 h on bitter gourd surface. It was clear that it was safe to use PC-0.5 on bitter gourd.

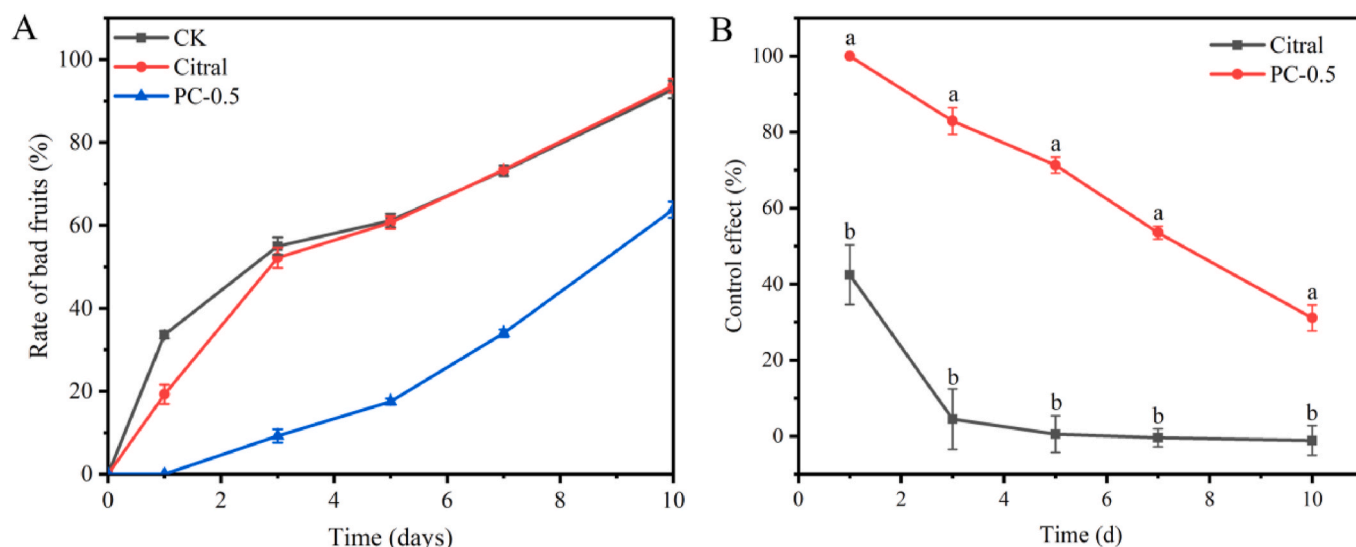


Fig. 9. (A) Bad fruits rate of bitter gourd for samples, (B) Control effect of samples against melon fly.

3.9. Efficacies of samples against melon fly

In order to study the control effect of PC-0.5 against melon fly under field conditions, the bad fruits situation of bitter gourd was investigated to calculate bad fruits rate and the control effect against melon fly. As indicated in Fig. 9A, PC-0.5 and free citral with the same citral concentration were sprayed to control melon fly, as a comparison, CK without any treatment was investigated. The bad fruits rate for free citral treatment was close to CK at the third day, which was significantly higher than PC-0.5, and the bad fruits rate for free citral was still 29.01% higher than that of PC-0.5 until the 10th day. It was clear that PC-0.5 effectively reduced the bad fruits rate of bitter gourd. As indicated in Fig. 9B, the control effect of PC-0.5 was higher than that of free citral all along. For free citral treatment, the control effect rapidly decreased from 45.47% before the first day to 4.49% at the third day, which had less control effect against melon fly from the third day. However, the control effect of PC-0.5 reached 100% at the first day, still 82.95% at third day, and the value 53.52% at 7th day was far higher than 0.42% of free citral treatment. The effects of two treatments exhibited significant differences. Results revealed that PC-0.5 could efficiently control melon fly for a longer time.

4. Conclusions

In this work, PC-0.5 was successfully developed embedded citral into PU film with simple blending, which displayed desirable properties, such as excellent sustained release and adhesion behavior. The results showed that the chemical resistance of composites could be tailored via controlling citral content, PC-0.5 with great water resistance could be thoroughly washed off by alcohol without worrying about the safety of that on crops. Besides, composites prepared exhibited ideal adhesion behavior on bitter gourds even under rainfall washing, sustained release citral under field conditions, resulting in long-lasting repellent behavior against melon fly. Compared with other drug delivery systems, this technology was safe enough, low cost and simple processing. It provides a potential approach to control melon fly, which has great value for plant essential oil applied in agriculture.

Declaration of competing interest

The authors declare that they have no known competing financial interests or personal relationships that could have appeared to influence the work reported in this paper.

Acknowledgments

This work was sponsored by Innovation Team of Modern Agricultural Industry Technology System of Guangdong Province (2019KJ140), National Key R&D Program of China (2018YFD0200300).

References

- Ahn, B.U., Lee, S.K., Lee, S.K., Park, J.H., Kim, B.K., 2008. UV curable polyurethane dispersions from polyisocyanate and organosilane. *Prog. Org. Coating* 62, 258–264.
- Azeredo, H.M.C., Waldron, K.W., 2016. Crosslinking in polysaccharide and protein films and coatings for food contact - a review. *Trends Food Sci. Technol.* 52, 109–122.
- Chauhan, N., Malik, A., Sharma, S., 2018. Repellency potential of essential oils against housefly, *Musca domestica* L. *Environ. Sci. Pollut. Res.* 25, 4707–4714.
- Dhillon, M.K., Singh, R., Naresh, J.S., Sharma, H.C., 2005. The melon fruit fly, *Bactrocera cucurbitae*: a review of its biology and management. *J. Insect Sci.* 5, 16.
- Diabate, S., Martin, T., Murungi, L.K., Fiaboe, K.K.M., Subramanian, S., Wesonga, J., Deletre, E., 2019. Repellent activity of *Cymbopogon citratus* and *Tagetes minuta* and their specific volatiles against *Megalurothrips sjostedti*. *J. Appl. Entomol.* 143, 855–866.
- Feng, Y., Deng, Q., Hu, J., Peng, C., Wu, Q., Xu, Z., 2018. Study on gel weight fraction of ultraviolet-cured acrylic adhesives. *Chem. Pap.* 73, 517–524.
- Gao, F., Zhou, H., Shen, Z., Zhu, G., Hao, L., Chen, H., Xu, H., Zhou, X., 2020. Long-lasting anti-bacterial activity and bacteriostatic mechanism of tea tree oil adsorbed on the amino-functionalized mesoporous silica-coated by PAA. *Colloids Surf. B Biointerfaces* 188, 110784.
- Gao, Y., Duan, L.J., Guan, S., Gao, G.H., Cheng, Y., Ren, X.Y., Wang, Y.R., 2017. The effect of hydrophobic alkyl chain length on the mechanical properties of latex particle hydrogels. *RSC Adv.* 7, 44673–44679.
- Gupta, S., Sharma, R.K., Gajbhiye, V.T., Gupta, R.K., 2012. Residue behavior of combination mix formulations in/on bittergourd and their efficacy against melon fruitfly. *Bull. Environ. Contam. Toxicol.* 89, 1258–1263.
- Gurunathan, T., Rao, C.R.K., Narayan, R., Raju, K., 2013. Synthesis, characterization and corrosion evaluation on new cationomeric polyurethane water dispersions and their polyaniline composites. *Prog. Org. Coating* 76, 639–647.
- Jia, X., Sheng, W.B., Li, W., Tong, Y.B., Liu, Z.Y., Zhou, F., 2014. Adhesive polydopamine coated avermectin microcapsules for prolonging foliar pesticide retention. *ACS Appl. Mater. Interfaces* 6, 19552–19558.
- Ju, J., Xie, Y.F., Yu, H., Guo, Y.H., Cheng, Y.L., Zhang, R.R., Yao, W.R., 2020. Synergistic inhibition effect of citral and eugenol against *Aspergillus Niger* and their application in bread preservation. *Food Chem.* 310, 7.
- Kalin, M., Polajnar, M., 2014. The wetting of steel, DLC coatings, ceramics and polymers with oils and water: the importance and correlations of surface energy, surface tension, contact angle and spreading. *Appl. Surf. Sci.* 293, 97–108.
- Kandakoor, S.B., Chakravarthy, A.K., Rashmi, M.A., Verghese, A., 2019. Effect of elevated carbon dioxide and temperature on biology of melon fruit fly, *Bactrocera cucurbitae* Coquillett (Tephritidae: Diptera). *Afr. Entomol.* 27, 36–42.
- Klungness, L., Jang, E., Mau, R., Vargas, R., Sugano, J., Fujitani, E., 2005. New approaches to sanitation in a cropping system susceptible to tephritid fruit flies (Diptera: Tephritidae) in Hawaii. *J. Appl. Sci. Environ. Manag.* 9, 5–15.
- Liang, H., Wang, S., He, H., Wang, M., Liu, L., Lu, J., Zhang, Y., Zhang, C., 2018a. Aqueous anionic polyurethane dispersions from castor oil. *Ind. Crop. Prod.* 122, 182–189.

- Liang, H.Y., Liu, L.X., Lu, J.Y., Chen, M.T., Zhang, C.Q., 2018b. Castor oil-based cationic waterborne polyurethane dispersions: storage stability, thermo-physical properties and antibacterial properties. *Ind. Crop. Prod.* 117, 169–178.
- Liang, W.L., Yu, A.X., Wang, G.D., Zheng, F., Hu, P.T., Jia, J.L., Xu, H.H., 2018c. A novel water-based chitosan-La pesticide nanocarrier enhancing defense responses in rice (*Oryza sativa* L.) growth. *Carbohydr. Polym.* 199, 437–444.
- Nisar, T., Wang, Z.C., Yang, X., Tian, Y., Iqbal, M., Guo, Y.R., 2018. Characterization of citrus pectin films integrated with clove bud essential oil: physical, thermal, barrier, antioxidant and antibacterial properties. *Int. J. Biol. Macromol.* 106, 670–680.
- Oyedele, A.O., Gbolade, A.A., Sosan, M.B., Adewoyin, F.B., Soyelu, O.L., Orafidiya, O.O., 2002. Formulation of an effective mosquito-repellent topical product from lemongrass oil. *Phytomedicine* 9, 259–262.
- Pascual-Villalobos, M.J., Canto-Tejero, M., Vallejo, R., Guirao, P., Rodríguez-Rojo, S., Cocero, M.J., 2017. Use of nanoemulsions of plant essential oils as aphid repellents. *Ind. Crop. Prod.* 110, 45–57.
- Prokopy, R.J., Miller, N.W., Pinero, J.C., Barry, J.D., Tran, L.C., Oride, L., Vargas, R.L., 2003. Effectiveness of GF-120 fruit fly bait spray applied to border area plants for control of melon flies (Diptera : Tephritidae). *J. Econ. Entomol.* 96, 1485–1493.
- Qin, H., Zhang, H., Li, L.X., Zhou, X.T., Li, J.P., Kan, C.Y., 2017. Preparation and properties of lambda-cyhalothrin/polyurethane drug-loaded nanoemulsions. *RSC Adv.* 7, 52684–52693.
- Rolere, S., Bottier, C., Vaysse, L., Sainte-Beuve, J., Bonfils, F., 2016. Characterisation of macrogel composition from industrial natural rubber samples: influence of proteins on the macrogel crosslink density. *Express Polym. Lett.* 10, 408–419.
- Schultz, N., Metreveli, G., Franzreb, M., Frimmel, F.H., Syltatk, C., 2008. Zeta potential measurement as a diagnostic tool in enzyme immobilisation. *Colloids Surf. B Biointerfaces* 66, 39–44.
- Sen, K., Dhar, P.P., Samanta, A., 2019. Field screening of different genotypes of bitter gourd for infestation with the melon fruit fly, *Bactrocera cucurbitae* (Coquillett) in two agro-climatic zones of West Bengal, India. *Int. J. Trop. Insect Sci.* 39, 273–282.
- Sunil, Thippaiah, M., Jagadish, K.S., Chakravarthy, A.K., 2016. Efficacy of insecticides against melon fruit fly *Bactrocera cucurbitae* (Coquillett) in bitter gourd. *Entomol.* 41, 233–238.
- Wu, H., Fu, C.C., Yu, D.D., Feng, J.T., Zhang, X., Ma, Z.Q., 2013. Repellent activity screening of 11 kinds of essential oils against *Aedes albopictus* Skuse: microcapsule preparation of *Herba Schizonepetae* oil and repellent bioassay on hand skin. *Trans. R. Soc. Trop. Med. Hyg.* 107, 471–479.
- Yang, F.L., Zhu, F., Lei, C.L., 2012. Insecticidal activities of garlic substances against adults of grain moth, *Sitotroga cerealella* (Lepidoptera: gelechiidae). *Insect Sci.* 19, 205–212.
- Yang, K., Wang, C.F., You, C.X., Geng, Z.F., Sun, R.Q., Guo, S.S., Du, S.S., Liu, Z.L., Deng, Z.W., 2014. Bioactivity of essential oil of *Litsea cubeba* from China and its main compounds against two stored product insects. *J. Asia-Pac. Entomol.* 17, 459–466.
- Yang, Y.H., Li, X.Z., Zhang, S., 2018. Preparation methods and release kinetics of *Litsea cubeba* essential oil microcapsules. *RSC Adv.* 8, 29980–29987.
- Yu, F.F., Cao, L.W., Meng, Z.H., Lin, N.B., Liu, X.Y., 2016. Crosslinked waterborne polyurethane with high waterproof performance. *Polym. Chem.* 7, 3913–3922.
- Zhang, C.Q., Garrison, T.F., Madbouly, S.A., Kessler, M.R., 2017. Recent advances in vegetable oil-based polymers and their composites. *Prog. Polym. Sci.* 71, 91–143.
- Zhang, H., Qin, H., Li, L.X., Zhou, X.T., Wang, W., Kan, C.Y., 2018. Preparation and characterization of controlled-release avermectin/Castor oil-based polyurethane nanoemulsions. *J. Agric. Food Chem.* 66, 6552–6560.
- Zheng, F., Li, Y.C., Zhang, Z.X., Jia, J.L., Hu, P.T., Zhang, C.Q., Xu, H.H., 2020. Novel strategy with an eco-friendly polyurethane system to improve rainfastness of tea saponin for highly efficient rice blast control. *J. Clean. Prod.* 264, 11.

Development of Multifunctional Avermectin Poly(succinimide) Nanoparticles to Improve Bioactivity and Transportation in Rice

Guodong Wang,^{†,‡,§} Yuyan Xiao,^{†,§} Hanhong Xu,^{*,†,§} Pengtong Hu,^{†,‡} Wenlong Liang,[†] Lijuan Xie,[‡] and Jinliang Jia^{*,†,‡}

[†]State Key Laboratory for Conservation and Utilization of Subtropical Agro-bioresources, South China Agricultural University, Guangzhou, Guangdong 510642, China

[‡]College of Materials and Energy, South China Agricultural University, Guangzhou, Guangdong 510642, China

Supporting Information

ABSTRACT: Avermectin (AVM) as a nonsystemic pesticide possesses a low effective utilization rate. Studies of the multifunctional pesticide delivery system for improving biological activity are developing prosperously. In this study, multifunctional avermectin/polysuccinimide with glycine methyl ester nanoparticles (AVM-PGA) were prepared by the self-assembly process. The AVM loading capacity was up to 23.7%. After 24 h of UV irradiation, there was still about 70% of AVM remaining in PGA₄₂ nanocarriers, as opposed to less than 5% of the free-form AVM. The rising ambient pH promoted the release of AVM using an in vitro releasing test, revealing a favorable pH-responsively controlled-release property. The mortality rate of *Plutella xylostella* with 2.5 µg/mL of AVM content of AVM-PGA₄₂ was 96.3% after 48 h, while that of free AVM was only 51.5%. In addition, the AVM could be detected in stems and all leaves treated with AVM-PGA₄₂ nanoparticles, whereas rare AVM was detected only in treated leaves for the free-form AVM, which achieved the transportation of nanocarriers carrying AVM in rice for the first time. Furthermore, the PGA nanoparticles performed a good growth promoting effect on rice. These results show that the AVM-PGA₄₂ nanopesticides have a great potential application prospect to control the pest and improve the drug utilization efficiency on agriculture.

KEYWORDS: polysuccinimide, avermectin, biological activity, transportation, growth promotion

1. INTRODUCTION

Pesticides play a crucial role in agriculture, which are used extensively to control weeds, pests, and crop diseases. Unfortunately, most pesticides are lost and degradation caused by environmental factors,^{1,2} and no more than 0.1% of effective ingredients can actually reach target organisms.³ As a result, the frequency of the applications is enhanced to achieve the desired effect. This overuse of pesticides has brought on a series of problems, such as environmental pollution, health hazards, pesticide resistance, and pesticide residues.^{4,5} Biopesticides with their broad insecticidal spectrum, strong selectivity, and low environmental toxicity have been regarded as an effective tool to reduce the harm of pesticides.⁶

Avermectin B1a (AVM), as one of the most effective nonsystemic biopesticides, was widely used in agriculture.⁷ However, due to its special 16-membered ring macrolide structure, AVM is sensitive to oxidation and photodegradation, which results in weak light stability and short half-life.^{8–10} Besides, excess organic solvent is employed to maintain effective activity because of the poor water solubility of AVM, which not only increases costs but also exacerbates pollution.^{11,12} Hence, to solve these weaknesses of AVM, different AVM nanoformulations have been investigated. For example, Li et al.¹³ prepared a lignin-based microsphere to encapsulate AVM via self-assembly, and demonstrated that the AVM microsphere not only revealed controlled release characteristics but also prolonged the half-life of AVM under UV irradiation. Jia et al.¹⁴ employed polydopamine (PDA)

microcapsules to encapsulate AVM, which protected AVM against photodegradation, as well as showed good sustained-release properties and adhesion properties. Liang et al.¹⁵ utilized chitosan as a carrier to load AVM, exhibited that the drug was rapidly released under alkaline conditions and had an ability to resist photolysis. However, most of these strategies only focus on improving the release performance and UV-shielding property to increase the duration of efficacy of AVM,^{16,17} and no research has been reported to improve the uptake and transportation of AVM in plant. As a nonsystemic pesticide, only a small quantity of AVM could enter the leaves by osmotic action, and most of the drug is unable to be absorbed and transported by plant, which results in a low effective utilization.¹⁸ Therefore, it is extremely important to establish a multifunctional AVM delivery system which is controllable and UV-resistant in vitro, and also could be absorbed and transported by plant in vivo.

Polymeric nanomaterials in aqueous solution have been extensively studied.^{19–21} Polysuccinimide (PSI) is a nontoxic polymer with the characteristics of biocompatible and sustainable, which is widely used in food, medical and cosmetics industries.²² To meet the different requirements, numerous groups such as hydrazone bonds,^{23–25} carboxyls^{26,27}

Received: June 24, 2018

Revised: September 8, 2018

Accepted: October 9, 2018

Published: October 9, 2018

and amines^{28,29} can be readily incorporated onto PSI backbone to form multifarious biodegradable copolymers. Moreover, the polymeric nanoparticles with a hydrophilic shell and hydrophobic core can show high loading capacity.³⁰ In the area of agriculture, amino acid transporters play a pivotal part in the long-distance transport of plant.³¹ Researchers have found that the phloem transportability of amino acid esters—pesticide conjugates could be detected with the aids of endogenous amino acid transporters in plant.^{32,33} Hence, the simplest amino acid ester, glycine methyl ester (GlyOMe) is chosen as a basic nutrient and transported group, which is incorporated onto PSI backbone to achieve drug load and transportation.

Herein, the synthesis of PSI/GlyOMe-based nanocarriers encapsulating AVM (AVM-PGA) via self-assembly behavior was described. The chemical structure of nanoparticles was explored by transmission electron microscopy (TEM), scanning electron microscopy (SEM), FTIR spectroscopy, and ¹H NMR spectroscopy. The AVM controlled-release and UV-shielding properties were both investigated. Furthermore, after the treatment of AVM-PGA₄₂ on rice leaves, the concentrations of AVM were detected in different parts of rice over a period of 3 days. Besides, the biological activity was evaluated by using AVM-PGA₄₂ nanoparticles to cultivate *Plutella xylostella*, and the growth promoting effect on rice seedlings treated with PGA nanoparticles was determined.

2. MATERIALS AND METHODS

2.1. Materials. Polysuccinimide ($M_w = 7k$ Da, 99%) was purchased from Hubei YuanChengSaichuang Technology Co., Ltd. (China). Glycine methyl ester hydrochloride (HGlyOMe, 99%) was provided by Shanghai Hanhong Scientific Co., Ltd. (China). Dibutylamine (DBA) and dimethyl sulfoxide (DMSO) were purchased from Shanghai Lingfeng Scientific Co., Ltd. (China). Tween 80 was provided by Tianjin Fuyu Fine Chemical Co., Ltd. (China). Avermectin B1a (original pesticide) with a purity of 96% was provided by Zhejiang Heben Technology Co., Ltd. (China). Acetonitrile and methanol at HPLC grade were obtained from Beijing DingGuoChangsheng Biotechnology Co., Ltd. (China). All others reagents were used without extra purification. Rice seeds (Huahang 12) were supplied by South China Agricultural University (Guangzhou, China).

2.2. Synthesis of Different Functionalized PGA. Functionalized PGA nanoparticles were prepared referring to previous reports with little modifications.³⁴ To synthesis copolymers with different functional degrees, three mol feed ratios (10:5, 10:3, 10:2) were carried out. For example, for an obtaining copolymer at the feed ratio of 10:5, 0.97 g of PSI (0.01 mol succinimide repeating unit) was dissolved into 10 mL of DMSO. Then 0.625 g (0.005 mol) of HGlyOMe and 0.646 g (0.005 mol) of DBA were dissolved in 5 mL DMSO and added to the PSI solution with vigorous stirred for 12 h at room temperature. To form the PGA nanoparticles, the resulting solution was added to 200 mL of citric acid buffer with the pH of 2.5 drop by drop. Finally, PGA was obtained by centrifugation (10 000 r/min), washing three times with deionized water and freeze-drying overnight.

2.3. Preparation of AVM-PGA. After dissolving 100 mg of PGA nanoparticles in 5 mL of DMSO, 100 mg of AVM was added into the as-prepared solution with gentle stirring to form a mixed organic phase. Then the mixture was added dropwise to 45 mL of deionized water under vigorously stirring at room temperature for 1 h. The result solution was transferred to the dialysis bags ($M_w = 3500$ Da) and dialyzed for 5 h.³⁵ The AVM-loaded nanoparticles were acquired after centrifugation (10 000 r/min), washed, and freeze-dried.

2.4. Loading Capacity and Encapsulation Efficiency. Ten mg of AVM-PGA was dissolved in of 3 mL of ethanol and transferred into an ultrasonic bath for 2 h to completely disassociate the AVM. The resulting suspension was centrifuged (10 000 r/min, 10 min), and the

supernatant collected. The amount of AVM in supernatant was determined by UV-vis spectroscopy at 245 nm with the help of AVM calibration curve ($R^2 = 0.999$) in ethanol. Each measurement was analyzed in triplicate. The AVM loading capacity (LC) and encapsulation efficiency (EE) were respectively calculated by the following equations:

$$LC = \frac{\text{weight of AVM loaded}}{\text{weight of AVM-PGA}} \times 100\% \quad (1)$$

$$EE = \frac{\text{AVM loading}}{\text{total amount of AVM}} \times 100\% \quad (2)$$

2.5. Characterization. The morphology of nanoparticles was inspected using a transmission electron microscopy (TEM) (Tecnai G2 F30, FEI Co., U.S.A.) and a scanning electron microscopy (SEM) instrument (Nova Nano 450, FEI Co., U.S.A.). The structure of nanoparticles was carried out by a Fourier transform infrared spectrometer (FTIR) (Vertex 70, Bruker Co., Germany) with nuclear magnetic resonance spectrometer (Bruker AV III 600, Bruker Co., Germany). The AVM concentration in release test as well as photodegradation test was determined by a UV-vis spectrophotometer (UV 2550, Shimadzu Co., Japan) with the wavelength of 245 nm. The concentration levels of AVM in different parts of the rice were measured by an Agilent 1290 HPLC equipped with a reversed-phase column (ZORBAX SB-C₁₈, 3.5 μ m, 50 \times 2.1 mm², Agilent Co., U.S.A.) at 30 °C. The solution of methanol and water (98:2, v/v) was used as a mobile phase at a flow rate of 1.0 mL/min, along with the injection volume of 10 μ L. The excitation wavelength and emission wavelength were 365 and 470 nm, respectively.

2.6. In Vitro Release Investigation. The release behavior of AVM from the synthetic AVM-PGA₄₂ at different pH values was estimated as follows:³⁶ 10 mg of AVM-PGA₄₂ nanoparticles were suspended in 3 mL of an ethanol-H₂O medium (50:50, v/v), and the suspension was injected into dialysis bags (MWCO = 3500 Da) with the help of an injection syringe, which was then soaked in 200 mL reagent bottles covering 150 mL of release medium with different pH values. The release system was kept by stirring at 120 r/min. The pH of release medium was adjusted by diluted hydrochloric acid and sodium hydroxide. At given time intervals, 3 mL of release medium was collected, and 3 mL of fresh medium was added into guarantee constant solution volume. The collected sample was analyzed on an AH-2800 UV-vis spectrophotometer at 245 nm to measure the release of AVM. The release amount of AVM was calculated by UV absorbance investigated by the standard curve of AVM (5–35 μ g/mL). All release experiments were repeated twice at room temperature.

2.7. Photodegradation Investigation. Three different functional AVM-PGA samples were used to evaluate the light stability. Each AVM-PGA sample that contained 5 mg of active ingredients of AVM was dispersed in 200 mL of ethanol solution, and then transferred to a 300 mL reagent bottle with a magnetic stirrer at 100 r/min. The samples were placed 20 cm under the UV radiation with an 8 W ultraviolet lamp that excitation wavelength was 254 nm in a black box (40 \times 30 \times 40 cm³). At regular periods, 1 mL of sample was withdrawn and analyzed by UV analysis. The degradation rate of technical grade AVM was also measured in a similar way and acted as a control group. The entire experiment was carried out at room temperature.

2.8. Insecticidal Activity Investigation. Healthy larvae of *Plutella xylostella* were proved by South China Agricultural University, Guangdong, China, and nourished on the cabbage (*Brassica rapa*). The cultivating conditions were 26 \pm 1 °C and 80% relative humidity with a photoperiod of 16-h light-8-h dark (16L: 8D).

To survey the insecticidal activity of AVM-PGA₄₂ and AVM, a modification of leaf-dipping assay was used.³⁷ The experiment was divided into technical grade (AVM) group and the AVM-PGA₄₂ group. The technical grade group was dissolved in acetone and diluted in deionized water containing Tween 80 (0.1%), while the AVM-PGA₄₂ group was directly dispersed in Tween 80 (0.1%). *Brassica*

rapa cabbage seedlings incubated in the greenhouse were collected, and kept the same weight for each treatment group. The seedlings were dipped into each treatment solution for 30 s and left to dry for 2 h at room temperature. After air-drying, the treated diet was placed into plastic cylindrical boxes (2.8 cm diameter, 4.0 cm height) lined with filter paper, then 12 third-instar larvae of *Plutella xylostella* were released into each box. Mortalities were determined after being treated for 48 h. All treatments were performed with three replicates.

2.9. Distribution Test. **2.9.1. Seed Sterilization and Plant Growth.** Rice seeds of Huahang12 collected from South China Agricultural University were used in this study. The seeds were surface-sterilized with 0.5% (v/v) NaClO for 1 h. Rice seeds were then immersed in deionized water at 37 °C for 48 h in the dark, and were transferred to moistened paper placed within Petri dishes. Seeds of rice were incubated at 30 °C for a further 24 h. After germination, the starting point of the nutrient solution for the seedlings was Hoagland's solution containing the macronutrients $\text{Mg}_2\text{SO}_4 \cdot 7\text{H}_2\text{O}$ (4 mM), $\text{CaCl}_2 \cdot 2\text{H}_2\text{O}$ (5 mM), KH_2PO_4 (1 mM), $(\text{NH}_4)_2\text{SO}_4$ (0.18 mM), $\text{Ca}(\text{NO}_3)_2$ (0.18 mM), KNO_3 (0.3 mM), KCl (5 mM), and KH_2PO_4 (0.09 mM), $\text{Fe}_2\text{SO}_4 \cdot 7\text{H}_2\text{O}$ (0.1 mM), Na_2EDTA (0.1 mM), MES (0.5 mM), and the micronutrients $\text{MnSO}_4 \cdot \text{H}_2\text{O}$ (9 μM), $\text{ZnSO}_4 \cdot 7\text{H}_2\text{O}$ (0.7 μM), $\text{CuSO}_4 \cdot 5\text{H}_2\text{O}$ (0.3 μM), KNO_3 (3 μM), $(\text{NH}_4)_6\text{Mo}_7\text{O}_{24} \cdot 4\text{H}_2\text{O}$ (1 μM), and $\text{Na}_2\text{B}_4\text{O}_7 \cdot 10\text{H}_2\text{O}$ (46 μM). The solution was refreshed every 3 days. Rice seedlings were performed in a plant growth chamber with a light/dark photoperiod of 14:10 h, air temperature of 30:25 °C and 15 000 LX illuminance for hydroponic culture.

2.9.2. Distribution of PGA_{42} in Rice Plant. The PGA_{42} was dispersed in sterile distilled water prior to exposure. 0.1 mg/mL of AVM- PGA_{42} was used in the distribution study. Five-week-old rice which in good growth condition was taken after cleaned and dried with soft paper. The rice was lay down the experimental table, then 0.2 mL of AVM- PGA_{42} aqueous solution was added on one of the middle leaves from rice plant drop by drop using a pipet and placed 30 min until the liquid naturally dried. In order to figure out the distribution behavior of AVM- PGA_{42} nanoparticles, the rice seedlings were incubated in test solution (pH = 5.8, 0.5 mM CaCl_2) with 0.1 mg/mL for AVM- PGA_{42} time-dependent distribution experiment, and the samples were collected at 6, 12, 24, 48, 72 h after AVM- PGA_{42} treatment on rice seedlings. Each treatment was repeated three times. As shown in Figure 1, the concentrations of AVM were measured in

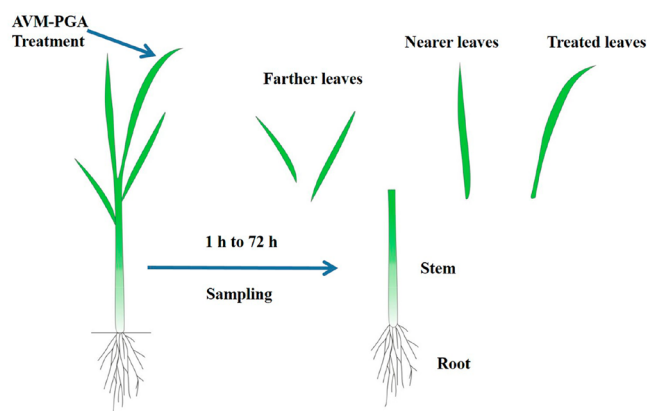


Figure 1. Sampling for the experiment of AVM- PGA_{42} distribution in rice.

five parts of rice, i.e., the roots, stem, and leaves (treated, nearer, farther), over a period of 72 h using high performance liquid chromatography (HPLC) with fluorescence detector.

At the 6, 12, 24, 48, and 72 h after the treatment, the roots, stems, and leaves (treated, nearer, farther) were quickly rinsed in ice cold distilled water, and then placed in aerated ice cold distilled water for 20 min.³⁸ The roots, stems, and leaves were washed once again with distilled water and blotted dry with tissue papers. Then the roots and

leaves (treated, nearer, farther) of the rice seedlings were cut into pieces and the fresh weight of those were determined. Then samples were put into mortar and ground with liquid nitrogen. After that, samples were extracted with 10.0 mL of acetonitrile, the roots or stem samples mixture were sonicated for 20 min and leaves sonicated for 30 min, respectively. 1.0 g of sodium chloride and 4.0 g of anhydrous magnesium sulfate were then added to remove water. After 20 min of ultrasound treatment, the mixture was centrifuged at 3000 r/min for 5 min. 0.5 mL aliquot of supernatant was transferred to a new centrifuge, mixed with 0.5 mL 1-methylimidazole-acetonitrile (1:1, v/v) reagents by vortex for 2 min to homogeneity and reacted in the dark at room temperature for 5 min. Before the sample was reacted in a dark place for 20 min, 0.5 mL of trifluoroacetic anhydride-acetonitrile (1:1, v/v) was added to the mixture and shaken by vortex for 2 min. The reaction solution was filtered through a 0.22- μm , lipophilicity PTFE needle filter for subsequent HPLC analysis.

2.10. Growth Promotion Investigation. To survey the capacity of PGA_{42} nanocarriers for plant promotion in adverse environment, two different pH culture conditions (7.0 and 8.5) were set. The rice seedlings were selected as a model plant and the agar culture medium was selected as the nutriment. The method of seed germination was same as described above.

When the seeds coleoptiles were ca. 1.0 cm in length, its root system was slowly inserted into the 250 mL beakers containing 200 mL 0.9% (w/v) agar in which the concentrations of PGA_{42} copolymers were 6.25, 12.5, 25, 50, and 100 $\mu\text{g/mL}$, ten seeds as a treatment. Beakers were kept in an illumination incubator at 16:8 h photoperiod, 28:25 °C light/dark cycle, 60% relative humidity, and 15 000 LX illuminance. After a month of incubation in agar culture medium, the rice seedlings were transplanted to the 250 mL beakers that filled with soil for further cultivation.³⁹ Plants were then replaced into the illumination incubator. And water management was carried out based on the model of rice cultivation. The testing block design was entirely randomized. Plant height and fresh weight were recorded after 75 days of growing.

2.11. Examination of Contact Angle of Rice Leaves. The rice that had been treated with different concentrations of PGA_{42} was picked up. Without damaging the morphological structure of rice leaves, a portion of the leaf between the main vein and the edge of the leaf was cut as a test sample, which was then stuck smoothly on the glass slide. The prepared leaf samples were transferred to the stage of the contact angle measuring instrument, keeping the slide completely in the field of screen. Ten μL of deionized water in the pipet was gently dripped on the rice leaves. When the droplet state on the leaf surface became stable, the image was quickly captured, and the corresponding contact angle values were recorded. All treatments were performed with three replicates.

2.12. Statistical Analysis. All of the data were expressed as means values and standard deviations, which were statistically analyzed using the SPSS version 22.

3. RESULTS AND DISCUSSION

3.1. FTIR Analysis. The FTIR spectra of PSI, PGA, and HGlyOMe were shown in Figure 2(a). As for PSI, the peak at 2950 cm^{-1} was assigned to $-\text{CH}_2-$, the absorption band at 1720 cm^{-1} was ascribed to $\text{C}=\text{O}$, and the peak at 1790 cm^{-1} represented the coupling effect of the adjacent carbonyl, indicating the presence of a five-membered ring cyclic imides structure.^{40,41} With regard to PGA, the absorption band between 3000 and 3400 cm^{-1} was attributed to the stretching vibration of N-H, the characteristic absorption band located at 1635 cm^{-1} was assigned to stretching vibration of $\text{C}=\text{O}$ in newly formed $-\text{CONH}-$. And the peak at 1036 cm^{-1} correspond to the stretching vibration of C-N mixed with C-C, implying existence of HGlyOMe.⁴² These measurements demonstrated that HGlyOMe was grafted successfully onto the architecture of PSI. As shown in Figure 2(b), the strong absorption peaks at 2974 and 2879 cm^{-1} were contributed by

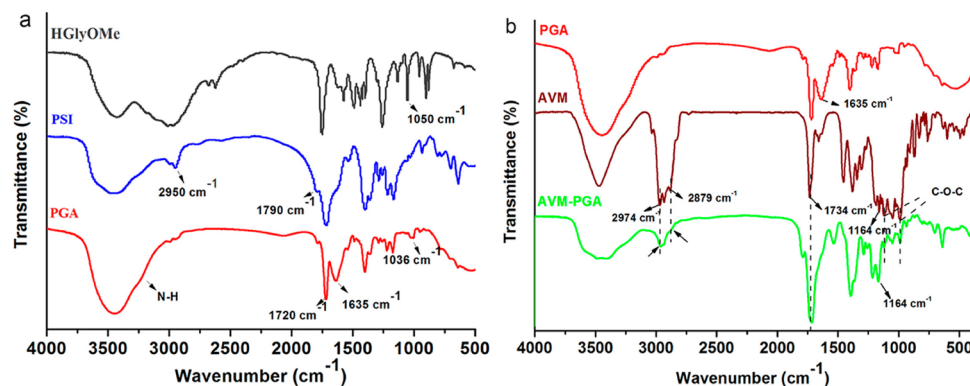


Figure 2. FTIR spectra of (a) PSI, PGA, and HGlyOMe; (b) PGA, AVM, and AVM-PGA.

$-\text{CH}_3$ stretching vibrations⁴³ and a sharp peak at 1734 cm^{-1} originated from the $\text{C}=\text{O}$ stretching vibration⁴⁴ in the AVM spectrum. Besides, the broad bands in the range of $989\text{--}1120\text{ cm}^{-1}$ were assigned to $\text{C}-\text{O}-\text{C}$ stretching vibration,⁴⁵ and the characteristic peak at 1164 cm^{-1} belonged to macrocyclic lactone $\text{C}-\text{O}-\text{C}$ stretching vibration. Comparing with the spectrum of AVM-PGA, the same peaks at 2974 , 2879 , 1734 , 1164 , and $989\text{--}1120\text{ cm}^{-1}$ were appeared, which belonged to the characteristic peaks of AVM. However, the peak at 1635 cm^{-1} was ascribed to the $\text{C}=\text{O}$ stretching vibration from PGA, which disappeared in the AVM-PGA spectrum because of the peak superposition. Thus, the results confirmed that the AVM was loaded successfully in the PGA nanocarriers.

3.2. ^1H NMR Analysis of Synthetic Product. In order to further confirm the structure and degree of functionalization of the synthesized PGA, the ^1H NMR spectra in $(\text{CD}_3)_2\text{SO}$ was recorded and displayed in Figure 3. Curve (b) showed the ^1H

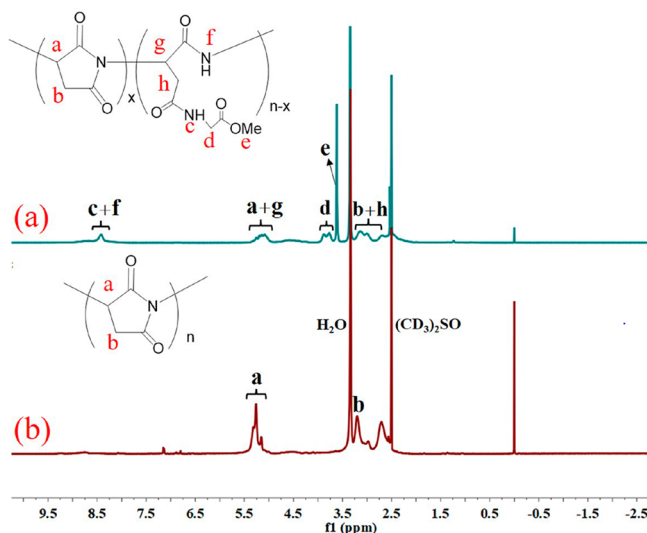


Figure 3. ^1H NMR spectra of PGA (a) and PSI (b).

NMR Spectrum of PSI, the signals at 3.34 and 2.50 ppm represented the H_2O and $(\text{CD}_3)_2\text{SO}$ residual peaks, respectively. The signal in the shift range $5.14\text{--}5.33\text{ ppm}$ was assigned to $-\text{CH}-$, and the signal at 3.20 ppm was attributed $-\text{CH}_2-$. It was seen from curve (a) that the shift range $8.42\text{--}8.73\text{ ppm}$ was ascribed to $-\text{NH}-$ in newly formed $-\text{CONH}-$. Additionally, $5.07\text{--}5.31\text{ ppm}$ were the signals of $-\text{CH}-$. The shift range $3.73\text{--}3.89\text{ ppm}$ was ascribed to

$-\text{CH}_2-$ in $-\text{CH}_2\text{COOCH}_3$, and 3.61 ppm was the signal of $-\text{CH}_3$.^{34,46,47} Thereby, the PGA had been successfully synthesized. The degree of functionalization for the copolymers was 12% , 24% and 42% , respectively, which was calculated by comparing the integrated intensity of $-\text{CH}_3$ to the integrated intensity of $-\text{CH}-$ (Figure S1 of the Supporting Information, SI). Additionally, the loading capacity and encapsulation efficiency were listed in Table S1, respectively. Due to the highest drug loading capacity of 42% functional PGA (PGA_{42}) with 23.7% , we chose it for follow-up experiments.

3.3. Morphology Analysis. The morphology of PGA_{42} nanocarriers was observed by TEM and SEM. As shown in Figure 4(a–c), the synthetic PGA_{42} copolymer possessed a nearly spherical structure with an average size of $56.8 \pm 4.5\text{ nm}$. The morphology of nanoparticles was not uniform indicating the overlapping layers of nanoparticles and the reason for aggregation was the stronger viscosity in the PGA_{42} nanoparticles.

3.4. Release Profiles of AVM. The release behavior of AVM under different pH conditions was investigated. In Figure 5, it showed that the entire release process was slow indicating the favorable control release ability of AVM- PGA_{42} . Compared with the values of 7.0 and 5.5 , the pH of 8.5 presented excellent release ability, resulting from the hydrolysis of the succinimidyl main chain of PSI units.⁴⁸ Eventually, 85.1% of AVM was released in the pH values of 8.5 after 192 h , whereas in pH 5.5 and 7.0 release buffer, the final accumulative release rate was 34.2% and 62.9% , respectively. Obviously, the release of AVM was intensified at the alkaline condition because of more likely to collapse of the nanoparticles. As a result, the PGA_{42} nanocarriers possessed good pH responsiveness and sustained release capability. In addition, the result of release mechanism investigation showed that the data corresponded to the Higuchi model best because of the highest R^2 compared with other models (Table S2 of the SI). It indicated that the release of AVM from AVM- PGA_{42} nanoparticles followed Fickian diffusion mechanism. Videlicet, AVM released from AVM- PGA_{42} nanoparticles mainly through diffusion effect.

3.5. UV Radiation Resistance Behavior. Table 1 showed the decomposition rate of the AVM-PGA under UV irradiation. As a reference, three different functionalized AVM-PGA samples were selected for photostability testing. After 6 h of radiation, the technical AVM had almost 40% of the decomposition, while the degradation rate of all samples just over 10% . Moreover, the original AVM reached 95% of the degradation through 24 h of UV exposure, but the content of

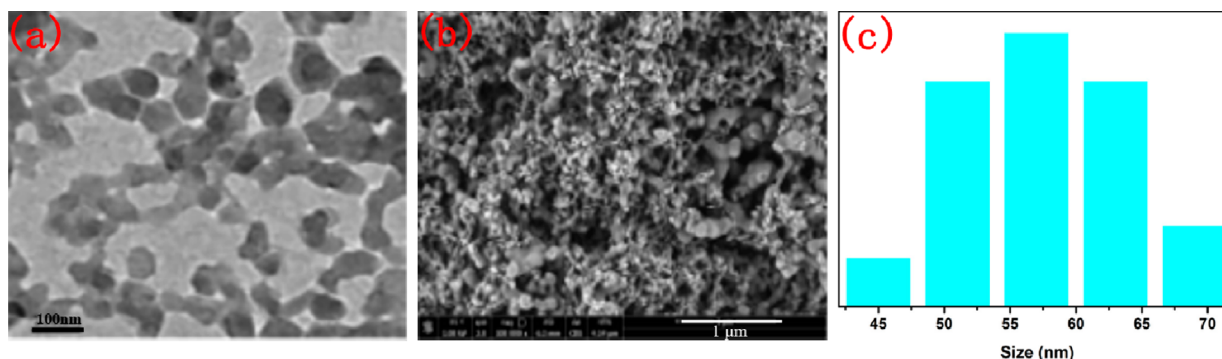


Figure 4. TEM image (a), SEM image (b), and particle size distribution (c) of PGA₄₂.

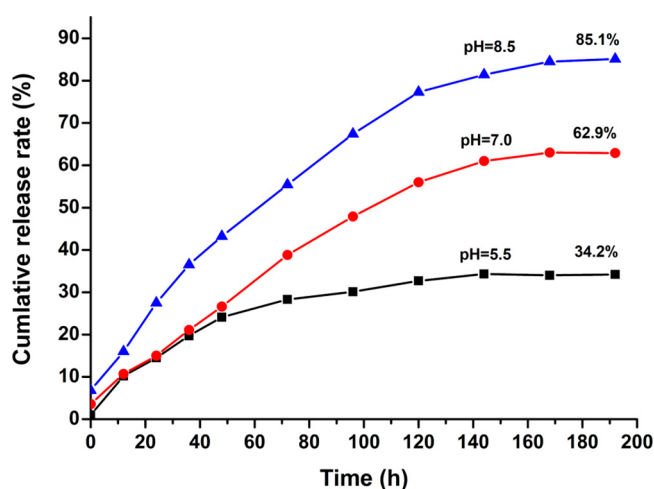


Figure 5. Release profiles of AVM at different pH values.

enfolded AVM in all PGA samples was still approximately 70%. Evidently, all samples decomposition rates were much slower than the original AVM. Besides, the degradation rates of AVM in three different functionalized samples were similar, showing that the PGA nanocarriers had a stable property of antiphotodegradation. The obtained data substantiated that PGA could greatly cut down the ultraviolet radiation on AVM molecules and prevent them from degrading. In summary, with good UV-shielding capability, the as-synthesized AVM-PGA can prolong the validity period and enhance the utilization efficiency of AVM.

3.6. Biological Activity Investigation of AVM-PGA₄₂

The excellent pH responsiveness and remarkable photostability of AVM-PGA₄₂ revealed great potential in biological activity. To evaluate the activity of PGA₄₂ formulations against *Plutella*

xylostella, AVM-PGA₄₂ was selected as a model formulation compared with AVM. Five increasing concentrations were defined as 0.3125, 0.625, 1.25, 2.5, and 5.0 $\mu\text{g/mL}$ for both AVM-PGA₄₂ and AVM, respectively.

Mortality of the test insects was investigated 48 h after treatment. As shown in Figure 6, the AVM molecule mortality

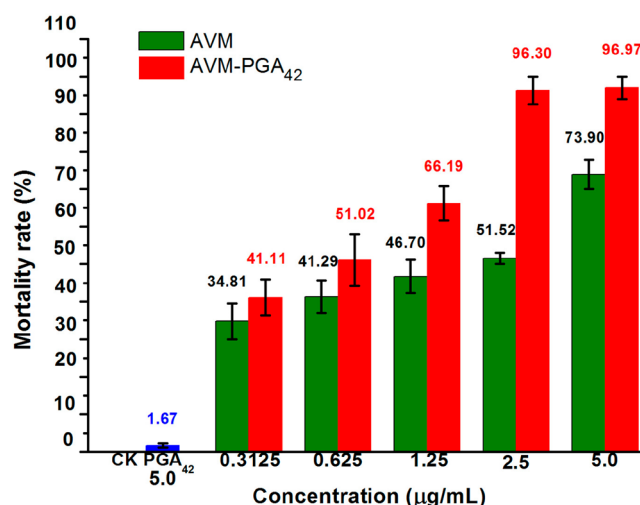


Figure 6. Insecticidal activities of AVM-PGA₄₂ and AVM against *Plutella xylostella*.

values varied from 34.81% to 73.90%, whereas the AVM-PGA₄₂ group exhibited higher mortality values ranging from 41.11% to 96.97%. Furthermore, all AVM-PGA₄₂ treatments showed better activity against *Plutella xylostella* than that AVM group at the any concentration of the assay. For the concentration of 2.5 $\mu\text{g/mL}$, the mortality rate of AVM-PGA₄₂ group was 96.30%, which was relatively higher than that

Table 1. AVM-PGA Stability under UV Radiation at 254 nm

tests at different time (h)	degradation rate (%)			
	AVM technical grade	AVM-PGA ₄₂	AVM-PGA ₂₄	AVM-PGA ₁₂
1	5.21	1.70	2.02	1.64
2	9.47	3.41	3.73	3.27
3	14.42	5.79	6.27	5.51
6	38.52	10.76	12.74	11.11
9	50.21	18.24	17.35	15.69
12	58.32	22.09	21.48	20.40
15	77.26	25.39	24.98	24.32
24	95.33	31.52	30.94	29.85

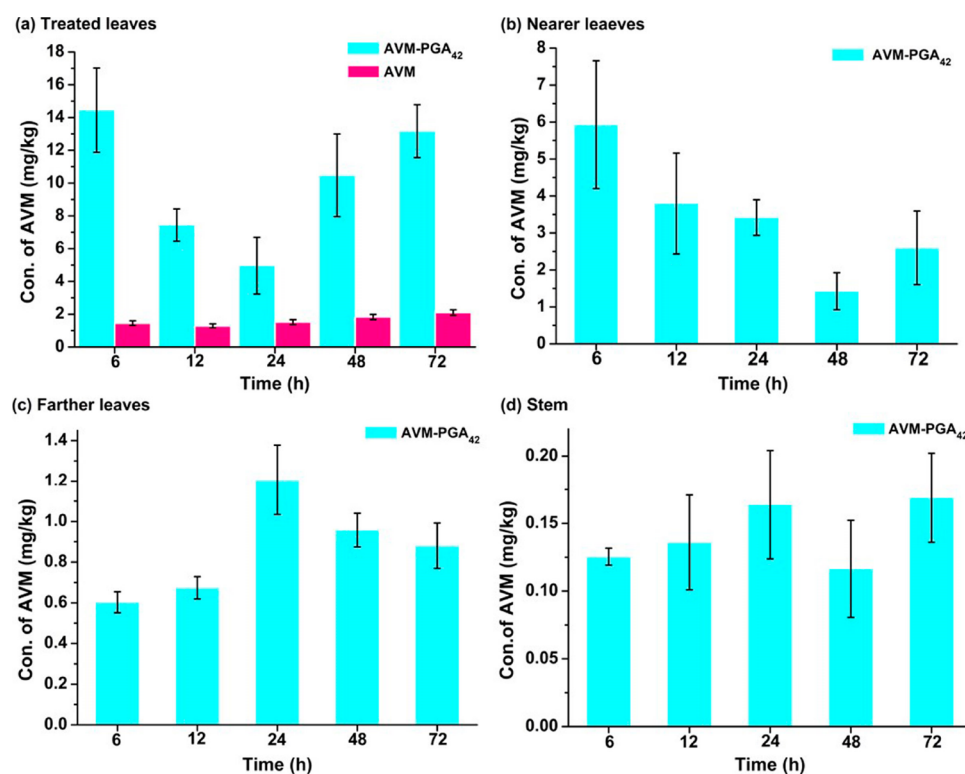


Figure 7. Distribution of AVM-PGA₄₂ in rice: (a) treated leaves, (b) nearer leaves, (c) farther leaves, and (d) stems.

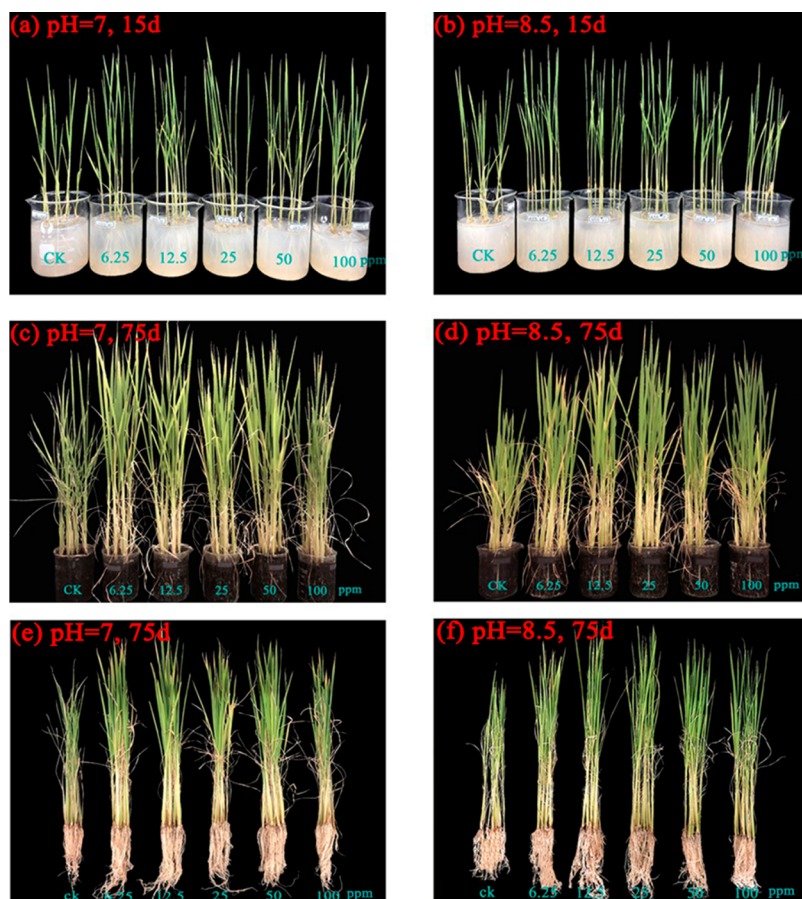


Figure 8. Photo images of rice plant treated with PGA₄₂ of different concentrations in two cultivation environments: (a, c, e) pH = 7 and (b, d, f) pH = 8.5 at 15 days (a, b) and 75 days (c–f) after planting.

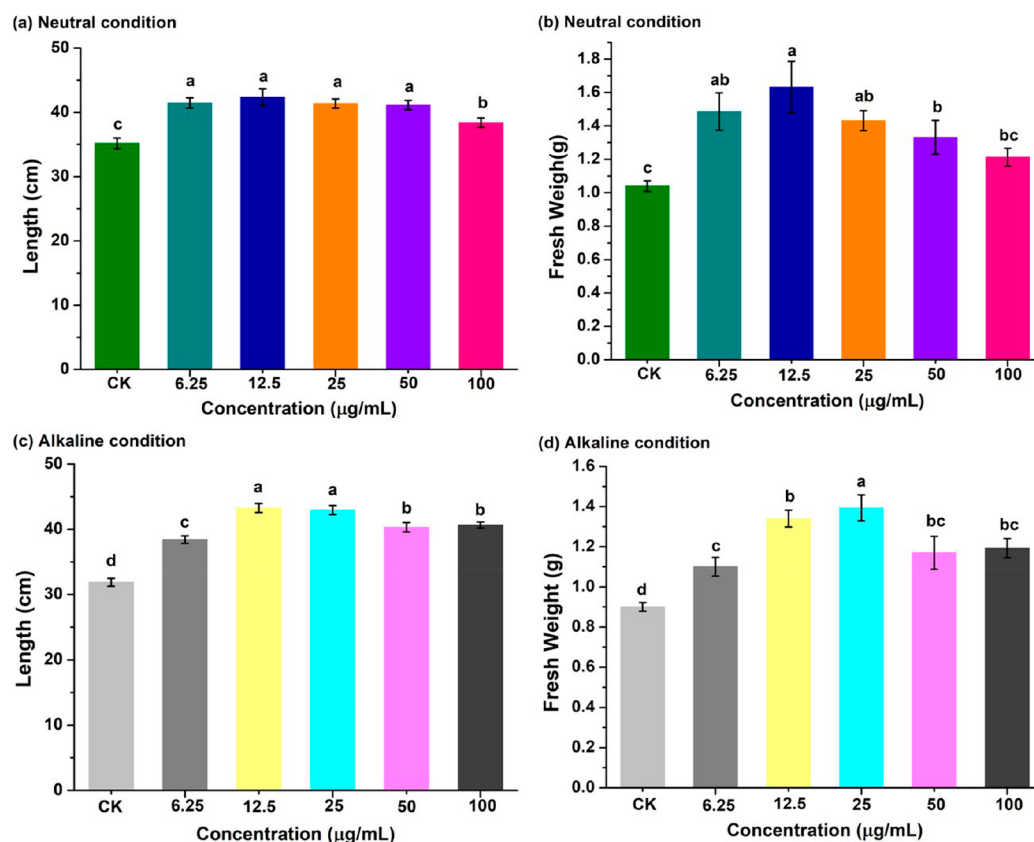


Figure 9. Plant height and fresh weight of the rice after 75 days of cultivation under different pH conditions: (a, b) pH = 7, and (c, d) pH = 8.5. Graph represents mean \pm SE followed by same letter is not significantly different at $p \leq 0.05$ as determined by Tukey-Kramer HSD.

treated with AVM group (51.52%). In addition, water and 5.0 $\mu\text{g/mL}$ of PGA₄₂ as control revealed that PGA₄₂ was nearly nontoxic to the *Plutella xylostella*. Compared with AVM, AVM-PGA₄₂ nanoparticles could exhibit better insecticidal activity because of the smaller particle size of PGA₄₂ nanoparticles. When AVM was loaded, the specific surface area of the drug had been greatly improved, so that the contact ability of the target tissue was greatly increased. Thus, AVM-PGA₄₂ nanopesticides could exhibit a superior insecticidal effect. In summary, PGA₄₂ nanocarriers could reduce the dosage of AVM in pest control.

3.7. Uptake and Distribution of AVM-PGA₄₂ Nanoparticles in Rice. Figure 7(a) showed that the amount of AVM dealt with AVM-PGA₄₂ in the treated leaves decreased gradually with time, from 14.3 mg/kg in 6 h to 4.96 mg/kg in 24 h, which marked the lowest accumulation level, and then increased to 13.2 mg/kg in 72 h. As shown in Figure 7(b), the amount of AVM in nearer leaves decreased from 5.80 mg/kg in 6 h to 1.43 mg/kg in 48 h and then increased to 3.2 mg/kg in 72 h. The amount of AVM in farther leaves showed in Figure 7(c) increased from 0.59 mg/kg in 6 h to 1.21 mg/kg in 24 h and then decreased to 0.85 mg/kg in 72 h. The amount of AVM in stem was 0.18 mg/kg during 72 h in Figure 7(d). In general, it was higher in the nearer leaves than in the farther leaves and stems. This showed that AVM-PGA₄₂ might be more beneficial to acropetal, rather than basipetal, distribution in rice plants. However, when only AVM was used in rice plants, in 6, 12, 24, 48, 72 h, a small amount was detected on the treated leaves, but not in other parts of rice. It stated that AVM possessed the permeability and no ability of transport. The results of the study showed that treatment of AVM-PGA₄₂

on rice plants resulted in the distribution and translocation of AVM to different rice plant parts, i.e. the stem and the nearer, farther, and treated leaves. Hence, AVM-PGA₄₂ demonstrated a better uptake and transportation performance in the leaves and stems of rice, which suggested that PGA₄₂ as nanocarriers could improve the inhalation of nonsystemic pesticides in rice. As can be seen, it provides a theoretical basis for the absorption and directional transportation of pesticides in plants.

3.8. Growth Promotion Observation. In order to evaluate the promotion effect of PGA₄₂ nanocarriers on growth of rice, two pH values (7.0 and 8.5) were set as different growth environment, and the rice growth vigor at different stages was exhibited in Figure 8. At different growth stages, the rice treated with different concentrations of PGA₄₂ nanocarriers was better growth than that of CK, and the plant height and fresh weight of the rice after 75 days of cultivation were measured.

Figure 9(a, b) showed the growth situation of the rice in neutral cultivation conditions. As we can see, the plant height and fresh weight of rice treated with PGA₄₂ nanocarriers were significantly different from those of CK in all five concentrations, and all showing different degrees of increase. The plant height and fresh weight had reached a dramatic difference at 6.25 $\mu\text{g/mL}$. The plant height and fresh weight both reached the peak at 12.5 $\mu\text{g/mL}$, and increased by 20.18% and 45.28%, respectively. However, the level of treatment above 25 $\mu\text{g/mL}$ had decreased, and the most remarkable reduction happened to 100 $\mu\text{g/mL}$. The growth situation of the rice in alkaline cultivation conditions as shown in Figure 9(c, d), the effects of five concentrations of PGA₄₂ nanocarriers

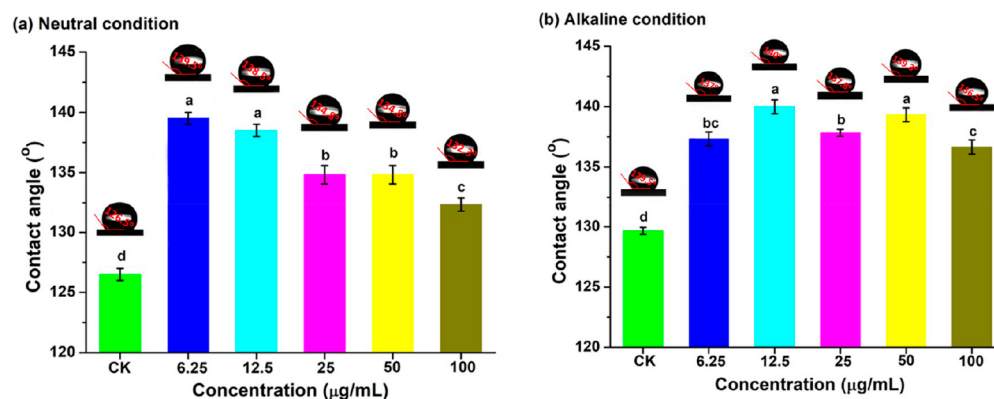


Figure 10. Contact angle of rice leaves treated by PGA₄₂ in different pH treatments: (a) 7.0, (b) 8.5. Graph represents mean \pm SE followed by same letter is not significantly different at $p \leq 0.05$ as determined by Tukey-Kramer HSD.

on rice growth were very similar to those under neutral conditions. The plant height and fresh weight showed different degrees of increase, which increased by 34.37% and 54.44% at 12.5 $\mu\text{g/mL}$, respectively. The overall growth revealed a trend of increasing first and then decreasing. The plant height peaked at 12.5 $\mu\text{g/mL}$ as well as fresh weight peaked at 25 $\mu\text{g/mL}$, and the decline phenomenon of them could be found with levels above 25 $\mu\text{g/mL}$.

Under alkaline conditions, the plant height and fresh weight of CK were lower than that of CK under neutral conditions, which may be caused by the alkali damage. However, the effect of promoting growth under alkaline condition was better than that under neutral condition. Due to more PGA₄₂ nanoparticles hydrolyzed under alkaline conditions, the content of poly(aspartic acid) was increased,⁴⁸ which led to a better growth promoting effect.⁴⁹ Thus, PGA₄₂ could promote rice growth and reduce the influence of alkaline environment on rice growth. That is to say, PGA₄₂ as nanocarriers of pesticides possessed a significant growth-promoting effect on the rice.

3.9. Contact Angle Experiment. The moisture on the leaf surface was a crucial source of moisture for the growth of pathogenic bacteria.⁵⁰ Many pathogenic spores could only germinate on the leaf and infect the plant body under suitable moisture conditions.^{51–53} It was generally recognized that too much leaf surface water would increase the risk of plants suffering from pests and diseases.⁵⁴ The contact angle, as a most direct indicator of wettability, was frequently used to determine the degree of wettability.

Figure 10 manifested the contact angle of rice leaves treated by PGA₄₂ in different pH treatments. Whether in neutral or alkaline conditions, the leaf contact angles of rice treated with five concentrations of PGA₄₂ rose in varying degrees compared with CK. Under neutral conditions, the contact angle compared to CK enhanced most significantly at 6.25 $\mu\text{g/mL}$ and 12.5 $\mu\text{g/mL}$, increasing by 13° and 12°, respectively. Whereas the contact angle decreased gradually along with the increasing concentration, and the most obvious decline occurred at 100 $\mu\text{g/mL}$. The contact angle of alkaline treatment increased by an average of 9.5° compared to CK. At the concentration of 12.5 $\mu\text{g/mL}$, the contact angle rose to 140°, whereas that of CK was only 129.5°. The data obtained revealed that the wetting performance of the leaves was greatly depressed after being treated with PGA₄₂ nanocarriers. Although the wettability was weakened, the ability of rice to resist pathogenic bacteria was enhanced.⁵⁵

In conclusion, multifunctional AVM-PGA nanoparticles were successfully synthesized. The nanoparticles were characterized by FITR, ¹H NMR, TEM, and SEM measurements. The study demonstrated PGA₄₂ nanocarriers had the remarkable antiphotolysis ability and controlled release behavior. Meanwhile, AVM-PGA₄₂ nanoparticles displayed a more superior control effect on *Plutella xylostella* rather than free-form AVM. PGA₄₂ as nanocarriers could improve the uptake and transportation of nonsystemic AVM in rice and it tended to acropetal accumulate. Finally, PGA₄₂ nanoparticles not only exhibited a good promoting effect on the growth of rice, but also enhanced the ability to resist pathogenic bacteria. All these performances showed that AVM-PGA₄₂ nanoparticles would possess promising application in controlling the pest and improving the pesticides utilization efficiency.

■ ASSOCIATED CONTENT

Supporting Information

The Supporting Information is available free of charge on the ACS Publications website at DOI: 10.1021/acs.jafc.8b03295.

Figure S1. The ¹H NMR spectra of PGA₁₂ (a), PGA₂₄ (b) and PGA₄₂ (c); Figure S2. The ¹³C NMR spectra of PGA₄₂; Table S1. Loading capacity and encapsulation efficiency of AVM for nanocarriers with different functionalization; Figure S3. Dynamic light scattering size distributions of PGA₄₂ and AVM-PGA₄₂; Figure S4. The linear fit chart of drug release model, Zero-order model (a), First-order model (b) and Higuchi model (c); and Table S2. Kinetic Parameters of AVM Released from AVM-PGA₄₂ with pH of 5.5, 7.0, and 8.5 (PDF)

■ AUTHOR INFORMATION

Corresponding Authors

*E-mail: hbxu@scau.edu.cn (H.X.).

*E-mail: jiajinliang@scau.edu.cn (J.J.).

ORCID

Hanhong Xu: 0000-0001-7841-2396

Author Contributions

[§]These authors contributed equally to this work.

Funding

The authors are grateful for the financial support provided by the National Key R&D Program of China (2018YFD0200300), and Key Platform of Department of Education of Guangdong Province (2017KZDXM007).

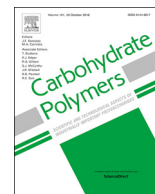
Notes

The authors declare no competing financial interest.

REFERENCES

- (1) Ghormade, V.; Deshpande, M. V.; Paknikar, K. M. Perspectives for nano-biotechnology enabled protection and nutrition of plants. *Biotechnol. Adv.* **2011**, *29*, 792–803.
- (2) Margni, M.; Rossier, D.; Crettaz, P.; Joliet, O. Life cycle impact assessment of pesticides on human health and ecosystems. *Agric. Ecosyst. Environ.* **2002**, *93*, 379–392.
- (3) Liu, B.; Wang, Y.; Yang, F.; Wang, X.; Shen, H.; Cui, H.; Wu, D. Construction of a controlled-release delivery system for pesticides using biodegradable PLA-based microcapsules. *Colloids Surf., B* **2016**, *144*, 38–45.
- (4) Forim, M. R.; Costa, E. S.; Da Silva, M. F. D. G.; Fernandes, J. B.; Mondego, J. M.; Boiça Junior, A. L. Development of a new method to prepare nano-/microparticles loaded with extracts of *Azadirachta indica*, their characterization and use in controlling *Plutella xylostella*. *J. Agric. Food Chem.* **2013**, *61*, 9131–9139.
- (5) Enserink, M.; Hines, P. J.; Vignieri, S. N.; Wigginton, N. S.; Yeston, J. S. The pesticide paradox. *Science* **2013**, *341*, 728–729.
- (6) Thakore, Y. The biopesticide market for global agricultural use. *Ind. Biotechnol.* **2006**, *2*, 194–208.
- (7) Lasota, J. A.; Dybas, R. A. Avermectins, a novel class of compounds: implications for use in arthropod pest control. *Annu. Rev. Entomol.* **1991**, *36*, 91–117.
- (8) Liu, W. G.; Zhu, X. Y.; Yin, M. M.; Chen, F. L. Photodegradation of three abamectin liquid formulations. *J. Agro-Environ. Sci.* **2012**, *31*, 1906–1912.
- (9) Escalada, J. P.; Gianotti, J.; Pajares, A.; Massad, W. A.; Amatguerrí, F.; García, N. A. Photodegradation of the acaricide abamectin: a kinetic study. *J. Agric. Food Chem.* **2008**, *56*, 7355–7359.
- (10) Mrozik, H.; Eskola, P.; Reynolds, G. F.; Arison, B. H.; Smith, G. M.; Fisher, M. H. Photoisomers of avermectins. *J. Org. Chem.* **1988**, *53*, 1820–1823.
- (11) Engelskirchen, S.; Maurer, R.; Levy, T.; Berghaus, R.; Auweter, H.; Glatter, O. Highly concentrated emulsified microemulsions as solvent-free plant protection formulations. *J. Colloid Interface Sci.* **2012**, *388*, 151–161.
- (12) Voinova, O. N.; Kalacheva, G. S.; Grodnitskaya, I. D.; Volova, T. G. Microbial polymers as a degradable carrier for pesticide delivery. *Appl. Biochem. Microbiol.* **2009**, *45*, 384–388.
- (13) Li, Y.; Zhou, M.; Pang, Y.; Qiu, X. Lignin-Based Microsphere: Preparation and performance on encapsulating the pesticide avermectin. *ACS Sustainable Chem. Eng.* **2017**, *5*, 3321–3328.
- (14) Jia, X.; Sheng, W.; Li, W.; Tong, Y.; Liu, Z.; Zhou, F. Adhesive Polydopamine coated avermectin microcapsules for prolonging foliar pesticide retention. *ACS Appl. Mater. Interfaces* **2014**, *6*, 19552–19558.
- (15) Liang, W.; Yu, A.; Wang, G.; Zheng, F.; Jia, J.; Xu, H. Chitosan-based nanoparticles of avermectin to control pine wood nematodes. *Int. J. Biol. Macromol.* **2018**, *112*, 258–263.
- (16) Zhang, H.; Qin, H.; Li, L.; Zhou, X.; Wang, W.; Kan, C. Preparation and characterization of controlled-release avermectin/castor oil-based polyurethane nanoemulsions. *J. Agric. Food Chem.* **2018**, *66*, 6552–6560.
- (17) Li, Y.; Yang, D.; Lu, S.; Lao, S.; Qiu, X. Modified lignin with anionic surfactant and its application in controlled release of avermectin. *J. Agric. Food Chem.* **2018**, *66*, 3457–3464.
- (18) Macconnell, J. G.; Demchak, R. J.; Preiser, F. A.; Dybas, R. A. Relative stability, toxicity, and penetrability of abamectin and its 8,9-oxide. *J. Agric. Food Chem.* **1989**, *37*, 1498–1501.
- (19) Tian, J.; Jiang, R.; Gao, P.; Xu, D.; Mao, L.; Zeng, G.; Liu, M.; Deng, F.; Zhang, X.; Wei, Y. Synthesis and cell imaging applications of amphiphilic AIE-active poly(amino acid)s. *Mater. Sci. Eng., C* **2017**, *79*, 563–569.
- (20) Zhang, X.; Han, L.; Liu, M.; Wang, K.; Tao, L.; Wan, Q.; Wei, Y. Recent progress and advances in redox-responsive polymers as controlled delivery nanoparticles. *Mater. Chem. Front.* **2017**, *1*, 807–822.
- (21) Zhang, X.; Wang, S.; Xu, L.; Feng, L.; Ji, Y.; Tao, L.; Li, S.; Wei, Y. Biocompatible polydopamine fluorescent organic nanoparticles: facile preparation and cell imaging. *Nanoscale* **2012**, *4*, 5581–5584.
- (22) Hernández-González, M.; Pérez Berumen, C. M.; Sánchez Ruiz, H.; Ruiz Salazar, C. V.; Hernández Paz, J. F.; Olivas-Armendáriz, I.; Martel-Estrada, S. A.; Rodríguez González, C. A. Polysuccinimide functionalized with oregano's essential oil extracts, an antimicrobial extended release bio-material. *Mater. Lett.* **2017**, *191*, 73–76.
- (23) Lu, C.; Li, B.; Liu, N.; Wu, G.; Gao, H.; Ma, J. A hydrazone crosslinked zwitterionic polypeptide nanogel as a platform for controlled drug delivery. *RSC Adv.* **2014**, *4*, 50301–50311.
- (24) Lee, M.; Jeong, J.; Kim, D. Intracellular uptake and pH-dependent release of doxorubicin from the self-assembled micelles based on amphiphilic polyaspartamide graft copolymers. *Biomacromolecules* **2015**, *16*, 136–144.
- (25) Wang, X.; Wu, G.; Lu, C.; Zhao, W.; Wang, Y.; Fan, Y.; Gao, H.; Ma, J. A novel delivery system of doxorubicin with high load and pH-responsive release from the nanoparticles of poly (α,β -aspartic acid) derivative. *Eur. J. Pharm. Sci.* **2012**, *47*, 256–264.
- (26) Xu, M.; Zhao, Y.; Feng, M. Polyaspartamide derivative nanoparticles with tunable surface charge achieve highly efficient cellular uptake and low cytotoxicity. *Langmuir* **2012**, *28*, 11310–11318.
- (27) Casadei, M. A.; Pitarresi, G.; Calabrese, R.; Paolicelli, P.; Giammona, G. Biodegradable and pH-sensitive hydrogels for potential colon-specific drug delivery: characterization and in vitro release studies. *Biomacromolecules* **2008**, *9*, 43–49.
- (28) Moon, J. R.; Kim, M. W.; Kim, D.; Jeong, J. H.; Kim, J. Synthesis and self-assembly behavior of novel polyaspartamide derivatives for anti-tumor drug delivery. *Colloid Polym. Sci.* **2011**, *289*, 63–71.
- (29) Gu, X.; Wang, J.; Liu, X.; Zhao, D.; Wang, Y.; Gao, H.; Wu, G. Temperature-responsive drug delivery systems based on polyaspartamides with isopropylamine pendant groups. *Soft Matter* **2013**, *9*, 7267–7273.
- (30) Xin, X.; He, Z.; Hill, M. R.; Niedz, R. P.; Jiang, X.; Sumerlin, B. S. Efficiency of biodegradable and pH-responsive polysuccinimide nanoparticles (PSI-NPs) as smart nanodelivery systems in grapefruit: in vitro cellular investigation. *Macromol. Biosci.* **2018**, *18*, 1800159.
- (31) Fischer, W.; André, B.; Rentsch, D.; Krolkiewicz, S.; Tegeder, M.; Breikreuz, K.; Frommer, W. B. Amino acid transport in plants. *Trends Plant Sci.* **1998**, *3*, 188–195.
- (32) Yao, G.; Wen, Y.; Zhao, C.; Xu, H. Novel amino acid ester-chlorantraniliprole conjugates: design, synthesis, phloem accumulation and bioactivity. *Pest Manage. Sci.* **2017**, *73*, 2131–2137.
- (33) Xie, Y.; Zhao, J.; Wang, C.; Yu, A.; Liu, N.; Chen, L.; Lin, F.; Xu, H. Glycinergic-Fipronil uptake is mediated by an amino acid carrier system and induces the expression of amino acid transporter genes in *ricinus communis* seedlings. *J. Agric. Food Chem.* **2016**, *64*, 3810–3818.
- (34) Torma, V.; Gyenes, T.; Szakács, Z.; Noszál, B.; Némethy, Á.; Zrínyi, M. Novel amino acid-based polymers for pharmaceutical applications. *Polym. Bull.* **2007**, *59*, 311–318.
- (35) Tong, Y.; Wu, Y.; Zhao, C.; Xu, Y.; Lu, J.; Xiang, S.; Zong, F.; Wu, X. Polymeric nanoparticles as a metolachlor carrier: water-based formulation for hydrophobic pesticides and absorption by plants. *J. Agric. Food Chem.* **2017**, *65*, 7371–7378.
- (36) Wang, X.; Zhao, J. Encapsulation of the herbicide picloram by using polyelectrolyte biopolymers as layer-by-layer materials. *J. Agric. Food Chem.* **2013**, *61*, 3789–3796.
- (37) Kim, J.; Yeon, S.; Kim, H.; Ahn, Y. Larvicidal activity against *Plutella xylostella* of cordycepin from the fruiting body of cordyceps militaris. *Pest Manage. Sci.* **2002**, *58*, 713–717.
- (38) Meharg, A. A.; Jardine, L. Arsenite transport into paddy rice (*Oryza sativa*) roots. *New Phytol.* **2003**, *157*, 39–44.

- (39) Tan, W.; Hou, N.; Pang, S.; Zhu, X.; Li, Z.; Wen, L.; Duan, L. Improved biological effects of uniconazole using porous hollow silica nanoparticles as carriers. *Pest Manage. Sci.* **2012**, *68*, 437–443.
- (40) Chen, J.; Xu, L.; Han, J.; Su, M.; Wu, Q. Synthesis of modified polyaspartic acid and evaluation of its scale inhibition and dispersion capacity. *Desalination* **2015**, *358*, 42–48.
- (41) Yeh, J.; Yang, H.; Hsu, Y.; Su, C.; Lee, T.; Lou, S. Synthesis and characteristics of biodegradable and temperature responsive polymeric micelles based on poly(aspartic acid)-g-poly(N-isopropylacrylamide-co-N,N-dimethylacrylamide). *Colloids Surf., A* **2013**, *421*, 1–8.
- (42) Migahed, M. A.; Rashwan, S. M.; Kamel, M. M.; Habib, R. E. Synthesis, characterization of polyaspartic acid-glycine adduct and evaluation of their performance as scale and corrosion inhibitor in desalination water plants. *J. Mol. Liq.* **2016**, *224*, 849–858.
- (43) Zhao, D.; Zhang, Y.; Lv, L.; Li, J. Preparation and release of avermectin-loaded cellulose acetate ultrafinefibers. *Polym. Eng. Sci.* **2013**, *53*, 609–614.
- (44) Liang, W.; Yu, A.; Wang, G.; Zheng, F.; Hu, P.; Jia, J.; Xu, H. A novel water-based chitosan-La pesticide nanocarrier enhancing defense responses in rice (*Oryza sativa* L) growth. *Carbohydr. Polym.* **2018**, *199*, 437–444.
- (45) Sheng, W. B.; Li, W.; Zhang, G. X.; Tong, Y. B.; Liu, Z. Y.; Jia, X. Study on the UV-shielding and controlled-release properties of a polydopamine coating for avermectin. *New J. Chem.* **2015**, *39*, 2752–2757.
- (46) Chitsiga, T.; Daramola, M. O.; Wagner, N.; Ngoy, J. Effect of the presence of water-soluble amines on the carbon dioxide (CO₂) adsorption capacity of amine-grafted poly-succinimide (PSI) adsorbent during CO₂ capture. *Energy Procedia* **2016**, *86*, 90–105.
- (47) Gong, C.; Shan, M.; Li, B.; Wu, G. A pH and redox dual stimuli-responsive poly(amino acid) derivative for controlled drug release. *Colloids Surf., B* **2016**, *146*, 396–405.
- (48) Hill, M. R.; MacKrell, E. J.; Forsthoefel, C. P.; Jensen, S. P.; Chen, M.; Moore, G. A.; He, Z. L.; Sumerlin, B. S. Biodegradable and pH-responsive nanoparticles designed for site-specific delivery in agriculture. *Biomacromolecules* **2015**, *16*, 1276–1282.
- (49) Koskan, L. P.; Meah, A. R. Y.; Sander, J. L.; Ross, R. J. Method and composition for enhanced plant productivity comprising fertilizer and cross-linker polyamino acid. 1999, US5861356A.
- (50) Müller, C.; Riederer, M. Plant surface properties in chemical ecology. *J. Chem. Ecol.* **2005**, *31*, 2621–2651.
- (51) Kuo, K.; Hoch, H. C. Germination of *Phyllosticta ampellicida* Pycnidiospores: prerequisite of adhesion to the substratum and the relationship of substratum wettability. *Fungal Genet. Biol.* **1996**, *20*, 18–29.
- (52) Pinon, J.; Frey, P.; Husson, C. Wettability of poplar leaves influences dew formation and infection by *Melampsora larici-populina*. *Plant Dis.* **2006**, *90*, 177–184.
- (53) Watanabe, T.; Yamaguchi, I. Evaluation of wettability of plant leaf surfaces. *J. Pestic. Sci.* **1991**, *16*, 491–498.
- (54) Bunster, L.; Fokkema, N. J.; Schippers, B. Effect of surface-active pseudomonas spp. on Leaf Wettability. *Appl. Environ. Microbiol.* **1989**, *55*, 1340–1345.
- (55) Kumar, N.; Pandey, S.; Bhattacharya, A.; Ahuja, P. S. Do leaf surface characteristics affect *Agrobacterium* infection in tea [*Camellia sinensis* (L.) O Kuntze]? *J. Biosci.* **2004**, *29*, 309–317.



A novel water-based chitosan-La pesticide nanocarrier enhancing defense responses in rice (*Oryza sativa* L) growth

Wenlong Liang^a, Aixin Yu^a, Guodong Wang^{a,b}, Feng Zheng^{a,b}, Pengtong Hu^{a,b}, Jinliang Jia^{a,b,*}, Hanhong Xu^{a,*}

^a State Key Laboratory for Conservation and Utilization of Subtropical Agro- bioresources, South China Agricultural University, Guangzhou 510642, PR China

^b College of Materials and Energy, South China Agricultural University, Guangzhou 510642, PR China

ARTICLE INFO

Keywords:

Chitosan oligosaccharide
Lanthanum
Avermectin
Magnaporthe grisea
Oryza sativa L.
Plant growth

ABSTRACT

To relieve the environmental pressure from overusing conventional pesticides formulations, the study of a new environmentally friendly and multifunctional formulation is so very urgent. Here, we firstly reported a lanthanum-modified chitosan oligosaccharide nanoparticles (Cos-La) prepared by a simple ionic cross-linking method to load avermectin (AVM). The loading capacity of AVM-loaded Cos-La was up to 46.3%. As a water-based formulation, Cos-La could effectively improve the persistence of AVM over 25% and reduce the photolysis rate of AVM around 20%. Furthermore, different concentrations of Cos-La were used to cultivate rice. The treated rice exhibited growth promotion effects in terms of plant height and fresh weight. With the increase in the treating concentration of Cos-La nanoparticles, the wettability of rice tended to reduce, which indicated it might lower the risk of plant diseases and pests. Further, Cos-La treated rice showed significant defense response for rice blast and the effect was two times more than equivalent Cos and $\text{LaCl}_3 \cdot 7\text{H}_2\text{O}$ mixture solution. These results showed that Cos-La not only could improve the stability and persistence of pesticides, but also could effectively promote the growth and improve the disease resistance of crops. Cos-La nanoparticles would be a promising and environmentally friendly nanocarrier of pesticides in agricultural scenarios.

1. Introduction

With continuous increase of the world population, the demand for sufficient quantity and quality of food is becoming more and more eager. It has been estimated that global food production is expected to increase 70–100% in order to feed the explosively growing population in 2050 (Tomlinson, 2013). Agricultural production continuously suffered from a large number of insect pests, diseases, and weeds leading to 40% losses to the tune of US \$2000 billion per year (Peshin & Dhawan, 2009). To reduce these losses and improve productivity, the use of pesticides became necessary. According to statistical research, pesticides have enhanced the yield of total worldwide crop over 30% every year (Lamberth, Jeanmart, Luksch, & Plant, 2013). It is well-known that the use of conventional pesticides formulation is the major method to control plant diseases and insect pests (Jia et al., 2017). However, the indiscriminately overuse of conventional pesticides formulation leads to degradation of agro-ecosystems and soil health, high pesticide residue, environmental pollution (Gevao, Semple, & Jones, 2000; Wan et al., 2013) and pesticide resistance (Naqqash, Gokce, Bakhsh, & Salim, 2016). These serious damages result from not only the

low efficiency of conventional pesticides formulation, but also the high use of organic solvent and surfactants in formulation, such as methylbenzene, xylene and nonylphenol surfactant (Engelskirchen et al., 2012). Thus, the development of a new water-based, release-controlled and environmentally friendly formulation is very urgent (Liu et al., 2013).

Over the past decade, the appearance of nanotechnology was potential to revolutionize agricultural practices (Scott & Chen, 1987). The use of nanoparticles in pesticide delivery had created many opportunities for safe application of conventional pesticides (Arasoglu et al., 2016; Mora-Huertas, Fessi, & Elaissari, 2010) and more and more water-based and eco-friendly nanopesticides formulations were reported lately. Those researches reports were mainly aimed at improving water dispersibility, persistence and stability of pesticides (Guan, Zhang, Tang, Wang, & Cui, 2017; Tong et al., 2017). However, there were no specific researches on whether the carriers had other biological functions such as promoting plants growth and activating defense responses to phytopathogen. Hence, we plan to prepare water-based multifunction nanoparticles in order to enhance biological functions of nanopesticides.

* Corresponding authors.

E-mail addresses: jjiajinliang@scau.edu.cn (J. Jia), hwxu@scau.edu.cn (H. Xu).

<https://doi.org/10.1016/j.carbpol.2018.07.042>

Received 25 April 2018; Received in revised form 12 July 2018; Accepted 13 July 2018

0144-8617/ © 2018 Elsevier Ltd. All rights reserved.

It is well-known that chitosan as a natural polymer has been widely used for nano-pharmaceuticals (Hu, Wang, Li, Zeng, & Huang, 2011; Li & Huang, 2012). Nevertheless, the use of chitosan in nanocarrier of pesticides is in initial stage. In the plant system, chitosan had been reported to promote plant growth and improve multifaceted disease resistance (El Hadrami, Adam, El Hadrami, & Daayf, 2010). Besides, results of research indicated that supplying the rare earth elements similarly had beneficial effect on plant growth and disease resistance (Diatloff, Smith, & Asher, 1995). Meanwhile, the rare earth elements-modified chitosan complex had been reported for improving the bioactivity of chitosan to improve bactericidal activity (Ou, Wu, Li, Wang, & Zhang, 2013). Therefore, the rare earth elements-modified chitosan would be a more potential material for preparing multifunctional nanopesticide formulation compared with chitosan and rare earth elements.

Here, a lanthanum-modified chitosan oligosaccharide (Cos-La) nanoparticle was firstly reported. The nanoparticles were prepared by simple ionic cross-linking between chitosan oligosaccharide (Cos) and lanthanum-citric acid complex (CA-La). The avermectin (AVM) which was a typical pesticide of poor water solubility, photosensitivity and low persistence was loaded in Cos-La nanoparticles (AVM-Cos-La) successfully. The nanoparticles were evaluated by fourier transform infrared (FT-IR), X-ray diffraction (XRD), electron microscope, dynamic light scattering (DLS), energy dispersive spectrometer (EDS) and X-ray photoelectron spectroscopy (XPS) in order to study the mechanism of the formation of Cos-La and AVM loading process. Furthermore, the release-controlled ability and photostability of AVM-Cos-La were evaluated. In order to explore the other biological application of Cos-La, different concentrations of Cos-La were used to cultivate rice and then the growth situation and disease resistance of rice were investigated.

2. Materials and methods

2.1. Materials

Chitosan oligosaccharide (1500–2000 Da, 99%) with a deacetylation degree of 85.49% was purchased from the Haidebei Marine Bioengineering (Jinan) Co., Ltd. Lanthanum(III) chloride heptahydrate ($\text{LaCl}_3 \cdot 7\text{H}_2\text{O}$) was purchased from Nine-Dinn Chemistry (Shanghai) Co., Ltd. Citric acid monohydrate (CA) was obtained from RichJoint Chemical Reagents (Shanghai) Co., Ltd. Avermectin (AVM) with a purity of 96% was provided by Fengning Chemistry (Hebei) Co., Ltd. Silwet L-77 was purchased from Biotopped (Beijing) Co., Ltd. Dialysis tube (MWCO, 3500) was purchased from Yuanye Bio-Technology (Shanghai) Co., Ltd. HCl, NaOH, CH_2Cl_2 and KBr were analytical grade from Taiwei Biochemical technology (Guangzhou) Co., Ltd.

2.2. Synthesis of Cos-La nanoparticles

The CA-La solution was prepared by the following procedure. Citric acid monohydrate (105 mg, 0.5 mmol) and $\text{LaCl}_3 \cdot 7\text{H}_2\text{O}$ (37.1 mg, 0.1 mmol) were dissolved in 25 mL distilled water. NaOH (1 mol/L) and HCl (1 mol/L) solution were used to adjust the pH value to 6 and the mixed solution was agitated gently at 25 °C for 0.5 h. The transparent CA-La complex solution was obtained and the CA-La (18.3 mg) was obtained by the solid precipitating out from the CA-La complex solution.

Cos-La nanoparticles were synthesized as similar with the literature (Lin et al., 2015). In briefly, 350 mg of Cos was dissolved in 25 mL distilled water. 25 mL of CA-La complex solution was added to the Cos solution with stirring at 25 °C for 2 h. The resulting Cos-La nanoparticles (278 mg) were harvested by centrifugation (8000 r/min for 10 min), rinsed three times in distilled water and freeze-dried.

2.3. Preparation of AVM-loaded Cos-La nanoparticles

AVM-loaded Cos-La nanoparticles were prepared by the similar to above method. 350 mg of Cos was dissolved in 20 mL distilled water. After dissolving 175 mg of AVM in 10 mL of CH_2Cl_2 , the organic phase was added to the Cos solution and vigorously stirred for 30 min to obtain an emulsion. At the same time, citric acid monohydrate (105 mg, 0.5 mmol) and $\text{LaCl}_3 \cdot 7\text{H}_2\text{O}$ (37.1 mg, 0.1 mmol) were dissolved in 20 mL distilled water and adjusted the pH to 6 with stirring for 0.5 h. 20 mL of complex solution was added to the emulsion over 2 h with gentle stirring at 25 °C. The AVM-Cos-La nanoparticles (247 mg) were harvested by centrifugation (8000 r/min for 10 min), rinsed several times in distilled water and freeze-dried.

To determine AVM loading efficiency (LE) and encapsulation efficiency (EE), 10 mg of freeze-dried AVM-Cos-La nanoparticles were added to 3 mL of ethanol, and the suspension subjected to ultrasonication using ultrasonic cleaner (Kunshan Ultrasonic Instruments, KQ2200DB) for 4 h to completely disassociate the AVM. The supernatant was collected by centrifugation (8000 r/min for 10 min) and then using UV-vis spectroscopy (Shimadzu, UV-2550) to determine the concentration of AVM in supernatant. The LE and EE were calculated as follows:

$$\text{LE (\%)} = \left(\frac{M}{M_0} \right) \times 100\% \quad (1)$$

$$\text{EE (\%)} = \left(\frac{M}{W} \right) \times 100\% \quad (2)$$

Where M is the mass of AVM in Cos-La nanoparticles, M_0 is the mass of AVM-Cos-La nanoparticle and W is the total amount of AVM used for nanoparticles preparation.

2.4. Characterization of nanoparticles

The size and morphology of Cos-La nanoparticles were determined by DLS with a Zetasizer NanoZSE (Malvern Instruments), TEM with a Tecnai 12 device (Fei, The Netherlands) and SEM using a Merlin Compact (Zeiss, Germany). The structure and compositions were characterized by FT-IR, EDS, XPS and ICP-OES. The FT-IR spectra were obtained using VERTEX 70 spectrometer (Bruker, Germany). Energy disperse spectra were determined by EDS Inca X-max (Oxford Instruments). XPS was carried out by using Escalab 250Xi (Thermo Scientific). La element content of Cos-La nanoparticles was obtained by ICP-OES 730 (Agilent). XRD patterns of nanoparticles were obtained by UltimaIV X-ray diffractometer (Rigaku).

2.5. Controlled-release of the AVM-Cos-La nanoparticles

The drug releasing profile of the Cos-La nanoparticles was measured by the dialysis method (Zhang et al., 2017). AVM-Cos-La nanoparticles containing 5 mg of AVM were dispersed to 1 mL of ethanol/water mixture (2:1, v/v) and moved into the dialysis bags (MWCO, 3500 Da). The dialysis bag was immersed into 150 mL of ethanol/water mixture (2:1, v/v) release media in a jar. The jar was then placed onto a magnetic stirrer with gentle agitation under the room temperature. 3 mL of the release medium was taken at the predesigned interval, and the released amount of AVM was obtained by UV-vis spectroscopy. The release medium was put back to the tester after the measurement and 5 mg of pure AVM as control.

2.6. Photodegradation behavior of AVM-Cos-La nanoparticles

The photostability of the AVM-Cos-La drug-loaded system was evaluated according to the method (Liang et al., 2017). 60 mg of AVM-Cos-La nanoparticles were irradiated at room temperature by an UV lamp (254 nm, 8 W). The sample was spread out on a petri dish and the

light source was at a distance of 15 cm. 10 mg of sample was collected at predesigned interval and then the remaining AVM was analyzed at 245 nm by UV–vis spectroscopy. The pure AVM was chosen as control.

2.7. Plant material and growth condition

The effect of Cos-La nanoparticles on plant growth was assessed according to the paper (Tan et al., 2012). Seeds of rice (*Oryza sativa* L.) cultivar huahang 36 were sterilized with 10% sodium hypochlorite solution for 10 min. After washing 3 times with distilled water, the seeds were incubated in 5 mL of different concentration of Cos-La nanoparticles (6.25, 12.5, 25, 50 and 100 $\mu\text{g/mL}$), water, mixture solution of Cos and $\text{LaCl}_3 \cdot 7\text{H}_2\text{O}$ (Cos/La, 100 $\mu\text{g/mL}$) at 28 °C until germination, respectively. After 6 days, ten germinated seeds of each group were planted in a 50 mL centrifuge tube that was filled with 45 mL of corresponding concentration of Cos-La nanoparticles, water and Cos/La hogland solution, respectively. These centrifuge tubes were placed in a growth chamber (Yiheng Technology, MGC-300 A) with a 16/8 h photoperiod, 28/25 °C day/night temperature and 15,000 LX illumination intensity. The fresh hogland solution was added to the 45 mL scale line of centrifuge tube daily. The plant height and fresh weight of the seedlings were recorded after two weeks.

2.8. The wettability evaluation of rice leaves

The wettability of plants surface had important influence on retention, adsorption and filtration of air pollutants (Neinhuis & Barthlott, 1998), interception of rain (Holder, 2007) and especially the infection of plant diseases and insect pests (Bunster, Fokkema, & Schippers, 1989; Pinon, Frey, & Husson, 2006). It was believed that excessive water retention on the leaf surface can increase the risk of plant diseases and pests (Kumar, Pandey, Bhattacharya, & Ahuja, 2004). To evaluate whether the Cos-La could change the wettability of plant, the experiment was done as following:

A healthy rice leaf was randomly selected from the seedling that was cultivated with different concentration of Cos-La nanoparticles and water in the promoting growth experiment. The degree of water repellency of the rice leaf surface was determined by measuring the contact angle of a 10 μL water droplet placed by micropipette on each leaf mouthed on glass slides using double sided tape. The contact angle was obtained by optical contact angle measuring device (OCA20).

2.9. Evaluation of Cos-La nanoparticles in protection of rice from blast disease

Blast-susceptible seedlings of rice (*Oryza sativa* L.) cultivar Lijiangxintuanheigu were planted in green house condition. After 15 days, the seedlings were subjected to foliar spray of equally volume of 1000 $\mu\text{g/mL}$ of Cos/La and Cos-La with 0.5% Silwet L-77 (Choudhary et al., 2017). Treating seedlings with Cos/La and Cos-La 7 days later, the seedlings were infected by *Magnaporthe grisea* (*M. grisea*) as described (Hamer, Howard, Chumley, & Valent, 1987) and then morbidity was evaluated after 4 days of infection by the statistical relative amount of *M. grisea*.

The relative amounts of *M. grisea* were calculated by the $\Delta\Delta\text{Ct}$ (cycle threshold) method (Livak & Schmittgen, 2001). Ct values were analyzed using RT-qPCR (Bio-rad, CFX96). *M. grisea* gene *pot2* was chosen as target gene and rice resistance gene *pi-ta* as endogenous control gene. The two primers reported by Berruyer, Poussier, Kankanala, Mosquera, and Valent (2006).

3. Results and discussion

3.1. Synthesis and characterization of nanoparticles

As shown in Scheme 1, the Cos-La nanoparticles were prepared by

two simple steps. The addition of CA-La that was synthesized by citric acid and $\text{LaCl}_3 \cdot 7\text{H}_2\text{O}$ was included to provide ionic cross-linking. The Cos-La nanoparticles were formed by an electrostatic interaction between the positively charged amino groups on the surface of chitosan oligosaccharide and the negatively charged carboxy groups on the CA-La complex. La content was 4.83% (w/w) in the nanoparticles carried out by ICP-OES. Through this simple method, AVM could be loaded when the Cos-La nanoparticles were formed.

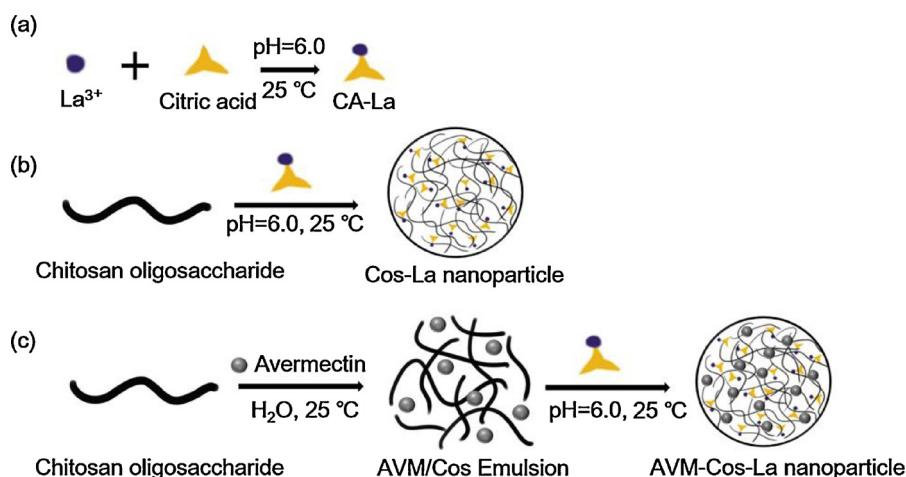
3.1.1. Determination of Cos-La nanoparticles morphology

Fig. 1(a) and (d) shows the morphology and size of Cos-La nanoparticles which were spherical in shape and a size range was 310 ± 19 nm. The particle size distribution was calculated by randomly sampling at least 200 nanoparticles from TEM image. Some nanoparticles were gathering and the surface was rough which was validated by the results of SEM in Fig. 1(b). It was observed that Cos-La nanoparticles were comprised of a dense network structure of interpenetrating polymer chains cross-linked to each other by CA-La complex (Tang, Huang, & Lim, 2003). The average size of the Cos-La nanoparticles measured by Zetasizer were 333.1 nm and with narrow size distribution (PDI-0.425) in Fig. 1(c). The slightly high PDI was due to the uncontrolled crosslinking and assembling during the formation of nanoparticles without adding other auxiliaries (Bulbake, Doppalapudi, Kommineni, & Khan, 2017; Mozafari, Danaei, Javanmard, Raji, & Maherani, 2017). The size difference between TEM and DLS analyses was due to different principle involved in these two techniques. The DLS measurement involves hydro-dynamic state of nanoparticles whereas it was dry state in TEM measurement (Ali, Rajendran, & Joshi, 2011).

3.1.2. FT-IR and XRD analysis

The FT-IR spectra of Cos, CA, CA-La and Cos-La were shown as Fig. 2(a). The broad and prominent peak at 3441.63 cm^{-1} and 2928.54 cm^{-1} were observed on Cos which was assigned to O–H, N–H stretching and aliphatic asymmetrical C–H stretching vibration in methylene (Jiang et al., 2016) respectively. Two strong peaks obtained at 1640 cm^{-1} and 1526 cm^{-1} showed the presence of amide I (C=O, stretching) and amide II (N–H, bending). The absorption band at 1075 cm^{-1} belonged to C–O stretching vibration on Cos. In the spectrum of CA, the broad and strong band ranging from 3200 cm^{-1} to 3600 cm^{-1} was due to the O–H stretching, while the peaks at 1742 cm^{-1} and 1703 cm^{-1} were assigned to C=O stretching vibration from the carboxyl (Zuo & Balasubramanian, 2013). Comparing with the spectrum of CA-La, two new peaks were observed at 1716 cm^{-1} and 1587 cm^{-1} , which indicated the carboxyl on the citric acid reacted with La^{3+} . After the formation of Cos-La nanoparticles, the peak at 1640 cm^{-1} , 1526 cm^{-1} in Cos and 1742 cm^{-1} , 1703 cm^{-1} in CA were disappeared, while a new peak at 1581 cm^{-1} was appeared. Moreover, the C–O peak in 1075 cm^{-1} was retained. These results confirmed that the nanoparticles formed from an electrostatic interaction between the carboxyl in citric acid and the amino groups in Cos. As shown in Fig. 2(b), the peak at 1734 cm^{-1} represented the C=O bond carried by AVM (Liang et al., 2018), and was also recognized in the spectrum generated by the AVM-Cos-La nanoparticles, which confirmed the successful encapsulation of AVM within the Cos-La nanoparticles.

The X-ray powder diffraction is a rapid analytical technique primarily used for phase identification of crystalline material and can provide information on unit cell dimensions. The XRD patterns of Cos and Cos-La presented in Fig. 2(c). The patterns of Cos showed certain sharp peaks at 11.3° , 16° , 18.1° and multiple peaks around 24.3° . The peaks correspond to a hydrated crystalline structure and an amorphous structure of Cos, respectively (Rhim, Hong, Park, & Ng, 2006). The patterns of Cos-La nanoparticles were observed at 11.3° , 18.7° and 23.4° . From the reduction and broadening of peaks compared with Cos, it was concluded that the crystallinity of nanoparticles was found to be reduced caused by both a reduction in crystallite size and an increase in



Scheme 1. Schematic illustrations of preparation of (a) CA-La, (b) Cos-La nanoparticle and (c) AVM-Cos-La nanoparticle.

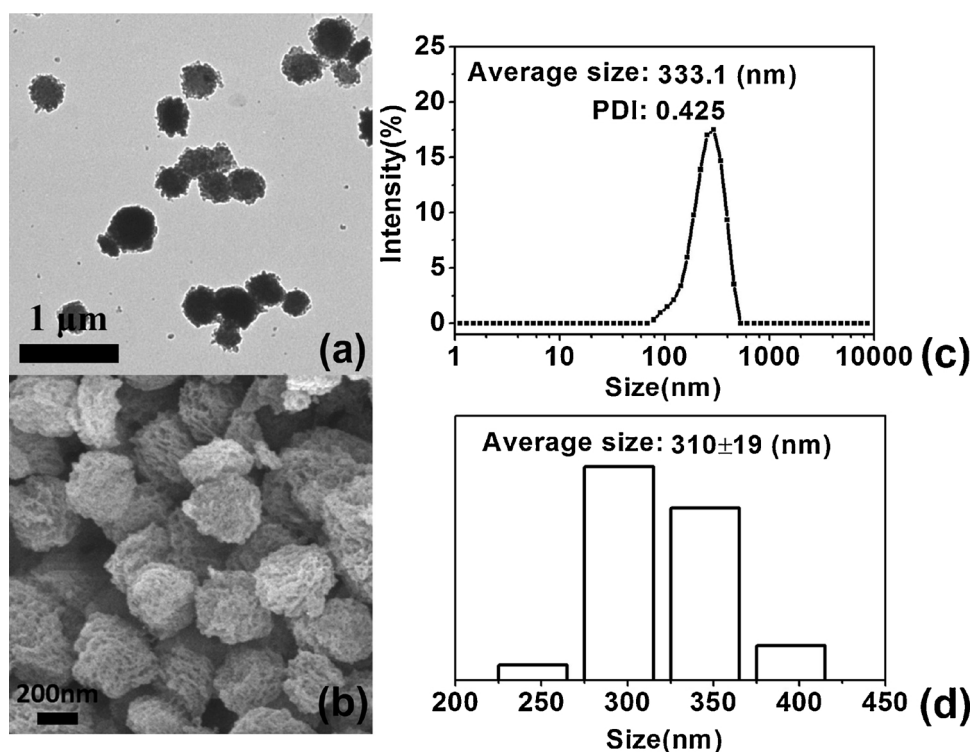


Fig. 1. The characterizations of morphology and size: (a) TEM of Cos-La, (b) SEM of Cos-La and (c) Dynamic light scattering of Cos-La nanoparticles (d) Topography of the nanoparticles size in TEM.

lattice strain (Lemine, 2009). As shown in Fig. 2(d), the XRD pattern of AVM showed many sharp peaks between 10° and 30° , and that indicated AVM had high crystallinity. However, a lower degree of crystallization was exhibited by the AVM packaged in Cos-La nanoparticles compared with pure AVM. It concluded that the Cos-La nanoparticles could increase drug dispersion and decrease the amount of the crystalline phase in the nano-formulation (Huang et al., 2016).

3.1.3. Energy spectrum analysis

To further confirm the mechanism of the formation for nanoparticles, the nanoparticles were analyzed by EDS and XPS. Fig. 1S showed a representative EDS statistic of the elements (C, O, N, La) identified and the same elements identified were consistent with the XPS survey scan of Cos-La in Fig. 3. The La weight percentage is around 4.9%, which was much the same as the result from ICP-OES. Besides, the La element was uniformly distributed on the surface of

nanoparticles.

As shown in Fig. 3, the La 3d spectra showed the La 3d states in the XPS spectra appeared a doublet. The energy peak appearing on the high energy side of La $3d_{5/2}$ peak was satellite peak (Yang, Li, Yu, Zhang, & Huang, 2008). The binding energy at 834.9 eV was attributed La^{3+} which was shifted compared with the reference value 836 eV (Moulder, Stickle, Sobol, & Bomben, 1995). The reducing binding energy indicated the La^{3+} combined with CA by coordination reaction.

It was known that there was only a peak at 399.5 eV on pure Cos according to the reference which was assigned to $\text{N}-\text{C}=\text{O}$ and NH_2 chemical bindings (Vieira, Oliveira, Guibal, Rodríguez-Castellón, & Beppu, 2011). However, there were two peaks identified in the N 1s spectra of Cos-La. The peak at 399.5 eV was retained and a new peak at 401.5 eV appeared which was assigned to NH_3^+ (Lindberg et al., 1983). The upward shift of the binding energy of the peak concluded that some NH_2 on the Cos were in the form of NH_3^+ (Bourbigot, Bras, Gengembre,

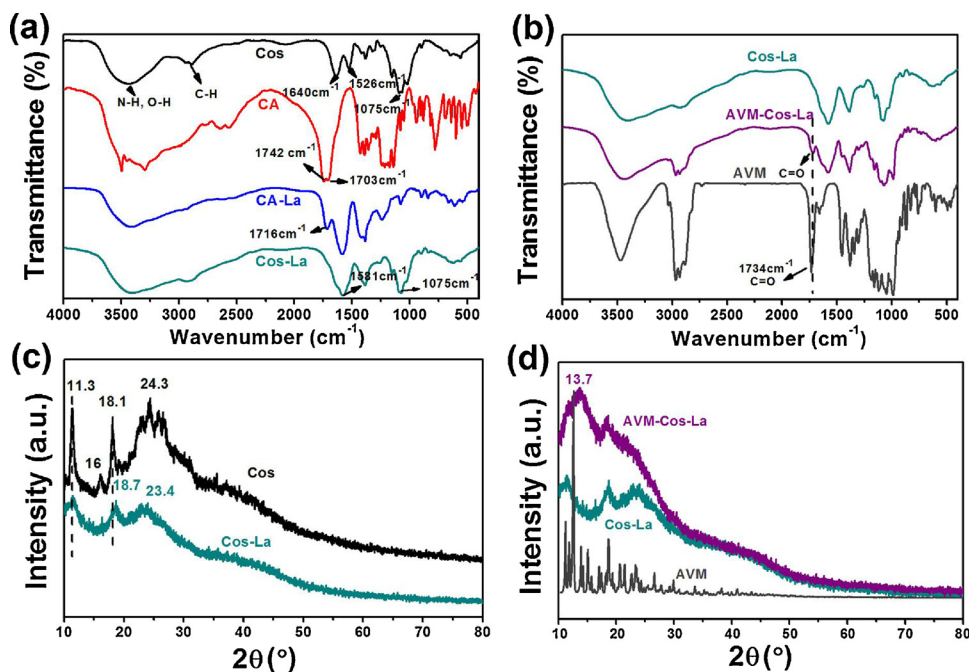


Fig. 2. FT-IR spectra of (a) Cos, CA, CA-La, Cos-La (b) AVM-Cos-La, AVM. X-ray diffraction patterns of (c) Cos, Cos-La and (d) AVM-Cos-La, Cos-La, AVM.

& Delobel, 1994) as it was expected from ionic bindings with carboxyl and the La element didn't bond with Cos. The results showed that only the ionic cross-linkages existed between protonated amine groups and carboxyl in Cos-La nanoparticles.

3.2. AVM-loading and release studies of Cos-La

The AVM-loading capacity and encapsulation efficiency of the AVM-Cos-La nanoparticles were calculated by the standard curve of AVM. It was possible to estimate that the LE reached up to 46.3% and the EE was around 65.3%. The in vitro release profile of pure AVM and AVM

from Cos-La nanoparticles were shown in Fig. 4. Perceptibly, the release of AVM from Cos-La nanoparticles was small difference with pure AVM before 36 h because of drug burst release, which was resulted from the high loading efficiency (Yeo & Park, 2007). However, the AVM release from Cos-La became gentler and the pure AVM maintained a high release speed after 48 h. Until the tenth day, the cumulative release rate of pure AVM was 93.6%, while the AVM release from Cos-La was only 67.5%. It was indicated that Cos-La could prolong the leaching time of AVM to enhance utilization efficacy.

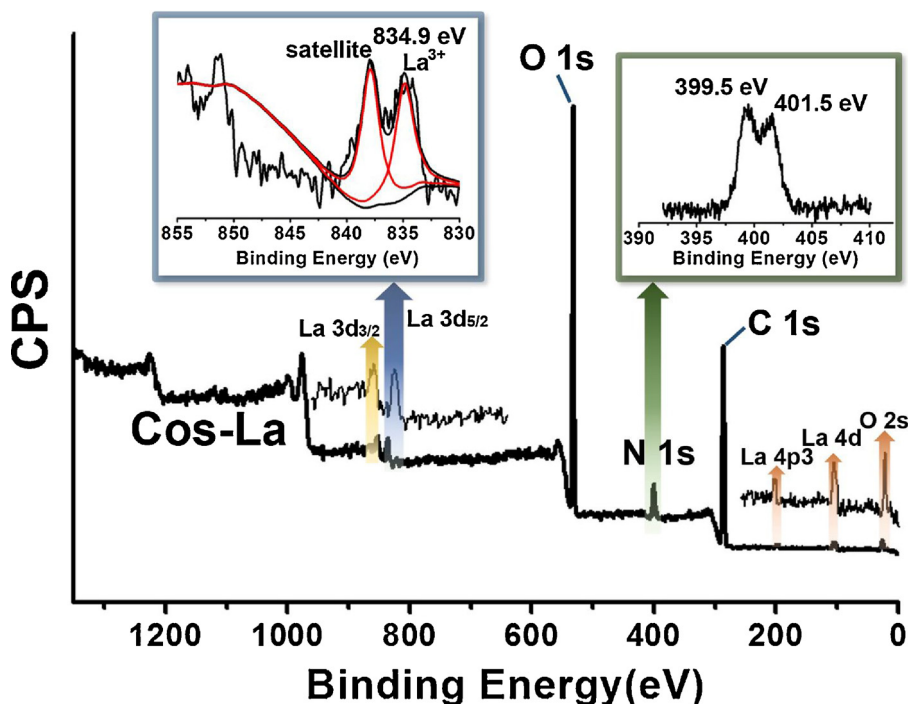


Fig. 3. X-ray photoelectron spectroscopy of Cos-La nanoparticles.

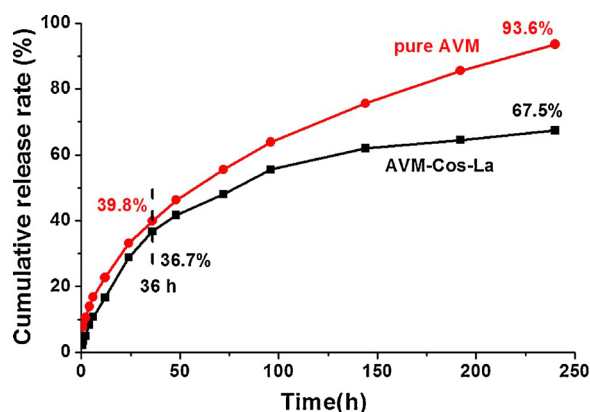


Fig. 4. In vitro release profile of pure AVM and AVM from Cos-La nanoparticles.

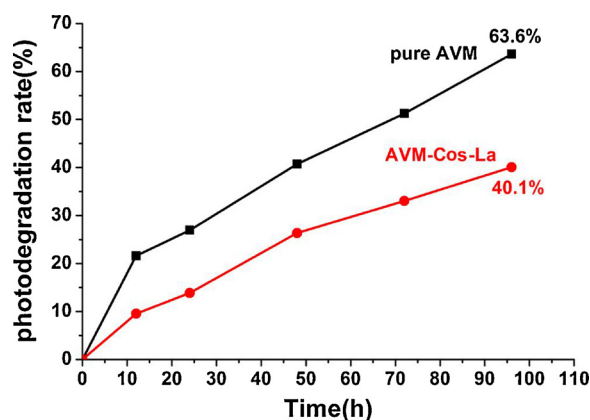


Fig. 5. The response curve of the photolysis rate of pure AVM and AVM-Cos-La.

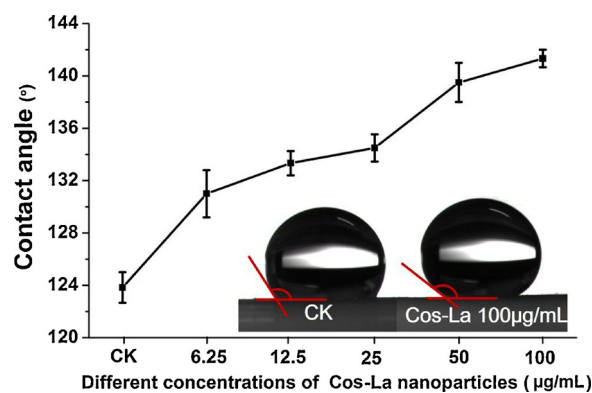


Fig. 7. The change of contact angle on rice leaf surface after hydroponics experiments.

3.3. Photostability of the AVM-Cos-La nanoparticles

As a bio-pesticide, AVM was very prone to degradation upon exposure to UV light. In order to improve the photostability of them, encapsulation formulation is seemingly practical. The degradation rate of AVM induced by UV irradiation is illustrated in Fig. 5. These results clearly showed that the photodegradation rate of pure AVM was very fast, with 63.6% degradation after 96 h of exposure to continuous UV light irradiation. At the same time, the photodegradation rates of the AVM loaded in Cos-La were only 40.1%, indicating that Cos-La nanoparticles were probably as a carrier to protect the light sensitive drug.

3.4. Effect of Cos-La nanoparticles on plant growth

To evaluate the effect of Cos-La nanoparticles on growth of rice, length of aboveground parts and fresh weight of rice were recorded. The Cos-La nanoparticles (100, 50, 25, 12.5, 6.25 μg/mL) significantly enhanced the growth of rice in hydroponics experiments by statistical

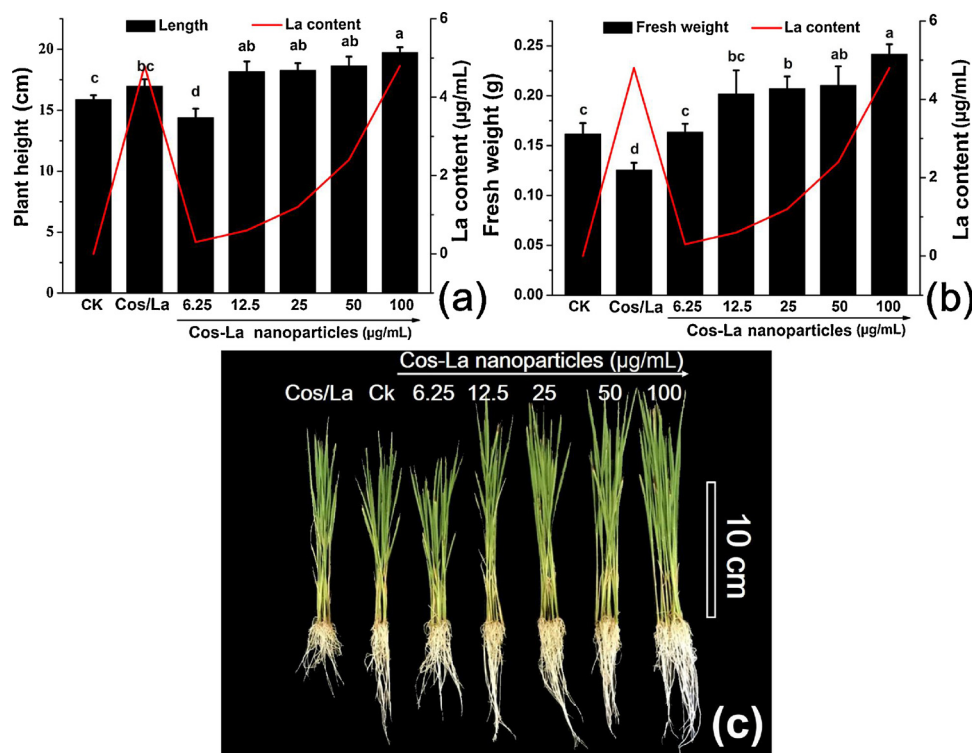


Fig. 6. Effect of Cos-La nanoparticles on (a) plant height, (b) fresh weight and (c) effect of Cos-La nanoparticles on plant growth of rice in hydroponics experiments. Graph represents mean \pm SE followed by same letter is not significantly different at $p \leq 0.05$ as determined by Tukey-Kramer HSD.

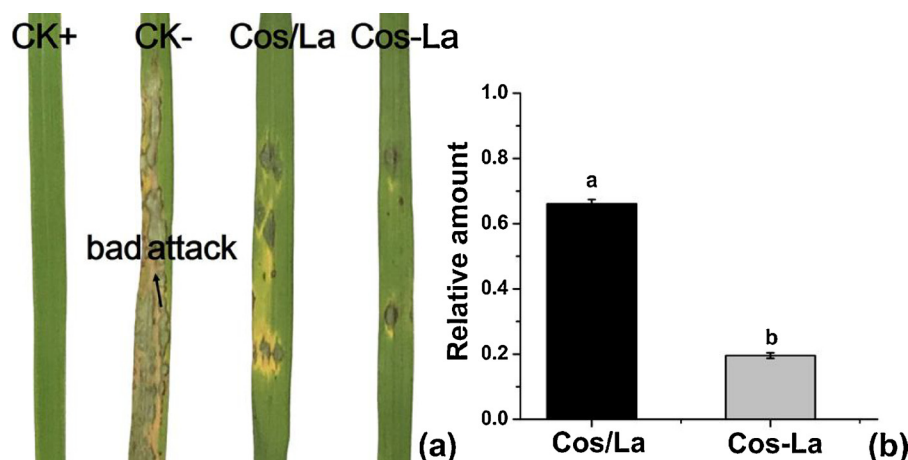


Fig. 8. Suppression of blast disease on rice (a) effect of Cos-La nanoparticles on suppressing blast disease of rice in pot experiment (b) relative amount of blast fungus. Graph represents mean \pm SE followed by same letter is not significantly different at $p \leq 0.05$ as determined by Tukey-Kramer HSD.

analyses as compared to control (CK) and Cos/La were shown in Fig. 6. As shown in Fig. 6(a), The increase in the plant height of rice treated with Cos-La nanoparticles were from 2.3 cm to 3.9 cm and 1.2 cm to 2.8 cm compared with CK and Cos/La, respectively. The increase in the fresh weight of rice treated with Cos-La nanoparticles were from 0.00187 g to 0.07993 g and from 0.03804 g to 0.1161 g compared with CK and Cos/La respectively presented in Fig. 6(b). With the increasing treating concentrations of Cos-La nanoparticles, the length and fresh weight of rice tended to grow. To confirm the optimal concentrations of Cos-La nanoparticles for enhancing the growth of rice, tenfold concentrations of Cos-La were used to cultivate rice with the same method. The optimal concentration was within 125 $\mu\text{g/mL}$ to 250 $\mu\text{g/mL}$ presented in Fig. 2S.

3.5. Change of contact angle on leaf surface

The side view of water droplets on rice leaves surface treated with Cos-La were shown in Fig. 7. It was obvious that contact angle for the rice leaves after cultivating with Cos-La nanoparticles was increased compared with CK. With the increasing treating concentrations of Cos-La nanoparticles, the contact angle tended to increase that were from 7.2° to 17.5°. The increase of contact angle indicated the wettability of rice leaves was reduced. Because excessive water retention on the leaf surface can increase the risk of plant diseases and pests, Cos-La nanoparticles could reduce the wettability of rice that might lower the risk of plant diseases and pests (Chandler & Thomas, 1991).

3.6. The suppression of leaf blast on rice

Cos/La (1000 $\mu\text{g/mL}$) and Cos-La (1000 $\mu\text{g/mL}$) had no inhibitory activity against growth of *M. grisea* under in-vitro condition shown in Fig. 3S. However, suppression of disease symptom was observed in vivo under pot experiment shown in Fig. 8(a). CK+ was the normal rice leaf without treating anything. CK- was rice blast infected rice. It showed that the severe symptoms of rice blast were appeared on the leaf after 4 days of fungal inoculation. Contrarily, the illness was mild for the blast infected rice after treating with Cos/La and Cos-La, respectively. These results indicated that both the Cos/La solution and Cos-La nanoparticles could stimulate some defense mechanism in rice to alleviate the morbidity of rice blast (Manikandan & Sathiyabama, 2016) but the efficacy of Cos-La nanoparticles was better. To quantitatively analyze the different efficacy between Cos/La and Cos-La, relative amount of *M. grisea* in the infected rice was calculated in Fig. 8(b). Amount of *M. grisea* in the infected rice treated with Cos/La were two times more than the rice treated with Cos-La. It concluded that the Cos-La nanocarrier could effectively improve the disease resistance of rice for blast

compared with the free Cos and La^{3+} .

4. Conclusions

Cos-La nanoparticles were prepared by a simple ionic cross-linking and packaged AVM successfully. Furthermore, the Cos-La and AVM-Cos-La nanoparticles were characterized by FT-IR, XRD, DLS, EDS and XPS. The mechanism of formation and drug loading process were analyzed. Furthering performance evaluation indicated that Cos-La nanopesticides not only improved the water dispersibility, stability and persistence of AVM without adding toxic organic solvents and surfactant, but also effectively promoted the growth and improved the disease resistance of crops. That was a water-based, release-controlled, environmentally friendly and multifunctional pesticide formulation, which would expand the application of novel nanopesticides formulation used in integrated plant diseases and insect pests management.

Acknowledgments

Financial support was provided by the National Key R&D Program of China (2018YFD0200300), and Science and Technology Program of Guangdong (Grant 2015B020230012).

Appendix A. Supplementary data

Supplementary material related to this article can be found, in the online version, at doi:<https://doi.org/10.1016/j.carbpol.2018.07.042>.

References

- Ali, S. W., Rajendran, S., & Joshi, M. (2011). Synthesis and characterization of chitosan and silver loaded chitosan nanoparticles for bioactive polyester. *Carbohydrate Polymers*, 83(2), 438–446.
- Arasoglu, T., Mansuroglu, B., Derman, S., Gumus, B., Kocyigit, B., Acar, T., et al. (2016). Enhancement of antifungal activity of juglone (5-hydroxy-1,4-naphthoquinone) using a poly(d,l-lactic-co-glycolic acid) (PLGA) nanoparticle system. *Journal of Agricultural and Food Chemistry*, 64(38), 7087–7094.
- Berruyer, R., Poussier, S., Kankanala, P., Mosquera, G., & Valent, B. (2006). Quantitative and qualitative influence of inoculation methods on in planta growth of rice blast fungus. *Phytopathology*, 96(4), 346–355.
- Bourbigot, S., Bras, M. L., Gengembre, L., & Delobel, R. (1994). XPS study of an in-tumescent coating application to the ammonium polyphosphate/pentaerythritol fire-retardant system. *Applied Surface Science*, 81(3), 299–307.
- Bulbake, U., Doppalapudi, S., Kommineni, N., & Khan, W. (2017). Liposomal formulations in clinical use: An updated review. *Pharmaceutics*, 9(2).
- Bunster, L., Fokkema, N. J., & Schippers, B. (1989). Effect of surface-active *Pseudomonas* spp. on leaf wettability. *Applied and Environmental Microbiology*, 55(6), 1340–1345.
- Chandler, L. D., & Thomas, C. E. (1991). Effect of leaf miner feeding activity on the incidence of Alternaria leaf blight lesions on muskmelon leaves. *Plant Disease*, 75(9), 930–940.

- Choudhary, R. C., Kumaraswamy, R. V., Kumari, S., Sharma, S. S., Pal, A., Raliya, R., et al. (2017). Cu-chitosan nanoparticle boost defense responses and plant growth in maize (*Zea mays* L.). *Scientific Reports*, 7(1), 9754.
- Diatloff, E., Smith, F. W., & Asher, C. J. (1995). Rare earth elements and plant growth: I. Effects of lanthanum and cerium on root elongation of corn and mungbean. *Journal of Plant Nutrition*, 18(10), 1963–1976.
- El Hadrami, A., Adam, L. R., El Hadrami, I., & Daayf, F. (2010). Chitosan in plant protection. *Marine Drugs*, 8(4), 968–987.
- Engelskirchen, S., Maurer, R., Levy, T., Berghaus, R., Auweter, H., & Glatter, O. (2012). Highly concentrated emulsified microemulsions as solvent-free plant protection formulations. *Journal of Colloid & Interface Science*, 388(1), 151–161.
- Gevao, B., Semple, K. T., & Jones, K. C. (2000). Bound pesticide residues in soils: A review. *Environmental Pollution*, 108(1), 3–14.
- Guan, W., Zhang, W., Tang, L., Wang, Y., & Cui, H. (2017). Fabrication of novel avermectin nanoemulsion using a polyurethane emulsifier with cleavable disulfide bonds. *Journal of Agricultural and Food Chemistry*, 66(26), 6569–6577.
- Hamer, J. E., Howard, R. J., Chumley, F. G., & Valent, B. (1987). A mechanism for surface attachment in spores of a plant pathogenic fungus. *Science*, 239, 288–290.
- Holder, C. D. (2007). Leaf water repellency of species in Guatemala and Colorado (USA) and its significance to forest hydrology studies. *Journal of Hydrology*, 336(1–2), 147–154.
- Hu, B., Wang, S. S., Li, J., Zeng, X. X., & Huang, Q. R. (2011). Assembly of bioactive peptide-chitosan nanocomplexes. *Journal of Physical Chemistry B*, 115(23), 7515–7523.
- Huang, P., Zeng, B., Mai, Z., Deng, J., Fang, Y., Huang, W., et al. (2016). Novel drug delivery nanosystems based on out-inside bifunctionalized mesoporous silica yolk-shell magnetic nanostars used as nanocarriers for curcumin. *Journal of Materials Chemistry B*, 4(1), 46–56.
- Jia, J. L., Jin, X. Y., Zhu, L., Zhang, Z. X., Liang, W. L., Wang, G. D., et al. (2017). Enhanced intracellular uptake in vitro by glucose-functionalized nanopesticides. *New Journal of Chemistry*, 41(19), 11398–11404.
- Jiang, W., Zhou, Z., Wang, D., Zhou, X., Tao, R., Yang, Y., et al. (2016). Transglutaminase catalyzed hydrolyzed wheat gliadin grafted with chitosan oligosaccharide and its characterization. *Carbohydrate Polymers*, 153, 105–114.
- Kumar, N., Pandey, S., Bhattacharya, A., & Ahuja, P. S. (2004). Do leaf surface characteristics affect Agrobacterium infection in tea [*Camellia sinensis* (L.) O Kuntze]? *Journal of Bioscience*, 29, 309–317.
- Lamberth, C., Jeanmart, S., Luksch, T., & Plant, A. (2013). Current challenges and trends in the discovery of agrochemicals. *Science*, 341(6147), 742–746.
- Lemine, O. M. (2009). Microstructural characterisation of nanoparticles using, XRD line profiles analysis, FE-SEM and FT-IR. *Superlattices and Microstructures*, 45(6), 576–582.
- Li, J., & Huang, Q. (2012). Rheological properties of chitosan-tripolyphosphate complexes: From suspensions to microgels. *Carbohydrate Polymers*, 87(2), 1670–1677.
- Liang, J., Yu, M., Guo, L., Cui, B., Zhao, X., Sun, C., et al. (2017). Bioinspired development of p(St-MAA)-avermectin nanoparticles with high affinity for foliage to enhance folia retention. *Journal of Agricultural and Food Chemistry*, 66(26), 6578–6584.
- Liang, W., Yu, A., Wang, G., Zheng, F., Jia, J., & Xu, H. (2018). Chitosan-based nanoparticles of avermectin to control pine wood nematodes. *International Journal of Biological Macromolecules*, 112, 258–263.
- Lin, M., Wang, D., Liu, S., Huang, T., Sun, B., Cui, Y., et al. (2015). Cupreous complex-loaded chitosan nanoparticles for photothermal therapy and chemotherapy of oral epithelial carcinoma. *ACS Applied Materials & Interfaces*, 7(37), 20801–20812.
- Lindberg, B., Maripuu, R., Siegbahn, K., Larsson, R., Golander, C. G., & Eriksson, J. C. (1983). ESCA studies of heparinized and related surfaces: 1. Model surfaces on steel substrates. *Journal of Colloid & Interface Science*, 95(2), 308–321.
- Liu, Y., Sun, Y., He, S., Zhu, Y., Ao, M., Li, J., et al. (2013). Synthesis and characterization of gibberellin-chitosan conjugate for controlled-release applications. *International Journal of Biological Macromolecules*, 57, 213–217.
- Livak, K. J., & Schmittgen, T. D. (2001). Analysis of relative gene expression data using real-time quantitative PCR and the 2(-Delta Delta C(T)) method. *Methods*, 25(4), 402–408.
- Manikandan, A., & Sathiyabama, M. (2016). Preparation of chitosan nanoparticles and its effect on detached rice leaves infected with *Pyricularia grisea*. *International Journal of Biological Macromolecules*, 84, 58–61.
- Mora-Huertas, C. E., Fessi, H., & Elaissari, A. (2010). Polymer-based nanocapsules for drug delivery. *International Journal of Pharmaceutics*, 385(1–2), 113–142.
- Moulder, J. F., Stickle, W. F., Sobol, P. E., & Bomben, K. D. (1995). *Handbook of X ray photoelectron spectroscopy: A reference book of standard spectra for identification and interpretation of Xps data*. Eden Prairie: Physical Electronics.
- Mozafari, M. R., Danaei, M., Javanmard, R., Raji, M., & Maherani, B. (2017). Nanoscale lipidic carrier systems: Importance of preparation method and solvents. *Global Journal of Nanomedicine*, 2, 555593.
- Naqqash, M. N., Gokce, A., Bakhsh, A., & Salim, M. (2016). Insecticide resistance and its molecular basis in urban insect pests. *Parasitology Research*, 115(4), 1363–1373.
- Neinhuis, C., & Barthlott, W. (1998). Seasonal changes of leaf surface contamination in Beech, Oak, and ginkgo in relation to leaf micromorphology and wettability. *New Phytologist*, 138, 91–98.
- Ou, Y., Wu, Y., Li, H., Wang, K., & Zhang, D. (2013). Synthesis, characterization and antibacterial activity of hybrid materials of rare earth and chitosan. *Journal of the Chinese Society of Rare Earths*, 31(2), 211–216.
- Peshin, R., & Dhawan, A. K. (2009). *Integrated pest management: Innovation-development process*. Netherlands: Springer.
- Pinon, J., Frey, P., & Husson, C. (2006). Wettability of poplar leaves influences dew formation and infection by *Melampsora larici-populina*. *Plant Disease*, 90(2), 177–184.
- Rhim, J. W., Hong, S. I., Park, H. M., & Ng, P. K. (2006). Preparation and characterization of chitosan-based nanocomposite films with antimicrobial activity. *Journal of Agricultural and Food Chemistry*, 54, 5814–5822.
- Scott, N., & Chen, H. (1987). Nanoscale science and engineering for agriculture and food systems. *Industrial Biotechnology*, 9(1), 17–18.
- Tan, W. M., Hou, N., Pang, S., Zhu, X. F., Li, Z. H., Wen, L. X., et al. (2012). Improved biological effects of uniconazole using porous hollow silica nanoparticles as carriers. *Pest Management Science*, 68(3), 437–443.
- Tang, E. S. K., Huang, M., & Lim, L. Y. (2003). Ultrasonication of chitosan and chitosan nanoparticles. *International Journal of Pharmaceutics*, 265(1–2), 103–114.
- Tomlinson, I. (2013). Doubling food production to feed the 9 billion: A critical perspective on a key discourse of food security in the UK. *Journal of Rural Studies*, 29, 81–90.
- Tong, Y., Wu, Y., Zhao, C., Xu, Y., Lu, J., Xiang, S., et al. (2017). Polymeric nanoparticles as a metolachlor carrier: Water-based formulation for hydrophobic pesticides and absorption by plants. *Journal of Agricultural and Food Chemistry*, 65(34), 7371–7378.
- Vieira, R. S., Oliveira, M. L. M., Guibal, E., Rodríguez-Castellón, E., & Beppu, M. M. (2011). Copper, mercury and chromium adsorption on natural and crosslinked chitosan films: An XPS investigation of mechanism. *Colloids and Surfaces A: Physicochemical and Engineering Aspects*, 374(1–3), 108–114.
- Wan, N. F., Ji, X. Y., Jiang, J. X., Deng, X., Huang, K. H., & Li, B. (2013). An eco-engineering assessment index for chemical pesticide pollution management strategies to complex agro-ecosystems. *Ecological Engineering*, 52, 203–210.
- Yang, L., Li, J., Yu, X., Zhang, M., & Huang, X. (2008). Lanthanum-based conversion coating on Mg–8 Li alloy. *Applied Surface Science*, 255(5), 2338–2341.
- Yeo, Y., & Park, K. N. (2007). Control of encapsulation efficiency and initial burst in polymeric microparticle systems. *Archives of Pharmacological Research*, 27, 1–12.
- Zhang, H., Qin, H., Li, L., Zhou, X., Wang, W., & Kan, C. (2017). Preparation and characterization of controlled-release avermectin/castor oil-based polyurethane nanomulsions. *Journal of Agricultural and Food Chemistry*, 66(26), 6552–6560.
- Zuo, X., & Balasubramanian, R. (2013). Evaluation of a novel chitosan polymer-based adsorbent for the removal of chromium (III) in aqueous solutions. *Carbohydrate Polymers*, 92(2), 2181–2186.



Chitosan-based nanoparticles of avermectin to control pine wood nematodes

Wenlong Liang^a, Aixin Yu^a, Guodong Wang^{a,b}, Feng Zheng^{a,b}, Jinliang Jia^{a,b,*}, Hanhong Xu^{a,*}

^a State Key Laboratory for Conservation and Utilization of Subtropical Agro-bioresources, South China Agricultural University, Guangzhou 510642, PR China

^b College of Materials and Energy, South China Agricultural University, Guangzhou 510642, PR China

ARTICLE INFO

Article history:

Received 21 December 2017

Received in revised form 22 January 2018

Accepted 26 January 2018

Available online 31 January 2018

Keywords:

Chitosan

Poly- γ -glutamic acid

Nematocidal activity

ABSTRACT

Pine wood nematode disease is a most devastating disease of pine trees. Avermectin (AVM) is a widely used bio-nematocide which can effectively to kill the pine wood nematode (PWN). However, its poor solubility in water and rapid photolysis are responsible for its poor bioavailability, which causes environmental pollution because of excessive applied rates. Here, a simple electrostatic interaction method was used to encapsulate AVM within nanoparticles composed of poly- γ -glutamic acid (γ -PGA) and chitosan (CS). The loading capacity of the resulting AVM-CS/ γ -PGA nanoparticles was as much as 30.5%. The encapsulation of AVM within these nanoparticles reduced its losses by more than 20.0% through photolysis. An in vitro test showed that the rate of release of AVM from the nanoparticles was dependent on the ambient pH, with rapid release occurring in an alkaline environment. The mortality rate of nematodes which were treated with 1 ppm of AVM content of AVM-CS/ γ -PGA was 98.6% after 24 h, while one of free AVM was only 69.9%. In addition, FITC-labeled CS/ γ -PGA nanoparticles (FITC-CS/ γ -PGA) showed that the nanoparticles could enrich in intestines and head of nematodes. All of these results showed that those nanoparticles of AVM are a potential multifunctional formulation to control the pest and reduce environment pollution.

© 2018 Elsevier B.V. All rights reserved.

1. Introduction

The pinewood nematode, a native of North America, is the causal agent of pine wilt disease, and has been responsible for the demise of millions of pine trees in China [1]. In the past decades, several different control measures against pine wilt disease have been developed, such as physical eradication by removing infected trees, aerial application of insecticide to kill the nematode's vector, the pine sawyer (*Monochamus* spp.), and trunk injection of an antinematodal compound to control the nematode itself. However, these are not very effective methods to control the PWN. The bio-nematocide avermectin is toxic to a wide variety of plant parasitic nematodes, including PWN. However, its conventional formulation suffers from poor water solubility and high environmental lability. In order to effectively using AVM, people have to use organic solvent and surfactants which led to environmental pollution and threats to human health [2–4]. And for the controlling of pine nematode, traditional method is by injecting the AVM into the trunk [5,6]. But this approach costs a lot of human resources and the bacterial also can infect the tree by wound that caused by injection. As it is not move systemically through the tree, the conventional application of

AVM cannot fully eradicate PWN, so does not provide a cure for pine wilt disease.

With the development of nanomaterials, biopolymer nanoparticles are regarded as potent drug delivery vehicles because they enable a controlled, sustained and targeted release of the drug, while in themselves being biodegradable, biocompatible and non-toxic [7]. Although biopolymer nanoparticles are widely used in the medical field, less attention has been paid to their exploitation in agriculture [8]. Besides, most conventional pesticides are inefficient because of their sensitivity to environmental variables such as light, pH and temperature. As a result, only a small proportion of the effective compound ever reaches its target site and their application at best reduces, rather than removes the pressure imposed by pests and pathogens [9]. A potential advantage of encapsulating a pesticide within a biopolymer nanoparticle is that it can reduce the amount of pesticide currently required to maintain agricultural productivity [10]. The transfer of this technology to the field of plant pathology requires that the nanoparticles, as well as being biocompatible and biodegradable, can be demonstrated to reduce the environmental lability of the encapsulated pesticide and maybe are small enough to enter the plants. In addition, it will be important that when present in an aqueous environment (as pertains in the plant vascular system), the pesticide released from the nanoparticles is bioactive.

The biopolymer chitosan (CS) is a partially de-acetylated form of chitin, in which the D-glucosamine repeating units are linked by β -(1-4)

* Corresponding authors.

E-mail addresses: jjiajinliang@scau.edu.cn (J. Jia), hxxu@scau.edu.cn (H. Xu).

glycosidic bonds [11], it has been widely exploited as a drug delivery vehicle in the medicinal context [12]. In the agricultural context, CS has been shown to act as a stimulator of plant growth [13], an antimicrobial agent [14] and a regulator of plant immunity [15]. Poly- γ -glutamic acid (γ -PGA) on the other hand, is an anionic polypeptide produced by species within the genus *Bacillus* [16]. It has a high chelating ability, moist function, and is readily biodegradable [17]. Along with certain other polyamino acids, they are considered to have promising applications in the agricultural field because they enhance plants' ability to absorb nutrients, thereby promoting their growth [18]. Based on the positively charged surface of CS and the negatively charged one of γ -PGA, CS/ γ -PGA polyelectrolyte complexes is benefited to us to form various kinds of nanomaterials in simple method.

Here, the synthesis of CS/ γ -PGA-based nanoparticles encapsulating AVM that improve performance of AVM to control PWN was described, achieved via the electrostatic interaction method. The nanoparticles were evaluated by Fourier transform infrared (FTIR), UV–visible spectroscopy (UV), fluorophotometer, transmission electron microscopy (TEM). In order to show that CS/ γ -PGA nanoparticles were a multifunctional formulation to AVM, photolysis experiments of avermectin in CS/ γ -PGA nanoparticles were measured. Besides, the bioactivity was assay by using AVM-CS/ γ -PGA nanoparticles to cultivate PWN and the in vivo imaging of nematodes that were treated with FITC labeling CS/ γ -PGA nanoparticles was studied.

2. Materials and methods

2.1. Experimental materials

CS (85% deacetylation, 200 CPS) was purchased from Haidebei Marine Bioengineering Co., Ltd. (Jinan, China), while the source of γ -PGA (M_w = 10 – 12 KDa) was from Realin Biotechnology Co., Ltd. (Xi'an, China). Tripolyphosphate (TPP) was obtained from Damao Chemical Reagent Factory (Tianjin, China). Other reagents used were of analytical grade.

2.2. Preparation of AVM-CS/ γ -PGA and FITC-CS/ γ -PGA

CS/ γ -PGA nanoparticles were prepared via a poly-electrolyte self-assembly method [19] with minor modifications. Briefly, 1% (w/v) solution of CS was prepared in 1% (v/v) aqueous glacial acetic acid at room temperature until the solution became transparent. 25 mL of 1% (w/v) aqueous γ -PGA was added to 25 mL of the CS solution with constant stirring at 50 °C for 1.5 h and then cooled to ambient temperature. After dissolving 0.375 g of AVM in 5 mL of CH_2Cl_2 , the organic phase was added to the CS/ γ -PGA mixture and vigorously stirred for 30 min to obtain an emulsion. 50 mL of aqueous 0.5% (w/v) TPP was added to the emulsion drop-by-drop over 1 h with gentle stirring at room temperature. The resulting crosslinked nanoparticles were harvested by centrifugation (8000 r/min for 10 min), rinsed three times in distilled water and freeze-dried.

FITC-labeled CS/ γ -PGA (FITC-CS/ γ -PGA) was prepared by reacting the FITC isothiocyanate group with the primary amino group of CS [20]. Briefly, 5 mL of ethanolic 0.01% (w/v) FITC was added to 25 mL of 1% (w/v) CS dissolved in 1% (v/v) aqueous glacial acetic acid, and the mixture was stirred at room temperature for 3 h in the dark. Subsequently, 25 mL of 1% (w/v) aqueous γ -PGA was vigorously stirred into the FITC/CS mixture for 1.5 h. 50 mL of aqueous 0.5% (w/v) TPP was added drop-by-drop over 1 h with gentle stirring at room temperature to affect crosslinking. The FITC-CS/ γ -PGA nanoparticles were harvested by centrifugation (8000 r/min for 10 min), rinsed several times in distilled water and freeze-dried.

2.3. Encapsulation efficiency and loading capacity

The encapsulation efficiency (EE) and loading capacity (LC) were assessed in the method [21] with minor modifications. Briefly, 10 mg

of freeze-dried AVM-CS/ γ -PGA nanoparticles were added to 3 mL of ethanol, and the suspension subjected to ultrasonication for 4 h to completely disassociate the AVM. The suspension was centrifuged (8000 r/min, 10 min) and the supernatant collected. The concentration of the AVM was determined spectrophotometrically at 245 nm, using a UV–visible spectroscopy (Shimadzu UV-2550). The amount of AVM was calculated by calibration curve of free AVM in ethanol (R^2 = 0.999). All measurements were carried out triplicate and mean values were reported. The AVM-loading capacity (LC) and the encapsulation efficiency (EE) of the AVM-CS/ γ -PGA nanoparticles were calculated from the following expressions:

$$LC = \frac{\text{mass of pesticides in nanoparticles}}{\text{total mass of nanoparticles}} \times 100\% \quad (1)$$

$$EE = \frac{\text{mass of pesticides in nanoparticles}}{\text{total mass of pesticides used for nanoparticles preparation}} \times 100\% \quad (2)$$

2.4. Characterization of nanoparticles

The size, morphology and structure of the nanoparticles were characterized using transmission electron microscopy (TEM), Fourier transform infrared (FTIR) spectrometry and fluorophotometer (Shimadzu, RF-5301PC). The TEM employed a Tecnai 12 device (Fei, The Netherlands) operating at a maximum accelerating voltage of 100 kV. FT-IR spectra were obtained following the KBr pellet method using a VERTEX 70 spectrometer (Bruker, Germany), scanning over the range 400–4000 cm^{-1} .

2.5. In vitro release of AVM-CS/ γ -PGA

The effect of varying the pH on the release of AVM from AVM-CS/ γ -PGA nanoparticles was quantified by suspending 20 mg of freeze-dried material in 3 mL of 20% ethanol phosphate buffer (pH 5.5, pH 7.0 or pH 8.5). The suspension was dialyzed (cut off M_w of 8–14 KDa) against 100 mL of the same buffer at the appropriate pH at room temperature. Periodically, 3 mL of the release medium was removed and an equal volume of fresh buffer solution was then replaced in the mixture. The each of absorbance of these aliquots was measured as above at 245 nm, and used to derive the AVM concentration. Cumulative percentage of AVM released calculated using the following equation:

$$\text{Cumulative release percentage} = \sum_{t=0}^t \frac{M_t}{M_0} \times 100\%$$

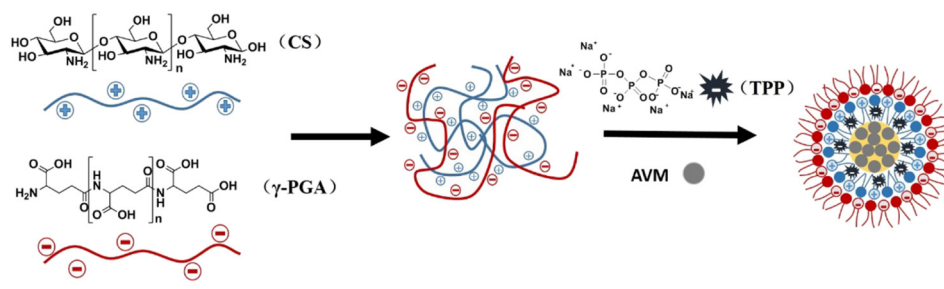
where M_t is the cumulative amount of AVM released to each sampling time point, t is time of released of AVM-loaded and M_0 is the initial weight of the AVM-loaded in the sample.

2.6. Photolysis experiments of avermectin in CS/ γ -PGA nanoparticles

The sensitivity to light irradiation of the AVM encapsulated within CS/ γ -PGA nanoparticles were compared to that of pure AVM (0.1 mg/mL). 0.33 mg/mL suspension of AVM-CS/ γ -PGA in ethanol was divided into equal aliquots of 3 mL and placed into centrifuge tubes, which were irradiated by UV light (254 nm, 8 W). The distance of the light source from suspension surface was 15 cm [22]. Periodically, a tube was selected for UV-spectrometric analysis to determine the remaining concentration of AVM.

2.7. Nematicidal assay

For the nematocidal assay, PWN were exposed to a 1 mL aqueous solution of either AVM or AVM-CS/ γ -PGA in 12-well plates for 24 h, with



Scheme 1. Schematic illustrations of preparation of AVM-CS/γ-PGA nanoparticles.

each well containing 30 ± 5 nematodes [23]. The assay was performed in triplicate. The chosen concentrations of AVM and the AVM content of the AVM-CS/γ-PGA nanoparticles were 0.0625, 0.125, 0.25, 0.5 and 1 ppm. Control wells contained either deionized water or 1 ppm of CS/γ-PGA. After 24 h, the mortality of PWN was counted under the microscope. If the posture of nematode is “C” or “J”, it will indicate the nematode has been dead.

2.8. Imaging of *Caenorhabditis elegans*

C. elegans were cultivated as described elsewhere [24]. Uniform *C. elegans* were transferred into 1 mL of 100 ppm FITC-CS/γ-PGA for 12 h, after which the worms were rinsed in distilled water. They were then imaged by fluorescence microscopy (model BX51, Olympus Corp).

3. Results and discussion

As shown in Scheme 1. The AVM-CS/γ-PGA nanoparticles self-assembled immediately upon the mixing of the AVM-containing organic phase with the CS/γ-PGA mixture. The drop-wise addition of TPP was included to provide ionic cross-linking. The nanoparticles were formed by an electrostatic interaction between the positively charged amino groups present on the surface of CS and the negatively charged carboxy groups on the surface of γ-PGA [25]. Compared with other pesticide emulsions, nanoparticles produced by self-assembly benefit from a simple preparation protocol, high stability and a reduced requirement for potentially toxic organic solvents.

3.1. Composition and morphology of nanoparticles

The FT-IR spectra of CS, γ-PGA, the CS/γ-PGA, AVM and the AVM-CS/γ-PGA were shown as Fig. 1a. The peaks generated at 1590 cm^{-1} and 1665 cm^{-1} represented the N—H bending of the CS amide II and amide I moieties, respectively [26]. The 895 cm^{-1} peak was assigned to C—O bond stretching and vibration. The peaks at 1590 cm^{-1} and 1408 cm^{-1} represented the carboxy ions present in γ-PGA. The

spectrum produced by the CS/γ-PGA nanoparticles featured a shift of the N—H deformation peak from 1590 cm^{-1} to 1540 cm^{-1} , while the C—O peak in 895 cm^{-1} was retained unchanged. These measurements confirmed that the CS/γ-PGA nanoparticles formed from an electrostatic interaction between the carboxy in γ-PGA and the amino groups in CS. The peak at 1734 cm^{-1} represented the C=O bond carried by AVM, and was also recognized in the spectrum generated by the AVM-CS/γ-PGA nanoparticles, which confirmed the successful encapsulation of AVM within the CS/γ-PGA nanoparticles. In order to further study the mechanism of CS/γ-PGA nanoparticles, FITC labeling CS/γ-PGA (FITC-CS/γ-PGA) were synthesized. The character emission peaks of FITC in 520 nm was shown in FITC-CS/γ-PGA (Fig. 1b) and it confirmed that FITC labeled CS/γ-PGA successfully.

The TEM images of the CS/γ-PGA nanoparticles show that their mean size was $61 \pm 4.5\text{ nm}$ and $56 \pm 2.6\text{ nm}$ under pH 7.0 and pH 5.5 respectively. The nanoparticles were spherical under weakly acidic (pH 5.5) or neutral (pH 7.0) conditions but the size of nanoparticles (pH 5.5) were slightly smaller than the neutral (Fig. 2a,b). It indicated that the structure of nanoparticles were more compact under the weakly acidic. Besides, under mildly alkaline conditions (pH 8.5), they lost their integrity and formed heterogeneously-sized aggregates (Fig. 2c). At this pH, CS lost protons, which would have undermined the structure of the nanoparticle [27]. As a result, the expectation was that the release of AVM from AVM-CS/γ-PGA nanoparticles would be slow over the mildly acidic to neutral pH range, but rapid under alkaline conditions.

3.2. AVM loading and release

The AVM-loading capacity and encapsulation efficiency of the CS/γ-PGA nanoparticles are both important variables. By means of the standard curve, it was possible to estimate that the LC of AVM was around 30.5% and the EE around 34.7%. As predicted, the release of AVM from the AVM-CS/γ-PGA nanoparticles at pH 5.5 was slower than at pH 7.0, while that at pH 8.5 was quite rapid (Fig. 3). At the very beginning, the release of AVM had already reach about 20% under the three pH

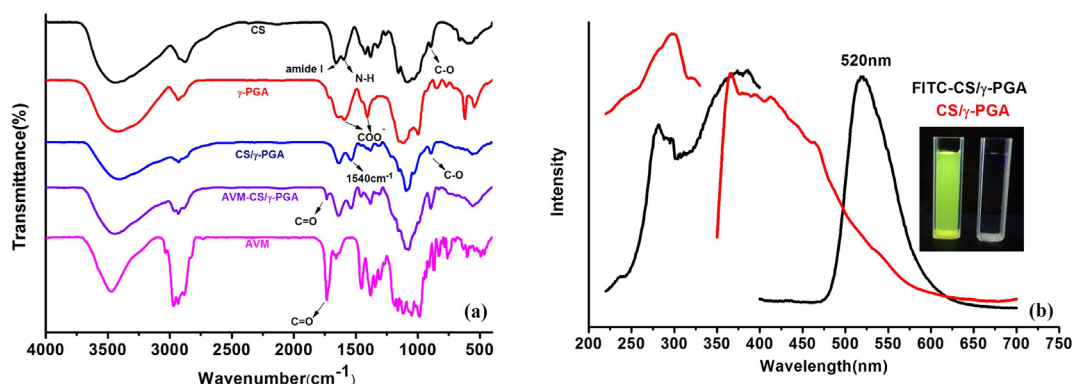


Fig. 1. (a) FT-IR spectra of CS, γ-PGA, CS/γ-PGA, AVM-CS/γ-PGA, AVM and (b) fluorescence spectra of CS/γ-PGA and FITC-CS/γ-PGA.

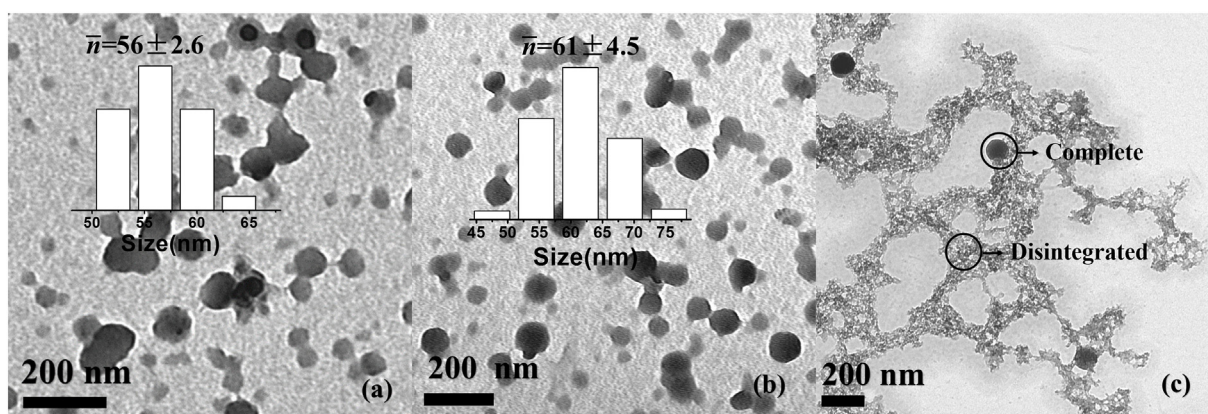


Fig. 2. TEM of CS/γ-PGA nanoparticles at distinct pH value: (a) pH 5.5, (b) pH 7.0 and (c) pH 8.5.

conditions because of drug burst release [28]. After 72 h, the release rate of AVM tends to be saturated and the maximal release rate was 69.1%, 60.4%, 57.6% in pH 8.5, 7.0, 5.5, respectively. The inhibited release of AVM from CS/γ-PGA at pH 5.5 was likely because of the high stability of the nanoparticles in an acidic environment resulting from the strong electrostatic interaction between the CS and γ-PGA, while the release of AVM was facilitated at the alkaline pH as a result of the disintegration of the nanoparticles. The results showed that AVM-CS/γ-PGA nanoparticles could better to release AVM under alkaline condition.

3.3. The study of photolysis of AVM-CS/γ-PGA

The degradation rate of AVM induced by UV irradiation is illustrated in Fig. 4. After a 1 h period of irradiation, 18.0% of the free AVM had become degraded, and 12.8% of the encapsulated AVM from CS/γ-PGA had become degraded. The small difference of photolytic rate was caused by initial burst release of pesticide. By 12 h, the loss rate is 76.6% in AVM and 50.7% in AVM-CS/γ-PGA, respectively. Thus CS/γ-PGA nanoparticles at least partially protected the AVM from decomposing under the UV irradiation. It is able to enlarge AVM effect time in agriculture under the natural environment.

3.4. The nematocidal activity of AVM-CS/γ-PGA

As shown in Fig. 5, the nematocidal activity of AVM-CS/γ-PGA nanoparticles is illustrated. 1 ppm of CS/γ-PGA and the water as control showed that CS/γ-PGA had relatively low toxicity to the nematodes and the nematodes can survive under the normal physiology condition

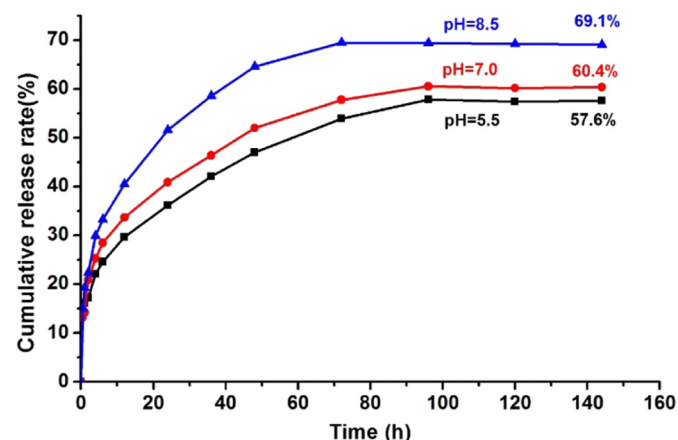


Fig. 3. In vitro release profile of AVM from CS/γ-PGA at different pH.

within 24 h. While the nematodes were treated with different concentration (0.0625, 0.125, 0.25, 0.5, 1 ppm) of AVM and the same AVM content of AVM-CS/γ-PGA after 24 h. A large number of nematode which were treated with AVM-CS/γ-PGA deaths can be observed under the

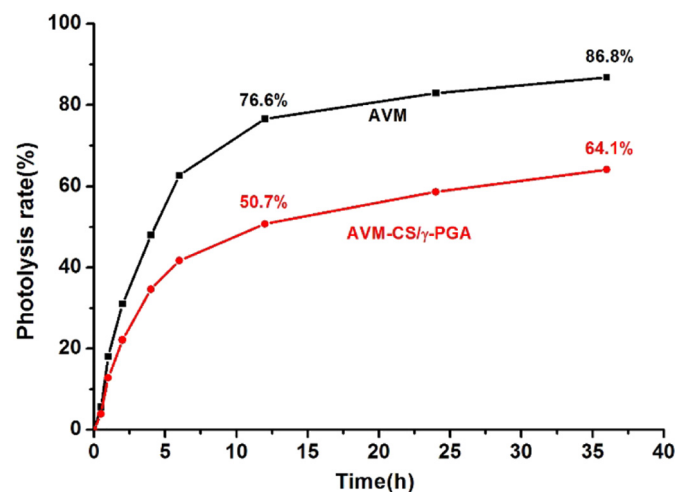


Fig. 4. The response curve of the photolysis rate of AVM and AVM-CS/γ-PGA.

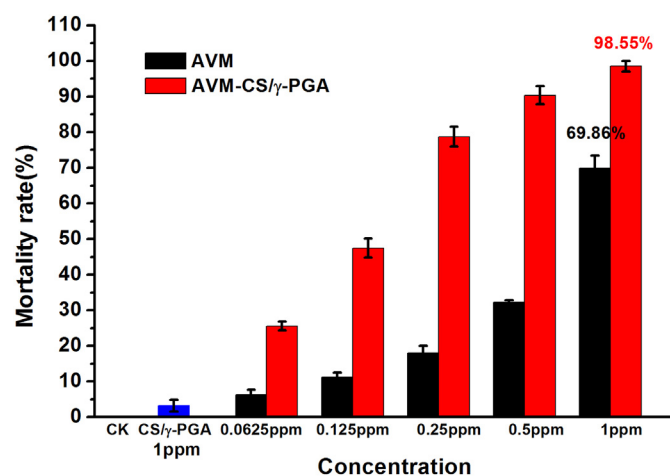


Fig. 5. Nematode mortality of live nematodes treated with AVM-CS/γ-PGA, AVM and CS/γ-PGA in different concentration.

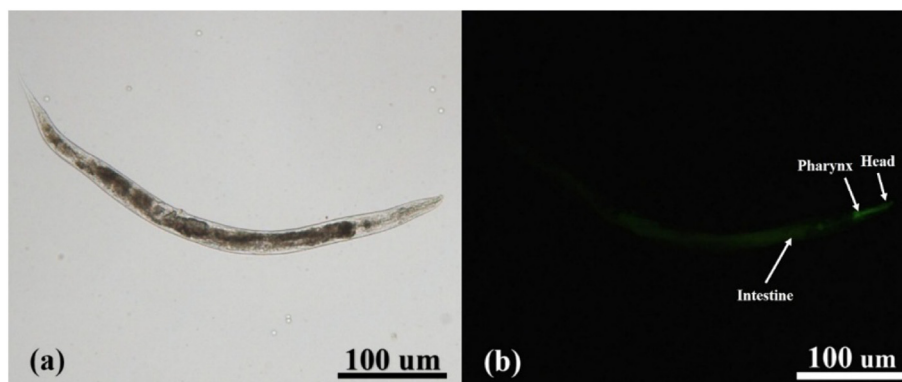


Fig. 6. Light microscopy images of FITC-CS/γ-PGA -treated *C. elegans*.

microscope after 24 h. While was relatively few mortality rate of nematode which were treated with AVM. The bioassay demonstrated that exposure of PWN to 1 ppm of AVM-CS/γ-PGA resulted in a very high mortality rate (98.6% after 24 h), a level which was considerably higher than that induced by free AVM (69.9%). The improved performance of the encapsulated form of AVM may derive from its better dispersion in an aqueous environment.

3.5. The in vivo imaging of FITC-CS/γ-PGA-Treated *C. elegans*

In order to further study the mechanism of nematocidal activity of CS/γ-PGA nanoparticles, FITC-labeled CS/γ-PGA (FITC-CS/γ-PGA) was synthesized. A typical fluorescence model *C. elegans* was used for fluorescence imaging object. As mentioned, the use of water as exposure media reflected that the dispersity of FITC-CS/γ-PGA was preserved upon incubation with *C. elegans* for 12 h. The fluorescence emitted by the FITC was clearly visible in the worms' intestine, head and pharynx (Fig. 6b), which indicates that FITC-CS/γ-PGA entered the worms primarily through the intestinal tract by ingestion and at the same time showed that there was no toxic or anti-feedant effect associated with the FITC-CS/γ-PGA [29]. It demonstrated that the CS/γ-PGA nanoparticles had good dispersion in the water and made the nanoparticles more easily enrich in the intestine and head of *C. elegans*.

4. Conclusion

AVM-CS/γ-PGA nanoparticles with high loading capacity were synthesized by a simple electrostatic interaction. AVM-CS/γ-PGA nanoparticles were evaluated by FTIR, UV, TEM, fluorophotometer and fluorescence microscope. The results showed that the AVM in the CS/γ-PGA nanoparticles was rapidly released under alkaline conditions and had good ability to resist photolysis. Besides, AVM-CS/γ-PGA nanoparticles were more effectively to kill PWN than free AVM under the water. Meanwhile, the CS/γ-PGA nanocarriers with FITC were more easily enrich in the intestine and head of nematodes by fluorescence microscope. The results show that AVM-CS/γ-PGA nanopesticides are a potential multifunctional formulation to control pest and lower environmental pollution.

Author contributions

The manuscript was written through contributions of all authors. All authors declared no competing financial interests.

Acknowledgment

This work was financially supported by National Science Foundation (Grant 31401781) of China and Science and Technology Program of Guangdong (Grant 2015B020230012).

References

- [1] B.J. Yang, Q.L. Wang, Distribution of the pinewood nematode in China and susceptibility of some Chinese and exotic pines to the nematode, *Can. J. For. Res.* 19 (1989) 1527–1530.
- [2] O.N. Voinovich, G.S. Kalacheva, I.D. Grodnitskaya, T.G. Volova, Microbial polymers as a degradable carrier for pesticide delivery, *Appl. Biochem. Microbiol.* 45 (2009) 384–388.
- [3] Y.J. Tong, Y. Wu, C.Y. Zhao, Y. Xu, J.Q. Lu, S. Xiang, F.L. Zong, X.M. Wu, Polymeric nanoparticles as a metolachlor carrier: water-based formulation for hydrophobic pesticides and absorption by plants, *J. Agric. Food Chem.* 65 (2017) 7371–7378.
- [4] S. Engelskirchen, R. Maurer, T. Levy, R. Berghaus, H. Auweter, O. Glatter, Highly concentrated emulsified microemulsions as solvent-free plant protection formulations, *J. Colloid Interface Sci.* 388 (2012) 151–161.
- [5] Z. Zhen, Y.T. Gong, X.J. Huang, H.G. Yu, L.Q. Bai, J.F. Hu, Efficacy of four nematocides against the reproduction and development of pinewood nematode, *Bursaphelenchus xylophilus*, *J. Nematol.* 47 (2) (2015) 126–132.
- [6] Q.F. Han, L.L. Ling, H.S. Diao, Z.Y. Kuang, The test of controlling pine wood nematode disease by method of inject trunk and treatment of root application of insecticide, *G. D. Forestry Sci. Technol.* 26 (5) (2010) 72–74.
- [7] C.H. Wu, T.T. Wu, Z.X. Fang, J.W. Zheng, S. Xu, S.G. Chen, Y.Q. Hu, X.Q. Ye, Formation, characterization and release kinetics of chitosan/γ-PGA encapsulated nisin nanoparticles, *RSC Adv.* 6 (2016) 46686–46695.
- [8] M.R. Hill, E.J. MacKrell, C.P. Forsthoefel, S.P. Jensen, M.S. Chen, G.A. Moore, Z.L. He, B. S. Sumerlin, Biodegradable and pH-responsive nanoparticles designed for site-specific delivery in agriculture, *Biomacromolecules* 16 (2015) 1276–1282.
- [9] J.K. Syers, A.E. Johnston, D. Curtin, Efficiency of soil and fertilizer phosphorus use: reconciling changing concepts of soil phosphorus behaviour with agronomic information, *FAO Fertilizer and Plant Nutrition Bulletin* 18, Food and Agriculture Organization of the United Nations Rome, 2008.
- [10] M.S. Chen, S.P. Jensen, M.R. Hill, G. Moore, Z.L. He, B.S. Sumerlin, Synthesis of amphiphilic polysuccinimide star copolymers for responsive delivery in plants, *Chem. Commun.* 51 (47) (2015) 9694–9697.
- [11] Y.H. Bian, D.W. Gao, Y.P. Liu, N. Li, X.W. Zhang, R.Y. Zheng, Q.Q. Wang, L.Y. Luo, K. Dai, Preparation and study on anti-tumor effect of chitosan-coated oleonic acid liposomes, *RSC Adv.* 5 (2015) 18725–18732.
- [12] M. Rinaudo, Chitin and chitosan: properties and applications, *Prog. Polym. Sci.* 31 (7) (2006) 603–632.
- [13] P.G. Chatelain, M.E. Pintado, M.W. Vasconcelos, Evaluation of chitoooligosaccharide application on mineral accumulation and plant growth in *Phaseolus vulgaris*, *Plant Sci.* 215 (2014) 134–140.
- [14] L.Y. Yang, P. Zhao, L. Wang, I. Filippus, X.H. Meng, Synergistic effect of oligochitosan and silicon on inhibition of *Monilinia fructicola* infections, *J. Sci. Food Agric.* 90 (2010) 630–634.
- [15] H. Yin, X.M. Zhao, Y.G. Du, Oligochitosan: a plant diseases vaccine—a review, *J. Carbohydr. Polym.* 82 (2010) 1–8.
- [16] D.W. Tang, S.H. Yu, Y.C. Ho, F.L. Mi, P.L. Kuo, H.W. Sung, Heparinized chitosan/poly(γ-glutamic acid) nanoparticles for multi-functional delivery of fibroblast growth factor and heparin, *Biomaterials* 31 (2010) 9320–9332.
- [17] M. Ashiuchi, Occurrence and biosynthetic mechanism of poly-γ-glutamic acid, in: Y. Hamano (Ed.), *Amino-Acid Homopolymers Occurring in Nature*, Springer, Berlin, Heidelberg 2010, pp. 77–93.
- [18] L.P. Koskan, A. Meah, J.L. Sanders, R.J. Ross, Method and composition for enhanced hydropic plant productivity with polyamino acids, U.S. Patent 5783523 A (1998).
- [19] A. Esmaeili, A. Asgari, In vitro release and biological activities of *Carum copticum* essential oil (CEO) loaded chitosan nanoparticles, *Int. J. Biol. Macromol.* 81 (2015) 283–290.
- [20] J. Thongborisute, H. Takeuchi, H. Yamamoto, Y. Kawashima, Visualization of the penetrative and mucoadhesive properties of chitosan and chitosan-coated liposomes through the rat intestine, *J. Liposome. Res.* 16 (2006) 127–141.
- [21] X.L. Yang, X.J. Ju, X.T. Mu, W. Wang, R. Xie, Z. Liu, L.Y. Chu, Core-shell chitosan microcapsules for programmed sequential drug release, *ACS Appl. Mater. Interfaces* 8 (2016) 10524–10534.

- [22] Y. Wang, H.X. Cui, C.J. Sun, X. Zhao, B. Cui, Construction and evaluation of controlled-release delivery system of Abamectin using porous silica nanoparticles as carriers, *Nanoscale Res. Lett.* 9 (2014) 655.
- [23] L. Gonzalez-Moragas, S.M. Yu, E. Carenza, A. Laromaine, A. Roig, Protective effects of bovine serum albumin on superparamagnetic iron oxide nanoparticles evaluated in the nematode *Caenorhabditis elegans*, *ACS Biomater. Sci. Eng.* 1 (2015) 1129–1138.
- [24] J. Chen, C.R. Guo, M. Wang, L. Huang, L.P. Wang, C.C. Mi, J. Li, X.X. Fang, C.B. Mao, S.K. Xu, Controllable synthesis of NaYF₄: Yb, Er upconversion nanophosphors and their application to in vivo imaging of *Caenorhabditis elegans*, *J. Mater. Chem.* 21 (2011) 2632.
- [25] A.R. Dudhani, S.L. Kosaraju, Bioadhesive chitosan nanoparticles: preparation and characterization, *Carbohydr. Polym.* 81 (2010) 243–251.
- [26] Z.X. Liao, S.F. Peng, Y.L. Chiu, C.W. Hsiao, H.Y. Liu, W.H. Lim, H.M. Lu, H.W. Sung, Enhancement of efficiency of chitosan-based complexes for gene transfection with poly(γ -glutamic acid) by augmenting their cellular uptake and intra cellular unpackage, *J. Control. Release* 193 (2014) 304–315.
- [27] J. Li, Z. He, C.R. Guo, L.P. Wang, S.K. Xu, Synthesis of carbon nanohorns/chitosan/quantum dots nanocomposite and its applications in cells labeling and in vivo imaging, *J. Lumin.* 145 (2014) 74–80.
- [28] Y. Yeo, K.N. Park, Control of encapsulation efficiency and initial burst in polymeric microparticle systems, *Arch. Pharm. Res.* 27 (2004) 1–12.
- [29] C. Fang-Yen, L. Avery, A.D. Samuel, Two size-selective mechanisms specifically trap bacteria-sized food particles in *Caenorhabditis elegans*, *Proc. Natl. Acad. Sci. U. S. A.* 106 (47) (2009) 20093–20096.

高效输导咯菌腈纳米杀菌剂的制备及其性能研究

黄炜柔, 何亮亨, 朱 丽, 邓文杰, 贾金亮*
(华南农业大学 材料与能源学院, 广东 广州 510642)

摘要: 为提高杀菌剂对香蕉枯萎病病灶部位的靶向积累, 以苯丙氨酸 (Phenylalanine, PHE) 和聚琥珀酰亚胺 (Polysuccinimide, PSI) 为原料, 构建靶向高分子纳米载体 (PSI-PHE) 负载咯菌腈 (Fludioxonil, FLU), 制备出苯丙氨酸介导的咯菌腈纳米杀菌剂 (FLU@PSI-PHE)。采用红外光谱、激光粒度仪、热重分析和 X 射线衍射手段等表征了原药与高分子载体之间的互作关系及载药率。研究结果表明, 水合粒径约 531 nm 的 FLU@PSI-PHE 纳米颗粒载药率高达 45.96%, 其在蓖麻韧皮部的输导剂量为 1.27 $\mu\text{g}/\text{mL}$, 显示出高效韧皮部输导效果。对比低剂量 FLU 原药, 活性成分含量相同的 FLU@PSI-PHE 纳米颗粒对香蕉枯萎病的抑菌活性基本相当。氨基酸介导的咯菌腈纳米杀菌剂在植物维管组织中高效输导, 为香蕉枯萎病的靶向治疗提供了新的技术手段。

关键词: 氨基酸; 输导; 香蕉枯萎病; 纳米载体

中图分类号: S482.92

文献标志码: A

文章编号: 1674-5663(2024)01-0026-06

Preparation and properties of efficiently translocated fludioxonil nanofungicide

HUANG Weirou, HE Liangheng, ZHU Li, DENG Wenjie, JIA Jinliang*
(College of Materials and Energy, South China Agricultural University, Guangzhou 510642, China)

Abstract: In order to improve the targeted accumulation of fungicides on the lesion locations against Fusarium wilt in bananas, polymer nanocarriers (PSI-PHE) were constructed with polysuccinimide (PSI) and phenylalanine (PHE). Then fludioxonil (FLU) was loaded into the nanocarriers to produce PHE-guided nanoparticles (FLU@PSI-PHE). The infrared spectroscopy, hydrodynamic size, zeta potential, thermogravimetric analysis and X-ray diffraction analysis were explored to characterize the interaction and loading capacity between nanocarriers and FLU. The results showed that the loading capacity of FLU@PSI-PHE nanoparticles with 531 nm by hydrodynamic size was up to 45.96%, and the translocation dose of the castor phloem was 1.27 $\mu\text{g}/\text{mL}$, showing efficient phloem delivery effect. Compared with low doses of FLU, FLU@PSI-PHE nanoparticles with the same active ingredient content showed basically equal antifungal activity against Fusarium wilt in bananas. Amino acid-mediated FLU@PSI-PHE could be efficiently translocated in plant vascular tissues, which provides new technology for targeted treatment of banana Fusarium wilt.

Key words: amino acid; translocation; banana Fusarium wilt; nanocarriers

香蕉枯萎病是香蕉产业上一种土传性、毁灭性的维管组织病害, 被称为“香蕉癌症”^[1]。香蕉根部的球茎部位由于受尖孢镰刀菌古巴专化型 (*Fusarium oxysporum* f. sp. *cubense*, Foc) 侵染, 导致其维管组织功能遭到破坏, 最后因水分和养分不足而枯萎死亡^[2-3]。香蕉枯萎病已严重威胁和制约了我国香蕉产业的可持续发展^[4-5]。

香蕉枯萎病的防治一直是世界性难题, 目前尚缺乏一种能直接作用维管组织有效防治香蕉枯萎病的理想药剂^[6]。不少内吸性杀菌剂在离体条件下可以明显抑制尖孢镰刀菌古巴专化型活性, 但在香蕉活体植株内却不能表现出同等的防治效果^[7-8]。原因是内吸性杀菌剂施药时会迅速往植物叶片等蒸腾作用旺盛部位输导, 难以在植物维管组织中积

收稿日期: 2023-09-23

基金项目: 广东省重点领域研发计划 (2023B0202080001)、广东省自然科学基金 (2023A1515010609) 和广东省现代农业产业技术体系创新团队专项 (2019KJ140)。

第275页, 共289页

作者简介: 黄炜柔 (2002-), 女, 广东梅州人, 在读本科生。* 通信作者: E-mail: jiajinliang@scau.edu.cn

累^[3].虽然大多杀菌剂可用于防治植物的叶部病害,但无法防治香蕉枯萎病等维管束病害^[9].因此,开发能在植物维管组织中靶向积累的杀菌剂已成为香蕉枯萎病防治的关键问题.

2021年课题组Wu等^[10]研究发现甘氨酸甲酯修饰聚琥珀酰亚胺后的高分子纳米载体携带咯菌腈(FLU@PGA)纳米颗粒可在香蕉苗的病灶部位有一定的积累.据此,本研究选用香蕉枯萎病发病前后含量变化显著的苯丙氨酸为关键的导向基团,结合徐汉虹教授提出的导向农药理念^[11],构建氨基酸介导的靶向纳米载体,负载咯菌腈制备得到一种新型靶向纳米杀菌剂,进一步提高现有杀菌剂在植物维管组织韧皮部中的传导剂量,希望能为解决体外高活性杀菌剂在香蕉苗体内脱靶难题提供新思路.

1 材料与方法

1.1 试验材料

聚琥珀酰亚胺(Polysuccinimide,PSI),分子量10 000,苯丙氨酸(Phenylalanine,PHE),上海麦克林生化科技有限公司;咯菌腈(Fludioxonil,FLU),纯度98%,上海吉至生化科技有限公司;二甲基亚砜(Dimethyl Sulfoxide,DMSO)、乙腈,天津市富宇精细化工有限公司;去离子水,自制;盐酸(体积分数36.0%~38.0%),广东广试试剂科技有限公司.

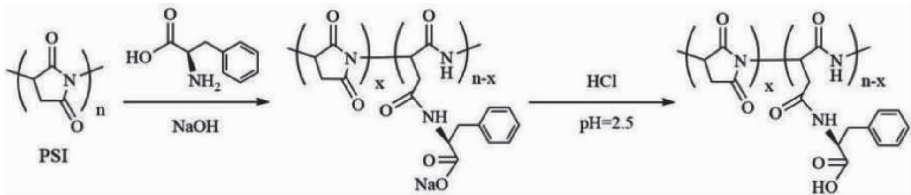


图1 PSI-PHE纳米载体的合成示意图

1.3.2 材料的结构表征

红外光谱测试:利用傅里叶红外光谱仪,采用KBr压片法,设置4 000~500 cm⁻¹波数范围分析样品特征峰.

水合粒径及Zeta电势测试:取一定量样品于去离子水中,利用激光粒度分析仪测定样品的水合粒径及Zeta电势.

X射线衍射(X-ray diffraction,XRD)测试:称量0.10 g样品,利用X射线多晶粉末仪分析样品的物相结构,扫描角度为10~80°,扫描速率为1(°)/min.

热重分析(Thermogravimetric Analysis,TGA)测试:利用热重分析仪,在30~800℃的氮气流中对

1.2 试验仪器

Nicolet IS10 傅里叶交换红外光谱仪,赛默飞世尔科技公司;N5000 紫外可见分光光度计,上海佑科仪器仪表有限公司;Zetasizer Nano ZSE 激光粒度分析仪,英国马尔文仪器有限公司;Ultima IV X 射线多晶粉末仪,日本理学公司;TG 209 F1 Libra TM 热重分析仪,德国耐驰仪器制造有限公司;EVO MA 15 扫描式电子显微镜,德国蔡司;LGJ-10 真空冷冻干燥机,北京松源华兴科技发展有限公司;LC-10F 液相色谱仪,天津博纳艾杰尔科技有限公司.

1.3 试验方法

1.3.1 材料的制备

PSI-PHE 纳米载体合成:0.970 6 g 聚琥珀酰亚胺溶解于DMSO,配制一定量的苯丙氨酸和等摩尔量的氢氧化钠水溶液.将苯丙氨酸钠盐溶液缓慢滴加到PSI溶液中剧烈搅拌24 h.加入盐酸,将混合溶液滴加到pH 2.5的柠檬酸缓冲液中析出,形成纳米载体颗粒,离心、清洗、冻干得到PSI-PHE纳米载体备用.其合成途径如图1所示.

FLU@PSI-PHE 纳米颗粒合成:质量比1:1的PSI-PHE纳米载体和咯菌腈溶解于DMSO.在45 mL剧烈搅拌的去离子水中依次加入一定量的盐酸和DMSO混合液,反应0.5 h,离心、清洗、冻干得到FLU@PSI-PHE纳米颗粒.

10 mg 样品进行测定,气体流速为20 mL/min,升温速率为10℃/min.

扫描电子显微镜(Scanning Electron Microscope,SEM)测试:利用扫描电子显微镜观察样品形貌,加速电压为3.0 kV.

1.3.3 材料的性能研究

FLU 标准曲线的建立:称取一定量的咯菌腈,利用乙腈定容于棕色容量瓶,得到1 000 μg/mL的标准母液和一系列浓度梯度为25.0、37.5、50.0、62.5和75.0 μg/mL的标准溶液.采用紫外分光光度计在296 nm波长下测定不同浓度溶液的吸光度,

纳米杀菌剂载药率和包封率的测定:称量10 mg

的 FLU@PSI-PHE 纳米颗粒溶解于 4 mL 乙腈中, 超声、过滤得样品溶液. 以乙腈为参比液, 利用吸光度值和公式(1)、(2)计算纳米杀菌剂的载药率和包封率.

$$\text{载药率}\% = \frac{m_{\text{载药}}}{M_{\text{总}}} \times 100, \quad (1)$$

$$\text{包封率}\% = \frac{m_{\text{载药}}}{M_{\text{投}}} \times 100. \quad (2)$$

式中, $m_{\text{载药}}$ 为纳米载药颗粒中咯菌腈的质量; $M_{\text{总}}$ 为纳米载药颗粒的总质量; $M_{\text{投}}$ 为投入载药体系中咯菌腈的总质量.

蓖麻韧皮部输导试验: 取一定数量的蓖麻, 剥开胚乳, 将子叶浸泡在 pH 5.0 的含 FLU@PSI-PHE 纳米颗粒的缓冲溶液中, 收集前 2 h 的蓖麻韧皮部流出液, 乙腈稀释. 以咯菌腈为对照, 采用高效液相色谱法对韧皮部汁液中的咯菌腈进行定量分析. 检测波长 296 nm, 流动相 $V(\text{甲醇}):V(\text{水})=93:7$, 流速 1 mL/min, 进样量 10 μL .

菌丝生长速率法测定尖孢镰刀菌古巴专化型菌丝活性试验: 配制 100 mg/L 的 FLU@PSI-PHE 溶液和 FLU 的 DMSO 溶液. 将 FLU@PSI-PHE 溶液和 FLU 溶液分别与马铃薯葡萄糖琼脂培养基混合制成等体积系列浓度平板培养基, 空白的马铃薯葡萄糖琼脂培养基作对照, 每个处理重复 5 次. 平板接菌后置于 28 $^{\circ}\text{C}$ 恒温培养箱中培养 10~12 d, 采用十字交叉法垂直测量菌落直径.

2 结果与分析

2.1 材料结构的表征分析

2.1.1 红外光谱分析

图 2(a) 为 PSI、PSI-PHE、FLU 和 FLU@PSI-

PHE 的红外光谱图. 对于 PSI, 峰值为 1 790 cm^{-1} 归属于两个相邻羰基的耦合作用; 峰值为 1 720 cm^{-1} 是由五元环内 C=O 键伸缩振动产生的, 说明 PSI 高分子有一个五元环酰亚胺结构的存在^[12-13]. 与 PSI 对比, PSI-PHE 纳米载体在 3 600~3 400 cm^{-1} 波数范围内和在 1 400 cm^{-1} 处分别有较宽和峰形尖锐的吸收峰, 对应于苯丙氨酸中 O-H 键的伸缩振动和面内变形振动^[14]; 在 3 400~3 000 cm^{-1} 之间和 1 650 cm^{-1} 处的吸收峰分别由反应新形成的酰胺键中 N-H 键和 C=O 键伸缩振动所产生; 1 540 cm^{-1} 峰归因于新形成的酰胺键中 N-H 键弯曲振动与 C-N 键伸缩振动的耦合作用, 表明 PSI-PHE 纳米载体被成功制备^[15].

对比 FLU@PSI-PHE 纳米颗粒和 FLU 的红外光谱, 发现两者在 2 220、3 140 和 3 290 cm^{-1} 处都有特征吸收峰出现, 分别归属于 C \equiv N 键、C-H 键和 N-H 键的伸缩振动^[10]. 在 FLU@PSI-PHE 光谱中, 特征吸收峰 1 650 cm^{-1} 强度变小是因 FLU 和 PSI-PHE 之间的相互作用^[10], 说明药物 FLU 被 PSI-PHE 纳米载体成功负载.

2.1.2 X 射线衍射分析

图 2(b) 为 FLU、PSI-PHE 和 FLU@PSI-PHE 的 XRD 图. 对于 FLU, 在 2θ 为 25.8 $^{\circ}$ 左右有一个尖锐的特征峰; 在 14.8 $^{\circ}$ 和 19.9 $^{\circ}$ 附近出现了衍射峰. 对比 PSI-PHE 和 FLU@PSI-PHE 的 XRD 图谱, 两者峰形大致相同, 说明 FLU@PSI-PHE 纳米颗粒和 PSI-PHE 纳米载体的晶型基本一致. 但主要区别为 FLU@PSI-PHE 在 14.8、19.9 和 25.8 $^{\circ}$ 处有衍射峰, 对应 FLU 的特征衍射峰, 表明 PSI-PHE 纳米载体负载原药 FLU 后, 未改变 PSI-PHE 纳米载体结构.

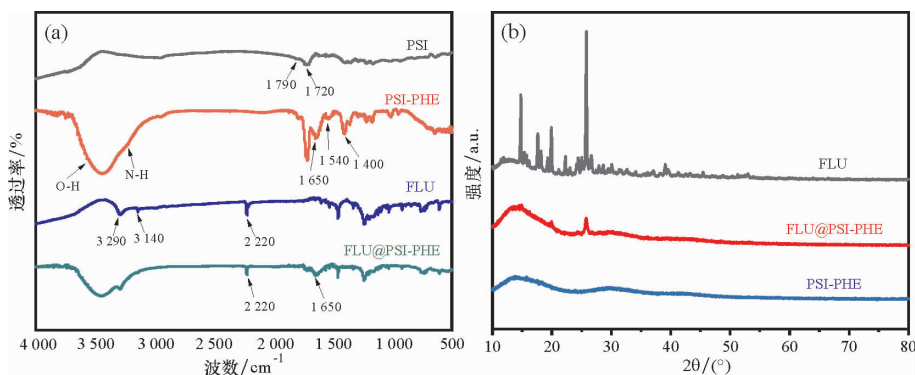


图 2 PSI、PSI-PHE、FLU、FLU@PSI-PHE 的红外光谱图(a); FLU、PSI-PHE、FLU@PSI-PHE 的 XRD 图(b)

2.1.3 水合粒径、Zeta 电势及 SEM 分析

图 3(a)、(b) 分别为 PSI-PHE 和 FLU@PSI-PHE 的粒径与 Zeta 电势图. PSI-PHE 纳米载体和

FLU@PSI-PHE 纳米颗粒的水合粒径分别为 295 nm 和 531 nm. PSI-PHE 纳米载体和 FLU@PSI-PHE 纳米颗粒的 Zeta 电势分别为 -21.2 mV 和 -27 mV,

两者在水中均带负电荷. FLU@ PSI-PHE 纳米颗粒的 Zeta 电势绝对值比纳米载体大, 带电粒子排斥力较大, 不易聚集^[16], 表明 FLU@ PSI-PHE 纳米

颗粒在水中具有更强的稳定性. 由图 3(c) FLU@ PSI-PHE 的 SEM 可知, FLU@ PSI-PHE 纳米颗粒表面褶皱, 可增大其载药接触面积.

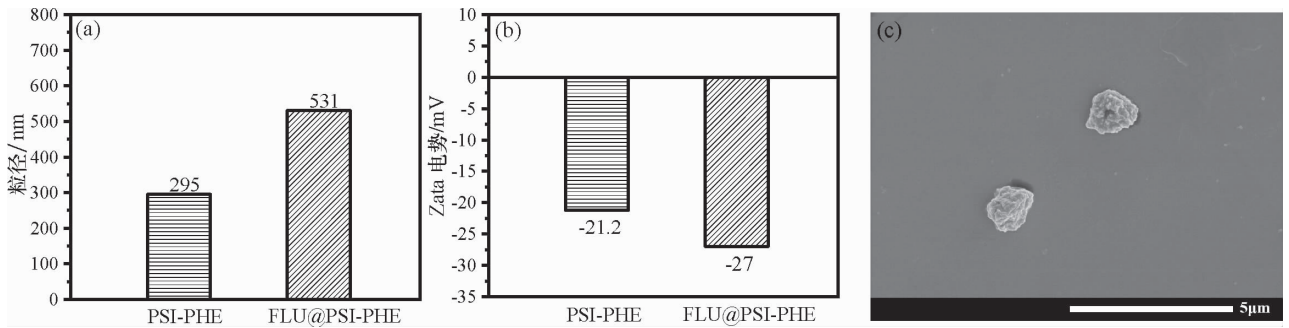


图3 PSI-PHE 和 FLU@PSI-PHE 的粒径图(a); PSI-PHE 和 FLU@PSI-PHE 的 Zeta 电势图(b); FLU@PSI-PHE 的 SEM 图(c)

2.1.4 热重分析

图 4(a)、(b)和(c)分别为 FLU、PSI-PHE 和 FLU@ PSI-PHE 的 TG 和 DTG 图谱. 由图 4 中 TGA 曲线可知, FLU 在 170 ~ 308 ℃ 发生失重, 失重率为 98.37%. PSI-PHE 纳米载体失重分为三个阶段, 第一阶段从 30 ~ 100 ℃, 失重率为 7.01%, 为表面附着水分子失重引起; 第二阶段从 100 ~ 330 ℃, 失重率为 8.59%, 可能为 PSI 主链五元环断裂分解的影响^[10]. 第三阶段为 330 ~ 800 ℃, 失重率为 49.21%, 为 PSI-PHE 中的酰胺键断开, 高分子聚合物支链断裂分解失重造成. FLU@ PSI-PHE 热解

曲线分为 4 个阶段, 其中 177 ~ 280 ℃ 失重率最高, 达 60.79%, 可能是因为 FLU 受热分解造成的^[10]. 后 2 个阶段的失重率为 6.17% 和 22.92%, 分别来自 PSI 主链五元环的断裂和支链酰胺键的断裂失重. 由 DTG 曲线可知, FLU 和 PSI-PHE 的失重率最高温度分别为 303 ℃ 和 384 ℃, 而 FLU@ PSI-PHE 失重率最高温度为 252 ℃. 可能是因为载药率 45.96% 的 FLU@ PSI-PHE (见 2.2.1), 同时受 170 ℃ 时 FLU 分解温度和 304 ℃ 左右 PSI-PHE 主链分解温度的影响^[10], 导致 FLU@ PSI-PHE 纳米颗粒最大失重率的温度提前.

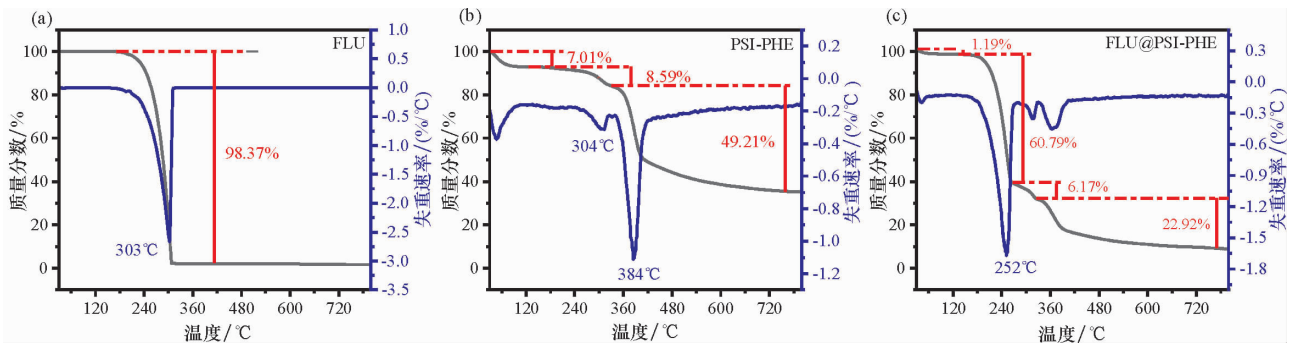


图4 FLU(a)、PSI-PHE(b)和 FLU@PSI-PHE(c)的热重图谱

2.2 纳米杀菌剂性能分析

2.2.1 纳米杀菌剂载药率和包封率分析

图 5 为咯菌腈溶液在 296 nm 波长下的标准曲线. 以吸光度对浓度进行线性拟合, 所得线性回归方程为 $y = 0.012\ 3x + 0.041\ 6$, $R^2 = 0.998\ 5$, 表明线性关系良好. 采用紫外分光光度法测得样品溶液的吸光度为 0.190, 结合咯菌腈溶液在 296 nm 下的标准曲线, 得到样品溶液的浓度为 48.26 μg/mL. 纳米咯菌腈总质量 $M_{总}$ 为 0.010 5 g, 结合公式(1)计算 FLU@ PSI-PHE 纳米颗粒的载药率为 45.96%. 第 278 页, 共 289 页

结合公式(2)计算 FLU@ PSI-PHE 纳米颗粒的包封率为 65.75%, 说明两亲性苯丙氨酸纳米载体负载咯菌腈分子具备较高的载药率.

2.2.2 输导剂量分析

结合图 6(a)和 6(b)的蓖麻韧皮部试验, 图 6(c)显示 FLU 原药、FLU@ PSI-PHE 和课题组前期制备的 FLU@ PGA 咯菌腈纳米颗粒^[10]在蓖麻韧皮部中咯菌腈含量的检测结果. 如图所示, 对于原药咯菌腈, 在韧皮部汁液中未能检测到咯菌腈, 表明咯菌腈无法自主在植物韧皮部中输导. 前期课题组 Wu 等^[10]制备的 FLU@ PGA 咯菌腈纳米颗粒, 其

韧皮部汁液中咯菌腈含量为 0.1 μg/mL. 对比本试验中 FLU@ PSI-PHE 纳米颗粒, 咯菌腈在蓖麻韧皮部汁液中检测含量为 1.27 μg/mL, 表明 PSI-PHE 纳米载体可携带咯菌腈分子在蓖麻韧皮部中进行输导. 相比于前期 PGA 纳米载体, PSI-PHE 纳米载体在蓖麻韧皮部中的输导剂量提高了 12.7 倍, 表明苯丙氨酸介导的 PSI-PHE 纳米载体在模式植物蓖麻的韧皮部位具有较强的传导能力, 为后期香蕉枯萎病的靶向防治奠定了科学基础.

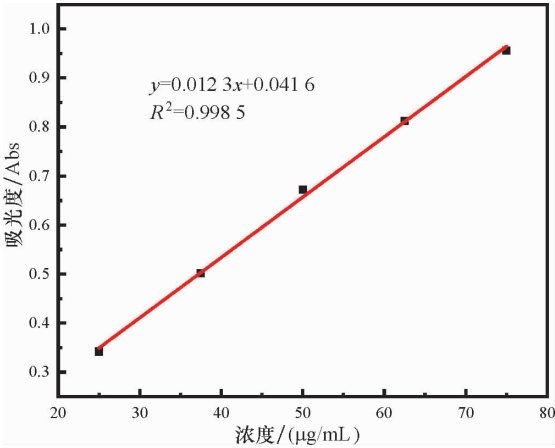


图 5 咯菌腈在 296 nm 波长下的标准曲线

2.2.3 体外抑菌活性分析

图 7 为载药率 45.96% 的 FLU@ PSI-PHE 纳米

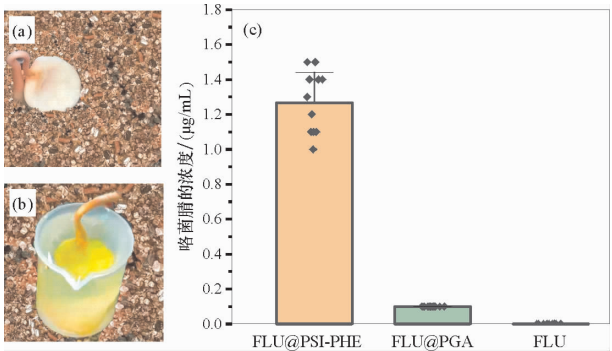


图 6 蓖麻及蓖麻韧皮部输导试验图 (a、b) ;
蓖麻韧皮部汁液所含咯菌腈含量 (c)

颗粒和原药 FLU 对尖孢镰刀菌的体外抗真菌活性对比图. 图 7(b) 结果表明, 在相同药物浓度范围内(0.125 ~ 2 mg/L), FLU@ PSI-PHE 纳米颗粒和原药 FLU 对尖孢镰刀菌都有明显的抑制效果. 当浓度为 0.125、0.25 mg/L 的培养基, FLU@ PSI-PHE 纳米颗粒和原药 FLU 对尖孢镰刀菌的抑菌圈大小基本相当; 浓度为 0.5、1 和 2 mg/L 的培养基, 原药 FLU 抑菌圈直径小于 FLU@ PSI-PHE 纳米颗粒. 因此, FLU@ PSI-PHE 纳米颗粒在较低药物浓度时的抑菌活性与原药 FLU 基本相当, 可能是因为 FLU@ PSI-PHE 纳米颗粒的凸释现象引起低浓度药物早期基本释放完全, 表现出和 FLU 原药活性大致相同^[14].

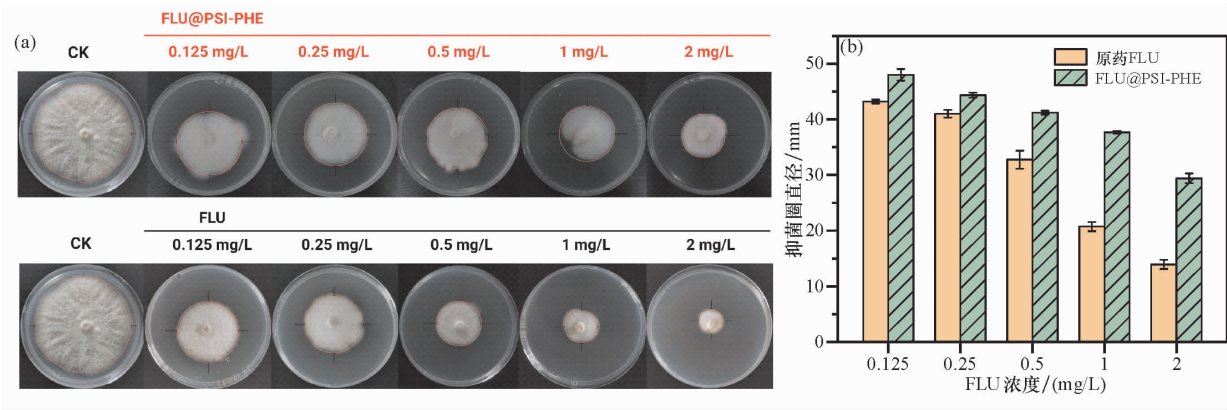


图 7 FLU@ PSI-PHE 和 FLU 对尖孢镰刀菌的体外抗菌活性对比图

3 讨论与结论

苯丙氨酸与聚琥珀酰亚胺高分子进行开环反应, 耦合形成 PSI-PHE 靶向纳米载体, 利用物理方式包覆咯菌腈, 制备了 FLU@ PSI-PHE 纳米颗粒. 通过红外光谱、粒度、热重、Zeta 电势和 X 射线衍射分析, 发现 FLU@ PSI-PHE 纳米颗粒的水合粒径约为 531 nm, 载药率高达 45.96%. 所构建的苯丙氨酸介导的 FLU@ PSI-PHE 纳米杀菌剂在蓖麻韧皮部汁液中的咯菌腈含量为 1.27 μg/mL, 显著

提高了咯菌腈在植物韧皮部的输导效果, 且 FLU@ PSI-PHE 纳米杀菌剂在低剂量时对香蕉枯萎病菌表现出良好的抑制作用. 本研究制备的苯丙氨酸纳米载体可显著增加农药有效成分在植物韧皮部中靶向积累, 实现提高农药利用率的目的.

参考文献:

[1] 李华平, 李云锋, 聂燕芳. 香蕉枯萎病的发生及防控研究现状[J]. 华南农业大学学报, 2019, 40(5): 128-136.
[2] DITA M, BARQUERO M, HECK D, et al. Fusarium wilt of ba-

nana: current knowledge on epidemiology and research needs toward sustainable disease management[J]. *Frontiers in Plant Science*, 2018, 9: 1468.

[3] 吴瀚翔, 陈志彬, 肖春霞, 等. 咯菌腈羧酸衍生物内吸传导性及对香蕉枯萎病的防效测定[J]. *植物保护学报*, 2021, 48(4): 789–797.

[4] DOU T X, SHAO X H, HU C H, et al. Host-induced gene silencing of Foc TR4 ERG6/11 genes exhibits superior resistance to Fusarium wilt of banana[J]. *Plant Biotechnology Journal*, 2020, 18: 11–13.

[5] WANG L, XING M, DI R, et al. Isolation, identification and antifungal activities of *Streptomyces aureovorticillatus* HN6[J]. *Journal of Plant Pathology and Microbiology*, 2015(6): 281.

[6] BUBICI G, KAUSHAL M, PRIGIGALLO M I, et al. Biological control agents against Fusarium wilt of banana[J]. *Frontiers in Microbiology*, 2019, 10: 616.

[7] 茹祥, 曾涛, 莫坤联, 等. 海南吊罗山原始林区抗香蕉枯萎病土壤放线菌的分离及田间防治效果试验[J]. *中国农学通报*, 2012, 28(13): 97–102.

[8] 蒲小明, 林壁润, 沈会芳, 等. 防治香蕉枯萎病胶囊药剂研制与应用[J]. *植物保护*, 2015, 41(1): 185–189.

[9] GHAG S B, SHEKHAWAT U K S, GANAPATHI T R. Fusarium wilt of banana: biology, epidemiology and management[J]. *International Journal of Pest Management*, 2015, 61: 250–263.

[10] WU H X, HU P T, XU Y, et al. Phloem delivery of fludioxonil by plant amino acid transporter-mediated polysuccinimide nanocarriers for controlling Fusarium wilt in banana[J]. *Journal of Agricultural Food and Chemistry*, 2021, 69(9): 2668–2678.

[11] 徐汉虹, 张志祥, 查友贵. 中国植物性农药开发前景[J]. *农药*, 2003, 42(3): 1–10.

[12] CHEN J X, XU L H, HAN J, et al. Synthesis of modified polyaspartic acid and evaluation of its scale inhibition and dispersion capacity[J]. *Desalination*, 2015, 358: 42–48.

[13] YE H J C, YANG H H, HSU Y T, et al. Synthesis and characteristics of biodegradable and temperature responsive polymeric micelles based on poly (aspartic acid)-g-poly (N-isopropylacrylamide-co-N, N-dimethylacrylamide) [J]. *Colloids and Surfaces A: Physicochemical and Engineering Aspects*, 2013, 421: 1–8.

[14] ZHAO M, ZHOU H J, HAO L, et al. A high-efficient nano pesticide-fertilizer combination fabricated by amino acid modified cellulose based carriers[J]. *Pest Management Science*, 2022, 78: 506–520.

[15] YE X, LIU M C, ZHAO N, et al. Targeted delivery of emamectin benzoate by functionalized polysuccinimide nanoparticles for the flowering cabbage and controlling *Plutella xylostella* [J]. *Pest Management Science*, 2022, 78: 758–776.

[16] 宋璇, 秦迎丹, 孙晨, 等. 不同 Zeta 电位纳米脂蛋白载体的物理稳定性评价[J]. *中国医院药学杂志*, 2023, 43(12): 1342–1346.

【责任编辑 林江娇】

(上接第 25 页)

[26] CHUACHAROEN T, SABLIOV C M. Stability and controlled release of lutein loaded in zein nanoparticles with and without lecithin and pluronic F127 surfactants[J]. *Colloids and Surfaces A: Physicochemical and Engineering Aspects*, 2016, 503: 11–18.

[27] HUANG X, GE X, WANG Y. Single-layer and double-layer zein-gum arabic nanoencapsulations: Preparation, structural characterization, thermal properties, and controlled release in the gastrointestinal tract[J]. *Journal of Food Science*, 2022, 87(10): 4580–4595.

[28] FAN H, DU C, DING L, et al. Effects of nitric oxide on the germination of cucumber seeds and antioxidant enzymes under salinity stress[J]. *Acta Physiologiae Plantarum*, 2013, 35(9): 2707–2719.

[29] DAWOOD M G. *Stimulating Plant Tolerance Against Abiotic Stress Through Seed Priming* [M]. Singapore: Springer Singapore, 2018.

[30] 范翠枝, 吴馨怡, 关欣, 等. 油菜素内酯浸种对盐胁迫番茄种子萌发的影响及其生理机制[J]. *生态学报*, 2021, 41(5): 1857–1867.

[31] AHMAD P, HASHEM A, ABD-ALLAH E F, et al. Role of Trichoderma harzianum in mitigating NaCl stress in Indian mustard (Brassica juncea L) through antioxidative defense system[J]. *Frontiers in Plant Science*, 2015, 6: 868.

[32] SHU H, NI W, GUO S, et al. Root-applied brassinolide can alleviate the NaCl injuries on cotton[J]. *Acta Physiologiae Plantarum*, 2015, 37: 1–11.

[33] 黄珂. NaCl 胁迫下湿地植物的形态变化及其对生理应激的影响[J]. *山东农业大学学报(自然科学版)*, 2023, 54(3): 373–377.

[34] 施雨. 褪黑素对盐胁迫下紫花苜蓿种子萌发及幼苗生长生理特性的影响[D]. 扬州: 扬州大学, 2022.

[35] NOLAN T M, HSU C W, ZHANG J, et al. Brassinosteroid gene regulatory networks at cellular resolution in the Arabidopsis root [J]. *Science*, 2023, 379(6639): 1314–1326.

[36] MU D, FENG N, ZHENG D, et al. Physiological mechanism of exogenous brassinolide alleviating salt stress injury in rice seedlings [J]. *Scientific Reports*, 2022, 12(1): 20439.

【责任编辑 林江娇】

证书号第6215149号



发明专利证书

发明名称：一种酶响应纳米农药及制备方法与应用

发明人：贾金亮;赵宁;徐汉虹;朱丽;何亮亨

专利号：ZL 2022 1 1160312.X

专利申请日：2022年09月22日

专利权人：华南农业大学

地址：510642 广东省广州市天河区五山路483号

授权公告日：2023年08月08日

授权公告号：CN 115530163 B

国家知识产权局依照中华人民共和国专利法进行审查，决定授予专利权，颁发发明专利证书并在专利登记簿上予以登记。专利权自授权公告之日起生效。专利权期限为二十年，自申请日起算。

专利证书记载专利权登记时的法律状况。专利权的转移、质押、无效、终止、恢复和专利权人的姓名或名称、国籍、地址变更等事项记载在专利登记簿上。



局长
申长雨

申长雨



证书号 第6215149号

专利权人应当依照专利法及其实施细则规定缴纳年费。本专利的年费应当在每年09月22日前缴纳。
未按照规定缴纳年费的，专利权自应当缴纳年费期满之日起终止。

申请日时本专利记载的申请人、发明人信息如下：

申请人：

华南农业大学

发明人：

贾金亮;赵宁;徐汉虹;朱丽;何亮亨

证书号第 4408730 号



发明专利证书

发明名称：一种植物韧皮部输导的纳米农药的制备方法及应用

发明人：贾金亮;胡鹏通;吴瀚翔;徐汉虹;朱丽;庄秀涵

专利号：ZL 2020 1 0455763.0

专利申请日：2020 年 05 月 26 日

专利权人：华南农业大学

地址：510642 广东省广州市天河区五山路 483 号

授权公告日：2021 年 05 月 07 日

授权公告号：CN 111567541 B

国家知识产权局依照中华人民共和国专利法进行审查，决定授予专利权，颁发发明专利证书并在专利登记簿上予以登记。专利权自授权公告之日起生效。专利权期限为二十年，自申请日起算。

专利证书记载专利权登记时的法律状况。专利权的转移、质押、无效、终止、恢复和专利权人的姓名或名称、国籍、地址变更等事项记载在专利登记簿上。



局长
申长雨

申长雨



第 1 页 (共 2 页)

其他第 283 页, 共 289 页

证书号第 4408730 号



专利权人应当依照专利法及其实施细则规定缴纳年费。本专利的年费应当在每年 05 月 26 日前缴纳。未按照规定缴纳年费的，专利权自应当缴纳年费期满之日起终止。

申请日时本专利记载的申请人、发明人信息如下：

申请人：

华南农业大学

发明人：

贾金亮；胡鹏通；吴瀚翔；徐汉虹；朱丽；庄秀涵



荣誉证书

黄炜柔、黄怡、李桐莹、黄盈 同学：

在第十二届“华港杯”广东大学生材料创新大赛总决赛中，荣获

三等奖

特发此证，以资鼓励。

作品名称：苯丙氨酸纳米杀菌剂对香蕉枯萎病的靶向治疗

指导教师：贾金亮、朱丽

承办单位：

暨南大学化学与材料学院

化学与材料学院

合作单位：

广东省本科高校材料类

专业教学指导委员会

（南方科技大学代章）

主办单位：

广东省材料研究学会

二〇二三年三月



荣誉证书

赵宇、刘美晨、何亮亨、邢文杰、刘文裕同学：

在第十二届“华港杯”广东大学生材料创新大赛分赛区决赛中，荣获

三等奖

特发此证，以资鼓励。

作品名称：酶控木质素基纳米阿维菌素的制备及其应用

指导教师：贾金亮

承办单位

暨南大学化学与材料学院

化学与材料学院

主办单位

广东省材料研究学会

二〇二三年三月



荣誉证书

赖静云、黄斯静、张纯仪、徐梦如、张燕恒同学

在广东第十届大学生材料创新大赛中，荣获总决赛

三等奖

特发此证，以资鼓励。

作品名：水基壳寡糖/铜纳米载体

指导老师：贾金亮

主办单位：
广东省材料研究学会



合作单位：
广东省本科高校材料类专业教学指导委员会

(南方科技大学代章)



承办单位：
广东工业大学材料与能源学院



二〇二〇年十二月二十日



荣誉证书

庄秀涵、张万景、罗倩、汤晓曼、朱国辉同学
在广东第十届大学生材料创新大赛高分子材料分赛区中荣获

三等奖

特发此证，以资鼓励。

作品名：甲维盐纳米悬浮剂的制备及其应用
指导老师：贾金亮

主办单位：
广东省材料研究学会

合作单位：
广东省本科高校材料类专业教学指导委员会
(南方科技大学代章)

承办单位：
广东工业大学材料与能源学院

二〇二〇年十二月十九日

教职工业绩成果报表

姓 名	贾金亮	工 号	30002577	所在单位	材料与化学工程学院		
年 龄	47	职 称	副教授	学 历	博士研究生 毕业	学 位	农学博士学位
岗位类别	专业技术	一级分类	教师	二级分类	教学科研型	岗位级别	专业技术岗 位6级
年度考核结果		2015年：合格； 2016年：合格； 2017年：合格； 2018年：优秀； 2019年：合格； 2020年：合格； 2021年：合格； 2022年：优秀； 2023年：合格； 2024年：合格； 2025年：合格					
		【教学工作业绩】					
		1. 本科生课程（理论课）					
		学年学期	课程名称	是否合上	课程大类	计划学时	
		2007-2008-2	基础化学实验BⅡ	否	必修		
		2007-2008-2	基础化学实验BⅡ	否	必修		
		2007-2008-2	基础化学实验BⅡ	否	必修		
		2007-2008-2	基础化学实验BⅡ	否	必修		
		2007-2008-2	基础化学实验BⅡ	否	必修		
		2008-2009-1	物理化学	否	必修		
		2008-2009-1	物理化学	否	必修		
		2008-2009-1	物理化学	否	必修		
		2008-2009-2	基础化学实验BⅡ	否	必修		
		2008-2009-2	基础化学实验BⅡ	否	必修		
		2008-2009-2	基础化学实验BⅡ	否	必修		
		2008-2009-2	基础化学实验AⅡ	否	必修		
		2009-2010-1	物理化学	否	必修		
		2009-2010-1	物理化学	否	必修		
		2009-2010-1	基础化学实验AⅢ	否	必修		
		2009-2010-1	基础化学实验AⅢ	否	必修		
		2009-2010-2	农药学概论	否	限选		
		2009-2010-2	基础化学实验Ⅱ	否	必修		
		2009-2010-2	基础化学实验Ⅱ	否	必修		
		2009-2010-2	基础化学实验Ⅱ	否	实践		